RIKEN Accelerator Progress Report

2005

vol. 39

BOOK & CD-ROM

独立行政法人理化学研究所
RIKEN

CONTENTS

2. Atomic and Solid-State Physics

Frontispiece

Progress in RIBF Accelerators

A Universal slow RI-beam facility (SLOWRI): Development and first results

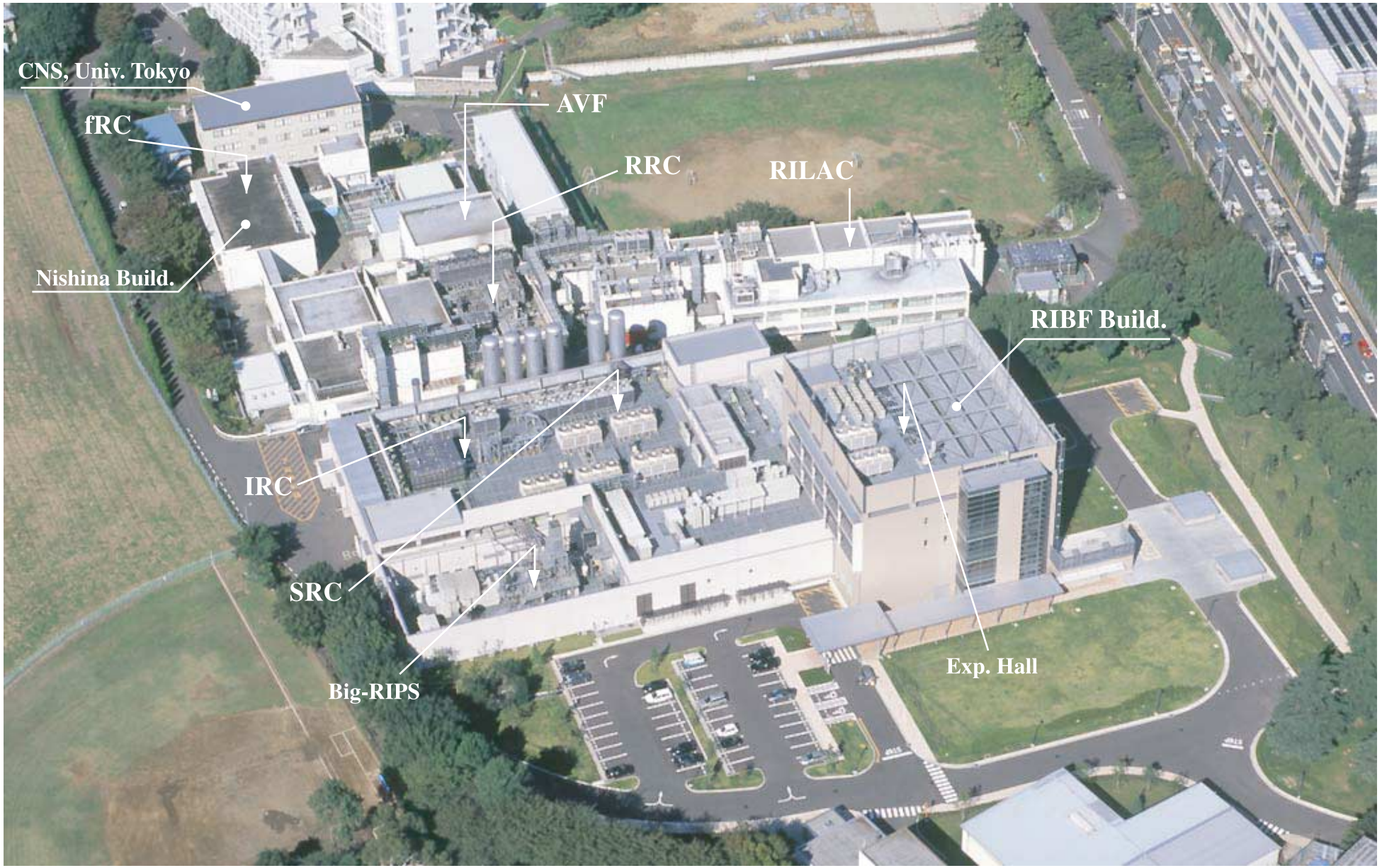

Fig. 1. Bird's-eye view of RIBF (RI-Beam Factory) and RARF (RIKEN Accelerator Research Facility) buildings. The construction of the RIBF building was completed in May, 2005. The arrows indicate the positions of the accelerators (RILAC, AVF, RRC, fRC, IRC, and SRC) and the Big-RIPS.

Fig. 2. SRC (Superconducting Ring Cyclotron).
K-value : 2,500 MeV
R_{inj} / R_{ext} : 3.56 m / 5.36 m
Total weight of magnets : 8,100 t
RF frequency : 18 - 38 MHz
No. of RF resonators : 4 + 1 (FT)
No. of sector magnets : 6
Max. magnetic field : 3.8 T
Harmonics : 6

Fig. 3. IRC (Intermediate-stage Ring Cyclotron).
K-value : 980 MeV
No. of sector magnets : 4
R_{inj} / R_{ext} : 2.77 m / 4.15 m
Max. magnetic field : 1.9 T
Total weight of magnets : 2,720 t
Harmonics : 7
RF frequency : 18 - 38 MHz
No. of RF resonators : 2 + 1 (FT)

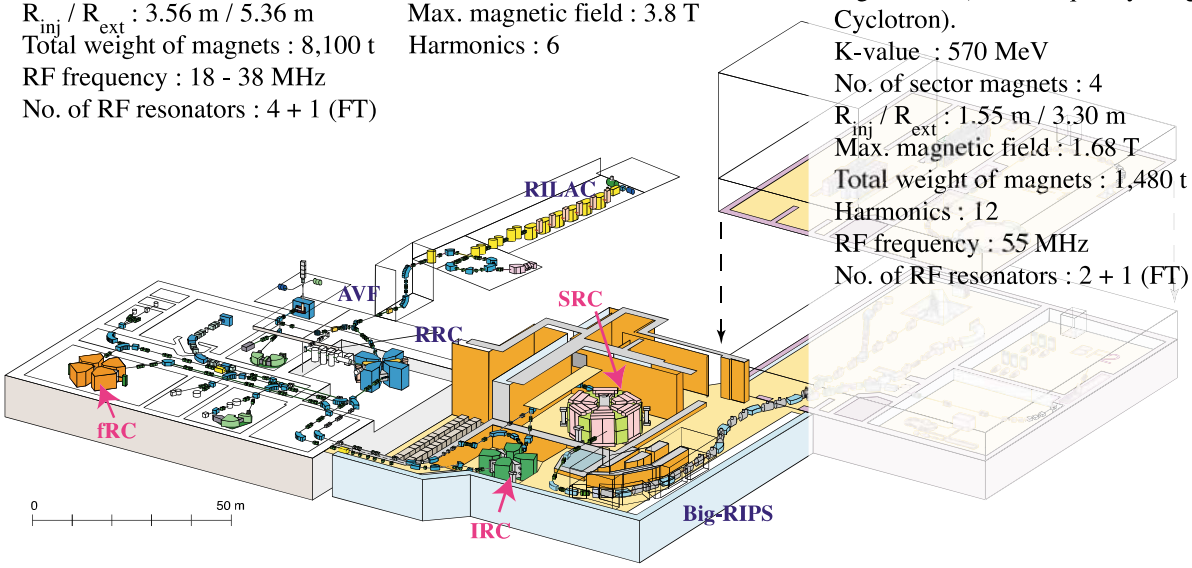

Fig. 5. Layout of three new cyclotrons.

Fig. 4. fRC (fixed-frequency Ring Cyclotron).
K-value : 570 MeV
No. of sector magnets : 4
R_{inj} / R_{ext} : 1.55 m / 3.30 m
Max. magnetic field : 1.68 T
Total weight of magnets : 1,480 t
Harmonics : 12
RF frequency : 55 MHz
No. of RF resonators : 2 + 1 (FT)

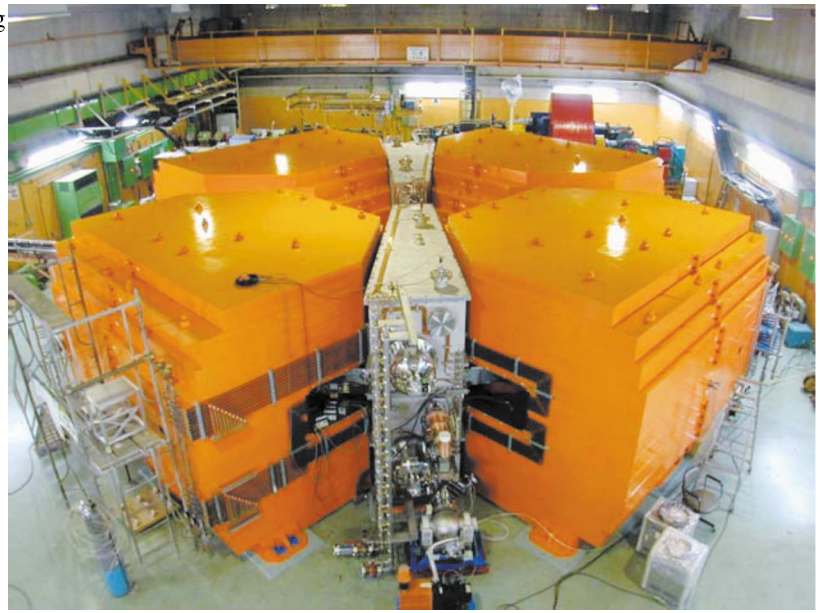

A universal slow RI-beam facility (SLOWRI) Development and first results (pp. 41, 157)

The prototype SLOWRI facility

A Universal slow radioactive ion beam facility (SLOWRI) is planned as one of the principal facilities of RIBF. A prototype setup for SLOWRI which is based on the rf ion guide technique has been tested at the projectile fragment separator RIPS obtaining an overall efficiency of ≈5% for a ≈100A Mev ^{8}Li ion beam. Laser spectroscopy of radioactive Be isotopes has also been performed.

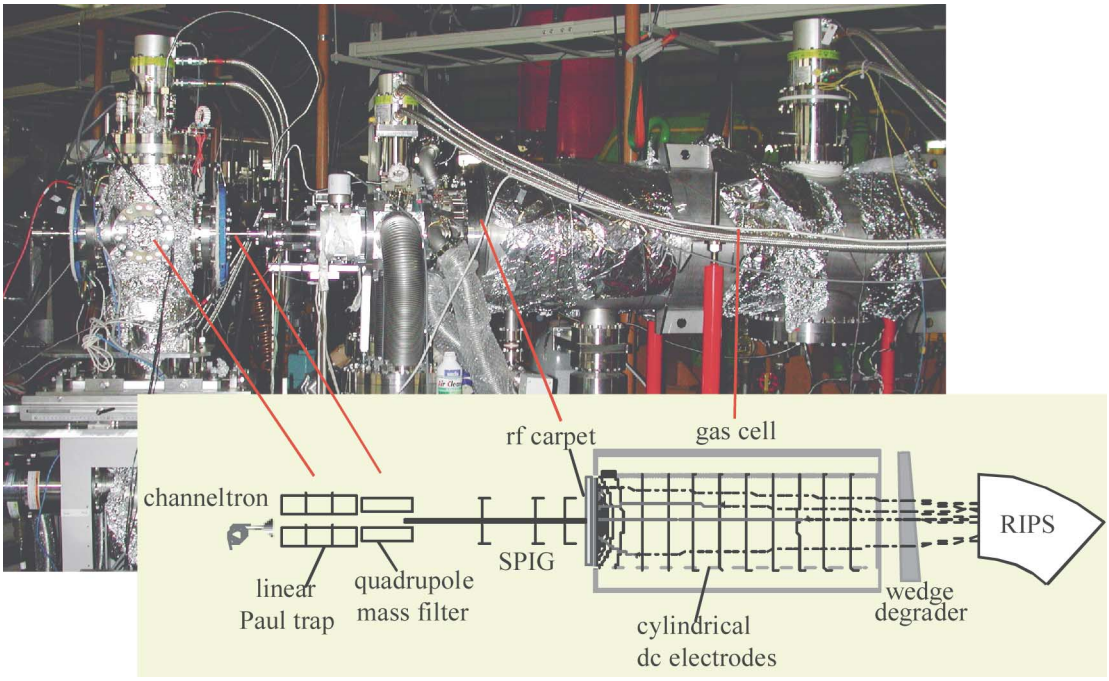

Fig. 1. High energy radioactive Be isotope beam from RIPS are decelerated and cooled in the gas catcher cell. The thermalized ions are accumulated and extracted into vacuum by combined dc and rf electric fields. The extracted slow ions are transported to an ion trap via a rf sixpole ion beam guide (SPIG) and a quadrupole mass filter.

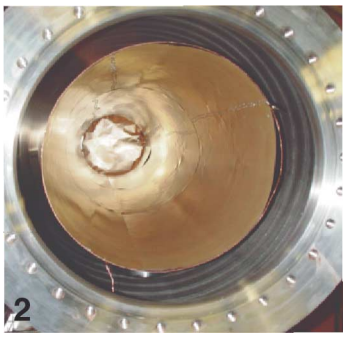

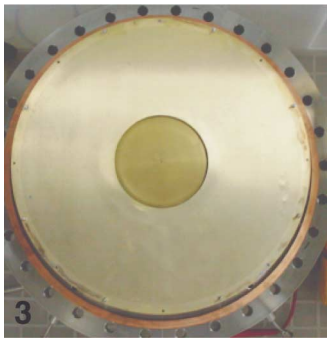

Fig. 2. The cylindrical dc electrode tube viewed from the bottom of the gas cell.

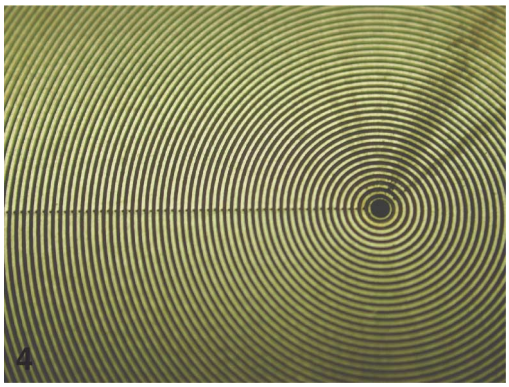

Fig. 3., 4. The rf carpet electrode assembly and its central part. Rf voltages are applied to alternate ring electrodes to form an ion-barrier field on the carpet which keeps the ions away from the surface and a dc field which due to different dc offset voltages on the electrodes pushes the ions towards the exit nozzle at the center.

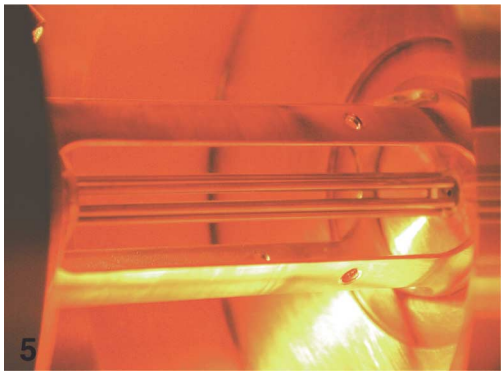

Fig. 5. The SPIG device located right behind the nozzle of the rf carpet which moves the ions through differential pumping sections.

Laser Spectroscopy of $^{7}Be^{+}$ and $^{10}Be^{+}$ ions trapped in an on-line ion trap

The first physics experiment at the prototype SLOWRI was atomic spectroscopy of trapped Be isotopes with the goal of measuring the isotope shifts and hyperfine structures. In the year 2005, $^{10}Be^{+}$ and $^{7}Be^{+}$ ions were trapped and their optical transition wavelengths were determined, for the first time, with an accuracy of 3×10^{-8}.

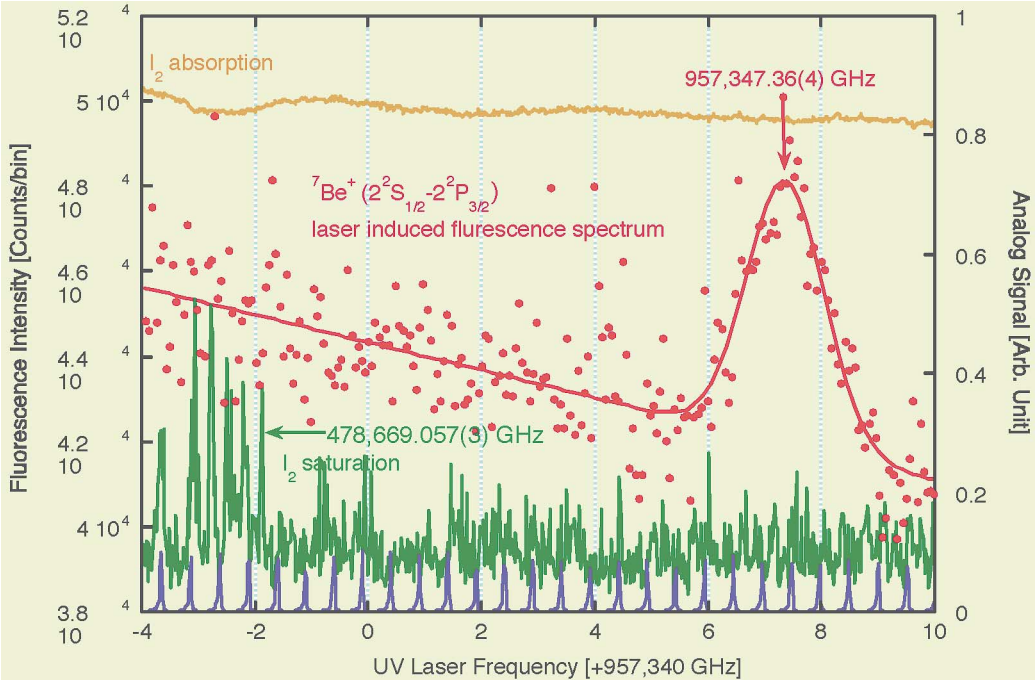

Fig. 6. The resonant frequency of buffer gas cooled $^{7}Be^{+}$ ions in an ion trap was determined to 957,347.36(4) GHz (preliminary). The absolute frequency was calibrated using a 250.7 MHz reference cavity (blue signal) and the saturation absorption of iodine molecules (green line).

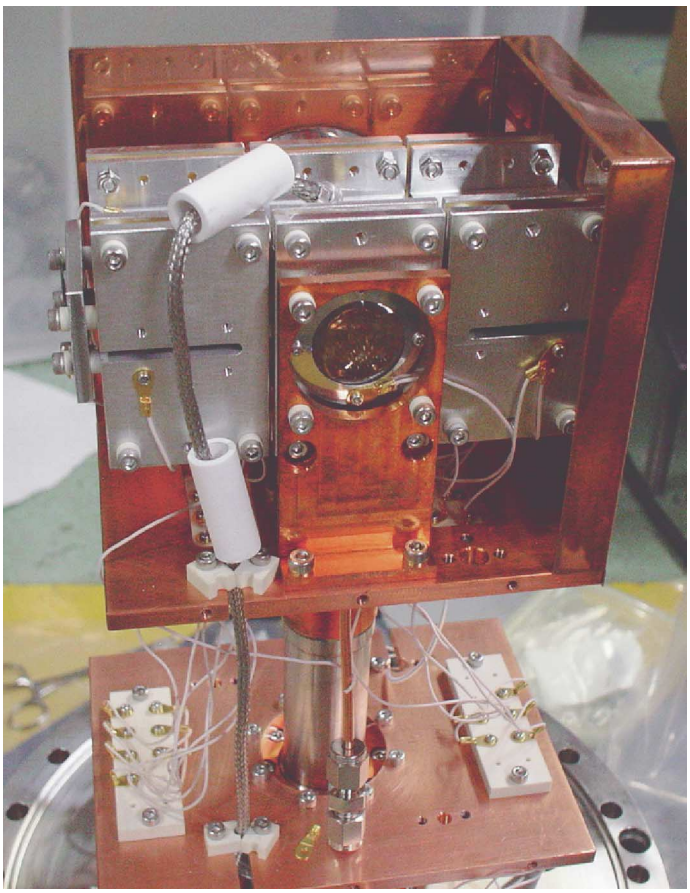

Fig.7. The linear rf ion trap used for laser spectroscopy. The trap electrodes are mounted on a cryogenic cooling head. Heat shieldings of the first stage and parts of the second stage were removed in the photograph. The hyperbolic quadrupole electrodes are segmented into three sections to form an axial trapping field.

I. PREFACE

This issue of RIKEN Accelerator Progress Report reports on progress of accelerator-based research activities in RIKEN Accelerator Research Facility (RARF) up to October 2005. The research programs involve a variety of fields such as experimental and theoretical nuclear physics, nuclear chemistry, radiation biology, atomic physics, condensed matter physics, plant mutation, material characterization, application to space science, accelerator physics and engineering, laser technology, and computational technology in terms of accelerator or radiation application. These activities involved a few hundred researchers from domestic and foreign institutions together with laboratories and Centers in RIKEN.

Major research activities of the RARF are based on the heavy-ion accelerator complex consisting of the $K = 540$ MeV RIKEN Ring Cyclotron (RRC), the energy variable heavy-ion linear accelerator (RILAC), and the $K = 70$ MeV azimuthally varying field (AVF) cyclotron. Heavy-ion beams of a variety of elements with energies ranging from a few A MeV to 135A MeV are provided. Vector and tensor polarized deuterons are also available. The three accelerators have been used in various configurations. The RRC operates either with the AVF or the RILAC as the injector. The AVF has been providing beams of ions of mass numbers up to 60, whereas the RILAC can accelerate heavier ions. An energy booster called CSM (Charge State Multiplier) installed in collaboration with CNS, the University of Tokyo, is used to raise the maximum beam energy from the RILAC. This enabled to deliver high-intensity beams of intermediate mass elements such as Kr up to 64A MeV from RRC. In addition, RILAC and RRC can be operated separately, when the AVF is used to inject ions to the RRC. This allows for long runs with RILAC beams like the experiment of super-heavy element search. Two thirds of the RRC research beam time is used for nuclear physics and nuclear astrophysics, and remaining one third is used for atomic physics, material science, nuclear chemistry, radiation biology and others. The major part of the nuclear physics research was performed with fast RI (Radioactive Isotope) beams provided by the fragment separator RIPS. The AVF beam time was used also for fields other than nuclear physics.

The RI Beam Factory (RIBF) project is to provide wider variety of RI beams with higher intensities. Its first stage includes construction of three cyclotrons, fRC, IRC and SRC, which accelerates ions up to uranium to 350 A MeV, and a large-acceptance superconducting two-stage in-flight RI-beam separator called BigRIPS. Commissioning will be in the year 2006. A highlight of the RIBF construction this year is the completion of the superconducting sector magnets of the SRC. Exciting the magnets with the designed maximum-current has been achieved.

Many international collaborations are performed. Among them are two large-size collaboration programs using overseas accelerator facilities: one is the muon science project at ISIS in collaboration with the Rutherford-Appleton Laboratory (RAL), and the other is the spin physics program at RHIC in collaboration with the Brookhaven National Laboratory (BNL). The pulsed muon-beam facility at ISIS has been operating steadily. At BNL, the RHIC spin project achieved the first mile stone by observing the neutral-pion production asymmetry with use of 3.8/pb of the data taken from January to June of 2005. The data of polarized proton collisions were transferred online to Wako to be analyzed in the PHENIX Computer Center in Japan, which is a part of RIKEN Super Combined Cluster. Although the results are still preliminary, the model of large gluon polarization is seemingly denied. We have collaborated with the CNS for improving the AVF cyclotron, and operating a CNS-built ECR ion-source and the low-energy RI beam separator (CRIB) to use the low-energy beam from the AVF. A Wien filter system attached to the CRIB improved the purity of secondary beams. The CNS installed a particle analyzer for high resolution studies with the beams from the AVF. The resolution of 80 keV (FWHM) was achieved for the ^{28}Si(α,^{6}He)^{26}Si reaction.

Highlights of the year for the research at the accelerator complex of RARF are as follows. (1) The second event indicating the production of the isotope ^{278}113 has been observed. (2) In-beam γ- and particle-spectroscopy has been performed for various proton- or neutron-rich nuclei, such as ^{6}He, ^{14}Be, ^{19}C, ^{20,27,28}Ne, ^{30,31}Na, ^{33,34}Mg, ^{34}Si and ^{60,62}Cr excited by Coulomb excitation, proton- and α-inelastic scattering, neutron removal reactions, and nucleon transfer reactions. Many new levels have been identified, and measured transition strengths have revealed new feature of nuclear structure. (3) Reactions involved in stellar burning processes have been studied either indirectly by the Coulomb dissociation method or directly with the low-energy RI beams from the CRIB. The ^{8}Li(α,γ)^{11}B reaction was studied down to the Gamow energy of around 0.5 MeV by using low energy ^{8}Li beams. (4) The nuclear moment study in the neutron-rich sd-shell region has been continued. In this year the electric quadrupole moment of ^{32}Al has been de-

termined. (5) Coulomb dissociation of the hallo nuclei ^{11}Li has been studied in detail. Low-energy behavior of the dipole strength function in ^{11}Li was established. (6) A pilot device for a slow RI-beam facility (SLOWRI) using an rf ion guide has enabled laser spectroscopy of $^{10}Be^{+}$ ions in an on-line trap for the first time. (7) Importance of indirect action of heavy-ion irradiation in killing V79 cells was identified at the very high LET of 2106 KeV/μm. Other related research activities are: Three nucleon system with strangeness $S = -1$ has been found and named as $S^0(3115)$ as a candidate of deeply bound kaonic system, K^-pnn with the binding energy about 200 MeV. An electron plasma in a quadrupole magnetic field has been compressed for the first time, which provides a unique scheme to synthesize a well-collimated spin-polarized antihydrogen beam for the CPT symmetry test.

Construction of the RIBF has been going well. The sector magnets and rf resonators for the fRC have been assembled at the factory. The magnetic spectrometer SMART has been decommissioned to use its site for installing the fRC. The power tests of the rf systems for the IRC are being carried out. Assembling of the superconducting sector magnets for the SRC has completed in summer. As mentioned earlier, we succeeded in cooling-down and exciting the magnets at 3.75 T with the maximum currents of 5,000 A and 3,000 A for the main and trim coils, respectively. The R&D's on the production of uranium ions, a candidate of the ions used for the first beam, have been carried out. At present 16+ ions with more than 2 particle-μA are extracted from the 18 GHz ECR source.

The construction of the RI-beam separator BigRIPS and the follwing RI-beam delivery line is in progress for their completion in early 2007. The magnets of the BigRIPS are installed, and the superconducting quadrupoles in the first stage have been cooled down to test the cryogenic plant. Beam line components such as focal plane chambers, high-power production target and high-power beam dump have also been fabricated. The RI-beam delivery line works as a spectrometer for particled emitted at around zero degree from secondary reactions. The magnets for the beam line are under fabrication in the same design as those of BigRIPS.

For experimental installation of RIBF, various research and developments are being performed. The feasibility studies of a novel experimental technique for e-RI scattering, SCRIT (Self-Confining Radioactive Ion Target), are underway at the electron storage ring KSR of Kyoto University. Trapping of externally injected ions on the electron beam has been confirmed. Conceptual design of an isochronous ring for mass measurements of short-lived and rarely-produced nuclei is in progress. Elements of the heavy-ion synclotron TARNII has been transferred to RIKEN from KEK. They will be used for the injection line connecting the BigRIPS and the ring. Detector developments for a large acceptance spectrometer (SAMURAI) have progressed together with the spectrometer design. Design of a high-resolution spectrometer (SHARAQ) and its dispersion-matched beam line has started. For creation of highly polarized RI beams using primary beams from IRC delivered to the RIPS, developments of a new system using the atomic beam method are underway.

This year, the organization structure for the accelerator-based research has been changed. The former Cyclotron Center, the Experimental Equipment Sub-Group of the Accelerator-based Research Group and RIBF Project Group have been unified, and a new organization, "Accelerator Research Program" in the Frontier Research System, has been established. Together with related laboratories in the Discovery Research Institute, a new Center covering the entire accelerator-based research activities will be created in the year 2006.

T. Motobayashi
Chief Scientist
Heavy Ion Nuclear Physics Laboratory

RILAC operation

E. Ikezawa, M. Kase, O. Kamigaito, T. Nakagawa, N. Sakamoto, H. Okuno, N. Inabe, M. Wakasugi, N. Fukunishi, M. Kobayashi-Komiyama, M. Kidera, Y. Higurashi, H. Ryuto, S. Kohara, M. Fujimaki, M. Nagase, T. Kageyama, S. Yokouchi, A. Yoneda, T. Aihara,* T. Ohki,* H. Yamauchi,* A. Uchiyama,* K. Oyamada,* R. Koyama,* A. Goto, and Y. Yano

Throughout this reporting period, RILAC has been in steady operation and has supplied various ion beams for various experiments. Table 1 shows the statistics for the RILAC operation from January 1 through December 31, 2005. We reduced planned maintenance, and carried out experiments in RILAC in August 2005. Therefore, compared with that one year ago, the operation time of RILAC increased by approximately 24%. The percentage of beam service time used by the RIKEN Ring Cyclotron (RRC) was approximately 35% of the total RILAC beam service time. ^{4}He, ^{40}Ar, ^{58}Fe, ^{58}Ni, ^{70}Zn, and ^{131}Xe ions accelerated by RILAC were injected into RRC.

Table 2 shows a summary of the beam service time of the RILAC standalone allotted to the search for the heaviest elements, and to the study of radiation chemistry, accelerator mass spectrometry, and instrumentation.

Research experiments on the heaviest elements have been carried out with a gas-filled recoil isotope separator (GARIS) at the e3 beam line of RILAC since 2002. This year, the experiments were carried out for 4 days in January, 31 days from March through April, 3 days in May, 21 days in August, 46 days from September through October, and 23 days from November through December. More than 1 pμA of the 5 MeV/u ^{70}Zn beam was supplied to the experiments. The total beam service time for the experiments was 2671 hours. As a result, a convincing candidate event for the isotope of the 113th element was observed for the second time on April 2, 2005. In 2006, the experiment will be carried out intensively at RILAC.

Table 3 shows the statistics for the operation time on which RILAC ion beams were delivered using the RFQ linac with an 18 GHz ECR ion source (18G-ECRIS) and a superconducting ECR ion source (SC-ECRIS). The percentages of the operation time used by 18G-ECRIS and SC-ECRIS were approximately 80% and 20% of the total operation time, respectively. The ion beams of 7 elements were used in the various experiments and beam acceleration tests.

For the RIBF project, the production of uranium ions using the 18G-ECRIS began at an ion source room of RILAC on October 31, 2005. We tested the production of uranium ions using the slow supply of UF_6 gas from an airtight container owing to vapor pressure at room temperature. Uranium ion beams, such U^{21+} of 13 eμA intensity at an rf power of 400 W, were obtained for the first time in Japan. Its acceleration test with RILAC and RRC will start in spring 2006. We already received official licenses of the uranium handling and acceleration in April 2004 and January 2005, respectively.

We experienced the following machine problems during this reporting period.

(1) Part of the chamber wall (6 mm-thick stainless steel) of the 90° bending magnet (DMe1) had a

Table 1. Statistics for RILAC operation from January 1 through December 31, 2005.

Operation time of RILAC	5401 hr
Beam service time of RILAC	4567 hr
Machine trouble	142 hr
Beam service time of RILAC standalone	2976 hr
Beam transport to RRC	1591 hr

Table 2. Beam service time of RILAC standalone allocated to different research groups.

	Total time (hr)	%
Search for heaviest elements	2671	89.8
Radiation chemistry	96	3.2
Accelerator mass spectrometry	86	2.9
Instrumentation	123	4.1
Total	2976	100.0

Table 3. Operation statistics for RILAC ion beams delivered using RFQ linac with two ion sources (18G-ECRIS and SC-ECRIS). The operation times using SC-ECRIS are in parentheses.

Ion	Mass	Charge state	Total time (hr)
He	4	1	288 (192)
N	14	3	72 (72)
Ar	40	8, 9, 11	1752 (792)
Fe	58	13	168
Ni	58	9	96
Zn	70	16	2905
Xe	131	19	120
Total			5401 (1056)

* SHI Accelerator Service, Ltd.

vacuum leak caused by the heat of the converged ion beam that hit it. The leaky part was soldered. In addition, a vacuum chamber of DMe1 was newly designed and manufactured. The internal surface of the new chamber was fortified with 1 mm-thick tantalum plates. One week of scheduled beam time was cancelled for the repair.

(2) A new water pump of the deionized water circuit for RILAC had a terminal breakdown again. This time, a heat exchanger of the same system had a water leak at about the same time. Two weeks of scheduled beam time was cancelled for some repairs.

(3) The final vacuum tubes of the No. 2 and 3 final rf amplifiers have been replaced with new ones, because they were worn out after many years of operation. A final vacuum tube of the RFQ final rf amplifier also had a problem and was replaced with a new one.

(4) In the No. 5 cavity, the rf contact fingers of the shorting plate melted due to excessive rf current. Three weeks of scheduled beam time was cancelled for the repair.

RRC operation

M. Kase, N. Inabe, E. Ikezawa, T. Kageyama, N. Fukunishi, T. Nakagawa, O. Kamigaito, H. Ryuto, H. Okuno, N. Sakamoto, M. Kidera, M. Wakasugi, M. Kobayashi-Komiyama, Y. Higurashi, M. Nagase, S. Kohara, M. Fujimaki, A. Yoneda, S. Yokouchi, Y. Ohshiro,[*1] N. Tsukiori,[*2] R. Ohta,[*2] Y. Kotaka,[*2] K. Kobayashi,[*2] M. Nishida,[*2] K. Masuda,[*2] S. Fukuzawa,[*2] T. Nakamura,[*2] A. Goto, and Y. Yano

Table 1 shows the statistics of the RIKEN Ring Cyclotron (RRC) operation from Jan. to Dec. 2005. In spite of a fund limitations for electric power in the fiscal year 2004, the RARF accelerators were operated for 435 hours from January to March 2005. The total operation hours per year, which had decreased by 15% in 2004, was recovered to the level of 2003. Unscheduled shutdown took place frequently during the first half of 2005 due to machine problems and power limitations. Table 2 shows the beam service time for each beam course ranging from rooms E1 to E6 of the Nishina Memorial Bldg.

Room E1 has been used for many purposes since 1987 when the Riken Accelerator Research Facility (RARF) started. In 2005, simulation tests of a beam dump in the Big-RIPS were performed at E1b using a 63 MeV/nucleon ^{40}Ar beam with a power of approximately 2 kW. At the beginning of next year, all the beam lines in room E1 will be removed and converted into the new beam transport line of the RIBF. The use of the E1 beam lines for general purposes was terminated at the end of 2005.

Table 1. Operation statistice of RRC in 2005.

Operation time of RRC	5657	(5091) hr
Beam service time	4128	(3421) hr
Machine trouble	1464	(736) hr
Nuclear physics experiment	78	(78) %
Non-nuclear physics experiment	22	(22) %
RILAC-RRC operation	33	(23) %
AVF-RRC operation	67	(77) %

Figures in parentheses are data obtained in 2004.

The first experiment was performed using a particle analyzer (PA), which was installed at the E2a beam course in room E2 by CNS (the Center of Nuclear Study, the Univ. of Tokyo) in 2001. The beam course of E2b was used in heavy-ion channeling experiments using a parallel beam of 92 MeV/nucleon ^{56}Fe.

Two long-term nuclear physics experiments (more than ten days) were carried out from April to June with the spectrograph SMART in room E4 using a 135 MeV/nucleon polarized deuteron beam. After these experiments, the use of the SMART was stopped. Subdivision of the SMART begun in July and some parts including the large dipole magnet (PD1) were transported to the RIBF experiment building for future use.

In roon E5, biology experiments have been constantly carried out since 1989. These experiments range in many fields such as radiation biology, mutation breeding, plant physiology, and cell biology. Recently a new target system with an automatic target-exchanging mechanism was installed. The successive irradiations of many targets have become more efficient. Experiment has been reduced on average as shown in Table 2.

Approximately 62% of the total beam time was devoted to experiments using secondary beams (RI beams) produced at the RIPS by projectile fragmentations. In particular, RIPS experiments using a 63 MeV/u ^{40}Ar beam were carried out with priority this year. Two long-term continuous operations of the 63 MeV/u ^{40}Ar beam were performed from February to April and from October to November. The operation of RILAC-CSM-RRC continuously supplied the

Table 2. RRC beam time for each beam course in 2005.

Target room	Beam course	Total time (hr)	No. of experiments
E1	E1b	30 (0)	3 (0)
	E1c	47 (0)	3 (0)
E2	E2a-PA	178 (34)	3 (2)
	E2b	106 (100)	2 (2)
E3	E3a	70 (62)	3 (2)
	E3b	42 (120)	2 (6)
E4	SMART	882 (189)	6 (6)
E5	E5a	0 (48)	0 (2)
	E5b	140 (183)	29 (27)
E6-RIPS	RIPS	2599 (2650)	23 (27)
RRC/D(MS)		34	3

Note: Figures in parentheses are data obtained in 2004.

*1 Center of Nuclear Science, University of Tokyo
*2 Sumiju Accelerator Service Ltd.

beam for seven RIPS experiments.

Unscheduled shutdown occurred repeatedly in the first half of 2005. In February, while an annual inspection of the cogeneration system (CGS) was underway, the RRC had to stop due to shortage of electric power caused by the large power consumption for heating as a result of the very cold weather. Problems with concerning the rf amplifiers for the RRC cavities occurred frequently. A spark discharge around the final-stage electrotube damaged electronics parts. After the optimum set of parameters was carefully determined, the above troubles became less frequent.

During operation with a high-intensity beam, a leak occurred in the vacuum chamber inside the analysing magnet located just after a charge stripper, probably when a stripper foil was broken. A septum of electrostatic deflection channel (EDC) in the RRC extraction system was also damaged by beam irradiation due to a mistake in operation. A beam interlock system was introduced in the summer to prevent accelerator devices from receiving these damages. It functions by stopping a beam immediately when an abnormal beam current is detected.

After the SMART was subdivided in June, the construction of the fRC (fixed-frequency ring cyclotron) started in August and assembly finished in December. After wiring and piping, the fRC will be ready in March 2006. The construction of beam transport lines around fRC will start in March 2006 and finish three months later. During this period, the RRC beam service will not be available.

The beam commissioning of the RIBF will start in 2006. As the first step, a beam test of fRC will be carried out in June. The beam commissioning including IRC and SRC will start in autumn of 2006. The RRC beam service in 2006 will be interrupted considerably. Estimated beam service time is 30% of that in 2005.

The operation time of the RILAC-RRC was very limited because most of the available beam time of RILAC was devoted to the experiment search for $Z = 113$ elements. Some users, who had been using the beams from the RILAC-RRC, were requested to use the beams from AVF-RRC instead, if possible.

AVF operation

T. Kageyama, Y. Ohshiro,[*1] M. Kase, N. Inabe, N. Fukunishi, T. Nakagawa, O. Kamigaito, H. Ryuto, H. Okuno, N. Sakamoto, M. Kidera, M. Wakasugi, M. Kobayashi-Komiyama, Y. Higurashi, M. Nagase, S. Kohara, A. Yoneda, S. Yokouchi, N. Tsukiori,[*2] R. Ohta,[*2] Y. Kotaka,[*2] K. Kobayashi,[*2] M. Nishida,[*2] K. Masuda,[*2] S. Fukuzawa,[*2] T. Nakamura,[*2] A. Goto, and Y. Yano

Table 1 shows the statistics of the AVF cyclotron (AVF) operation from January to December 2005. Approximately 80% of AVF operation time was spent injecting the beam into the RRC in 2005. This percentage is expected to decrease markedly after the RIBF commissioning starts in the following years and, as a result, the standalone use of AVF will take priority. The three types of ion sources shown in Fig. 1 have been producing various ion beams since 2003. Table 2 shows a list of all the beams accelerated with AVF in 2005. Table 3 shows the operation time for each ion source.

In the case of ions heavier than Ar, the 10 GHz ECR ion source is mainly used. For lighter ions, both the 10 GHz ECR and Hyper-ECR ion source are used alternatively. The polarized ion source (PIS) was used continuously in April and June 2005 to supply a polarized deuteron beam to the final SMART experiments. Since then, the PIS has not been used for a long duration.

In the standalone use, the various beams were delivered either to the CRIB in the E7 room or the beam course of C03 in the AVF accelerator room. At the CRIB, eleven nuclear physics experiments were carried out using low-energy secondary beams. The Center of Nuclear Study, The University of Tokyo (CNS), has promoted these CRIB experiments in collaboration with RIKEN. At C03, many types of radioisotope have been produced using mainly proton beams for the purpose of radiochemistry.

An 8.6 MeV/u $^{7}Li^{3+}$ beam was successfully extracted for the first time from the AVF in June 2005 with an intensity of 400 pnA, which was sufficiently strong for the CRIB experiment. A melting pot with metallic lithium was inserted into the plasma of the Hyper ECR ion source. It worked well for more than three days.

The upgrade of the AVF has been in progress in cooperation with CNS. The flattop acceleration system was added to the AVF cavities in 2002. A high-power operation with the flattop system was restricted due to the damage of a ceramic insulation part of the rf amplifier. The improvement of the ceramic part is now underway. The power supplies for the sector magnets were improved to increase the maximum energy of the light ion beam at the beginning of 2005. The maximum current of the main coil was increased from

Table 1. Operation statistics of AVF in 2005.

Total operation time	4858 hr	
Beam tuning	1262 hr	26%
Injection to RRC	2799 hr	58%
AVF standalone	715 hr	16%
Beam course		
E7a (CRIB)	535 hr	
E7b	36 hr	
C03	262 hr	

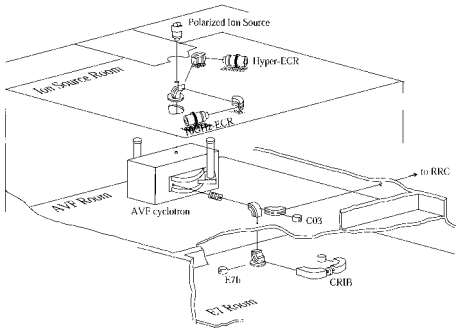

Fig. 1. Overview of AVF and its injection beam lines and extraction beam lines.

Table 2. Ion species and operation times.

Ion species	Ion source	Operation time (hr)	
		RRC injectio	AVF
p	10ECR & H-ECR	161	202
Polarized d	PIS	889	
$^{4}He^{2+}$	10ECR & H-ECR		168
$^{7}Li^{3+}$	H-ECR		320
$^{12}C^{4+}$	10ECR & H-ECR	629	
$^{13}C^{4+}$	10ECR & H-ECR	408	
$^{14}N^{4+}$	10ECR & H-ECR	127	
$^{15}N^{6+}$	H-ECR		48
$^{19}F^{7+}$	10ECR		36
$^{18}O^{5+}$	10ECR		36
$^{18}O^{6+}$	10ECR	96	48
$^{20}Ne^{6+}$	10ECR & H-ECR	201	
$^{22}Ne^{7+}$	10ECR	168	72
$^{24}Mg^{8+}$	10ECR		96
$^{40}Ar^{11+}$	10ECR & H-ECR	1043	
$^{56}Fe^{15+}$	10ECR	299	
$^{58}Ni^{15+}$	10ECR	60	

10ECR: 10 GHz-ECR ion source
PSI: Polarized ion source
H-ECR: Hyper-ECR ion source

Table 3. Operation times of ion sources.

Ion source	Operation time (hr)	Fraction (%)
10 GHz ECRIS	2791	54%
Hyper ECRIS	1470	29%
Polarized Ion Source	889	17%

*1 Center of Nuclear Science, the University of Tokyo
*2 Sumiju Accelerator Service Ltd.

1100 A to 1200 A. The two sets of power supplies for the trim coils were also improved. As a result, the K-value of the AVF increased from 70 to 78 MeV. The maximum energy of $^{15}N^{5+}$ beam was increased beyond 9 MeV/nucleon, extending the availability of RI beams by the CRIB in E7. Acceleration tests have not been performed yet, because of the lack of both input electric power and a sufficient capacity of the water cooling system.

According to the agreement between RIKEN and CNS, the AVF beam should be used in regular-course experiment for students of the Physics Department of the University of Tokyo starting 2002. Four sets of one-day experiments were performed from September to December in 2005. Eight students participated in each experiment on elastic scattering or gamma spectroscopy using a 6 MeV/u alpha beam from the AVF. The total number of students has increased by 25% compared with that in the first year of 2002.

Problems with the AVF occurred mainly in March 2005. The position control mechanism of the gradient collector in the extraction system of the AVF broke down. A water leak into the vacuum chamber occurred at the septum electrode of the deflector. A high-voltage cable, which sustains the power feed into one of the rf amplifier, was damaged. A radial probe had difficulty in performing smooth operation owing to the failure of mechanical coupling in June. These problems caused a total of 141 hr of unscheduled shutdown for the AVF-RRC beam time and a total of 80 hr for the AVF standalone beam time.

Operation of tandem accelerator

T. Kobayashi and K. Ogiwara

The 1.7 MV tandem accelerator (Pelletron) was operated for a total of 125 days for experiments during the annual report period from Nov. 1, 2004 to Oct. 31, 2005. The number of operation days increased by approximately 30% that of the previous year due to the participation of a new experimental group for semiconductor materials. A total of 32 days was spent for machine inspection, troubleshooting and beam testing including shutdown and recovery for electric power failure. The details of the problems during this period and the days required for repair are as follows.

(1) Leakage of SF_6 (4 days)

The isolation gas SF_6 leaked from the high-pressure tank in November. The leakage occurred at the seal of the corona-detection electrode. The electrode was exchanged and SF_6 was added from a gas cylinder.

(2) Wear of carbon sheaves (3 days)

There are four sheaves for charge transfer in the HV generator. One of them wore out in January and the HV became unstable. The wear amount of carbon depends on the tension of the charge transfer chain and the lifetime is approximately 3–5 years.

(3) Damage of charge transfer chain (3 days)

The charge transfer chain consists of aluminum pellets and nylon joints. In January, one of the joints was broken. The cause of this accident is not clear. However, no abnormality was found in other joints by careful investigation.

(4) Contamination of quartz tube in He ion source (8 days)

This trouble occurred frequently during this period and was due to metallic Rb vapor used for the production of He^- ions. The productivity of He ions markedly drops with contamination. Recently, we have prevented the backward diffusion of Rb vapor by flowing He gas continuously during and after operation. By this method, contamination has been suppressed.

The accelerated ion species during this period were H^+, He^+ and B^+ with energies from 1.6 to 2.5 MeV summarized in Table 1.

Experimental studies on the following subjects were performed, and are still in progress.

(1) Nuclear reaction analysis (NRA) using $^1H(^{11}B,\alpha)2\alpha$ reaction (67 days)

(a) The state of hydrogen in Nb-based and Ta-based alloys, and V as investigated by the channeling method

(b) Effect of irradiation on the state of hydrogen in metals

(2) Particle-induced X-ray emission (PIXE) (18 days)

(a) Development and application of highly sensitive high-resolution in-air PIXE system for chemical state analysis

(b) Trace element analysis of biological and environmental samples using energy dispersive X-ray spectrometry

(3) Analysis using elastic scattering (40 days)

(a) Rutherford backscattering spectrometry (RBS) analysis of polymers, carbon materials, GaN, AlGaN and ZnO.

(b) Elastic recoil detection (ERD) analysis of diamond-like carbon (DLC) thin films and ion-implanted polymers for determining hydrogen content.

The total time in days, which was spent for each experiment, is shown in parentheses.

Table 1. Beam conditions and analysis techniques of Pelletron accelerator.

Ion	Energy [MeV]	Beam current [nA]	Analysis	Operation time [days]
$^1H^+$	1.6–2.5	30–50	PIXE	18
$^4He^+$	2.0–2.3	5–20	RBS, ERDA	40
$^{11}B^+$	2.0	1.0–1.5	NRA	67

^{16}C inelastic scattering studied with the microscopic coupled-channels method†

M. Takashina, Y. Kanada-En'yo,[*1] and Y. Sakuragi[*2]

[Nuclear reaction, unstable nuclei]

Recently, the opposite deformations between proton and neutron densities in C isotopes have been theoretically suggested[1,2] by the method of antisymmetrized molecular dynamics (AMD): The proton density has an oblate deformation, whereas the neutron density has a prolate deformation, and the symmetry axis of proton distribution is perpendicular to that of neutron distribution in ^{10}C and ^{16}C. According to Ref. 2, the 2_1^+ state of ^{16}C is a rotational excited state, and the rotational axis is perpendicular to the neutron symmetry axis. In this excitation mechanism, the proton transition strength is reduced, and the $0_1^+ \to 2_1^+$ transition is dominated by the neutron excitation.

To search for the possible difference between proton and neutron contributions to the excitation of the 2_1^+ state in ^{16}C, an inelastic scattering experiment of ^{16}C on ^{208}Pb target was performed[3] applying the Coulomb-nuclear interference method. The analysis was carried out using the deformed potential model, and the proton and neutron transition matrix elements, M_p and M_n, were extracted. However, the phenomenological analysis done in Ref. 3 contains some assumptions, and hence, it seems inappropriate to compare the M_p and M_n evaluated in Ref. 3 with those calculated theoretically.

To test the ^{16}C internal wave function, we should directly link the cross section with the wave function by calculating the differential cross sections of the inelastic scattering of ^{16}C on ^{208}Pb target by the microscopic coupled-channels (MCC) method, and compare the calculated result with the experimental reaction data measured in Ref. 3.

In the MCC calculation, the diagonal and coupling potentials are given by the double-folding model:

$$V_{\alpha(ij)\alpha'(k\ell)}(\mathbf{R}) = \int \rho_{ik}^{(a)}(\mathbf{r}_a)\rho_{j\ell}^{(A)}(\mathbf{r}_A) \times v_{NN}(\mathbf{r}_a + \mathbf{R} - \mathbf{r}_A)d\mathbf{r}_a d\mathbf{r}_A, \quad (1)$$

where $\rho_{ik}^{(a)}$ ($\rho_{j\ell}^{(A)}$) represents the transition density of the ^{16}C (^{208}Pb) nucleus between the state i (j) in channel α and the state k (ℓ) in channel α', and v_{NN} is the DDM3Y interaction.[4]

Here, we use the AMD wave function to calculate $\rho_{ik}^{(a)}(\mathbf{r}_a)$. In Ref. 2, two versions of the ^{16}C internal wave function are obtained, changing the strength of the spin-orbit force, (i) $u_{ls} = 900$ MeV and (ii) $u_{ls} = 1500$ MeV. In addition, we also use the AMD wave function for which the strength of the spin-orbit force is set to (iii) $u_{ls} = 2000$ MeV so as to reduce the $B(E2)$, close to the experimental value. The $B(E2)$ values obtained with these three wave functions are $B(E2; 2_1^+ \to 0_1^+) = 1.9$, 1.4, and 0.93 e^2fm^4, respectively. The density distribution of the ^{208}Pb nucleus is obtained by unfolding the measured charge form factor with the realistic proton charge form factor and it is assumed that the shape of the neutron density is the same as that of the proton density, namely $\rho_n(\mathbf{r}) = (N/Z)\rho_p(\mathbf{r})$.

The results are shown in Fig. 1. It is found that the MCC calculations with the AMD wave functions (i) and (ii) reproduce the experimental data fairly well without introducing any normalization factor for the calculated differential cross sections, whereas the result with the wave function of case (iii) severely underestimates the measured differential cross sections.

We conclude that the AMD wave function (i) predicts the neutron excitation strength of ^{16}C reasonably well, and that the MCC calculation is a useful tool to link the inelastic scattering data with the internal wave functions obtained theoretically.

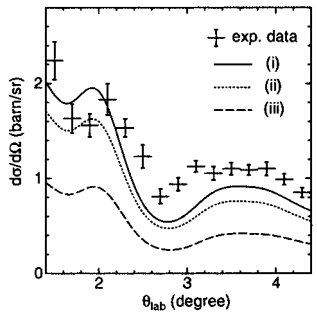

Fig. 1. Results of MCC calculations with AMD wave functions (i), (ii) and (iii) shown by solid, dotted and dashed curves, respectively.

References
1) Y. Kanada-En'yo and H. Horiuchi: Prog. Theor. Phys. Suppl. No. 142, 205 (2001).
2) Y. Kanada-En'yo: Phys. Rev. C **71**, 014310 (2005).
3) Z. Elekes et al.: Phys. Lett. B **586**, 34 (2004).
4) M. El-Azab Farid and G. R. Satchler: Nucl. Phys. A **438**, 525 (1985).

† Condensed from the article in Phys. Rev. C **71**, 054602 (2005)

*1 Institute of Particle and Nuclear Studies, High Energy Accelerator Research Organization (KEK)
*2 Department of Physics, Osaka City University

Coulomb breakup effects on elastic cross section of ^{6}He+^{209}Bi scattering near Coulomb barrier energies

T. Matsumoto, T. Egami,[*1] K. Ogata,[*1] Y. Iseri,[*2] M. Kamimura, and M. Yahiro[*1]

[Nuclear reaction, unstable nuclei]

Recently, Keeley *et al.*[1] have analyzed ^{6}He+^{209}Bi scattering at 19 and 22.5 MeV near the Coulomb barrier energy[2,3] by the continuum-discretized coupled-channels method (CDCC)[4] that is a fully quantum-mechanical method for describing the scattering of a three-body system. In the analysis, the ^{6}He+^{209}Bi system was assumed to be the ^2n+^{4}He+^{209}Bi three-body system, that is, the neutron pair in ^{6}He was treated as a single particle, di-neutron (^2n). Their calculation, however, did not reproduce the experimental data of the elastic and total reaction cross sections. This indicates that the ^{6}He+^{209}Bi scattering cannot be described by the three-body model. Since ^{6}He is well known as a two-neutron halo nucleus, its structure should be described by the n+n+^{4}He three-body system rather than the ^2n+^{4}He two-body one. Thus, it is necessary to analyze the ^{6}He+^{209}Bi scattering using the n+n+^{4}He+^{209}Bi four-body model.

In our previous work,[5] we proposed four-body CDCC that is an extension of CDCC and describes four-body breakup processes. In four-body CDCC, three-body breakup continuum of the projectile is discretized by diagonalizing the internal Hamiltonian in a space spanned by the Gaussian basis functions. Thus far, the Gaussian basis function has been used with success for solving bound-state problems of few-body systems. The approach is called the Gaussian expansion method (GEM).[6] Four-body CDCC was successfully applied to ^{6}He+^{12}C scattering at 18 and 229.8 MeV in which only nuclear breakup was significant.[7] The elastic and breakup cross sections calculated with four-body CDCC are found to converge as the number of Gaussian basis functions is increased. This indicates that the set of discretized continuum states obtained with GEM forms a complete set with good accuracy in a finite region of space that is important for the four-body reaction process concerned. Furthermore, Egami *et al.*[8] showed the applicability of CDCC with GEM to Coulomb breakup processes for ^{8}B+^{58}Ni scattering at 25.8 MeV. Thus, it is expected that four-body CDCC with GEM accurately describes four-body breakup reactions near the Coulomb barrier energy.

In this work, we analyze ^{6}He+^{209}Bi scattering at 19 and 22.5 MeV by four-body CDCC in which the scattering is described by the n+n+^{4}He+^{209}Bi model. This is the first application of four-body CDCC to low-energy scattering in which both nuclear and Coulomb breakup processes are significant.

It is found that four-body CDCC reproduces the angular distribution of the measured elastic cross sections as shown in Fig. 1. Also the calculated total reaction cross sections are in good agreement with the experimental data. Meanwhile the CDCC calculation based on the di-neutron model of ^{6}He, i.e., the ^2n+^{4}He+^{209}Bi three-body model, does not reproduce the data. We thus conclude that the n+n+^{4}He+^{209}Bi four-body reaction model is necessary to accurately describe the ^{6}He+^{209}Bi scattering. Four-body CDCC is indispensable to analyze low-energy ^{6}He scattering in which both nuclear and Coulomb breakup processes are significant.

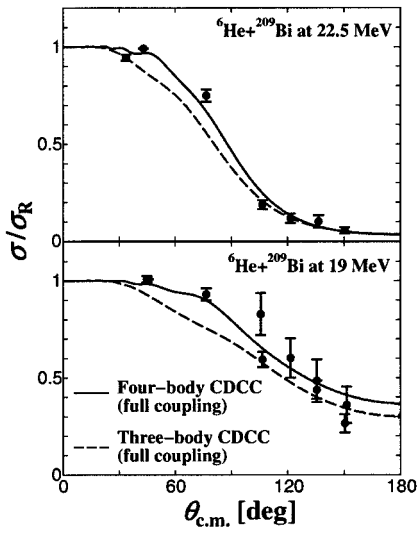

Fig. 1. Angular distribution of the elastic differential cross section as a ratio to the Rutherford cross section for ^{6}He+^{209}Bi scattering at 19 and 22.5 MeV.

[*1] Department of Physics, Kyushu University
[*2] Department of Physics, Chiba-Keizai College

References

1) N. Keeley et al.: Phys. Rev. C **68**, 054601 (2003).
2) E. F. Aguilera et al.: Phys. Rev. Lett. **84**, 5058 (2000).
3) E. F. Aguilera et al.: Phys. Rev. C **63**, 061603(R) (2001).
4) M. Kamimura et al.: Prog. Theor. Phys. Suppl. **89**, 1 (1986).
5) T. Matsumoto et al.: Phys. Rev. C **70**, 061601 (2004).
6) For a review, E. Hiyama et al.: Prog. Part. Nucl. Phys. **51**, 223 (2003).
7) T. Matsumoto et al.: Phys. Rev. C **68**, 064607 (2003).
8) T. Egami et al.: Phys. Rev. C **70**, 047604 (2004).

Reaction cross section described by a black sphere approximation of nuclei†

A. Kohama, K. Iida, and K. Oyamatsu*

[Nuclear reaction, reaction cross section, nuclear radius, unstable nuclei]

The size of atomic nuclei is considered to be well deduced from empirical data for the proton-nucleus elastic differential cross section, $d\sigma_{\rm el}/d\Omega$, and the total reaction cross section, $\sigma_R \equiv \sigma_T - \sigma_{\rm el}$, where σ_T is the total cross section.[1] Thus far, the analysis that respects both data in deducing the nuclear size has not been completed in particular for proton incident energies, T_p, higher than 800 MeV.

In this work, we identify a length scale that simultaneously accounts for the observed proton-nucleus reaction cross section and diffraction peak in the proton elastic differential cross section. This scale is the nuclear radius, a, deduced from proton elastic scattering data of incident energies higher than ∼800 MeV, by assuming that the target nucleus is a "black" sphere.[2]

We determine a in such a way that the c.m. scattering angle $[\theta_{\rm c.m.} \equiv 2\sin^{-1}(q/2p)]$ of the first maximum for the Fraunhofer diffraction agrees with that measured by proton-nucleus elastic scattering, θ_M. Here, we define the zeroth peak as that whose angle corresponds to $\theta_{\rm c.m.} = 0$. The radius, a, and the angle, θ_M, are then related by

$$2pa\sin(\theta_M/2) = 5.1356\cdots. \quad (1)$$

It is useful to identify this radius multiplied by $\sqrt{3/5}$ with the root-mean-square matter radius of the target nucleus:

$$r_{\rm BS} \equiv \sqrt{3/5}a. \quad (2)$$

The factor $\sqrt{3/5}$ originates from the assumption that the density distribution of the black sphere is uniform.

We have two significant results, while finalizing a systematic analysis of the existing data for proton elastic scattering off stable nuclei ranging from He to Pb at proton incident energies above ∼800 MeV. First, the values of $r_{\rm BS}$ obtained from Eq. (2) are systematically larger than the root-mean-square radius r_m deduced from elaborate scattering theory for $A < 50$, although they agree quite well with each other for $A > 50$. This suggests a significant deviation of the nucleon distribution from the rectangular one for $A < 50$, which is consistent with the behavior of the empirical charge distribution.[3] Second, the absorption cross section, $\sigma_{\rm BS}$ $(= \pi a^2)$, is consistent with the empirical total reaction cross section for C, Sn, and Pb to within error bars as shown in Fig. 1. This consistency persists in the case of the interaction cross section measured for a carbon target. We thus see the dual role of a as a black sphere radius and as a reaction radius.

We now prepare for future possible application of the black sphere approximation to neutron-rich unstable nuclei expected to be produced at RIKEN and GSI.

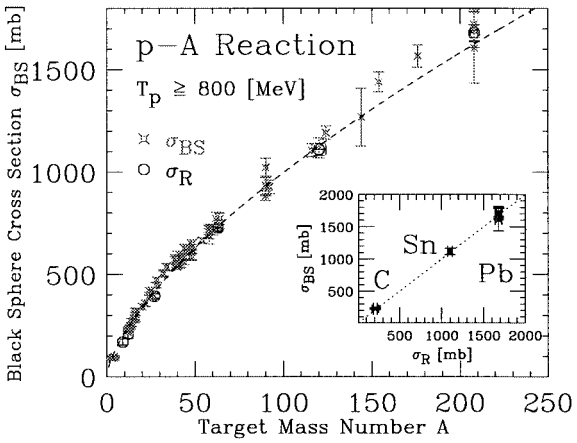

Fig. 1. Absorption cross section, $\sigma_{\rm BS}$ $(= \pi a^2)$, of a proton of $T_p \geq 800$ MeV by a target nucleus of mass number A. For comparison, we plot the empirical data for the proton-nucleus total reaction cross section, σ_R (○), which are listed in Ref. 4 for ^{9}Be, ^{12}C, ^{27}Al, Cu, Sn, and Pb. For the latter three elements the value of σ_R is the average over the isotopic abundance in a target. For these data, we set A as the mass number of the most abundant isotope and assign the uncertainty in A due to the natural abundance. The dashed curve denotes $(5/3)\pi(0.94A^{1/3})^2$ fm^2. Inset: $\sigma_{\rm BS}$ vs σ_R for ^{12}C, Sn, and Pb. The dotted line represents $\sigma_{\rm BS} = \sigma_R$.

References

1) C. J. Batty, E. Friedman, H. J. Gils, and H. Rebel: Adv. Nucl. Phys. **19**, 1 (1989).
2) A. Kohama, K. Iida, and K. Oyamatsu: Phys. Rev. C **69**, 064316 (2004).
3) B. Frois, C. N. Papanicolas, and S. E. Williamson: in *Modern Topics in Electron Scattering*, edited by B. Frois and I. Sick (World Scientific, Singapore, 1991), p. 352.
4) W. Bauhoff: At. Data Nucl. Data Tables **35**, 429 (1986).

† Condensed from the article in Phys. Rev. C **72**, 024602 (2005)

* Department of Media Theories and Production, Aichi Shukutoku University

Study of oxygen isotopes by charge- and parity-projected Hartree-Fock method

S. Sugimoto,[*1] K. Ikeda, and H. Toki[*2]

[Nuclear structure, tensor force, mean field model]

Recently, we have proposed a mean-field-type framework that treats the correlation by the tensor force by mixing parities and charges in single-particle states.[1] We applied this method to alpha particles and found that the tensor correlation can be exploited. The tensor force should have effects on the structure of nuclei over the whole mass region and, therefore, it is interesting to apply our method to heavier mass nuclei. In this paper, we report the application of our method to oxygen isotopes.

As we mentioned above, we mix parities (positive and negative) and charge states (proton and neutron) in a single-particle state. A Slater determinant, which is composed of such single-particle states with mixing of parities and charges, does not have a good parity and a good charge number. To a exploit state with a good parity and a good charge number, we perform the parity and charge projections. By considering the variation of the projected wave function with respect to single-particle states, we obtain a Hartree-Fock-like equation, namely, the charge- and parity-projected Hartree-Fock (CPPHF) equation. In our method (the CPPHF method), we solve the CPPHF equation self-consistently.[1]

We take the Hamiltonian in the following form,

$$H = \sum_{i=1}^{A}\left(-\frac{\hbar^2}{2M}\Delta_i\right) + V_{\rm C} + V_{\rm 3B} + V_{\rm T} + V_{\rm LS} + V_{\rm Coul} - E_{\rm CM}. \quad (1)$$

Here, the first term is the kinetic energy. $V_{\rm C}$, $V_{\rm 3B}$, $V_{\rm T}$, $V_{\rm LS}$, and $V_{\rm Coul}$ are the potential energies from the central force, three-body force, tensor force, LS force, and Coulomb force, respectively. We subtract the energy of the center of mass motion $E_{\rm CM}$. For the central and three-body forces, we adopt the modified Volkov No.1 force.[2] For the tensor and LS forces we adopt the G3RS force.[3] We strengthen the tensor force by multiplying the $\tau_1 \cdot \tau_2$ part in the tensor force by $x_{\rm T}$ to take into account correlations that cannot be treated in the CPPHF method. We also multiply the attraction part of the triple-even channel in the central force by the factor $x_{\rm TE}$ and the three-body force by $x_{\rm 3B}$ to reproduce the binding energy and the charge radius of ^{16}O.

In Table 1, the result for the sub-closed-shell oxygen isotopes is shown. In the calculation we take $x_{\rm T} = 1.5$, $x_{\rm TE} = 1.04$, and $x_{\rm 3B} = 1.55$. We also multiply the LS force by a factor of 2. It is required to reproduce the binding energy of ^{14}O and ^{22}O reasonably. From the table we can see that relatively large energy gains come from the tensor force. These are much larger than the energy gains from the LS force. The potential energies from the tensor force have a shell-structure dependence, which is of the same order as that of the LS force. This suggests that the tensor force has an effect on the shell structure of the nuclei. To study the effect of the tensor force on shell structure, we need to investigate single-particle structure and now we are trying to calculate the 1-particle states like ^{17}O. We hope we will show the result in the near future.

Table 1. Result for sub-closed-shell oxygen isotopes in CPPHF method. E, K, and V are the total energy, the kinetic energy including the correction for the center of mass motion, and the potential energy, respectively. $V_{\rm T}$ and $V_{\rm LS}$ are the contributions to the potential energy from the tensor and LS forces, respectively. They are give in MeV. $R_{\rm m}$ is the matter radius in fm.

	E	K	V	$V_{\rm T}$	$V_{\rm LS}$	$R_{\rm m}$
^{14}O	−100.4	272.9	−373.4	−75.3	−11.9	2.43
^{16}O	−127.6	253.9	−381.6	−38.3	−1.0	2.60
^{22}O	−153.8	371.4	−525.3	−40.5	−19.4	2.93
^{24}O	−164.4	415.7	−580.1	−57.6	−19.7	3.03
^{28}O	−175.8	442.9	−618.7	−45.1	−1.9	3.27

References

1) S. Sugimoto, K. Ikeda, and H. Toki: Nucl. Phys. A **740**, 77 (2004).
2) T. Ando, K. Ikeda, and A. Tohsaki-Suzuki: Prog. Theor. Phys. **64**, 1608 (1980).
3) R. Tamagaki: Prog. Theor. Phys. **39**, 91 (1968).

*1 Department of Physics, Graduate School of Science, Kyoto University
*2 Research Center for Nuclear Physics, Osaka University

Tensor correlation in neutron halo nuclei

T. Myo,[*1] K. Katō,[*2] H. Toki,[*1] and K. Ikeda

[Nuclear structure, unstable nuclei, cluster model, tensor force]

The tensor force is an essential component in nuclear force and plays an important role in the nuclear structure.[1] In this report, we investigate the role of the tensor force in neutron halo nuclei ^{6}He and ^{11}Li. In most theoretical studies of halo nuclei, the core+n+n model is often used, where an inert core is assumed, such as the $(0s)^4$ of ^{4}He in ^{6}He. In this picture, the tensor force cannot work in the core or in the coupling between core and valence neutrons. Thus, the tensor correlation in neutron halo nuclei has not been realized. For ^{11}Li, the mechanism of the lowering of the $1s$ orbit is still unclear. It is also of interest to examine the effect of the tensor correlation on this problem.

We consider the tensor correlation as follows. The tensor force tends to change the parity of the single particle orbit due to the $(\boldsymbol{\sigma}\cdot\boldsymbol{r})$ operator. This is a result of the one pion exchange potential, namely, the pion. Then, in ^{4}He, the $0s$ and $0p$ orbits can be coupled by the tensor force, and we extend the model space into $(0s)^4+(0s)^2(0p)^2$.[2–5] In fact, we take up to the $2p2h$ excitation of $0s+0p+sd$ shells to include the tensor correlation in ^{4}He. We employ Akaishi's effective NN force[5] derived from the G-matrix theory. We use the harmonic oscillator basis for a single particle orbit and determine the length parameter of each orbit variationally. The obtained wave function has narrow $0p$ and $0d$ orbits, which represent the higher shell effect of the tensor force. Among the $2p2h$ components, $(0p_{1/2})^2(0s_{1/2})^{-2}$ is well mixed, about 5%. The expectation value of the tensor force is -40.1 MeV.

We also solve the coupled ^{4}He+n problem with tensor correlation. Since the Pauli blocking mainly occurs in the $1/2^-$ state from the large $0p_{1/2}$ component in ^{4}He, splitting of $1/2^-$–$3/2^-$ can arise in ^{5}He. We start from the microscopic ^{4}He-n potential, KKNN,[6] and make a new ^{4}He-n potential including the tensor correlation with weakening of the LS part of KKNN by about half. In the new model, the d-wave behavior is improved, as shown in Fig. 1.[4] We also solve the coupled three-body model of ^{6}He shown in Fig. 2, where the Pauli-blocking effect occurs in the 0_2^+ state related to the $0p_{1/2}$ orbit.

We found that the tensor correlation strongly affects the properties of the $0p_{1/2}$ orbit. This seems crucial in the s-state problem in ^{11}Li. To confirm this, we solve the coupled ^{9}Li+n+n model for ^{11}Li, where we include the $2p2h$ excitation from $0s$ to $0p$ orbits in ^{9}Li. In ^{11}Li, the $0p_{1/2}$ orbits in ^{9}Li couple to the p-wave

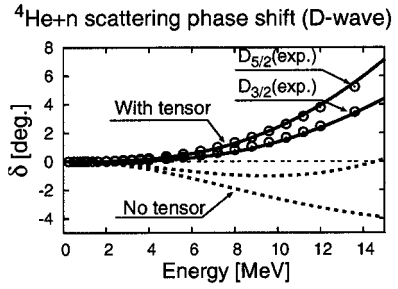

Fig. 1. ^{4}He+n d-wave phase shifts with tensor correlation.

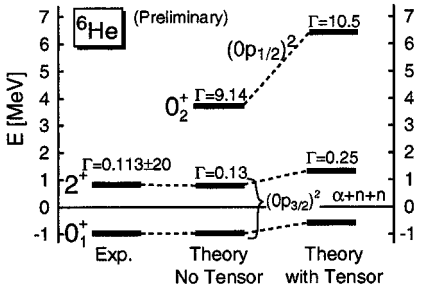

Fig. 2. ^{6}He spectrum with tensor correlation.

valence neutrons. This produces the Pauli-blocking effect, and the p-state energy of ^{11}Li is lost. The results are shown in Table 1. We confirm that the s-state mixing increases when considering the tensor correlation in comparison with the single channel case. In fact, the contribution of the tensor force decreases by 5.6 MeV in ^{11}Li in comparison with isolated ^{9}Li.

Table 1. Properties of ^{9}Li and ^{11}Li. P is the probability.

		Single	Couple	Expt.
^{9}Li	E [MeV]	—	-39.7	-45.3
	$\langle V_T\rangle$ [MeV]	—	-19.8	—
	$P(2p2h)$ [%]	—	7.2	—
^{11}Li	$P((1s)^2)$ [%]	2.3	21.6	~ 50
	R_m [fm]	2.88	3.08	3.12 ± 0.16 3.53 ± 0.06

*1 Research Center for Nuclear Physics, Osaka University
*2 Graduate School of Science, Hokkaido University

References
1) Y. Akaishi et al.: Int. Rev. Nucl. Phys. **4**, 259 (1988).
2) T. Terasawa: Prog. Theor. Phys. **23**, 87 (1960).
3) S. Sugimoto et al.: Nucl. Phys. A **740**, 77 (2004).
4) T. Myo et al.: Prog. Theor. Phys. **113**, 763 (2005).
5) Y. Akaishi: Nucl. Phys. A **738**, 80 (2004).
6) H. Kanada et al.: Prog. Theor. Phys. **61**, 1327 (1979).

Three-body cluster states in ^{11}C and ^{11}B

Y. Kanada-En'yo*

[Nuclear structure, unstable nuclei, cluster]

In ^{12}C, it is known that 3α-cluster states develop in excited states such as the 0_2^+ (7.65 MeV) state. Tohsaki et al.[1,2] proposed that 0_2^+ is a dilute state which is considered to be a weakly interacting gas of 3 α particles. There is a question whether such loosely bound multicluster states may appear in other nuclear systems. Our aim is to study the structure of excited states of ^{11}C and ^{11}B and search for dilute cluster states composed of three weakly interacting clusters.

The present study has been motivated by the recent measurements of Gamov-Teller (GT) transitions ^{11}B$\rightarrow^{11}$C* with high energy resolutions.[3] In the experiments, it has been found that GT transitions into the $3/2_3^-$ (8.10 MeV) state of ^{11}C are extremely weak compared with other low-lying states. Abnormal features of $3/2_3^-$ have been known also in the mirror nucleus ^{11}B. For example, the $3/2_3^-$ of ^{11}B has relatively weak $M1$ transitions into the lower states compared with strong transitions among other low-lying states. Moreover, it is also mysterious that in shell model calculations, no theoretical state can be assigned to $3/2_3^-$. These facts indicate that $3/2_3^-$ may have an exotic structure different from those of normal shell-model-like states, and is a candidate for the three-center cluster state.

In the present work, we apply the method of antisymmetrized molecular dynamics (AMD). We perform energy variation after spin parity projection (VAP) within the AMD model space, as was done in previous studies.[4,5]

In Table 1, the calculated excitation energies and GT transition strengths for the negative parity states of ^{11}C are shown compared with the experimental data. The present calculations well reproduce the experimental $B(GT;^{11}\mathrm{B}\rightarrow^{11}\mathrm{C})$ values. The calculations also agree well with the $M1$ transition strengths in ^{11}B and ^{11}C. As mentioned before, the characteristic properties of ^{11}C($3/2_3^-$, 8.10 MeV) and ^{11}B($3/2_3^-$, 8.65 MeV) are small $B(GT)$ and $B(M1)$. In the present calculations, the quenching of GT and $M1$ transitions for the $3/2_3^-$ states can be described by their exotic structure. Namely, the $3/2_3^-$ states exhibit the well-developed $2\alpha + {}^3$He and $2\alpha + t$ clustering, and therefore, they have a small transition overlap with the other normal low-lying states.

By analyzing the wave function of the excited states, we find that ^{11}C($3/2_3^-$) is a three-center cluster state with loosely bound $2\alpha + {}^3$He. The features of the loose binding of ^{11}C($3/2_3^-$) are very similar to those of ^{12}C(0_2^+, 7.65 MeV), which is known to be a dilute gaslike 3α state. Therefore, we consider that ^{11}C($3/2_3^-$, 8.10 MeV) and ^{11}B($3/2_3^-$,8.56 MeV) are candidates for dilute gaslike cluster states with $2\alpha + {}^3$He and $2\alpha + t$, respectively.

Another interesting result of the present work is that the $5/2_2^-$ state is described by a mixture of two components. The dominant component is the state with the intrinsic spin excitation, and the other one contains cluster correlations in terms of the $SU(3)$ limit clustering. Moreover, in the present calculations, we find many ^{7}Li + α and ^{7}Be + α cluster states in the higher negative parity states as well as in the positive parity states.

It is concluded that various types of cluster states appear in the excited states of ^{11}C and ^{11}B. A new revelation in the present work is that ^{11}C($3/2_3^-$, 8.10 MeV) and ^{11}B($3/2_3^-$, 8.56 MeV) are considered to be three-center cluster states with loosely bound $2\alpha + {}^3$He and $2\alpha + t$, respectively.

Table 1. Gamov-Teller transition strengths from $^{11}\mathrm{B}_{g.s.}$ to ^{11}C and excitation energies. The theoretical values were calculated by the AMD (VAP) method. The adopted interaction consists of the central force of MV1 ($m = 0.62$, $b = h = 0.25$), the spin-orbit force of GSRS ($u_I = -u_{II} = 2800$ MeV), and Coulomb force. The experimental data are taken from Ref. 3.

	exp.		theor.	
J_k^π	E_x	$B(GT)$	E_x	$B(GT)$
$3/2_1^-$	0.0	0.345(8)	0.0	0.40
$1/2_1^-$	2.00	0.440(22)	2.8	0.43
$5/2_1^-$	4.32	0.526(27)	3.6	0.70
$3/2_2^-$	4.80	0.525(27)	5.8	0.67
$7/2_1^-$	6.48	–	5.4	–
$3/2_3^-$	8.10	0.005(2)	10.5	0.02
$5/2_2^-$	8.42	0.461(23)	10.5	0.56

References
1) A. Tohsaki et al.: Phys. Rev. Lett. **87**, 192501 (2001).
2) Y. Funaki et al.: Phys. Rev. C **67**, 051306 (2003).
3) Y. Fujita et al.: Phys. Rev. C **70**, 011306(R) (2004).
4) Y. Kanada-En'yo: Phys. Rev. Lett. **81**, 5291 (1998).
5) Y. Kanada-En'yo, H. Horiuchi, and A. Doté: Phys. Rev. C **60**, 064304 (1999).

* Yukawa Institute for Theoretical Physics, Kyoto University

Alpha particle condensation in ^{12}C

Y. Funaki, A. Tohsaki,[*1] H. Horiuchi, P. Schuck,[*2] and G. Röpke[*3]

[Nuclear structure, cluster model, alpha particle]

Recently, we proposed that near the $n\alpha$ breakup threshold in self-conjugate $4n$ nuclei, there exist Bose-Einstein condensed states in which self-bound α particles weakly interact like a gas and occupy the same lowest $0s$ state, obeying Bose statistics.[1)] We investigated the structures of ^{12}C and ^{16}O using a new α-cluster wave function of the α-cluster condensate type, and identified the 0_2^+ state of ^{12}C (Hoyle state), observed at 0.38 MeV above the 3α threshold, and the 0_5^+ state of ^{16}O, observed at 0.44 MeV below the 4α threshold, as a candidate of the 3α condensed state and a possible candidate of the 4α condensed state, respectively.

According to the above proposal, we conducted a more detailed analysis of the excited state of ^{12}C observed near the 3α threshold, using a deformed alpha condensate wave function which only slightly deviates from the spherical one introduced in Ref. 1. The alpha condensed wave function extended to a deformed functional space can be written as,[2)]

$$\Phi_{n\alpha} \propto \mathcal{A}\Big[\prod_{i=1}^{n} \exp\Big(-2\sum_{k=x,y,z}\frac{(\boldsymbol{X}_i)_k^2}{B_k^2}\Big)\phi(\alpha_i)\Big]. \qquad (1)$$

Here, $\phi(\alpha_i) \propto \exp[-(1/2b^2)\sum_j^4(\boldsymbol{r}_{j(i)} - \boldsymbol{X}_i)^2]$ and $\boldsymbol{X}_i = \sum_j^4 \boldsymbol{r}_{j(i)}/4$, with $j(i) \equiv 4(i-1)+j$, are the internal wave functions and center-of-mass coordinates of the i-th α cluster, respectively. This wave function has the characteristic feature that all center-of-mass motions of the constituent alpha clusters occupy the same deformed Gaussian orbit, $\exp(-2\sum_{k=x,y,z} X_k^2/B_k^2)$. This feature is maintained as long as the variational parameter B_k is a sufficiently large value that the action of the antisymmetrizer, $\mathcal{A}$, is weak and can be neglected. We impose an axial symmetric restriction, $B_x = B_y \neq B_z$ for simplicity in all calculations.

For the 3α cluster states of ^{12}C, detailed analysis was already conducted by several authors about a quarter-century ago.[3)] In particular, complete 3α calculation with a fully microscopic model was performed by solving the following RGM equation, $\langle\phi_\alpha^3|(H - E)|\mathcal{A}\{\chi(\boldsymbol{s},\boldsymbol{t})\phi_\alpha^3\}\rangle = 0$, $\boldsymbol{s}$ and $\boldsymbol{t}$ being the Jacobi coordinates of the center-of-mass motion of three α clusters. The calculated 0_2^+ wave function well reproduced most of the observed experimental data, such as the binding energy, $B(E2)$ value, and inelastic electron scattering form factor. We found that the 0_2^+ wave function obtained by solving the RGM equation has a large squared overlap value of 97% with the single condensate wave function of a 3α gaslike structure which is projected onto J^π=0^+, using Eq. (1).[4)] Considering the fact that the RGM equation was solved without any model assumption for the inter-alpha motions, this result gives definitive theoretical evidence that the 0_2^+ state can be understood to be a 3α condensed state.

Besides the 0_2^+ state, the former theoretical works[3)] indicated the existence of the 2_2^+ state, which is located at about 3.0 MeV above the 3α threshold and has a typical 3α cluster structure, though this state had been unknown experimentally. However, recently, the 2_2^+ state was observed at 2.6 ± 0.3 MeV above the 3α threshold, together with the α-decay width, 1.0 ± 0.3 MeV.[5)] Since this state is observed as a resonance with non small α-decay width, it should be treated beyond the bound-state approximation in which a proper boundary condition is imposed. As one of the proper treatments, we applied the analytic continuation in the coupling constant (ACCC) method to the present formalism, which enables us to calculate the resonance energy and width.[6)]

The calculated binding energy and width are 2.1 MeV and 0.64 MeV, respectively, with the use of Volkov No.1 force as the effective nuclear force, and are in good agreement with the experimental values. We found that the resonance 2_2^+ wave function can be described by the single condensate wave function of the 3α gaslike structure which is projected onto J^π=2^+, using Eq. (1). By a simple analysis of the single condensate wave function with $J^\pi = 2^+$, we found that the 2_2^+ state is obtained by promoting just one α cluster out of the condensate of the 0_2^+ state into a D-wave. This implies that the 2_2^+ state has a structure similar to that of the 0_2^+ state which has a gaslike structure composed of 3α clusters and exhibits the Bose-condensate character.

*1 Suzuki Corporation
*2 Institut de Physique Nucléaire, France
*3 Institut für Physik, Universität Rostock, Germany

References

1) A. Tohsaki, H. Horiuchi, P. Schuck, and G. Röpke: Phys. Rev. Lett. **87**, 192501 (2001).
2) Y. Funaki, H. Horiuchi, A. Tohsaki, P. Schuck, and G. Röpke: Prog. Theor. Phys. **108**, 297 (2002).
3) For example, Y. Fujiwara, H. Horiuchi, K. Ikeda, M. Kamimura, K. Katō, Y. Suzuki, and E. Uegaki: Prog. Theor. Phys. Suppl. No. 68, 29 (1980).
4) Y. Funaki, A. Tohsaki, H. Horiuchi, P. Schuck, and G. Röpke: Phys. Rev. C **67**, 051306 (R) (2003).
5) M. Itoh et al.: Nucl. Phys. A **738**, 268 (2004).
6) Y. Funaki, H. Horiuchi, A. Tohsaki, P. Schuck, and G. Röpke: Eur. Phys. J. A **24**, 321 (2005).

Molecular-orbital and di-nuclei states of ^{22}Ne

M. Kimura* and H. Horiuchi

[Nuclear structure, cluster structure]

The successful description of Be isotopes by assuming a molecular-orbital structure (2α cluster core plus covalently valence neutrons) suggests a new type of clustering which is peculiar to neutron-rich isotopes. It will be of importance to investigate whether the molecular-orbital structure exists not only in Be isotopes but also in heavier systems.

Ne isotopes are one of the promising candidates of such heavier systems, since ^{20}Ne has a prominent α+^{16}O clustering in its ground state and many excited states. In this work, we have investigated the structure of ^{22}Ne focusing on the α clustering by combining the theoretical framework of the deformed-basis AMD and α+^{18}O(0^+_1) cluster model. By calculation, we have obtained the ground state and many excited states of ^{22}Ne. Among the obtained states, the spectra of the excited bands which show considerable α clustering are plotted in Fig. 1, together with that of the ground band.

The excited bands with the prominent α clustering are categorized into two types. The first type is the molecular-orbital band in which the system has an α+^{16}O cluster core and two valence neutrons orbit around the core. The K^π=0^+_2, 0^-_1 and 1^- bands belong to this type. The K^π=0^+_2 and 0^-_1 bands have similar intrinsic wave functions in which two valance neutrons occupy the orbital that is elongated along the α+^{16}O clustering of the core (Fig. 2). This orbital can be decomposed into the $1s0d$ orbital around ^{16}O and the $0p$ orbital around α, and is considered as an analogue of the $\sigma_{1/2}$-molecular-orbital of Be isotopes. The most important difference between the present σ-orbital and that of the Be isotopes is the parity asymmetry of the present one which is due to the parity asymmetry of the cluster core. The prominent parity-asymmetry of the total system of the σ^2 molecular-orbital states leads to the existence of the parity-doublet bands of K^π=0^+_2 and 0^-_1 in ^{22}Ne with almost the same intrinsic wave function. In the K^π=1^- band, one of the valence neutrons occupies the σ-orbital and the other occupies the parity-symmetric orbital which has the dominant component of the $0d_{5/2}$ orbital. These three bands are built on the states around the α+^{18}O threshold energy and correspond to the states with the prominent α reduced widths experimentally observed in the α transfer reaction.[1] Indeed the calculated and observed excitation energies and α reduced widths show good agreement.

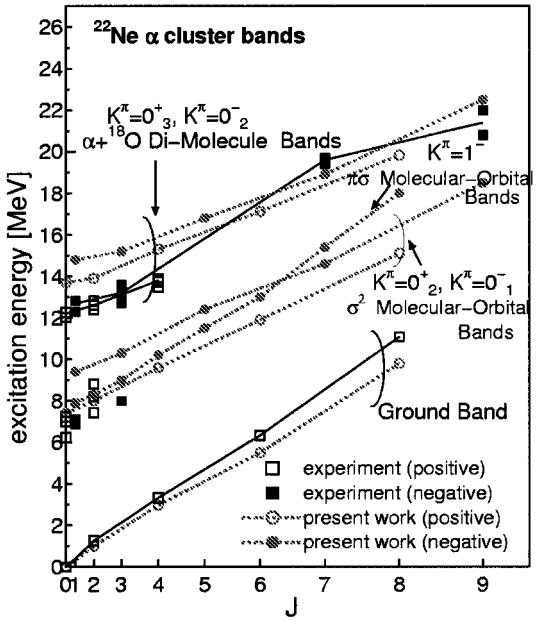

Fig. 1. Observed and calculated level schemes of excited bands with α clustering and ground band.

The second type is the di-molecule band in which the system is divided into α and ^{18}O clusters. The K^π=0^+_3 and 0^-_2 bands belong to this type. Their excitation energies are higher than that of the molecular-orbital band and the α+^{18}O threshold energy. In these bands, two valence neutrons orbit only around the ^{16}O. We consider that these bands correspond to the observed α+^{18}O molecular resonances,[2] since the calculated and observed α reduced widths show qualitative agreement.

From the present results, we suggest the two different kinds of α cluster structure in ^{22}Ne. The first one is the molecular-orbital structure and the second one is the di-molecule structure.

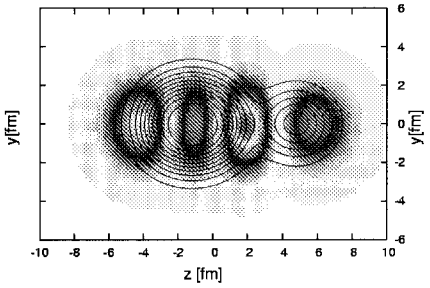

Fig. 2. Density plot for σ-orbital (gray scaled plot) and for α+^{16}O core (contour lines) of K^π=0^-_1 band.

* Yukawa Institute for Theoretical Physics, Kyoto University

References

1) W. Scholz et al.: Phys. Rev. C **6**, 893 (1972).
2) V. Z. Goldberg et al.: Phys. Rev. C **69**, 024602 (2004).

Many-body correlations among weakly bound neutrons

M. Yamagami

[Nuclear structure, pairing correlations, low-frequency vibrational excitations]

One of the most important features of unstable nuclei is the presence of weakly bound nucleons and their coupling to continuum states. In light neutron-rich nuclei, such as ^{11}Be and ^{11}Li, one or two weakly bound neutrons with low orbital angular momentum ℓ form neutron halos, and their coupling to particle continuum leads to soft $E1$ excitations. In medium and heavy mass regions, on the other hand, many weakly bound neutrons are present (e.g., eight weakly bound neutrons above the $N = 50$ shell closure in $^{86}_{28}\mathrm{Ni}_{58}$), and we may expect more exotic collective excitations as a consequence of the coherent motions among them.

In this study, I clarify several distinctive features of many-body correlations in the nuclei close to the neutron drip line by investigating pairing correlations and low-frequency vibrational excitations within the framework of the Hartree-Fock-Bogoliubov (HFB) method and quasiparticle random phase approximation (QRPA).

In HFB, the spatial structure of the two-component single-quasiparticle wave function is determined not only by the single-particle energy and ℓ but also by pairing correlations, and the asymptotic behaviors of the lower component $v_{lj}(E_{lj,n}, r)$ and the upper component $u_{lj}(E_{lj,n}, r)$ are different because of the boundary conditions at infinity.[1] The spatial structure of the pairing density

$$\tilde{\rho}(r) = -\frac{1}{4\pi r^2}\sum_{lj,n}(2j+1)u_{lj}(E_{lj,n},r)v_{lj}(E_{lj,n},r)$$

is determined by the competition between the spatial extent of the lower and upper components, and it is very sensitive to ℓ. Because of the strong coupling to continuum states, the contribution of the quasiparticle states with low-ℓ to the pairing density has a spatially large extent that leads to the enhancement of the pairing energy as approaching the neutron drip line[2] (see Fig. 1).

The similar competitive mechanism brings about the strong transition strength of low-frequency vibrational excitations. Within the QRPA, vibrational excitations are described by the coherent superposition of two-quasiparticle states, and the coherency is sensitive to the spatial structure defined by

$$F^{(ph)}_{kk'}(\vec{r}) = u_k(E_k,\vec{r})\,\hat{O}(\vec{r})\,v_{k'}(E'_{k'},\vec{r})\,. \qquad (1)$$

Here, $\hat{O}(\vec{r})$ is one-body transition operator, and $\hat{O}(\vec{r}) = r^2Y_2(\hat{r})$ for isoscalar quadrupole excitations. In Fig. 2, the $B(E2, 0^+_1 \rightarrow 2^+_1)$ values in neutron-rich Ni isotopes obtained by the HFB plus QRPA calculation with Skyrme SLy4 force are shown. The strong coherent motions among weakly bound neutrons, and the correlations between neutrons and protons lead to the large $B(E2)$ values. By comparing the results of QRPA with the resonant BCS approximation and RPA, the crucial role of the change in the spatial structure of the quasiparticle wave functions by pairing correlations in HFB is evident.[2]

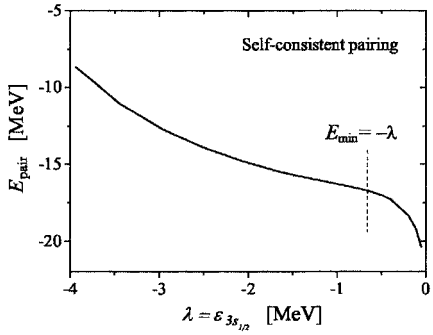

Fig. 1. The pairing energy obtained by the Woods-Saxon potential plus HFB pairing model is shown as a function of $\lambda = \varepsilon_{3s_{1/2}}$. The boundary of the continuum region, where all quasiparticle states are in the continuum, is indicated.

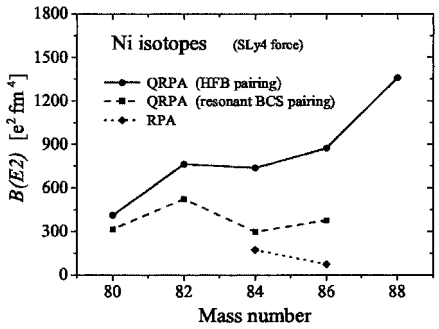

Fig. 2. The $B(E2, 0^+_1 \rightarrow 2^+_1)$ values in neutron-rich Ni isotopes obtained by HFB plus QRPA, resonant BCS plus QRPA, and RPA calculations with Skyrme SLy4 force.

References

1) J. Dobaczewski, W. Nazarewicz, T. R. Werner, J. F. Berger, C. R. Chinn, and J. Dechargé: Phys. Rev. C **53**, 2809 (1996).
2) M. Yamagami: Phys. Rev. C **72**, 064308 (2005).

Calculations of lowest 2^+ states of Ni isotopes using quasiparticle random-phase approximation

J. Terasaki*

[Nuclear structure, quasiparticle random-phase approximation, unstable nuclei]

The study of unstable nuclei is one of the important subjects in current nuclear physics. A question may be addressed for the neutron-rich unstable region as follows: since the neutron drip line is anticipated to be far from the stable line, many of the nuclei in the region have much more excess neutrons than excess protons. Then the nuclear surface may consist of only the neutrons with a tail longer than that of the protons. In addition, coupling effects become important between the discrete- and continuum-energy single-particle states, as the neutron number approaches the drip lines. Do any new features, then, appear in the observables of excited states? In this report, we show results of the calculations of the lowest 2^+ states of even Ni nuclei from the proton to neutron drip lines using the quasiparticle random-phase approximation (QRPA) with the Skyrme and volume-type pairing interactions (for details of the method, see Ref. 1).

The results and experimental data are shown in Fig. 1. The Ni isotopic chain has a rise in the energy E_{2+} and a downward slope of the transition probability $B(E2; 0^+ \rightarrow 2^+)$ at $N = 28$ and 40 in the experimental data. Normally, this behavior is attributed to the magic number; that is, there is a shell gap at the neutron chemical potential of the ground state. It is known, however, that ^{68}Ni does not show any irregularity in the systematics of the two-neutron separation energy; thus, this nucleus is not doubly magic. This anomaly is explained in terms of the single-particle level scheme.[5] Since the Ni isotopic chain has an anomaly as ^{68}Ni, it is necessary to investigate if there occur any other anomalies in more neutron-rich Ni.

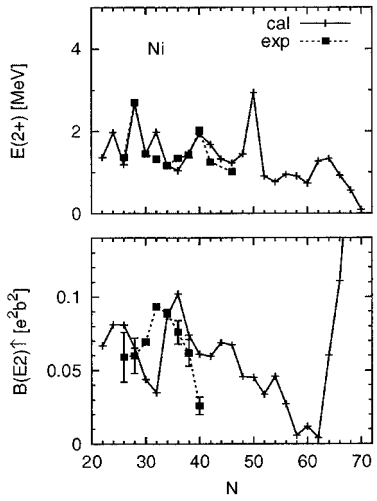

Fig. 1. Energies (upper) and $B(E2; 0^+ \rightarrow 2^+)$ (lower) of lowest 2^+ states of even Ni isotopes. The experimental data were taken from Refs. 2–4. The Skyrme parameter set SkM* and the volume-type delta pairing interaction are used.

The energies are reproduced well by the calculation with the parameter set SkM*. The peak of the theoretical transition probability at $N = 36$ is, however, shifted from the experimental data, and the decrease at $N = 40$ of the calculation is not enough. Currently, no anomaly is found at the neutron-rich frontier of this chain concerning the experimental data of the lowest 2^+ states.

The calculation predicts a decrease in $B(E2; 0^+ \rightarrow 2^+)$ values for $N > 46$ on average until $N = 58$. We have performed the QRPA calculations also using the parameter sets SLy4 and SkO′. The global behaviors of those calculations are similar to that of the SkM* calculation; however, the $B(E2; 0^+ \rightarrow 2^+)$ values of SLy4 is twice that of the SkM* calculation at $N = 34$ and 36, and an eigenvalue of the QRPA equation with SkO′ was found to be imaginary for the two nuclei — therefore, the ground states of SkO′ are deformed. The transition probabilities with SLy4 and SkO′ are almost 0 at $N = 40$. These three calculations have very similar $B(E2; 0^+ \rightarrow 2^+)$ values at each of $N = 28,\ 38,\ 46$, and 50, and these values are close to the experimental data at $N = 28$ and 38. Thus, it will be interesting to see if the predictions at $N = 46$ and 50 are realistic.

The author thanks the members of Motobayashi Heavy-Ion Nuclear Physics Laboratory for valuable discussions.

References

1) J. Terasaki et al.: Phys. Rev. C **71**, 034310 (2005).
2) S. Raman et al.: At. Data Nucl. Data Tables **78**, 1 (2001).
3) S. Kanno et al.: Private communication.
4) K. Yamada et al.: Eur. Phy. J. A **25**, Suppl. 1, 409 (2005).
5) K. Langanke et al.: Phys. Rev. C **67**, 044314 (2003).

* School of Physics, Peking University, P.R. China

Shape coexistence of $N = 20$ isotopes studied by the Monte Carlo shell model

Y. Utsuno,[*1] T. Otsuka,[*2] T. Mizusaki,[*3] and M. Honma[*4]

[Nuclear structure, shell model, unstable nuclei]

It has been recently argued[1] that shell structure narrowing toward unstable nuclei plays a primary role in the disappearance of the magic structure. In the case of the $N = 20$ region, the SDPF-M interaction introduced in a previous paper[2] has such a feature. It is then of much interest to examine the validity of this narrowing shell structure by comparing between experiment and theory.

It is well established that $N = 20$ isotones near the stability line have several low-lying states dominated by the intruder state (i.e. the one with two-particle two-hole excited configurations beyond the $N = 20$ core). Since their positions are sensitively influenced by the $N = 20$ shell gap, they are a good measure for the present purpose. In this study, we systematically investigate the position of the intruder state obtained by Monte Carlo shell model (MCSM) calculation with the valence shell including part of the pf shell. The numerical computations have been carried out with the Alphleet and Alphleet-2 parallel computer systems as a RIKEN-CNS collaboration project on large-scale nuclear structure calculations.

Figure 1 compares the energy levels of ^{36}S between experiment and calculation. Whereas for the sd-shell calculation some levels such as the 0_2^+ ones are missing, the MCSM calculation, incorporating the lower part of the pf shell, has succeeded in reproducing most of them. This agreement indicates that the width of the shell gap in the SDPF-M interaction adopted in the present study is appropriate. Together with the results of our calculations for unstable nuclei,[3] the $N = 20$ shell gap most probably varies in moving from stable to unstable nuclei.

We finally stress the importance of the full-configuration shell-model calculation by MCSM. In Fig. 2, the location of the intruder state by MCSM is compared with the locations with truncated calculations, revealing that the result strongly depends on the truncation scheme adopted. Hence, not until the correlation is properly taken into account can one discuss the position of the intruder state and its relation to the shell gap.

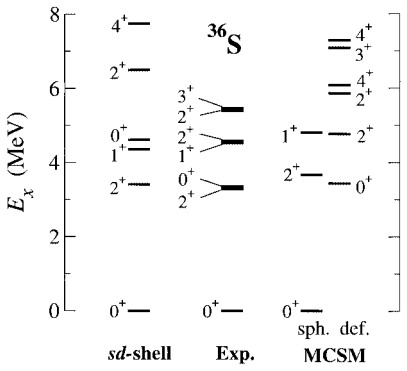

Fig. 1. Energy levels of ^{36}S compared between experiment and shell-model calculations (see the text for details).

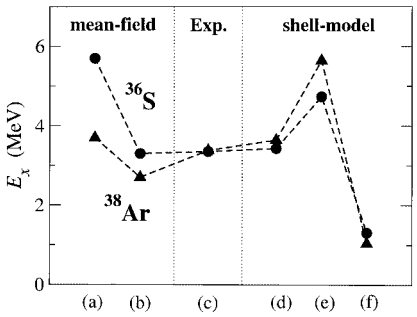

Fig. 2. Excitation energies of the 0_2^+ states in ^{36}S and ^{38}Ar compared between the experiment (Exp.) (c) and shell-model calculations with various truncations. (a) and (b) are the mean-field (Hartree-Fock) approximation with and without the angular-momentum projection, respectively. (d), (e) and (f) denote spherical-shell-model based truncations: (d) is the MCSM calculation, while (e) and (f) correspond to calculations by truncating up to the $2p2h$ excitation with and without the mixing of the $0p0h$ configurations, respectively.

*1 Japan Atomic Energy Agency
*2 Department of Physics and Center for Nuclear Study, University of Tokyo
*3 Institute of Natural Sciences, Senshu University
*4 Center for Mathematical Sciences, University of Aizu

References

1) T. Otsuka, R. Fujimoto, Y. Utsuno, B. A. Brown, M. Honma, and T. Mizusaki: Phys. Rev. Lett. **87**, 082502 (2001).
2) Y. Utsuno, T. Otsuka, T. Mizusaki, and M. Honma: Phys. Rev. C **60**, 054315 (1999).
3) Y. Utsuno, T. Otsuka, T. Glasmacher, T. Mizusaki, and M. Honma: Phys. Rev. C **70**, 044307 (2004).

A search for a unified effective interaction for Monte Carlo shell model calculations (VII)†

M. Honma,[*1] T. Otsuka,[*2,*3] B. A. Brown,[*4] and T. Mizusaki[*3,*5]

[Shell model, effective interaction]

The Monte Carlo shell model[1] (MCSM) has enabled us to apply the nuclear shell model to various problems in a huge model space. We have been investigating[2] a possibility to construct an effective interaction which can be used for a unified description of many nuclei in a huge model space with a reasonable predictive power, and have published a possible solution GXPF1[3] for pf-shell nuclei. Since the GXPF1 was determined by using experimental energy data mainly of stable nuclei, it is a challenging test to apply this interaction to describe/predict the structure of unstable nuclei.

Figure 1 shows excitation energies $E_x(2_1^+)$ for Ca, Ti and Cr isotopes. It is seen that the GXPF1 successfully describes the variation of E_x for all these isotope chains, including the increase of E_x at $N = 28$ shell closure. Another increase of E_x appears at $N = 32$, which can be interpreted as an indication of a shell gap resulting from the spin-orbit splitting between the $p_{3/2}$ and $p_{1/2}$ orbits. One interesting result obtained by GXPF1 is the third increase of E_x at $N = 34$ for Ca and Ti, which is attributed to the energy gap between the neutron $f_{5/2}$ and $p_{1/2}$ orbits. However, it turned out that the measured $E_x(2_1^+)$ for ^{56}Ti was lower than the GXPF1 prediction by 0.4 MeV.[5] A good correspondence between the measured and the calculated high-spin level structure for ^{54}Ti suggests the validity of the predicted effective single-particle energy (ESPE) for the $p_{3/2}$ and $f_{5/2}$ orbits at least near $N = 32$.[6] Therefore, we have searched for a solution of this problem without modifying the ESPE of these orbits.

We have found that the following two modifications are enough: (1) The monopole pairing strengths between the orbits $f_{7/2}$-$f_{7/2}$, $f_{5/2}$-$p_{1/2}$, and $p_{1/2}$-$p_{1/2}$ are made more repulsive by 0.2, 0.5 and 0.5 MeV, respectively. (2) The strength of a quadrupole-quadrupole (QQ) interaction $[(f_{5/2})^\dagger(\tilde{p}_{1/2})]^{(2)} \cdot [(p_{1/2})^\dagger(\tilde{f}_{5/2})]^{(2)}$ is made much stronger, i.e., changed from -0.23 to -0.58 MeV, keeping the monopole centroid unchanged. In total, five two-body matrix elements have been modified. This modified GXPF1 is referred to as GXPF1A. It can be seen in Fig. 1 that GXPF1A gives better description of the systematics of $E_x(2^+)$ than GXPF1 for almost all nuclei. We have confirmed that it is also true for high-spin states of ^{54}Ti. In ^{54}Ca, $E_x(2^+)$ is decreased from 3.8 MeV to 3.0 MeV. Nevertheless, this excitation energy is higher than that of ^{52}Ca (2.56 MeV experimentally), suggesting the appearance of the $N = 34$ shell closure in the Ca isotopes.

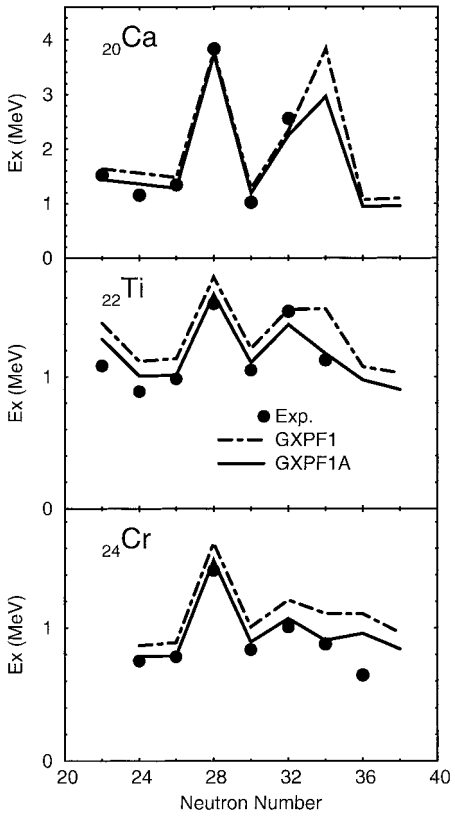

Fig. 1. Systematics of $E_x(2_1^+)$. Experimental data (closed circle) are compared to shell-model results obtained by a code MSHELL[4] with effective interactions GXPF1 (dod-dashed line) and GXPF1A (solid line).

References

1) T. Otsuka et al.: Phys. Rev. Lett. **81**, 1588 (1998).
2) M. Honma et al.: RIKEN Accel. Prog. Rep. **33**, 16 (2000); RIKEN Accel. Prog. Rep. **34**, 15 (2001); RIKEN Accel. Prog. Rep. **35**, 12 (2002); RIKEN Accel. Prog. Rep. **36**, 21 (2003); RIKEN Accel. Prog. Rep. **37**, 17 (2004); RIKEN Accel. Prog. Rep. **38**, 29 (2005).
3) M. Honma et al.: Phys. Rev. C **65**, 061301(R) (2002); Phys. Rev. C **69**, 034335 (2004).
4) T. Mizusaki: RIKEN Accel. Prog. Rep. **33**, 14 (2000).
5) S. N. Liddick et al.: Phys. Rev. Lett. **92**, 072502 (2004).
6) R. V. F. Janssens et al.: Phys. Lett. B **546**, 55 (2002).

† Condensed from the article in Eur. Phys. J. A **25**, Suppl. 1, 499 (2005)

*1 Center for Mathematical Sciences, University of Aizu
*2 Department of Physics, University of Tokyo
*3 Center for Nuclear Study, University of Tokyo
*4 National Superconducting Cyclotron Laboratory and Department of Physics and Astronomy, Michigan State University, USA
*5 Institute of Natural Sciences, Senshu University

Origin of $J = 0$ dominance in two-body random interaction†

N. Shimizu*1 and T. Otsuka*1,*2

[Nuclear structure, shell model, quantum chaos]

The properties of the ground state with a random interaction have been attracting much interest since Johnson, Bertsch and Dean reported that the angular momentum of such a ground state is predominantly $J = 0$.[1)] In other words, in a shell model calculation in the *sd* shell with 6 neutrons, the ground-state spin becomes $J = 0$ with a probability of 76% with randomly generated two-body matrix elements, whereas only 9.8% of the Hilbert space of 6 neutrons in the *sd* shell is $J = 0$.[1)]

Since this striking report,[1)] many studies have been carried out.[2–5)] The major points can be summarized as follows.

(1) A $J = 0$ ground state is dominant even if the pairing interaction is switched off in a random interaction.
(2) No collectivity can be seen.
(3) No general connection to symmetries has been established.

In particular, the basic mechanism for the preponderance of the $J = 0$ ground state is not yet established, except for special cases with some algebraic structures.[3,4)] We briefly show a possible mechanism in this report.

As in previous works,[1–5)] the following shell model Hamiltonian is diagonalized:

$$H = \Sigma_{ijklL} v^{(L)}_{ijkl} ([a^\dagger_i a^\dagger_j]^{(L)} [a_l a_k]^{(L)}), \quad (1)$$

where some mathematical details are omitted for brevity. Here, i, j, k and l denote single-particle orbits, L means their coupled angular momenta, and v stands for a two-body matrix element. In the discussions below, the v's are generated as random numbers so as to obey the Gaussian distribution, and this system is usually called a two-body random ensemble (TBRE). In the Hamiltonian above, single-particle energies are assumed to be zero because they are not essential.

In considering the properties of the ground state of the random interaction discussed above, we propose the following Ansatz.

- A certain type of random interaction mixes various states strongly in a chaotic manner without preferences, in eigenstates of a many-body system.
- In this situation, the binding energy can become maximum when the wave function is invariant with respect to transformations of coordinates, because all orientations should be equal.
- The highest symmetries are then given to the ground state; a distortion of the wave function results in a loss of binding energy.

At this point, we note that a randomly generated interaction does not necessarily fulfill the above feature of mixing. Namely, such an interaction can have certain dynamics *accidentally*. If such an accidental dynamics is absent, a random two-body interaction may mix various states with no preferred orientation in any sense. The invariance with respect to orientation occurs in the level of a many-body wave function. Thus, the quantum chaotic mixing can produce the maximum binding energy, while the wave function acquires the highest symmetry for its relevant transformation. This will be called the chaotic realization of (highest) symmetry.

The application of the above mechanism to the rotational invariant system causes the ground state for an even number of particles to be of $J = 0$. This is the case well known from Ref. 1. The same mechanism is also applied to systems having isospin symmetry (T) and parity symmetry (P), which leads us to conclude that the ground state for an even number of particles should be of $P = +$ and $T = 0$. The detailed verification of this mechanism and its applications can be found in Ref. 6.

This work was supported by grants from the MEXT of Japan, including a Grant-in-Aid for Specially Promoted Research (13002001), and by the RIKEN-CNS project on nuclear structure calculation.[7)]

References

1) C. W. Johnson, G. F. Bertsch, and D. J. Dean: Phys. Rev. Lett. **80**, 2749 (1998).
2) R. Bijker and A. Frank: Phys. Rev. Lett. **84**, 420 (2000); Phys. Rev. C **62**, 014303 (2000).
3) P. Chau Huu-Tai, A. Frank, N. A. Smirnova, and P. Van Isacker: Phys. Rev. C **66**, 061302 (2002).
4) Y. M. Zhao, A. Arima, and N. Yoshinaga: Phys. Rev. C **66**, 064322 (2002); Phys. Rev. C **66**, 064323 (2002).
5) M. Horoi, A. Volya, and V. Zelevinsky: Phys. Rev. C **66**, 024319 (2002).
6) T. Otsuka and N. Shimizu: AIP Conf. Proc. **777**, 135 (2004).
7) N. Shimizu, T. Otsuka, N. Itagaki, T. Mizusaki, M. Honma, and Y. Utsuno: Annu. Rep. 2004, Center of Nuclear Study, University of Tokyo, 95, (2004).

† Condensed from the article in AIP Conf. Proc. **777**, 135 (2004).

*1 Department of Physics, University of Tokyo
*2 Center for Nuclear Study, University of Tokyo

Estimation of ground-state energy and spin-zero dominance

N. Yoshinaga,[*1] A. Arima, and Y. M. Zhao[*2]

[Nuclear shell model, spin-zero dominance]

The ground states of all even-even nuclei have angular momenta equal to zero, $I = 0$, and positive parity, $\pi = +$. This feature was believed to be a consequence of the attractive short-range interaction between nucleons. However, a predominance of $I^\pi = 0^+$ ground states was discovered by Johnson, Bertsch and Dean in 1998 using the two-body random ensemble (TBRE).[1] Since then many efforts have been devoted to understanding and solving this problem from various viewpoints. See Ref. 2 for a recent review. The purpose of this Report is to obtain a semi-empirical formula for evaluating the ground-state energy in terms of the average energy (centroid), the standard deviation (width), and the number of spin I states. On the basis of this formula, we study the problem of spin-zero ground state (0 g.s.) dominance in the presence of the TBRE.

In order to simplify our argument, we take a single j^n configuration for fermions. The Hamiltonian that we take is as follows:

$$\hat{H} = \sum_{J=0,\mathrm{even}}^{2j-1} \sqrt{2J+1}\, G_J \left[A^{\dagger(J)} \tilde{A}^{(J)}\right]^{(0)}, \qquad (1)$$

where G_J's are two-body interactions between fermions, and are assumed to follow the TBRE,

$$\rho(G_J) = \frac{1}{\sqrt{2\pi}} \exp\left(-G_J^2/2\right). \qquad (2)$$

Then the variance of eigenenergies around the average energy (the width squared) is denoted as

$$\left(\sigma_I\left\{G_J\right\}\right)^2 \equiv \frac{1}{d_I} \mathrm{Tr}\left[\left(\hat{H} - \bar{E}_I\right)^2\right], \qquad (3)$$

where d_I indicates the dimension of the Hamiltonian matrix.

Let us estimate the ground-state energy of the Hamiltonian $\hat{H}$ by assuming that it can be expressed in terms of the average energy ($\bar{E}_I$), the width ($\sigma_I\left\{G_J\right\}$) and the number of states (d_I) as

$$E_I^{(\mathrm{min})} = \bar{E}_I - \Phi(d_I)\, \sigma_I\left\{G_J\right\}, \qquad (4)$$

where $\Phi(d_I)$ is assumed to depend only on the dimension of the Hamiltonian matrix and to take the following form:

$$\Phi(d_I) = \sqrt{a \ln d_I + b}. \qquad (5)$$

Here, the parameters $a = 0.99$ and $b = 0.36$ are determined phenomenologically.

In Fig. 1 (a), we show $P(0)$'s of four fermions in single-j shells. The diamonds are obtained by performing 1000 runs of the TBRE Hamiltonian. The squares are the empirical prediction,[3] $P_{\mathrm{emp}}(0)$'s, and the triangles are the results of the present method (the width-prediction method). It is seen that both predictions well describe the staggering behavior of $P(0)$'s, although a slight disagreement in the case of the empirical prediction is seen for $j = 27/2$ and $j = 29/2$. In Fig. 1 (b), $P(I^{\max})$'s are shown for three cases. It is seen that a slight staggering of the TBRE results is better reproduced by the width-prediction method proposed in this paper.

To summarize, we proposed a new analytical expression to evaluate the ground-state energy of spin I states. With this simple formula, a remarkably successful description of the spin I ground-state probabilities was obtained in the presence of the TBRE.

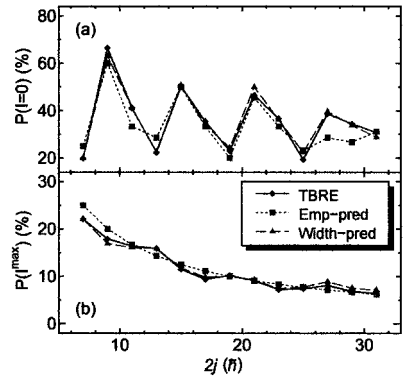

Fig. 1. (a) $P(0)$'s of four fermions in single-j shell. The diamonds are obtained by performing 1000 runs of the TBRE Hamiltonian. The squares are obtained by the emp-prediction method and the triangles, by the width-prediction method. (b) The same figure as in (a), but for $P(I^{\max})$.

References

1) C. W. Johnson, G. F. Bertsch, and D. J. Dean: Phys. Rev. Lett. **80**, 2749 (1998).
2) Y. M. Zhao, A. Arima, and N. Yoshinaga: Phys. Rep. **400**, 1 (2004).
3) Y. M. Zhao, A. Arima, and N. Yoshinaga: Phys. Rev. C **66**, 034302 (2002).

*1 Department of Physics, Saitama University
*2 Department of Physics, Shanghai Jiao Tong University, China

Band structure in doubly-odd nuclei with mass around 130†

K. Higashiyama*1 and N. Yoshinaga*2

[Nuclear structure, pair-truncated shell model, chopsticks configurations]

A number of $\Delta I = 1$ doublet bands built on the unique-parity $0h_{11/2}$ valence neutron and proton orbitals have been observed in many doubly-odd nuclei in the mass $A \sim 130$ region. These bands had been interpreted as the manifestation of "chirality" by Frauendorf and Meng using the three-dimensional tilted axis cranking model.[1] Theoretical investigations of the doublet bands were carried out within the framework of the phenomenological core-particle-hole coupling model[2,3] and the particle-rotor model,[4,5] and the results supported the interpretation of the doublet bands of the chiral structure. These models, however, disregarded the intrinsic degrees of freedom of the even-even core.

Recently, we have studied the band structure with the $\nu h_{11/2} \otimes \pi h_{11/2}$ configuration in the doubly-odd nuclei in the mass region by means of a pair-truncated shell model (PTSM).[6] In the PTSM, the shell-model basis states of doubly-odd nuclei are constructed by adding an unpaired neutron and an unpaired proton to the even-even core, which consists of angular momentum zero (S) and two (D) collective pairs. In this work we use the pairing plus quadrupole type interaction, whose force strengths are determined to reproduce the energy levels of the even-even nuclei in the mass $A \sim 130$ region.[6]

The theoretical partial level scheme with the $\nu h_{11/2} \otimes \pi h_{11/2}$ configuration for ^{134}La is shown in Fig. 1. The solid arrows indicate $E2$ transitions, and the dotted arrows indicate $M1$ transitions. The numerals on the right side of the $E2$ transitions denote the $B(E2; I \to I-2)$ values (in $e^2\mathrm{b}^2$), and those beneath the $M1$ transitions denote the $B(M1; I \to I-1)$ values (in μ_N^2). The states within four $\Delta I = 2$ $E2$ bands with the bandhead states of 8_1^+, 9_1^+, 10_1^+ and 11_1^+ are connected by the strong $E2$ transitions to the same members of the $\Delta I = 2$ $E2$ bands, and by the strong $M1$ transitions to the states in the neighboring $\Delta I = 2$ $E2$ bands. This result reproduces well the experimental energy levels of the yrast and yrare bands, and the ratios $B(M1; I \to I-1)/B(E2; I \to I-2)$ for the yrast states.

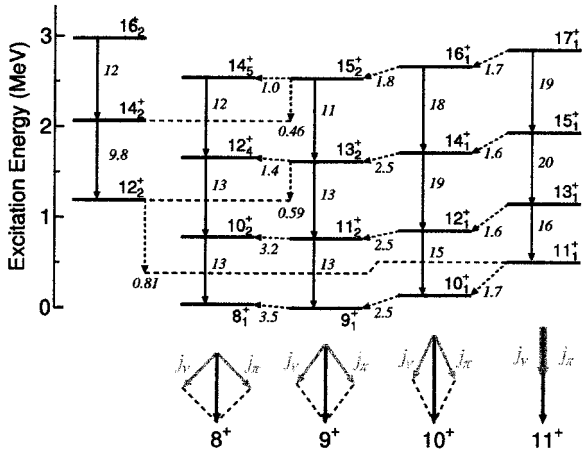

Fig. 1. Partial level scheme of ^{134}La by PTSM calculation.

In search of the microscopic origin of electromagnetic properties, we analyze the reduced matrix elements of $M1$ operators, and compare the $B(M1)$ values for the two-nucleon system of one neutron and one proton both in the same $0h_{11/2}$ orbital with those of actual calculations. We also calculate the effective angles between the angular momenta of the neutrons and protons in the $0h_{11/2}$ orbitals. The closing of two angular momenta enhances the $B(M1)$ values, and the odd-spin yrast states (I) ($I \geq 11$) have a fully aligned configuration of two angular momenta with angular momentum 11. Similarly, the even-spin yrast states ($I-1$), odd-spin states ($I-2$) and even-spin states ($I-3$) are formed mainly with the configurations of angular momenta 10, 9, and 8, respectively. The schematic illustrations of these configurations (chopsticks configurations) are presented below each $\Delta I = 2$ $E2$ band in Fig. 1. Since quadrupole collectivity plays an important role in describing the $\Delta I = 2$ $E2$ bands, we conclude that the level scheme of ^{134}La arises from the chopsticks configurations of the unpaired nucleons in the $0h_{11/2}$ orbitals, weakly coupled with the quadrupole collective excitations of the even-even part of the nucleus. Similar situations are also obtained in ^{132}Cs, ^{130}Cs and ^{132}La.

References

1) S. Frauendorf and J. Meng: Nucl. Phys. A **617**, 131 (1997).
2) K. Starosta et al.: Phys. Rev. C **65**, 044328 (2002).
3) T. Koike et al.: Phys. Rev. C **67**, 044319 (2003).
4) D. J. Hartley et al.: Phys. Rev. C **64**, 031304(R) (2001).
5) J. Peng, J. Meng, and S. Q. Zhang: Phys. Rev. C **68**, 044324 (2003).
6) N. Yoshinaga and K. Higashiyama: Phys. Rev. C **69**, 054309 (2004).

† Condensed from the article in Phys. Rev. C **72**, 024315 (2005)

*1 Department of Physics, University of Tokyo
*2 Department of Physics, Saitama University

Backbending phenomena in $A \sim 130$ region described using a pair-truncated shell model†

N. Yoshinaga*1 and K. Higashiyama*2

[Nuclear structure, pair-truncated shell model, backbending phenomena]

Until now, many theoretical investigations have been carried out on low-lying states of even-even nuclei with mass around 130, which exhibit many interesting features from the soft triaxial deformation. However, there is a limited number of microscopic researches on backbending phenomena around spin 10 due to the difficulty of a theoretical treatment. Recently, we have proposed the pair-truncated shell model (PTSM) that describes the nuclear collective motions and the excitations of single-particle degrees of freedom on the same footing.[1,2)]

In the SD+H version of the PTSM,[1)] an even-nucleon system is constructed from angular momentum zero (S) and two (D) collective pairs, and non-collective H pairs, which are made by two nucleons in the $0h_{11/2}$ orbital, on the closed-shell core $|-\rangle$ as

$$|S^{n_s} D^{n_d} H^{n_h} I\eta\rangle = (S^\dagger)^{n_s} (D^\dagger)^{n_d} (H^\dagger)^{n_h} |-\rangle\,, \qquad (1)$$

where I is the total spin of the nuclear state, η is an additional quantum number required to completely specify the system, and $2(n_s + n_d + n_h)$ is the number of valence nucleons. Then, a basis state of any even-even nucleus is constructed as a product of $|S_\nu^{n_s} D_\nu^{n_d} H_\nu^{n_h} I_\nu \eta_\nu\rangle$ and $|S_\pi^{n_s} D_\pi^{n_d} H_\pi^{n_h} I_\nu \eta_\pi\rangle$. In the present calculation, we use the pairing plus quadrupole type interactions.

In Fig. 1, the energy spectrum obtained by the PTSM is compared with experimental data for ^{132}Ce. The calculation reproduces well the energy levels of the even-spin yrast band, especially the sudden decrease of level spacing occurring between the 10_1^+ and 12_1^+ states. The calculated quasi-γ band appears lower in energy than that in the experiment, but the 5_1^+ and 6_2^+ states are higher in energy. However, our results give a good description of the staggering seen in 2_2^+, 3_1^+, 4_2^+, and 5_1^+ states in the quasi-γ band.

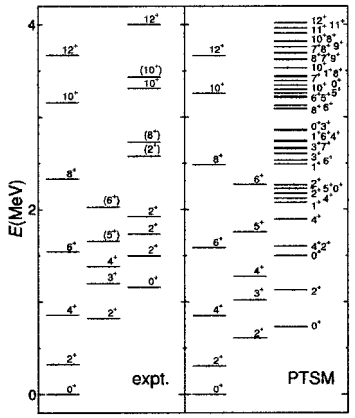

Fig. 1. Experimental energy levels of ^{132}Ce (expt.) compared with those of PTSM calculation.

In Fig. 2, calculated $B(E2)$ values in the yrast band are compared with the experimental data for ^{132}Ce. For low-spin states, we suspect that experimental data might be erroneous, because theoretically it is impossible to produce a smaller value for $B(E2; 4_1^+ \to 2_1^+)$ than $B(E2; 2_1^+ \to 0_1^+)$ in any existing collective models. A salient feature of the backbending phenomena is the appearance of a drop in the experimental $B(E2)$ value, and it is confirmed that such a behavior is well simulated by the PTSM.

From the results of the expectation numbers of D and H pairs (results not shown), it is found that the S and D collective pairs play essential roles in describing the low-lying states, and the effect of the alignment of two $0h_{11/2}$ neutrons becomes apparent above 10_1^+ states. We conclude that the truncation scheme extended to the SD+H subspace by including the intruder configurations provides an effective and minimal shell model space just enough to describe the yrast band, γ band and backbending phenomena.

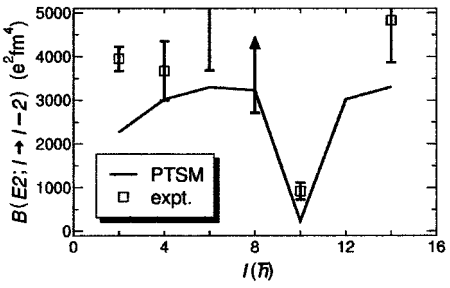

Fig. 2. Comparison of yrast $B(E2)$ values in PTSM with experimental data (expt.).

† Condensed from the article in Phys. Rev. C **71**, 014305 (2005)

*1 Department of Physics, Saitama University
*2 Department of Physics, University of Tokyo

References

1) K. Higashiyama, N. Yoshinaga, and K. Tanabe: Phys. Rev. C **67**, 044305 (2003).
2) N. Yoshinaga and K. Higashiyama: Phys. Rev. C **69**, 054309 (2004); K. Higashiyama, N. Yoshinaga, and K. Tanabe: Phys. Rev. C **72**, 024315 (2005).

Self-consistent random-phase approximation at finite temperature within the picket-fence model

N. Dinh Dang, A. Volya,[*1] and K. Tanabe[*2]

[Nuclear structure, random-phase approximation, canonical and grand canonical ensemble]

The random-phase approximation (RPA) is recognized as a powerful method for treating collective dynamics of small amplitudes motion in many-body systems. As with any approximate theory extensions and improvements immediately followed the original technique. One of major extensions of the RPA is the so-called finite-temperature random-phase approximation (FT-RPA)[1)] for the microscopic description of highly excited nuclei (hot nuclei). Here, as in the standard statistical approach to nuclear study, the observables are replaced with the average over the statistical ensemble at a given temperature T, which corresponds to the excitation energy. Traditionally, in the construction of FT-RPA equations, the collective dynamics is built on thermodynamic states, which are assumed to have particle occupation numbers given by the Fermi-Dirac distribution of free particles, neglecting the correlations between them. The correctness of this substitution has been taken for granted for years, although it is clear that the single-particle occupation numbers in general should not follow the distribution of free particles because of correlations between them generated by interactions.

In the present paper the self-consistent RPA (SCRPA)[2)] has been extended to finite temperature, where the single-particle occupation number is calculated self-consistently. The use of the double-time Green function's method releases the present approach from the constraints of perturbation theory and allows the calculations of the single-particle damping to be carried out in a straightforward manner. The focus of the present study is the region where the BCS has no solution but the RPA is still well valid, so that a recourse to the SCRPA is highly desirable. The results of numerical calculations performed within the picket-fence model of pairing, whose details are given in,[2)] show that, except for the lowest-energy level, the results obtained within the SCRPA are rather similar to those given by the RPA, where the occupation numbers are assumed to have the form of the Fermi-Dirac distribution for non-interacting fermions. As compared to the RPA, the SCRPA indeed offers a slightly better agreement with the exact solutions for the thermodynamic quantities such as the total energy and excitation energy as functions of temperature. Nonetheless, the difference from 1 (0) for the hole (particle) occupation numbers obtained at $T \sim 0$ within the SCRPA because of the ground state correlations beyond RPA does not affect significantly the integrated quantities obtained within the RPA such as the energy-weighted sum of strength and Landau splitting. This indicates that, in realistic calculations for high-lying states such as giant resonances, the conventional RPA at finite temperature might be sufficient and more convenient than the computationally expensive SCRPA. For the first excited states, however, cares should be taken, in particular for light systems at the large interaction strength, to ensure that the correlation effects are properly included.

References

1) A. V. Ignatyuk: *Statistical Properties of Excited Atomic Nuclei* (Energoatomizdat, Moscow, 1983); M. H. Sommermann: Ann. Phys. (N.Y.) **51**, 163 (1983); D. Vautherin and N. Vinh Mau: Nucl. Phys. A **422**, 140 (1984); N. Dinh Dang: J. Phys. G **11**, 125 (1985); K. Tanabe and K. Sugawara-Tanabe: Phys. Lett. B **172**, 129 (1986); N. Dinh Dang: Z. Phys. A **335**, 253 (1990); K. Tanabe and N. D. Dang: Phys. Rev. C **62**, 024310 (2000).

2) J. Dukelsky and P. Schuck: Phys. Lett. B **464**, 164 (1999); J. G. Hirsch, A. Mariano, J. Dukelsky, and P. Schuck: Ann. Phys. **296**, 187 (2002); N. D. Dang: Phys. Rev. C **71**, 024302 (2005).

*1 Department of Physics, Florida State University, USA
*2 Department of Physics, Saitama University

Effect of thermal pairing within thermal shape-fluctuation model on giant-dipole-resonance width at low temperature

P. Arumugam* and N. Dinh Dang

[Nuclear structure, giant dipole resonance, thermal shape fluctuations, pairing]

One of the key issues, which remain to be understood about the hot and rotating nuclei, is the variation of the width of giant dipole resonance (GDR) as a function of temperature (T) and spin (I). Thermal shape fluctuation models,[1] which are quite successful in hot GDR studies, have failed to explain the recently observed low-T quenching of the GDR width. Microscopic models such as the phonon damping model attribute this behavior to the fluctuations in the pairing field.[2] In the present work, for the first time, we attempt to explain this behavior in a relatively macroscopic approach. We have taken care of pairing fluctuations along with the thermal shape fluctuations to calculate the GDR width in hot nuclei. The free energies are calculated using the Nilsson-Strutinsky method extended to finite temperature and taking care of the pairing correlations properly. The GDR observables are related to the shape of the nuclei through a simple anisotropic harmonic oscillator model with a separable dipole-dipole interaction. Considering the fluctuations, the observables are averaged over the shape parameters and pairing gap.

Our study reveals that the observed quenching of GDR width at low T in the nuclei ^{120}Sn and ^{148}Au can be understood in terms of simple shape effects caused by the pairing correlations. The fluctuations in pairing leads to a slowly vanishing pairing gap and hence influence the structural properties even at moderate temperatures ($\sim$1 MeV). We observe that the low-T structure and hence the GDR width are quite sensitive to the change of the pairing field (See Fig. 1). This enables us to validate the pairing prescription and the parameters involved. We infer that if the the fluctuations are treated properly, GDR could be more precise in yielding the structure information.

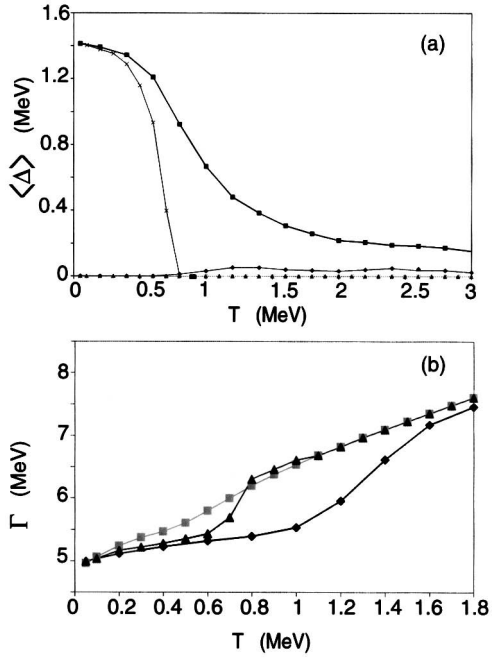

Fig. 1. (a) Pairing gaps for ^{120}Sn averaged over thermal shape fluctuations versus temperature. Lines with triangles and crosses are the usual BCS proton and neutron pairing gaps, respectively, while those with diamonds and squares denote the corresponding pairing gaps, which also include thermal fluctuations of pairing fields. (b) GDR widths for ^{120}Sn versus temperature. Lines with squares, triangles, and diamonds denote the widths obtained without pairing, including BCS pairing, and thermally fluctuating pairing field from (a), respectively.

References

1) W. E. Ormand, P. F. Bortignon, and R. A. Broglia: Phys. Rev. Lett. **77**, 607 (1966).

2) N. D. Dang and A. Arima: Phys. Rev. Lett. **80**, 4145 (1998); N. D. Dang and A. Arima: Nucl. Phys. A **636**, 427 (1998).

* Centro de Física das Interacções Fundamentais, Instituto Superior Técnico, Portugal

Study of nuclear structure change in framework of 3D-CHFB + GCM

Y. Hashimoto[*1] and T. Horibata[*2]

[HFB, tilted axis rotation, generator coordinate method]

Description of nuclei within the mean field approximation has been considered as an extremely effective approach and it helps us to understand the dynamics of nuclear collective motion either from the qualitative or quantitative point of view. The combination of the Hartree-Fock-Bogoliubov theory and the cranking model, CHFB, provides us a powerful tool in analyzing the characteristic feature of nuclear collective motion and has revealed the intimate mechanism underlying the nuclear rotational motion step by step. We expect that the rotational motion of a deformed nucleus can take place about an axis which is tilted from the principal axes of the mass quadrupole moment, tilted-axis rotation (TAR), besides the occurrence of the usual principal-axis rotation (PAR).[1–3] Recently, a band structure which represents the wobbling motion occurring about one of the principal axes has been observed.[4,5] Since the wobbling mode is considered as a quantum mechanical motion, it requires the existence of nuclear fully asymmetric shape in three-dimensional space.

The question we address is the following: What are the microscopic relationships among the PAR, wobbling motion and TAR? We have started a project on establishing a theoretical framework with the purpose of understanding the microscopic mechanism underlying the generation of the wobbling motion and the transformation into the TAR from a unified viewpoint. We take advantage of the traditional generator coordinate method (GCM) based on the CHFB in building up the mean field. In the ideal case, the nuclear quadrupole moments and the angles of the rotation vector tilted from the principal axes are treated as the generator coordinates. In the practical case, however, the quadrupole moments are evaluated in the mean field approximation. Attention is paid to the coordinates of the angles of the rotation vector so that we can cover the physically important area in an effective way. Horibata and Onishi performed the GCM calculations based on the two-dimensional cranking along the prime meridian. They have pointed out several interesting modes of motion including TAR and wobbling motion within the restricted space on the prime meridian.[1)]

We are now at the stage of trial and error to set up a suitable coordinate system which covers the physical area including the wobbling motion and TAR in the three-dimensional space of angles of the rotation vector. The GCM norm kernel in ^{182}Os with the angular momentum $J = 18$ is calculated in the restricted area of the "north-east" quarter region including the cranking solution about the principal x-axis, using the pairing plus quadrupole (P+QQ) force. In Fig. 1, we show the overlap between the wave function of the PA rotation and each wave function of the tilted-axis CHFB on the mesh points. The PAR state with $J = 18$ is in the band crossing region, where Horibata and Onishi pointed out that the γ -deformation changes markedly from the g-band to the s-band.[1)] Nevertheless, no remarkable change in the norm kernel is seen in the figure when we go to the east from the prime meridian. We are now investigating the nuclear structure change in a wide area including the band crossing region.

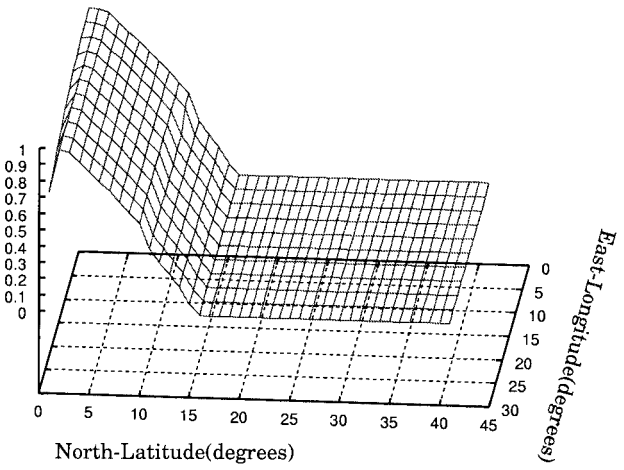

Fig. 1. Example of norm overlap kernel.

References

1) T. Horibata and N. Onishi: Nucl. Phys. A **596**, 251 (1996).
2) S. Frauendorf: Rev. Mod. Phys. **73**, 463 (2001).
3) A. Bohr and B. R. Mottelson: *Nuclear Structure*, Vol.II (Benjamin, Reading, New York, 1975).
4) S. W. Ødegård et al.: Phys. Rev. Lett. **86**, 5866 (2001).
5) I. Hamamoto and G. B. Hagemann: Phys. Rev. C **67**, 014319 (2003).

*1 Graduate School of Pure and Applied Sciences, University of Tsukuba
*2 Faculty of Software and Information Technology, Aomori University

Decay modes of heavy and superheavy nuclei predicted by KTUY mass formula†

H. Koura*1 and T. Tachibana*2

[Binding energies and masses, α decay, β decay, decay by proton emission, spontaneous fission, $220 \leq A$]

We present a chart of decay modes for α-decay, β-decay, proton emission and spontaneous fission ranging from light nuclei to superheavy nuclei including unknown ones using a phenomenological atomic mass formula[1] and some decay models. A bulk term of this mass formula is expressed as a function of proton number Z, neutron number N and mass number A to represent the global feature of atomic masses. Microscopic features including shell effect and deformation are calculated from a modified Woods-Saxon single-particle potential.[2] These calculated masses are applied to the estimation of the decay Q values of α-decay, β-decay and proton emission. For the calculation of the decay rates of α-decay, proton emission and spontaneous fission, a one-dimensional WKB method is applied.[3] Beta decay rate is calculated using the gross theory.[4]

Figure 1 shows the calculated partial half-lives of these four decays along $Z = 101$. One of the notable features is that spontaneous fission is quite sensitive to nucleon number because of the shell effect. The curves of proton emission and α decay increase with neutron number, but the proton curve increases more steeply. The β-decay line is almost flat far off the β-stable region in comparison with other decay modes. (The peak at $N = 154$ comes from even-odd effect with small Q values.)

Figure 2 shows estimated dominant decay modes in the nuclear chart including the superheavy nuclidic region. We find some regions of fissioning nuclei at about $Z \approx 108$, $N \approx 168$, and nuclei from $Z \approx 100$, $N \approx 190$ to heavier nuclei. The former region is qualitatively consistent with recent experimental α-decay chains measured at Dubna, which terminate by fission. The latter region indicates that the production of suspected double-magic super heavy nucleus $^{298}[114]_{184}$ by the r-process nucleosynthesis in supernova is not expected because β-decay after the r-process near $A \approx 300$ or more is impeded by fission in that region (See Fig. 2). We also calculate total half-lives in the "island of stability for the superheavy nuclei," and obtain $^{294}\mathrm{Ds}_{184}$ as the α-decay-dominant nucleus with the longest half-life on the β-stability line of our mass formula of the order of 100 years, having an ambiguity of 100–1/100 times.

We also estimate nuclei beyond the superheavy ones and find the next "island of stability" on $N = 228$ in the neutron-poor region. This results from the larger fission barrier height due to the shell closure of 228 for neutrons. Another region with a similar property is located near $N = 126$ outside the proton drip line. In the neutron-rich region, most nuclei are β-decay-dominant and have relatively long total half-lives at least in the order of 1 ms. The partial half-lives of other decays are longer than that of β-decay.

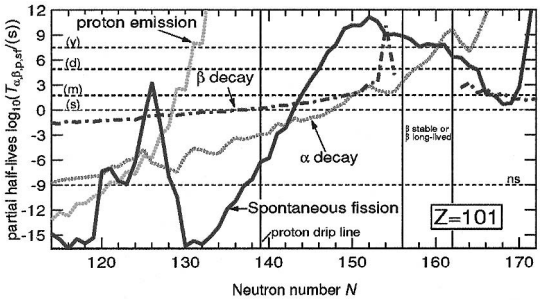

Fig. 1. Transition of partial half-lives of four decay modes along $Z = 101$.

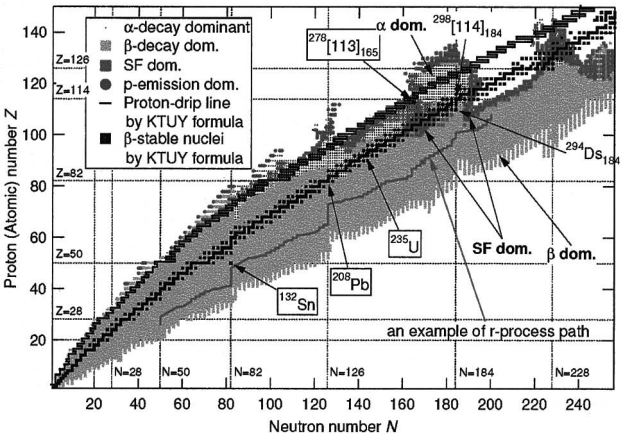

Fig. 2. Shortest partial half-lives among α-decay, β-decay, spontaneous fission and proton emission.

† Condensed from the part of article in Butsuri (Bull. Phys. Soc. Jpn.) **60**, 717 (2005)

*1 Advanced Science Research Center, Japan Atomic Energy Agency

*2 Advanced Research Institute for Science and Engineering, Waseda University

References

1) H. Koura et al.: Prog. Theor. Phys. **113**, 305 (2005).
2) H. Koura et al.: Nucl. Phys. A **671**, 91 (2000).
3) H. Koura: AIP Conf. Proc. **704**, 60 (2004), .
4) T. Tachibana et al.: Proc. Int. Conf. on Exotic Nuclei and Atomic Masses, Arles, France, 1995-6, edited by M. de Simon and O. Sorlin (Editions Frontueres, Gif-Yvette, 1995), p. 763.

Development of 2-D supernova model for r-process nucleosynthesis

Y. Motizuki and H. Madokoro

[Supernova explosion, nucleosynthesis]

Rapid neutron-capture process (r-process) nucleosynthesis is necessary to explain the origin of about half the natural elements heavier than iron. The r-process is one of the most complex nucleosynthesis to explore because of the numerous difficulties still affecting the description of both the explosive astrophysical conditions believed to induce the process and the nuclear properties of the exotic neutron-rich nuclei involved.

It should be noted that the r-process site has remained totally unknown to date. Currently, no astrophysical model can consistently predict the neutron densities required for a successful r-process. The "hot bubble" or postexplosion outflows expected from protoneutron stars within seconds after successful core-collapse supernovae[1] is thought to be a likely candidate site. However, recent models of spherical (1-D) neutrino-driven winds from protoneutron stars fail to induce robust r-process nucleosynthesis up to and beyond the third ($A \approx 195$) r-process peak.[2] Nevertheless, core-collapse supernovae are generally believed to be the first candidate to induce r-process nucleosynthesis.

Under this situation in which 1-D nucleosynthesis may have difficulties occurring, we developed an axially symmetric (2-D) supernova model to be applied to r-process nucleosynthesis. Our numerical code was based on Ref. 3, in which the mechanism of core-collapse supernovae was investigated. The following points were our main concerns in the development of the 2-D model.

(1) The "butterfly structure" that appeared in the vicinity of the z-axis in Ref. 3 was removed.
(2) The simulated space was enlarged up to 60,000 km: The equation of state employed was updated accordingly.
(3) Neutrino-matter interactions and the electron degeneracy parameter were incorporated without approximations that are valid under high-temperature and high-density conditions, which are usually considered in simulations of the core-collapse phase and initial (< 500 ms) evolution phase after the explosion.
(4) The outer boundary condition was changed.
(5) Neutrino luminosity decay and the time evolution of the electron fraction were considered.
(6) Nuclear statistical equilibrium was incorporated with an accurate treatment of the partition function.

The simulated time was then extended to several seconds after the shock stall. Figures 1 and 2 show the entropy distributions in 1-D and 2-D models, respectively. Here, the initial neutrino temperature was taken to be 5.4 MeV for both models. Comparing Figs. 1 and 2, we see that entropy evolution remarkably differs between 1-D and 2-D calculations. Since nuclear reaction rate is determined by the local temperature and density found in entropy maps, it is naturally expected that the resulting nucleosynthesis in the 2-D model will be very different from that in the 1-D model. The r-process nucleosynthetic calculations employing these models as input of a supernova environment are in progress.

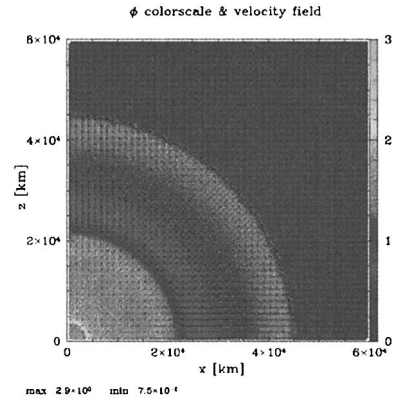

Fig. 1. Entropy map in our 1-D supernova model 4.7 sec after shock stall.

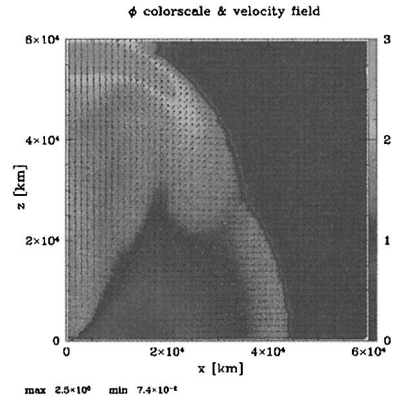

Fig. 2. The same map as that in Fig. 1, but for 2-D model.

References

1) S. E. Woosley et al.: Astrophys. J. **433**, 229 (1994).
2) K. Takahashi et al.: Astron. Astrophys. **286**, 857 (1994).
3) T. Shimizu et al.: Astrophys. J. **552**, 756 (2001).

2-D simulation of core-collapse supernova explosion caused by anisotropic neutrino flux

H. Madokoro, T. Shimizu, and Y. Motizuki

[Shock waves, hydrodynamics, stars:neutron, supernova:general]

We study the mechanism of core-collapse supernovae by using two-dimensional numerical code. Special attention is paid to effects of anisotropic neutrino radiation from the proto-neutron star on the explosion dynamics. We have shown[1–3] that anisotropy of $\sim$ 5–10 percent in the neutrino radiation can greatly increase the explosion energies when the total neutrino luminosity is fixed, and then lead to a successful explosion. In these studies, however, the profile of anisotropy in the neutrino flux was assumed because we did not solve the region inside the proto-neutron star. It is expected that anisotropy will naturally appear as a result of multidimensional effects such as rotation and convection in the course of core-collapse, bounce, and shock propagation. Therefore, as the next step, we have performed two-dimensional core-collapse simulations starting from the rotating progenitor model developed by Heger et al.[4]

Figure 1 shows a contour plot of entropy distribution with velocity fields at $t = 20$ ms after bounce. It is seen that the shock wave is stalled at $r \sim 100$ km. The radius of the neutrino sphere is $r \sim 52$ km (on the pole) and ~ 55 km (on the equatorial plane), which is deformed in a oblate shape due to rotation. We can estimate the degree of anisotropy in the neutrino flux as follows: If the deformed neutrino sphere is regarded as a Maclaurin spheroid, the ratio of the neutrino flux along the polar axis (l_z) to that on the equatorial plane (l_x) becomes $l_z/l_x = R_x/R_z$,[1] where R_x and R_z represent the equatorial and polar radius of the neutrino sphere, respectively. Our calculation gives $R_x/R_z \sim 1.05$. This implies that the neutrino flux has an anisotropy of $\sim 5\%$.

In Fig. 2, a result of our previous study with assumed anisotropy[1–3] is shown. We can see that the anisotropy of $\sim 5\%$, which we obtained in the present core-collapse simulation, is sufficient to increase the explosion energy compared with that of the spherical model.

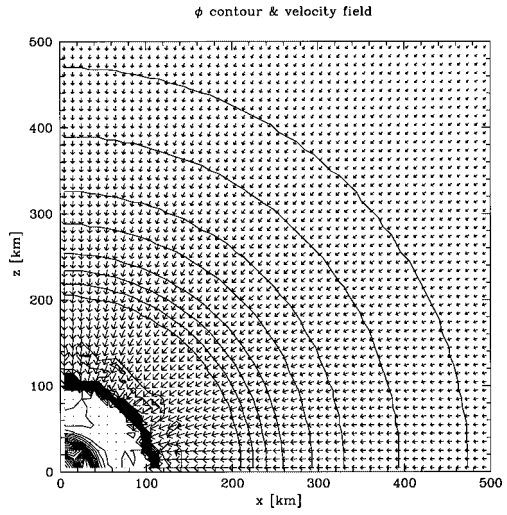

Fig. 1. Contour plot of entropy distribution with velocity fields at $t = 20$ ms after bounce for rotating model. The stalled shock wave is represented by crowded contour lines at $r \sim 100$ km. The deformed neutrino sphere is located at $r \sim 52$–55 km.

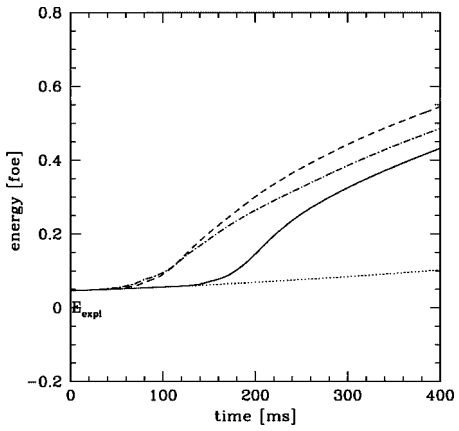

Fig. 2. Evolution of explosion energies for models under assumption of anisotropic neutrino radiation: anisotropy of 5% (solid line), of 10% (dashed line), of 15% (dot-dashed line), and spherical explosion (dotted line). Note that anisotropic models will explode, while the spherical model fails.

References

1) T. M. Shimizu et al.: Astrophys. J. **552**, 756 (2001).
2) H. Madokoro, T. Shimizu, and Y. Motizuki: Astrophys. J. **592**, 1035 (2003).
3) H. Madokoro, T. Shimizu, and Y. Motizuki: Pub. Astron. Soc. Jpn. **56**, 663 (2004).
4) A. Heger et al.: Astrophys. J. **528**, 368 (2000).

EOS dependence of supernova neutrinos from the collapse of massive stars

K. Sumiyoshi,[*1,*2] S. Yamada,[*3] H. Suzuki,[*4] and H. Toki[*5]

[Equation of state, supernova, neutrino]

Massive stars having more than ∼10 solar masses ($M_\odot$) end their lives by the gravitational collapse after the iron core is formed. For the massive stars of ∼10–20 $M_\odot$, the spectacular events known as supernova explosions occur through the launch of shock wave by the bounce of core at high density. Stars more massive than ∼20 $M_\odot$ may have different fates since they usually have larger iron cores. They are too massive to have the stellar explosion and the outcome will be a formation of black hole. The detection of neutrinos is a clear and unique identification of such events and it is important to quantitatively predict the neutrino signals from the black hole formation.

To predict the time profile of neutrino burst and the energy spectrum of neutrinos during the evolution, we perform elaborated simulations of ν-radiation hydrodynamics under the spherical symmetry.[1)] We follow the evolution from the beginning of gravitational core-collapse to find when and how the black hole is formed from a massive star. In order to determine the final fate, we perform the simulations for a long time scale (∼1 s), which has not been explored before.

The microphysics such as equation of state (EOS) of dense matter is playing significant roles[2)] in the ν-radiation hydrodynamics. In order to assess the influence of dense matter, we adopt two sets of realistic EOS for the simulations of black-hole-forming massive stars. We make comparisons of the evolutions of central core from the initial collapse up to the black hole formation for the first time. This enables us to probe dense matter at extremely high density and temperature through the properties of neutrino signals.

The subroutine of EOS by Lattimer and Swesty (LS-EOS),[3)] which is a conventional choice, is based on the compressible liquid drop model for nuclei together with dripped nucleons. On the other hand, the data table of EOS by Shen et al. (SH-EOS)[4)] is newly constructed in the relativistic nuclear many body frameworks. It is to be noted that the nuclear interaction to derive SH-EOS is constrained by the properties of unstable nuclei, which are available recently in radioactive nuclear beams facilities.

The average energies of neutrinos emitted from the central core of a 40 $M_\odot$ star in two simulations with LS-EOS and SH-EOS are shown as a function of time after bounce in Fig. 1. The rise of average energies comes from the temperature increase by the contraction of newly born neutron stars since its mass increases due to the matter accretion. The mass of neutron star finally exceeds the maximum mass and the black hole is formed by the dynamical collapse. The end points in the figure correspond to the births of black hole. It is interesting that the different timing of black hole formation for models with LS-EOS and SH-EOS is reflected in the different timing of the termination of neutrino emissions. The LS-EOS is softer than SH-EOS, therefore, it leads to the smaller maximum mass and the earlier formation of black hole. This difference in neutrino signals will provide us with the information on EOS.[5)] A terrestrial detection of neutrino bursts from the black hole formation in future will put a new constraint on the EOS at high density and temperature.

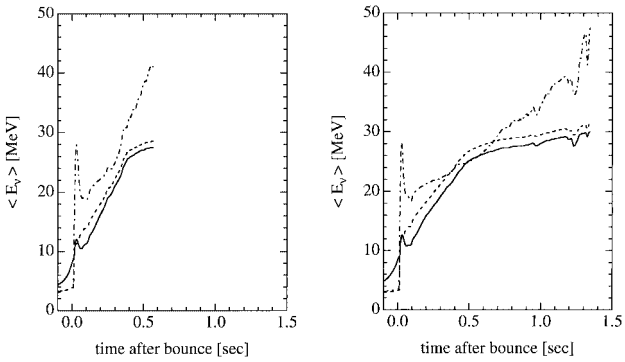

Fig. 1. Average energies of ν_e (solid), $\bar{\nu}_e$ (dashed) and $\nu_{\mu/\tau}$ (dot-dashed) as a function of time after bounce in two simulations with LS-EOS (left) and SH-EOS (right).

*1 Numazu College of Technology
*2 National Astronomical Observatory of Japan
*3 Science & Engineering, Waseda University
*4 Faculty of Science and Technology, Tokyo University of Science
*5 Research Center for Nuclear Physics, Osaka University

References

1) K. Sumiyoshi, S. Yamada, H. Suzuki, H. Shen, S. Chiba, and H. Toki: Astrophys. J. **629**, 922 (2005).
2) K. Sumiyoshi, H. Suzuki, S. Yamada, and H. Toki: Nucl. Phys. A **730**, 227 (2004).
3) J. M. Lattimer and F. D. Swesty: Nucl. Phys. A **535**, 331 (1991).
4) H. Shen, H. Toki, K. Oyamatsu, and K. Sumiyoshi: Nucl. Phys. A **637**, 435 (1998).
5) K. Sumiyoshi, S. Yamada, H. Suzuki, and S. Chiba: submitted to Phys. Rev. Lett.

Momentum correlation in the three-body decay of high-density $\bar{K}$ nuclear clusters: $NNNK^- \to N + N + \Lambda^\dagger$

P. Kienle,[*1] Y. Akaishi,[*2] and T. Yamazaki[*3]

[Kaonic nuclei]

A method is proposed to probe the size of dense $\bar{K}$ nuclear clusters[1–4] by observing the momentum correlation in their 3-body decay products, such as $[pppK^-]_{(T=1)} \to \Lambda + p + p$ and $[ppnK^-]_{(T=0)} \to \Lambda + p + n$. The calculated momentum correlation pattern expressed in a Dalitz plane shows characteristic features, reflecting the size/density and the angular momentum of the parent $\bar{K}$ cluster, as shown in Fig. 1. The ridges on the right-hand and left-hand sides correspond to the "participant" proton and the "spectator" proton, respectively. For the "normal core" the ridges are very sharp, peaked around at X_{max} and at X_{min}, reflecting that the spectator nucleon carries out only a small momentum. On the other hand, for the "shrunk core," the variation is very much broadened, since the spectator nucleon takes out a larger momentum and in turn the participants momenta are reduced. Thus, the nuclear shrinkage predicted can be experimentally examined by observing the three-body correlation.

References

1) Y. Akaishi and T. Yamazaki: Phys. Rev. C **65**, 044005 (2002).
2) T. Yamazaki and Y. Akaishi: Phys. Lett. B **535**, 70 (2002).
3) A. Doté, H. Horiuchi, Y. Akaishi, and T. Yamazaki: Phys. Lett. B **590**, 51 (2004).
4) A. Doté, H. Horiuchi, Y. Akaishi, and T. Yamazaki: Phys. Rev. C **70**, 044313 (2004).

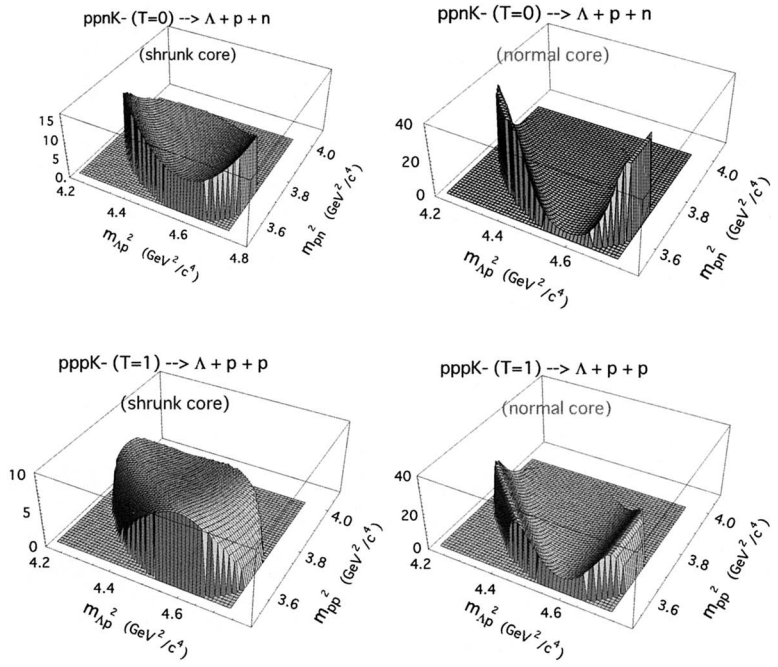

Fig. 1. Calculated density distributions in three-dimensional presentation of Dalitz plots in the decay of $ppnK^-(T=0)$ (Upper) and $pppK^-(T=1)$ (Lower) of $M = 3115\,\mathrm{MeV}/c^2$. (Left) "shrunk core" and (Right) "normal core."

† Condensed from the article in Phys. Lett. B **632**, 187 (2006)

*1 Technische Universität München and Stephan Meyer Institute, Germany
*2 College of Science and Technology, Nihon University
*3 Department of Physics, University of Tokyo

Shear viscosity coefficient studied by molecular dynamics

Y. Akimura,[*1,*2] T. Maruyama,[*2] N. Yoshinaga,[*1] and S. Chiba[*2]

[Quark gluon plasma, viscosity, molecular dynamics]

From experimental analyses,[1–3] it is considered that quark gluon plasma (QGP) produced in RHIC is not a weakly coupled gas but a strongly coupled liquid. The ratio of shear viscosity to entropy is a good criterion for determining whether a system behaves as a gas or a liquid. A theoretical study by quenched lattice QCD was performed on the matter viscosity at above the critical temperature.[4] The viscosity per entropy density η/s was found to be much smaller than 1, which indicates the matter is extremely smooth. However, the dynamics of quarks and anti-quarks, which seems very important, was not considered in the study. Here, we study the shear viscosity of quark matter by molecular dynamics (MD) which is a natural framework for investigating dynamical quantities.

We prepare a cubic box in which the same number of u, d quarks and their anti-quarks are contained, and impose a periodic boundary condition. The number of quarks and anti-quarks for $q\bar{q}$ matter is determined using a derivative of the thermodynamical potential with respect to the chemical potential, where no interaction is assumed. To simulate quark many-body system at a finite temperature, we give appropriate initial values for the position and momentum of i-th quark, $\mathbf{R}_i$ and $\mathbf{P}_i$, and solve the following equations,

$$\dot{\mathbf{R}}_i = \frac{\partial H}{\partial \mathbf{P}_i}, \quad \dot{\mathbf{P}}_i = -\frac{\partial H}{\partial \mathbf{R}_i}, \tag{1}$$

where H is the Hamiltonian used in Ref. 5 without the meson exchange potentials. The equations of motion were solved for several thousands fm/c after the system reached equilibrium. The shear viscosity η can be calculated using the Green-Kubo relation,[6]

$$\eta = \frac{1}{T_{\rm eff} V} \int_0^\infty \big\langle J_{xy}(t) \cdot J_{xy}(0) \big\rangle dt, \tag{2}$$

where $T_{\rm eff}$ is the effective temperature defined in Ref. 7 and J_{xy} is the stress tensor in the x-y direction,

$$J_{xy}(t) = \sum_{i=1}^{N} \left(x_i \cdot \left(-\frac{\partial H}{\partial y_i} \right) + \frac{\partial H}{\partial P_{i,x}} \cdot P_{i,y} \right). \tag{3}$$

To discuss the ratio of the shear viscosity to the entropy density, thermodynamic quantities in MD are calculated as

$$s = \frac{\varepsilon + P}{T_{\rm eff}}, \; PV = NT_{\rm eff} + \frac{1}{3} \sum_{i=1}^{N} \mathbf{R}_i \cdot \left(-\frac{\partial H}{\partial \mathbf{R}_i} \right), \tag{4}$$

where s is the entropy density, ε is the energy density and P is the pressure.

Simulation is performed using a box size of 10 fm for a low-temperature region and 4 fm for a high-temperature region. Figure 1 shows the ratio of shear viscosity to the entropy density. In the low-temperature region, where quarks form mesons, η/s is larger than one. The value decreases as the temperature increases. Around 130 MeV, where quarks are deconfined, η/s takes a value smaller than one. This value is of the same order as that of the lattice calculation of Ref. 4 and suggests that quarks behave like a liquid. Above 130 MeV, η/s increases linearly. This means that the motion of quarks is more dominant than their interaction at high-temperature. If an effect of the asymptotic freedom was taken into account, η/s at high-temperature would become larger. The investigation of viscosity for the finite baryon density is in progress.

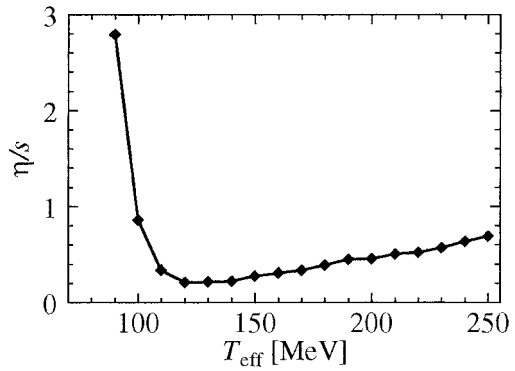

Fig. 1. Temperature dependence of ratio of shear viscosity to entropy density for $q\bar{q}$ matter.

[*1] Department of Physics, Saitama University
[*2] Japan Atomic Energy Agency

References

1) PHOBOS Collaboration, B. B. Back et al.: Nucl. Phys. A **757**, 28 (2005).
2) STAR Collaboration, J. Adams et al.: Nucl. Phys. A **757**, 102 (2005).
3) PHENIX Collaboration, K. Adcox et al.: Nucl. Phys. A **757**, 184 (2005).
4) A. Nakamura and S. Sakai: Phys. Rev. Lett. **94**, 072305 (2005).
5) Y. Akimura et al.: Eur. Phys. J. A **25**, 405 (2005).
6) J. P. Hansen and I. R. McDonald: *Theory of Simple Liquids, 2nd ed.* (Academic Press, London, 1986).
7) S. Chikazumi et al.: Phys. Rev. C **63**, 024602 (2001).

Color superconductivity and neutron star structure†

S. Lawley,*1 W. Bentz,*2 and A. W. Thomas*3

[Matter at high density, neutron matter]

The equation of state (EOS) at very high baryon densities, like in the center of a neutron star, is a very active field of recent research. Theoretically it is expected that the matter undergoes a phase transition from nuclear matter (NM) to quark matter (QM), where the latter is most likely in a color superconducting state (SQM). The basic parameter which controls this phase transition is the pairing strength between the quarks in the scalar diquark channel ($J = T = 0$, color $\overline{3}$). In this work, we report on the results for the equation of state of charge neutral matter in β-equilibrium and the masses of compact stars obtained by using the flavor SU(2) Nambu-Jona-Lasinio (NJL) model, which is an effective quark theory based on QCD.

The effective potential for NM is[1] $V^{\rm NM} = V_{\rm vac} + V_{\rm N} + V_\omega + V_\rho + V_{\rm e}$, where the vacuum term $V_{\rm vac}$ accounts for the polarization of the quark Dirac sea, $V_{\rm N}$ represents the Fermi motion of the nucleons which are described as quark-diquark bound states in the NJL model, V_ω and V_ρ arise from the isoscalar and isovector mean vector fields respectively, and $V_{\rm e}$ is the electron contribution. For QM we have[2] $V^{\rm QM} = V_{\rm vac} + V_{\rm Q} + V_{\rm e} + V_\Delta$, where the vacuum and electron terms are as above and the term for the Fermi motion of the quarks $V_{\rm Q}$ is analogous to $V_{\rm N}$, but referring to up and down quarks. The effect of the quark pairing is expressed by the term V_Δ, which involves the gap and a coupling constant (G_s) for the pairing interaction in the scalar diquark channel, which we express as $G_s = r_s\, G_\pi$. Here r_s is a parameter, and the coupling constant in the pionic channel (G_π) is fixed by reproducing the pion mass. The NM/QM mixed state is constructed by using the Gibbs conditions of phase equilibrium.[3]

In Fig. 1 we show the EOS corresponding to the cases $r_s = 0$ and $r_s = 0.25$, and in Fig. 2 we show the resulting star sequences. (The results for the pure NM case are also shown for comparison.) In the first case, for central densities between $3.7\rho_0$ and $6.0\rho_0$ ($\rho_0 = 0.15\,\mathrm{fm}^{-3}$), stable hybrid stars exist with a NM/QM phase in the center. In the second case, stable hybrid stars exist with central densities between $2.3\rho_0$ and $5.0\rho_0$ with a very small region of NM/SQM mixed phase in the center, and for central densities between $6.0\rho_0$ and $15.0\rho_0$ stable quark stars exist, which are composed of SQM in the central region. Comparison of these two cases indicates that color superconductivity has a major effect on the EOS: With increasing r_s, both the density and the pressure for the phase transition to QM are reduced, the EOS becomes softer, and the star masses decrease for given central density.

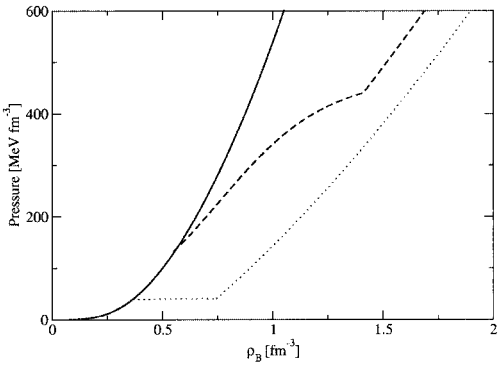

Fig. 1. Pressure vs. baryon density for pure NM (solid line) and the transition to QM for $r_s = 0$ (dashed line) and $r_s = 0.25$ (dotted line).

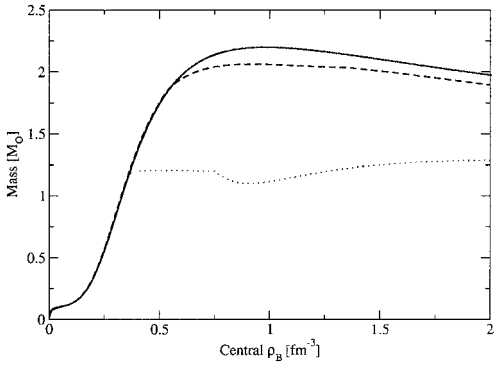

Fig. 2. Star masses vs. central density for the 3 cases of Fig. 1.

References

1) W. Bentz and A. W. Thomas: Nucl. Phys. A **696**, 138 (2001).
2) W. Bentz, T. Horikawa, N. Ishii, and A. W. Thomas: Nucl. Phys. A **720**, 95 (2003).
3) N. K. Glendenning: *Compact Stars* (Springer, New York, 2000).

† Condensed from an article by S. Lawley, W. Bentz, and A. W. Thomas: Phys. Lett. B **632**, 495 (2006)

*1 Department of Physics, University of Adelaide, Australia
*2 Department of Physics, Tokai University
*3 Jefferson Laboratory, USA

The polarized EMC effect†

I. C. Cloet,*1 W. Bentz,*2 and A. W. Thomas*1

[Nuclear structure functions, spin dependence, effective quark theories]

Recent works[1] have shown that the EMC effect for the spin-independent nuclear structure functions can be successfully described in terms of the self consistent scalar and vector fields which couple to the quarks inside the nucleons. The individual nucleons in this approach are described as bound states of a quark and a diquark, where both the scalar and axial vector diquark channels are taken into account.[2] Predictions for the spin-dependent counterpart of the EMC effect have also been made in this model.

The calculations of Ref. 1 have been carried out in nuclear matter, and in this work we present results for finite nuclei. First studies of the polarized EMC effect should concentrate on light to medium heavy nuclei with valence proton particles or holes carrying the nuclear spin. Examples are ^{11}B and ^{15}N, which have a relatively simple structure so that one can investigate the effects of the medium on the quark substructure without too many complications caused by the nuclear many body problem.

We report on the results for ^{11}B in this work. It is assumed that the nucleons move in average scalar and vector fields, for which we take Woods-Saxon forms for simplicity. From the wave functions we obtain the spin dependent light cone momentum distributions of the nucleons.[3] To get the quark distributions in the nucleons, we use the quark-diquark model of Ref. 2, where the mean nuclear fields are incorporated into the constituent quark and diquark propagators. The convolution formalism is then applied to calculate the quark light cone momentum distributions in the nucleus.

The results for the polarized up and down quark distributions for the $p_{3/2}$ proton hole state are shown in Fig. 1 for the low energy scale $Q_0 = 0.4\,\mathrm{GeV}$. The dotted line shows the distribution in a free proton, the dashed line shows the result including the effective mean scalar field which applies to the $p_{3/2}$ state, the dotted-dashed line shows the result including the Fermi motion, and the solid line also includes the effective mean vector field. Figure 2 shows the resulting polarized EMC ratio for the nucleus ^{11}B (dashed line) in comparison to the unpolarized one (solid line) and the experimental data for the ^{12}C nucleus. For the unpolarized case, where all nucleons contribute, this ratio is defined as usual by $\overline{F}_{2A}/F_{2N}$, where $\overline{F}_{2A}$ is the nuclear structure function per nucleon and F_{2N} is the average of the free proton and neutron structure functions. For the polarized case, the ratio is defined as $\frac{g_{1A}}{g_{1p}}/P$, where we divide out the nuclear polarization factor (P) so that the ratio becomes 1 for the case of no medium modifications. The comparison of these two ratios shows that the medium modifications are more important for the case of the spin-dependent structure function than for the spin-independent one.

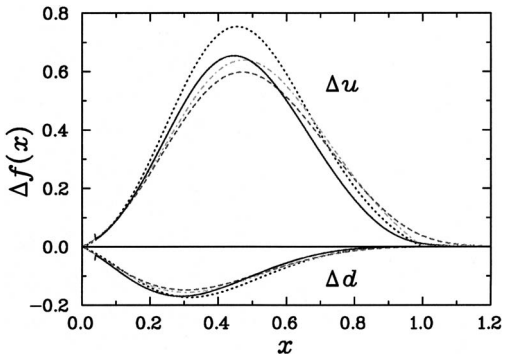

Fig. 1. The polarized up and down quark distribution for the $p_{3/2}$ proton state.

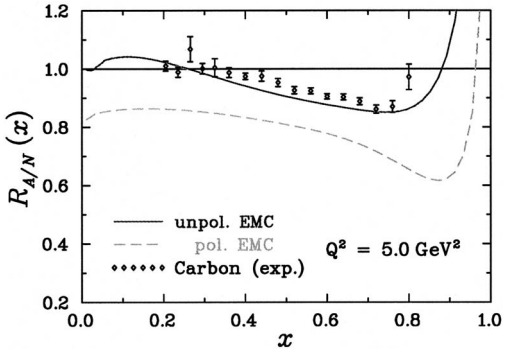

Fig. 2. Polarized (dashed line) and unpolarized (solid line) EMC ratios for ^{11}B. The experimental data of the unpolarized ratio for ^{12}C are shown for comparison.

References

1) I. C. Cloet, W. Bentz, and A. W. Thomas: Phys. Rev. Lett. **95**, 052302 (2005).
2) I. C. Cloet, W. Bentz, and A. W. Thomas: Phys. Lett. B **621**, 246 (2005).
3) R. L. Jaffe and A. Manohar: Nucl. Phys. B **321**, 343 (1989).

† Condensed from an article by I. C. Cloet, W. Bentz, and A. W. Thomas, to be published.

*1 Jefferson Laboratories, USA
*2 Department of Physics, Tokai University

Measurement of the vector analyzing power for the $\vec{p}$+^{6}He elastic scattering at 71 A MeV using polarized proton solid target

S. Sakaguchi,[*1] T. Uesaka,[*1] T. Wakui,[*2] N. Aoi, Y. Hashimoto,[*3] M. Ichikawa,[*4] Y. Ichikawa,[*5] K. Itoh,[*6] M. Itoh,[*2] H. Iwasaki,[*5] T. Kawabata,[*1] T. Kawahara,[*7] H. Kuboki,[*5] Y. Maeda,[*1] R. Matsuo,[*4] T. Nakao,[*5] H. Okamura,[*2] H. Sakai,[*5] N. Sakamoto, Y. Sasamoto,[*1] M. Sasano,[*5] Y. Satou,[*3] K. Sekiguchi, M. Shinohara,[*3] K. Suda,[*1] D. Suzuki,[*5] Y. Takahashi,[*5] A. Tamii,[*8] K. Yako,[*5] and M. Yamaguchi

[Nuclear structure, polarized target, unstable nuclei]

To extract a variety of spin-dependent information on nuclear reaction and the structure of unstable nuclei, we have constructed a polarized proton solid target applicable in RI beam experiments.[1] The target was first used in an experiment in 2003, where analyzing power was measured for the $\vec{p}$+^{6}He elastic scattering at 71 A MeV.[2] Here, we obtained a result that directly contradicts the predictions of optical models.[3,4]

To derive the underlying physics, we carried out an analyzing power measurement for the $\vec{p}$+^{6}He elastic scattering with higher statistics and improved resolution in 2005. Simultaneous with the analyzing power measurement, we also measured the target polarization via the $\vec{p}$+^{4}He elastic scattering at 80 A MeV whose analyzing power is already known.[5] The polarization measurement was carried out because the absolute value of the polarization cannot be, in our target, determined by nuclear magnetic resonance (NMR) measurement alone, whereas the value is required for the normalization of analyzing power.

The experiment was performed at RIKEN Accelarator Research Facility using a 92 A MeV ^{12}C primary beam. A 71 A MeV ^{6}He beam was separated using the RIKEN Projectile Fragment Separator (RIPS) and the beam bombarded the polarized proton solid target with a thickness of 113 mg/cm^2. The typical beam intensity was 300 kcps. The target material was a naphthalene crystal with a size of ϕ14 mm × 1 mm^t. For the elimination of spurious asymmetry, the direction of the polarization was reversed three times during the beam time by the 180-degree NMR pulse method. A schemetic view of the experimental setup is shown in Fig. 1. Leading particles were detected using a multiwire drift chamber (MWDC) and $\Delta E - E$ plastic scintillator hodoscopes with thicknesses of 5 and 100 mm. Recoiled particles were detected using single-wire drift chambers and CsI scintillators on the left and right sides of the beam line.

$\vec{p}$+^{4,6}He elastic scattering events were selected by identifying the particles and requiring a kinematical consistency for them. By counting left/right (L/R) scattering events in the cases of polarization up/down (↑/↓), we obtained yields as $N_L^{\uparrow}$, $N_R^{\uparrow}$, $N_L^{\downarrow}$ and $N_R^{\downarrow}$. Analyzing power and target polarization are deduced using the relation

$$A_y = \frac{1}{P_y} \frac{\sqrt{N_{\uparrow L} \cdot N_{\downarrow R}} - \sqrt{N_{\downarrow L} \cdot N_{\uparrow R}}}{\sqrt{N_{\uparrow L} \cdot N_{\downarrow R}} + \sqrt{N_{\downarrow L} \cdot N_{\uparrow R}}}, \quad (1)$$

by cancelling spurious asymmetry. The target polarization was 13.5±3.9% on the average and 19.7±5.6% at the maximum. The preliminary result of analyzing power is shown in Fig. 2 as indicated by the closed circles. Further analysis is now in progress.

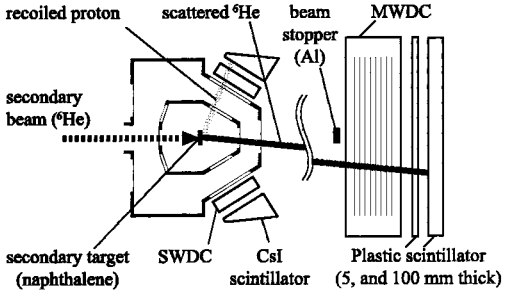

Fig. 1. Schematic view of experimental setup.

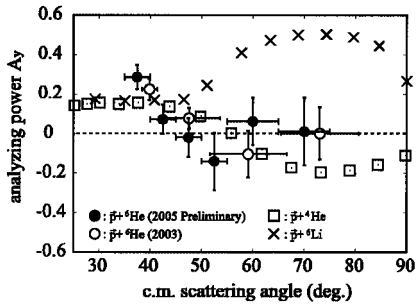

Fig. 2. Analyzing power for $\vec{p}$+^{6}He, ^{6}Li, and ^{4}He.

*1 Center for Nuclear Study, University of Tokyo
*2 Cyclotron and Radioisotope Center, Tohoku University
*3 Department of Physics, Tokyo Institute of Technology
*4 Department of Physics, Tohoku University
*5 Department of Physics, University of Tokyo
*6 Department of Physics, Saitama University
*7 Department of Physics, Toho University
*8 Research Center for Nuclear Physics, Osaka University

References

1) T. Wakui et al.: Nucl. Instrum. Methods Phys. Res. A **550**, 521 (2005).
2) M. Hatano et al.: Eur. Phys. J. A **25**, 255 (2005).
3) S. P. Weppner et al.: Phys. Rev. C **61**, 044601 (2000).
4) D. Gupta et al.: Nucl. Phys. A **674**, 77 (2000).
5) H. Togawa et al.: RCNP Ann. Rep. **1987**, 1.

Inelastic proton scattering of ^{6}He

Y. Hashimoto,[*1] T. Nakamura,[*1] Y. Satou,[*1] T. Sugimoto,[*1] Y. Kondo,[*1] N. Matsui,[*1] T. Okumura,[*1] T. Nakabayashi,[*1] M. Shinohara,[*1] N. Fukuda, S. Takeuchi, N. Aoi, T. Gomi, Y. Yanagisawa, T. Motobayashi, T. Kobayashi,[*2] H. Otsu, Y. Matsuda,[*2] N. Endo,[*2] M. Kitayama,[*2] Y. Togano,[*3] S. Kawai,[*3] H. Sakurai, H. J. Ong,[*4] T. K. Onishi,[*4] M. Tamaki,[*5] S. Shimoura,[*5] and M. Ishihara

[Nuclear reactions: ^{6}He(p,p′)^{6}He, inelastic proton scattering]

We have investigated the first 2^+ excited state at $E_x = 1.8$ MeV of ^{6}He by proton inelastic scattering. ^{6}He has a two-neutron halo structure characterized by a three-body nature with no bound binary subsystems, which is called the Borromean system. Previous theoretical studies predicted that the first 2^+ excited state of ^{6}He is a three-body related resonance.[1–3] Recently, the three-body breakup $^6\mathrm{He} \rightarrow {}^4\mathrm{He} + \mathrm{n} + \mathrm{n}$ was studied using a ^{6}He ion beam of 240 MeV/nucleon incident on carbon and lead targets at GSI.[4] At GANIL, inelastic proton scattering of ^{6}He was studied using a missing mass method, where they detected only ^{4}He and a recoiled proton.[5,6] Here, we study the structure of $^6\mathrm{He}(2^+)$ using an invariant mass method, where we have measured all the decay products from this state. We extract the energy spectrum and the angular distribution, which may have information on the three-body structure. We also study the two-body correlations by examining the Dalitz plot.

The experiment was performed at the RIPS beam line at the RIKEN Accelerator Research Facility. A secondary ^{6}He beam was produced using a 100 MeV/nucleon ^{18}O primary beam incident on a ^{9}Be target with a 1.1 g/cm^2 thickness. The secondary beam was purified through the RIPS separator, and was transported to the last focal point of RIPS (F3) where a secondary target of liquid hydrogen with a thickness of 229 mg/cm^2 was installed. Particle identification of the incident beam was achieved using the ΔE and time of flight (TOF) measured at the second focal point of RIPS (F2) event by event. The intensity of ^{6}He separated by RIPS was approximately 2×10^4 cps with a purity of 97%. The energy was 70 MeV/nucleon at F3. The position and incident angle of the secondary beam were measured using two parallel-plate avalanche counters. The magnetic spectrometer system equipped with a multiwire drift chamber, a drift chamber, and a plastic scintillator hodoscope (HOD) was used for detecting a charged particle fragment. Particle identification of this fragment was carried out by combining ΔE and TOF information from HOD, and magnetic rigidity information from the drift chambers. Three layers of plastic scintillator arrays were used for detecting two neutrons. The upstream, middle and downstream layers had 26, 30 and 30 pieces of plastic scintillator rod, respectively. The constituent rod of the first and second layers had dimensions of $6\times6\times214$ cm^3, and that of the third layer had dimensions of $6\times6\times108$ cm^3. By imposing the proper kinematical condition, we excluded cross-talk events, which could be mixed with true two-neutron events.

Figure 1 shows the preliminary relative energy spectrum of $^4\mathrm{He} + \mathrm{n} + \mathrm{n}$. We have analyzed this peak by fitting it with a Breit-Wigner parameterization for the resonance and arbitrary background function, which roughly explains the strength of approximately 2 MeV. The obtained resonance energy is 0.85±0.04 MeV in relative energy, which is consistent with the known value of 0.824.[4] The total inelastic cross section is 18.0±0.7(stat.)±1.9(syst.) mb (preliminary). Further analysis is now in progress including the study of three-body decay characteristics using the Dalitz plot.

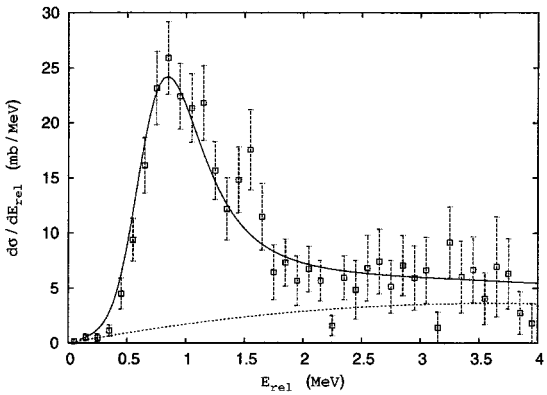

Fig. 1. Relative energy spectrum observed for ^{1}H(^{6}He, ^{4}He+n+n) reaction at 70 MeV/nucleon. The data are fitted with the Breit-Wigner function (solid curve) plus background (dashed curve).

*1 Department of Physics, Tokyo Institute of Technology
*2 Department of Physics, Tohoku University
*3 Department of Physics, Rikkyo University
*4 Department of Physics, University of Tokyo
*5 Center for Nuclear Study, University of Tokyo

References
1) B. V. Danilin et al.: Phys. Rev. C **55**, R577 (1997).
2) B. V. Danilin, I. J. Thompson, J. S. Vaagen, and M. V. Zhukov: Nucl. Phys. A **632**, 383 (1998).
3) E. Nielsen, D. V. Fedorov, A. S. Jensen, and E. Garrido: Phys. Rep. **347**, 373 (2001).
4) T. Aumann et al.: Phys. Rev. C **59**, 3 (1999).
5) A. Lagoyannis et al.: Phys. Lett. B **518**, 27 (2001).
6) S. V. Stepantsov et al.: Phys. Lett. B **542**, 35 (2002).

Confirmation of validity of s-wave approximation for ^{6}Li(d,p$_0$) reaction at incident energy of 90 keV

M. Yamaguchi, Y. Tagishi, and M. Tanifuji*

[Nuclear reaction, resonance]

We confirmed the validity of the s-wave approximation for ^{6}Li(d,p$_0$) reaction. In our previous publications[1–3] we proposed a novel method for studying reaction mechanism by extracting resonant component from analyzing powers at very low incident energy, and applied it to the ^{6}Li + d reactions which are affected by a resonance level of ^{8}Be at E_x = 22.2 MeV. In this study, we assumed the isotropic behavior of the reaction, which was to be confirmed later in a separate measurement.

In the framework of IMA (Invariant Amplitude Method),[4] the angular distribution of the differential cross section for ^{6}Li(d, p$_0$) reaction is represented as

$$\frac{d\sigma_{\rm p}(\theta)}{d\theta} = a(1 + 2P_\sigma \cos\theta), \quad (1)$$

where a and P_σ are arbitrary parameters. Using the yields of proton and α-particle, $N_{\rm p}(\theta)$ and $N_\alpha(\theta)$, respectively, the yield ratio of proton and α-particle is represented as

$$X(\theta) \equiv N_{\rm p}(\theta)/N_\alpha(\theta) = (a/b) \times (1 + 2P_\sigma \cos\theta), \quad (2)$$

where b is the differential cross section of ^{6}Li(d, α), which is isotropic. $X(\theta)$ is canceled by the differences in solid-angles between the detectors, and becomes isotropic if the s-wave approximation is valid.

The experiment was performed at the University of Tsukuba, Tandem Accelerator Center (UTTAC). The scattering chamber was directly connected to the deuteron ion source. The deuteron beam was accelerated up to 90 keV and impinged on a target. Figure 1 shows the placement of the detectors and target, which was a layer of lithium carbonate Li_2CO_3 10 μg/cm^2 thick on an aluminum backing 15 μm thick. The enrichment of ^{6}Li was 95%. The energy loss in the layer of lithium carbonate was approximately 8 keV. A slit with a diameter of 5 mm was placed at the distance of 150 mm upstream from the target. We placed 12 Si-SSDs around the target from the scattering angle of 0° to 165° every 15 degrees for measuring the proton and α-particle. Each detector was placed at the distance of 140 mm from the target and has the solid angle of 2.6 msr.

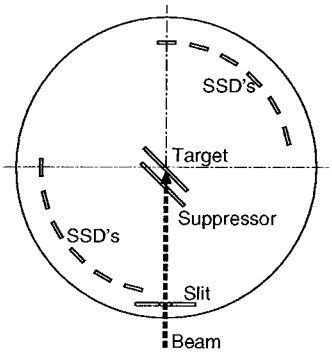

Fig. 1. Layout in scattering chamber.

The experimental results are shown in Fig. 2. The horizontal axis is the scattering angle in the center mass system. The vertical axis is the yield ratio, $X(\theta)$. The error bars only include statistically significant values. The quantities a/b and P_σ are treated as free parameters and determined to fit the experimental data of $X(\theta)$ by the maximum-likelihood method. The derived parameters are $P_\sigma = 0.009 \pm 0.014$ and $a/b = 0.572 \pm 0.011$. We found that the anisotropic parameter, P_σ, is consistent with zero and hence the mixture by the p-wave is negligible.

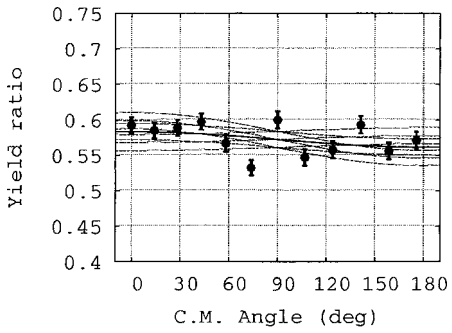

Fig. 2. Yield ratio of proton and α-particle. The solid line is for $P_\sigma = 0.009$ and $a/b = 0.572$. The dashed lines are for $P_\sigma = 0.009 \pm 0.014$ and $a/b = 0.572 \pm 0.011$.

References

1) M. Yamaguchi, Y. Tagishi, Y. Aoki, T. Iizuka, T. Nagatomo, T. Shinba, N. Yoshimaru, Y. Yamato, T. Katabuchi, and M. Tanifuji: in press.
2) M. Yamaguchi, N. Yoshimaru, and Y. Tagishi: UTTAC Ann. Rep. **2003**, 17 (2004).
3) T. Iizuka, M. Yamaguchi, N. Kawachi, N. Yoshimaru, K. Shiga, and Y. Tagishi: UTTAC Ann. Rep. **2001**, 32 (2002).
4) M. Tanifuji and H. Kameyama: Phys. Rev. C **60**, 034607 (1999).

* Department of Physics, Hosei University

Laser spectroscopy of $^{10}Be^{+}$ in an on-line ion trap

T. Nakamura, M. Wada, K. Okada,[*1] A. Takamine,[*2] Y. Ishida, S. Shiba,[*3] Y. Yamazaki, T. Kambara, Y. Kanai, T. M. Kojima, Y. Nakai, N. Oshima, A. Yoshida, T. Kubo, S. Ohtani,[*3] K. Noda,[*4] I. Katayama,[*5] G. Jegou, V. Lioubimov,[*6] H. Wollnik,[*7] V. Varentsov,[*8] and H. A. Schuessler[*6]

[On-line ion trap, laser spectroscopy, $^{10}Be^{+}$, isotope shift]

We have developed an on-line ion trap for storing unstable nuclear ions extracted from an rf ion guide system.[1] Recently, we have succeeded in the on-line trapping of $^{10}Be^{+}$ ions provided by RIPS, and have measured the frequency of the $2^2P_{3/2} - 2^2S_{1/2}$ transition ν_0^{10} of laser-cooled $^{10}Be^{+}$ ions by laser spectroscopy. From the measurement, we derived the isotope shift (IS) between $^{10}Be^{+}$ and $^{9}Be^{+}$. This IS consists of the field shift (FS) and the mass shift (MS). The FS is due to the different distributions of the nuclear charge, which has s dominant effect for heavier ions but is negligible for Be isotopes. The MS also consists of two parts; the normal mass shift (NMS) and the specific mass shift (SMS). The NMS is due to the reduced mass of atomic electrons. For isotopes of mass M_A and M_B, the NMS is expressed as

$$\delta\nu_{\mathrm{NMS}}(B-A) = \frac{m_e(M_B - M_A)}{M_A(M_B + m_e)}\nu^A, \qquad (1)$$

where m_e is the electron mass and ν^A is the transition frequency of the isotope of mass m_A. The SMS is due to the mass polarization effect. It can be described by

$$\Delta\nu_{\mathrm{SMS}}(B-A) = \left(\frac{1}{M_A + m_e} - \frac{1}{M_B + m_e}\right)\Delta K, \qquad (2)$$

where ΔK is the difference in mass polarization parameter K between the states, and K is defined by the momentum of the k-th electron $\vec{p}_k$ of the N electron system as

$$K = \sum_{i>j}^{N} \langle \vec{p}_i \cdot \vec{p}_j \rangle \,. \qquad (3)$$

Some theoretical calculations of the mass polarization parameter for Be^{+} have been reported.[2–4]

In the experiment, a laser system was used that contained of a cw tunable ring dye laser (Coherent: 899-21) with a cw SHG unit (Coherent: MBD-200). The frequency of the dye laser was monitored by a wavelength meter (Advantest: TQ8325) and by the magnitude of the iodine absorption signal. Both were used to calibrate the absolute frequencies by comparison with the iodine atlas.[5] Figure 1 shows the laser-induced fluorescence (LIF) spectra together with the iodine spectra and the resonance frequencies of $^{9,10}Be^{+}$. From the observed resonance frequencies with compensations due to the Zeeman and hfs shifts under an external field $B = 0.54\,\mathrm{mT}$, we obtain $\nu_0^{10} = 957\,413.92(54)\,\mathrm{GHz}$ and $\nu_0^{9} = 957\,396.52(50)\,\mathrm{GHz}$, and their IS $\delta\nu = 17.40(104)\,\mathrm{GHz}$. The NMS is estimated to $\delta\nu_{\mathrm{NMS}} = 5.83\,\mathrm{GHz}$ from Eq. (1), then the SMS is $\delta\nu_{\mathrm{SMS}} = 11.57(104)\,\mathrm{GHz}$. Finally, ΔK derived from the SMS using Eq. (2) is shown in Table 1 with theoretical results[2–4] which are in good agreement within experimental error. This result is helpful when we set laser frequencies for other isotopes, such as $^{7}Be^{+}$ and $^{11}Be^{+}$, which are our main objects to perform precise hyperfine structure spectroscopy for nuclear structure study.

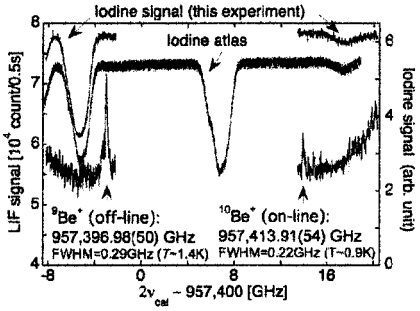

Fig. 1. Experimental results.

Table 1. Comparison between present and theoretical ΔK's. Deviations were compared with the experimental error σ.

Reference	ΔK [au]	deviation
present result	0.289(26)	–
Prasad et al. (1966)[2]	0.3296	1.6σ
Chung et al. (1991, 1993)[3]	0.2881	0.03σ
Yamanaka (1998)[4]	0.2852604	0.14σ

*1 Department of Physics, Sophia University
*2 Graduate School of Art and Science, University of Tokyo
*3 Institute for Laser Science, University of Electro-Communications
*4 National Institute for Radiological Science
*5 High Energy Accelerator Research Organization (KEK)
*6 Department of Physics, Texas A&M University, USA
*7 II. Physikalisches Institute, Giessen University, Germany
*8 Kholopin Radium Institute, Russia

References

1) A. Takamine et al.: Rev. Sci. Instrum. **76**, 103503 (2005).
2) S. S. Prasad et al.: Proc. Phys. Soc. **87**, 159 (1966).
3) K. T. Chung: Phys. Rev. A **44**, 5421 (1991); K. T. Chung and X.-W. Zhu: Physica Scr. **48**, 292 (1993).
4) N. Yamanaka: Phys. Lett. A **243**, 132 (1998).
5) H. Kato et al.: *Doppler-Free High Resolution Spectral Atlas of Iodine Molecule 15000 to 19000 cm*$^{-1}$ (Japan Society for the Promotion of Science, Tokyo, 2000).

^{6}He+^{6}He cluster states in ^{12}Be *via* α-inelastic scattering

A. Saito,[*1] S. Shimoura,[*1] T. Minemura,[*2] Y. U. Matsuyama,[*3] H. Baba, H. Akiyoshi, N. Aoi, T. Gomi,[*4] Y. Higurashi, K. Ieki,[*3] N. Imai,[*2] N. Iwasa,[*5] H. Iwasaki,[*6] S. Kanno,[*3] S. Kubono,[*1] M. Kunibu,[*3] S. Michimasa, T. Motobayashi, T. Nakamura,[*7] H. Sakurai, M. Serata,[*3] E. Takeshita,[*3] S. Takeuchi, T. Teranishi,[*8] K. Ue,[*6] K. Yamada, and Y. Yanagisawa

[Nuclear reactions, ^{4}He(^{12}Be,^{6}He^{6}He)]

The cluster structure in neutron-rich beryllium isotopes is one of the most interesting phenomena in unstable nuclei. We aimed at searching for excited states with low spins, such as 0^+ and 2^+, which may lie just above the ^{6}He+^{6}He decay threshold. The α-inelastic scattering at 60 A MeV based on the inverse kinematics using a liquid helium target[1)] was used to populate these excited states. The one-step direct-reaction process is dominant at this energy. In the present work, the angular correlations between decay particles are also compared with DWBA predictions. Since the density of levels is rather high, the multipole decomposition analysis (MDA) with the DWBA was used. The details of the experimental setup are described in Ref. 2.

The DWBA analyses for α-inelastic scattering were performed using the computer code TWOFNR.[3)] A single-folding model with density-dependent effective nucleon-α interactions was used in the DWBA calculations.[4)] The details of the transition densities are described in Ref. 5. The parameters were adjusted to reproduce the ^{12}Be(α,α')^{12}Be*(2_1^+) reaction.[6)] The MDA has been used including angular correlations of decay particles as well as the angular distribution of inelastic scattering. Only even-spin states can be populated since the final state is two identical spin-0 particles. The expected maximum angular momentum is assumed to be $\Delta L = 4$ at this energy. Therefore, the multipoles of $\Delta L = 0$, 2, and 4, are included in the MDA.

Figure 1 shows examples of fits to (a) the angular distribution of inelastic scattering, and the angular correlation between two ^{6}He particles with respect to (b) the beam direction and (c) the momentum transfer. The dashed, dotted, and dash-dotted curves are for $\Delta L = 0$, 2, and 4, respectively. The gray dashed, gray dotted, and gray dash-dotted curves indicate the contributions of interferences of 0⊗2, 0⊗4, and 2⊗4, respectively. The solid curves show the sum of all contributions, i.e., the coherent sum of the multipoles. These curves include the experimental resolutions estimated by Monte Carlo simulations.

Figure 2 shows the excitation energy spectra for multipoles of ΔL=0, 2, and 4 deduced by the MDA. In Figs. 2 (a) and (b), the peaks indicated by closed arrows are newly observed states for $\Delta L = 0$ and 2, respectively. For the $\Delta L = 4$ spectrum, the previously reported levels are indicated with open arrows. No distinct peaks are observed because of large statistical errors.

The lowest 0^+ and 2^+ states, together with 4^+–8^+ levels,[7)] may form a rotational band with $\hbar^2/2\mathcal{I} = 139$ keV, which corresponds to a developed ^{6}He+^{6}He cluster structure. By assuming that all rotational bands have similar moments of inertia, the third lowest 0^+ and 2^+ states may be connected to the previously observed 6^+ state at 18.6 MeV.[7)]

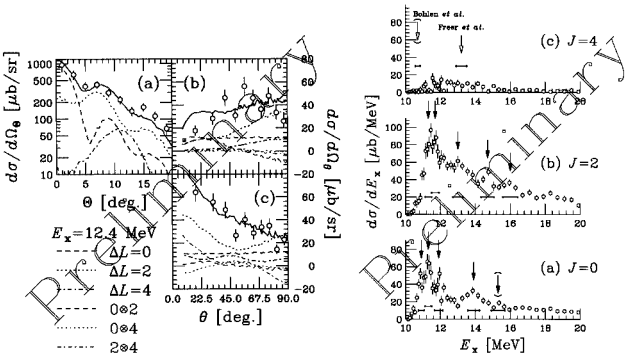

Fig. 1. (left) Example of a fit with $\Delta L = 0$, 2, and 4, to (a) the angular distribution of inelastic scattering, and the angular correlation with respect to (b) the beam direction and (c) the momentum transfer.

Fig. 2. (right) Decay-energy spectra for (a) $\Delta L = 0$, (b) $\Delta L = 2$, and (c) $\Delta L = 4$, for the ^{4}He(^{12}Be, ^{6}He^{6}He) reaction.

*1 Center for Nuclear Study, University of Tokyo
*2 Institute for Particle and Nuclear Studies, High Energy Accelerator Research Organization (KEK)
*3 Department of Physics, Rikkyo University
*4 National Institute of Radiological Sciences
*5 Department of Physics, Tohoku University
*6 Department of Physics, University of Tokyo
*7 Department of Physics, Tokyo Institute of Technology
*8 Department of Physics, Kyushu University

References

1) H. Ryuto et al.: Nucl. Instrum. Methods Phys. Res. A **555**, 1 (2005).
2) A. Saito et al.: RIKEN Accel. Prog. Rep. **37**, 48 (2004).
3) M. Igarashi: DWBA code TWOFNR, unpublished.
4) A. Kolomiets et al.: Phys. Rev. C **61**, 34312 (2000).
5) G. R. Satchler et al.: Nucl. Phys. A **472**, 215 (1987).
6) S. Shimoura: Nucl. Phys. **738**, 162 (2004).
7) M. Freer et al.: Phys. Rev. Lett. **82**, 1383 (1999).

^{8}Li(α,n)^{11}B reaction measurement using monolithic silicon telescope

S. Nishimura, M. Kurata-Nishimura, H. Fujikawa,[*1] A. Guilherme,[*1] J. J. He,[*1] S. Kubono,[*1] H. Yamaguchi,[*1] T. Teranishi,[*2] Y. Wakabayashi,[*2] S. Bishop, M. Kurokawa, T. Kishida, and T. Motobayashi

[Astrophysics, unstable nuclei]

The ^{8}Li(α,n)^{11}B reaction has recently been identified as one of the important reaction paths for passing through the valley of A = 8 in the synthesis of ^{12}C and heavy elements at the early stages of Big Bang. Similarly, the inclusion of the pathway that involves the ^{8}Li(α,n)^{11}B reaction in r-process nucleosynthesis changes the final heavy nuclei abundances according to full network calculations.[1,2)]

Various experiments over the past decade have attempted to determine the cross section of the ^{8}Li(α,n)^{11}B reaction.[3–6)] However, previous measurements have produced inconsistent results and have been unable to study the lowest resonances of interest due to difficulties in particle identification of low-energy ^{11}B ions from the background particles, which mainly consist of elastically scattered ^{8}Li ions and α particles as well as the decay products of ^{8}Li.

A new approach for exploring the low-energy nuclear reactions has been investigated on the simulation code GEANT4.[7,8)] Our studies show that the application of a monolithic detector,[9)] consisting of five ultrathin silicon pads (ΔE) of 1 μm thickness supported by 508-μm-thick silicon detector (E), would enable us to measure the low energy nuclear reactions in the gas target.[10)] A first attempt of ^{8}Li(α,n)^{11}B reaction measurement using the monolithic silicon detector array was performed in the inverse kinematics at CRIB. The primary beam of ^{7}Li ions was accelerated up to 24 MeV and was impinged on a deuteron gas target at F0. ^{8}Li nuclei produced via the reaction d(^{7}Li,p)^{8}Li were then momentum-filtered from the intense ^{7}Li primary beam by an aperture inserted at the dispersive focal plane at F1. In addition, a Wien filter in conjunction with the time-of-flight information among the RF and two PPACs enabled us to extract pure ^{8}Li ions at the detector section of F3. The energies of ^{8}Li ions passing through 7 μm Mylar foil, two tracking detectors (PPACs), and the entrance window of gas cell (2 μm thick Mylar foil) were decreased to 0.25 ± 0.05 MeV/u corresponding to the E_{cm} of $\sim$ 0.5 MeV. The incident ^{8}Li beam and reaction products in the 6 cm He gas cell at the gas pressure of 100 Torr were detected by 18 sets of monolithic silicon detectors at the downstream end of the gas target. The intensity of the ^{8}Li beam was approximately $1\sim5\times10^{3}$ cps after the gas cell window. Moreover, the He gas cell was surrounded by an array of neutron detectors and γ-ray detectors to measure any coincident neutrons and the γ rays corresponding to the decay of excited states in ^{11}B. Figures 1 (a) and (b) show the preliminary results obtained using the monolithic silicon detectors, where the different spectra were obtained between the ^{4}He gas pressures of 0 and 100 Torr. The large amount of events below 2000 ch corresponds to the incident ^{8}Li ions directly implanted to the monolithic silicon detectors. The cluster in large ΔE region indicates the reaction products of ^{11}B from the ^{8}Li(α,n)^{11}B reaction. Our preliminary results show that the monolithic silicon detector array has sufficient capability for efficiently identifying the ^{8}Li(α,n)^{11}B reaction even at the E_{cm} of approximately 0.5 MeV.

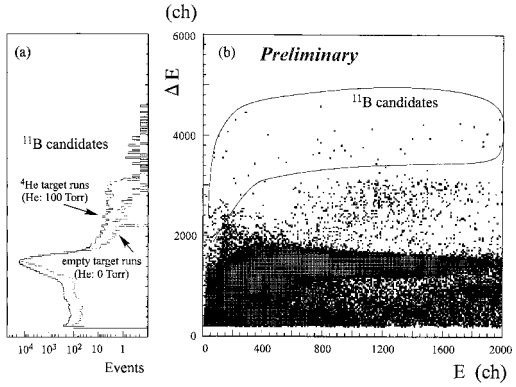

Fig. 1. (a) Comparison of ΔE spectrum between empty target runs and ^{4}He target runs. (b) Correlation between energy deposited in ΔE and E layers. There are clusters at large ΔE area where the reaction products of the ^{11}B are expected from the ^{8}Li(α,n)^{11}B reaction.

*1 Center for Nuclear Study, Graduate School of Science, University of Tokyo
*2 Department of Physics, Kyushu University

References

1) M. Terasawa et al.: Astrophys. J. **562**, 470 (2001).
2) T. Kajino et al.: Nucl. Phys. A **704**, 165c (2002).
3) X. Gu et al.: Phys. Lett. B **343**, 31 (1995).
4) R. N. Boyd et al.: Phys. Rev. Lett. **68**, 1283 (1992).
5) Y. Mizoi et al.: Phys. Rev. C **6206**, 5801 (2000).
6) S. Cherubini et al.: Eur. Phys. J. A **20**, 355 (2004).
7) M. K-Nishimura et al.: RIKEN Accel. Prog. Rep. **37**, 183 (2004).
8) M. K-Nishimura et al.: Nucl. Phys. A **758**, 162c (2005).
9) A. Musumarra et al.: Nucl. Instrum. Methods Phys. Res. A **409**, 414 (1998).
10) S. Nishimura et al.: RIKEN Accel. Prog. Rep. **38**, 142 (2005).

Elastic scattering and Coulomb dissociation of ^{8}B on Pb, liquid hydrogen and liquid helium targets

S. Bishop, T. Motobayashi, N. Aoi, H. Baba, T. Gomi, Y. Ichikawa,[*1] N. Imai,[*1] N. Iwasa,[*2] H. Iwasaki,[*1] S. Kawai,[*3] Y. Kondo,[*4] T. Nakamura,[*4] T. Nakao,[*1] S. Nishimura, T. Ohnishi, T. K. Onishi,[*1] H. J. Ong,[*1] S. Ota,[*5,6] A. Perera, S. Shimoura,[*5] T. Sumikama, D. Suzuki,[*1] H. Suzuki,[*1] M. K. Suzuki,[*1] S. Takeuchi, M. Tamaki,[*5] K. Tanaka, Y. Togano,[*3] and Y. Yanagisawa

[^{8}B, elastic scattering, Coulomb dissociation, nuclear astrophysics, S-factor]

The solar ^{7}Be$(p,\gamma)^8$B reaction has been the object of intense experimental and theoretical studies for more than 30 years. This reaction is responsible for producing the detectable solar neutrino flux.[1] An outstanding problem in nuclear astrophysics is the determination of the zero-energy astrophysical S-factor for the ^{7}Be$(p,\gamma)^8$B reaction. The cross section of the proton capture on ^{7}Be can be determined by measuring the dissociation of ^{8}B in the presence of a known photon flux provided by the Coulomb field of a target nucleus. Studies of this sort have been previously performed employing Pb targets; however, such studies have shown that the break-up cross section of ^{8}B on Pb, while dominated by *E1* electromagnetic interaction, also contains contributions from *E2*, *M1*, and perhaps non-negligible nuclear break-up contributions. Determination of these higher order contributions are desired to determine the S-factor to a higher degree of accuracy.

To this end, a Coulomb dissociation experiment of ^{8}B was performed at the RIKEN RIPS facility using Pb (57 mg/cm^2), liquid helium (130 mg/cm^2) and liquid hydrogen (63 mg/cm^2) secondary targets, positioned at the achromatic focal plane of RIPS. Use of these three targets will provide the necessary information to disentangle the multipole and nuclear contributions to the ^{8}B break-up cross section. Production of the secondary 72 MeV/u ^{8}B beam was done using a 135 MeV/u primary ^{12}C beam impinging on a 1.5 mm thick production target of pure nickel. The ^{8}B secondary beam intensity was $\approx$ 150 kcps and had a purity of 76%. The incident ^{8}B beam momentum, **p**, was made using two PPAC detectors located 1.91 m and 1.61 m upstream of the secondary target position; detection of the charged particle reaction products, and their momentum and energy, was performed using a 1×1 m^2 segmented plastic scintillator hodoscope[2] positioned 3.86 m downstream of the secondary target position. The total angular resolution of this detector set-up has been determined as 4.4 mrad. Gamma-ray detection for break-up into the first excited state of ^{7}Be was performed using the γ-ray detector array DALI2.[3]

The break-up data will be analyzed using a distorted-wave theory, combined with a GEANT Monte Carlo code which simulates the incident beam emittance, the angular resolution of the PPACs, the response functions of all 132 DALI2 detectors, and the timing and position responses of the 29 hodoscope scintillator bars. From the analysis of ^{8}B elastic scattering angular distributions, constraints on a phenominological optical potential, or a microscopically constructed potential, such as a double-folding model, will be obtained.

Presently, preliminary ^{8}B elastic scattering angular distributions have been extracted from the data and are shown in Fig. 1. These distributions are now being analyzed, as a first attempt, within the framework of the Woods-Saxon optical potential formalism. Comparison between theoretical and experimental elastic angular distributions will determine optical parameters for the aforementioned constraints. Additionally, this analysis will test the extendability, into a much lower mass and energy range, of the energy, proton number and neutron number, dependence of the optical potential parameters previously determined in broader global studies[4,5] of proton elastic scattering data.

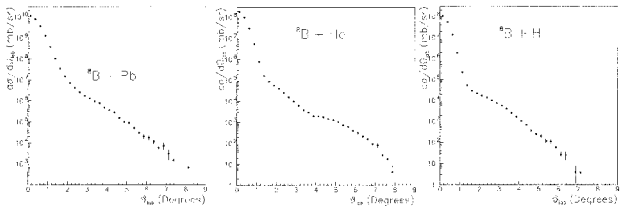

Fig. 1. ^{8}B elastic scattering angular distributions for Pb (left), liquid helium (centre) and liquid hydrogen (right) targets.

References

1) J. N. Bahcall: Phys. Rev. **135**, B137 (1964).
2) I. Hisanaga et al.: RIKEN Accel. Prog. Rep. **31**, 162 (1998).
3) S. Takeuchi et al.: RIKEN Accel. Prog. Rep. **36**, 148 (2003).
4) R. L. Varner et al.: Phys. Rep. **201**, 57 (1991).
5) F. D. Becchetti, Jr. and G. W. Greenlees: Phys. Rev. **182**, 1190 (1969).

[*1] Department of Physics, University of Tokyo
[*2] Department of Physics, Tohoku University
[*3] Department of Physics, Rikkyo University
[*4] Department of Physics, Tokyo Institute of Technology
[*5] Center for Nuclear Study, University of Tokyo
[*6] Department of Physics, Kyoto University

Proton inelastic scattering of ^{14}Be

Y. Kondo,[*1] T. Nakamura,[*1] Y. Satou,[*1] T. Sugimoto,[*1] N. Matsui,[*1] Y. Hashimoto,[*1] T. Okumura,[*1] T. Nakabayashi,[*1] M. Shinohara,[*1] N. Aoi, N. Endo,[*2] N. Fukuda, T. Gomi, S. Kawai,[*3] M. Kitayama,[*2] T. Kobayashi,[*2] Y. Matsuda,[*2] T. Motobayashi, T. K. Onishi,[*4] H. J. Ong,[*4] H. Otsu, H. Sakurai, S. Shimoura,[*5] S. Takeuchi, M. Tamaki,[*5] Y. Togano,[*3] Y. Yanagisawa, and M. Ishihara

[Nuclear reactions: ^{14}Be+p, proton inelastic scattering, invariant mass method]

We have studied the proton inelastic scattering of the neutron-rich nucleus ^{14}Be using a liquid hydrogen target. Disappearance of the magic number $N = 8$ in ^{12}Be has been revealed from the systematics of the excitation energy of the 2^+ state in even-even beryllium isotopes. A large quadrupole deformation length has been also obtained for ^{12}Be from the inelastic cross section of the $0^+_{\rm g.s.} \rightarrow 2^+$ transition on a proton target.[1)] Information regarding the 2^+ state in the neighboring nucleus ^{14}Be is important to understand the shell-closure melting at $N = 8$. Recently, the first 2^+ state above the two-neutron separation energy $S_{2n} = 1.34\,$MeV[2)] in ^{14}Be has been observed at 1.67 MeV in a breakup reaction on a carbon target.[3)] This energy is smaller than that of ^{12}Be. The mechanism for lowering the 2^+ level compared with ^{12}Be is not well understood yet.

In the present study, we aim at investigating the deformation and shell structure of ^{14}Be by studying proton inelastic scattering. Since the proton and carbon targets have different sensitivities to the protons and neutrons in the ^{14}Be nucleus, the proton and neutron transition quadrupole matrix elements M_p and M_n can be deduced independently by comparing the deformation lengths obtained from the inelastic cross sections using the proton and carbon targets.[4)] In addition, other excited states can be observed in this experiment because the proton target, which has an isovector component, is more accessible to various states than the carbon target, which is an isoscalar probe.

Since no bound excited states exist in ^{14}Be, we need to measure the states in the continuum region. Here, we adopt the invariant mass method to investigate the unbound excited states with a kinematically complete measurement in proton inelastic scattering. In this reaction, ^{14}Be is broken up by the proton target into ^{12}Be and two neutrons because ^{13}Be has no bound states. By measuring the momentum vectors of the breakup fragments, the relative energy of ^{12}Be+$2n$ can be deduced via the invariant mass method.

The experiment was performed at the in-flight radioactive-isotope beam separator, RIPS.[5)] A primary ^{18}O beam at 100 MeV/nucleon bombarded a Be target with 6 mm thickness to produce a secondary ^{14}Be beam. Particle identification of the secondary beam was carried out event-by-event using the time-of-flight (TOF) information between a cyclotron RF and a 1-mm-thick plastic scintillator placed at the second focal point of RIPS. The ^{14}Be ion bombarded a liquid hydrogen target with a thickness of 228 mg/cm^2. The energy of the ^{14}Be beam at the center of the liquid hydrogen target was 69 MeV/nucleon. The incident angle of the ^{14}Be beam was measured by two sets of parallel-plate avalanche counters[6)] placed upstream of the liquid hydrogen target.

The neutrons were detected by a six-layered neutron hodoscope array (NEUT), which consists of 56 bars with dimensions of 6 cm × 6 cm × 2.1 m and 30 bars of 6 cm × 6 cm × 1.1 m. The front side of NEUT was equipped with a thin layer of plastic scintillators to reject the charged particle background. The momentum vectors of the neutrons were reconstructed from the hit position and TOF.

The ^{12}Be fragment emitted in the breakup reaction was bent by a large-gap dipole magnet, was detected and traced by two multi wire drift chambers located at the entrance and exit of the magnet, and penetrated a hodoscope (HOD), which consists of seven plastic scintillator slats of 1 cm thickness. Particle identification of the breakup charged fragment was performed by combining the ΔE and TOF information from HOD with the magnetic rigidity information obtained from the trace. The momentum vector of the charged fragment was deduced from the TOF and trace.

Forty-eight blocks of NaI(Tl) scintillators surrounding the liquid hydrogen target were used to examine whether ^{12}Be is in the excited state by detecting de-excitation γ rays. Each scintillator crystal has a size of 6 cm × 6 cm × 12 cm. Data analysis is now in progress.

*1 Department of Physics, Tokyo Institute of Technology
*2 Department of Physics, Tohoku University
*3 Department of Physics, Rikkyo University
*4 Department of Physics, University of Tokyo
*5 Center for Nuclear Study, University of Tokyo

References

1) H. Iwasaki et. al.: Phys. Lett. B **481**, 7 (2000).
2) G. Audi and A. H. Wapstra: Nucl. Phys. A **565**, 66 (1993).
3) T. Sugimoto et. al.: private communication.
4) A. M. Bernstien, V. R. Brown, and V. A. Madsen: Comments Nucl. Part. Phys. **11**, 203 (1983).
5) T. Kubo et. al.: Nucl. Instrum. Methods Phys. Res. B **70**, 309 (1992).
6) H. Kumagai et. al.: Nucl. Instrum. Methods Phys. Res. A **470**, 562 (2001).

Invariant-mass spectroscopy of ^{14}Be

T. Sugimoto,[*1] T. Nakamura,[*1] N. Fukuda, M. Miura,[*1] Y. Kondo,[*1] N. Aoi, H. Baba, D. Bazin,[*2] T. Gomi, H. Hasegawa,[*3] Y. Hashimoto,[*1] N. Imai,[*4] T. Kobayashi,[*5] T. Kubo, T. Motobayashi, A. Saito,[*6] H. Sakurai, S. Shimoura,[*6] A. M. Vinodkumar,[*7] K. Watanabe,[*5] Y. X. Watanabe,[*4] T. Yakushiji,[*5] Y. Yanagisawa, K. Yoneda, and M. Ishihara

[Nuclear reactions: C(^{14}Be, ^{12}Be $2n$), nuclear breakup]

Recently, shell quenching at $N = 8$ in ^{12}Be has been suggested by experimental investigations of the low-lying first 2^+ state and intruder first 1^- state.[1–4] To discuss the change in the shell stability of beryllium isotopes, systematic studies of these excited states are important. As for the most neutron-rich beryllium isotope ^{14}Be, although the location of the first 2^+ state is a key to understand the shell stability, bound excited states in ^{14}Be have never been found. In the present study, we aim at observing the first 2^+ state of ^{14}Be in the particle-unbound region to discuss the shell stability and deformation property of this nucleus.

The experiment was performed at the RIPS beam line of the RIKEN Accelerator Research Facility. The secondary ^{14}Be beam was produced by the projectile fragmentation from ^{18}O at 100 A MeV. A carbon target was used to excite ^{14}Be to a discrete state. The excited ^{14}Be broke up into $^{12}\mathrm{Be}+n+n$. By measuring the four momenta of the outgoing ^{12}Be and neutrons, decay energy was extracted from the reconstructed invariant mass, and angular distribution was obtained. Details of the experimental setup are described in the previous report.[5]

Figure 1 shows the decay-energy spectrum of the $^{12}\mathrm{Be}+n+n$ system. A narrow peak at approximately 0.3 MeV was clearly observed. The spectrum was fitted with a Breit-Wigner shape corresponding to the peak and quasi-free scattering shape as background. Since the daughter nucleus ^{12}Be has excited states, it is necessary to identify the final state of ^{12}Be by examining the γ-ray spectrum. Since the cross section measured in coincidence with γ-ray emission was found to be the order of 10^{-3} times that without γ-ray emission, the peak in the decay-energy spectrum should be associated with the ground state of ^{12}Be. Thus, the observed peak at $E_\mathrm{d} = 0.3$ MeV is assigned to be the first excited state of ^{14}Be, with the excitation energy extracted from E_d as $E_\mathrm{ex} = 1.56 \pm 0.15$ MeV (preliminary).

The spin of the first excited state can be determined from the angular distribution of the inelastically scattered $^{12}\mathrm{Be} + n + n$ system as shown in the inset of Fig. 1. The distribution is compared with the distorted-wave coupled-channel calculation using the `ECIS97` code with the optical potential parameters obtained in the $^{11}\mathrm{Be} + ^{12}\mathrm{C}$ reaction at 47 A MeV.[6] The transferred angular momentum $\Delta L = 2$ is consistent with the experimental data, and we thus assigned J^π of the observed peak as 2^+. Compared with the cross section associated with the peak, the deformation length was extracted as $\delta = 1.44 \pm 0.16$ fm (preliminary).

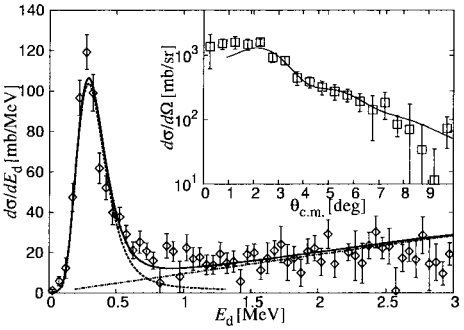

Fig. 1. Decay-energy spectrum of $^{12}\mathrm{Be} + n + n$ system. The spectrum was fitted with the Breit-Wigner shape (dashed curve) and quasi-free scattering shape (dot-dashed curve). The inset shows the angular distribution of the inelastically scattered $^{12}\mathrm{Be} + n + n$ system. The solid line shows the theoretical calculation assuming $\Delta L = 2$.

A shell-model calculation analysis was also performed. The excitation energy was well reproduced ($E_\mathrm{ex} = 1.48$ MeV) using a effective interaction proposed in Ref. 7, while the deformation length was not reproduced. Further analysis to discuss the shell stability and deformation property of beryllium isotopes is now in progress.

*1 Department of Physics, Tokyo Institute of Technology
*2 National Superconducting Cyclotron Laboratory, Michigan State University, USA
*3 Department of Physics, Rikkyo University
*4 High Energy Accelerator Research Organization (KEK)
*5 Department of Physics, Tohoku University
*6 Center for Nuclear Study, University of Tokyo
*7 Department of Chemistry, Oregon State University, USA

References

1) F. Ajzenberg-Selove: Nucl. Phys. A **506**, 1 (1990).
2) A. Navin et al.: Phys. Rev. Lett. **85**, 266 (2000).
3) H. Iwasaki et al.: Phys. Lett. B **481**, 7 (2000).
4) H. Iwasaki et al.: Phys. Lett. B **491**, 8 (2000).
5) T. Sugimoto et al.: RIKEN Accel. Prog. Rep. **37**, 59 (2004).
6) M. Takashina et al.: Phys. Rev. C **67**, 037601 (2003).
7) T. Suzuki et al.: Phys. Rev. C **67**, 044302 (2003).

Isoscalar monopole and dipole strengths in ^{14}O

H. Baba, S. Shimoura,[*1] T. Minemura, Y. U. Matsuyama,[*2] A. Saito,[*1] H. Akiyoshi, N. Aoi, T. Gomi, Y. Higurashi, K. Ieki,[*2] N. Imai,[*3] N. Iwasa,[*4] H. Iwasaki,[*5] S. Kanno,[*2] S. Kubono,[*1] M. Kunibu,[*2] S. Michimasa, T. Motobayashi, T. Nakamura,[*6] H. Sakurai, M. Serata,[*2] E. Takeshita,[*2] S. Takeuchi, T. Teranishi,[*7] K. Ue,[*4] K. Yamada, and Y. Yanagisawa

[Nuclear reactions: ^{14}O(α,α'), 60 A MeV, inelastic α scattering]

Intermediate-energy RI beams enable us to investigate excited unstable nuclei using secondary reactions in inverse kinematics. As a probe for excitation, inelastic α scattering is useful for exciting isoscalar states and is the best tool for investigating isoscalar monopole and dipole excitations. They are compressional excitations called the "breathing mode" and the "squeezing mode", respectively, and are relevant to the incompressibility of nuclear matter. For light stable nuclei, isoscalar multipole strength has been studied[1,2] using 60 A MeV α and discussed with regard to compressional responses. To start studies of isoscalar compressional responses in unstable nuclei, we performed an experiment of inelastic scattering of 60 A MeV α on the light unstable nucleus ^{14}O in inverse kinematics.

The experiment was carried out at the RIKEN RIPS course. A 60 A MeV secondary beam of ^{14}O was transmitted to a liquid ^{4}He target of 120 mg/cm^2 thickness. Decay particles were detected in coincidence by a ΔE-$E1$-$E2$ plastic scintillator hodoscope. In this work, the following decay channels were measured: ^{14}O$^* \rightarrow$ ^{13}N + p, ^{12}C + p + p, ^{12}C$^*_1$ + p + p, ^{10}C + α, and ^{10}C$^*_1$ + α. Excitation energy and angular distribution were deduced from the momentum vectors of the decay products.

To obtain the strength distributions, we carried out multipole decomposition (MD) analysis[3] with the DWBA calculation. In this work, the DWBA calculation was carried out using the single-folding model with a density-dependent nucleon-α interaction. Details are described in Ref. 4. For the measured decay channels, the integrated EWSR values of up to 25.0 MeV deduced from the MD analysis were determined to be as 45±11% and 61±14% of the isoscalar monopole and dipole EWSRs, respectively. The obtained EWSR fractions, which are shown in Fig. 1, fragmented in a wide excitation energy range and no massive resonance peaks were found. The experimental results cannot strictly be compared with results of other experiments higher than 13.8 MeV excitation energy, because the decay channel of $\alpha + \alpha + \alpha$ + p + p, which has a 13.8 MeV threshold energy, was not measured in this experiment. Nevertheless, the monopole and dipole strength distributions of ^{14}O and the light stable nuclei of ^{12}C and ^{16}O are in some agreement. Therefore, this fragmented distribution without massive peaks may be common in light nuclei, regardless stable or unstable.

In Fig. 1, additional monopole and dipole strengths to the known 0^+ and 1^- states were identified at E = 6–9 MeV. This energy region corresponds to the bound states in the mirror nucleus ^{14}C, where neither 0^+ nor 1^- state was found, these strengths may come from the continuum. Similar low-energy isoscalar monopole and dipole responses have been predicted in the neutron drip line nucleus ^{28}O.[5,6] In addition to the soft-dipole mode, this low-lying isoscalar compressional response is a new characteristic transition in unstable nuclei.

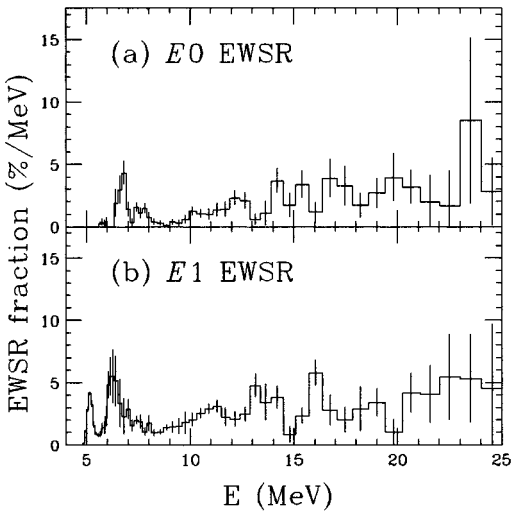

Fig. 1. Decomposed EWSR fractions of monopole and dipole responses. The strengths fragmented in a wide excitation energy range without massive peaks.

*1 Center for Nuclear Study, University of Tokyo
*2 Department of Physics, Rikkyo University
*3 Institute of Particle and Nuclear Studies, High Energy Accelerator Research Organization (KEK)
*4 Department of Physics, Tohoku University
*5 Department of Physics, University of Tokyo
*6 Department of Physics, Tokyo Institute of Technology
*7 Department of Physics, Kyushu University

References

1) B. John et al.: Phys. Rev. C **68**, 014305 (2003).
2) Y.-W. Lui et al.: Phys. Rev. C **64**, 064308 (2001).
3) M. Itoh et al.: Phys. Lett. B **549**, 58 (2002).
4) H. Baba et al.: CNS Annu. Rep. **2003**, 5 (2004).
5) I. Hamamoto and H. Sagawa: Phys. Rev. C **53**, R1492 (1996).
6) I. Hamamoto et al.: Phys. Rev. C **57**, R1064 (1998).

Decoupling of valence neutrons from core in ^{17}B†

Zs. Dombrádi,[*1] Z. Elekes,[*1] R. Kanungo, H. Baba,[*2] Zs. Fülöp,[*1] J. Gibelin,[*3] Á. Horváth,[*4] E. Ideguchi,[*5] Y. Ichikawa,[*5] N. Iwasa,[*6] H. Iwasaki,[*5] S. Kanno,[*2] S. Kawai,[*2] Y. Kondo,[*2] T. Motobayashi, M. Notani,[*5] T. Ohnishi,[*5] A. Ozawa, H. Sakurai,[*5] S. Shimoura,[*5] E. Takeshita,[*2] S. Takeuchi, I. Tanihata,[*7] Y. Togano,[*2] C. Wu, Y. Yamaguchi, Y. Yanagisawa, A. Yoshida, and K. Yoshida

[Nuclear structure, unstable nuclei, proton inelastic scattering, ^{17}B, neutron decoupling]

Recently, an extremely large $M_n/M_p \sim 4N/Z$ ratio has been observed in ^{16}C.[1)] In this nucleus, a neutron effective charge of $e_n = 0.15$ was deduced[1)] and can be considered as a clear indication of the decoupling of the valence neutrons from the ^{14}C core. ^{17}B is another nucleus where a significant decoupling may take place because an anomalous electric quadrupole moment of its ground state was measured at $Q = 38.6 \pm 1.5$ mb.[2)] In order to check this idea by deducing the neutron deformation, we studied the inelastic scattering of ^{17}B in inverse kinematics. In the present experiment, we employed the technique of in-beam γ-ray spectroscopy, incorporating inelastic proton scattering and utilizing a liquid hydrogen target for enhancement of luminosity. The experiment was performed at the RIPS beamline of the RIKEN accelerator research facility (for details see Ref. 3). Figure 1 shows the Doppler-corrected spectra of γ-rays with and without the secondary liquid hydrogen target. A single peak at 1089 (15) keV can be seen in the bottom panel (subtraction of top and middle panels), which corresponds to the transition between the first excited state and the ground state. To derive the quadrupole deformation parameter ($\beta_2^{pp'}$), a distorted–wave calculation was performed. In this way, we obtained $\beta_2^{pp'} = 0.57 \pm 0.05$. From a comparison with the previously determined electric quadrupole moment, we deduced the deformation parameters of the neutron and proton distributions to be $\beta_n \sim 0.6$ and $\beta_p = 0.36$, respectively. By exploiting this information on the neutron and proton deformations of ^{17}B, an upper limit on the neutron effective charge of $e_n < 0.12$ has been deduced (for detailed analysis, see Ref. 3). This value is in a good agreement with the one deduced in Ref. 2 of $e_n \approx 0.1$ and is 4 times smaller than the one characteristic for nuclei close to the stability in this mass region.

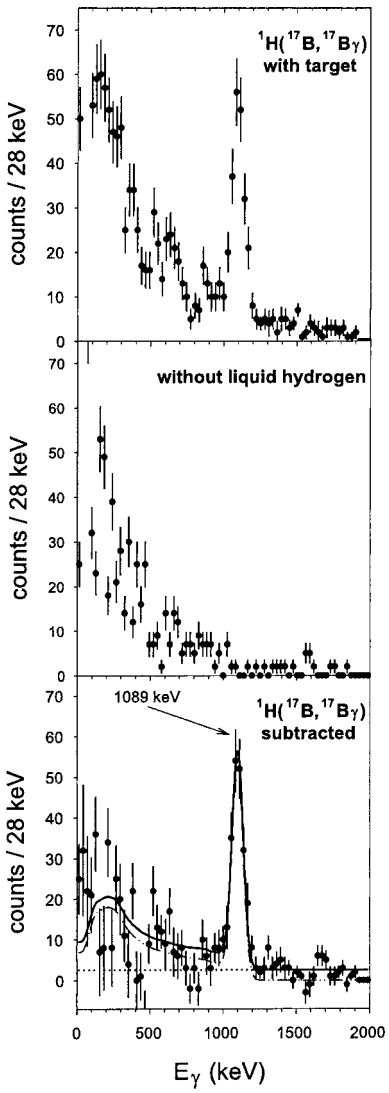

Fig. 1. Doppler-corrected spectra of γ-rays emerging from the ^{1}H(^{17}B,^{17}B) reaction can be seen in the top panel. The middle spectrum is taken without the liquid hydrogen, whereas the spectrum in the bottom panel is produced by subtracting the two spectra.

† Condensed from the article in Phys. Lett. B **621**, 81 (2005)

*1 Insitute of Nuclear Research (ATOMKI), Hungary
*2 Rikkyo University
*3 Institut de Physique Nucléaire, France
*4 Eötvös Lóránd University, Hungary
*5 University of Tokyo
*6 Tohoku University
*7 TRIUMF, Canada

References

1) Z. Elekes et al.: Phys. Lett. B **586**, 34 (2004).
2) H. Ogawa et al.: Phys. Rev. C **67**, 064308 (2003).
3) Zs. Dombrádi et al.: Phys. Lett. B **621**, 81 (2005).

Structure of ^{17}B studied by proton inelastic scattering

M. Shinohara,[*1] T. Nakamura,[*1] Y. Satou,[*1] T. Sugimoto,[*1] Y. Kondo,[*1] N. Matsui,[*1] T. Okumura,[*1] Y. Hashimoto,[*1] T. Nakabayashi,[*1] T. Motobayashi, N. Aoi, N. Fukuda, Y. Yanagisawa, S. Takeuchi, T. Gomi, T. Kobayashi,[*2] H. Otsu,[*2] Y. Matsuda,[*2] N. Endo,[*2] M. Kitayama,[*2] H. Sakurai, T. K. Onishi,[*3] H. J. Ong,[*3] S. Shimoura,[*4] M. Tamaki,[*4] Y. Togano,[*5] S. Kawai[*5] and M. Ishihara

[Nuclear structure, ^{1}H(^{17}B,^{17}B*) reaction, In-beam γ-ray spectroscopy]

Recently, different matter distributions of protons and neutrons in the ^{16}C nucleus have been suggested experimentally and theoretically.[1,2] It is interesting to determine whether this phenomenon also occurs for neighboring nuclei such as ^{17}B. In this report, we present the results of in-beam γ-ray spectroscopy using the ^{1}H(^{17}B,^{17}B*) reaction. In the previous study of the ^{12}C(^{17}B,^{17}B*) reaction, we observed the first excited state at $E_{\rm ex} = 1.07(1)$ MeV, and determined the deformation length $\delta^{\rm C}$ to be 1.20(8) fm.[3] The present work has a different sensitivity to protons and neutrons from that with the ^{12}C target. Then, we have determined the deformation length with proton target, $\delta^{\rm p}$, from an angular distribution of the ^{1}H(^{17}B,^{17}B*) reaction cross section. By combining the results of $\delta^{\rm p}$ and $\delta^{\rm C}$, the transition matrix elements for protons ($M_{\rm p}$) and neutrons ($M_{\rm n}$) are extracted.

The experiment was performed using the RIPS radioactive beam separator at RIKEN. A secondary beam of ^{17}B was produced by the fragmentation reaction of a 110 MeV/nucleon primary ^{22}Ne beam incident on a 6 mm Be target. The secondary beam was identified event-by-event using the TOF-ΔE method. The intensity and purity of the ^{17}B beam were 0.3 kcps and 26%, respectively. The ^{17}B beam bombarded a 120 mg/cm^2 liquid hydrogen target placed at the third focal plane. The average beam energy was 60 MeV/nucleon in the middle of the target. The incident position and angle upon the target were measured by two PPACs. The ejectiles were momentum-analyzed using a large-gap dipole magnet equipped with two drift chambers, and were detected using a plastic scintillator hodoscope.

De-excitation γ rays were detected by the DALI system, which consists of 48 blocks of NaI(Tl) scintillators placed around the liquid hydrogen target. Each scintillator crystal has a rectangular shape with a dimension of $6 \times 6 \times 12$ cm^3. For 0.662 MeV γ rays from a standard ^{137}Cs source, the efficiency and resolution were typically 9% and 9% (FWHM), respectively. Figure 1 shows the Doppler-shift corrected γ-ray energy spectrum. We observed a clear peak corresponding to the decay from the first excited state. The hatched area

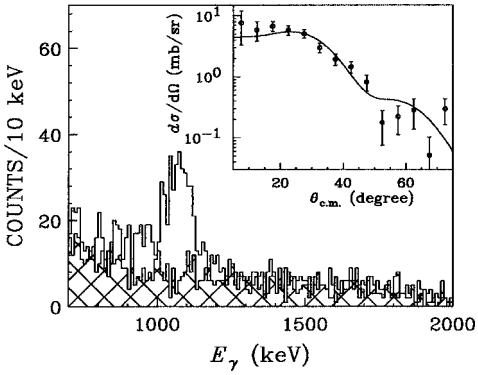

Fig. 1. Doppler-shift corrected γ-ray energy spectrum in ^{1}H(^{17}B,^{17}B*) reaction. The hached area represents the background. The insert shows the angular distribution of the inelastically scattered ^{17}B. The solid line is the DWBA calculation result.

in Fig. 1 shows the background spectrum obtained for the uncorrelated events with ^{17}B. The peak energy was 1.07(1) MeV, which is in agreement with previous works: 1.07(1) MeV[3] and 1.089(15) MeV[4].

The scattering angles of the ejectiles were measured by the drift chamber placed just downstream of the target. The insert in Fig. 1 shows the angular distribution of the inelastically scattered ^{17}B. The solid line shows the result of the DWBA analysis based on the code ECIS97 with $\Delta L^\pi = 2^+$. The experimental data is well reproduced by assuming the $\Delta L^\pi = 2^+$, which is consistent with the result of the previous ^{12}C(^{17}B,^{17}B*) reaction measurement. From the angular distribution, we have determined $\delta^{\rm p} = 1.22(8)$ fm. The obtained $\delta^{\rm p}$, together with $\delta^{\rm C}$, allows us to determine the transition matrix elements $M_{\rm p}$ and $M_{\rm n}$ for the ^{1}H(^{17}B,^{17}B*) reaction. Futhermore, by including the static Q moment for the ground state of ^{17}B,[5] we expect to improve the accuracies of $M_{\rm p}$ and $M_{\rm n}$, and to extract the effective charges for protons ($e_{\rm p}$) and neutrons ($e_{\rm n}$) in ^{17}B. Detailed analysis is now in progress.

*1 Tokyo Institute of Technology
*2 Tohoku University
*3 University of Tokyo
*4 Center for Nuclear Study, University of Tokyo
*5 Rikkyo University

References
1) N. Imai et al.: Phys. Rev. Lett. **92**, 062501 (2004).
2) Y. Kanada-En'yo: Phys. Rev. C **71**, 014310 (2005).
3) Y. Kondo et al.: Phys. Rev. C **71**, 044611 (2005).
4) Zs. Dombrádi et al.: Phys. Lett. B **621**, 81 (2005).
5) H. Ogawa et al.: Phys. Rev. C **67**, 064308 (2003).

Low-lying excited states of ^{17}C and ^{19}C†

Z. Elekes,[*1] Zs. Dombrádi,[*1] R. Kanungo, H. Baba,[*2] Zs. Fülöp,[*1] J. Gibelin,[*3] Á. Horváth,[*4] E. Ideguchi,[*5] Y. Ichikawa,[*5] N. Iwasa,[*6] H. Iwasaki,[*5] S. Kanno,[*2] S. Kawai,[*2] Y. Kondo,[*2] T. Motobayashi, M. Notani,[*5] T. Ohnishi,[*5] A. Ozawa, H. Sakurai,[*5] S. Shimoura,[*5] E. Takeshita,[*2] S. Takeuchi, I. Tanihata,[*7] Y. Togano,[*2] C. Wu, Y. Yamaguchi, Y. Yanagisawa, A. Yoshida, and K. Yoshida

[Nuclear structure, unstable nuclei, proton inelastic scattering, ^{17,19}C, bound excited states]

We have investigated the properties of the bound excited states in ^{17,19}C nuclei via the (p,p'γ) process in inverse kinematics at intermediate energy. The experiment was carried out at the RIKEN radioactive isotope separator RIPS. The details of the setup can be found in Ref. 1. Here, we focus on the results achieved. In the Doppler corrected spectrum, two peaks associated with the prompt decays of excited states in ^{19}C are found at 72(4) and 197(6) keV. The spectrum of ^{17}C showed two strong peaks at 210(4) and 331(6) keV establishing two low-lying excited states for this nucleus. The constructed level schemes and tentatively assigned spin/parities can be seen in Figs. 1 and 2. It is shown that the shell model gives a qualitative description of the results by predicting two excited states below 600 keV indepedent of the effective interactions applied. Furthermore, in analyzing the cross sections, a distorted wave calculation was performed using the ECIS79[2] code. During the analysis, the standard collective form factors were used for obtaining the "matter" deformation parameters (β_2) for the different transitions. As a result for ^{19}C, it can be concluded that having a $1/2^+$ ground state and the excited states of $3/2^+$-197(6) keV and $5/2^+$-269(8) keV result in $\beta_2(269\,\mathrm{keV}) = 0.29 \pm 0.03$. This relatively small deformation parameter suggests a basically single particle nature for the transition with some collective component. For ^{17}C, to reproduce the cross sections starting with a $3/2^+$ ground state, a $\beta_2 = 0.52 \pm 0.04$ is needed if the excited state has a spin of 5/2. This suggests that the ^{17}C nucleus is strongly deformed.

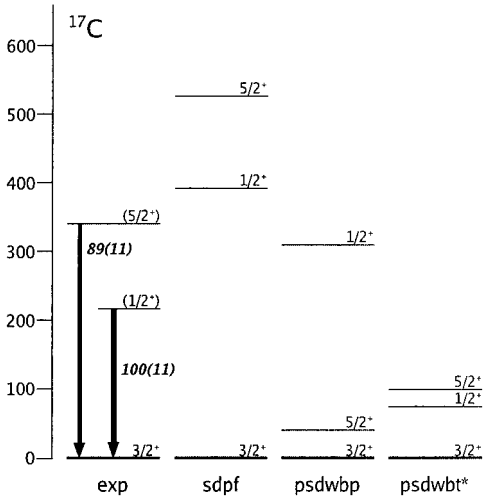

Fig. 1. Experimental level scheme for ^{17}C nucleus plotted together with *sdpf*,[3] *psdwbp*[4] and *psdwbt**[5] theoretical predictions. The arrows indicate the relative γ transition strengths observed in the $^{19}\mathrm{C} \rightarrow {}^{17}\mathrm{C}$ two-neutron removal rection.

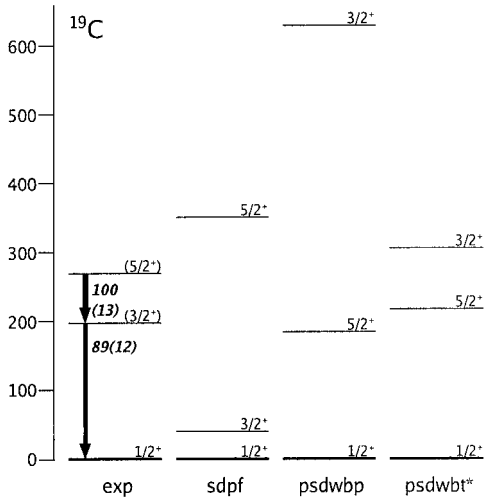

Fig. 2. Experimental level scheme for ^{19}C nucleus plotted together with *sdpf*,[3] *psdwbp*[4] and *psdwbt**[5] theoretical predictions. The arrows indicate the relative γ transition strengths observed in (p,p') reaction.

† Condensed from the article in Phys. Lett. B **614**, 174 (2005)

*1 Insitute of Nuclear Research, ATOMKI, Hungary
*2 Rikkyo University
*3 Institut de Physique Nucléaire, France
*4 Eötvös Lóránd University, Hungary
*5 University of Tokyo
*6 Tohoku University
*7 TRIUMF, Canada

References

1) Z. Elekes et al.: Phys. Lett. B **614**, 174 (2005).
2) J. Raynal: Phys. Rev. C **23**, 2571 (1981).
3) R. Fujimoto: Ph.D. Thesis, University of Tokyo (2003).
4) E. K. Warburton et al.: Phys. Rev. C **46**, 923 (1992).
5) O. Sorlin et al.: AIP Conf. Proc. **701**, 31 (2004).

Inelastic proton scattering of ^{19}C

Y. Satou,[*1] T. Nakamura,[*1] N. Fukuda, T. Sugimoto,[*1] Y. Kondo,[*1] N. Matsui,[*1] Y. Hashimoto,[*1] T. Nakabayashi,[*1] T. Okumura,[*1] M. Shinohara,[*1] T. Motobayashi, Y. Yanagisawa, N. Aoi, S. Takeuchi, T. Gomi, Y. Togano,[*2] S. Kawai,[*2] H. Sakurai, H. J. Ong,[*3] T. K. Onishi,[*3] S. Shimoura,[*4] M. Tamaki,[*4] T. Kobayashi,[*5] H. Otsu,[*5] Y. Matsuda,[*5] N. Endo,[*5] M. Kitayama,[*5] and M. Ishihara

[Nuclear reaction, unstable nuclei]

Nucleon-induced inelastic and charge exchange reactions, such as (p, p') and (p, n) reactions, have been one of the major tools for studying nuclear structures. Various combinations of spin, isospin, momentum and energy transfers are available in such reactions. We applied the (p, p') reaction in inverse kinematics to a structural study of the one-neutron halo nucleus ^{19}C, specifically in search of unbound excited states in this nucleus. The measurement was carried out by the invariant mass method, where the momentum vectors of all (or part of) the reaction products are measured and an invariant mass is constructed from them. This method is well suited for the spectroscopy of halo nuclei, which are often characterized by an extremely low particle decay threshold.[1,2)]

A ^{19}C beam with an energy of 70 MeV/nucleon was produced using RIPS from a 110 MeV/nucleon ^{22}Ne primary beam with an intensity of 100 pnA. The production target was a 6-mm-thick Be plate; the aluminum energy degrader used had a thickness of 3.03 mm. The typical intensity at F3 was 260 cps at a momentum setting of $\Delta P/P = \pm 3\%$.

Figure 1 shows the layout of the experiment. A cryogenic hydrogen target was used as experimental target, the thickness of which (120 mg/cm^2) was carefully chosen so as not to deteriorate invariant mass resolution, but to obtain a high counting rate. Outgoing neutrons were detected by a neutron counter hodoscope, consisting of plastic scintillators with a total volume of 400 l and located 5 m downstream of the target. Outgoing charged particles (^{18}C) were analyzed using a dipole magnet and detected by a plastic counter hodoscope associated with a multiwire drift chamber (FDC3). A He bag was placed along the charged particle path to minimize multiple Coulomb scattering effects.

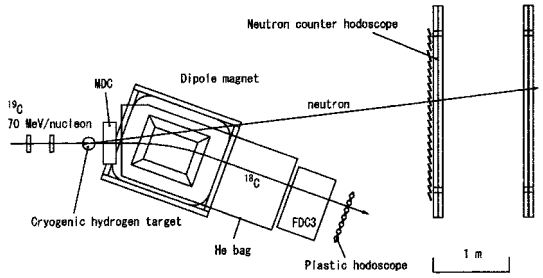

Fig. 1. Layout of experiment.

In the present experiment, a multiwire drift chamber (MDC), having a sense wire configuration of X-U-X'-V-X'-U'-X-V' and a sensitive area of 190 mm(H) × 140 mm(V), was installed at the entrance of the dipole magnet. It was used not only to improve the angular resolution but also to facilitate the mass identification of charged particles. A mass resolution of $A/\Delta A$(FWHM) ≈ 60 was attained by exploiting the ion optical property of the dipole magnet, given as transfer matrix element, and the track information obtained from both FDC3 and MDC.

Figure 2 shows a preliminary invariant mass spectrum of the ^{1}H(^{19}C,^{18}C $+ n$) reaction obtained in this experiment. The effects due to finite detector acceptance are not corrected. A peak can be clearly seen at approximately 0.9 MeV despite the background. This peak was observed for the first time in this measurement. Further analysis is in progress to determine J^π of this peak, and to clarify structures related to ^{19}C.

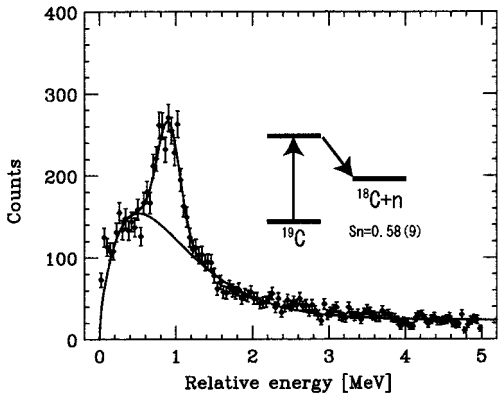

Fig. 2. Invariant mass spectrum observed for the ^{1}H(^{19}C, ^{18}C $+ n$) reaction at 70 MeV/nucleon.

*1 Department of Physics, Tokyo Institute of Technology
*2 Department of Physics, Rikkyo University
*3 Department of Physics, University of Tokyo
*4 Center for Nuclear Study, University of Tokyo
*5 Department of Physics, Tohoku University

References

1) T. Nakamura et al.: Phys. Rev. Lett. **83**, 1112 (1999).
2) N. Fukuda et al.: Phys. Rev. C **70**, 054606 (2004).

In-beam γ-ray spectroscopy of ^{19}N and ^{20}N

T. Okumura,[*1] T. Nakamura,[*1] Y. Satou,[*1] N. Fukuda, T. Sugimoto,[*1] Y. Kondo,[*1] N. Matsui,[*1] Y. Hashimoto,[*1] T. Nakabayashi,[*1] M. Shinohara,[*1] T. Motobayashi, Y. Yanagisawa, N. Aoi, S. Takeuchi, T. Gomi, Y. Togano,[*2] S. Kawai,[*2] H. Sakurai, H. J. Ong,[*3] T. K. Onishi,[*3] S. Shimoura,[*4] M. Tamaki,[*4] T. Kobayashi,[*5] H. Otsu,[*5] Y. Matsuda,[*5] N. Endo,[*5] M. Kitayama,[*5] and M. Ishihara

[Nuclear Reaction: ^{1}H(^{21}N,^{19,20}N*)X, γ-ray spectroscopy]

We have investigated low-lying excited states of the neutron-rich nitrogen isotopes ^{19}N and ^{20}N using in-beam γ-ray spectroscopy applied for the fragmentation of ^{21}N. Excited states of these neutron-rich nitrogen isotopes have not been well studied yet. In particular, no excited states have been observed for ^{20}N. In-beam γ-ray spectroscopy has been found to be a powerful method of locating low-lying bound excited states of such nuclei. This is the first application of in-beam γ-ray spectroscopy to the analysis of the neutron-rich nitrogen isotopes ^{19}N and ^{20}N.

The experiment was performed at the RIKEN Projectile fragment Separator (RIPS).[1)] A 6.0-mm-thick ^{9}Be production target was bombarded with a 110 MeV/nucleon ^{22}Ne beam. We obtained a secondary ^{21}N beam with an energy of 72 MeV/nucleon, and an intensity of about 60 cps. The purity of the ^{21}N beam was about 3%.

The particle identification of the secondary beam was performed by combining the pulse height of a plastic scintillator at the second focal point (F2PL) and the time-of-flight (TOF) information obtained from the RF signal of the cyclotron and the timing signal of the F2PL. The position and angle of the incident beam at the secondary target were measured using two parallel-plate avalanche counters (PPACs) placed at the third focal point. The secondary target was liquid hydrogen ($LiqH_2$) with a thickness of 120 mg/cm^2. The de-excitation γ rays from excited states of the projectile fragments were detected using 48 blocks of NaI(Tl) scintillators surrounding the secondary target. Each scintillator crystal was $6 \times 6 \times 12$ cm^3.

Outgoing nitrogen isotopes downstream of the secondary target were analyzed using a magnetic spectrometer equipped with two drift chambers (MDC and FDC3) and plastic scintillators (hodoscope). The particle identification of outgoing nitrogen isotopes was performed by combining ΔE and TOF information from the hodoscope, and magnetic rigidity information from MDC and FDC3.

The upper and lower panels in Fig. 1 show the preliminary Doppler-shift-corrected γ-ray energy spectra obtained in coincidence with the outgoing ^{19}N and ^{20}N from the $LiqH_2$ target, respectively. Peaks are observed at 534 ± 20 keV and 1104 ± 49 keV in the case of ^{19}N, and at 612 ± 21 keV and 850 ± 17 keV in the case of ^{20}N. The peaks for ^{19}N are compared with known levels, as shown in Fig. 2.[2)] The observed peaks are assigned to γ rays coming from 1650 keV to 1110 keV and from 1110 keV to ground state. Further analysis to determine of these peaks is now in progress.

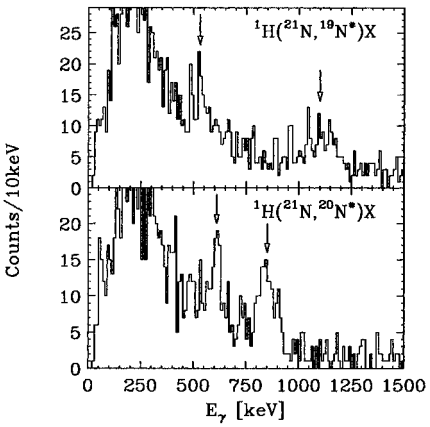

Fig. 1. Doppler-shift-corrected γ-ray energy spectra for ^{19}N (upper) and ^{20}N (lower).

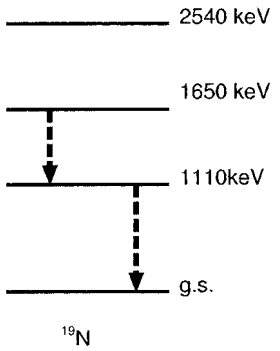

Fig. 2. Known levels of ^{19}N. Possible assignments of observed peaks are shown by dashed arrows.

*1 Department of Physics, Tokyo Institute of Technology
*2 Department of Physics, Rikkyo University
*3 Department of Physics, University of Tokyo
*4 Center for Nuclear Study, University of Tokyo
*5 Department of Physics, Tohoku University

References

1) T. Kubo et al.: Nucl. Instrum. Methods Phys. Res. B **70**, 309 (1992).
2) R. B. Firestone et al.: Table of Isotopes

Study of ^{22,23}O nuclear structure by ^{22}O+^{2}H reaction

Z. Elekes,[*1] Zs. Dombrádi,[*1] S. Bishop, Zs. Fülöp,[*1] J. Gibelin,[*2] T. Gomi, Y. Hashimoto,[*3] N. Imai, N. Iwasa,[*4] H. Iwasaki,[*5] G. Kalinka,[*1] Y. Kondo,[*3] A. A. Korsheninnikov,[*6] K. Kurita,[*7] M. Kurokawa, N. Matsui,[*3] T. Motobayashi, T. Nakamura,[*3] T. Nakao,[*5] E. Yu. Nikolskii,[*6] T. K. Ohnishi, T. Okumura,[*3] S. Ota,[*8] A. Perera, A. Saito,[*5] H. Sakurai,[*5] Y. Satou,[*3] D. Sohler,[*1] T. Sumikama, D. Suzuki,[*7] M. Suzuki,[*7] H. Takeda,[*5] S. Takeuchi, Y. Togano,[*7] and Y. Yanagisawa

[Nuclear structure, unstable nuclei, transfer reaction, single-particle energies, gamma-ray spectroscopy]

To understand the rapid change in the location of the neutron dripline between O and F species, we investigated the nuclear structure of the neutron–rich ^{22,23}O nuclei. Since the details of the experiment can be found in Ref. 1, here we concentrate on the results. By studying the Doppler–corrected gamma-ray spectrum from the ^{22}O(d,d') reaction, the excitation cross section for the first excited state in ^{22}O has been determined to be $\sigma(0_1^+ \rightarrow 2_1^+) = 19 \pm 3$ mb. From distorted wave analysis, we derived the "matter" deformation length $\delta_M = 0.77 \pm 0.07$ fm, which corresponds to a moderate mass deformation of $\beta_M = 0.23 \pm 0.02$. We can compare this result with the data from the ^{22}O+^{197}Au reaction,[2] where the proton deformation (β_p) was derived to be between 0.2 and 0.24. This means that the neutron deformation of ^{22}O is very close the proton deformation taking into account the mass deformation determined in the present study, i.e, the $N = 14$ subshell closure makes both the proton and neutron distributions nearly spherical in ^{22}O.

To populate the first excited state in ^{23}O, which is expected to be unbound, we studied the neutron transfer reaction ^{2}H(^{22}O,^{23}O)^{1}H in which the excited ^{23}O nucleus decays by emitting a neutron and an ^{22}O isotope. The two preliminary excitation energy spectra can be found in Fig. 1. Both of them were produced by selecting neutrons with their light outputs larger than 5 MeV of the electron–equivalent energy to cut the gamma-ray-induced events out, and by requiring multiplicities M $\leq$ 4 to eliminate the events caused by cosmic ray radiation. Panel (a) shows a spectrum with 20 ns $\leq$ TOF $\leq$ 58 ns between the secondary target and the neutron detectors, while panel (b) shows a spectrum with 20 ns $\leq$ TOF $\leq$ 45 ns focussing on the low-energy part of the excitation energy spectrum. It is clearly visible that the lowest energy peak is at 4 MeV, which most probably corresponds to the first excited state of ^{23}O with the $d_{3/2}$ neutron single–particle nature. Furthermore, thorough analyses of the angular distributions are now in progress to confirm these arguments.

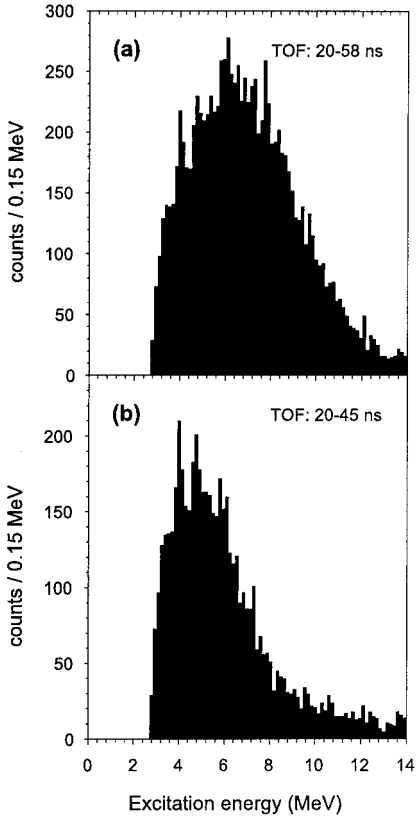

Fig. 1. Excitation energy spectrum of ^{23}O from ^{22}O(d,p) reaction.

References

1) Z. Elekes et al.: RIKEN Accel. Prog. Rep. **38**, 50 (2005).
2) P. G. Thirolf et al.: Phys. Lett. B **485**, 16 (2000).

*1 ATOMKI, Hungary
*2 Institut de Physique Nucléaire, France
*3 Tokyo Institute of Technology
*4 Tohoku University
*5 University of Tokyo
*6 Kurchatov Institute, Russia
*7 Rikkyo University
*8 Kyoto University

Proton single-particle states in ^{23}F

S. Michimasa, S. Shimoura,[*1] H. Iwasaki,[*2] M. Tamaki,[*1] S. Ota,[*3] N. Aoi, H. Baba, N. Iwasa,[*4] S. Kanno,[*5] S. Kubono,[*1] K. Kurita,[*5] M. Kurokawa, T. Minemura, T. Motobayashi, M. Notani,[*6] H. J. Ong,[*2] A. Saito,[*1] H. Sakurai, S. Takeuchi, E. Takeshita,[*5] Y. Yanagisawa, and A. Yoshida

[Nuclear reactions: ^{4}He(^{22}O,^{23}F*), ^{4}He(^{23}F,^{23}F*), ^{4}He(^{24}F,^{23}F*), ^{4}He(^{25}Ne,^{23}F*), single-particle state, In-beam γ-ray spectroscopy]

We have measured de-excited γ rays from ^{23}F produced by the proton transfer reaction ^{4}He(^{22}O,^{23}F*), the inelastic scattering ^{4}He(^{23}F,^{23}F*), the neutron knockout reaction ^{4}He(^{24}F,^{23}F*), and the two nucleon knockout reaction ^{4}He(^{25}Ne,^{23}F*).

The experiment was performed at the RIPS beam line in RIKEN. ^{40}Ar ions were accelerated up to 63 MeV/nucleon using the linear accelerator scheme of RFQ-RILAC-CSM-RRC. The average intensity of the primary beam was ∼500 particle nA. The primary target was ^{9}Be with a thickness of 1 mm. The secondary beam was a cocktail of ^{22}O, ^{23}F, ^{24}F and ^{25}Ne, and produced by their projectile fragmentation reaction. The averaged beam energies of ^{22}O, ^{23}F, ^{24}F and ^{25}Ne were 35.0, 41.5, 36.0 and 42.7 MeV/nucleon, and these intensities were 2×10^3, 6×10^2, 5×10^2 and 1×10^3 cps, respectively. The secondary beam bombarded a liquid helium target[1] of 100 mg/cm^2 with havar foil windows. The reaction products were identified using a telescope consisting of 9 SSDs and 36 NaI(Tl) scintillators.[2] The scattering angles of the reaction products were measured using three PPACs. De-excitation γ rays from the reaction products were detected using 150 NaI(Tl) scintillators[3] surrounding the secondary target.

In the analysis, we examined the coincidences of multiple γ rays in the above-mentioned reactions and reconstructed the γ-decay scheme in ^{23}F as shown in Fig. 1. The level energies with underlines show newly observed excited states in the present experiment. The bar graphs on the right side of the excitation energies show the relative cross sections to populate these excited states. In these relative cross sections, one can observe that the 2268- and 4059-keV states are strongly populated by the proton transfer reaction, but hardly populated by the neutron knockout reaction. This strongly suggests that these states have a proton single-particle nature. Furthermore, the cross sections for these states by α inelastic scattering may indicate that the 2268- and 4059-keV states have proton single-particle configurations of $s_{1/2}$ and $d_{3/2}$, respectively. The angular distributions of scattered ^{23}F ions

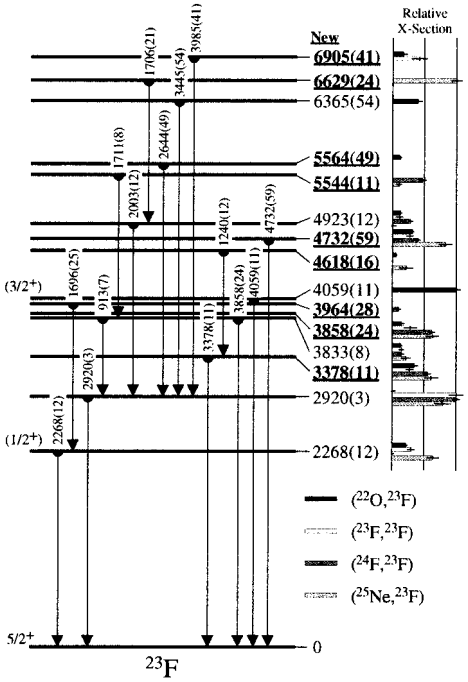

Fig. 1. Proposed level and γ-decay scheme in ^{23}F. The level energies with underlines show newly observed excited states in the present experiment. The bars on the right side of excitation energies show the relative cross sections to populate these states.

for these states were consistent with the spin-parity assignments.

The excitation energies of these proton single-particle states are compared with the shell-model calculations on the basis of the USD[4] and SDPF-M[5] effective interactions. These states are located at higher energies than the predictions by ∼500 keV, although other states correspond to the predictions within 100 keV. This may indicate that the shell gaps of $d_{5/2}$-$d_{3/2}$ and $d_{5/2}$-$s_{1/2}$ in ^{23}F are wider than those in stable nuclei.

*1 Center for Nuclear Study, University of Tokyo
*2 Department of Physics, University of Tokyo
*3 Department of Physics, Kyoto University
*4 Department of Physics, Tohoku University
*5 Department of Physics, Rikkyo University
*6 Argonne National Laboratory, USA

References

1) H. Ryuto et al.: Nucl. Instrum. Methods Phys. Res. A **555**, 1 (2005).
2) M. Tamaki et al.: CNS-REP-59, 76 (2003).
3) S. Takeuchi et al.: RIKEN Accel. Prog. Rep. **36**, 148 (2003).
4) B. H. Wildenthal et al.: Prog. Part. Nucl. Phys. **11**, 5 (1984).
5) Y. Utsuno et al.: Phys. Rev. C **64**, 011301 (1999).

Coulomb excitation measurement for ^{18}Ne with precise angular distribution

K. Yamada, N. Iwasa,[*1] S. Bishop, Z. Elekes,[*2] J. Gibelin,[*3] M. Hosoi,[*4] K. Ieki,[*5] K. Ishikawa,[*6] H. Iwasaki,[*7] S. Kawai,[*5] Y. Kondo,[*6] S. Kubono,[*8] K. Kurita,[*5] M. Kurokawa, N. Matsui,[*6] T. Minemura,[*9] H. Morikawa,[*5] T. Nakamura,[*6] M. Niikura,[*8] M. Notani,[*10] S. Ota,[*11] A. Saito,[*8] H. Sakurai, S. Shimoura,[*8] K. Sugawara,[*4] T. Sugimoto,[*6] H. Suzuki,[*7] T. Suzuki,[*4] E. Takeshita,[*5] S. Takeuchi, I. Tanihata,[*12] T. Teranishi,[*13] Y. Togano,[*5] K. Yamaguchi,[*5] Y. Yanagisawa, and T. Motobayashi

[Nuclear reactions: Pb(^{18}Ne,^{18}Neγ), $E(^{18}\mathrm{Ne}) = 50\,A$MeV, Coulomb excitation]

The comparison of $B(\mathrm{E2}; 0^+_{\mathrm{g.s.}} \rightarrow 2^+_1)$ in the mirror nuclei ^{18}O and ^{18}Ne is of interest to understand the core polarization mechanism and evolution of the shell structure, because each of these isotopes has a pair of valence nucleons outside the doubly magic ^{16}O core.[1] The B(E2) for ^{18}O is well-known, whereas the one for the unstable nucleus ^{18}Ne is not. The previous work on intermediate-energy Coulomb excitation measurement[2] reported a B(E2) value that markedly disagreed with two lifetime measurements.[3,4] The Coulomb excitation measurement has a large ambiguity for the treatment of nuclear excitation components due to the lack of angular distribution data.[4] The present study is aimed at providing Coulomb excitation data with a precise angular distribution to resolve the ambiguity.

A secondary beam of ^{18}Ne was produced by the projectile fragmentation of a 135 AMeV ^{24}Mg beam on a 1.35-mm-thick nickel target at RIPS. The ^{18}Ne beam irradiated a lead target of 226 mg/cm^2 thickness with a typical intensity of 800 counts per second. The average energy of the beam was 50 AMeV in the middle of the lead target. The experimental setup is the same as the one described in Ref. 5.

Figure 1 shows the Doppler-corrected γ-ray spectrum measured in coincidence with inelastically scattered ^{18}Ne. A single distinct peak can be seen at 1.9 MeV, which corresponds to the 1887 keV γ-ray of the $2^+_1 \rightarrow 0^+_{\mathrm{g.s.}}$ transition in ^{18}Ne. The total photopeak efficiency was 12% for 1887 keV photons from the ^{18}Ne nucleus in flight with $v/c \approx 0.3$. The possible contribution to the photopeak yield given by feeding γ-rays from the second 2^+ excited state should be considered to derive the proper excitation cross section. By fitting

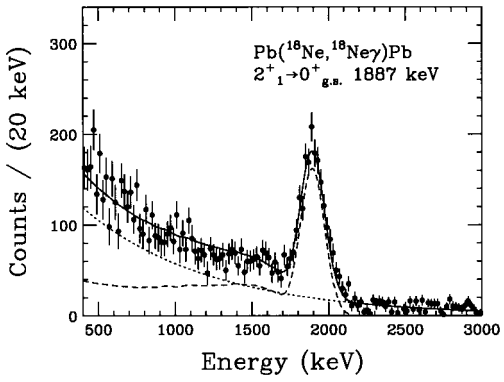

Fig. 1. Doppler-corrected γ-ray spectrum obtained for ^{18}Ne inelastically scattered on lead target. The solid curve indicates the result of peak-fit analysis, where a simulated line shape (dashed curve) and an exponential background (dotted curve) were taken.

the detector response for corresponding 1.7 MeV γ-rays to the spectrum (not shown in Fig. 1), the contribution was evaluated to be 5.5±5.5% for the photopeak yield. The obtained ^{18}Ne(Pb, Pb′) cross section consists of a neutron excitation component and a proton excitation component. To extract the B(E2) of ^{18}Ne, the neutron excitation component is subtracted, which is derived from the B(E2) of ^{18}O assuming isospin symmetry. The proton excitation component is further divided into nuclear excitation and Coulomb excitation, both of which can evidently be decomposed and related to B(E2) using DWBA calculation. The resultant $B(\mathrm{E2}; 0^+_{\mathrm{g.s.}} \rightarrow 2^+_1)$ of ^{18}Ne is $180 \pm 26\,e^2\mathrm{fm}^4$, which is consistent with the lifetime measurement,[4] indicating that the disagreement may not depend on the experimental method. Further analysis of the angular distribution is in progress.

*1 Department of Physics, Tohoku University
*2 ATOMKI, Hungary
*3 Institute de Physique Nucléaire, Orsay, France
*4 Department of Physics, Saitama University
*5 Department of Physics, Rikkyo University
*6 Department of Physics, Tokyo Institute and Technology
*7 Department of Physics, University of Tokyo
*8 Center for Nuclear Study, University of Tokyo
*9 High Energy Accelerator Research Organization (KEK)
*10 Argonne National Laboratory, USA
*11 Department of Physics, Kyoto University
*12 TRIUMF, Canada
*13 Department of Physics, Kyushu University

References

1) R. Sherr and H. T. Fortune: Phys. Rev. C **58**, 3292 (1998).
2) L. A. Riley et al.: Phys. Rev. C **62**, 034306 (2000).
3) A. B. McDonald et al.: Nucl. Phys. A **258**, 152 (1976).
4) L. A. Riley et al.: Phys. Rev. C **68**, 044309 (2003).
5) N. Iwasa et al.: RIKEN Accel. Prog. Rep. **38**, 58 (2005).

Search for low-lying dipole strength in the neutron-rich nucleus ^{26}Ne

J. Gibelin,[*1,*2,*3] N. Aoi, H. Baba, D. Beaumel,[*2] Y. Blumenfeld,[*2] Z. Elekes,[*4] N. Frascaria,[*2] N. Fukuda, T. Gomi,[*5] K. Ishikawa,[*6] Y. Kondo,[*6] T. Kubo, V. Lima,[*2] T. Motobayashi, T. Nakamura,[*6] A. Saito,[*3] Y. Satou,[*6] E. Takeshita,[*3] S. Takeuchi, T. Teranishi,[*7] Y. Togano,[*3] A. M. Vinodkumar,[*6] Y. Yanagisawa, and K. Yoshida

[Coulomb excitation, low-lying strength, radioactive beam, ^{26}Ne]

How the Giant Dipole Resonance strength evolves when going from stable to weakly bound nuclei with an extreme neutron-to-proton ratio is an interesting question.[1,2] Recent theoretical approaches based on mean field calculation predict that in the neutron-rich nucleus ^{26}Ne, almost 5% of the Thomas-Reiche-Kuhn (TRK) energy weighted sum rule is exhausted by a strength centered at approximatly 8 MeV.[3] This region of energy is located between the one-neutron and two-neutron emission thresholds. To confirm this prediction, we performed the Coulomb excitation of ^{26}Ne at intermediate energies on a lead target and used the invariant mass method to reconstruct $B(E1)$ strength.

A secondary ^{26}Ne beam was produced through the fragmentation of a 95 A.MeV ^{40}Ar primary beam on a 2-mm-thick ^{9}Be target. The intensity obtained was $\sim 5.10^3$ pps with an incident energy of 58 MeV/nucleon and a purity of 80%. It was tracked with two parallel-plate avalanche counters impinged on a 230 mg/cm^2 ^{nat}Pb. The outgoing charged fragments were measured using a set of telescopes placed 1.2 m upstream of the target, which consisted of two layers (X and Y) of silicon strip detectors (SSD) and a layer of 3-mm-thick Si(Li) from the charged-particle detector MUST.[4] An unambiguous mass and charge identification of all projectile-like fragments was achieved using the E-ΔE method. In-beam γ-rays were detected using the 4π-γ-detector DALI2.[5] The hodoscope for neutron detection was an array of 4 layers of 29 plastic rods each, placed 3.5 m downstream of the target. Its total intrinsic efficiency for the detection of one 60 MeV neutron was calculated to be $\sim$25%. Finally, 29 thin plastic rods were used to cover the front face of the wall in order to veto charged particles as well as to provide an active beam stopper.

The excitation energy spectrum of ^{26}Ne for the ^{25}Ne+n decay channel take into account all possible excited states of ^{25}Ne.[6] Furthermore, the method enables us to deduce the corresponding decay branching ratio. We observed an enhancement of the cross section at $E^* \sim 9$ MeV. The analysis of the differential cross section allowed a multipole decomposition of these states. The result of the fit of this distribution using ECIS 97 calculation and the hypothesis that the nuclear and Coulomb deformation lengths are equal is presented in Fig. 1. We deduce that 5.2 ± 2.1% of the TRK is exhausted by our structure centred at $E^* \sim 9$ MeV, which corresponds to a $B(E1) = 0.54 \pm 0.18$ e^{2}fm^2, in agreement with Cao and Ma[3] calculations in the framework of QRRPA. Other models[7–9] predict similar results for the existence of a low-lying state. However they are divergent on the collectivity and the configurations involved. In the future, a comparison of our results with calculated branching ratios should enable the discrimination between different approaches.

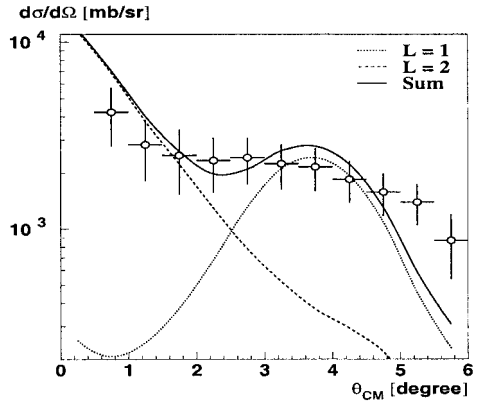

Fig. 1. Angular distribution of scattered ^{26}Ne on lead target for excitation energies between one- and two-neutron emission thresholds, fitted with theoretical $L = 1$ and $L = 2$ distributions.

*1 On leave for Lawrence Berkeley National Laboratory, USA
*2 Institut de Physique Nucléaire, France
*3 Department of Physics, Rikkyo University
*4 Department of Physics, Tokyo Institute of Technology
*5 National Institute of Radiological Sciences
*6 ATOMKI, Hungary
*7 Department of Physics, Kyushu University

References

1) A. Leistenschneider et al.: Phys. Rev. Lett. **86**, 5442 (2001).
2) P. Adrich et al.: Phys. Rev. Lett. **95**, 132501 (2005).
3) L.-G. Cao and Z.-Y. Ma: Phys. Rev. C **71**, 034305 (2005).
4) Y. Blumenfeld et al.: Nucl. Instrum. Methods A **421**, 471 (1999).
5) S. Takeuchi et al.: RIKEN Accel. Prog. Rep. **36**, 148 (2003).
6) J. Gibelin et al.: RIKEN Accel. Prog. Rep. **38**, 53 (2005).
7) E. Khan et al.: Private communication (2005).
8) S. Péru et al.: Private communication (2005).
9) P. Ring et al.: Private communication (2005).

Measurement of $B(E2; 0^+ \rightarrow 2_1^+)$ value in ^{26}Ne

J. Gibelin,[*1,*2,*3] N. Aoi, H. Baba, D. Beaumel,[*2] Y. Blumenfeld,[*2] Z. Elekes,[*4] N. Frascaria,[*2] N. Fukuda, T. Gomi, K. Ishikawa,[*5] Y. Kondo,[*5] T. Kubo, V. Lima,[*2] T. Motobayashi, T. Nakamura,[*5] A. Saito,[*3] Y. Satou,[*5] E. Takeshita,[*3] S. Takeuchi, T. Teranishi,[*6] Y. Togano,[*3] A. M. Vinodkumar,[*5] Y. Yanagisawa, and K. Yoshida

[Coulomb excitation, B(E2), radioactive beam, ^{26}Ne]

We performed the experimental Coulomb excitation of a secondary radioactive beam of ^{26}Ne using the RIKEN Projectile fragment Separator. This secondary ^{26}Ne beam was produced by the fragmentation of a 95 A.MeV ^{40}Ar primary beam on a 2-mm-thick ^{9}Be target. The intensity obtained was $\sim 5 \times 10^3$ pps with an incident energy of 58 A.MeV and a purity of 80%. It was tracked with two parallel-plate avalanche counters[1] before impinging on a 230 mg/cm^2 ^{nat}Pb. The outgoing charged fragments were measured using a hodoscope placed 1.2 m downstream of the target, which consisted of two layers (X and Y) of silicon strip detectors (SSD) and a layer of 3-mm-thick Si(Li) from the charged-particle detector MUST.[2] The unambiguous mass and charge identification of all projectile-like fragments were obtained using the E-ΔE method. In-beam γ-rays were detected using the 4π NaI detector DALI2.[3]

We extracted the integrated cross section for the excitation of the 2_1^+ state of ^{26}Ne (68(8) mb) by identifying its 2018 keV γ-decay. Using the ECIS 97 code with the optical parameters of ^{20}Ne at 40 MeV/n impinging on ^{208}Pb[4] and on the basis of the hypothesis that the nuclear ($\delta_N^{L=2}$) and the Coulomb ($\delta_C^{L=2}$) deformation lengths are equal, we deduced a $B(E2) = 87(13)\,e^2fm^4$, which reproduces both the integrated excited cross section and the corresponding experimental angular distribution of inelastically scattered ^{26}Ne ions, as shown in Fig. 1.

Our $B(E2)$ value disagrees with the previous value of $B(E2) = 228(41)\,e^2fm^4$ reported by Pritychenko et al..[5] Note that by using their method, which supposes that the γ-ray emission cross section is a pure Coulomb excitation, we extracted a $B(E2) = 230(30)\,e^2fm^4$, which is in excellent agreement with their result. The corresponding angular distribution is plotted in Fig. 1 (dashed line) showing a shape different from that obtained in the experiment. The discrepancy in the two results thus comes from the fact that our first method takes into account the nuclear excitation component.

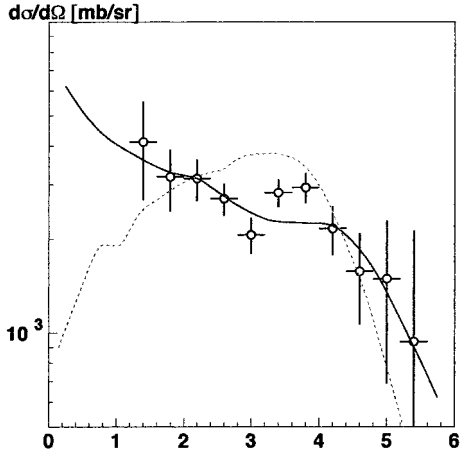

Fig. 1. Scattering angular distribution for first 2^+ excited state of ^{26}Ne on lead target compared with ECIS 97 calculation: solid line, for the case in which $\beta_N = 0.32$ and $\beta_C = 0.31$; dashed line, results of calculation with pure Coulomb excitation ($\beta_n = 0.0$). Both provide an integrated cross section of 68 mb. Note that the deformation lengths are correlated to deformation parameters *via* the relations $\delta_N = \beta_N R_N$ and $\delta_C = \beta_C R_C$ where R_N and R_C are the nuclear and Coulomb radii, respectively.

References
1) H. Kumagai et al.: Nucl. Instrum. Methods Phys. Res. A **470**, 562 (2001).
2) Y. Blumenfeld et al.: Nucl. Instrum. Methods Phys. Res. A **421**, 471 (1991).
3) S. Takeuchi et al.: RIKEN Accel. Prog. Rep. **36**, 148 (2003).
4) T. Suomijärvi et al.: Nucl. Phys. A **491**, 314 (1989).
5) B. Pritychenko et al.: Phys. Lett. B **461**, 322 (1999).

*1 On leave for Lawrence Berkeley National Laboratory, USA
*2 Institut de Physique Nucléaire, France
*3 Department of Physics, Rikkyo University
*4 Department of Physics, Tokyo Institute of Technology
*5 ATOMKI, Hungary
*6 Department of Physics, Kyushu University

Quadrupole collectivity of ^{28}Ne and the boundary of the island of inversion†

H. Iwasaki,[*1] T. Motobayashi, H. Sakurai, K. Yoneda, T. Gomi, N. Aoi, N. Fukuda, Zs. Fülöp,[*2] U. Futakami,[*3] Z. Gacsi,[*2] Y. Higurashi, N. Imai,[*4] N. Iwasa,[*5] T. Kubo, M. Kunibu,[*3] M. Kurokawa, Z. Liu,[*6] T. Minemura, A. Saito,[*7] M. Serata, S. Shimoura,[*7] S. Takeuchi, Y. X. Watanabe,[*4] K. Yamada, Y. Yanagisawa, and M. Ishihara

[Nuclear reactions: Pb, C(^{28}Ne,^{28}Neγ), $E(^{28}\mathrm{Ne})$=46A MeV, intermediate-energy Coulomb excitation, deduced B(E2)]

We report a recent result of $B(\mathrm{E2}\uparrow)$ for the $0^+_{g.s.}\rightarrow 2^+_1$ excitation in ^{28}Ne obtained by intermediate-energy heavy-ion inelastic scattering in reversed kinematics.[1] As the most neutron-rich even-even isotope along the $N = 18$ line, ^{28}Ne attracts much attention[2,3] because of its location close to the 'island of inversion' where an enhancement of quadrupole deformation is possible. A sudden decrease of $E(2^+_1)$ at $N = 18$ among the neutron-rich Ne isotopes (^{26}Ne: 2.02 MeV,[3] ^{28}Ne: 1.29 MeV,[2,3] and ^{30}Ne: 0.79 MeV[4]) suggests that a tendency towards deformation occurs at ^{28}Ne. A large $B(\mathrm{E2}\uparrow)$ value reported in an earlier study of intermediate-energy Coulomb excitation[2] might imply large deformation of ^{28}Ne, however a definite conclusion cannot be made due to the relatively large experimental uncertainties. Thus, further experimental effort towards a precise determination of $B(\mathrm{E2}\uparrow)$ of ^{28}Ne is called for.

The experiment was performed at the RIPS facility in RIKEN using the same experimental arrangement described in Ref. 5. The ^{28}Ne beam with a typical intensity of 100 counts per second was produced by RIPS and was directed onto the reaction target placed at the final focal plane of RIPS. Two different targets of 693-mg/cm^2-thick Pb and 339-mg/cm^2-thick C were used to excite the projectiles. The angle-integrated cross sections for the 2^+_1 excitation of ^{28}Ne were obtained to be 93(13) mb and 36(6) mb, respectively, for the ^{28}Ne+Pb and ^{28}Ne+C inelastic scattering, from the measurement of de-excitation γ-rays in coincidence with the scattered ^{28}Ne particles. To obtain the reduced E2 transition probability $B(\mathrm{E2}\uparrow)$, a distorted wave calculation was performed using the coupled channel code ECIS79 in a similar fashion to that used in Ref. 5. The $B(\mathrm{E2}\uparrow)$ value was deduced from the 2^+_1 excitation cross section with the lead target, while the measurement with the carbon target was used to evaluate possible contributions from nuclear excitations. We thus obtained $B(\mathrm{E2}; 0^+_{\mathrm{g.s.}} \rightarrow 2^+_1) = 132(23)$ e^{2}fm^4, which is smaller than the previously reported value[2] of 269(136) e^{2}fm^4 with small overlap of the errors. Unexpectedly, the present result of $B(\mathrm{E2}\uparrow)$ turns out to be even smaller than that of the less neutron-rich isotope ^{26}Ne ($B(\mathrm{E2}\uparrow)$=228(41) e^{2}fm^4),[2] which contrasts sharply to the considerable decrease of $E(2^+_1)$ from ^{26}Ne to ^{28}Ne.

One possible scenario related to the suppression of $B(\mathrm{E2}\uparrow)$ for ^{28}Ne follows from a naive shell-model picture as follows. For isotopes located just on the boundary of the 'island of inversion', a delicate interplay between the normal ($0\hbar\omega$) and intruder ($2\hbar\omega$) configurations prevails. Away from the island, the $0\hbar\omega$ configurations dominate both the ground state and the 2^+_1 state, while the $2\hbar\omega$ configurations occur at higher excitation energies. Degeneracy between these two configurations is gradually promoted near the island of inversion. Since the 0^+–2^+ level spacing in the $2\hbar\omega$ configuration is smaller than that in the $0\hbar\omega$ one, configuration mixing firstly occurs between the two unperturbed 2^+ states with the $0\hbar\omega$ and $2\hbar\omega$ configurations, pushing down the 2^+_1 energy in ^{28}Ne.[2] In this circumstance, deformation is promoted mostly in the 2^+_1 state, while the ground state remains rather spherical. As for the E2 strength, the small overlap between the ground state and the 2^+_1 state may lead to a hindered $B(\mathrm{E2}\uparrow)$ in ^{28}Ne, despite the lowered $E(2^+_1)$.[2] A similar argument has been made for ^{34}Si, where both the $E(2^+_1)$ and $B(\mathrm{E2}\uparrow)$ values are found to be considerably small with respect to the $0\hbar\omega$ shell model calculations.[6] Since both of the ^{28}Ne and ^{34}Si nuclei are located between the regions of the 'normal' (^{26}Ne and ^{36}S) and 'deformed' (^{30}Ne and ^{32}Mg) nuclei, the suppressed collectivity presently observed in ^{28}Ne can be a characteristic feature of nuclei lying on the very boundary of the island of inversion.

† Condensed from the article in Phys. Lett. B **620**, 118 (2005)
*1 Department of Physics, University of Tokyo
*2 ATOMKI, Hungary
*3 Department of Physics, Rikkyo University
*4 High Energy Accelerator Research Organization (KEK)
*5 Department of Physics, Tohoku University
*6 Institute of Modern Physics, China
*7 Center for Nuclear Study, University of Tokyo

References
1) H. Iwasaki et al.: Phys. Lett. B **620**, 118 (2005).
2) B. V. Pritychenko et al.: Phys. Lett. B **461**, 322 (1999).
3) F. Azaiez: Nucl. Phys. A **704**, 37c (2002).
4) Y. Yanagisawa et al.: Phys. Lett. B **566**, 84 (2003).
5) H. Iwasaki et al.: Phys. Lett. B **522**, 227 (2001).
6) R. W. Ibbotson et al.: Phys. Rev. Lett. **80**, 2081 (1998).

Coulomb excitation of ^{20}Mg

N. Iwasa,[*1] S. Bishop, Z. Elekes,[*2] J. Gibelin,[*3,*4] M. Hosoi,[*5] K. Ieki,[*3] K. Ishikawa,[*6] H. Iwasaki,[*7] S. Kawai,[*3] S. Kubono,[*8] K. Kurita,[*3] M. Kurokawa, N. Matsui,[*6] T. Minemura,[*9] H. Morikawa,[*3] T. Nakamura,[*6] M. Niikura,[*8] M. Notani,[*10] S. Ota,[*11] A. Saito,[*8] H. Sakurai, S. Shimoura,[*8] K. Sugawara,[*5] T. Sugimoto,[*6] H. Suzuki,[*7] T. Suzuki,[*5] I. Tanihata,[*12] E. Takeshita,[*2] S. Takeuchi, T. Teranishi,[*13] Y. Togano,[*3] K. Yamada, K. Yamaguchi,[*3] Y. Yanagisawa, and T. Motobayashi

[Nuclear reactions: Pb(^{20}Mg,^{20}Mgγ), $E(^{20}\mathrm{Mg}) = 58$ A MeV, Coulomb excitation]

The energies of the first 2^+ states and the reduced transition probabilities B(E2) of even-even nuclei are one of the fundamental quantities for studying the collective character of nuclei. We studied the ^{20}Mg nucleus, which lies near the proton drip line, by measuring the Coulomb excitation in reverse kinematics.

A radioactive ^{20}Mg beam was produced by RIPS in cooperation with the RF deflector[1] and bombarded a lead target with a thickness of 226 mg/cm^2 placed at the final achromatic focal plane of RIPS. The beam energy at the center of the target was 58 A MeV. Deexcitation γ rays were measured using an array of 68 NaI(Tl) detectors (DALI)[2] surrounding the target in coincidence with scattered ^{20}Mg measured by 9 silicon counter telescopes arranged in a 3×3 matrix. The details of the experimental setup were previously described in Ref. 3.

Figure 1 shows the angular distribution of inelastically scattered ^{20}Mg measured in coincidence with the gamma line at 1.61 ± 0.06 MeV, which was tentatively assigned to the transition of $2_1^+ \rightarrow 0_1^+$.[3] The curves in the figure represent the results of Monte Carlo simulations based on theoretical $\ell = 2$ angular distributions obtained using a coupled channel code ECIS79. The experimental angular distribution is well reproduced, indicating that the assumption of the $\ell = 2$ transition is valid.

In the ECIS79 calculation, optical potential parameters were obtained for the elastic scattering data of 84 A MeV ^{17}O+Pb(dashed),[4] 40 A MeV ^{20}Ne+Pb (solid),[5] and 41 A MeV ^{40}Ar+Pb(dot-dashed).[6] The coupling potentials were obtained by the collective deformation model with the Coulomb and nuclear deformation parameters β_2^C and β_2^n. β_2^C is directly related to B(E2) as $\beta_2^C = 4\pi\sqrt{B(\mathrm{E2})/3ZeR^2}$, whereas β_2^n affects the nuclear interaction between ^{20}Mg and lead. We adopted the Bernstein method,[7] which deduces β_2^n from the proton and neutron transition matrix elements M_p and M_n, respectively. M_p is related to B(E2) and hence to β_2^C. M_n was fixed to be M_p of the mirror nuclei ^{20}O from its known B(E2),[8] assuming charge symmetry. β_2^C was adjusted to reproduce the cross section.

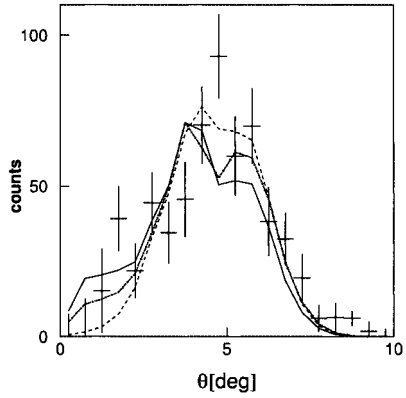

Fig. 1. Angular distributions of scattered ^{20}Mg in coincidence with gamma line at 1.61 MeV in ^{nat}Pb(^{20}Mg, ^{20}Mgγ) reaction. The curves represent results of Monte Carlo simulations.

The preliminary experimental B(E2$\uparrow$) was deduced to be 229 ± 24 (exp.) $\pm$ 78 (theo.) e^2fm^4. Theoretical ambiguity was estimated by accounting the uncertainties regarding a choice of optical potentials and the assumption for β_2^n.

*1 Department of Physics, Tohoku University
*2 ATOMKI, Hungary
*3 Department of Physics, Rikkyo University
*4 Institut de Physique Nucléaire, France
*5 Department of Physics, Saitama University
*6 Department of Physics, Tokyo Institute and Technology
*7 Department of Physics, University of Tokyo
*8 Center for Nuclear Study, University of Tokyo
*9 High Energy Accelerator Research Organization (KEK)
*10 Argonne National Laboratory, USA
*11 Department of Physics, Kyoto University
*12 TRIUMF, Canada
*13 Department of Physics, Kyushu University

References

1) K. Yamada et al.: Nucl. Phys. A **746**, 156 (2004).
2) T. Motobayashi et al.: Phys. Lett. B **346**, 9 (1995).
3) N. Iwasa et al.: RIKEN Accel. Prog. Rep. **38**, 58 (2005).
4) J. Barrette et al.: Phys. Lett. B **209**, 182 (1988).
5) T. Suomaijärvi et al.: Nucl. Phys. A **491**, 314 (1989).
6) T. Suomaijärvi et al.: Nucl. Phys. A **509**, 369 (1990).
7) A. M. Bernstein et al.: Phys. Rev. Lett. **42**, 425 (1979).
8) S. Raman et al.: At. Data Nucl. Data Tables **78**, 1 (2001).

Progress in analyzing proton resonant states in ^{22}Mg

J. J. He,[*1] S. Kubono,[*1] T. Teranishi,[*1,*2] M. Notani,[*1,*3] H. Baba,[*1] S. Nishimura, J. Y. Moon,[*4] M. Nishimura, S. Michimasa,[*1] H. Iwasaki,[*5] Y. Yanagisawa, N. Hokoiwa,[*2] M. Kibe,[*2] J. H. Lee,[*4] S. Kato,[*6] Y. Gono, and C. S. Lee,[*4]

[Proton resonant state, nuclear astrophysics]

The nuclear structure of the ^{22}Mg nucleus has received much interest recently because of its role in determining relevant astrophysical reaction rates.[1,2] The properties of resonant states above the proton threshold (Q_p=5.508 MeV) have been investigated at TRIUMF.[3–5] On the basis of these studies, the conclusion is that the resonance at E_x=5.714 MeV dominates at nova temperatures and the resonance at E_x=6.332 MeV dominates above T=1.1 GK. Therefore, we would like to investigate the resonant properties of those high-energy states in ^{22}Mg. In particular, the resonant states above the α threshold (Q_α=8.14 MeV) are relevant to the stellar ^{18}Ne(α, p)^{21}Na reaction, which is probably one of the key reactions for the breakout from the hot CNO cycle in X-ray bursters.[2] The excited states around the 8.14 MeV region were investigated previously,[6,7] however, the spin parities have not been determined yet. In this work, the excited states in ^{22}Mg were scanned from 6.3 to 9.0 MeV by a thick-target method.[8] It may provide useful information for evaluating the reaction rate of the ^{18}Ne(α, p)^{21}Na,[2] as well as for studying the nuclear structure in ^{22}Mg.

The experiment was performed using the CNS radioactive-ion-beam separator (CRIB).[9] The experimental setup was previously reported[10] in detail. This report will only show the recent results.

The center-of-mass energies (E_{cm}) were deduced using the elastic scattering kinematics of ^{21}Na+p with correction of the energy loss of particles in the target. The overall energy resolutions (FWHM) of E_{cm} at θ_{cm}=172° (SET1) are approximately 20 keV (at E_{cm}=0.5 MeV) to 45 keV (at E_{cm}=3.5 MeV). While those at θ_{cm}=146° (SET2) are approximately 20 to 70 keV. The systematic errors of E_{cm} are caused mainly by the uncertainty of proton energy calibration. In SET1, they are approximately ±12 keV (at E_{cm}=1.0 MeV) to ±20 keV (at E_{cm}=3.5 MeV) and approximately ±13 keV to ±30 keV in SET2.

The first excitation energy in ^{21}Na is only 0.33 MeV, and it is impossible to distinguish the inelastic scattering events from elastic ones in this work. Thus, the contribution from inelastic scattering ^{21}Na(p, p')^{21}Na was not considered in the report.

Figure 1 shows the center-of-mass differential cross sections for the ^{21}Na+p elastic scattering at two angles. Only statistical errors were included in the figure. The region studied by the TRIUMF group is indicated, where two resonant states at E_x=6.61 and 6.81 MeV agree very well with their respective 6.615 and 6.795 MeV states[5] within uncertainties. Beyond that, several resonances were observed, and particularly one or two resonances were observed above the α threshold. Not all resonances were indicated due to the complexity. The previously observed 7.60 MeV[7] and 8.54 MeV[6] states were clearly seen in the figure. The spectroscopic information of the 8.54 MeV state will be very useful for evaluating the rate of ^{18}Ne(α, p)^{21}Na reaction.

Later on, the cross-sectional data will be analyzed by the R-matrix code SAMMY-M6-BETA.[11]

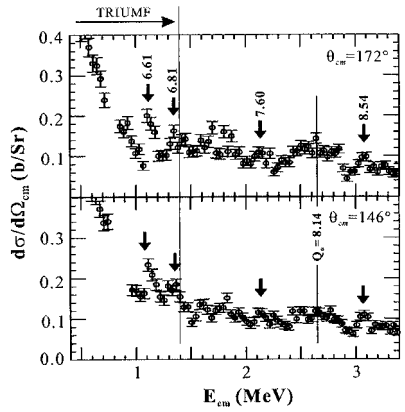

Fig. 1. Center-of-mass differential cross sections for ^{21}Na+p elastic scattering at two different angles.

References

1) M. Wiescher and K. Langanke: Z. Phys. A **325**, 309 (2002).
2) M. Wiescher et al.: J. Phys. G **25**, 133 (1999).
3) S. Bishop et al.: Phys. Rev. Lett. **90**, 162501 (2003).
4) J. M. D'Auria et al.: Phys. Rev. C **69**, 065803 (2004).
5) C. Ruiz et al.: Phys. Rev. C **71**, 025802 (2005).
6) A. A. Chen et al.: Phys. Rev. C **63**, 065807 (2001).
7) J. A. Caggiano et al.: Phys. Rev. C **66**, 015804 (2002).
8) S. Kubono: Nucl. Phys. A **693**, 221 (2001).
9) Y. Yanagisawa et al.: Nucl. Instrum. Methods Phys. Res. A **539**, 74 (2005).
10) J. J. He et al.: CNS Annu. Rep. **2003**, 34 (2004).
11) N. M. Larson: ORNL/TM-9179/R5, Oak Ridge National Laboratory (2000).

*1 Center of Nuclear Study, University of Tokyo
*2 Department of Physics, Kyushu University
*3 Argonne National Laboratory, USA
*4 Department of Physics, Chung-Ang University, Korea
*5 Department of Physics, University of Tokyo
*6 Department of Physics, Yamagata University

Measurement of proton transfer reaction ^{4}He(^{32}Mg,^{33}Alγ)

S. Ota,[*1] S. Shimoura,[*2] N. Aoi, E. Takeshita,[*3] S. Takeuchi, H. Suzuki,[*4] H. Baba, T. Fukuchi,[*3] T. Fukui,[*1] Y. Hashimoto,[*5] E. Ideguchi,[*2] K. Ieki,[*3] N. Iwasa,[*6] H. Iwasaki,[*4] S. Kanno,[*3] Y. Kondo,[*5] T. Kubo, K. Kurita,[*3] T. Minemura, S. Michimasa, T. Motobayashi, T. Murakami,[*1] T. Nakabayashi,[*5] T. Nakamura,[*5] M. Niikura,[*2] T. Okumura,[*5] T. K. Onishi,[*4] H. Sakurai, M. Shinohara,[*5] R. Sugo,[*3] D. Suzuki,[*4] M. K. Suzuki,[*4] M. Tamaki,[*2] K. Tanaka, Y. Togano,[*3] Y. Wakabayashi,[*7] and K. Yamada

[(α,t) Reaction, ^{33}Al, liquid helium, GRAPE, STQ]

A picture of the evolution of the shell structure is being obtained on the basis of the experimental result about the magicity loss in the $N = 8, 20$ neutron-rich nuclei. The shell structure formed by the mean field depends on the nuclear deformation, the isospin of the nuclei, or the occupation number of single-particle orbits. Systematic studies on single-particle states as functions of the number of protons and neutrons provide information on the change in shell structure. Among $N = 20$ nuclei, ^{32}Mg is known to be well deformed[1] while ^{34}Si is believed to be spherical in its ground state. The property of the ground state in the ^{33}Al nucleus has been studied via beta decay measurement and the decay of ^{33}Al is described well by an *sd*-shell model calculation.[2] In an other experiment, the candidate $2p2h$ state is found at an energy of 730 keV consistent with the shell model prediction.[3] These two different experiments suggest that those two states in ^{33}Al may be normally spherical. However, the shell structure in other excited states is not clear since the single-particle orbits may reflect the deformed mean field provided by the ^{32}Mg core. In the present study, we aim at clarifying the shell structure of ^{33}Al by finding new excited states and assigning their spins, parities and spectroscopic factors through a measurement of ^{4}He(^{32}Mg,^{33}Alγ) reaction.

The experiment was performed at the RIKEN Accelerator Facility with the RIKEN Projectile fragment Separator (RIPS).[4] A ^{32}Mg beam was produced by projectile fragmentation of ^{40}Ar at 63 MeV/nucleon bombarding 1-mm-thick carbon and separated by RIPS. The ^{32}Mg beam was contaminated with other neutron-rich isotopes such as ^{33,34}Al and ^{35,36}Si. These isotopes were identified event-by-event based on the information of the time-of-flight between two plastic scintillators of 0.1 mm thickness, at positions F2 and F3, and energy loss in a Si detector of 100 μm thickness. The energy of the ^{32}Mg beam at F3 was 40 ± 2 MeV/nucleon. The ^{32}Mg beam bombarded the liquid-helium target,[5] whose thickness was estimated to be approximately 150 mg/cm^2 from the velocity difference of outgoing particles between the case with helium and the case without it. Gamma rays emitted from the in-flight ^{33}Al were detected by Gamma-Ray detector Array with Position and Energy sensitivity (GRAPE)[6] surrounding the target. This consists of 17 pairs of segmented planar germanium detectors. Three PPACs[7] were placed upstream of the target for monitoring incident particles and two PPACs were placed downstream for outgoing particles, which provide the position information of the reaction point and the scattering angle of outgoing particles. The resolutions of the position at the reaction point and the scattering angle were estimated to be approximately 1 mm and 2 mrad, respectively. Outgoing particles were identified event-by-event by the TOF-ΔE-E method. The TOF was obtained from the timing information of two plastic scintillators of 300 μm thickness placed downstream of the target with a 3.8 m flight length. We had a new focus (F4) after the liquid-helium target by Super conducting Triplet Quadrupole (STQ)[8] magnets to strike a balance between the long flight path and the small array of particle detectors. For the ΔE- and E-detectors, 2×2 matrix Si detectors of 100 μm thickness were located after the STQ magnets with a 10×10 cm^2 active area, and 6×6 matrix NaI(Tl) detectors[9] of 50 mm thickness were located after the Si detectors with a 21×21 cm^2 active area, respectively.

Data analysis is in progress.

[*1] Department of Physics, Kyoto University
[*2] Center for Nuclear Study, University of Tokyo
[*3] Department of Physics, Rikkyo University
[*4] Department of Physics, University of Tokyo
[*5] Department of Physics, Tokyo Institute of Technology
[*6] Department of Physics, Tohoku University
[*7] Department of Physics, Kyushu University

References

1) T. Motobayashi et al.: Phys. Lett. B **346**, 9 (1995).
2) A. C. Morton et al.: Phys. Lett. B **544**, 274 (2002).
3) W. Mittig et al.: Eur. Phys. J. A **15**, 157 (2002).
4) T. Kubo et al.: Nucl. Instrum. Methods Phys. Res. B **70**, 309 (1992).
5) H. Ryuto et al.: Nucl. Instrum. Methods Phys. Res. A **555**, 1 (2005).
6) S. Shimoura et al.: Nucl. Instrum. Methods Phys. Res. A **525**, 188 (2004).
7) H. Kumagai et al.: Nucl. Instrum. Methods Phys. Res. A **470**, 562 (2001).
8) N. Aoi et al.: RIKEN Accel. Prog. Rep. **38**, 176 (2005).
9) M. Niikura et al.: RIKEN Accel. Prog. Rep. **37**, 155 (2004).

Alpha inelastic scattering on ^{32}Mg

T. Fukui,[*1] S. Shimoura,[*2] T. Murakami,[*1] S. Ota,[*1] N. Aoi, E. Takeshita,[*3] S. Takeuchi, H. Suzuki,[*4] H. Baba, T. Fukuchi,[*3] Y. Hashimoto,[*5] E. Ideguchi,[*2] K. Ieki,[*3] N. Iwasa,[*6] H. Iwasaki,[*4] S. Kanno,[*3] Y. Kondo,[*5] T. Kubo, K. Kurita,[*3] S. Michimasa, T. Minemura, T. Motobayashi, T. Nakabayashi,[*5] T. Nakamura,[*5] M. Niikura,[*2] T. K. Ohnishi,[*4] T. Okumura,[*5] H. Sakurai, M. Shinohara,[*5] R. Sugo,[*3] D. Suzuki,[*4] M. K. Suzuki,[*4] M. Tamaki,[*2] K. Tanaka, Y. Togano,[*3] Y. Wakabayashi,[*7] and K. Yamada

[Nuclear reactions, ^{4}He(^{32}Mg,^{32}Mg γ), alpha inelastic scattering]

We performed high-resolution in-beam γ-spectroscopy of the neutron-rich $N = 20$ nucleus ^{32}Mg excited by an alpha inelastic scattering at 42 MeV/nucleon in inverse kinematics. As the study of the excited states in ^{32}Mg is one of the keys for understanding structural change in neutron-rich nuclei having $N \sim 20$ (island of inversion), many studies have been performed and several excited states reported in ^{32}Mg.[1–3] However, the spins and parities have not been assigned except for the ground and first excited states.

In the present experiment, we aim at deducing population yield for each excited state and determining its spin and parity by using the angular distribution of the measured alpha inelastic scattering. Since some γ transitions may have similar energies, high-resolution γ spectroscopy is necessary to provide unambiguous assignments of the transitions. In order to deduce transition energies emitted from a fast-moving particle at high energy resolution, emission angle with respect to the momentum vector of the particle should be determined at a good resolution. On the basis of this requirement, we used a Ge detector array named GRAPE[4] having position sensitivity and five sets of tracking detectors for the γ ray and a charged particle.

The experiment was performed at the RIKEN Accelerator Facility with the RIKEN projectile-fragment separator (RIPS).[5] A secondary beam of ^{32}Mg was produced by projectile fragmentation of an ^{40}Ar primary beam on a carbon target at 63 MeV/nucleon. The ^{32}Mg beam at 42 MeV/nucleon was separated by RIPS and used to bombard a liquid He target of 150 mg/cm^2 thickness. The beam particles were identified using time-of-flight (TOF) and energy-loss (ΔE) measured using plastic scintillators located at the second and third foci of RIPS. The beam was tracked by three sets of parallel-plate avalanche counters (PPACs).[6] The ejectile was identified by the TOF-ΔE-E method. The TOF was measured using two plastic scintillators located at the entrance and exit of the TOF spectrometer.[7] ΔE and E were measured using a detector telescope consisting of 100-μm Si detectors and NaI(Tl) detectors. The direction of the ejectile was measured using two sets of PPACs located downstream of the target. γ rays from the ejectiles were detected by the GRAPE consisting of 17 position-sensitive Ge detectors. The Doppler shift of each event was corrected on the basis of TOF and tracking information of the ejectile and the detection position of γ rays in the Ge detector deduced by pulse-shape analysis (PSA).[4]

Figure 1 shows a preliminary Doppler-shift-corrected spectrum of γ rays from the ^{4}He(^{32}Mg,^{32}Mg γ) reaction. In the present analysis, an energy resolution of 28 keV (FWHM) for the 885-keV transition ($2_1^+ \rightarrow 0_1^+$) of ^{32}Mg was achieved with PSA, whereas 36 keV was obtained without PSA. Careful analysis taking into account the integral and differential nonlinearity of ADCs and gain drift throughout the experiment is in progress.

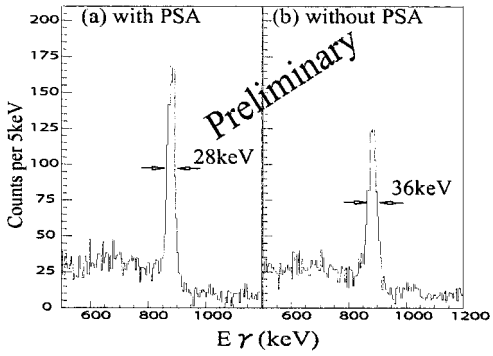

Fig. 1. Doppler-shift-corrected γ-ray energy spectrum of ^{4}He(^{32}Mg,^{32}Mg γ) reaction (a) with and (b) without pulse shape analysis.

[*1] Kyoto University
[*2] Center for Nuclear Study, University of Tokyo
[*3] Rikkyo University
[*4] University of Tokyo
[*5] Tokyo Institute of Technology
[*6] Touhoku University
[*7] Kyushyu University

References
1) T. Motobayashi et al.: Phys. Lett. B **346**, 9 (1995).
2) G. Klotz et al.: Phys. Rev. C **47**, 2502 (1993).
3) F. Azaiez et al.: Eur. Phys. J. A **15**, 93 (2002).
4) S. Shimoura: Nucl. Instrum. Methods Phys. Res. A **525**, 188 (2004).
5) T. Kubo et al.: Nucl. Instrum. Methods Phys. Res. B **70**, 309 (1992).
6) H. Kumagai et al.: Nucl. Instrum. Methods Phys. Res. A **470**, 562 (2001).
7) N. Aoi et al.: RIKEN Accel. Prog. Rep. **38**, 176 (2005).

Proton inelastic scattering on ^{32}Mg and ^{34}Si

S. Takeuchi, N. Aoi, H. Baba,[*1] T. Fukui,[*2] Y. Hashimoto,[*3] K. Ieki,[*4] N. Imai,[*5] H. Iwasaki,[*6] S. Kanno,[*4] Y. Kondo,[*3] T. Kubo, K. Kurita,[*4] T. Minemura,[*5] T. Motobayashi, T. Nakabayashi,[*3] T. Nakamura,[*3] T. Okumura,[*3] T. K. Onishi,[*6] S. Ota,[*2] H. Sakurai,[*6] S. Shimoura,[*1] R. Sugo,[*4] D. Suzuki,[*6] H. Suzuki,[*6] M. K. Suzuki,[*6] E. Takeshita,[*4] M. Tamaki,[*1] K. Tanaka, Y. Togano,[*4] and K. Yamada

[Nuclear structure, in-beam γ-ray spectroscopy]

Proton inelastic scattering was applied to ^{32}Mg and ^{34}Si nuclei located at and around the island of inversion. These nuclei were studied by β-γ spectroscopy and Coulomb excitation reaction to investigate collective motions or shape coexistence characteristic for the island of inversion. In these studies, excitation energies of higher states were obtained;[1–4] however, the spins and parities of the states other than the 2^+ state are still unknown. In the present study, de-excitation γ rays from inelastically scattered particles were detected and analyzed by γ-γ analysis to obtain cross sections and spin-parity information.

^{32}Mg and ^{34}Si beams were produced by projectile fragmentation reaction of a 94 MeV/nucleon ^{40}Ar primary beam with 370 mg/cm^2 and 231 mg/cm^2 ^{9}Be production targets for ^{32}Mg and ^{34}Si, respectively. The secondary beams were separated using RIPS[5] and identified event-by-event using ΔE and the time-of-flight (TOF) method between F2 and F3 foci using a Si detector and two plastic scintillators. The energy and intensity were 56 MeV/nucleon and 700 cps for ^{32}Mg and 65 MeV/nucleon and 12 kcps for ^{34}Si.

The secondary beams bombarded the liquid hydrogen target[6] with a thickness of 160 mg/cm^2. Inelastically scattered particles were analyzed using the recently developed TOF spectrometer.[7] It consists of a Si detector, NaI(Tl) detectors,[8] two plastic scintillators and Superconducting Triplet Quadrupole (STQ) magnets.[9] The obtained mass resolution for Mg and Si isotopes was around 1.5% in FWHM. With this high mass resolution, contaminations in ^{32}Mg and ^{34}Si mass gates were reduced to as low as 1%. De-excitation γ rays were detected using DALI2[10] which consists of 160 NaI(Tl) crystals surrounding the reaction target. The typical energy resolution and efficiency are respectively 8% and 21% for 1 MeV γ ray emitted from fast moving particles ($\beta \simeq 0.3$).

Figure 1 shows the Doppler-corrected γ-ray spectra for ^{32}Mg(p,p$'$) and ^{34}Si(p,p$'$). De-excitation γ rays from known 2^+ states and from other higher states are clearly observed in γ-ray spectra for both nuclei.

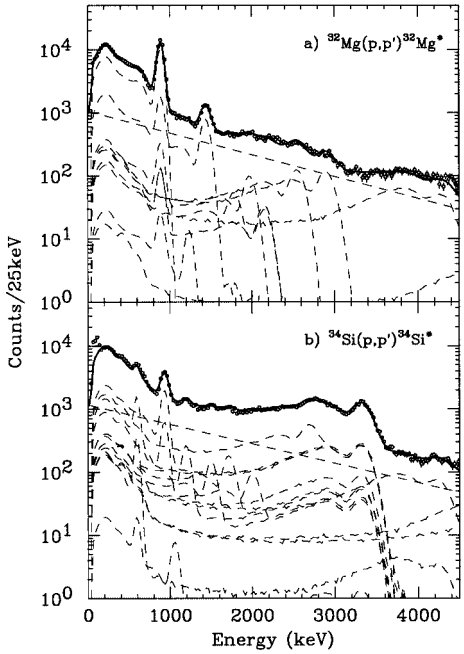

Fig. 1. Doppler-corrected γ-ray spectra for a) ^{32}Mg(p,p$'$)^{32}Mg* and b) ^{34}Si(p,p$'$)^{34}Si*.

The solid curves show the results of fit consisting of the response functions of DALI2 and an exponential background shown by dashed curves. Using the fitting results together with the γ-γ analysis, the level scheme and cross sections to each state can be determined. The spin and parity assignments can also be obtained by γ-γ angular correlation analysis.

*1 Center for Nuclear Study, University of Tokyo
*2 Department of Physics, Kyoto University
*3 Department of Physics, Tokyo Institute of Technology
*4 Department of Physics, Rikkyo University
*5 Institute of Particle and Nuclear Studies, High Energy Accelerator Research Organization (KEK)
*6 Department of Physics, University of Tokyo

References

1) G. Klotz et al.: Phys. Rev. C **47**, 2502 (1993).
2) S. Nummela et al.: Phys. Rev. C **63**, 044316 (2001).
3) R. W. Ibbotson et al.: Phys. Rev. Lett. **80**, 2081 (1998).
4) T. Motobayashi et al.: Phys. Lett. B **346**, 9 (1995).
5) T. Kubo et al.: Nucl. Instrum. Methods Phys. Res. B **70**, 309 (1992).
6) H. Ryuto et al.: Nucl. Instrum. Methods Phys. Res. A **555**, 1 (2005).
7) N. Aoi et al.: RIKEN Accel. Prog. Rep. **38**, 176 (2005).
8) M. Tamaki et al.: CNS-REP-59, 76 (2003).
9) K. Kusaka et al.: IEEE Trans. Appl. Supercond. **14**, 310 (2004).
10) S. Takeuchi et al.: RIKEN Accel. Prog. Rep. **36**, 148 (2003).

Weak-coupling structure of proton resonances in ^{23}Al

J. J. He,[*1] S. Kubono,[*1] T. Teranishi,[*1,*2] M. Notani,[*1,*3] H. Baba,[*1] S. Nishimura, J. Y. Moon,[*4] M. Nishimura, S. Michimasa,[*1] H. Iwasaki,[*5] Y. Yanagisawa, N. Hokoiwa,[*2] M. Kibe,[*2] J. H. Lee,[*4] S. Kato,[*6] Y. Gono, and C. S. Lee[*4]

[Proton resonant state, weak-coupling, R-matrix]

In the present work, the proton resonant states in ^{23}Al have been investigated by resonant elastic and inelastic scattering of a ^{22}Mg RI beam on a thick hydrogen target.[1] The resonance energies, proton partial widths and spin parities are determined for several resonant states by an R-matrix analysis of the excitation functions. The weak-coupling structure of these states has been studied.

The experiment was performed using the CNS radioactive ion beam separator (CRIB).[2] The experimental details are described in Ref. 3. By analyzing the recoiled-proton energy spectra measured at different angles, a new level scheme of ^{23}Al is proposed as shown in Fig. 1.[4] The 3.00-MeV and 3.95-MeV states are newly observed, and the states at 3.14 and 3.26 MeV could correspond to an observed broad peak at E_x = 3.204 MeV reported in an earlier study with the ^{24}Mg(^{7}Li,^{8}He)^{23}Al reaction.[5] Via proton emission, the excited state at 3.00 MeV decays to the ground state in ^{22}Mg, while the excited states at 3.14, 3.26 and 3.95 MeV mainly decay to the first excited state (2^+, 1.25 MeV) in ^{22}Mg.

The measured elastic and inelastic scattering cross sections were analyzed using the R-matrix code SAMMY-M6-BETA.[6,7] Table 1 lists the resonant properties, energies, spin parities and proton partial widths to the ground state (Γ_p) and to the first excited state ($\Gamma_{p'}$) in ^{22}Mg.

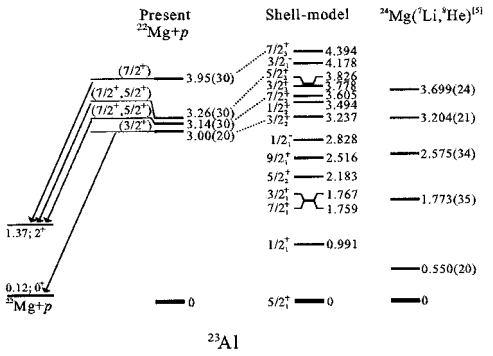

Fig. 1. New level scheme of ^{23}Al constructed in this work. The calculated levels are shown for comparison.

Table 1. Resonant properties determined in this work. The widths are for the inelastic channels for the last three states. The predicted J_n^π indicates the nth level of the same J^π. (widths in keV)

E_x	$2J^\pi$	$2J_n^\pi$	$\Gamma^{exp}_{p,(p')}$	$\Gamma^{cal}_{p,(p')}$	Coupling
3.00	(3^+)	3_2^+	32(5)	44	$0^+\otimes 1d_{3/2}$
3.14	(7^+, 5^+)	7_2^+	30(20)	6	$2^+\otimes 1d_{3/2}$
3.26	(7^+, 5^+)	5_3^+	30(20)	10	mixed
3.95	(7^+)	7_3^+	30(20)	18	$2^+\otimes 1d_{3/2}$

The shell-model calculations have been performed with an OXBASH[8] code. The calculations were carried out in a complete model space *spsdpf* using an isospin-conserving WBT interaction.[9] The calculated levels are shown in Fig. 1. The calculated energies of positive-parity states agree very well with those observed in the mirror ^{23}Ne nucleus, and the calculated C^2S factors are also in good agreement with those determined from the (d, p) reaction.[7] To study the weak-coupling structure in ^{23}Al, the spectroscopic factors of the excited states in the A = 23 nucleus for the single-particle structure with the A = 22 core in its ground (or the first excited) state were calculated. As shown in the last column of Table 1, their main configurations can be explained by the weak coupling of a valence proton with the ^{22}Mg core, in the ground (0^+) and first excited states (2^+). These expected coupling schemes are in good agreement with the experimental observations for the proton decay. In addition, the proton partial widths were calculated[10] as listed in Table 1. The experimental values are in reasonable agreement with the calculated ones.

*1 Center of Nuclear Study, University of Tokyo
*2 Department of Physics, Kyushu University
*3 Argonne National Laboratory, USA
*4 Department of Physics, Chung-Ang University, Korea
*5 Department of Physics, University of Tokyo
*6 Department of Physics, Yamagata University

References
1) S. Kubono: Nucl. Phys. A **693**, 221 (2001).
2) Y. Yanagisawa et al.: Nucl. Instrum. Methods Phys. Res. A **539**, 74 (2005).
3) J. J. He et al.: CNS Annu. Rep. **2003**, 34 (2004).
4) J. J. He et al.: CNS Annu. Rep. **2004**, 3 (2005).
5) J. A. Caggiano et al.: Phys. Rev. C **64**, 025802 (2001).
6) N. M. Larson: ORNL/TM-9179/R5, Oak Ridge National Laboratory (2000).
7) J. J. He et al.: Phys. Rev. C, (2005), to be submitted.
8) B. A. Brown et al.: MSU-NSCL report number 1289 (1988).
9) E. K. Warburton et al.: Phys. Rev. C **46**, 923 (1992).
10) C. Iliadis: Nucl. Phys. A **618**, 166 (1997).

β-delayed proton and γ-ray spectroscopy of ^{24}Si

Y. Ichikawa,[*1] T. Kubo, N. Aoi, V. Banerjee,[*2] A. Chakrabarti,[*2] N. Fukuda, H. Iwasaki,[*1] S. Kubono,[*3] T. Motobayashi, T. Nakabayashi,[*4] T. Nakamura,[*4] T. Nakao,[*1] T. Okumura,[*4] H. J. Ong,[*1] T. K. Onishi,[*1] D. Suzuki,[*1] H. Suzuki,[*1] M. K. Suzuki,[*1] T. Teranishi,[*5] K. N. Yamada, H. Yamaguchi,[*3] K. Yoneda, and H. Sakurai

[β-delayed proton, β-delayed γ, ^{24}Si]

We investigated the β-decay properties of the ^{24}Si nucleus, by β-delayed proton and γ-ray spectroscopy. ^{24}Si with an isospin value of $T_z = -2$ is a very proton-rich nucleus near the drip line. The structure of proton-rich nuclei provides a useful platform to investigate isospin symmetry, as well as to test the applicability of the effective interaction of the shell model in a proton-rich region. The β decay of very proton-rich nuclei is characterized by its large Q_β value in contrast to a small threshold for the proton emission of the daughter nucleus. It is thus essential to perform measurements that cover not only β-delayed γ decay, but also β-delayed proton emission, to obtain a complete β-decay scheme. Here, we report our measurement of β-delayed protons and γ rays from ^{24}Si.

The experiment was performed at the RIKEN Projectile Fragment Separator (RIPS) facility. A radioactive beam of ^{24}Si was produced by the projectile fragmentation of a 100 A MeV ^{28}Si beam with a 3.0-mm-thick Be target. To determine the half-life of ^{24}Si, a pulsed beam was used; the beam-on and beam-off cycles were chosen to be 500 ms and 500 ms, respectively.

The measurement of β-delayed protons and γ rays was performed using separate setups. Figure 1 shows a schematic view of the setup for β-delayed proton measurement. Two aluminum foils were set in a chamber, along the beam line to stop ^{24}Si beam. Each stopper foil had a 2.8 μm thickness and was placed at a tilted angle of 15 degrees with respect to the beam axis. On both sides of the foils, four sets of proton telescopes were installed to detect and identify the protons. Each proton telescope was composed of a gas ΔE and silicon E detectors. The gas detector, which consisted of three electrodes, was used to measure the energy loss (ΔE) of the protons. Each electrode was made of a wire-mesh sheet with dimensions of 50 mm $\times$ 50 mm, the transmission factor was 95%. The center electrode was used as an anode, while both ends were connected to the ground. The ΔE detectors was operated at 300 V in the proportional region. The chamber was filled with 20 Torr P10 (Ar 90% + CH_4 10%) gas. Behind the gas detector, four 450-μm-thick silicon detectors were set to measure the energy (E) of the protons. To obtain a clean spectrum of the protons, it is necessary to reduce background contributions attributed to β rays. Using the ΔE and E information from the telescopes, we could distinguish the protons from the β rays.

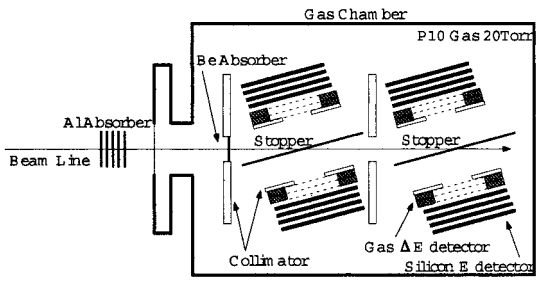

Fig. 1. Setup for β-delayed proton measurement.

Figure 2 shows the setup for β-delayed γ-ray measurement. A plastic scintillator with a thickness of 10 mm was placed at a tilted angle of 45 degrees with respect to the beam line. γ rays were detected by a Clover Ge detector, equipped with a BGO active Compton shield.

In the measurement of β-delayed protons, we succeeded in obtaining ten times larger statistics than those obtained in the previous experiment.[1)] The branching ratios of the relevant β decay are to be determined with a higher accuracy. In addition, we found a new β branch to the bound excited state in ^{24}Al by the β-delayed γ ray measurement. The present data will enable us to deduce the absolute values of the branching ratios for the β decay of ^{24}Si, leading to both unbound and bound states in ^{24}Al. Analysis of the data is soon to be finished.

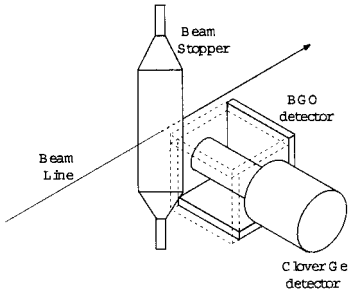

Fig. 2. Setup for β-delayed γ-ray measurement.

*1 Department of Physics, University of Tokyo
*2 Variable Energy Cyclotron Centre, India
*3 Center for Nuclear Study, University of Tokyo
*4 Department of Physics, Tokyo Institute of Technology
*5 Department of Physics, Kyushu University

Reference

1) V. Banerjee et al.: Phys. Rev. C **63**, 024307-1 (2001).

Investigation of stellar reaction rate for ^{26}Si(p,γ)^{27}P by Coulomb dissociation of ^{27}P

Y. Togano,[*1] T. Gomi,[*2] T. Motobayashi, Y. Ando,[*1] N. Aoi, H. Baba, K. Demichi,[*1] Z. Elekes,[*3] N. Fukuda, Zs. Fülöp,[*3] U. Futakami,[*1] H. Hasegawa,[*1] Y. Higurashi, K. Ieki,[*1] N. Imai,[*4] M. Ishihara, K. Ishikawa,[*5] N. Iwasa,[*6] H. Iwasaki,[*7] S. Kanno,[*1] Y. Kondo,[*5] T. Kubo, S. Kubono,[*8] M. Kunibu,[*1] K. Kurita,[*1] Y. U. Matsuyama,[*1] S. Michimasa, T. Minemura, M. Miura,[*5] H. Murakami,[*1] T. Nakamura,[*5] M. Notani,[*9] S. Ota,[*10] A. Saito,[*8] H. Sakurai, M. Serata,[*1] S. Shimoura,[*8] T. Sugimoto,[*5] E. Takeshita,[*1] S. Takeuchi, K. Ue,[*7] K. Yamada, Y. Yanagisawa, K. Yoneda, and A. Yoshida

[^{208}Pb(^{27}P,p^{26}Si)^{208}Pb, Coulomb dissociation, nuclear astrophysics]

The stellar ^{26}Si(p,γ)^{27}P reaction has been investigated in terms of the Coulomb dissociation of ^{27}P. The γ decay widths of low-lying resonant states in ^{27}P were deduced to investigate the resonant capture reaction rate.

This reaction is suggested to affect the synthesis of ^{26}Al, whose 1.8 MeV γ-line distribution, which is emitted by its β decay, in the galaxy[1] is observed by satellite telescopes. Since the β decay of ^{26}Si feeds only the isomeric state of ^{26}Al, which subsequently β decays to the ground state of ^{26}Mg, ^{26}Si does not contribute to astrophysical γ rays. However, in a high-density photon bath of an X-ray burst or supernovae, the statistical equilibrium is achieved among low-lying states in ^{26}Al[2] and consequently, ^{26}Si causes the 1.8 MeV γ rays. Therefore, the destruction of ^{26}Si by proton capture is important in estimating the synthesis of ^{26}Al on the basis of the equilibrium.

An experiment was performed at the RIPS beam line on the RIKEN Accelerator Research Facility. The details of the experimental setup are described in Ref. 3.

The γ decay widths Γ_γ of the three states with resonance energies of 0.34, 0.72, and 1.15 MeV are extracted from the experimental results. As discussed in Ref. 4, Γ_γ for the first excited state is experimentally estimated to be $(3.7 \pm 2.2) \times 10^{-3}$ eV by assuming the E2/M1 mixing ratio. The widths of the second and third excited states are determined directly from the experimental cross sections alone because the transitions to the ground state are induced by almost pure E2 transitions. They are determined to be $(1.82 \pm 0.28) \times 10^{-4}$ eV and $(3.77 \pm 0.74) \times 10^{-4}$ eV, respectively.

The astrophysical reaction rate of ^{26}Si(p,γ)^{27}P was calculated using the deduced Γ_γs. Figure 1 shows the temperature dependence of the rate. The three solid curves represent the present estimations of the resonant capture reaction rates through the three states. The dotted curves show the margins of error. The resonance parameters, except for Γ_γ of the first and second excited states, were adopted from Caggiano et al.[5] The dashed curve represents the direct capture component calculated by Caggiano et al.[5] The spins and parities of the states were deduced by assuming that ^{27}P has a level structure analogous to that of the mirror nucleus ^{27}Mg.[6] The resultant reaction rate indicates that resonant capture through the first excited state of ^{27}P is the dominant process above 0.1 GK, and those through the second and third excited state give negligible contributions.

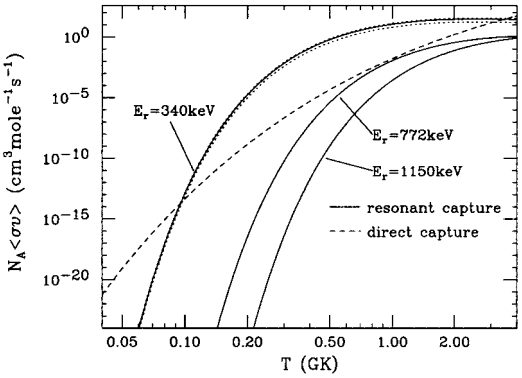

Fig. 1. Reaction rate of ^{26}Si(p,γ)^{27}P as a function of temperature of stars obtained in the present study.

[*1] Rikkyo University
[*2] National Institute of Radiological Sciences
[*3] ATOMKI, Hungary
[*4] High Energy Accelarator Research Organization (KEK)
[*5] Tokyo Institute of Technology
[*6] Tohoku University
[*7] University of Tokyo
[*8] Center for Nuclear Study, University of Tokyo
[*9] Argonne, USA
[*10] Kyoto University

References
1) R. Diehl et al.: Astron. Astrophys. Suppl. **97**, 181 (1993).
2) A. Coc et al.: Phys. Rev. C **61**, 015801 (1999).
3) Y. Togano et al.: RIKEN Accel. Prog. Rep. **37**, 69 (2004).
4) Y. Togano et al.: Proc. of Nuclear Physics in Astrophysics II, Debrecen, Hungary, 2005-5 (Springer), to be published in Eur. Phys. J. A.
5) J. A. Caggiano et al.: Phys. Rev. C **64**, 025802 (2001).
6) P. M. Endt: Nucl. Phys. A **521**, 1 (1990).

Measurement of spin and magnetic moment of ^{23}Al

A. Ozawa,[*1] K. Matsuta,[*2] T. Nagatomo,[*1,*2] M. Mihara,[*2] K. Yamada, T. Yamaguchi,[*3] T. Ohtsubo,[*4] S. Momota,[*5] T. Izumikawa,[*5,*6] T. Sumikama, Y. Nakashima,[*2] H. Fujiwara,[*2] S. Kumashiro,[*2] R. Matsumiya,[*2] M. Ota,[*4] D. Shinojima,[*4] H. Tanaka,[*4] T. Yasuno,[*1] S. Nakajima,[*3] T. Suzuki,[*3] K. Yoshida, K. Muranaka,[*3] T. Maemura,[*3] A. Chiba,[*1] Y. Utsuno,[*7] M. Fukuda,[*2] K. Tanaka, I. Tanihata,[*8] Y. Nojiri,[*5] T. Minamisono,[*2,*9] J. R. Alonso,[*10] G. F. Krebs,[*10] and J. Symons[*10]

[Nuclear structure: ^{23}Al, β-NMR method, g-factor]

^{23}Al is one of the potential candidates for the proton-halo nucleus because its proton separation energy is quite small (125 keV). Recently, the large reaction cross section of ^{23}Al has been measured although the error is still large.[1)] The authors of Ref. 1 analyzed the measurement data using a Glauber model with a simple core nucleus (^{22}Mg) and a valence proton (p) configuration. According to their analysis, the density distribution of ^{23}Al should have a halo-like long tail. Because the density of loosely bound s-wave proton can be extended, it is suggested that the spin and parity (J^π) of ^{23}Al might be $1/2^+$. However, J^π of its mirror partner ^{23}Ne is $5/2^+$. Thus, if the ground-state J^π of ^{23}Al is $1/2^+$, a proton halo structure can be anticipated but mirror symmetry is broken between the bound ground states of mirror pairs. Magnetic moment allows us to determine J^π directly because magnetic moment is largely different for different spins. Therefore, we measured the magnetic moment of ^{23}Al.

The ^{23}Al nuclei were produced through the projectile fragmentation process. The primary beam of ^{28}Si was accelerated up to 135 A MeV using the RIKEN ring cyclotron. The Be target thickness was 4.0 mm. Only the fragments ejected at the angle 1.0 ± 0.6 deg were separated by the fragment separator RIPS. In the separator, the momentum of the fragments was analyzed, and only the fragments with a momentum $2.0 \pm 0.5\%$ larger than the central momentum were selected. To sweep the contaminants of ^{23}Al, an RF deflector[2)] was installed at the achromatic focus F2 of the RIPS. The selected fragments were slowed down by an energy degrader and were implanted in a Si catcher of 0.6 mm thickness placed in a strong magnetic field H_0 of 3.0005 ± 0.0006 kOe. The polarization of the ^{23}Al is detected by the β-ray asymmetry in the plastic counter telescope. An RF magnetic field H_1 of approximately 13 Oe was applied to induce transitions between magnetic sublevels. An NMR spectrum for wide frequency modulation (FM) of $\pm$500 kHz is shown in the upper part of Fig. 1. We found the resonance of approximately 3600 kHz. To determine the resonance more precisely, we performed measurements with a narrow FM of $\pm$200 kHz. The result of the NMR spectrum is shown in the lower part of Fig. 1.

We performed shell-model calculations (OXBASH) to assign J^π of ^{23}Al. For ^{23}Al, our shell-model calculations show $g = +3.410$ for $J^\pi = 1/2^+$ and $g = +1.575$ for $J^\pi = 5/2^+$. The calculated values are indicated by the arrows in Fig. 1. Here, the nucleon g-factors in the free space were used for the calculations. The present experimental g-factor is well reproduced by the shell-model value for the ground-state J^π of $5/2^+$ as shown in Fig. 1.

The ground-state J^π of ^{23}Al can give the strong restriction to the possible structure of the nucleus. Because the proton separation energy of ^{23}Al is very small, a core nucleus and a valence proton (^{22}Mg+p) structure can be anticipated. If we assume the ^{22}Mg+p structure, J^π of $5/2^+$ allows three cases of configurations: 1) the ground state of ^{22}Mg ($J^\pi = 0^+$) couples to the d-wave valence proton; 2) the first excited state of ^{22}Mg ($E_x = 1.25$ MeV, $J^\pi = 2^+$) couples to the s-wave valence proton; and 3) the first excited state of ^{22}Mg couples to the d-wave valence proton. Our shell-model calculations show that the configuration of case 1) is 71%, that of case 2) is only 0.2% and that of case 3) is 23%. Thus, the configuration with the d-wave valence proton is the most probable for ^{23}Al.

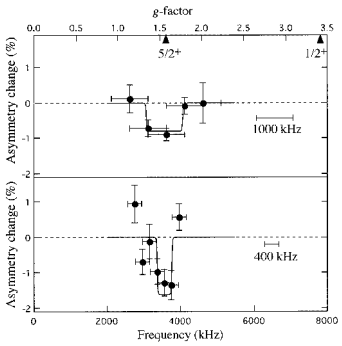

Fig. 1. Observed β-NMR spectra.

*1 University of Tsukuba
*2 Osaka University
*3 Saitama University
*4 Niigata University
*5 Kochi Institute of Technology
*6 Niigata University RI Center
*7 Japan Atomic Energy Research Institute
*8 TRIUMF, Canada
*9 Fukui University Technology
*10 Lawrence Berkeley National Laboratory, USA

References

1) X. Z. Cai et al.: Phys. Rev. C **65**, 024610 (2002).
2) K. Yamada et al.: Nucl. Phys. A **746**, 156c (2004).

Magnetic moments of $^{30}_{13}Al_{17}$ and $^{32}_{13}Al_{19}$†

H. Ueno, D. Kameda, G. Kijima,[*1] K. Asahi, A. Yoshimi, H. Miyoshi,[*1] K. Shimada,[*1] G. Kato,[*1] D. Nagae,[*1] S. Emori,[*1] T. Haseyama, H. Watanabe,[*2] and M. Tsukui[*1]

[Nuclear structure, spin-polarized radioactive beams, β-NMR method, measured ground-state magnetic moments of ^{30}Al and ^{32}Al, shell model]

Ground-state magnetic moments of ^{30}Al and ^{32}Al were measured by β-ray detected nuclear magnetic resonance (β-NMR) using radioactive-isotope beams spin-polarized in the projectile-fragmentation reaction.

A beam of ^{30}Al (^{32}Al) was obtained from the fragmentation of ^{40}Ar projectiles at an energy of $E = 95\ A$ MeV on a ^{93}Nb target of 0.13 (0.37) g/cm^2 thickness. In order to spin-polarize the ^{30}Al (^{32}Al) beam, the emission angle and outgoing momentum were selected. Thus, fragments emitted at angles $\theta_L = 1.3°$–$5.7°$ were accepted by RIPS using a beam swinger installed upstream of the target. A range of momentum $p = 12.4$–$12.7\,\mathrm{GeV}/c$ (12.2–$13.0\,\mathrm{GeV}/c$) was selected by a slit at the momentum-dispersive focal plane F1. This momentum range corresponds to 1.006–1.026 p_0 (0.975–1.034 p_0), where p_0 is a peak in the momentum distribution of the ^{30}Al (^{32}Al) beam. The spin-polarized fragments are isotope-separated and introduced into the NMR apparatus located at the final focus.

We employed β-NMR to determine the μ moment. In this method, β-rays emitted from the implanted fragments are detected with plastic scintillator telescopes located above and below the stopper. When the polarization P is altered due to the resonant spin reversal, a change appears in the β-ray up/down ratio. Thus, the resonance frequency ν_0 is derived from the observed peak or dip in the β-NMR spectrum. From the β-NMR spectra obtained for the ground states of ^{30}Al and ^{32}Al, we have determined the experimental μ moments, $|\mu_{\mathrm{exp}}(^{30}\mathrm{Al})| = 3.010(7)\ \mu_N$ and $|\mu_{\mathrm{exp}}(^{32}\mathrm{Al})| = 1.959(9)\ \mu_N$, for ^{30}Al and ^{32}Al, respectively, where μ_N is the nuclear magneton. No diamagnetic-shielding correction was performed for the present values, since the reported chemical shift of ^{27}Al in α-Al_2O_3[1] is negligible compared with the errors from other sources.

The experimental μ values were compared with shell-model calculations. The theoretical μ moments calculated with the USD interaction[2] are $+3.19\ \mu_N$ and $+2.06\ \mu_N$ for ^{30}Al and ^{32}Al, respectively, as listed in Table 1. In both cases, theoretical values are in agreement with the present experimental values within ~6%. Comparison was also carried out with experimental values of other aluminum isotopes.[3,4] As listed in Table 1, they agree well with each other. Thus, no prominent deviation was observed in all of these aluminum isotopes.

Table 1. Comparison of experimental magnetic moments (μ_{exp}) and shell-model predictions (μ_{SM}) for aluminum isotopes in unit of nuclear magneton. The differences are calculated assuming positive signs for the μ_{exp} values if the signs are not assigned.

isotope	I^π	μ_{exp}	μ_{SM}	$\mu_{\mathrm{SM}} - \mu_{\mathrm{exp}}$
^{26}Al	5^+	+2.804(4)	+2.95	0.14 (5.0 %)
^{27}Al	$5/2^+$	+3.6415069(7)	+3.75	0.11 (3.0 %)
^{28}Al	3^+	3.242(5)	+3.29	0.04 (1.3 %)
^{30}Al	3^+	3.010(7)	+3.19	0.18 (6.1 %)
^{31}Al	$5/2^+$	3.793(50)	+3.98	0.19 (5.0 %)
^{32}Al	1^+	1.959(9)	+2.06	0.10 (5.0 %)

With respect to ^{32}Al, an isomer state has been found recently at an excitation energy of $E_x = 956\,\mathrm{keV}$,[5] above the excited state at $E_x = 734\,\mathrm{keV}$.[5,6] Spin and parity $I^\pi = 2^+$ and 4^+ have been assigned to 734 keV and 956 keV levels, respectively, from the study of their γ-decay properties. It is pointed out in Ref. 5 that this ordering is unusual and the USD interaction fails to reproduce it. Since such disagreements between calculations carried out with the USD interaction and experimental observations are rare, this unusual level ordering of ^{32}Al might stem from the presence of the "island of inversion". In the present study, however, we found that the USD interaction can reproduce the experimental ground-state μ moment of ^{32}Al as well as that of ^{30}Al.

References
1) A. J. Woo: Bull. Korean Chem. Soc. **20**, 1205 (1999).
2) B. H. Wildenthal: Prog. Part. Nucl. Phys. **11**, 5 (1984).
3) D. Borremans et al.: Phys. Lett. B **537**, 45 (2002).
4) P. Raghavan: At. Data Nucl. Data Tables **42**, 189 (1989).
5) M. Robinson et al.: Phys. Rev. C **53**, R1465 (1996).
6) G. Klotz et al.: Phys. Rev. C **47**, 2502 (1993).

† Condensed from article in Phys. Lett. B **615**, 186 (2005)
*1 Department of Physics, Tokyo Institute of Technology
*2 Department of Nuclear Physics, The Australian National University, Australia

Precision measurements of magnetic moments of ^{31}Al and ^{32}Al

G. Kijima,[*1] H. Ueno, D. Kameda, M. Takemura,[*1] A. Yoshimi, K. Shimada,[*1] D. Nagae,[*1] M. Uchida,[*1] T. Haseyama, T. Arai,[*1] S. Suda,[*1] K. Takase,[*1] T. Inoue,[*1] H. Kawamura,[*2] and K. Asahi

[Nuclear structure, ^{31}Al, ^{32}Al, β-NMR method, magnetic moment]

We aim at studying the borderline of the "island of inversion"[1] through nuclear moment measurements for neutron-rich Al isotopes. We measured the magnetic moment (μ-moment) of ^{30}Al and ^{32}Al by the β-NMR method using a single-crystal α-Al_2O_3 stopper.[2] This sample is also useful for measuring electric quadrupole moments (Q-moments) because the electric field gradients at the Al site of the sample have been obtained precisely.[3,4] Applying the stopper to the Q-moment measurement for ^{32}Al, the eqQ interaction term is estimated to be 13 kHz/mb with the crystal of the c-axis parallel to the external static magnetic field. On the other hand, the obtained accuracy for the μ-moment of ^{32}Al corresponds to the frequency of $\pm$37 kHz at the static magnetic field of $B_0 \sim 500$ mT. This accuracy is not sufficient to determine the Q-moment precisely. In the case of ^{31}Al,[5] the situation is found to be more severe. It is necessary, therefore, to precisely obtain the μ-moments of ^{32}Al and ^{31}Al before the Q-moment measurements.

Spin-polarized ^{32}Al was obtained from the projectile fragmentation of 95 MeV/nucleon ^{40}Ar projectiles on a 367 mg/cm^2 thick Nb target. The ^{32}Al fragments ware separated using RIPS. To obtain spin-polarized ^{32}Al, the emission angle $\theta_L = 1.3°$–$5.7°$ and momenta $p_F = 12.3$–13.0 GeV/c were selected. In the case of ^{31}Al, a 128 mg/cm^2 thick Nb target was employed and $p_F = 12.6$–13.4 GeV/c were selected. Thus, the polarized fragments of ^{32}Al were implanted in a single-crystal Si stopper of 1 mm thickness to which the external static magnetic field $B_0 \sim$ 500 mT was applied. This material is available for precise μ-moment measurement for ^{31,32}Al because the μ-moment of ^{25}Al ($T_{1/2} = 7.2$ sec) was determined to be $|\mu(^{25}\mathrm{Al})| = (3.6455 \pm 0.012)\mu_\mathrm{N}$ with diamagnetic correction.[6] In addition, the Si stopper has an advantage in that no electric field gradient exists. In the β-NMR measurement, using the adiabatic fast passage method, an oscillating magnetic field perpendicular to the B_0 direction was applied to the stopper, which was located in the air of the experimental hall. We employed the beam pulsing method with the RF application.

The obtained β-NMR spectra for ^{32}Al and ^{31}Al are shown in Figs. 1 and 2, respectively. In Fig. 1, the largest β-ray asymmetry change was observed within the searched frequency region of 7415.5–7447.8 kHz with 4.1σ deviation, where σ denotes the standard deviation of the β-ray counts. Using this frequency region, the μ-moment of ^{32}Al was preliminarily determined to be $|\mu(^{32}\mathrm{Al})| = (1.947 \pm 0.004)\mu_\mathrm{N}$, where μ_N denotes the nuclear magneton. The error of the μ-moment was improved to be half of the previous value. From Fig. 2, the μ-moment of ^{31}Al was also determined to be $|\mu(^{31}\mathrm{Al})| = (3.818 \pm 0.008)\mu_\mathrm{N}$ in the frequency region of 5816.0–5841.4 kHz where the largest asymmetry change was observed. The precise μ-moments of ^{31,32}Al obtained are consistent with those of previous reports[2,5] within the errors. Thus, we employed the obtained μ-moments for the Q-moment measurements of ^{32}Al and ^{31}Al as stated earlier.

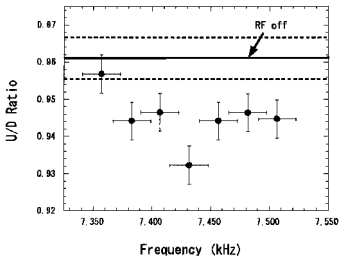

Fig. 1. β-NMR spectrum for ^{32}Al. The vertical bars indicate statistical errors, and the horizontal bars indicate the widths of swept frequency.

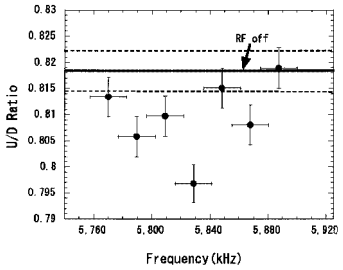

Fig. 2. β-NMR spectrum for ^{31}Al.

References
1) E. K. Warburton et al.: Phys. Rev. C **41**, 1147 (1990).
2) H. Ueno et al.: Phys. Lett. B **615**, 186 (2005).
3) D. Sundholm and J. Olsen: Phys. Rev. Lett. **68**, 927 (1992).
4) B. Filsinger et al.: J. Magn. Reson. **125**, 280 (1997).
5) D. Borremans et al.: Phys. Lett. B **537**, 45 (2002).
6) T. Minamisono et al.: Phys. Rev. B **14**, 376 (1976).

*1 Department of Physics, Tokyo Institute of Technology
*2 Rikkyo University

Electric quadrupole moments of ^{32}Al and ^{31}Al

D. Kameda, H. Ueno, K. Asahi, G. Kijima,[*1] M. Takemura,[*1] M. Uchida,[*1] A. Yoshimi, K. Shimada,[*1]
D. Nagae,[*1] T. Arai,[*1] T. Haseyama, K. Takase,[*1] S. Suda,[*1] T. Inoue,[*1]
J. Murata,[*2] H. Kawamura,[*2] and Y. Kobayashi

[Nuclear structure, spin-polarized RI beam, nuclear moments, β-NMR method]

The static electric qaudrupole moments (Q-moments) of ground-state ^{32}Al and ^{31}Al have been measured to study the nuclear deformations around the border of the "island of inversion".[1] In particular, the Q-moment of ^{32}Al is interesting in the determination of the *northern* border of the "island" along the neutron-rich $N = 19$ isotones.

The spin-polarized ^{31}Al and ^{32}Al beams were produced from the projectile fragmentation of 95 MeV/nucleon ^{40}Ar^{17+} projectiles on a Nb target. The target thickness for ^{31}Al (^{32}Al) was 0.13 g/cm^2 (0.37 g/cm^2). The separation of these isotopes was made using RIPS. To obtain spin-polarized fragments, selections were also made on the emission angle, $\theta = 1.3°$–$5.7°$, and the outgoing momentum of the ^{31}Al (^{32}Al) fragments, $p = 12.6$–13.4 GeV/c ($p = 12.3$–13.0 GeV/c). The polarized fragments were implanted in a single crystal α-Al_2O_3 sample to which the static magnetic field $B_0 \sim 500$ mT was applied. The experimental setup around the stopper was almost the same as that in the μ-moment experiment,[2] except the angle, θ_c, between the crystal c-axis and the B_0 direction. Specifically, two types of angle, $\theta_c = 90°$ and $\theta_c = 0°$, were employed. The former angle was used for searching the Q-moment in the initial stage of the experiment. The latter angle was used for the precise measurement.

In Fig. 1, the top and the bottom figures show the results of the Q-moment search for ^{32}Al($I^\pi = 1^+$) for $\theta_c = 90°$ and $\theta_c = 0°$, respectively. The vertical and horizontal axes denote the β-ray asymmetry change and the absolute value of the coupling constant of the quadrupole interaction, respectively. The Q-moment is obtained using the electric field gradient at the Al site of the α-Al_2O_3 sample, $eq = 70.9(5) \times 10^{19}$ V/m^2.[3,4] The vertical bars attached to the solid circles denote the statistics of the β-ray counts. Each horizontal bar of the solid circle indicates the Q-moment region which was searched by applying the RF field. Assuming that the region from ν_{Q_1} ($= |\frac{e^2qQ_1}{h}|$) to ν_{Q_2} ($= |\frac{e^2qQ_2}{h}|$) was searched using the $\theta_c = 90°$ setup, the frequency of the RF field would be swept in two different frequency regions, $[f_0 - \frac{3\nu_{Q_1}}{8} : f_0 - \frac{3\nu_{Q_2}}{8}]$ and $[f_0 + \frac{3\nu_{Q_1}}{8} : f_0 + \frac{3\nu_{Q_2}}{8}]$, where f_0 denotes the Larmor frequency. In the spectra, the magnetic resonance was clearly observed around 400 kHz in both $\theta_c = 90°$ and $\theta_c = 0°$ cases. In the bottom figure, we obtained the β-ray asymmetry change of 0.68(19)% in the region of 376.5–513.3 kHz which corresponds to the Q-moment region of 22–30 mb. The magnitude of the β-asymmetry change agrees with that obtained in the magnetic moment measurement.[2]

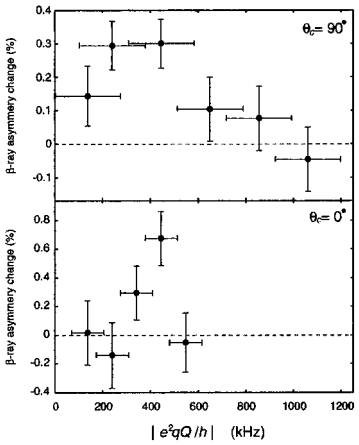

Fig. 1. Spectra of Q-moment measurement for ^{32}Al.

Figure 2 shows the result for ^{31}Al. We observed the magnetic resonance in the Q-moment region of 70–94 mb with the β-asymmetry change of 0.27(8)%. Further Q-moment search is needed for ^{31}Al.

Although analyses are now in progress, the obtained Q-moment of ^{32}Al shows that the shape of ^{32}Al is spherical. This indicates that ^{32}Al is located *out of* the "island of inversion".

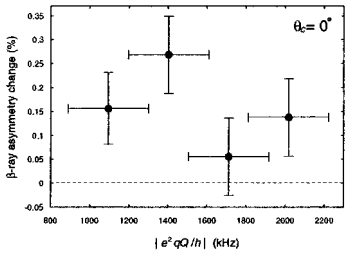

Fig. 2. Spectrum of Q-moment search for ^{31}Al holding crystal c-axis parallel to external static magnetic field.

*1 Tokyo Institute of Technology
*2 Rikkyo University

References
1) E. K. Warburton et al.: Phys. Rev. C **41**, 1147 (1990).
2) H. Ueno et al.: Phys. Lett. B **615**, 186 (2005).
3) D. Sundholm et al.: Phys. Rev. Lett. **68**, 927 (1992).
4) B. Filsinger et al.: J. Magn. Reson. **125**, 280 (1997).

Inelastic proton scattering on neutron-rich nuclei ^{60}Cr and ^{62}Cr

E. Takeshita,[*1] N. Aoi, S. Ota,[*2] S. Takeuchi, H. Suzuki,[*3] H. Baba,[*4] S. Bishop, T. Fukui,[*2] Y. Hashimoto,[*5] E. Ideguchi,[*4] K. Ieki,[*1] N. Imai,[*6] H. Iwasaki,[*3] S. Kanno,[*1] Y. Kondo,[*5] T. Kubo, K. Kurita,[*1] K. Kusaka, T. Minemura,[*6] T. Motobayashi, T. Nakabayashi,[*5] T. Nakamura,[*5] T. Nakao,[*3] M. Niikura,[*4] T. Okumura,[*5] H. J. Ong,[*3] T. K. Onishi,[*3] H. Sakurai,[*3] S. Shimoura,[*4] R. Sugo,[*1] D. Suzuki,[*3] M. K. Suzuki,[*3] M. Tamaki,[*4] K. Tanaka, Y. Togano,[*1] and K. Yamada

[Nuclear structure, ^{60,62}Cr(p,p′γ), inelastic scattering, unstable nuclei]

Inelastic proton scatterings on neutron-rich nuclei ^{60}Cr and ^{62}Cr were studied. The first 2^+ energies of $^{60}_{24}Cr_{36}$ and $^{62}_{24}Cr_{38}$ are significantly lower than those of the neighboring isotopes,[1] indicating the narrowering of the $N = 40$ sub-shell gap. When the $N = 40$ shell gap is narrowed, a large deformation is expected for such nuclei in this region, because the locations of these nuclei are close to the middle of the neutron pfg shell between $N = 28$ and 50. The deformation may be further enhanced by protons, which also favor such deformation because of their location in the middle of the $f_{7/2}$ shell between $Z = 20$ and 28. To study such deformation and collectivity, inelastic proton scatterings in inverse kinematics, H(^{60}Cr,^{60}Crγ) and H(^{62}Cr,^{62}Crγ), were performed by γ-ray spectroscopy.

Neutron-rich Cr isotopes were produced by the fragmentation of the 63 MeV/nucleon ^{70}Zn beam of the mean intensity 150 particle nA onto a ^{9}Be target of 95 mg/cm^2 thickness. These isotopes were separated by the RIKEN Projectile-Fragment Separator (RIPS).[2] The intensities of ^{60}Cr and ^{62}Cr were 10 cps and 12 cps, respectively. These nuclei bombarded a liquid hydrogen target[3] of 60 mg/cm^2 thickness. De-excitation γ rays from the inelastically scattered ^{60,62}Cr nuclei were detected by the NaI(Tl) scintillator array DALI2[4] located around the secondary target. The photo-peak efficiency and energy resolution for the 0.7 MeV γ ray were 26% and 11% (FWHM), respectively. Scattered particles were identified using a TOF-spectrometer[5] placed downstream of the secondary target, which is newly developed to improve the mass resolution of the scattered particles. In the present experiment, a maximum mass separation of 2.7 σ was achieved for the scattered particles.

Doppler-corrected γ-ray spectrum obtained in the H(^{60}Cr,^{60}Crγ) reaction shown in Fig. 1 (a) exhibits a pronounced peak at 650(5) keV. The peak at 210 keV is associated with ^{59}Cr, resulting from the contamination in the mass gate of the scattered particles. In the spectrum obtained in the H(^{62}Cr,^{62}Crγ) reaction shown in Fig. 1 (b), a clear peak is seen at 447(3) keV.

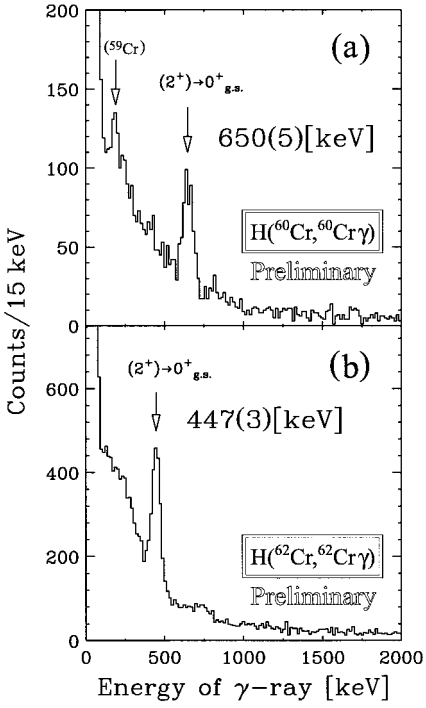

Fig. 1. γ-ray spectra obtained in inelastic proton scatterings of ^{60}Cr(a) and ^{62}Cr(b).

The energies of γ-ray peaks in ^{60}Cr and ^{62}Cr are consistent with the excitation energies of the states tentatively assigned to be the first 2^+ state in Ref. 1 (646(1) keV, 446(1) keV) The determination of the inelastic proton scattering cross sections is in progress.

References

1) O. Sorlin et al.: Eur. Phys. J. A **16**, 55 (2003).
2) T. Kubo et al.: Nucl. Instrum. Methods Phys. Res. B **70**, 309 (1992).
3) H. Ryuto et al.: Nucl. Instrum. Methods Phys. Res. A **555**, 1 (2005).
4) S. Takeuchi et al.: RIKEN Accel. Prog. Rep. **36**, 148 (2003).
5) N. Aoi et al.: RIKEN Accel. Prog. Rep. **38**, 176 (2005).

[*1] Department of Physics, Rikkyo University
[*2] Department of Physics, Kyoto University
[*3] Department of Physics, University of Tokyo
[*4] Center for Nuclear Study, University of Tokyo
[*5] Department of Physics, Tokyo Institute of Technology
[*6] High Energy Accelerator Research Organization (KEK)

Proton inelastic scattering on ^{74}Ni

S. Kanno,[*1] N. Aoi, W. F. Mueller,[*2] H. Sakurai,[*2] D. Bazin,[*2] M. D. Bowen,[*2] C. M. Campbell,[*2] J. M. Cook,[*2] D.-C. Dinca,[*2] A. Gade,[*2] T. Glasmacher,[*2] H. Iwasaki,[*2] T. Kubo, K. Kurita,[*1] T. Motobayashi, T. Nakamura,[*3] H. Suzuki,[*4] S. Takeuchi, J. R. Terry,[*2] K. Yoneda,[*2] and H. Zwahlen[*2]

[Nuclear structure, ^{74}Ni(p,p′ γ), 104 MeV/u, inelastic scattering, unstable nuclei]

A neutron-rich nucleus ^{74}Ni was studied by proton inelastic scattering to explore the evolution of magicity at $Z = 28$ in a very neutron rich region. Ni isotopes close to the stability line show rigid magicity, although neutron-rich Ni isotopes could loose the magicity due to their large neutron excess. As a tool for investigating nuclear magicity, the excitation energy of the first 2_1^+ state ($E_x(2_1^+)$) and the cross-section of the inelastic scattering to the 2_1^+state are used. $E_x(2_1^+)$'s are known for the Ni isotopes from ^{54}Ni to ^{76}Ni. However, inelastic scattering cross-section to the 2_1^+ states is obserbed only for Ni isotopes lighter than ^{68}Ni. In this work, the (p,p′) cross-section of very neutron rich Ni isotope ^{74}Ni is measured for the first time.

The experiment was performed at National Superconducting Cyclotron Laboratory in Michigan State University using an S800 spectrograph. A projectile fragmentation of ^{86}Kr on ^{9}Be target was used to produce the ^{74}Ni beam. The intensity of ^{74}Ni beam was typically 0.5 particle/sec. De-excitation γ rays were observed instead of recoil protons to identify the final states. The simultaneous counting of γ rays and scattered particles enable us to determine the reaction channel. Further information about the experimental setup, detectors and secondary beam is described in Ref. 1.

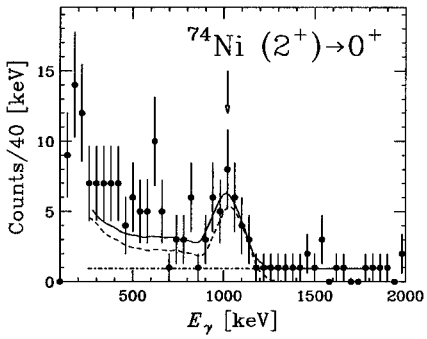

Fig. 1. γ-ray spectrum in coincidence with incoming and scattered ^{74}Ni ions. The solid curve is the fit to the spectrum, which consists of the response function (dashed curve) of γ-ray detectors and a background (dot-dashed curve).

Figure 1 shows the γ-ray spectrum obtained in coincidence with scattered ^{74}Ni, where a clear peak corresponding to the $2_1^+ \rightarrow 0_{g.s.}^+$ transition was observed. The energy of the peak is determined to be 1021(21) keV, which is consistent with the value (1024(1) keV) that has recently been obtained in the β-decay experiment of ^{74}Co.[2)]

The $E_x(2_1^+)$ obtained in this work is plotted in Fig. 2 together with the $E_x(2_1^+)$'s of the neighboring Ni isotopes. The $E_x(2_1^+)$ of ^{74}Ni is slightly lower than that of ^{72}Ni. Several theoretical calculations[3–5)] are also shown in Fig. 2 for comparison. All the calculations reproduce the tendency of the observed value. Further analysis is in progress to deduce the cross-section and deformation parameter from the γ-ray yield.

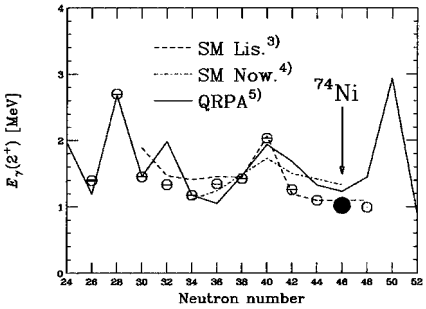

Fig. 2. $E_x(2^+)$ plotted as function of neutron number. The closed circle is the value obtained in this work; the open circles are experimental values.[2,6–9)] Dashed and dot-dashed lines indicate shell-model calculations based on NR78[3)] and S3V[4)] effective interactions. Solid line indicates QRPA calculation[5)] with SkM* parameter.

[*1] Rikkyo University
[*2] Michigan State University, USA
[*3] Tokyo Institute of Technology
[*4] University of Tokyo

References
1) S. Kanno et al.: RIKEN Accel. Prog. Rep. **38**, 66 (2005).
2) C. Mazzocchi et al.: Phys. Lett. B **622**, 45 (2005).
3) A. F. Lisetskiy et al.: Phys. Rev. C **70**, 044314 (2004).
4) O. Sorlin et al.: Phys. Rev. Lett. **88**, 092501 (2002).
5) J. Terasaki: Private communication.
6) K. Yamada et al.: Eur. Phys. J. A **25**, Suppl. 1, 409 (2005).
7) T. W. Burrows: Nucl. Data Sheets **97**, 1 (2002).
8) J. K. Tuli: Nucl. Data Sheets **103**, 389 (2004).
9) M. Sawicka et al.: Phys. Rev. C **68**, 044304 (2003).

Development of ^{134}Ce isomeric beam with spin orientation

H. Watanabe,[*1] H. Ueno, A. Yoshimi, D. Kameda, K. Shimada,[*2] D. Nagae,[*2]
T. Kishida, Y. Kobayashi, and K. Asahi [*2]

[Radioactive beam, isomer]

A nuclear spin ensemble in orientation can be produced by nuclear reaction. In particular, excited states populated by heavy-ion fusion reactions are highly oriented due to the large orbital angular momentum brought in perpendicularly to the direction of projectiles. Aligned isomeric states which have lifetimes ranging from a few tens of nanoseconds up to submicroseconds become excellent probes of the γ-ray time differential perturbed angular distribution (TDPAD) measurement for studies of nuclear moments and hyperfine interactions. The objective of this work is to exploit the spin-aligned isomeric beam of ^{134}Ce ($T_{1/2}$ = 308 ns, E_{ex} = 3.2 MeV, $I^{\pi} = 10^{+}$, $g = -0.183$) as a probe to investigate the magnetic ordering in Ce-based compounds and alloys from the microscopic viewpoint.

The isomer in ^{134}Ce has been produced via the ^{9}Be(^{131}Xe,6n)^{134}Ce reaction at an energy of 8 AMeV provided by the RIKEN Ring Cyclotron (RRC). According to a simulation using the LISE code[1] with an energy loss calculation based on the formula of Hubert,[2] the recoil energy of the ^{134}Ce beam emerging from the ^{9}Be target (7.5 μm thickness) is 6.1 AMeV on average. For this recoil energy, the simulation using a charge-state parametrization given by Winger[3] suggests that the Ce ions have a charge distribution around the most probable value $Q = 49+$. Even for a single charge state, there are various electronic configurations, for each of which the hyperfine interaction couples the electronic spin $\boldsymbol{J}$ to the nuclear spin $\boldsymbol{I}$. Together they precess around the total atomic spin $\boldsymbol{F} = \boldsymbol{J} + \boldsymbol{I}$. In the case of highly ionized atoms traveling in vacuum, the nuclear spin alignment is quickly attenuated due to the random walk-out in the direction of $\boldsymbol{J}$.[4] Furthermore, when the ions are transported through the magnetic elements, the electronic spins precess very rapidly in the external fields because of the large atomic magnetic moments. As a result, the initial nuclear spin alignment most likely disperses before the isomers arrive at the final focal point.

The methodology for preserving the nuclear spin alignment during the separation process is based on the fact that there are no hyperfine interactions in atomic states which have the singlet $^{1}S_0$ electronic configuration. In this experiment, the Ce ions at the $Q = 48+$ charge state, which is equivalent to the Ne-like closed atomic shell, were transported through the RIPS spectrometer. In such a situation, the precession of nuclear spin is only caused by the static interaction of the nuclear moment with the external magnetic fields, which never wipes out the alignment. Its precession angle can be calculated to be $-23.4°$ for the present spectrometer setup. Because the ions are deflected by 90° through the RIPS spectrometer, it is expected that the angular distribution of $E2$ transition is minimum and maximum at $-23.4°$ and 66.6°, respectively, with respect to the beam axis. Two Ge detectors were placed at these angles at the final focal plane to confirm the anisotropy of γ rays deexciting the isomeric state in ^{134}Ce. The measurements were carried out at three different values of magnetic rigidity which correspond to charge states $Q = 46+, 47+, 48+$ of the Ce ions. It is reasonable to assume that the alignment is completely lost during flight in the RIPS spectrometer due to the hyperfine interaction for $Q = 46+$ and $47+$. In order to eliminate systematic errors, the ratio between the number of counts measured using the two detectors for each charge state was normalized with that for $Q = 46+$ ions. This quantity, called double ratio (DR), is immune to differences in detection efficiency. The results of the DR for the 948 keV transition in ^{134}Ce are shown in Fig. 1. The experimental value of DR = 1.076(35) for $Q = 48+$ indicates a 11% preservation of alignment.

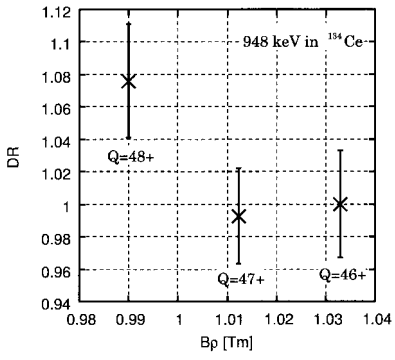

Fig. 1. Double ratios obtained for 948 keV transition in ^{134}Ce.

References

1) D. Bazin et al.: Nucl. Phys. Phys. A **701**, 661 (2002).
2) F. Hubert et al.: Nucl. Data Tables A **7**, 233 (1970).
3) J. A. Winger et al.: Nucl. Instrum. Methods Phys. Res. B **70**, 380 (1992).
4) I. Ben Zvi et al.: Nucl. Phys. A **121**, 592 (1968).

*1 Department of Nuclear Physics, The Australian National University, Australia
*2 Tokyo Institute of Technology

Study of high-spin states in $^{49-51}$Ti

M. Niikura,[*1] E. Ideguchi,[*1] T. Fukuchi,[*1] H. Baba, N. Hokoiwa,[*2] C. Ishida,[*3] H. Iwasaki,[*4] T. Koike,[*5] T. Komatsubara,[*6] T. Kubo, M. Kurokawa, S. Michimasa, K. Miyakawa,[*6] K. Morimoto, T. Ohnishi, S. Ota,[*7] A. Ozawa,[*6] S. Shimoura,[*1] T. Suda, M. Tamaki,[*1] I. Tanihata,[*8] Y. Wakabayashi,[*2] and K. Yoshida

[Nuclear reaction, ^{9}Be(^{46}Ar, xn)$^{55-x}$Ti, unstable nuclei, fusion reaction]

In-beam γ-ray spectroscopy with fusion-evaporation reactions is one of the most efficient methods for the study of the nuclear structure at high spin since large angular momentum can be brought into the system. However, nuclei produced by the fusion reaction using stable isotope beams are limited, in many cases, to the proton-rich side relative to the line of β-stability. In order to study high-spin states in the neutron-rich nuclei, $^{49-51}$Ti, we have performed an experiment using a neutron-rich secondary beam, ^{46}Ar.

The experiment was performed at the RIPS facility in RIKEN.[1] A ^{46}Ar beam of 4.0 $\pm$ 0.3 MeV/nucleon was used to bombarded a 10-μm-thick ^{9}Be target to induce the secondary fusion reaction, $^{9}\mathrm{Be}\left(^{46}\mathrm{Ar}, xn\right)^{55-x}\mathrm{Ti}$. Gamma rays emitted from the high-spin states of evaporation residues were detected by the CNS-GRAPE (Gamma-Ray detector Array with Position and Energy sensitivity)[2] placed around the secondary target. Details of the experimental setup are described in Ref. 3.

We have obtained the γ-ray spectrum for $^{49-51}$Ti, and known cascade gamma transitions up to spin $(19/2)^{-}$, (11^{+}) and (13/2,17/2) states[4–6] of $^{49-51}$Ti were clearly observed, respectively.[3]

In order to investigate higher-spin states, we performed a γ-γ coincidence analysis. In Fig. 1 γ-ray spectra gated by known γ rays of ^{51}Ti are shown. We confirmed coincidence relations between known γ rays and the observed new γ peak at 761 keV. Since this γ ray is in coincidence with all known cascade γ transitions of ^{51}Ti, it is placed above the known 3644 keV state (see right panel of Fig. 1).

In ^{49}Ti, four γ transitions with the energies of 1543, 963, 785 and 1093 keV were previously reported.[4] Figure 2 shows the total projected spectrum gated by known transitions of ^{49}Ti. We confirmed the coincidence relations between the four known γ transitions and, in addition, found a new γ peak at 2370 keV. Since this peak cannot be seen in the spectrum gated by the known transitions of ^{50,51}Ti, this new γ ray was assigned to a transition from ^{49}Ti. To interpret the excited levels, we performed shell-model calculations using the ANTOINE code.[7,8] The calculations reproduced the identified levels well.

Further analysis is still in progress.

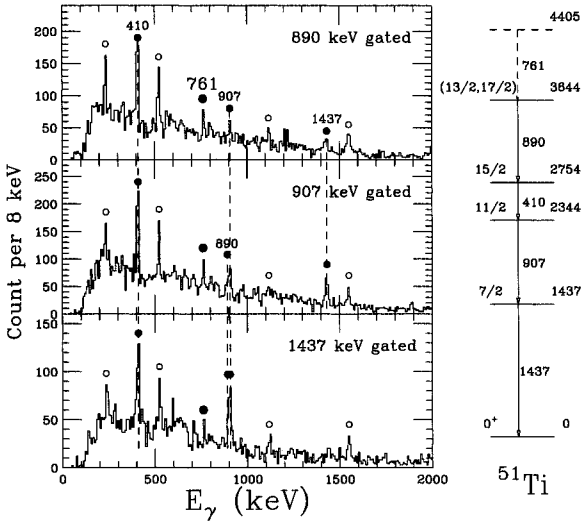

Fig. 1. γ-ray spectra gated by 890, 907 and 1437 keV of ^{51}Ti. Gamma rays from ^{51}Ti and ^{50}Ti are marked by closed and open circles, respectively.

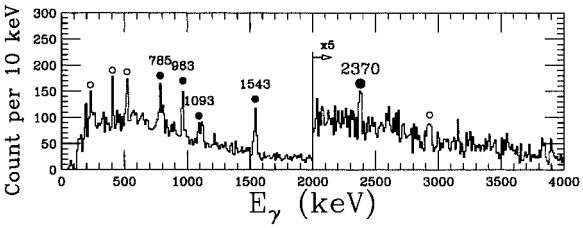

Fig. 2. Total projected spectrum gated by known transitions of ^{49}Ti. Gamma rays from ^{49}Ti and ^{50}Ti are marked by closed and open circles, respectively.

*1 Center for Nuclear Study, University of Tokyo
*2 Department of Physics, Kyushu University
*3 Department of Physics, Royal Institute of Technology, Sweden
*4 Department of Physics, University of Tokyo
*5 Department of Physics, Tohoku University
*6 Institute of Physics, University of Tsukuba
*7 Department of Physics, Kyoto University
*8 TRIUMF, Canada

References
1) T. Kubo et al.: Nucl. Instrum. Methods Phys. Res. B **461**, 309 (1992).
2) S. Shimoura: Nucl. Instrum. Methods Phys. Res. A **525**, 188 (2004).
3) E. Ideguchi et al.: AIP Conf. Proc. **764**, 136 (2004).
4) M. Behar et al.: Nucl. Phys. A **366**, 61 (1981).
5) B. Gass et al.: Phys. Rev. Lett. **40**, 1313 (1978).
6) S. E. Arnell et al.: Phys. Scr. **6**, 222 (1972).
7) E. Caurier: *Shell-model code ANTOINE* (Institut de Recherches Subatomiques, Strasbourg, 1989–2002).
8) E. Caurier and F. Nowacki: Acta Phys. Pol. B **30**, 705 (1999).

Search for high-spin isomers in $N = 51$ isotones using CRIB

Y. Wakabayashi,[*1,*2] A. Odahara,[*3] Y. Gono, T. Fukuchi,[*4] T. Teranishi,[*1] S. Kubono,[*2] H. Yamaguchi,[*2] A. Saito,[*2] E. Ideguchi,[*2] S. Nishimura, J. J. He,[*2] H. Fujikawa,[*2] A. Guilherme,[*2] S. Ota,[*5] J. Y. Moon,[*6] M. Notani,[*7] Y. Yanagisawa, S. Michimasa, S. Shimoura,[*2] H. Watanabe,[*8] T. Kishida, H. Baba, and T. Ishii[*9]

[High-spin isomer, $\gamma\gamma$ coincidence, unstable nuclear beams]

High-spin isomers are known in $N = 83$ isotones systematically.[1)] These isomers are of stretch-coupled configurations of valence nucleons excited by the breaking of neutron magic 82 and proton semimagic 64 cores. They are considered to be shape isomers because the isomerism is attributed to sudden shape changes from near-spherical to oblate shapes. To search for the same type of isomer in other mass regions, we selected $N = 51$ isotones, which have one neutron outside the magic 50 core and proton numbers close to the semimagic 40 core.

We developed a ^{17}N secondary beam using the low-energy radioisotope beam separator (CRIB)[2,3)] of the Center for Nuclear Study (CNS), University of Tokyo, to search for high-spin isomers in $N = 51$ isotones. Because the nuclei with $Z < 40$ of $N = 51$ isotones are close to the line of stability, it is difficult to produce high-spin states in these nuclei using reactions by combinations of stable beams and targets. Therefore, it is very effective to use radioisotope beams. By γ-ray spectroscopy, high-spin isomers can be searched for in the nuclei ^{90}Y, ^{89}Sr and ^{88}Rb produced by the α5n, αp5n, 2α3n evaporation channels in the fusion reaction of ^{82}Se+^{17}N, respectively.

An experiment that involved searching for isomers was carried out in Dec. 2004. A self-supporting ^{9}Be target of 2.3 mg/cm^2 thickness was bombarded by an $^{18}O^{8+}$ primary beam at 126 MeV to obtain a ^{17}N beam. The beam current was 0.55 particle μA at the primary target position. A parallel-plate avalanche counter (PPAC) was set at a dispersive focal plane (F1) for beam monitoring. To identify reaction products, a PPAC and a Si detector of 1.5 mm thickness were installed at an achromatic focal plane (F2) before the Wien Filter. A ^{82}Se secondary target of 4.9 mg/cm^2 thickness was placed at a final focal plane (F3). A PPAC and a 72-μm-thick Si detector were also placed just upstream and downstream of the secondary target, respectively, to distinguish the secondary fusion reaction products from the secondary beam. Two clover Ge detectors were set to measure the γ rays emitted from the nuclei produced by the secondary fusion reaction. These Ge detectors were surrounded by paraffin, cadmium and lead to reduce background γ rays from thermal neutron capture reaction products. The intensity and purity of the $^{17}N^{7+}$ secondary beam were 2.3×10^4 particles/s and 21%, respectively, at the secondary target position.

In this experiment, some γ rays from nuclei, such as ^{93}Nb, produced by the ^{82}Se+^{17}N reaction were observed, as shown in Fig. 1, which shows energy spectra obtained using Ge detectors. Spectrum (a) shows the total projection spectrum of the $\gamma\gamma$ prompt coincidence measurement. The gate width of prompt $\gamma\gamma$ timing was set to 200 nsec. Spectrum (b) shows a delayed $\gamma\gamma$ projection spectrum whose delayed time was set in the range of 1 to 2 μsec from prompt timing, where prompt and delayed indicate the condition of the time difference between two γ rays in coincidence.

In spectrum (a) in Fig. 1, a possible indication of the existence of the 1535 keV peak, which is the lowest transition feeding a long-lived isomer 7^+ ($T_{1/2}$ = 3.19 h), was obtained. This nucleus is one of the relevant nuclei in $N = 51$ isotones. A clearer indication can also be seen in (b) of Fig. 1. If these indications are proven in further data analyses, such as the optimization of various gate conditions, it means that there exists a relatively long lived isomer in ^{90}Y.

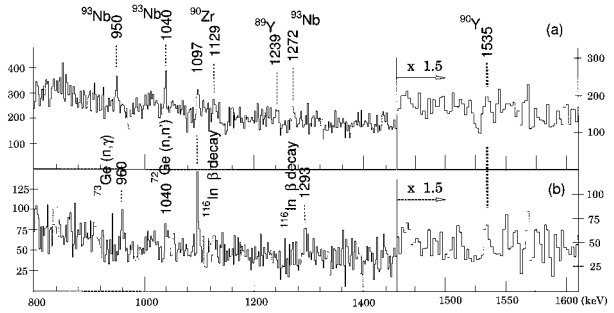

Fig. 1. Projection spectra of $\gamma\gamma$ coincidence under two time conditions. The time conditions of spectra (a) and (b) are given in the text.

*1 Department of Physics, Kyushu University
*2 Center for Nuclear Study, University of Tokyo
*3 Department of Physics, Osaka University
*4 Department of Physics, Rikkyo University
*5 Department of Physics, Kyoto University
*6 Chung-Ang University, Korea
*7 Physics Division, Argonne National Laboratory, USA
*8 Department of Nuclear Physics, The Australian National University, Australia
*9 Japan Atomic Energy Agency

References

1) Y. Gono et al.: Eur. Phys. J. A **13**, 5 (2002), and references therein.
2) S. Kubono et al.: Eur. Phys. J. A **13**, 217 (2002).
3) Y. Yanagisawa et al.: Nucl. Instrum. Methods Phys. Res. A **539**, 73 (2005).

Observation of second decay chain from $^{278}113$

K. Morita, K. Morimoto, D. Kaji, T. Akiyama,[*1] T. Suda, H. Haba, A. Yoshida, E. Ideguchi,[*2] S. Goto, F. Tokanai, H. Koura, A. Ozawa, T. Ohnishi, T. Yamaguchi, H. Kudo, K. Sueki, A. Yoneda, and N. Sato[*3]

[$^{278}113$, production and decay, gas-filled recoil ion separator]

We observed one decay chain, which was the convincing candidate event originating from an isotope of the 113th element, $^{278}113$ in the ^{209}Bi + ^{70}Zn reaction in 2004[1] at RIKEN Linear Accelerator (RILAC) facility. In continuing the experiment to search for more events in the same reaction for confirming the first event, we observed one more decay chain this year. The production cross sections of isotopes of the highest-atomic-number region in the fusion reaction become extremely small with the increase in atomic number. For example, according to our previous measurements in 2003 and 2004 to produce the isotope $^{278}113$ mentioned above, the cross section was deduced to be $55\ ^{+130}_{-45}$ fb (fb $= 10^{-39}$ cm^2). We carried out the reproduction experiment from January 20 to October 20, this year with several intermissions. The net irradiation time was 87.2 days. The second decay chain was observed at 2:18 (JST) on April 2.

All the experimental conditions were almost identical to those used in previous runs.[1] A ^{70}Zn ion beam of 353 MeV was extracted from RILAC. The absolute accuracy of the beam energy was ±0.6 MeV. Targets were prepared by the vacuum evaporation of metallic bismuth, onto carbon backing foils of 30 μg/cm^2 thickness. The thickness of the bismuth layer was about 450 μg/cm^2. The beam energy at the half-depth of targets was estimated to be 349.5 MeV. The reaction products were separated in-flight from the beam by a gas-filled recoil ion separator, GARIS,[1] and were guided into a detector box placed at the focal plane of GARIS. The separator was filled with helium gas at a pressure of 86 Pa. The magnetic rigidity of GARIS for evaporation residue measurement was set to be 2.09 Tm. The total dose of ^{70}Zn from Jan. to Oct. 2005 was 2.46×10^{19}.

The second chain was observed during irradiation. This decay chain consisted of four consecutive alpha decays followed by a spontaneous fission after the implantation of an evaporation residue in the focal plane detector of GARIS. Energies, time differences between events, positions in the detector of the event are listed in the second column of Table 1 together with those observed in previous runs (first column). In the table, ER denotes the evaporation residue, and SF denotes the spontaneous fission. In the third alpha decay of the second chain, decay energy was measured only partly because of the limited solid angle coverage (85%) of the detector box.

Table 1. Summary of observed events. Number in parentheses denotes an energy resolution in FWHM. ΔT: Time differences between events. Position: measured from the bottom of the detector.

	chain 1	chain 2	Nuclide
	E (MeV) ΔT Position	E (MeV) ΔT Position	
ER	36.75 - 30.3 mm	36.47 - 30.1 mm	
α_1	11.68 (0.04) 0.344 ms 30.5 mm	11.52 (0.04) 4.93 ms 30.2 mm	$^{278}113$
α_2	11.15 (0.07) 9.26 ms 30.4 mm	11.31 (0.07) 34.3 ms 29.6 mm	^{274}Rg
α_3	10.03 (0.07) 7.16 ms 29.8 mm	2.32 (escape) 1.63 s 29.5 mm	^{270}Mt
α_4	9.08 (0.04) 2.47 s 30.9 mm	9.77 (0.04) 1.31 s 29.7 mm	^{266}Bh
SF	204.1 40.9 s 30.3 mm	192.3 0.787 s 30.5 mm	^{262}Db

The observed decay is the same as that observed in the first decay chain. Decay times observed in both chains are consistent, indicating that they have the same origins. Decay energies in both chains show some discrepancies. However, considering that the observation in the rather widely distributed decay energies of the decay chains of odd-odd nucleus ^{272}Rg,[2] these two decay chains are consistently assigned to those originating from $^{278}113$. The production cross section is deduced from the present event to be 38^{+88}_{-32} fb, which agrees well with that obtained in previous runs. Then average production the cross section is deduced to be 45^{+59}_{-29} fb by combining the two values.

References

1) K. Morita, K. Morimoto, D. Kaji, T. Akiyama et al.: J. Phys. Soc. Jpn. **73**, 2593 (2004).
2) K. Morita, K. Morimoto, D. Kaji et al.: J. Phys. Soc. Jpn. **73**, 1738 (2004).

*1 Department of Physics, Saitama University
*2 Center for Nuclear Study, University of Tokyo
*3 Department of Physics, Tohoku University

Electron scattering from unstable nuclei by novel SCRIT method (III)

T. Suda, T. Emoto, Y. Furukawa,[*2] S. Ito, T. Koseki, K. Kurita,[*1] T. Masuda,[*1]
M. Nakamura, T. Tamae,[*2] M. Wakasugi, S. Wang, and Y. Yano

[SCRIT, electron scattering, luminosity determination]

We have been intensively carrying out feasibility studies for a novel SCRIT (Self-Confining RI Target) scheme[1] at an existing electron storage ring, KSR of Kyoto University, for future electron-RI scattering experiments.

As already reported,[2–4] the trapping of externally injected ions by circulating electron beams was clearly confirmed by detecting ions after some trapping period, on an order of a second, by extracting from the trapping potential.

This is not, however, direct evidence that all ions exist on the electron beam, since the ions can also spiral around the electron beam. The main effort made this year was, thus, to observe direct evidence of the spatial overlap of the ions with the electron beam; in another words, luminosity determination.

As a luminosity monitor, a high-energy γ-ray detector, BaF_2, was prepared for detecting bremsstrahlung from the trapped ions. During the series of test experiments, a huge background was revealed for the bremsstrahlung luminosity monitor. A typical counting rate of the BaF_2 detector was a few kHz, whereas the expected rate for a luminosity of $10^{25}\,/cm^2/s$ is 20 Hz. We found that the sources of the background are due to, 1) bremsstrahlung from residual gas ions trapped by the electron beam, and 2) electromagnetic showers produced at the beam pipe where the β_y of the ring parameters becomes maximum.

The number of trapped gas ions calculated from the BaF_2 counting rate is found to be consistent with the number of gas ions, which explains the beam life time of KSR. What we did in this year for this purpose are listed below.

- Ion clearer installation:
  An ion clearer is a pair of electrodes, which sandwiches the electron beam. By applying high voltage to the electrodes, one can effectively remove the trapped gas ions from the electron beam. A numerical simulation predicted a nearly one-order reduction of the number of trapped gas ions.
- New beam pipe installation:
  The background reduction due to the electromagnetic shower is realized by enlarging the aperture; inner diameter of the beam pipe. We designed new beam pipes at the quadruple magnets, where β_y is maximum (Fig. 1), to keep sufficiently large aperture for the storage electron beam.
- Collimator installation:
  In addition, a Geant simulation suggests that a collimator placed close to the circulating electron beam to remove the beam halo is effective in reducing the background from upstream. A thick collimator, having dimensions of ± 20 mm for vertical and ± 50 mm for horizontal, for a high-vacuum environment was installed inside the vacuum chamber.

After successful installation of the ion clearers, beam pipes and collimator, the whole electron ring, including the SCRIT prototype, was backed for about one week. Vacuum of tpically 10^{-8} Pa was achieved. Self-cleaning operation of KSR subsequently followed the backing to further improve the vacuum, which was completed by the end of November.

We are now ready to restart feasibility studies of the SCRIT scheme at KSR for determining the luminosity by observing the bremsstrahlung from trapped ions in SCRIT.

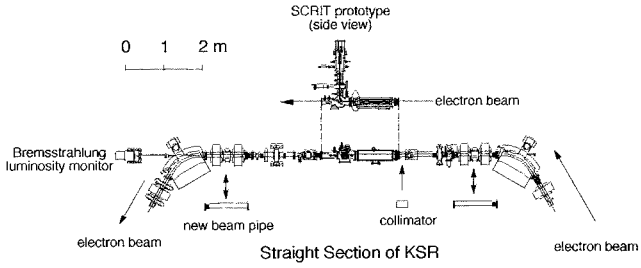

Fig. 1. Straight section of KSR, where the SCRIT prototype is installed. The bremsstrahlung luminosity monitor is positioned in the downstream of the straight section. The newly installed beam pipes at position where β_y becomes maximum are indicated.

References
1) M. Wakasugi, T. Suda, and Y. Yano: Nucl. Instrum. Methods Phys. Res. A **532**, 216 (2004).
2) T. Suda and M. Wakasugi: Prog. Part. Nucl. Phys. **55**, 417 (2005).
3) T. Suda et al.: RIKEN Accel. Prog. Rep. **38**, 71 (2005).
4) M. Wakasugi et al.: J. Part. Accel. Soc. Jpn. **2**, 59 (2005).

*1 Rikkyo Univesity
*2 Tohoku Univesity

Observation of medium modifications for ρ and ω mesons†

M. Naruki, H. En'yo, R. Muto, F. Sakuma,* T. Tabaru, and S. Yokkaichi,*
for the KEK-PS E325 Collaboration

[Vector meson, mass modification, chiral symmetry, QCD]

The experiment E325 has been performed at the KEK 12-GeV Proton Synchrotron to measure the invariant mass spectra of $\rho, \omega, \phi \rightarrow e^+e^-$ and $\phi \rightarrow K^+K^-$ decay modes simultaneously. This was the first dilepton measurement of the modification of the vector meson mass in a nucleus.

Figure 1 shows the invariant mass spectra of the e^+e^- pairs using all of the data taken in 2002. The invariant mass spectra were fitted with a combinatorial background and known hadronic sources: $\rho \rightarrow e^+e^-$, $\omega \rightarrow e^+e^-$, $\phi \rightarrow e^+e^-$, $\eta \rightarrow e^+e^-\gamma$, and $\omega \rightarrow e^+e^-\pi^0$. The background was evaluated by the event-mixing method. The mass resolution and the detector effect of our spectrometer were taken into account through the detector simulation using Geant4. The relative abundances of these components were determined by the fitting, except for the ratio of $\omega \rightarrow e^+e^-\pi^0$ to $\omega \rightarrow e^+e^-$ decay, which was fixed to in-vacuum branching ratios, 59/6.95 given by the PDG. The fit results are plotted with the solid lines in Fig. 1. The region from 0.6 to 0.76 GeV/c^2 was excluded from the fit.

A significant excess can be seen on the low-mass side of the ω peak, whereas the high-mass tail of ω can be reproduced with the expected shapes. After the acceptance correction, the 95% C.L. allowed parameter regions are obtained as $\rho/\omega < 0.15$ and $\rho/\omega < 0.31$ for C and Cu targets, respectively. These values are much smaller than one, as was previously measured in pp interactions at the same energy.[1] A possible explanation of the small ρ/ω is that the most of the ρ decay inside the nuclei due to their short lifetime, therefore the ρ with the vacuum shape is highly suppressed, and the modified ρ contributes to the excess.

A comparison has been made between the data and a model considering in-medium mass modification. In this model, mass decreases linearly as a function of the density ρ; $m(\rho)/m(0) \simeq 1-k(\rho/\rho_0)$.[2] A Woods-Saxon shape was used for the nuclear density distribution. We assumed that the vector mesons were generated at the surface of an incident hemisphere of the target nucleus. We fit the entire mass region of Fig. 1 with the modified shapes of ρ and ω. The fit results, after subtracting the combinatorial background and the shapes of $\eta \rightarrow e^+e^-\gamma$ and $\omega \rightarrow e^+e^-\pi^0$ are shown in Fig. 2. The spectra for both C and Cu targets can be reproduced quite well using this model. We obtained the shift parameter of $k = 0.092 \pm 0.002$. The best-fit

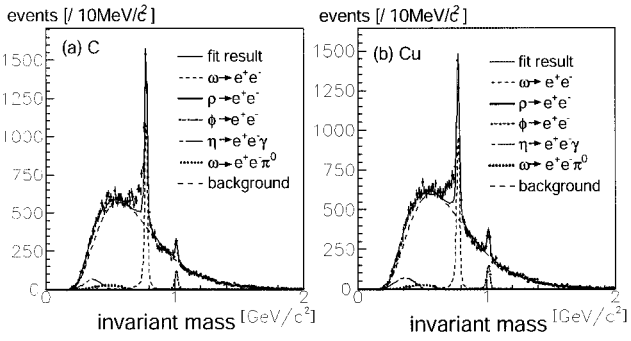

Fig. 1. Invariant mass spectra of e^+e^- for (a) C and (b) Cu targets. The solid lines are the best-fit results, which are the sums of the known hadronic decays. $\rho \rightarrow e^+e^-$ is not visible (see text).

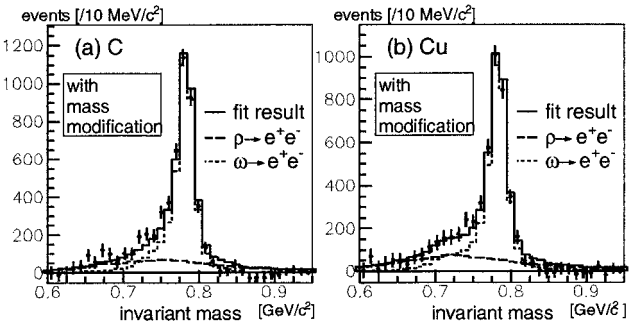

Fig. 2. Result of model calculation considering in-media modification for (a) C and (b) Cu targets. The background and the shapes of $\eta \rightarrow e^+e^-\gamma$ and $\omega \rightarrow e^+e^-\pi^0$ were subtracted. The shapes of $\omega \rightarrow e^+e^-$ (dotted) and $\rho \rightarrow e^+e^-$ (dash-dotted) were modified according to the model using the formula $m(\rho)/m(0) = 1-k(\rho/\rho_0)$ with $k = 0.092$.

ρ/ω ratios are 0.7 ± 0.1 and 0.9 ± 0.2 for the C and Cu targets, respectively. It is concluded that the observed modification can be understood with the model in which the masses of the ρ and ω mesons decrease by 9% at normal nuclear density. This value is consistent with the theoretical prediction.[2]

This work was partly funded by the RIKEN Special Postdoctoral Researchers Program. We thank the staff members of RIKEN Super Combined Cluster system and RIKEN-CCJ.

References

1) V. Blobel et al.: Phys. Lett. B **48**, 73 (1974).
2) T. Hatsuda and S. H. Lee: Phys. Rev. C **46**, R34 (1992).

† Condensed from the article in nucl-ex/0504016

* Department of Physics, Kyoto University

Nuclear mass number dependence of inclusive omega and phi meson productions in 12 GeV p-A collisions

T. Tabaru, H. En'yo, R. Muto, M. Naruki, F. Sakuma,* and S. Yokkaichi, for the KEK-PS E325 Collaboration

[Mass number dependence, vector meson]

The mass modification of mesons in nuclear matter has been studied recently. We, KEK-PS E325 experiment group, have reported that such modification has be seen in ρ^0/ω and ϕ meson productions in 12 GeV p+A collisions.[1–3] To understand such a phenomenon, basic measurements of meson production, such as the nuclear mass number dependence of production cross section, are important. In this article, we discuss the nuclear mass number dependence using the same data with which we observed the mass modification of mesons.

Introducing the parameter α representing the nuclear mass number dependence, the production cross section $\sigma(A)$ can be parameterized as $\sigma(A) = \sigma_0 A^\alpha$, for collisions of protons and nuclei with the mass number A. In the hadronic production of light mesons such as π and ρ mesons, the α parameter is about 2/3.[4,5] On the other hand, the α parameter is close to unity in hard reactions like J/ψ production.[5–7] The α parameter of ϕ mesons is measured as 0.81 to 0.96 at a collision energy $\sqrt{s_{NN}}$ of approximately 10 GeV.[8–10] In our experiment, ω and ϕ mesons were measured in medium-energy collisions of 12 GeV p+A ($\sqrt{s_{NN}} = 5.1$ GeV). At this collision energy, there has been no measurements of the α parameters of ω and ϕ mesons so far.

Our experiment was performed using the EP1-B beam line of the 12 GeV proton synchrotron in the High Energy Accelerator Research Organization (KEK). The proton beam was delivered onto carbon (C) and copper (Cu) targets, and the produced e^+e^- pairs were measured by our spectrometer covering the backward regions; the rapidity (y) range from 0.3 to 1.7 and transverse momentum (p_T) range below 1 GeV/c. The momenta of charged tracks were measured using cylindrical drift chambers in a magnetic field of 0.81 T·m. The electron ID was realized by the cascade operation of gas Čerenkov counters using isobutane and electromagnetic lead-glass calorimeters. The spectrometer acceptance was estimated by a GEANT4 simulation.

The measured invariant mass spectra were decomposed into correlated pairs from meson decays and uncorrelated pairs of combinatorial background. By breaking down the present spectra into these expected components, we obtained the yield of mesons in the region of $0.9 < y < 1.7$ and $p_T < 0.75$ GeV/c. Finally, the α parameter is obtained as shown in Fig. 1. The errors are statistical errors.

Although the mass difference between ω and ϕ mesons is small, we obtained it as the experimental result that the α parameter of ϕ meson production is larger than that of ω meson production. Similarly, the nuclear cascade simulation JAM[11] gives a larger α parameter for ϕ meson production than for ω meson production, as shown in Fig. 1. In the JAM calculation, the ω meson is produced from both primary and secondary reactions, while the ϕ meson is produced mainly from secondary reactions. This suggests that the difference in α parameters between ϕ and ω mesons is explained by the difference in the primary and secondary production ratio.

In the analysis, we have used CC-J and RSCC at RIKEN. We would like to thank the staff members of CC-J and RSCC for their support.

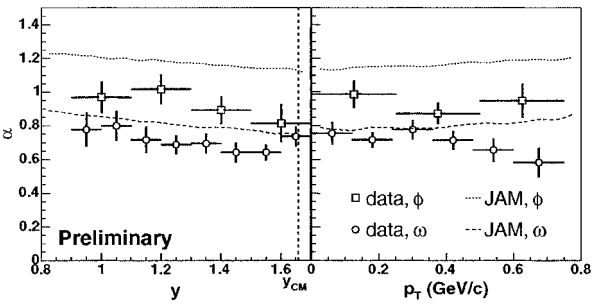

Fig. 1. α parameters of ϕ and ω mesons in present data (squares and circles) and JAM results (dotted and dashed lines).

References

1) K. Ozawa et al.: Phys. Rev. Lett. **86**, 5019 (2001).
2) M. Naruki et al.: nucl-ex/0504016.
3) R. Muto et al.: nucl-ex/0511019.
4) M. Ono et al.: Phys. Lett. B **84**, 515 (1979).
5) M. Binkley et al.: Phys. Rev. Lett. **37**, 571 (1976).
6) B. Alessandro et al.: Eur. Phys. J. C **33**, 31 (2004).
7) U. Husemann: Nucl. Phys. B **142**, 104 (2005).
8) C. Daum et al.: Z. Phys. C **18**, 1 (1983).
9) R. Bailey et al.: Z. Phys. C **24**, 111 (1984).
10) A. N. Aleev et al.: Czech. J. Phys. **42**, 11 (1992).
11) Y. Nara et al.: Phys. Rev. C **61**, 024901 (1999).

* Department of Physics, Kyoto University

Evidence for ϕ meson modification in nuclear medium†

R. Muto, H. En'yo, M. Naruki, F. Sakuma,* T. Tabaru, and S. Yokkaichi, for the KEK-PS E325 Collaboration

[QCD, chiral symmetry, normal nuclear density, mass modification, vector meson]

The KEK-PS E325 experiment was conducted at KEK Proton Synchrotron to detect possible in-medium modification of vector mesons. The invariant mass spectra of $\phi \to e^+e^-$ decays were measured in 12-GeV $p + A$ interactions. Data was obtained from 1997 to 2002. Copper and carbon targets were used to study the nuclear size dependence of e^+e^- invariant mass distributions.

We divided the data into three parts based on the $\beta\gamma$ values of the observed e^+e^- pairs, $\beta\gamma < 1.25$, $1.25 < \beta\gamma < 1.75$, and $1.75 < \beta\gamma$. We fitted each mass spectrum with a resonance shape of $\phi \to e^+e^-$ and a quadratic background curve (see Fig. 1). A significant excess over the expected mass spectrum on the low-mass side of the ϕ meson peak was observed in the lowest $\beta\gamma$ region of ϕ mesons ($\beta\gamma < 1.25$) with copper targets. However, in the middle- and high-$\beta\gamma$ regions ($\beta\gamma > 1.25$), the spectral shapes of ϕ mesons are well described by the Breit-Wigner shape when experimental effects such as multiple scattering and energy loss of particles, tracking performance with chamber resolution, and misalignment of tracking devices, are considered. This excess is considered to be the signal of the mass modification of the ϕ mesons in a target nucleus because the effect is visible only for slow ϕ mesons produced in a large target nucleus.

To evaluate the amount of excess N_{ex}, we repeated the same fit procedure to the spectrum except for the mass region where the excess was observed (from $0.95\,\mathrm{GeV}/c^2$ to $1.01\,\mathrm{GeV}/c^2$). We obtained N_{ex} as a yield of excess from the fit result. The ratio of excess to total ϕ yield, $N_{ex}/(N_{ex}+N_\phi)$, is plotted in Fig. 2. The excess is statistically significant for the copper target data in the lowest-$\beta\gamma$ bin, whereas it is marginal for the carbon target data.

We attempted to reproduce the $\beta\gamma$ dependence of the excess with a Monte-Carlo-type model calculation that includes the in-medium mass modification of the ϕ mesons based on the theoretical prediction.[1,2] We assumed the density dependence of the ϕ meson mass as $m_\phi(\rho)/m_\phi(0) = 1 - k(\rho/\rho_0)$, where ρ_0 is normal nuclear density.[1] To reproduce the large amount of excess in our data (29% for the lowest-$\beta\gamma$ bin for Cu), it is necessary to introduce a broadening of the total width of ϕ (Γ_ϕ), or at least of the partial width for $\phi \to e^+e^-$ decay ($\Gamma_{\phi\to ee}$). For the total width broadening, we adopted $\Gamma_\phi(\rho_0) \sim 47$ MeV/c^2 in accordance with Ref. 2. The density dependence of width $\Gamma_\phi(\rho)$ was assumed to be $\Gamma_\phi(\rho)/\Gamma_\phi(\rho_0) - 1 \propto \rho/\rho_0$ and the branching ratio $\Gamma_{\phi\to ee}/\Gamma_\phi$ remained unchanged in the medium. Figure 2 shows the $N_{ex}/(N_\phi + N_{ex})$ from the data and the model calculation with shift parameters k of 0.02 and 0.04. The tendency of the data is well reproduced by the model calculation with the shift parameter of $k = 0.04$.

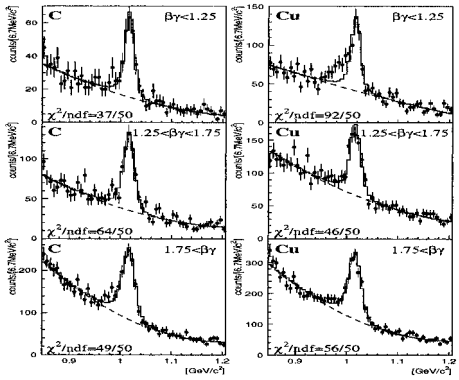

Fig. 1. Obtained e^+e^- distributions with fit results. Target and $\beta\gamma$ -region are shown in each panel. The points with error bars represent the data. The solid lines represent the fit results. The dotted lines represent the background curve.

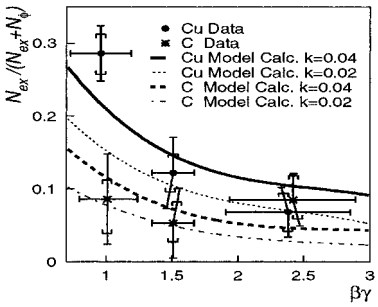

Fig. 2. $\beta\gamma$ dependence of $N_{ex}/(N_\phi + N_{ex})$ for both data and model calculation. The points represent the data and the lines represent the model calculation results.

In these analyses, we used the excellent cpu power of CC-J and RSCC at RIKEN.[3] We are grateful for the support from these computing facilities.

References

1) T. Hatsuda and S. H. Lee: Phys. Rev. C **45**, R34 (1992).
2) F. Klingl, T. Waas, and W. Weise: Phys. Lett. B **431**, 254 (1998).
3) S. Kametani et al.: RIKEN Accel. Prog. Rep. **39**, 224 (2006).

† Condensed from the article in nucl-ex/0511019

* Department of Physics, Kyoto University

Nuclear size dependence of ϕ meson production via e^+e^- and K^+K^- decay channel in 12 GeV p+A reaction at KEK-PS

F. Sakuma,* H. En'yo, M. Naruki, R. Muto, T. Tabaru, and S. Yokkaichi for KEK-PS E325 Collaboration

[Vector meson, in-medium modification, e^+e^-, K^+K^-]

In the experiment KEK-PS E325, we have measured e^+e^- and K^+K^- pairs produced in 12 GeV p+A reaction, in order to study the chiral property of dense nuclear matter through the analysis of invariant mass spectra. We have already reported the modification of ρ/ω meson spectra at normal nuclear matter density.[1,2] Moreover, we have recently observed the modification of the ϕ meson spectrum via the e^+e^- decay channel.[3] The simple toy model calculation in Ref. 3, it is assumed that the total and partial width change and the mass shift at normal nuclear matter density, reproduces the tendency of our data. The modification of the width of a ϕ meson is predicted as a consequence of modifications of kaon-nucleon interactions in a nuclear matter.[4] Therefore, the medium effect could be observed as a difference in partial width between $\phi \rightarrow e^+e^-(\Gamma_{\phi\rightarrow e^+e^-})$ and $\phi \rightarrow K^+K^-(\Gamma_{\phi\rightarrow K^+K^-})$. That is we could observe the difference in the nuclear size dependence of production cross section between the e^+e^- and the K^+K^- decay channel, because a larger modification is expected in a larger nucleus. We parametrize the nuclear size dependence of production cross section $\sigma(A)$ with α,

$$\sigma\,(A) = \sigma\,(A=1) \times A^{\alpha},$$

for the collisions between a proton and the nucleus with the mass number A. The difference in nuclear size dependence α is expected to be enhanced in slowly moving ϕ mesons that have a large probability of decay inside the nucleus. For example, if the ϕ meson is modified and $\Gamma_{\phi\rightarrow K^+K^-}/\Gamma_{\phi\rightarrow e^+e^-}$ increases in a nucleus, $N_{\phi\rightarrow K^+K^-}/N_{\phi\rightarrow e^+e^-}$ that we can observe becomes large, where N_ϕ is the number of ϕ mesons. Then, $\alpha_{\phi\rightarrow K^+K^-}$ should be larger than $\alpha_{\phi\rightarrow e^+e^-}$ in slowly moving ϕ mesons.

In the present article, we report the results of analysis of all the data taken in 2001/2002. In order to observe the nuclear size dependence, we accumulated data using two types of target, carbon and copper. A detailed description of the E325 spectrometer can be found elsewhere.[5] The detector acceptance is different between e^+e^- and K^+K^-, but there is an overlapping region.

To evaluate the yield of ϕ mesons, we fit mass spectra with the ϕ meson shape and the background shape. For the ϕ meson shape, we used the Breit-Wigner curve with a natural mass (1019.456 MeV/c^2) and decay width (4.26 MeV/c^2) convoluted over the detector response in Geant4 simulation[6] according to the kinematical distribution of ϕ mesons. The kinematical distribution of ϕ mesons was obtained by the nuclear cascade code JAM.[7] And for the background shape, we used the quadratic curve for e^+e^- and the event mixing method for K^+K^-.

The preliminary results for the α parameter obtained as functions of $\beta\gamma$ are plotted in Fig. 1. In this figure, $\alpha_{\phi\rightarrow K^+K^-}$ seems larger than $\alpha_{\phi\rightarrow e^+e^-}$ in the lower $\beta\gamma$ region. This suggests that $\Gamma_{\phi\rightarrow K^+K^-}/\Gamma_{\phi\rightarrow e^+e^-}$ is increased by the modification of the ϕ meson and kaon at normal nuclear matter density, as discussed above.

To expedite the analysis, we have used CC-J and RSCC at RIKEN. We would like to thank the staff members of CC-J and RSCC for support.

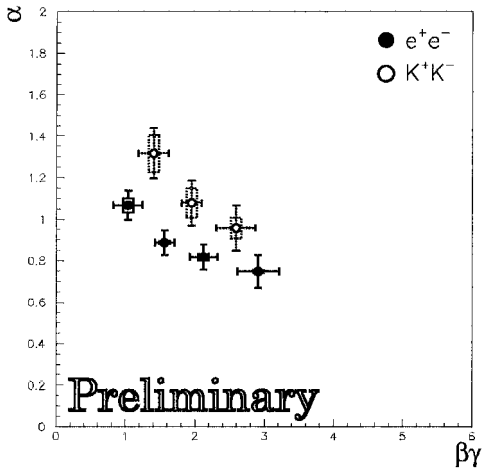

Fig. 1. Preliminary results for α parameter of $\phi \rightarrow e^+e^-$(closed circle) and $\phi \rightarrow K^+K^-$(open circle) shown as functions of $\beta\gamma$.

References

1) K. Ozawa et al.: Phys. Rev. Lett. **86**, 5019 (2001).
2) M. Naruki et al.: nucl-ex/0504016
3) R. Muto et al.: nucl-ex/0511019
4) F. Klingl, T. Waas, and W. Weise: Phys. Lett. B **431**, 254 (1998).
5) M. Sekimoto et al.: Nucl. Instrum. Methods Phys. Res. A **516**, 390 (2004).
6) http://geant4.web.cern.ch/geant4/
7) Y. Nara et al.: Phys. Rev. C **61**, 024901 (1999).

* Department of Physics, Kyoto University

Muon catalyzed fusion in non-equilibrium D_2+T_2 mixtures

K. Ishida, T. Matsuzaki, Y. Matsuda, M. Iwasaki, K. Nagamine,[*1] N. Kawamura,[*2] H. Imao,[*3] S. N. Nakamura,[*4] M. Kato,[*5] H. Sugai,[*5] A. Uritani,[*6] H. Harano,[*6] T. Matsumoto,[*6] and G. H. Eaton[*7]

[Muon, fusion, deuterium, tritium]

In muon catalyzed fusion (μCF) cycle, muonic molecule formation has to occur rapidly for a muon to catalyze many fusions during its lifetime (2.2 μs). It is considered that $dt\mu$ formation proceeds as follows, $(t\mu)_F + (\mathrm{DX})_{K_i\nu_i} \rightarrow [(dt\mu)xee]_{K_f\nu_f}$ ($x = d, t, \mathrm{X} = \mathrm{D}, \mathrm{T}$), where F is the hyperfine state and $K_i\nu_i$ and $K_f\nu_f$ are the rotational and vibrational states, respectively. Here, the sum of the initial kinetic energy and the energy released by $dt\mu$ formation is resonantly absorbed by the excitation ($K_f\nu_f$) of the final compound molecule, therefore, the formation rate is significantly enhanced compared with the rate by non-resonant (Auger) formation only. Theoretical calculations such as the temperature dependence of the formation rate are generally consistent with results for gas phase, but predict too small rates for liquids and solids. Thus, further investigation is necessary for a complete understanding of this phenomena.

In a previous measurement done at RIKEN-RAL Muon Facility, we have shown that dtμ formation rate with D_2 is significantly higher than that with DT.[1)] Because the resonance condition is also dependent on the rotational levels of the D_2 molecule, an experiment which varies the ortho- (rotational states $K_i = 0, 2, \ldots$) to para-D_2 ($K_i = 1, 3, \ldots$) composition ratio of the target will provide valuable additional inputs to the development of the theory.

Such a measurement was successfuly done first for ddμ formation in pure D_2 by our group.[2)] We have observed that the ddμ formation rates in ortho-rich liquid and solid D_2 decrease by about 30 % compared with those in normal D_2. It is predicted that the effect will be much more enhanced for dtμ formation because the dtμ molecule has a much shallower bound state and the resonance condition can be more sensitive to the initial molecular states. Several calculations suggest that dtμ formation rate with para-D_2 is much higher than that with ortho-D_2.

To test this prediction, we have recently carried out μCF measurements comparing ortho-rich D_2 and normal-D_2. Ortho-D_2 was selected primarily because it is more easily produced than para-D_2. Figure 1 shows the measured μCF cycling rate in each hour after D_2 (50%) and T_2 (50%) mixing. When we mix D_2 and T_2, an equilibrium state is gradually reached due to the reaction $D_2 + T_2 \rightleftharpoons 2DT$. Data were taken for the liquid state up to 96 h in the previous run with normal-D_2 (filled circles in Fig. 1) and up to 75 h in the new run with ortho-D_2 (open circles). In both cases, the target D/T gas was then warmed up to room temperature to accelerate the equilibration and was liquefied again to obtain data with a fully equilibrated target (filled and open squares).

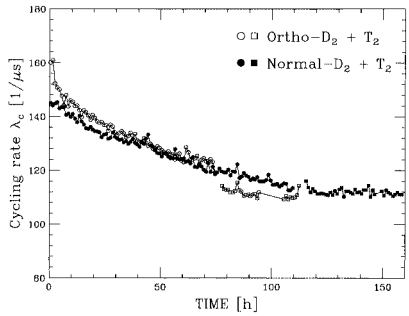

Fig. 1. μCF cycling rate as function of time after D_2 and T_2 mixing. Cases using normal-D_2 and ortho-D_2 are compared.

It can be observed that the cycling rate was enhanced by 30% in the non-equilibrium state just after D_2+T_2 mixing. The result is well explained by taking account of the higher resonant formation rate with D_2 and the equilibration process with a time constant of 56 h.

Concerning the ortho-para effect, the difference between the two conditions was not as large as expected. Two distinguished data points at the beginning of the ortho-D_2 data were actually the result of an accidentally introduced impurity.

We are not yet sure why the difference between normal-D_2 and ortho-D_2 was very small. It could be that the conversion of ortho-D_2 to normal-D_2 has occurred in less than two hours due to the presence of radioactive tritium. Another possibility is that the difference in dtμ formation rate is unexpectedly small. We plan to develop a method for *in-situ* gas analysis to distinguish between these possibilities.

*1 Physics Department, University of California, USA
*2 Muon Science Laboratory, High Energy Accelerator Research Organization (KEK)
*3 Department of Physics, University of Tokyo
*4 Department of Physics, Tohoku University
*5 Department of Radioisotopes, Japan Atomic Energy Agency
*6 Quantum Radiation Division, National Institute of Advanced Industrial Science and Technology
*7 ISIS, Rutherford Appleton Laboratory, UK

References

1) K. Ishida et al.: RIKEN Accel. Prog. Rep. **35**, 39 (2002).
2) H. Imao et al.: Phys. Lett. B **632**, 192 (2006).

Measurement of Doppler broadening width of K_α X-rays from $\mu^-\alpha$ atoms formed in muon sticking process of muon catalyzed t-t fusion

T. Matsuzaki, K. Ishida, N. Kawamura,[*1] H. Imao,[*1,*2] Y. Matsuda, M. Iwasaki, S. N. Nakamura,[*3] M. Kato,[*4] H. Sugai,[*4] G. H. Eaton,[*5] and K. Nagamine[*6]

[Muon catalyzed t-t fusion, muonic K_α X-rays, Doppler broadening width, particle correlations]

The muon catalyzed t-t fusion (t-t μCF) process proceeds spontaneously by stopping negative muons in a tritium (T_2) target. $t\mu^-$ atoms are formed by muons being bound to triton nuclei (t), and then collide with T_2 molecules without receiving any Coulomb repulsive force to form $tt\mu^-$ molecules. The t+t fusion reactions occur in the framework of $tt\mu^-$ molecules, and induce three-particle decays of an α-particle and two neutrons. After the fusion reaction, the muon is liberated and participates again in the next t-t μCF process. The t-t μCF process is described in Eq. (1), where the muon is 9-fold lighter than a proton or 207-fold heavier than an electron.

$$\begin{aligned} t + t + \mu^- &\rightarrow tt\mu^- \\ &\rightarrow \alpha + n + n + \mu^- + Q(11.33\,\mathrm{MeV}) \quad (1) \\ &\rightarrow \mu\alpha + n + n + Q \quad (2) \end{aligned}$$

This t+t reaction is very unique from the viewpoint of nuclear reaction mechanism, because the t+t system is formed in the $tt\mu^-$ molecule with a molecular binding energy, and decays to three particles. Therefore, the t+t reaction mechanism can be studied by observing the behavior of outgoing particles: two fusion neutrons and an α-particle.

With some probability, the liberated muon is captured by the α-particle to terminate the t-t μCF cycle described in Eq. (2); this phenomenon called muon sticking. In this process, the $\mu^-\alpha$ atom recoils in the target medium at a given kinetic energy by the reaction mechanism at the exit channel. In addition, characteristic muonic X-rays are emitted from the recoiling $\mu^-\alpha$ atoms; thereby, the observed X-ray lines show Doppler broadening which reflects the velocity distribution of $\mu^-\alpha$ atoms effective for the observation direction. By measuring the Doppler broadening width, we can determine the mean value in the velocity distribution of $\mu^-\alpha$ atoms, and obtain information on the mean kinetic energy of $\mu^-\alpha$ atoms, which is deeply dependent on the mechanism of three-particle decay at the exit channel.

*1 Meson Science Laboratory, High Energy Accelerator Research Organization
*2 Faculty of Science, University of Tokyo
*3 Department of Physics, Tohoku University
*4 Japan Atomic Energy Research Institute
*5 ISIS, Rutherford Appleton Laboratory, UK
*6 Physics Department, University of California, USA

We conducted X-ray measurements associated with the t-t μCF process using high-purity solid and liquid T_2 targets at the RIKEN-RAL Muon Facility.[1,2] We observed K_α X-rays originating from muonic helium atoms ($\mu^-\alpha$) formed by the muon sticking process,[3,4] and determined Doppler broadening widths ($\Delta E_\gamma = 0.147 +/- 0.014$ keV for the solid target and $0.138 +/- 0.029$ keV for the liquid target). Then, we obtained the mean total kinetic energies of $\mu\alpha^-$ atoms, ($E_{kin} = 1.9 +/- 0.4$ MeV for the solid target and $1.7 +/- 0.7$ MeV for the liquid target) and compared these energies with the calculated kinetic energies of α-particles assuming three limiting cases, namely, no particle correlations, n-n correlations and n-α correlations at the exit channel of t+t reactions. It was consequently shown that the obtained E_{kin} values were well in agreement with the kinetic energies calculated by reaction kinetics assuming either strong n-α particle correlations (sequential neutron decay through ^{5}He resonance states) or no particle correlations. The former case gave a continuous energy distribution from zero to a maximum of 3.8 MeV with a mean energy of 1.9 MeV, and the latter case gave the kinetic energies of 1.6–1.9 MeV through the $p_{3/2}$ resonance and 0.1–2.1 MeV through the $p_{1/2}$ resonance. On the other hand, the obtained E_{kin} values excluded clearly a possibility of n-n correlations because the calculation gave a monochromatic kinetic energy of 3.8 MeV. The measured t-t fusion neutrons in the previous work[5] showed a continuous energy spectrum with a maximum energy of 9 MeV, the shape of which was reasonably well reproduced by a simple model assuming n-α particle correlations. By combining the present results and the previous conclusion, it is most probable that strong n-α correlations are dominate in the three-particle decay at the exit channel of t+t reactions.

References

1) T. Matsuzaki et al.: Nucl. Instrum. Methods Phys. Res. A **465**, 365 (2001).
2) T. Matsuzaki et al.: Nucl. Instrum. Methods Phys. Res. A **480**, 812 (2002).
3) T. Matsuzaki et al.: Phys. Lett. B **465**, 74 (1999).
4) T. Matsuzaki et al.: RIKEN Accel. Prog. Rep. **38**, 75 (2004).
5) T. Matsuzaki et al.: Phys. Lett. B **527**, 43 (2002).

Dimuon measurement in Indium-Indium collisions at CERN/SPS

H. Ohnishi

[Heavy-ion collisions, quark-gluon plasma, charm quark]

Under normal conditions, elementary particles, quarks and gluons, are confined inside a hadron according to Quark Chromodynamics (QCD) which describes the dynamics of elementary particles. However, QCD also predicts that under extreme conditions, such as high temperature and/or high density, quarks and gluons will not be confined in hadrons. These conditions are expected at just after the big bang or in the core of the neutron star. This new state of matter, which consists of many body systems of quark-gluon, is called Quark-Gluon Plasma (QGP).

The use of high-energy heavy-ion collisions is one of the possible ways of creating nuclear matter with high energy density. Normal nuclear matter may then undergo a phase transition to a QGP. The previously observed J/ψ suppression[1] pattern in high-energy heavy-ion collisions at CERN-SPS seems to provide the first signal of color deconfinement. Simultaneously, an enhancement of dimuons in the Intermediate Mass Region (IMR, $1.5 < M_{\mu\mu} < 2.5\,\mathrm{GeV}$) is observed,[2] with the main contributions expected to be from the decays of charm mesons and dimuons from Drell-Yan processes. However, there have been no indications that this color condensate subsequently leads to a medium in thermal equilibrium, such as the QGP.

One of the relevant issues that the NA60 experiment intends to address is the origin of the enhancement of IMR dimuons. Two hypotheses are proposed: the enhancement of charm meson production in heavy-ion collisions, and thermal dimuon production from the created medium, which is a direct evidence of QGP formation. To clarify this issue, we must be able to isolate the considerable yield of dimuons coming from the decays of charm mesons. Due to the long life time of charm mesons, the origin of muons coming from charm meson decays will be offset from the primary vertex. Therefore, we need to perform secondary vertex measurements that provide approximately $50\,\mu$m resolution. To achieve the above requirement, the vertex telescope (VERTEL) is installed just after the target to track all produced particles with high precision. The VERTEL consists of a 16-plane tracking telescope in a 2.5 T magnetic field, built from radiation tolerant silicon pixel detectors developed for the ALICE experiment at CERN-LHC. The performance of the VERTEL was seriously investigated and the track offset resolution of the muon was achieved around $50\,\mu$m.

The experimental data of offset distribution taking into account the error for the tracking in the VERTEL (weighted offset) are shown in Fig. 1. Note that data are the same for the left and right figures. This distribution is then fitted with a superposition of the expected weighted offset distributions for prompt and charm meson decay contributions. The shape of the prompt sample contribution is evaluated with the measured J/ψ and ϕ offset distributions. On the other hand, the shape of the offset distribution produced by Monte-Carlo simulation is used for the charm meson decay contribution.

The left figure in Fig. 1 shows the results of the fit with the prompt contribution normalized to the expected Drell-Yan yield and the charm meson decay contribution left free. The fit result indicates that the expected distribution with this parameterization is too flat to describe the data. As a next step, we try to fit the data with the normalizations of both prompt and charm meson decay contributions as free parameters. The result is shown in the right figure of Fig. 1. This result is in good agreement with the data with a charm meson decay contribution compatible with the expected results, but requires two times more prompt contribution from the expected prompt yield. This result indicates that 1) there is an excess in IMR dimuons and 2) the source of the excess is due to the enhancement in the prompt dimuon. However, enhancement of the Drell-Yan yield is not observed.[3] Therefore, these results indicate that the source of the IMR dimuon enhancement is not from known sources such as the Drell-Yan or charm meson decay but rather from unknown sources such as a signal from thermal dimuons which is expected as a direct signal from QGP. The detailed evaluation of systematic uncertainty is in progress.

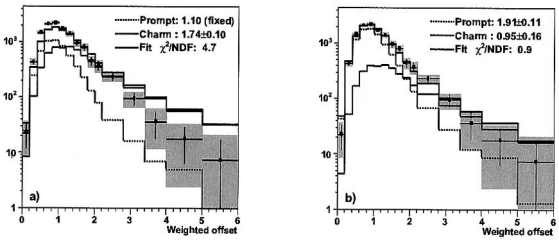

Fig. 1. Fit results of IMR dimuon weighted offset spectrum (left) with normalization of charm meson decay contribution as free parameter and (right) with normalization of charm meson decay and prompt contributions as free parameters.

References

1) M. C. Abreu et al.: Eur. Phys. J. C **39**, 335 (2005).
2) M. C. Abreu et al.: Eur. Phys. J. C **14**, 443 (2000).
3) R. Arnaldi et al.: Proc. Quark Matter 2005, Budapest, Hungary, 2005-8, to be published.

Eigenvalues of the time-delay matrix in overlapping resonances

I. Shimamura, J. F. McCann,[*1] and A. Igarashi[*2]

A scattering resonance is associated with rapid increase in the phase shift $\delta(E)$ with the scattering energy E. For an isolated resonance with a single open channel, $\delta(E)$ may be parameterized by the resonance position E_1 and width Γ_1 by the Breit-Wigner formula

$$\tan[\delta(E) - \delta_{\rm b}(E)] = -(\Gamma_1/2)(E - E_1), \qquad (1)$$

where the background phase shift $\delta_{\rm b}(E)$ varies slowly with E. A calculated phase shift may be fitted to (1) to obtain the parameters E_1 and Γ_1 as well as $\delta_{\rm b}(E)$.

When N (>1) open channels are coupled to a resonance, the N-by-N S matrix, which is an extension of the single-channel formula $S(E) \equiv \exp(2i\delta)$, shows rapid variation with E. This variation is parametrized not only by E_1 and Γ_1 but also by partial widths Γ_{1i} $(i = 1, \cdots, N)$ representing the decay into channels i, as well as the background S matrix, $S_{\rm b}(E)$.

Parameterization of the S matrix seems impractical when many channels, i.e., many fitting parameters $\{\Gamma_{1i}\}$ and E_1, are involved. However, Eq. (1) still applies to multichannel cases if Γ_1 is understood as the total width $\sum_i \Gamma_{1i}$ and if $\delta(E)$ and $\delta_{\rm b}(E)$ are taken to be the sum of the eigenphases $\delta_i(E)$ and the sum of the background eigenphases $\delta_{{\rm b},i}(E)$;[1)] $\delta_i(E)$ are defined by writing the diagonal elements of the diagonalized S matrix as $\exp(2i\delta_i)$, and $\delta_{{\rm b},i}(E)$ similarly defined by using $S_{\rm b}(E)$. This result is quite convenient for multichannel resonance analysis by parameter fitting.

Smith[2)] defined another useful matrix, the lifetime (or time-delay) matrix $Q(E)$, as an extension of the time delay in single-channel scattering.[3)] He proved that $Q(E) = i\hbar S(dS^\dagger/dE)$, where $S^\dagger$ is the Hermitian conjugate of S. The diagonal elements Q_{ii} have the physical meaning of the average time delay, over all exit channels, starting from the initial channel i.

The diagonal sum or the trace of the time-delay matrix, $\mathrm{Tr}\, Q$, is related to the eigenphase sum $\delta(E)$ by

$$2\hbar(d\delta/dE) = \mathrm{Tr}\, Q(E) \qquad (2)$$

if Eq. (1) is valid. In fact, Eq. (2) is a very general theorem valid for the $S(E)$ matrix or the eigenphase sum $\delta(E)$ of *any* form, as we proved recently.[4)]

In this work, we study the properties of $Q(E)$ and $\delta(E)$ for multichannel overlapping resonances at energies E_ν with widths Γ_ν. We prove the relation

$$\mathrm{Tr}\, Q(E) = \sum G_\nu(E) + 2\hbar(d\delta_{\rm b}/dE), \qquad (3)$$

where $G_\nu(E) = (\hbar\Gamma_\nu)/[(E - E_\nu)^2 + (\Gamma_\nu/2)^2]$. The equivalent integral form of the relation is

$$\delta(E) = -\sum \arctan[(\Gamma_\nu/2)/(E - E_\nu)] + \delta_{\rm b}(E). \qquad (4)$$

These results are quite useful in the analysis of overlapping resonances by parameter fitting.

For an overlapping double-resonance with a slowly varying background, all eigenvalues $q_i(E)$ of $Q(E)$ are nearly zero, except for two, which take a form

$$q_\pm \equiv (G_1 + G_2)/2 \pm [(G_1 - G_2)^2 + 4\beta G_1 G_2]^{1/2}/2, \qquad (5)$$

where β $(0 \le \beta \le 1)$ represents the strength of the interaction between the two overlapping resonances. Equation (5) shows a typical avoided crossing between two Lorentzian profiles. The two limiting cases of (5) are

$$\beta \to 0: \quad q_\pm \to G_i(E), \quad i = 1, 2,$$

where the two Lorentzians appear independently, and

$$\beta \to 1: \quad q_+ \to G_1(E) + G_2(E), \quad q_- \to 0,$$

where q_+ is the mere sum of the two Lorentzians.

We show an example of Ps^- consisting of an electron e^- and a positronium Ps, an electron-positron system (Fig. 1). Multichannel continuum states were calculated from hyperspherical coupled-channel (HSCC) equations; see Ref. 5 for detail. The two extreme overlapping cases are seen: (a) Strong avoidance for the symmetry $^1\mathrm{P^o}$ just below the threshold $E_{\rm th} = -0.0278$ a.u. for the breakup into $\mathrm{e}^- + \mathrm{Ps}(n{=}3)$ and (b) weak avoidance for symmetry $^1\mathrm{D^e}$ just above $E_{\rm th}$.

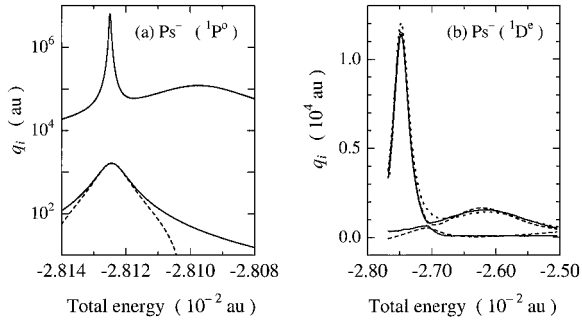

Fig. 1. Two largest eigenvalues q_i of $Q(E)$ for Ps^-. Solid curves: HSCC. Broken curves: fitting of Eq. (5). (a) $^1\mathrm{P^o}$. $\beta = 0.95$. The curve for q_1 is indistinguishable from the solid curve. (b) $^1\mathrm{D^e}$. $\beta = 0.10$.

*1 Department of Applied Mathematics and Theoretical Physics, Queen's University Belfast, UK
*2 Department of Applied Physics, Miyazaki University

References
1) A. U. Hazi: Phys. Rev. A **19**, 920 (1979).
2) F. T. Smith: Phys. Rev. **118**, 349 (1960).
3) E. P. Wigner: Phys. Rev. **98**, 145 (1955).
4) A. Igarashi and I. Shimamura: Phys. Rev. A **70**, 012706 (2004).
5) A. Igarashi, I. Shimamura, and N. Toshima: New J. Phys. **2**, 17 (2000); A. Igarashi and I. Shimamura: J. Phys. B **37**, 4221 (2004).

Measurement of resonant coherent excitation for channeling Li-like Fe ions using silicon surface barrier detector target

Y. Nakai, T. Ikeda, Y. Kanai, T. Kambara, N. Fukunishi, Y. Nakano,[*1] C. Kondo,[*2] T. Azuma,[*1] K. Komaki,[*2] and Y. Yamazaki[*2]

When the energy difference between two electronic states of an ion channeling through a crystal matches with one of the frequencies of the periodic crystal field, the ion is resonant-coherently excited. This excitation is referred to as "resonant coherent excitation (RCE)." Many RCE experiments have been performed to date. Nevertheless, we have recently observed RCE phenomena of an outer shell electron of systems with three or more electrons for the first time to our best knowledge using 83 MeV/u Fe^{23+} ions.[1)] In the observation of the 2s electron RCE to the $n = 3$ states, it was found that the RCE corresponding to optically forbidden transitions can be seen as well as optically allowed transitions, where the transitions to the $3s_{1/2}$, $3d_{3/2}$ and $3d_{5/2}$ states are optically forbidden and the transitions to the $3p_{1/2}$ and $3p_{3/2}$ states are optically allowed.

We have been considering two possible reasons for the observation of the optically forbidden transitions as well as optically allowed transitions. (1) The transitions from the $2s$ state to the $3s$ and $3d$ states are caused by transitions *via* the $3p$ component in the Stark-mixed $3s$ and $3d$ states. (2) Pure optically forbidden transitions with a large momentum transfer have to be considered. These effects are very small or zero at the channeling center. However, these two effects become more important with increasing distance from the channel center.

To obtain information on the distance where the transitions to the $3s$ and $3d$ states occur, we used a silicon surface barrier detector (SSD) target. This method has already been used for RCE measurement of 390 MeV/u hydrogen-like Ar ions.[2)] The energy deposit to the target crystal from channeling ions strongly depends on their oscillating orbits. The energy deposit increases with the amplitude of the oscillating orbit. Therefore, coincidence measurement between the final charge states of Fe ions and the energy deposit in the SSD gives information on the distance where the transitions to the $3s$ and $3d$ states occur.

An SSD target of approximately 10 μm thickness was vertically mounted so that the beam direction was near the [001] axis of the silicon crystal. The ions emerging from the SSD were deflected by an analyzing magnet located downstream of the SSD target to separate the final charge states. A two-dimensional position-sensitive detector (2D-PSD) was located 8 m downstream of the analyzing magnet, which detected Li-like, He-like, H-like and bare ions.

The fraction of Li-like ions ionized solely through RCE, $p(\theta, \Delta E) = 1 - f(\theta, \Delta E)/f_{\text{non-res}}(\Delta E)$,[2)] is shown in Fig. 1 as a function of θ and ΔE, where θ is the rotation angle from the [001] axis and ΔE is the energy deposit in the SSD target. $f(\theta, \Delta E)$ is the survival fraction of Li-like ions for each θ and ΔE.

$$f = N(\text{Li-like})/[N(\text{Li-like}) + N(\text{He-like}) + N(\text{H-like}) + N(\text{bare})]$$

Here, N is the number of Li-like, He-like, H-like and bare ions emerging from the SSD. $f_{\text{non-res}}(\Delta E)$ is the average survival fraction of Li-like ions in the off-resonance region.

In the low ΔE region, i.e., near the channeling center, only optically allowed transitions, $2s$-$3p$, have a large $p(\theta, \Delta E)$. Increasing ΔE, i.e., increasing the distance from the channel center (increasing the amplitude of the oscillating orbit), the $p(\theta, \Delta E)$ of the optically forbidden $2s$-$3s$ transition rapidly increases. On the other hand, those of the optically forbidden $2s$-$3d$ transitions do not increase so rapidly.

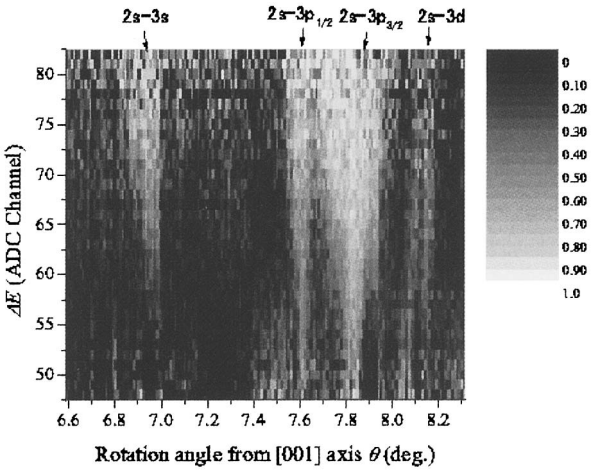

Fig. 1. Fraction of Li-like ions ionized solely through RCE, $p(\theta, \Delta E)$.

References

1) Y. Nakai et al.: Nucl. Instrum. Methods Phys. Res. B **230**, 784 (2005).
2) T. Azuma et al.: Phys. Rev. Lett. **83**, 528 (1999).

*1 Department of Physics, Tokyo Metropolitan University
*2 Institute of Physics, University of Tokyo

Ni-ion-induced charge collection measurements of SiC Schottky barrier diode

C. Kamezawa,[*1] Y. Satoh,[*1] N. Ikeda,[*1] S. Kuboyama,[*1] O. Shimada,[*2] H. Otomo,[*2] H. Ohira,[*2] N. Inabe, and M. Kase

Silicon carbide (SiC) is one of the candidates for the next-generation semiconductor materials. SiC devices can be possibly operated under harsh environments such as at very high temperature and in strong electric fields, as compared with Si devices.

In electronic devices, there are two types of radiation damage for semiconductors: one is caused by atomic displacement, and the other by ionization. However, SiC devices are inherently resistant to radiation effects, because the charge generated by radiations is small.

Most particular and well known among the above damages is the destructive breakdown of semiconductor devices, called single-event burnout (SEB). For space applications, there is a need to prevent the occurrence of SEB, which is caused by high-energy particles of different types and energies in space.

The SEB for Si devices is essentially triggered by a plasma column along the incident ion track in the depletion layer, e.g., epitaxial layer in a unipolar device, where plasma density is calculated from the electron-hole pair generation energy and linear energy transfer (LET) of the incident particle. However, the correlation between the energy loss of high-energy particles and damage in SiC materials remains unclear. In this work, we have performed a charge collection measurement of an Ni-ion strike to understand its physical mechanism for future space applications of SiC devices.

The SiC Schottky barrier diode used in this work as a simple SiC device was the commercially available Infineon SDP06S60, which has an epitaxial layer of $\sim$6 μm. The properties of irradiated Ni ions are shown in Table 1. The Ni ion has a sufficient projection range to pass through the active region of the sample device, provided the mold material on the chip surface is removed and irradiation is performed with a normal incidence from the Schottky contact surface to substrate.

Figure 1 shows the schematic diagram of the irradiation system for SiC-Schottky barrier diodes. The electron-hole pairs generated by incident Ni ions were collected by adjusting applied bias voltage. To investigate the behavior of the generated charges, a charge-sensitive preamplifier, the ORTEC 142B, was used to measure charge collection spectra.

Figure 2 shows the collected charge spectra of a sample as a function of reverse bias voltage. Here, the peak of the collected charge is shifted with an increase in bias voltage and an anomalously large charge collection with an excess charge collection efficiency of 100% is observed at a higher bias voltage.

To clarify the mechanism of the anomalously large charge collection, the charge at the peak of each spectrum was taken at room temperature and 70°C, as shown in Fig. 3. In this figure, the charge collection was suppressed by a temperature increase at higher voltages, although it was larger at lower voltages. This result suggests that the anomalously large charge is basically produced by an electron avalanche in the Schottky barrier, because the temperature increase reduces carrier mobility, which is sensitive to the yield of electron-hole pairs generated in the barrier.

Table 1. Property of Ni ion used in this study. LET and range derived using software of SRIM 2003.

Ion	Energy [MeV]	LET [MeV/mg·cm^{-2}]	Range [μm]
$^{58}Ni^{19+}$	366.3	2.64	40.71

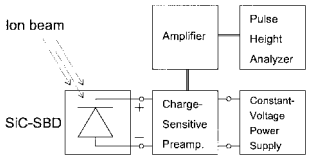

Fig. 1. Schematic diagram of irradiation and measurement system.

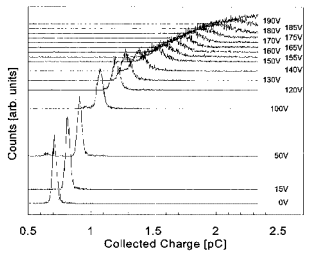

Fig. 2. Charge collection spectra obtained by Ni ion irradiation as function of reverse bias voltage.

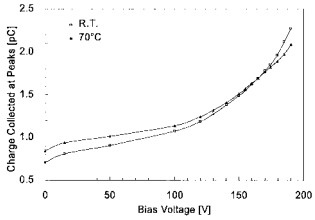

Fig. 3. Charges collected at peak of each spectrum at room temperature and 70°C.

*1 Institute of Aerospace Technology, Japan Aerospace Exploration Agency
*2 Ryoei Technica Corporation

Elastic waves from swift heavy-ion irradiations on solids

T. Kambara, K. Kageyama,* Y. Kanai, T. M. Kojima, Y. Nakai, A. Yoneda, and Y. Yamazaki

We have studied sound waves generated by fast heavy-ion irradiations on solid samples at the RIKEN Ring Cyclotron.[1–3] Samples of various solids have been irradiated with short-pulse beams of 3.8-GeV Ar ions and 3.54-GeV Xe ions and sound waves at ultrasonic frequencies have been observed on the surface at different directions from the beam spot. The angular dependence of the sound waveform, called radiation pattern, reflects the mechanical motion of the matter at the sound source, where stress and strain are generated by energy deposition from the ions.

We have observed marked differences in radiation patterns between the Ar and Xe irradiations on the same material. The waveforms from the Ar-ion irradiation are almost independent of the sound-wave direction, and contain only an isotropic compressional wave (P wave) generated at the end of the ion range. On the other hand, the 3.54-GeV Xe-ion irradiation generates more complicated waveforms, which are strongly dependent on the sound-wave direction and contain a shear wave (S wave) in addition to the P wave. The difference in waveforms between the Xe and Ar ions can be described as the difference of the mechanical boundary condition of the sound source due to different ion ranges in materials.

The purpose of the present experiment was to study the extent of the sound source through the dependence of the waveform on the ion-penetration depth. The experimental setup was almost the same as that reported previously.[1] An Ar beam was modulated to single bunches at a rate of 109 Hz, each of which was approximately 3-ns long and contained ions in the order of 10^3. The sample was a 10-mm-thick, 40 mm × 40 mm plate of polycrystalline aluminum. Sound signals were detected with a piezoelectric sensor attached to the sample at the center of the back side of the beam spot. The sample and sensor were mounted on a remote-controlled movable feedthrough so that different points on the sample were irradiated. The beam energy on the sample was adjusted with a degrader which was a 3- or 4-mm thick aluminum plate inserted in front of the sample.

Figure 1 shows sound waveforms from irradiation with 3.8-GeV Ar ions (a) without a degrader, (b) with the 3-mm-thick degrader, and (c) with the 4-mm-thick degrader. According to the TRIM code,[4] the range of 3.8-GeV Ar ions in Al is estimated to be 4.24 mm, so that the actual ranges in the sample are (a) 4.24 mm, (b) 1.24 mm and (c) 0.24 mm, respectively. For comparison, Fig. 1 (d) shows a waveform from the same sample irradiated with 3.54-GeV Xe ions without a degrader where the estimated ion range is 0.29 mm. The waveforms are averaged over up to 50 shots of ion bunches and normalized to 1000 ions. The graphs also show beam-bunch patterns observed with a secondary-electron monitor, and the origin of the time is set to the arrival of the beam bunch. The distances of the sensor relative to the epicenter are indicated on the right side of the graphs. The solid and dashed lines show the estimated arrival times of the direct P and S waves, assuming the sound source at the end of the ion range calculated with the TRIM code.

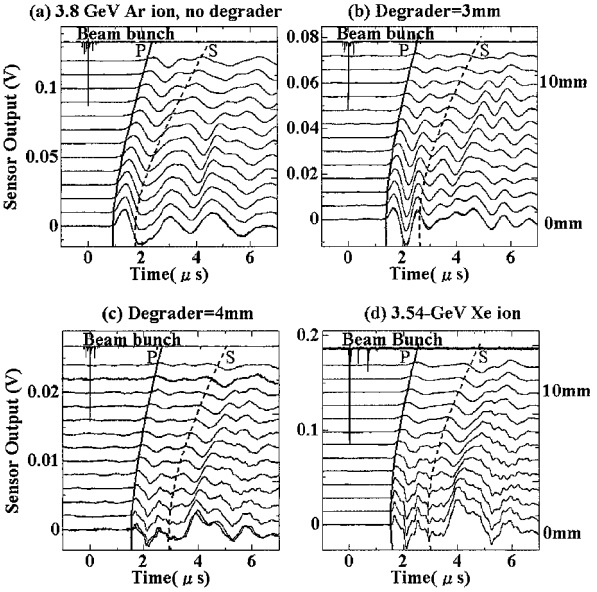

Fig. 1. Sound waveforms from Al irradiated with 3.8-GeV Ar ions with degrader thicknesses of (a) 0 mm, (b) 3 mm and (c) 4 mm, and (d) 3.54-GeV Xe ions without a degrader. On the right side are the distances between the sensor and the epicenter.

The radiation patterns of the Ar irradiation in Fig. 1 (a-c) apparently depend on the length of the ion range, and that with the shortest ion range (c) resembles that of the Xe irradiation (d) with a structure along the expected arrival time of the S wave.

References

1) T. Kambara, K. Kageyama, Y. Kanai, T. M. Kojima, Y. Nakai, A. Yoneda, and Y. Yamazaki: Nucl. Instrum. Methods Phys. Res. B **193**, 371 (2002).
2) T. Kambara: Nucl. Instrum. Methods Phys. Res. B **230**, 601 (2005).
3) T. Kambara: Nucl. Instrum. Methods Phys. Res. B **245**, 108 (2006).
4) J. F. Ziegler, J. P. Biersack, and U. Littmark: *The Stopping and Range of Ions in Solids* (Pergamon Press, New York, 1985).

* Department of Mechanical Engineering, Saitama University

Synthesis of Au nanoparticles by GeV-ion irradiation

N. Maeda,* F. Hori,* T. Kambara, T. Abe, and A. Iwase*

As metallic nanoparticles have some specific characteristics which are not observed in bulk metallic materials, they have been applied for various uses in some industrial fields. It is well known that γ-ray irradiation can reduce metallic ions in aqueous solutions and has been used for the synthesis of metallic nanoparticles[1]. However, electron or energetic ion irradiation has hardly been used for metallic nanoparticle synthesis. In this study, we have produced Au particles by irradiating aqueous solutions with swift heavy ions.

Samples used in the present experiment were dilute aqueous solutions with 0.5 m mol/l Au ions and 0.4 m mol/l Polyethylene Glycol Monostearate as surfactants. $NaAuCl_4 2H_2O$ was chosen as a precursor of Au^{3+} ions. Irradiation was performed at E5B beam line of the RIKEN ring cyclotron accelerator. The samples were irradiated with 1.6 GeV full-stripped C ions. The dose rate was approximately 2 Gy/sec and the absorption doses were 300, 600, 900 and 1200 Gy.

After C-ion irradiation, the optical absorption spectra of each solution were measured using an ultraviolet-visible spectrophotometer (UV-vis). Then, nanoparticles produced by the irradiation were directly observed by a transmission electron microscope (TEM) to determine their shapes and sizes.

Figure 1 shows the results of UV-vis measurements for irradiated samples. Large peaks appear at around 530 nm. These peaks correspond to the absorption by surface plasmon of the produced Au nanoparticles. The appearance and growth of the peak indicate that C-ion irradiation reduces Au^{3+} ions in the aqueous solution and produces Au nanoparticles. Figure 2 shows the TEM images of Au particles produced by C-ion irradiation. Figure 3 shows the size histogram of Au nanoparticles. The mean diameter value is approximately 20 nm, and the size of the Au particles is widely distributed from 9 nm to 50 nm. These results indicate that swift heavy-ion irradiation can be used for the synthesis of metallic nanosized particles.

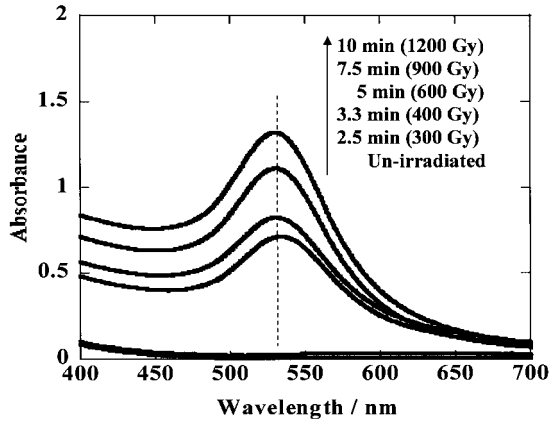

Fig. 1. UV-vis absorption spectra for aqueous solution irradiated with 1.6 GeV C ions.

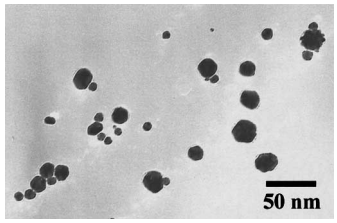

Fig. 2. TEM images of Au nanoparticles produced by 1.6 GeV C-ion irradiation.

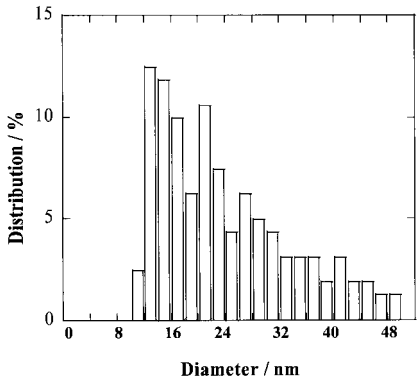

Fig. 3. Particle size histogram of Au nanoparticles.

Reference

1) T. Kinoshita, S. Seino, Y. Otome, Y. Mizukoshi, T. Nakagawa, T. Nakayama, T. Sekino, and K. Niihara: Mater. Res. Soc. Symp. Proc. **877E**, S6.30.1 (2005).

* Department of Materials Science, Osaka Prefecture University

Observation of hyperfine field on ^{17}N nucleus at P1 center in diamond

T. Arai,* M. Uchida,* H. Ueno, D. Kameda, M. Takemura,* A. Yoshimi, T. Haseyama, K. Shimada,* D. Nagae,* G. Kijima,* S. Suda,* T. Inoue,* K. Takase,* and K. Asahi

Nuclear spins in a diamond are known to show exclusively long relaxation times,[1] suggesting a possibility for their applications in nuclear spin-based quantum information technology, and in condensed matter and nuclear structure physics. In particular, an unpaired electron accompanied by each of impurity nuclear spins in a diamond may enable dynamic nuclear polarization and nuclear spin manipulation through hyperfine interactions. The P1 center in a diamond is one of the defect centers which accompany such an unpaired electron. The P1 center consists of a nitrogen atom substituting for a carbon atom[2] as shown in Fig. 1 (a). Because a nitrogen atom has five $2s2p$ electrons, an unpaired electron resides in the vicinity of nitrogen. A previous ESR study suggests that the unpaired electron is bound in one of the four antibonding orbitals between the nitrogen and surrounding carbon atoms, from the observed hyperfine splittings of an ESR line. However, such hyperfine fields on the extremely dilute nuclear spins are very difficult to observe by the conventional NMR technique. In this study, we measured the hyperfine field on a ^{17}N nucleus by the β-NMR method by implanting spin-polarized radioactive ^{17}N nuclei.

A beam of spin-polarized ^{17}N was produced from the fragmentation of ^{18}O projectiles at 70 MeV/nucleon on a 500-μm-thick Nb target.[3] The ^{17}N fragments were implanted in a diamond stopper at room temperature. The stopper, $10 \times 14\,\mathrm{mm}^2$ in area, was made up of 35 "tiles" ($2 \times 2 \times 1\,\mathrm{mm}^3$) of type Ib synthetic diamond. A static magnetic field $B_0 = 715\,\mathrm{mT}$ was applied in the [100] direction. Thus, all of the four N-C bonds were inclined at an angle of $\theta = 54.7°$ from the applied field.

The hyperfine coupling constant A has been determined from the ESR study,[4] as $A^2(\theta) = A_\parallel^2 \cos^2\theta + A_\perp^2 \sin^2\theta$ with a considerable anisotropy, $A_\parallel/(g_\mathrm{e}\mu_\mathrm{B}) = 4.085\,\mathrm{mT}$ and $A_\perp/(g_\mathrm{e}\mu_\mathrm{B}) = 2.918\,\mathrm{mT}$ for a ^{14}N nuclear spin. In a strong field limit of the external field $g_\mathrm{e}\mu_\mathrm{B}B_0 \gg A$, the nuclear spin transition takes place at resonance frequencies given by

$$h\nu_0 = \left| g_{17}\mu_\mathrm{N} \left[B_0 + \frac{A(\theta)}{g_{14}\mu_\mathrm{N}} m_\mathrm{s} \right] \right|, \qquad (1)$$

where μ_B and μ_N denote the Bohr magneton and nuclear magneton, and g_e and g_n ($= g_{14},\ g_{17}$) are the g-factors for the electron and nucleus (^{14}N or ^{17}N), respectively. The second term in the bracket represents the hyperfine field B_hf exerted on the ^{17}N nuclear spin by the electron in a substate m_s, and is calculated as $B_\mathrm{hf} = \pm 15.3\,\mathrm{T}$ for $m_\mathrm{s} = \pm 1/2$ at $\theta = 54.7°$.

An oscillating magnetic field B_1 was applied in the direction perpendicular to the B_0 field, to reverse ^{17}N nuclear spins by the adiabatic fast passage (AFP) technique. Inserting the g-factor for ^{17}N, $|g_{17}| = 0.704 \pm 0.004$,[3] ν_0 is calculated as $\nu_0^< = 78.3\,\mathrm{MHz}$ and $\nu_0^> = 85.9\,\mathrm{MHz}$, corresponding to $m_\mathrm{s} = -1/2$ and $m_\mathrm{s} = +1/2$. To cover these two frequencies, the frequency for the B_1 field was swept from 74 to 90 MHz in 60 ms. The observed change in the up-down asymmetry of the β-rays is shown in Fig. 1 (b). A significant asymmetry change of $0.14 \pm 0.04\%$ is observed.

The present crude β-NMR result indicates that the strength of the hyperfine field on ^{17}N at the P1 center takes a value between 13.1 and 17.5 T, in agreement with the structure of the P1 center previously proposed.[5] The observed size of the β-asymmetry change indicates that about 1/4 of the implanted N atoms stop in substitutional sites in a diamond, based on a comparison with the observed asymmetry change in a graphite stopper. The present finding implies the possibility that the spins of unstable nuclei may be polarized by implanting them in a diamond stopper by the dynamic polarization technique, and (stable) nuclear spins may be implanted externally to form a quantum information system.

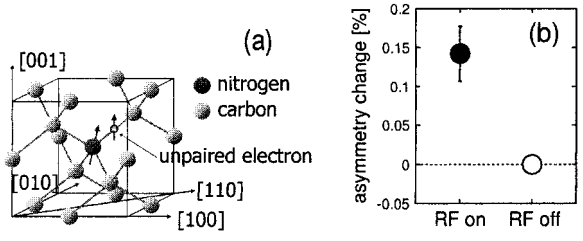

Fig. 1. (a) Crystalline structure of P1 center in diamond. (b) Obtained asymmetry change for ^{17}N in diamond under hyperfine field.

* Department of Physics, Tokyo Institute of Technology

References
1) E. C. Reynhardt and G. L. High: J. Chem. Phys. **109**, 4090 (1998).
2) J. H. N. Loubser and J. A. Van Wyk: Rep. Prog. Phys. **41**, 1201 (1978).
3) H. Ueno et al.: Phys. Rev. C **53**, 2142 (1996).
4) S. Zhang et al.: Phys. Rev. B **49**, 15392 (1994).
5) W. V. Smith et al.: Phys. Rev. **115**, 1546 (1959).

Online TDPAC measurements with the ^{19}F probe implanted in metal oxides

W. Sato,[*1] H. Ueno, Y. Itsuki,[*1] A. Yoshimi, K. Shimada,[*2] D. Kameda, D. Nagae,[*2] G. Kijima,[*2] M. Takemura,[*2] T. Arai,[*2] S. Suda,[*2] T. Inoue,[*2] K. Takase,[*2] A. Shinohara,[*1] Y. Kobayashi, and K. Asahi

Online time-differential perturbed angular correlation (TDPAC) spectroscopy is an effective method for extending the study fields in materials sciences because it enables the introduction of short-lived parent nuclei of PAC probes in samples by the RI beam production technique. In order to apply this method in condensed matter physics and chemistry, we have recently developed a new online TDPAC method at the RIKEN Accelerator Research Facility employing the ^{19}F probe, the β-decay product of ^{19}O.[1)] As the first application of this method to oxides, an online experiment was recently performed for a polycrystalline perovskite manganite $La_{0.7}Ca_{0.3}MnO_3$, which is known to show a colossal magnetoresistance (CMR) effect,[2)] for the purpose of providing insight into the mechanism of the magnetic phenomenon. We here briefly report the preliminary results of the experiments.

Polycrystalline $La_{0.7}Ca_{0.3}MnO_3$ was synthesized by a conventional solid-state reaction from stoichiometric amounts of La_2O_3, $CaCO_3$, and MnO_2. The formation of a single phase was corroborated by a powder X-ray diffraction measurement, and magnetization as a function of temperature was investigated. The obtained crystallographic and magnetic properties were found to show good agreement with those in literature.[3,4)] The powdered sample was pressed into a cylindrical aluminum holder with a size of 12 mmϕ×5 mm so that most of the incident beam can be stopped in it. The holder was attached to the tip of the cold head of a cryostat equipped with a temperature controller. The primary ^{22}Ne ions were accelerated to 110 MeV/u at a beam intensity of 250 pnA. A variety of radioactive nuclides were formed at the Be production target by a projectile-fragmentation reaction, and the secondary beam of interest, ^{19}O, was separated by the RIKEN projectile-fragment separator.[5)] A well-focused pulsed beam of 65 MeV/u was implanted in the sample disc, and online TDPAC measurements were performed on the (1357–197) keV cascade γ rays. In order to obtain better statistics of coincident events, we used sixteen BaF_2 scintillators and arranged them in four independent detector planes.

A preliminary TDPAC spectrum of ^{19}F implanted in the polycrystalline $La_{0.7}Ca_{0.3}MnO_3$ is shown in Fig. 1. The time-variant directional anisotropy $A_{22}G_{22}(t)$, which is given by a simple arithmetic operation as

$$A_{22}G_{22}(t) = \frac{2\,[N(\pi,\ t) - N(\pi/2,\ t)]}{N(\pi,\ t) + 2N(\pi/2,\ t)}, \qquad (1)$$

is plotted as a function of the time interval, t, between the cascade γ rays. Here, $N(\theta, t)$ denotes the number of coincident events observed at an angle, θ. An oscillatory structure is seen in the spectrum. The structure is considered to originate from the hyperfine interaction with the internal magnetic field and/or the electric quadrupole interaction with the extranuclear charge distribution. To obtain further microscopic information, investigation of the temperature dependence of the TDPAC spectra is needed. Precise data analysis is now in progress.

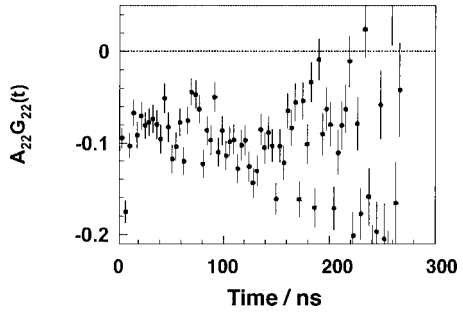

Fig. 1. TDPAC spectrum of ^{19}F implanted in powder $La_{0.7}Ca_{0.3}MnO_3$ at 200 K.

References

1) W. Sato et al.: J. Radioanal. Nucl. Chem. **255**, 183 (2003).
2) A. P. Ramirez: J. Phys. Condens. Matter **9**, 8171 (1997).
3) V. Chechersky et al.: Phys. Rev. B **59**, 497 (1999).
4) H. Y. Hwang et al.: Phys. Rev. Lett. **75**, 914 (1995).
5) T. Kubo et al.: Nucl. Instrum. Methods Phys. Res. B **70**, 309 (1992).

*1 Graduate School of Science, Osaka University
*2 Graduate School of Science and Engineering, Tokyo Institute of Technology

Effects of proton beam irradiation of chalcopyrite-type compound semiconductor solar cell material

K. Yoshino,[*1] M. Yamauchi,[*2] and K. Morimoto

I-III-VI_2 chalcopyrite semiconductors have been attractived for solar cell applications because of their direct-bandgap and high-optical-absorption. Indeed, $CuInGaSe_2$ solar cell energy conversion efficiencies of more than 19.5% have been reported.[1] Furthermore, radiation damages of the $CuInGaSe_2$ are very small in comparison with other solar cell materials such as poly-Si, single Si, amorphous-Si and InGaP.[2] On the other hand, Ag-III-VI_2 materials, such as $AgInSe_2$, are also promising candidate materials for solar cells. $AgInSe_2$ has a bandgap energy of 1.20 eV[3] and a melting point of 780°C, which are even better than $CuInSe_2$ for solar cell applications. An efficiency of 7.5% was reported for a solar cell which used a $AgInSe_2$ absorber on p-$AgInSe_2$/n-CdS.[4] However, little is known about the properties of $AgInSe_2$ thin films.

In our previous study,[5] $AgInSe_2$ thin films were prepared on a quartz glass substrate by evaporation method. After the evaporation, the samples were annealed at 600°C for 10 min. in an Ar atmosphere. Single-phase $AgInSe_2$, with a (112) orientation was present in the sample annealed at 600°C by X-ray diffraction (XRD). Measured lattice constant of the a-axis was close to the JCPDS value; however, the c-axis was larger than that of the JCPDS value. The $AgInSe_2$ film has n-type conductivity with a resistivity of 0.14 Ω cm, a carrier concentration of 2.5×10^{18} cm^{-3} and a mobility of 20 cm^2 $(V\ s)^{-1}$.

Here, a proton beam irradiation of the $AgInSe_2$ films was carried out using the AVF cylotron in RIKEN to obtain information on irradiation damages. The energies of the proton were from 0.8 to 4 MeV at a dose of 1×10^{15} cm^{-2}. The ranges of the proton are from approximately 10 to 100 μm. Protons passed through the sample because the thickness of the sample is approximately 1 μm. Hall measurements were carried out at room temperature using the Van der Pauw method for electrical characterization. Gold was used as an ohmic contact.

Figure 1 shows resistivity and mobility as functions of proton energy. Resistivity is constant at proton energies less than approximately 3 MeV and increases above 3 MeV. From the XRD measurements, the values of full width at half maximum of a (112) peak increase with increasing proton energy. This means that grain sizes decrease with increasing proton energy. Therefore, it is deduced that the decrease in mobility is due to the decrease in grain sizes. On the other hand, carrier concentration slightly increases with increasing proton energy. All irradiation samples have n-type conductivity. The conduction types are not changed by the proton irradiation. A type of carrier in the nonirradiated sample has already been reported as Se-vacancy.[5] Therefore, it is assumed that the increase in carrier concentration by proton irradiation is due to the increase in defects of Se-vacancy and/or interstitial hydrogen.

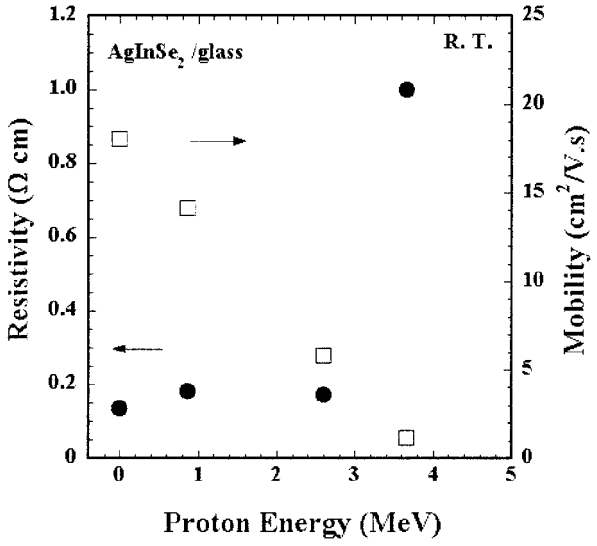

Fig. 1. Resistivity and mobility as functions of proton energy. White square and black circle indicate mobility and resistivity, respectively. A 0 MeV proton energy indicates nonirradiation.

References

1) M. A. Contreras, K. Ramanathan, J. Abushama, F. Hasoon, J. Keane, D. L. Young, B. Egaas, and R. Noufi: Prog. Photovolt. Res. Appl. **13**, 209 (2005).
2) M. Imaizumi, T. Sumita, S. Kawakita, K. Aoyamna, O. Anzawa, T. Aburaya, T. Hisamatsu, and S. Matsuda: Prog. Photovolt. Res. Appl. **13**, 93 (2005).
3) B. Tell, J. T. Shary, and H. M. Kasper: J. Appl. Phys. **43**, 2469 (1972).
4) P. P. Ramesh, O. M. Hussain, S. Uthanna, B. S. Naidu, and P. J. Reddy: Mater. Lett. **34**, 27 (1997).
5) H. Matsuo, K. Yoshino, and T. Ikari: Submitted to Phys. Stat. Sol.

*1 Department of Electrical and Electronic Engineering, University of Miyazaki
*2 Department of Applied Physics, University of Miyazaki

Ultra-short-pulse continuum of ion track and its universality

K. Kimura, M. Koshimizu,* H. Ryuto, K. Asai,* and M. Kase

Time-integrated luminescence spectra of ion-irradiated solid material are used to be mostly combinations of luminescence spectra known in photo- or electron irradiation, in spite of expectation that vast deposit energy could produce something new. Known spectra are due to self-trapped excitons (STE), excited defect or impurity centers, and/or recombination of electron and shallow trapping of holes. However, time-resolved measurements with a resolution of about 100 ps enable us to obtain quite different results. Some decay rates are enhanced extraordinarily. Moreover, a new ultra-fast luminescence continuum (UFLC) appears in time-resolved luminescence spectra within a few tens ps after an ion impact. Since UFLC was first observed for alumina,[1] it has been observed universally in all the heavy-ion irradiated insulator crystals except for diamonds. The luminescence can be characterized as follows[2]: UFLC covers a wavelength region from vacuum ultraviolet to visible. Its efficiency is largely dependent on the atomic number of a projectile ion, i.e. excitation density. The luminescence efficiency increases super linearly in many cases with increasing excitation density. This means that the precursors for luminescence interact multiply with each other. However, known excited states cannot be the precursors, which can be proved by kinetics using the shape of the decay curve. In addition to this, large chemical-composition dependence was observed. Also, the continuum has structures and their peaks appear at similar positions to those due to the known excited states although the UFLC is broadened. On balance, the precursors aforementioned may be electrons staying at higher quantum levels under potential of holes. A number of electrons are ejected radially from cylindrical region along the track core, and return back to the track core after thermalization.[2] The density of the electrons is so high that the interaction compels the electron-hole pairs strongly to release excess energy. The releasing is considered to occur not only via the phonon networks by bonds surrounding each hole but also via photo-emissions by the interaction between electron-hole pairs. At extremely high density, the emission may occur through the interactions among electrons near continuum levels and in the intermediate way of hole-trapping. We consider that this is UFLC. In case of alkali halides with large luminescence efficiencies, the hole is the neutral halogen atom which cannot have ionic bonds. This mechanism looks to explain the experimental results well. Now, we call UFLC track-luminescence continuum (TLC).

* Department of Applied Chemistry, Graduate School of Engineering, Tohoku University

Figure 1 gives two experimental results at RILAC: (a) shows TLC spectra of KI single crystal irradiated by 2 MeV/u Xe ions at 296 K. All luminescence belongs to TLC because STEs, being the principal sources of luminescence, cannot survive at this temperature. TLC has a structure comprised of two peaks and one shoulder. By photolysis near 4.2 K, STEs luminescence appears at I and II, but not at III. It is known that there are three types of STEs due to I, II, III but each alkali halide misses one or two STEs of the three. These missing STEs are virtual ones anticipated from comparisons of spectral peak positions of every STE.[3] The missing may mean that potential is too shallow to stabilize the electron into the potential minimum. However, TLC seems to break every spectral missing of alkali halides. The second example, given in Fig. 1 (b), is for N-ion irradiated MgO crystal at 3.3 K. This material is known to have evident free-exciton luminescence at 162.5 nm. TLC near time 0 shows coexistence of a sharp free-exciton band and TLC near 180 nm. In case of Xe-ion irradiation with much larger energy density, TLC was increased while the free-exciton band disappeared because the process for TLC precedes free-exciton formation. In this case also, there is a proposal of shrunk STE at 180 nm though negligibly weak.[4] The situation seems similar to the previous spectral missing.

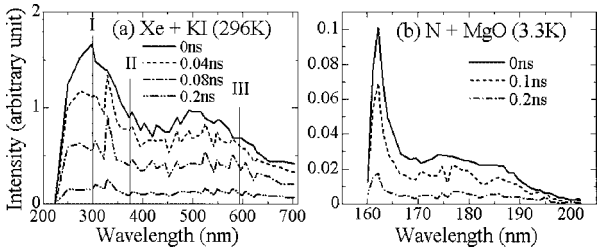

Fig. 1. (a) Time-resolved spectra of Xe-ion irradiated KI single crystal at 296 K. Bars I, II, and III are actual and anticipated appearance positions of STEs at 4 K, respectively. (b) Time-resolved spectra for N-ion irradiated MgO crystal at 3.3 K.

References

1) K. Kimura, J. Kaneko, S. Sharma, W. Hong, and N. Itoh: Phys. Rev. B **60**, 12626 (1999).
2) K. Kimura: Nucl. Instrum. Methods Phys. Res. B **212**, 123 (2003).
3) K. S. Song and R. T. Williams: in *Self-Trapped Excitons*, (Springer, Berlin, 1993), p. 168.
4) Z. A. Rachko and J. A. Valbis: Phys. Stat. Sol. (6) **98**, 161 (1979).

Temperature and excitation density dependence of ultrafast luminescence of ion-irradiated α-alumina

M. Koshimizu,* K. Kimura, H. Ryuto, K. Asai,* and M. Kase

Fast processes occurring along an ion trajectory, which are characterized by high-density electronic excitation and related processes such as interaction among excited states at a high density or that between excited electrons and a lattice system, has been a subject of intensive studies, because these processes should be profoundly related to the formation of an ion track. In particular, in insulators, the self-trapping of a hole or an exciton renders these processes even more complicated, and it is suggested that self-trapping may be relevant to the formation of an ion track. However, the behavior of the self-trapped holes (STHs) or excitons (STEs) is not well understood for high-density excitation, and the interaction among them should lead to the behavior which is entirely different from that for low-density excitation. In this study, to investigate the temporal behavior of STHs or STEs under high-density excitation, we measured the time-resolved luminescence spectra of α-alumina about which the relaxation of holes or excitons for low-density excitation has been discussed by many researchers.[1)]

The measured sample was a single crystal of α-alumina. The sample was irradiated with N, Ar, and Xe ions having energies of 2.0 MeV/nucleon. Excitation density by projectiles increases with increasing mass of the projectiles. Time-resolved luminescence spectra were obtained by the single-photon counting method.

Figure 1 shows the decay curves of luminescence observed under irradiation with N, Ar, and Xe with energies of 2.0 MeV/nucleon. In each case, the decay curve cannot be fitted with a single exponential function. In addition, in the case of Xe irradiation, there exists a fast component, which is distinctly different from the other components. This fast component is observed in a wide wavelength range, particularly longer than 200 nm, in contrast to the slow components. In addition, the decay rates of the slow components seem to depend on excitation density. It should be noted that the decay rates of these components are much higher than those observed for electron irradiation, and luminescence occurs at approximately the wavelength of luminescence due to STE.[1)]

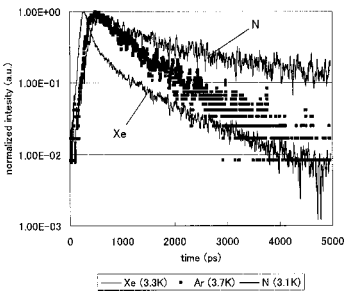

Fig. 1. Normalized decay curves of luminescence of α-alumina irradiated with N, Ar, and Xe. For N and Ar irradiation, the luminescence was observed at 172.7 nm, for Xe irradiation, 170.1 nm.

Figure 2 shows the normalized decay curves of the luminescence of Xe-irradiated α-alumina at 170.1 nm at different temperatures. The decay rate of the fast component seems to be independent of temperature in the measured temperature range. In contrast, the decay rate of the slow component markedly decreased with increasing temperature from 3.3 K to 7.0 K, and reached the minimum at 15 K.

Because the decay rates of both the fast and slow components depended on excitation density, the decay rates are certainly related to interactions among excited carriers. The threshold-like behavior of the intensity of the fast component, along with the weak temperature dependence, indicates that this component is related to the interaction between many 'hot' excited species accompanying lattice deformation similar to the STE, such as electron-hole plasma in semiconductors.[2)] The high decay rate is also explained by a large oscillator strength of such high-density excited species.[2)] In contrast, the slow components may be related to the interaction of a few excited species, such as STEs, with the lattice system, although it is necessary to measure the decay curves in a wider temperature range.

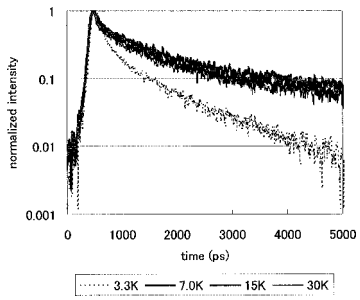

Fig. 2. Normalized decay curves of luminescence of Xe-irradiated α-alumina at 170.1 nm at different temperatures.

References

1) For review, see J. Valbis and N. Itoh: Radiat. Eff. Defects Solids **116**, 171 (1991).
2) C. Klingshirn and H. Haug: Phys. Rep. **70**, 315 (1981).

* Department of Applied Chemistry, Graduate School of Engineering, Tohoku University

Resonant electron capture and decay for N ions using metal microcapillary targets

Y. Iwai, Y. Kanai, Y. Nakai, T. Ikeda, M. Hoshino,[*1] H. Oyama, H. Masuda,[*2] K. Nishio,[*2] H. A. Torii,[*3] K. Komaki,[*3] and Y. Yamazaki

When a slow highly charged ion approaches a metal surface, the ion resonantly captures target valence electrons into its excited states above the surface and forms a multiply and highly excited state. To study the formation and decay of the excited state in the vacuum, X rays emitted from 2.3 keV/u N^{q_i+} ($q_i = 7$) ions transmitted through a thin Ni microcapillary foil were measured using a high-resolution soft X-ray spectrometer. X-ray intensity for each transition as a function of time after passing through microcapillaries was evaluated by cascade simulation, and the initial state distribution was reconstructed.

Ions (2.3 keV/u N^{7+}) are supplied by a 14.5 GHz Caprice electron cyclotron resonance ion source in RIKEN.[1)] The microcapillary target was $\sim$1 mm^2 in area with a thickness of $\sim$1 μm and had numerous straight holes of $\sim$200 nm diameter.[2)] When the ions impinge on the microcapillary target parallel to the capillary axis, a part of the ions that captured electrons from the capillary wall can pass through the capillary before hitting the capillary wall and multiply and highly excited ions are extracted in vacuum.[3)] The spectrometer consists of a concave grating and a charge-coupled device. Further details of the spectrometer and methods of data analysis are described below.[4)] X-ray spectra were taken at eight points (t_d = 0.0–6.0 ns) downstream of the target along the ion beam, where t_d is the time after passing through the target.

Figure 1 shows K X-ray intensities $I(t_d{:}q_i = 7)$ for np - 1s ($n = 2, 3$) and 1s2p ^{1,3}P - 1s^2 ^{1}S transitions as a function of t_d. The half-lives of $I(t_d < 1.5\,\text{ns})$ and $I(t_d \geq 1.5\,\text{ns})$ were $\sim$0.1 ns and $\sim$1 ns, respectively, except for 1s2p ^{3}P - 1s^2 ^{1}S transition. The half-life of 1s2p ^{3}P - 1s^2 ^{1}S transition was almost constant at $\sim$5 ns. This is consistent with the lifetime of 1s2p ^{3}P, *i.e.*, 4.9 ns.[5)]

The initial state distribution ($P^I(n, \ell{:}q_i)$) of the first electron transferred was calculated by cascade simulation for hydrogen-like ions. The np - 1s and 1snp - 1s^2 transitions were calculated by adopting the effective charges of $q_e = 7$ and 6, respectively. The average value of the initial state n-distribution was $\sim q_i + 1.5$ and the full widths at the half maximum of the distributions were $\delta n \sim 2$. The average value agreed with the prediction obtained using the classical over barrier model (COBM).[6)] The trend of n-distribution agreed with a report of the visible light spectroscopy.[7)] Combining the present result and the report, it was concluded that the average value of n-distribution in the broad ℓ-distribution was almost constant.

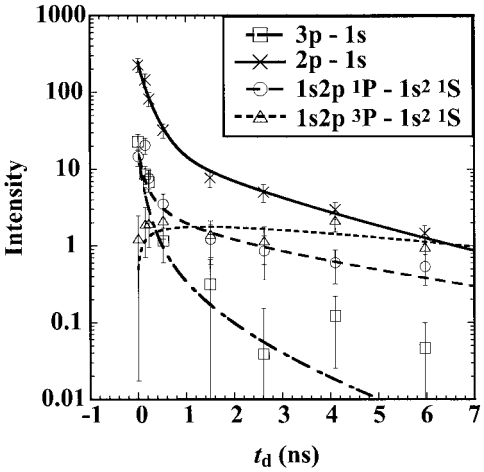

Fig. 1. Intensities for np - 1s ($n = 2, 3$) and 1s2p ^{1,3}P - 1s^2 ^{1}S transitions as function of time after passing through microcapillaries. Lines are results of cascade simulations considering Auger decay.

$I(t_d \geq 1.5)$ was reproduced by $P^I(n, \ell{:}q_i)$, however $I(t_d < 1.5)$ was not reproduced. Then, according to COBM, the initial state distribution ($P^{I^2}(n, \ell{:}q_i)$) of the second electron transferred was assumed to be $P^{I^2}(n, \ell{:}q_i) \approx P^I(n, \ell{:}q_i - 1)$. The distribution $P^A(n, \ell{:}q_i)$ after the Auger decay of ion that captured two electrons was calculated. The lines in Fig. 1 show the result of the cascade simulation by the combination of $P^I(n, \ell{:}q_i)$ with $P^A(n, \ell{:}q_i)$. Considering the Auger decay, $I(t_d < 1.5)$ was reproduced. The ions that passed the Auger decay were $\sim$50% of X ray emitting ions.

*1 Department of Physics, Sophia University
*2 Department of Applied Chemistry, Graduate School of Engineering, Tokyo Metropolitan University
*3 Institute of Physics, Graduate School of Arts and Sciences, University of Tokyo

References
1) Y. Kanai et al.: Phys. Scr. T **92**, 467 (2001).
2) H. Masuda et al.: Appl. Phys. Lett. **71**, 2770 (1997).
3) S. Ninomiya et al.: Phys. Rev. Lett. **78**, 4557 (1997).
4) Y. Iwai et al.: Nucl. Instrum. Methods Phys. Res. B **193**, 504 (2002).
5) W. R. Johnson et al.: Adv. At. Mol. Opt. Phys. **35**, 255 (1995).
6) J. Burgdörfer et al.: Phys. Rev. A **44**, 5674 (1991).
7) Y. Morishita et al.: Phys. Rev. A **70**, 012902 (2004).

Single- and double-electron capture processes in slow N^{5+}-He collisions

Y. Miyamoto,[*1] M. Hoshino,[*1] Y. Kanai, K. Otsuki,[*2] Y. Nakai, M. Kitajima,[*3] H. Tanaka,[*1] and Y. Yamazaki

We have measured angle-resolved energy gain spectra of N^{5+}-He collisions at impact energies of 340, 490, 580, and 670 eV, using the crossed-beam apparatus at the beamline-BL2 in the Slow Highly Charged Ion Beam Facility of RIKEN. The single- and double-electron capture processes in N^{5+}-He collisions have been studied intensively. However, most of these studies involved total cross section measurements,[1] except for a few partial cross section measurements for single-electron capture with VUV photon emission spectroscopy.[2,3] In particular, there has been no state-selective measurement of double capture. Because angular distributions become more sensitive to the shape of the interaction potentials with decreasing impact energy, state-selective angular distributions are expected to provide information on the interaction potentials for single- and double-electron capture processes. By analyzing data for double electron capture in detail, the final states reported for 670 eV last year[4] were identified as the states of $N^{3+}(1s^22p^2)$(peak 1), $N^{3+}(1s^22s3l)$(peak 2), $N^{3+}(1s^22p3l)$(peak 3 or peak 4) and $N^{3+}(1s^22s4l)$(peak 3 or peak 4).

Our purpose is to obtain the information on the shape of potential curves for the N^{5+}-He system. However, it is difficult to extract the shapes of interaction potentials directly from experimental angular distribution. As the first step, we calculate *ab-initio* adiabatic potential and discuss whether this potential can qualitatively explain our experimental results or not. It is sufficiently valuable to discuss the validity of such adiabatic potentials. In order to obtain the interaction potentials between $N^{(5-q)+} - He^{q+}(q = 0, 1, 2)$, singly and doubly excited configuration interaction (CI) calculations were performed using Alchemy software empolying the $7s6p4d3f$ Gaussian orbitals and the $6s4p$ Gaussian orbitals to guarantee the energy levels of the N-ion and He-ion/neutral, respectively. In the CI calcultions, the $1s$-orbital in the N ion was treated as a frozen core orbital. The results of the CI calculations are independent of the choice of the initial orbitals.

To evaluate these adiabatic potential curves, we have carried out the multichannel Landau-Zener calculations[5] (MCLZ) for single-electron capture channels, using the adiabatic potential curves that include the capture into the $N^{4+}(1s^23s)$, $N^{4+}(1s^23p)$, and $N^{4+}(1s^23d)$ states (not show in Fig. 1). Comparison of the present MCLZ calculations with experimental absolute cross sections measured by Beijers et al.,[3] showed that our calculations, particulaly those of the total and partial cross sections of the $N^{4+}(1s^23s)$ state, are in fairly good agreement with the measurement. Thus, our adiabatic potential energy curves are thought to be satisfactory for reproducing the experimental results. Figure 1 shows part of the *ab-initio* adiabatic potential curves for double electron capture channels, which we calculated in present work. Solid lines in Fig. 1 show the capture channels we obtained from our experimental results. We found, from these potential curves, the avoided crossing points are about 3.3, 4.8, and 5 atomic units(a.u.) for double-electron capture channels, which correspond to the capture into the $N^{3+}(1s^22s4l, 1s^22p3l)$, $N^{3+}(1s^22s3l)$, and $N^{3+}(1s^22p^2)$ states. From now on, we will compare our measured state-selective angular distributions with the augular distributions calculated using these adiabatic potential curves.

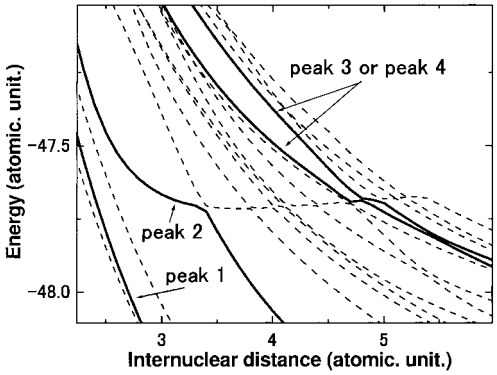

Fig. 1. Adiabatic potential curves calculated for double electron-capture process.

References

1) K. Ishii et al.: Phys. Rev. A **70**, 042716 (2004).
2) D. Dijkkemp et al.: J. Phys. B **18**, 4763(1985).
3) J. P. M. Beijers et al.: Phys. Rev. A **49**, 363 (1994).
4) Y. Miyamoto et al.: RIKEN. Accel. Prog. Rep. **38**, 92 (2005).
5) A. Salop and R. E. Olson: Phys. Rev. A **13**, 1312 (1979).

*1 Department of Physics, Sophia University
*2 The University of Electro-Communications
*3 Tokyo Institute of Technology

Charge-state correlations in large-angle scattering between Ne ion and Ar atom

M. Hoshino,[*1] T. Kambara, Y. Kanai, R. Schuch,[*2] and Y. Yamazaki

The interaction of slow highly charge ions (HCIs) with clean metal surfaces has been studied intensively over the past few years.[1)] The neutralization processes of HCIs from metal surfaces at large-angle scattering have been investigated in detail. To study these processes from a different viewpoint, we have been investigating the close collisions of slow HCIs with single atoms as the elementary processes of ion-surface interactions. We previously reported the measurements of charge-state correlations between recoil and scattered ions for 5 keV Ne^{q+}(q = 1, 2, and 3) on Ar.[2)] Recentry, we have measured the recoil-ion charge-state distributions for q = 3, 5, and 7 in the energy range of 5–63 keV. The mean charge states of both scattered and recoil ions were also measured at 5 keV. Here, we describe the results only for Ne^{7+}-Ar collisions.

The experiment was carried out at the Slow Highly-Charged Ion Beam Facility in RIKEN. The experimental setup has been reported elsewhere.[2)] A Ne-ion beam from a 14.5 GHz Caprice-type ECR ion source was collimated on a localized Ar gas from a needle. Scattered Ne ions and recoil Ar ions were detected in coincidence at 27° and 70° with respect to the beam direction using ion-detection telescopes. These angles are expected from the kinematics of elastic scattering of the Ne-Ar system. Each ion-detection telescope consists of a Time-of-Flight (TOF) drift tube to be set on electrostatic potential, and a two-dimensional position-sensitive detector. For each coincidence event, the time difference between the detections of the scattered and recoil ions (ΔTOF) and the positions of both ions were recorded, from which we can obtain the charge-state fraction of recoil ions (q_{Ar}).

Figure 1 (a) shows the mean charge states of recoil-ions ($\overline{q}_{\mathrm{Ar}}$) as a function of the impact energy in the collisions of Ne^{7+} with Ar. In Fig. 1 (a), the $\overline{q}_{\mathrm{Ar}}$ changed drastically from approximately 5 to 7 as a step function around the impact energy of 35 keV, at which the closest approach corresponds to the L-shell radius of the Ar atom. The same behavior was observed for the energy loss measurements in large-angle scattering between Ar^{+} and Ar at a higher impact energy region.[3)]

The fraction of each final charge state (q_{Ar}) from 3 to 8 is also shown in Fig. 1 (b). The fraction of q_{Ar} = 4 and 5 decrease by a factor of three as the impact energy increases. The fraction of q_{Ar} = 6 is almost independent of impact energy, but it seems to have a peak at approximately 35 keV. The fractions of q_{Ar} = 7 and 8 drastically increase at approximately 35 keV. A similar increase in q_{Ar} was observed in the case of Ne^{3+} and Ne^{5+} impacts.

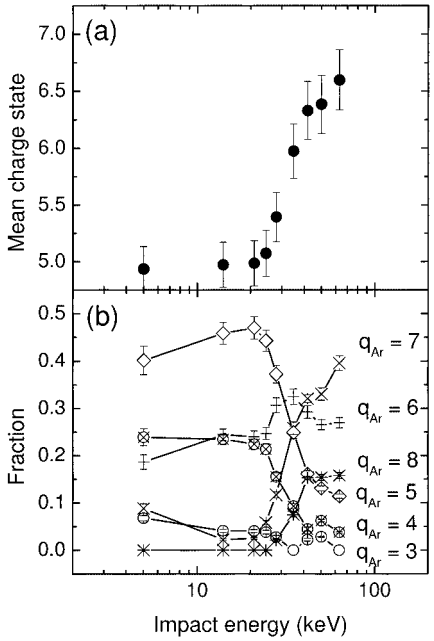

Fig. 1. Energy dependence of (a) mean charge states (•) and (b) fraction of recoil ions in collisions of Ne^{7+} with Ar. (○): q_{Ar} = 3. (⊗): q_{Ar} = 4. (◇): q_{Ar} = 5. (+): q_{Ar} = 6. (×): q_{Ar} = 7. (∗): q_{Ar} = 8.

In the measurements of mean charge-state correlations between scattered and recoil ions at 5 keV, we have found that the three-electron-capture and two-electron-loss channel gave the maximum contribution from ΔTOF shift for Ne^{7+}-Ar collisions. Therefore, we assumed that these five electrons in the M-shell of the Ar atom contribute in the reaction below 35 keV, whereas at higher energies the internuclear distance is close to the L-shell radius of Ar and the promotion of L-shell electrons may contribute to the increase in q_{Ar}.

References

1) S. Hustedt et al.: Phys. Rev. A **50**, 4993 (1995).
2) M. Hoshino et al.: Nucl. Instrum. Method Phys. Res. B **235**, 347 (2005).
3) E. Everhart and Q. C. Kessel: Phys. Rev. Lett. **14**, 247 (1965).

[*1] Department of Physics, Sophia University
[*2] Atomic Physics, Stockholm University, Sweden

Possible scheme for preparing microbeam of slow highly charged ions using tapered glass capillary

T. Ikeda, Y. Kanai, M. Hoshino,[*1] T. M. Kojima, T. Kambara, T. Nebiki,[*2] T. Narusawa,[*2] and Y. Yamazaki

We have started to develop a new technique for preparing micro/sub-microbeam of slow highly charged ions (HCIs) using a tapered glass capillary at RIKEN. We have succeeded in observing the guiding effect for the first time.

Recently, microbeams of ions have been utilized in various scientific fields. However, these microbeams are mainly composed of protons or He ions with energies higher than 1 MeV. On the other hand, microbeams of slow HCIs have not yet been fully utilized. The use of slow HCI microbeams could realize the pinpoint deposition of their large potential energy on the surface of a sample, and offer a unique opportunity of surface characterization by scanning microscopy. So far, microbeams are formed by collimation and focusing, using a double slit with a long interval and electromagnetic focusing lenses. This scheme requires a long beam line and beam intensity is diminished. Our new technique is based on the charge up inside an insulator tube. It can provide the microbeams of HCIs with a certain intensity through its compact setup.

When positive ions enter the glass capillary, they can make the inner wall positively charged up. The electric field prevents the following ions from coming in close contact with the wall. The beam is thus guided within the glass capillary and exits from the outlet, which is smaller than the inlet, and the density of the beam becomes higher (focusing effect). This makes it possible to realize a HCI microbeam without charge transfer or energy loss.

The glass capillaries employed in this study, as shown in Fig. 1, were 30–50 mm in length, 0.8 mm in inlet diameter and 0.9–24 μm in outlet diameter. They were made from borosilicate glass tubes 2 mm in outer diameter and 90 mm in length, these tubes melt at 820°C (softening temperature). A glass tube was heated in the midlength at the softening temperature, and pulled at a constant velocity to form a tapered glass capillary. The taper angle is determined by the temperature and pulling velocity. An outlet with a diameter of $\sim$0.1 μm can be fabricated by this method.

As shown in Fig. 2, Ar^{8+} ion beam of 8 keV from a 14.5 GHz ECR ion source was collimated by a 4-jaw slit so that the beam profile was about 1.5 mm square, and the intensity of the beam at the inlet of the glass capillary was varied in the range of 0.1 – several pA. An Al plate with 4 mmϕ holes was set in front of the glass capillary inlet so that any part of the initial beam cannot directly reach the downstream elements. Moreover, a stainless ring with an outer diameter of 6 mmϕ surrounding the inlet was also set. A deflector just behind the glass capillary was used for measuring the charge distribution of the transmitted beam. The transmitted ions were counted using a position sensitive detector (PSD) with MCP's and a wedge-and-strip type anode. The distance between the outlet of the glass capillary and the PSD was about 100 mm. A metal tube parallel to the glass capillary was installed to adjust the direction and position of the ion beam.

To confirm the guiding effect, the glass capillary (ϕ_{outlet} 24 μm) was tilted horizontally from $-5°$ to $+5°$. Figure 3 shows the tilting angle dependence of the peak position for the beam intensity of $\sim$0.1 pA at the inlet. The error was produced from the reading of the tilting dial. The open circles show the calculated positions. If the shape of the glass capillary is assumed to be trapezoid, the geometrical limit of the tilting angle for a direct beam is about 0.49°. Therefore, it is impossible to transmit ions in a tilting angle of more than 0.49° without the guiding effect.

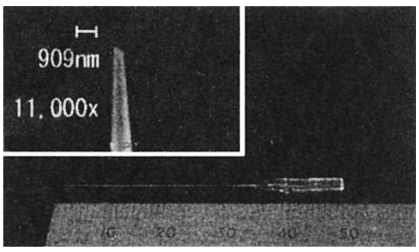

Fig. 1. Glass capillary: The inset is a magnified image of the outlet taken by SEM.

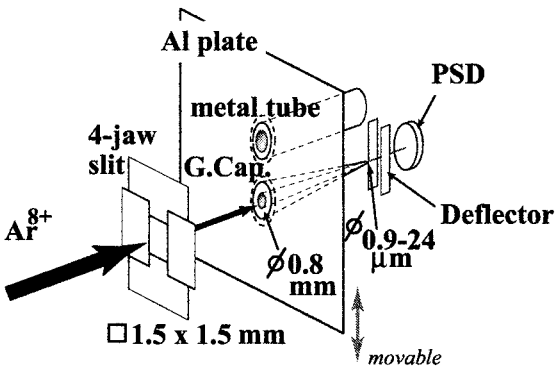

Fig. 2. Schematic view of setup: G. Cap. stands for glass capillary.

*1 Department of Physics, Sophia University
*2 Kochi University of Technology

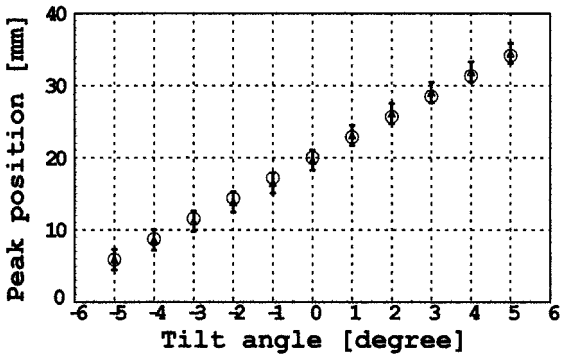

Fig. 3. Horizontal position at PSD vs tilting angle: The error was produced from the reading of the tilt dial. The open circles show the calculated positions.

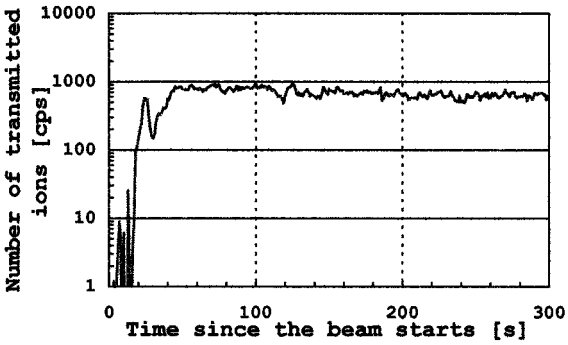

Fig. 4. Time dependence of number of transmitted ions: It took several s to start the transmission and several tens of seconds to saturate the transmission rate.

The probability of the charge transfer inside the glass capillary was also measured using the deflector applied at 140 or 280 V. As a result, the contamination by Ar^{7+} in the transmitted ions was at most 10% in the position distribution at the PSD for the tilting angle of 0° or 3°. This implies that most ions did not touch the inner wall. The beam spot at the PSD was smaller than 0.7 mmϕ (FWHM). The peak positions of Ar^{8+} and Ar^{7+} ions of 8 keV were calibrated from the results of the transmission with the metal tube.

Figure 4 shows the time dependence of the number of transmitted ions for the beam intensity of about 1 pA without tilting. The transmission continued for more than 1200 s. (We did not measure the number of transmitted ions longer than 1200 s) As shown in the plot, it took several s to start the transmission and several tens of seconds to saturate the transmission rate. These delays indicate that the inner wall was charged up by the ion beam so that the beam was properly guided. In the cases of ∼0.1 pA inputs, the transmission rate was not stable. The rise time of the transmission rate could be determined from the beam intensity and the discharge process of the glass surface. A small peak (at around $t = 25$ s in this plot) appears before the saturation. This phenomenon was observed in other results.

Guiding of slow Ne ions transmitted through nanocapillaries in polymer foils

Y. Kanai, M. Hoshino,[*1] T. Kambara, T. Ikeda, R. Hellhammer,[*2] N. Stolterfoht,[*2] and Y. Yamazaki

Recent observation[1)] has shown that slow highly charged ions are guided when transmitted through capillaries of large aspect ratio (100 nm in diameter and 10 μm in length) in a highly insulating polymer (PET: polyethylene terephthalate) foil. The guiding effect indicates that the inner walls of the insulator capillaries are charged in a self-organizing process so that close collisions with the surface are suppressed. In previous experiments,[1)] only horizontal distributions of transmitted ions were measured. In order to obtain more comprehensive information on the guiding effect, we started to measure the two-dimensional (2-D) images of transmitted ions through PET capillaries.

The experiments were performed at the Slow Highly Charged Ion Facility at RIKEN.[2)] Beams of 3.5–7 keV Ne^{7+} ions from a 14.5 GHz electron cyclotron resonance ion source were collimated to a diameter of 1 mm and a divergence of 0.5° at a 10-μm-thick PET-foil target. Typical beam currents were 0.01–0.2 nA. The PET foil had capillaries with a diameter of 200 nm, whose density was 4×10^6 holes/cm^2. The front and exit sides of the PET foil were evaporated with Au, producing a conducting film of $\sim$ 20 nm thickness to avoid charge up. 2-D images of transmitted ions were measured using a position-sensitive detector with micro channel plates and a wedge-and-strip anode.

Figure 1 shows 2-D images of transmitted ions at different tilt angles of the PET foil relative to the beam with 3.5 keV Ne^{7+}. By rotating the target tilt angle from 0° to 4°, the peak positions of transmitted ions moved to the capillary axis direction; that is, the deflection angle is nearly equal to the tilt angle. This indicates that the ions were guided by the capillaries. As is seen in Fig. 1, the 2-D images of transmitted ions are isotropic and the angular widths of transmitted ions are about 1°. This is in good agreement with the theoretical simulation,[3)] but different from the previous measurements,[1,4)] where a high-capillary-density (10^8 holes/cm^2) PET foil was used and the angular width of transmitted ions was about 3° for 7 keV Ne^{7+}.[4)] To discuss the relationship between the angular width of transmitted ions and the capillary density, we need more experiments in which the capillary density is changed.

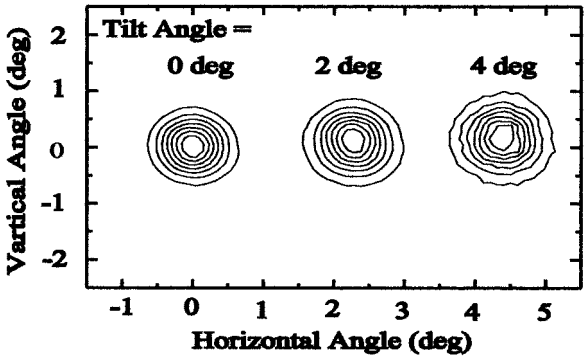

Fig. 1. 2-D images of ions transmitted through PET capillaries at tilt angle = 0°, 2°, and 4°. The beam energy is 7 keV.

Figure 2 shows the integrated intensity of transmitted Ne^{7+} ions as a function of tilt angle for beam energies of 3.5, 4.9, and 7 keV. As the beam energy becomes lower, ions with larger tilt angles can be guided. The maximum intensity is about 100 ions/pC, which corresponds to about 20% of the incident ions for each capillary being transmitted by the guiding effect. This efficiency does not depend on the beam energy and current under our experimental conditions; 3.5–7 keV and 0.01–0.2 nA.

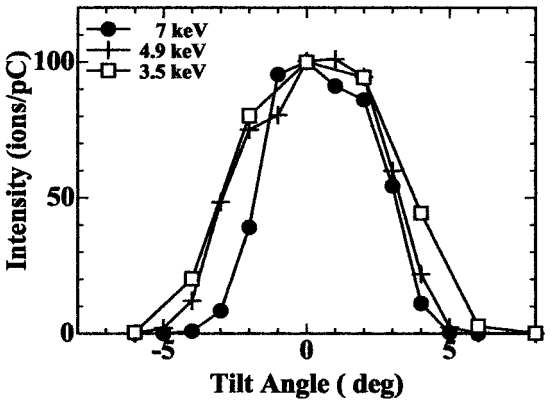

Fig. 2. Transmitted ion intensities for 3.5, 4.9, and 7 keV Ne^{7+} ions. Intensities are normalized by incident beam currents.

References

1) N. Stolterfoht et al.: Phys. Rev. Lett. **88**, 133201 (2002).
2) Y. Kanai et al.: Phys. Scr. T **92**, 467 (2001).
3) K. Schiessl et al.: Nucl. Instrum. Methods Phys. Res. B **232**, 228 (2005).
4) R. Hellhammer et al.: Nucl. Instrum. Methods Phys. Res. B **232**, 235 (2005).

*1 Department of Physics, Sophia University
*2 Hahn-Meitner Institute, Germany

Measurement of momentum distributions of multiply charged rare gas ions produced by an intense ($\sim 10^{17}$ W/cm^2) laser field

H. Shimada,* Y. Nakai, H. Oyama, K. Ando, A. Hatakeyama,* and Y. Yamazaki

With the advent of ultrafast laser technology, strong electric field of the order of one atomic unit or more (electric field of 1 a.u. $= 5.2 \times 10^{11}$ V/m, corresponding light intensity is 3.6×10^{16} W/cm^2) has become experimentally accessible. The ionization of an atom with such a strong field cannot be described in a perturbative manner and requires a different approach. If the adiabaticity condition

$$\frac{\omega}{F\sqrt{2I_P}} \ll 1$$

is fulfilled,[1] where ω and F represent the frequency and amplitude of the electric field of light, and I_P represents the ionization potential, the ionization is described as an escape of the electron from the atomic potential deformed by the quasi-static electric field. Under this adiabaticity condition, a tunneling model, known as the ADK model,[2] has been successfully applied to describe the measured ion yield. At high field strength, where the assumption of the tunneling model does not hold, a deviation from the ADK model has been predicted.[3] However, it has not been confirmed by ion yield measurements.

We report the deviation from the ADK model observed in ion momentum spectra. In this experiment, we have measured the momentum distributions of multiply charged Ar ions produced by an intense ($\sim$(0.2–1) $\times 10^{17}$ W/cm^2) laser field. Ultrashort ($\sim$200 fs, FWHM) pulses of linearly polarized near-infrared (775 nm) light were used. The ion momentum distributions along the light polarization direction were measured by the time-of-flight technique.

The measured momentum distributions of Ar ions are plotted in Fig. 1. Each distribution has a peak at zero momentum, and their widths increase monotonically with the charge states (open squares in Fig. 2).

These results were compared with model calculations. A calculation based on the ADK model gave narrower distributions (solid triangles in Fig. 2) than the experiment. This discrepancy can be attributed to the tunneling approximation that is inappropriate near the top of the potential barrier. Significantly improved results were obtained using more accurate ionization rate near the top of the barrier[3] (open triangles).

In summary, the momentum distributions of multiply charged Ar ions were measured. The distributions were compared using the calculation based on the quasi-static treatment of the electric field. The well-known ADK model has proven to be insufficient to correctly describe the momentum distributions. The use of the more accurate ionization rate near the top of the barrier improved the calculated results. From these results, we conclude that the ion momentum spectroscopy is more sensitive to the ionization model than the yield measurement.

* Graduate School of Arts and Sciences, University of Tokyo

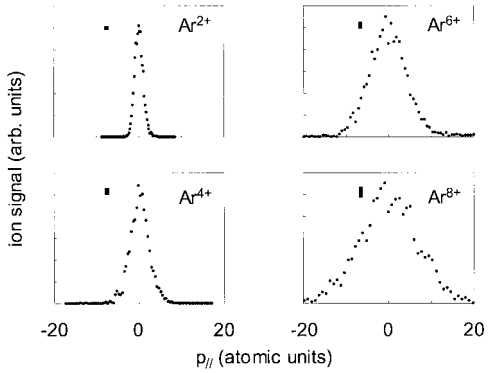

Fig. 1. Measured momentum distributions of Ar^{q+} (q = 2, 4, 6, 8) along light polarization direction. The vertical bars represent the magnitude of the experimental uncertainties at the top of the peak.

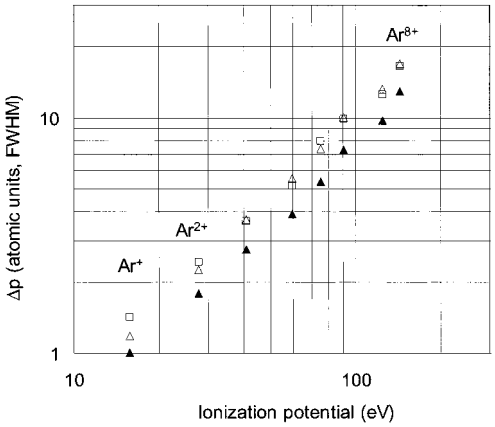

Fig. 2. Experimental and calculated widths of momentum distributions as a function of ionization potential. (□: experimental results, ▲: calculation employing ADK model. △: calculation employing improved rate at top of barrier.[3])

References

1) L. V. Keldysh: Zh. Eksp. Teor. Fiz. **47**, 1945 (1964); Sov. Phys. JETP **20**, 1307 (1965).
2) M. V. Ammosov, N. B. Delone, and V. P. Krainov: Zh. Eksp. Teor. Fiz. **91**, 2008 (1986); Sov. Phys. JETP **64**, 1191 (1986).
3) X. M. Tong and C. D. Lin: J. Phys. B **38**, 2593 (2005).

Space-charge shift in motional resonance of Ca^+ by simultaneously trapped molecular ions in a linear Paul trap

K. Okada,[*1] M. Wada, T. Takayanagi,[*1] T. Nakamura,[*2] I. Katayama,[*2] and S. Ohtani[*3]

An ion trap connected to an rf ion guide is used to accumulate an unstable ion beam in order to study the Bohr-Weisskopf effect of unstable alkaline earth ions.[1] In the initial stage of the experiment, buffer-gas cooling is applied as a simple and universal method of accumulating and cooling unstable ions which are injected from the ion guide. In such an experiment, it is important to know how many ions are trapped and how the ion cloud behaves in the ion trap.

In this short report, we present a new method of estimating the number of buffer-gas-cooled *invisible* molecular ions through laser-induced fluorescence (LIF) of simultaneously trapped *visible* Ca^+ ions. The systematic shift in the secular motion frequency of Ca^+ was measured as a function of the production time of molecular ions. The number of molecular ions was evaluated from the frequency shift using a newly developed simple pesudopotential model.

For a systematic measurement of the space-charge shift in the secular motion resonance of the Ca^+ ions, molecular ions were prepared by the succesive chemical reactions, $Ca^{+*} + O_2 \rightarrow CaO^+ + O$ and $CaO^+ + H_2 \rightarrow CaOH^+ + H$, where these reactions are triggered by the laser excitation of Ca^+ to the $3d\ ^2D_J$ state. The details of the experimental setup and the procedure are described elsewhere.[2,3] An important point is that the final products are $CaOH^+$ ions and the relative number of molecular ions can be controlled simply by turning the lasers on and off.

As shown in Fig. 1, we systematically measured the shift of the secular motion of Ca^+ ions as a function of the $Ca^{+*} + O_2$ reaction time to determine the dependence on the number of molecular ions. Since the shift in Fig. 1 is considered to be caused by the space-charge of simultaneously trapped molecular ions, the number of molecular ions can be estimated *nondestructively*.

To convert the space charge shift to the number of molecular ions produced, a simple pseudopotential model has been developed, the details of which will be pubulished elsewhere.[3] The secular frequency shifted by the space-charge potential is given by

$$\omega_{\rm obs} \cong \sqrt{\frac{k'_{x,y} - 2eaN_{\rm ion}}{m}}, \qquad (1)$$

where m and $N_{\rm ion}$ are the mass of Ca^+ ions and the total number of trapped molecular ions, respectively.

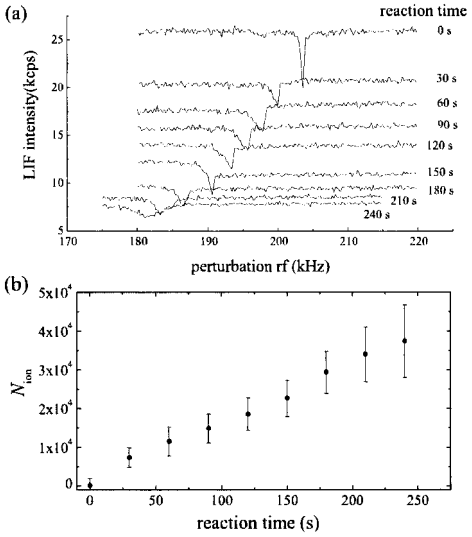

Fig. 1. (a) Sequential measurement of secular motion resonance of trapped Ca^+ ions as functions of $Ca^{+*} + O_2$ reaction time. (b) Evaluated number of molecular ions obtained from the frequency shifts in (a).

$k'_{x,y}$ is the radial trapping force constant for Ca^+. The space charge factor a can be determined by the least-squares fit of the calculated space-charge potential of molecular ions near the central region when the charge density distribution of the ions is assumed to be a Gaussian function.[3] Using Eq. (1), the number of molecular ions $N_{\rm ion}$ can be estimated. This equation is always applicable when the weak coupling condition is satisfied,[4] i.e., $|m_1 - m_2|/m_2 \gg |c/k_1|$ and $k_1 \gg |c|$, where m_1 and m_2 represent the masses of the two species of trapped ions. k_1 and c represent a trapping force constant for m_1 and the repelling force constant between two species of ions, respectively.

The space-charge potential of the trapped molecular ions can be numerically calculated using experimental values of $\omega_{x,y,z}$ and $T_{\rm ion}$. As shown in Fig. 1 (b), the shift of the Ca^+ spectra is converted to the number of trapped molecular ions. This new method can be applied for various partner ions in principle, as long as the weak coupling condition is satisfied between probe atomic ions and invisible ions.

*1 Department of Physics, Sophia University
*2 Institute for Particle and Nuclear Studies, High Energy Accelerator Research Organization
*3 Institute for Laser Science, University of Electro-Communications

References

1) M. Wada et al.: RIKEN Rev., No.31, 56 (2000).
2) K. Okada et al.: J. Phys. B **36**, 33 (2003).
3) K. Okada et al.: Jpn. J. Appl. Phys. **45**, 951 (2006).
4) K. Jungmann et al.: Phys. Rev. A **36**, 3451 (1987).

Excitation spectrum of Al atoms in He II

T. Itou,[*1] T. Furukawa,[*2] Y. Matsuo, A. Hatakeyama,[*3] T. Kobayashi, Y. Ota,[*1]
H. Odashima,[*1] and T. Shimoda[*2]

Superfluid helium (He II) is expected to be a suitable medium for instantly trapping atoms and ions of high kinetic energy. We are planning to measure the nuclear moments of atoms with unstable nuclei trapped in He II by the laser spectroscopic method.[1)] Atoms in He II show a large shift and broadening of their atomic excitation spectra, whereas the shift and broadening are relatively small in the emission stage, because implanted atoms reside in bubble-like cavities (He bubble).[2)] Taking advantage of this unique property, the optical pumping method, which has been achieved only for alkaline and alkali-like atoms to date, may be applicable to various atoms. The aluminium atom is important in nuclear physics because of the proton halo structure suggested from a recent study of proton-rich nuclei of Al. To achieve an efficient optical pumping, the wavelength of the laser should be at the peak position of the excitation spectrum in He II where absorption efficiency is maximum. However, a previously reported peak wavelength had large experimental uncertainties because the laser power correction was not sufficient.[3)] In this paper, we report laser-induced fluorescence (LIF) spectra of Al atoms obtained by removing the effect of excitation laser power dependence on its wavelength.

The experimental setup is shown in Fig. 1. The apparatus consisted of a cryostat chamber (Oxford) with quartz windows, a detection system, and three lasers. The bottom part of the cryostat contained liquid He. An open-top quartz cell ($70 \times 70 \times 70\,\mathrm{mm}^3$) was placed above the liquid surface and was filled with He II by transferring liquid He utilizing the fountain effect of He II. An Al sample held about 1 cm above the quartz cell was ablated with an output of the third harmonic generation of a Nd:YAG laser through one of the windows. Then, Al clusters produced by laser ablation were dissociated to disperse Al atoms in He II by the second harmonic output of another Nd:YAG laser. The implanted Al atoms whose densities are about 10^8–$10^{10}\,\mathrm{cm}^{-3}$ in He II were excited from the ground $^2P_{1/2}$ state to the $^2S_{1/2}$ excited state with a pulsed dye laser. Operating a variable ND-filter manually, the dye laser power was maintained weak and constant (approximately $0.1\,\mu$J/pulse). Thus, the implanted clusters were not dissociated any further, and LIF intensity is free from the effect of laser power. Emitted photons were collected with a photomultiplier tube (PMT) through a monochromator fixed at an Al emission wavelength of 397 nm, and the obtained signal was sent to a PC.

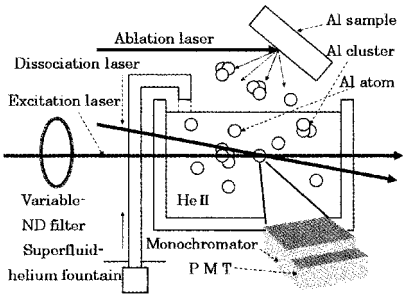

Fig. 1. Experimental setup.

Figure 2 shows an excitation spectrum of Al in He II. LIF intensity observed at 397 nm is plotted against excitation laser wavelengths from 345 nm to 370 nm. The peak position and width of the excitation spectrum are 354 nm and about 11 nm, respectively. The peak wavelength is found to be 4 nm shorter than that previously reported in Ref. 3. We are planning to apply the optical pumping method to Al atoms at the peak wavelength obtained in this experiment, and to measure the nuclear moments of proton-rich nuclei of Al.

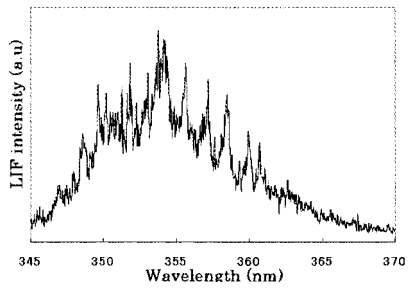

Fig. 2. Excitation spectrum of Al atom in He II. The large intensity variation in the spectrum is mainly caused by the fluctuation of the number of atoms implanted by laser ablation.

[*1] Department of Physics, Graduate School of Science and Technology, Meiji University
[*2] Department of Physics, Graduate School of Science, Osaka University
[*3] Institute of Physics, Graduate School of Arts and Sciences, The University of Tokyo

References

1) T. Furukawa et al.: RIKEN Accel. Prog. Rep. **38**, 99 (2005).
2) B. Tabbert, H. Günther, and G. zu Putlitz: J. Low Temp. Phys. **109**, 653 (1997).
3) Q. Hui, J. L. Persson, J. H. M. Beijersbergen, and M. Takami: Z. Phys. B **98**, 353 (1995).

Hyperfine-structure spectroscopy of stable ^{133}Cs atoms in He II

T. Furukawa,[*1] Y. Matsuo, A. Hatakeyama,[*2] T. Ito,[*3] Y. Ota,[*3] Y. Fukuyama,[*4]
T. Kobayashi, and T. Shimoda[*1]

We have been studying the hyperfine structures of impurity atoms in superfluid helium (He II) with the aim of establishing a versatile method for determining the nuclear moments of unstable nuclei.[1)] The atoms implanted in He II have a broadened absorption line spectrum ($\geq$ 10 nm) and a long spin relaxation time despite the broadened line.[2)] The broadened line spectrum is very promising for pumping various atomic species not only alkali atoms but also nonalkalis such as Al and Mg, because the broadened spectrum covers all of complicatedly split lines in many cases. Furthermore, the long spin relaxation time of Cs atoms in He II ($\geq$ 2 s) has been confirmed experimentally.[3)] Those phenomena suggest that He II is a suitable medium for measuring the hyperfine structure of an impurity atom, and for determining the nuclear moments from the hyperfine structure. We now report the measurement of a previously reported hyperfine transition in the ground state of Cs atoms ($|F\rangle : |4\rangle \rightarrow |3\rangle$) immersed in He II by the double resonance method[4)] to check our experimental system.

The double resonance method is based on the fact that the laser-induced fluorescence (LIF) intensity I observed with the irradiation of circularly polarized "pumping" light, tuned to the wavelength of the $D1$ excitation line of Cs atoms in He II, is related to the polarization of Cs atoms as

$$I \propto N_{\mathrm{Cs}} \times (1 - P_l \times P_z), \qquad (1)$$

where N_{Cs} is the number of Cs atoms, P_l is the polarization of pumping laser light, and P_{z} is the electronic spin polarization of the atoms.[5,6)] The details of the method are as follows. At the beginning of the measurement, Cs atoms are laser-sputtered and introduced into the optical detection region in He II where the pumping laser light and the microwave for hyperfine transition are both irradiated continuously.[3)] Next, the introduced Cs atoms are optically pumped and polarized by the irradiation of circularly polarized pumping laser light, then LIF intensity is decreased during a period shorter than 1 ms. Note that, if the hyperfine transition occurs on resonance, the polarized atoms are depolarized and LIF intensity increases compared with the off resonant case. Before and after the optical pumping, the linearly polarized pumping laser is irradiated to check the number of Cs atoms because LIF intensity with the linearly polarized laser light is related only to the number of Cs atoms deduced from Eq. (1). By sweeping the microwave frequency, we can search for hyperfine transition to determine hyperfine splitting energy. It should be noted that each of the hyperfine levels splits into Zeeman sublevels owing to an external magnetic field. Because of this effect, the different transition frequencies of $|F, m_F\rangle : |4, +4\rangle \rightarrow |3, +3\rangle$ and $|4, -4\rangle \rightarrow |3, -3\rangle$ are measured with the σ^+ and σ^- pumping lasers, respectively. Nonperturbed hyperfine splitting energy is obtained as an average of two resonant frequencies.[7)]

Figure 1 shows LIF intensity as a function of microwave frequency. With simple Lorentzian fittings, the resonant frequencies are determined preliminarily to be 9.25773(1) GHz in σ^+ pumping and 9.24352(1) GHz in σ^- pumping. Thus, the hyperfine coupling constant A of ^{133}Cs atoms immersed in He II is preliminarily determined as 2.312655(5) GHz, which is consistent with previous data[4)] and the error is 20 times smaller than the previous data. This value is slightly larger ($\simeq$0.6%) than that in vacuum, probably owing to the effects of He II pressure. The obtained narrow resonance line width of approximately 150 kHz and the resonant frequency close to that in vacuum (0.6% difference) are suitable for measuring nuclear moments within an uncertainty of 1% required for investigating the nuclear structure. Note that it is conceivable that there is no difference in the size of isotope atoms compressed in He II. To confirm this, we will next measure the hyperfine structures of ^{85,87}Rb isotopes.

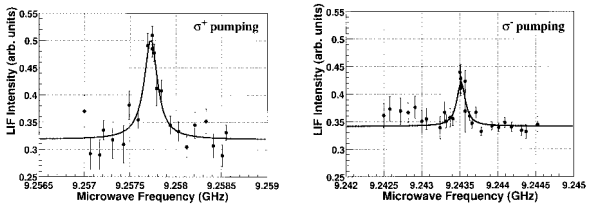

Fig. 1. Measured hyperfine transitions with σ^+ (left) and σ^-(right) pumping.

References

1) T. Furukawa et al.: Ann. Rep. (Osaka University Laboratory of Nuclear Studies) 27 (2002).
2) B. Tabbert, H. Günther, and G. zu Putlitz: J. Low Temp. Phys. **109**, 653 (1997).
3) T. Furukawa et al.: Phys. Rev. Lett. **96**, 095301 (2006).
4) Y. Takahashi et al.: Z. Phys. **98**, 391 (1995).
5) M. Arndt et al.: Phys. Rev. Lett. **74**, 1359 (1995).
6) S. Lang et al.: Phys. Rev. A **60**, 3867 (1999).
7) S. Lang et al.: Europhys. Lett. **30** (4), 233 (1995).

*1 Department of Physics, Osaka University
*2 Department of Basic Science, University of Tokyo
*3 Institute of Physics, Meiji University
*4 Spring-8

Research for acceleration of Al by Direct Plasma Injection Scheme

K. Sakakibara,[*1] M. Okamura, S. Kondrashev, H. Kashiwagi, and T. Kanesue[*2]

Linac is used in various fields, for example as a synchrotron injector, for the implantation and improvement of which is a very significant theme. However, in a low energy region between an ion source and an accelerator, space charge effect is very strong and it causes beam losses.

To resolve this, a new acceleration scheme for high-charge-state and high-intensity beam was invented. This scheme is called "Direct Plasma Injection Scheme (DPIS)." In DPIS, a laser ion source is used and connected to Radio Frequency Quadrupole (RFQ) linac directly without a beam transport line. It can prevent serious beam losses by space charge effect in Low Energy Beam Transport and possibly accelerate high-charge and high-intensity beam. We succeeded in accelerating C^{4+} (60 mA) using a CO_2 laser,[1)] and C^{6+} ions using a YAG laser.[2)]

As a new step, we will accelerate a heavier element Al using this scheme. Before the acceleration, we measured Al-laser-produced plasma properties. We also simulated the acceleration of Al using PTEQ-HI.

Figure 1 shows the experimental equipments for the Al plasma measurement. The glass laser has a wavelength of 1064 nm and its maximum energy is 4.39 J/cm^2 per shot. The laser was a courtesy of Center for Nuclear Study, Tokyo University. The spot size and pulse length are 1 cm and 40 ns, respectively. In the target chamber, the laser was focused using a convex lens (focal length: 100 mm) and was emitted to the target suspended by a supporting rod. We placed a Faraday cup (aperture 10 mm) and measured the total current of the plasma. An electrostatic analyzer was used to obtain charge distribution and signals were detected by a secondary electron multiplier (SEM).

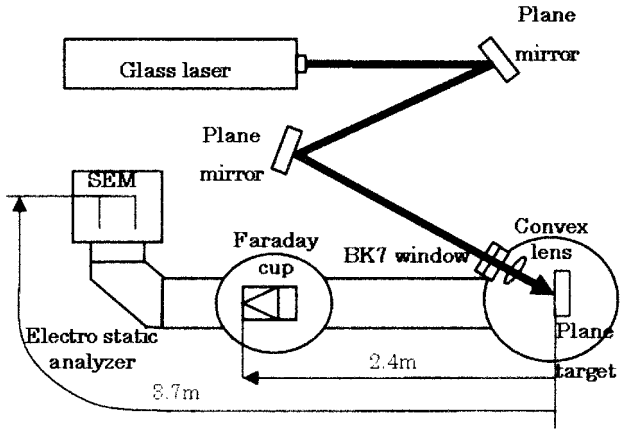

Fig. 1. Experimental setup.

We obtained Al plasma current and charge state distribution and were able to determine the number of ions produced in each charge state. We also did the simulation of Al ion acceleration. The simulation study was done using a multispecies beam tracking cord, PTEQ-HI, in the RFQ. Al^{9+} was selected as the target ion of acceleration. The beam current, including multiple charge states which will be injected to the RFQ can be estimated from the ion property. The acceleration performance of the Al^{9+} beam was investigated. In the simulation, we assumed that Al plasma included only Al^{6+} ~Al^{9+}. The total percentage of the simulated currents corresponded to 83.4% of all the currents of the measured plasma. The initial parameters are listed in Table 1.

The operating frequency and the extraction energy were 100 MHz and 100 keV/amu, respectively. The RF voltage was set to the design value of the RFQ for accelerating C^{4+} beam. The numbers of particles in the simulation are 3000 for Al^{9+} and 1500 for other charge states. We counted the particles which had more than 40% energy shift with respect to the synchronous particle as lost particles.

The result of the simulation shows that the expected current of Al^{9+} is about 42 mA (61.4% survive). Some portions of the Al^{8+}, Al^{7+} and Al^{6+} ions will be also accelerated. The simulated currents at the end of the RFQ were 54 mA (41.3%), 31.9 mA (24.1%) and 4.7 mA (8.8%).

The contents of the Al plasma induced by the glass laser were measured and we simulated the acceleration performance of the Al beam using our new RFQ. According to the simulation, 42 mA of Al^{9+} will be accelerated.

We will try heavier species up to gold this year to establish the DPIS as an intense heavy-ion production method.

Table 1. Initial parameter for PTEQ-HI.

Main particle	Al^{+9}
Injection beam current	68 mA
Injection energy	540 keV (total)

References
1) M. Okamura et al.: Laser Part. Beams **20**, 451 (2002).
2) H. Kashiwagi et al.: Rev. Sci. Instrum. **75**, 1569 (2004).

*1 Tokyo Institute of Technology
*2 Kyushu University

Shot-to-shot stability of ion generation by solid-state laser

T. Kanesue,[*1] S. Kondrashev,[*2] M. Okamura, and K. Sakakibara[*3]

To obtain higher-intensity highly charged heavy-ion beams, we are developing a new combination of the Laser Ion Source (LIS) and RFQ linac, the Direct Plasma Injection Scheme.[1)] We plan to accelerate ion species heavier than carbon this year. Previously, the ion yield from C, Al, Ti, Fe, Ge, Nb and Ta targets was measured. The main results obtained are presented in Ref. 2.

In this paper, we describe the shot-to-shot stability of ion yield generated by the solid-state Nd-glass laser: 3 J/30 ns, B. M. Industries model 511 DNS13 (courtesy of the Center for Nuclear Study, University of Tokyo).

A movable target was placed inside a vacuum chamber with a residual gas pressure of about 10^{-6} Torr. The use of a 3D manipulator enabled us to move the target with a minimal step of about 10 μm. A laser beam was focused on the target surface by a convex lens with a 100 mm focal length at an incident angle of about 30° from the target normal axis. A detailed description of the experimental setup is presented in Ref. 3.

The following procedure was applied to determine the best target position for the generation of the highest charge states for all elements: the target was moved along the direction normal to the surface in 0.25 mm steps and total ion current was measured using a Faraday cup (FC) for each target position. The target position with the maximal measured current and fastest arrival of ions to the FC was chosen for highly charged ion generation. The Al case is shown in Fig. 1. In this case, −2 mm was chosen as the best target position.

All the other elements tested have shown similar behaviors. After defining the target position as described above, the charge state and energy distributions of ions were measured. It was confirmed that the target position determined as described above provides the highest yield of highly charged ions.

To check the shot-to-shot stability of ion yield generation, ion current was measured for 5 laser shots at different spots with enough steps to use a fresh target surface and 5 shots at the same spot for 6 elements: Al, Fe, Ti, Ge, Nb, Ta.

The shot-to-shot stabilities in the case of different spots for Al, Fe, Ti, Ge, Nb and Ta targets were ±3%, ±5%, ±19%, ±19%, ±20% and ±16%, respectively, from the average FC peak current.

Typical FC signals are shown in Fig. 2 for the Al target in the case of the same spot laser shot. All 6 elements have shown similar tendencies: the first shot always produced the highest current and then current gradually decreased. Drastic changes were observed in the cases of Al, Fe, Ti and Ge targets: currents were reduced to 23%, 13%, 28% and 18%, respectively, of the first-shot current even in the second shot and remained small to the same extent in all subsequent shots. In the case of Nb and Ta targets, the changed second-shot currents were 77% and 97% of the first-shot current. It also gradually decreased. The smallest currents were 33% of the first shot in the fourth shot in the case of the Nb target, and 67% in the fifth shot in the case of the Ta target.

Al and Fe had stabilities below 5% on the fresh surface. Ge, Nb and Ta signals were more sensitive; they easily change by about ±20% even on the fresh surface.

It is important that the first laser shot onto the fresh target surface always provides the highest ion yield at the same target spot. For this reason, the target should be moved between laser shots to hit a fresh target surface. Such an approach will provide the highest and most stable ion yield.

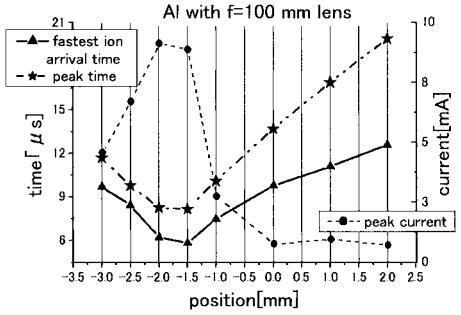

Fig. 1. The curves are for ion group arrival time, peak time, and FC peak current.

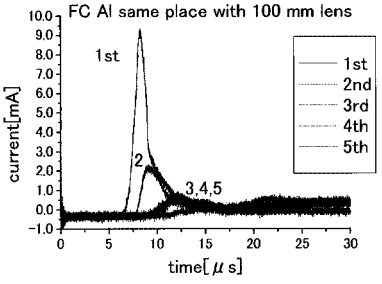

Fig. 2. FC signals (5 shots at the same spot).

*1 Department of Energy Science and Engineering, Kyushu University
*2 Institute of Theoretical and Experimental Physics, Russia
*3 Department of Energy Sciences, Tokyo Institute of Technology

References

1) T. Takeuchi et al.: Rev. Sci. Instrum. **73**, 764 (2002).
2) S. Kondrashev et al.: RIKEN Accel. Prog. Rep. **39**, 268 (2006).
3) K. Sakakibara et al.: RIKEN Accel. Prog. Rep. **39**, 105 (2006).

μSR study of magnetic property of α-$(BETS)_2I_3$

S. Ohira, R. Kato, N. Tajima, K. Hiraki,* and T. Takahashi*

Recently, many interesting physical properties of various organic conductors have been reported. The relationship between their magnetism and electric conductivity is now drawing much attention. α-$(BETS)_2I_3$ is an organic conductor having a quasi-2D layered structure. This salt exhibits a metal-insulator (MI) transition at $T_{MI} = 50$ K.[1,2] Below T_{MI}, ^{77}Se NMR[3] and magnetic susceptibility measurements showed a nonmagnetic state, while the observed magnetotransport suggests the existence of strong magnetic interactions at low temperatures with a large negative magnetoresistance under an external field applied perpendicular to the conducting layer.[4] Therefore, the magnetic state of this salt has not been clarified yet. We investigated the magnetic state of this material below T_{MI} by the μSR method. 60 mg of polycrystalline sample was packed in a silver foil and fixed on the sample holder of the cryostat. The experiment was carried out at the RIKEN-RAL Muon Facility in the Rutherford Appleton Laboratory.

In the ZF-μSR time spectra, the muon spin relaxation due to nuclear dipole fields was observed down to 1.8 K. The spectra are fitted with the relaxation function, $A(t) = A\exp[-(\lambda t)^{\beta}]$, where λ is the muon spin relaxation rate describing dynamical fluctuations and β is the exponent. The temperature dependences of λ and β are shown in Fig. 1. We note that λ starts to increase at $T_{MI} = 50$ K with decreasing temperature. This behavior is significantly different from magnetic transition, where λ should show a cusp. A similar temperature dependence is observed in some spin-singlet materials.[5,6] It has been suggested that thermally activated excitations across the magnetic gap are responsible for the relaxation. Therefore, our result indicates the nonmagnetic state below T_{MI}.

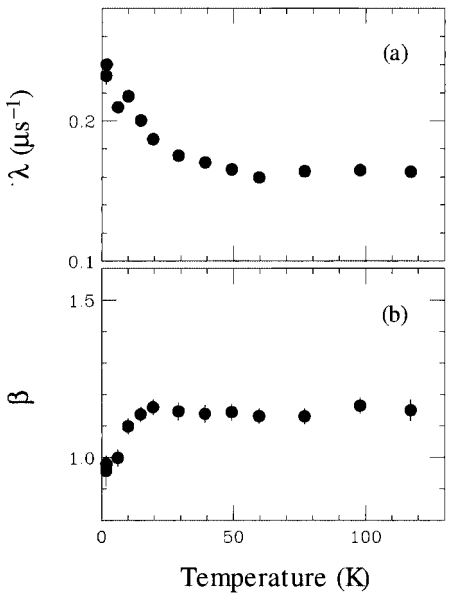

Fig. 1. Temperature dependences of (a) relaxation rate λ and (b) exponent β.

Another noteworthy change is observed in the temperature dependence of β at about 20 K. β shows a constant value ~1.2 above 20 K. At lower temperatures, however, it approaches 1, namely, the time spectra show an exponential relaxation. This suggests that another dynamical contribution to the muon spin relaxation appears below 20 K, as well as in another spin-singlet organic material.[6] This change is more clearly observed in the longitudinal-field (LF) μSR measurement. The amplitude of the dynamical component increases below 20 K, as shown in Fig. 2. The relaxation mechanism below ~20 K is expected to be different from that in the higher-temperature region. We consider that dilute defect spins, existing naturally or resulting from the implantation of the muon, provide an additional dynamical component. The existence of magnetic interactions as suggested by the magnetotransport measurement is also conceivable.

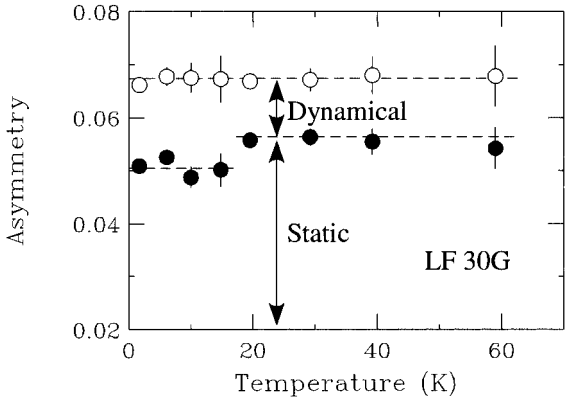

Fig. 2. Temperature dependence of amplitudes of dynamical and static components in the LF-μSR measurement at 30 G.

References

1) M. Inokuchi et al.: Bull. Chem. Soc. Jpn. **68**, 547 (1995).
2) N. Tajima et al.: J. Phys. Soc. Jpn. **69**, 543 (2000).
3) K. Hiraki et al.: Meeting Abstracts of Phys. Soc. Jpn. **59**, Issue 1, Part 4, 829 (2004).
4) N. Tajima et al.: Synth. Met. **86**, 1981 (1997).
5) S. J. Blundell et al.: J. Phys., Condens. Matter **9**, L119 (1997).
6) S. Ohira et al.: Physica B, in press.

* Department of Physics, Gakushuin University

Preparation of Th target for heavy element studies with GARIS

H. Haba, D. Kaji, T. Takabe,[*1] and H. Kikunaga[*2]

We plan to study the chemical properties of superheavy elements (SHEs) with atomic number $Z \geq 104$ by developing the gas-jet transport system coupled to the gas-filled recoil separator GARIS at the RIKEN Linear Accelerator Facility (RILAC).[1] SHE nuclides for the chemical experiments have been produced by heavy-ion induced fusion reactions on actinide targets such as ^{238}U, ^{248}Cm, and ^{249}Bk. Because of the extremely low production yields of SHEs, stable targets are desired for high-intensity heavy-ion bombardments for beam times of long duration. Thus, the actinide targets in oxide form have been prepared by electrodeposition from organic solutions (molecular-plating method). Recently, multitarget devices mounted on a rotating wheel have been developed to prevent the excessive heating of a stationary target.[2,3] However, it is still hard to prepare a large and uniform target layer by electrodeposition.

Using the GARIS and gas-jet transport system, we will first intend to study the chemical properties of elements 106 (Sg) and 108 (Hs). For this purpose, experiments searching for ^{265}Sg and ^{269}Hs using the ^{232}Th(^{40}Ar, $\alpha 3n$)^{265}Sg and ^{232}Th(^{40}Ar,$3n$)^{269}Hs reactions are in progress,[4] because high-intensity ^{40}Ar beams up to 10 particle μA (pμA) are expected at RILAC. Here, we report a technical development for preparing a large and uniform ThO_2 target by electrodeposition for irradiations using a rotating target system of GARIS.

Figure 1 shows a schematic view of the newly developed cell for electrodeposition. A Ti backing foil of 2.8 μm thickness placed on the water-cooled Ti block was used as the cathode, whereas a Pt plate of 0.1 mm thickness on another Ti block was used as the anode. A Teflon spacer perforated in the shape of a banana and of 10 mm thickness was sandwiched by the electrodes sealed using silicon rubbers perforated in the same banana shape and of 1 mm thickness. The active target area of 7.85 cm^2 is more than two times larger than those used in the previous Dubna and GSI experiments.[2,3]

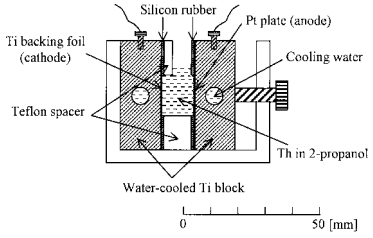

Fig. 1. Schematic view of cell for electrodeposition.

Five microliters of 0.01 M HNO_3 containing 2.7 mg of Th was mixed with 10 mL of 2-propanol, and the mixture was filled into the cell as shown in Fig. 1. Electrodeposition was carried out by applying a voltage of 600 V with current densities from 2 to 6 mA cm^{-2} for 20 min. During the electrodeposition, the Ti blocks were water-cooled at 10°C. After the electrodeposition, the target was heated in an electric furnace at 350°C for 20 min to obtain ThO_2. The target thickness of 320 ± 30 μg cm^{-2} averaged for the 16 targets was determined by α spectrometry on ^{232}Th. The deposition yield was not less than 90%. The uniformity of the target was investigated using the imaging plate Fujifilm BAS-MS 2325. The target densities are shown in Fig. 2 for each 1.0 mm × 1.0 mm pixel. Deviations in the target density are less than 8% except for the 2 mm outer edge of the target.

The 16 Th targets were arranged on the rotating wheel of 30 cm diameter and were irradiated by the 222.5 MeV ^{40}Ar beam (total dose of 1.3×10^{18} ions with beam currents up to 2 pμA).[4] The target wheel was rotated during the irradiation at 3000 rpm and cooled with He gas filled in GARIS at a pressure of 88 Pa. No damages or losses of the target material were observed after the irradiation on the basis of α spectrometry. In the near future, we will develop rotating U_3O_8 targets to study possible production of ^{283}112 for chemical studies of element 112 using the ^{238}U(^{48}Ca,$3n$)^{283}112 reaction.

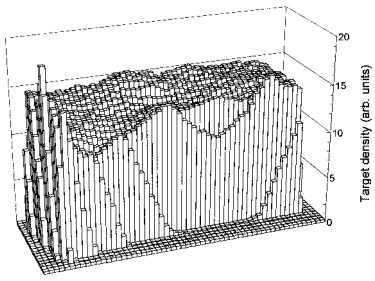

Fig. 2. Density distribution of Th target for each 1.0 mm × 1.0 mm pixel.

*1 Graduate School of Science, Osaka University
*2 Faculty of Science, Kanazawa University

References
1) H. Haba et al.: RIKEN Accel. Prog. Rep. **38**, 103 (2005).
2) Yu. V. Lobanov et al.: Nucl. Instrum. Methods Phys. Res. A **397**, 26 (1997).
3) K. Eberhardt et al.: Nucl. Instrum. Methods Phys. Res. A **521**, 208 (2004).
4) D. Kaji et al.: RIKEN Accel. Prog. Rep. **39**, 110 (2006).

Search for superheavy-element nuclides for chemical studies using ^{232}Th+^{40}Ar reaction

D. Kaji, H. Haba, K. Morimoto, T. Akiyama,[*1] K. Morita, N. Sato,[*2] T. Takabe,[*3] and A. Shinohara[*3]

Long-lived superheavy-element (SHE) nuclides for chemical studies were searched for in the ^{232}Th+^{40}Ar reaction using the gas-filled recoil separator (GARIS) at RIKEN. SHE nuclides near deformed shells of Z=108 and N=162 are of special interest. These nuclides have been reported as reaction products from ^{238}U- and ^{248}Cm-based reactions, such as ^{238}U(^{34}S,5n)^{267}Hs,[1] ^{248}Cm(^{22}Ne,xn)$^{266,\ 265}$Sg [x=4, 5][2] and ^{248}Cm(^{26}Mg,xn)$^{270,\ 269}$Hs [x=4, 5],[3] or decay products of ^{277}112 produced by the ^{208}Pb(^{70}Zn,n) reaction.[4] In this work, the ^{232}Th+^{40}Ar reaction is considered to be a candidate reaction that produces SHE nuclides. In this reaction, it is interesting from the reaction mechanism viewpoint whether the (HI,αxn) enhancement of the production cross section as described in Ref. 5 is observed or not.

The ^{232}ThO$_2$ target was irradiated with an ^{40}Ar^{11+} beam at two beam energies of 4.97 and 5.18 MeV/nucleon corresponding to excitation energies of 39.1 and 46.3 MeV, respectively. Excitation energy is deduced using the mass formula of KUTY.[6] The former beam energy was set to search for ^{232}Th(^{40}Ar,4n)^{268}Hs or ^{232}Th(^{40}Ar,αxn)$^{266,\ 265}$Sg [x=2, 3], and the latter was for ^{232}Th(^{40}Ar,5n)^{267}Hs or ^{232}Th(^{40}Ar,α3n)^{265}Sg. The ambiguity of the absolute beam energy was $\pm$0.3 MeV. The typical beam intensity on the target was 1.0 particle μA. The target was prepared by the electrodeposition of ^{232}Th onto a titanium backing foil of 2.8 μm thickness. Details of the target preparation are given in Ref. 7. Sixteen targets were mounted on a rotating wheel of 30 cm diameter. The wheel was rotated at 3000 rpm during the irradiation. The average thickness of each ^{232}Th layer was 320$\pm$30 μg/cm^2. Evaporation residues (ERs) recoiling out of the target were separated in-flight from the other charged particles, such as beam particles and target recoils by the GARIS. After passing two time-of-flight (TOF) pickups, the ERs were implanted into a position-sensitive silicon detector, where their decays were measured. The separator was filled with a helium gas at 86 Pa. The magnetic rigidity $B\rho$ in the measurement of the ERs was set to 2.04 Tm, which is estimated using our empirical formula.[8]

The target was irradiated with ^{40}Ar at doses of 3.0×10^{17} and 1.16×10^{18} at beam energies of 4.97 and 5.18 MeV/nucleon, respectively. No candidate α-decay and spontaneous fission (SF) decay due to the production of $^{267,\ 268}$Hs and $^{265,\ 266}$Sg were observed. The two-fold and three-fold correlation analyses of ER-α_1/SF and ER-α_1-α_2/SF were performed under the following conditions: ER-kinetic energy gate of 5 $\leq E_{ER} \leq$25 MeV, α-energy gate of 7 $\leq E_\alpha \leq$12 MeV, SF-energy gate of $E_{SF} \geq$ 50 MeV, position gate of $\Delta P \leq$2.0 mm and time gate of $\Delta\tau \leq$1000 sec. The 1-σ upper limit (confidence level=68%) of the cross section in each reaction is estimated to be 31 pb for ^{268}Hs, 185 pb for $^{266,\ 265}$Sg at 4.97 MeV/nucleon, and 8 pb for ^{267}Hs and 48 pb for ^{265}Sg at 5.18 MeV/nucleon, where the transmission efficiencies of the GARIS for xn and αxn emissions are estimated to be 24% and 4%, respectively. Transmission efficiency is deduced by taking the angular distribution of residual nuclei produced in each reaction, the multiple scattering of recoil ions with helium atoms and the geometrical transmission of TOF detectors into account. The transmission in αxn emission is smaller than that in xn emission, because the angular distribution is not forward-peaked but is side-peaked due to the large recoil effect induced by α-emission.

We will continue to search for SHE nuclides for chemical studies using the ^{232}Th+^{40}Ar reaction. In particular, the production of ^{269}Hs produced via ^{232}Th(^{40}Ar,3n) is interesting.

References

1) Yu. A. Lazarev et al.: Phys. Rev. Lett. **75**, 1903 (1995).
2) Yu. A. Lazarev et al.: Phys. Rev. Lett. **73**, 624 (1994); M. Schädel et al.: Nature **388**, 55 (1997); A. Türler et al.: Phys. Rev. C **57**, 1648 (1998).
3) Ch. E. Düllmann et al.: Nature **418**, 859 (2002); A. Türler et al.: Eur. Phys. J. A **17**, 505 (2003).
4) S. Hofmann et al.: Z. Phys. A **354**, 229 (1996); S. Hofmann et al.: Eur. Phys. J. A **14**, 147 (2002).
5) T. Nomura et al.: Proc. Int. Symp. on Heavy Ion Physics and Its Application, Lanzhaou, China, 1990-10 (World Scientific, Singapore, 1991), p. 349; T. Nomura et al.: Proc. Int. Symp. on Structure and Reactions of Unstable Nuclei, Niigata, 1991-6 (World Scientific, Singapore, 1992), p. 310.
6) H. Koura et al.: Nucl. Phys. A **674**, 47 (2000).
7) H. Haba et al.: RIKEN Accel. Prog. Rep. **39**, 109 (2006).
8) D. Kaji et al.: RIKEN Accel. Prog. Rep. **36**, 88 (2003); D. Kaji: Doctoral Dissertation, Niigata University, (2003).

[*1] Department of Physics, Saitama University
[*2] Department of Physics, Tohoku University
[*3] Department of Chemistry, Graduate School of Science, Osaka University

Development of online solvent extraction system using microchip

D. Saika,* Y. Kitamoto,* K. Matsuo,* Y. Tashiro,* T. Takabe,* T. Yoshimura,* W. Sato,* N. Takahashi,* H. Haba, S. Enomoto, and A. Shinohara*

We have developed a rapid reaction and measuring system for studying the chemical properties of heavy and trans-actinide elements. Their half-lives are so short that it is difficult to study their chemical behaviors by a conventional method. To overcome the difficulty, we used a microchip for solvent extraction. A microchip is a reactor vessel made of glass or plastics with etched channels of dozens to hundreds micrometers in width. Because molecules diffuse more rapidly in such a small vessel than in an ordinary vessel of a cm size, a diffusion-limited reaction can achieve equilibrium very rapidly in a microchip.[1] Here, we show the results of solvent extraction using a microchip for lanthanide elements as a simulation of actinides.

At first, we determined the time for the extraction of lanthanide radiotracers to reach equilibrium using TTA (thenoyl-trifluoroacetone) as a ligand. We used 0.1 M acetate buffer solution containing ^{153}Gd, ^{139}Ce, ^{88}Y, and ^{170}Tm as aqueous phase, and 0.044 M TTA-toluene solution as organic phase. Each solution was infused into the microchip using syringe pumps, and solvent reactions occurred during their contact at the liquid interface. We can vary their contact time by controlling the flow rate of syringe pumps and determined the time for the extraction of lanthanide to reach equilibrium. Their activities were measured by γ-ray spectrometry using a Ge detector and the extraction ratio D was derived using the equation $D = V_{\mathrm{aq}} \cdot A_{\mathrm{org}}/V_{\mathrm{org}} \cdot A_{\mathrm{aq}}$, where V is the volume and A is the radioactivity.

We applied the microchip method to online chemical experiments performed at RIKEN Ring Cyclotron E3b course. The $^{\mathrm{nat}}$Ta targets ($2\,\mu\mathrm{m} \times 30$ sheets) were irradiated with 135 MeV/nucleon ^{14}N ions, and many lanthanide radionuclides were produced by $^{\mathrm{nat}}$Ta (^{14}N, X) reaction. These radionuclides were transported to the hot laboratory within a few seconds by the gas-jet method,[2] and dissolved by an acetate buffer solution. This solution was infused to the microchip simultaneously with the TTA-toluene solution. Then, the radionuclides were rapidly extracted from the aqueous phase to the organic phase. It took less than 2 min to extract the species from the production of radionuclides to the measurement in this experiment.

To compare with the microchip method, we performed batch extraction. An aqueous solution containing radionuclides was mixed with TTA-toluene solution, shaken for 3 min, and separated by centrifugation.

The extraction ratios D of lanthanide elements are shown in Fig. 1. The D values of the microchip extraction method nearly correspond to those obtained by the batch extraction method. This result shows that heavier lanthanide elements are extracted more into the organic phase and the microchip method is applicable to online chemical experiments. The application is also expected for actinide elements because they have similar chemical properties to lanthanide elements.

We have confirmed that the equilibrium for the extraction of lanthanide is achieved within one second as shown in Fig. 2. These results show that the use of a microchip enables the extraction of heavy elements whose half-lives are in the order of seconds.

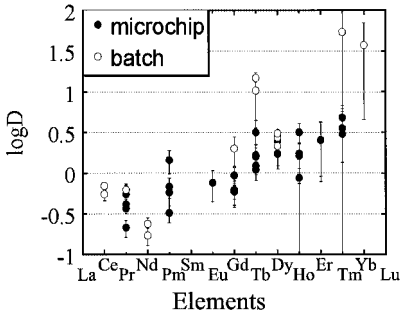

Fig. 1. Extraction ratios D of microchip and batch experiments.

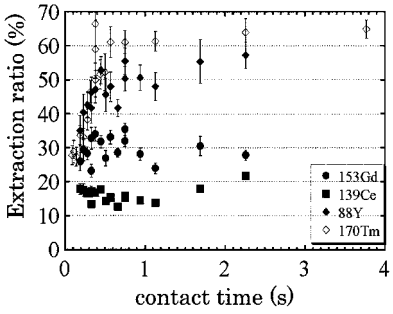

Fig. 2. Extraction rate of lanthanides using microchip.

References

1) H. Hisamoto et al.: Chem. Commun. **24**, 2662 (2001).
2) E. Stender, N. Trautmann, and G. Herrman: Radiochem. Radioanal. Lett. **42**, 291 (1980).

* Graduate School of Science, Osaka University

Development of capillary electrophoresis apparatus for heavy actinide chemistry

Y. Kitamoto,[*1] D. Saika,[*1] K. Matsuo,[*1] Y. Tashiro,[*1] T. Takabe,[*1] W. Sato,[*1] N. Takahashi,[*1] T. Yoshimura,[*1] T. Mitsugashira,[*2] H. Haba, S. Enomoto, and A. Shinohara[*1]

In the chemistry of heavy actinide and transactinide, the chemical isolation of a nuclide of interest is preferable. However, we cannot spend much time removing by-products, because of the short lifetimes of nuclides. Therefore, we need to obtain information on their chemical properties in their separation process. For this purpose, we have been developing a capillary electrophoresis (CE) system. CE enables us to separate the elements rapidly with a large number of theoretical stages. At the same time, the mobility of each element reflects their chemical properties such as the strength of metal-ligand interaction. A scheme of our system is illustrated in Fig. 1.

An analyte is typically detected by the on-capillary detection method,[1,2] because the solution volume treated by CE is limited to the order of 10 nL. However, it is quite difficult to detect heavy actinide and transactinide nuclides using this method, because we must detect α particles emitted from the analyte nuclides, which cannot penetrate through the capillary wall. Therefore, we tried to use the fraction collection method. The ion fractions coming out of the capillary are transferred into collection vials in microliters of the electrolyte solution.

The performance of CE with the fraction collecting apparatus was investigated using lanthanide multitracers and some actinide tracers. Lanthanide tracers were produced by the ^{197}Au (^{14}N, X) nuclear reaction in the E3b course of RIKEN Ring Cyclotron, irradiating ^{197}Au targets with 135 MeV/nucleon ^{14}N ions. The fused silica capillary with 60 cm in length and 75 μm i.d. was used. The applied voltage was 30 kV in positive. The analyte was hydrostatically injected into the capillary. The electrolytes were an aqueous solution of 12 mM α-HIB (α-hydroxyisobutyrate). For these experimental conditions, we followed the procedure of Quang et al.[3] Here, the pHs were adjusted to 2.98, 3.48 and 4.01. The ionic fractions transferred into collection vials were measured using Ge and Si semiconductor detectors.

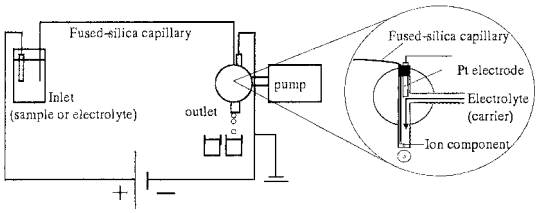

Fig. 1. Capillary electrophoresis/fraction collection apparatus for heavy actinide chemistry.

We assumed the equilibrium state of the following metal-ligand reaction as

$$M^{3+} + nL^{-} \quad \Leftrightarrow \quad [ML_n]^{(3-n)+},$$

where L is α-HIB. The mobility of the metal cations decreases with the coordination number of the ligand, because the mean charge of the complex becomes smaller.

The electrogram of each experiment is shown in Fig. 2. For every pH condition, the elements with smaller ionic radius passed through the capillary faster than those with larger ionic radius. When ionic radius is small, the surface charge is large in general. Therefore, the elements with smaller ionic radius seemed to attract ligand anions more strongly.

Also, the mobility of the elements with smaller ionic radius, which interact with ligands strongly, decreased with the increase in pH. At higher pH, the dissociation of ligand (α-HIB) is enhanced, and many metal cations form bonding with ligand anions. This is the reason why the mobility of these elements decreases with the increase in pH.

Moreover, at higher pH, the peaks become broad as a result of the interaction between metal cation and capillary wall. We are now trying to reduce this interaction treating the capillary wall.

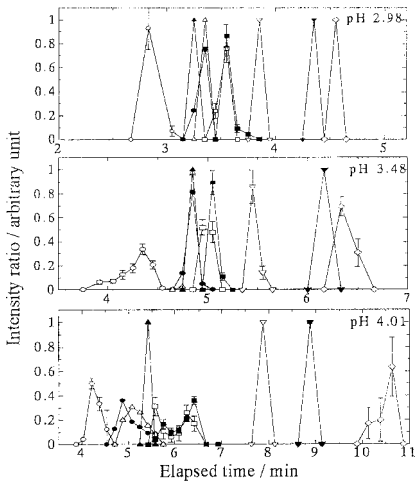

Fig. 2. Variation fo electrogram with pH values. ○: Ce, ●: Am, △: Cm, ▲: Pm, □: Eu, ■: Gd, ▽: Y, ▼: Tm, ◇: Yb.

*1 Department of Chemistry, Osaka University
*2 Institute for Materials Research, Tohoku University

References

1) P. Janos: Electrophoresis **24**, 1982 (2003).
2) S. L. Pentony et al.: Anal. Chem. **61**, 1642 (1989).
3) C. Quang et al.: J. Chromatogr. A **659**, 459 (1994).

Development of gas-jet transport system for superheavy element chemistry using the RIKEN K70 AVF Cyclotron

T. Takabe,* Y. Kitamoto,* D. Saika,* K. Matsuo,* Y. Tashiro,* T. Yoshimura,* H. Haba,* D. Kaji, and A. Shinohara*

A gas-jet transport system for superheavy element chemistry was installed at the C-03 beam line of the RIKEN K70 AVF Cyclotron. The gas-jet system has been widely used for delivering short-lived superheavy element nuclides, because its transport time is in the order of one second from the target chamber to various devices. In this work, the performance of the present system was investigated using W isotopes produced in the ^{nat}Gd(^{22}Ne,xn) reaction.

A schematic of the system is shown in Fig. 1. A ^{nat}Gd target of 0.18 mg/cm^2 thickness and 7 mm diameter was prepared by the electrodeposition onto a beryllium backing foil of 2.0 mg/cm^2 thickness. The 144-MeV ^{22}Ne^{7+} beam from the RIKEN K70 AVF Cyclotron passed through a beryllium vacuum window (1.9 mg/cm^2), a helium cooling gas (0.13 mg/cm^2), and the target backing. Finally, the beam entered the target material at 122 MeV. The average beam intensity was approximately 300 particle-nA (pnA). The reaction products recoiled out of the target were stopped in helium gas (∼90 kPa), attached to KCl aerosol particles generated by the sublimation of KCl powder, and were transported through a Teflon capillary (2.0 mm diameter, 10 m long) to the E7 irradiation room just beneath the C-03 beam line. They were collected on a glass filter (ADVANTEC GB-100R) and subjected to γ-spectrometry using an HPGe detector. In a separate experiment, all of the products recoiled out of the target were directly collected using an Al catcher foil (99.999% in purity) of 10 μm thickness placed just behind the ^{nat}Gd target. Thus, the gas-jet transport efficiency was deduced from the activities in the glass filter and Al catcher foil.

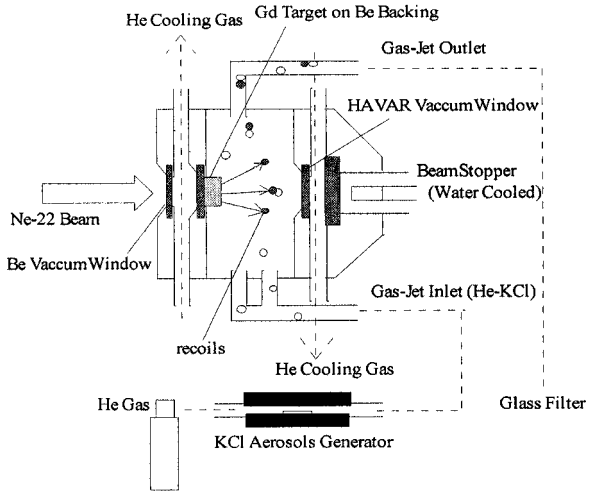

Fig. 1. Schematic of gas-jet transport system.

The optimum condition of the gas-jet system was first investigated as a function of the temperature of the KCl aerosol generator from 580°C to 640°C. It was found that the gas-jet transport efficiency increases with an increase in the temperature of the KCl aerosol generator and attains a plateau value at about 620°C. The gas-jet transport efficiency increases proportionally to the helium gas flow rate from 3 L/min to 5 L/min. Under the condition of the He-gas flow rate at 5 L/min, the inner pressure of the target chamber is almost equal to the pressure of the atmosphere. Thus, the temperature of the KCl aerosol generator of 620°C and the helium gas flow late of 4.5 L/min were determined as the optimum conditions. Under these conditions, the gas-jet transport efficiency was approximately 17%. The dependence of the gas-jet transport efficiency on beam intensity was also studied, because recently available high-intensity beams cause a serious problem in that the plasma created by these beams drastically decreases the gas-jet transport efficiency. In Fig. 2, the gas-jet transport efficiencies of ^{173}W, ^{24,25}Na, ^{28}Al, and ^{27}Mg are shown as a function of the beam intensities from 50 pnA to 300 pnA. The isotopes of ^{24,25}Na, ^{28}Al, and ^{27}Mg were produced in the interaction between the ^{22}Ne beam and the beryllium backing foil. As shown in Fig. 2, no decreasing trend of the gas-jet transport efficiency was observed up to the beam intensity of 300 pnA.

In the near future, we will perform an experiment to produce ^{255}No by the ^{238}U(^{22}Ne,5n)^{255}No reaction using the RIKEN K70 AVF Cyclotron.

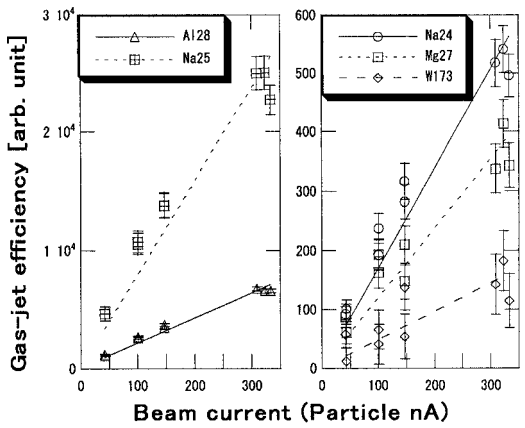

Fig. 2. Gas-jet efficiency as function of beam current.

* Department of Chemistry, Graduate School of Science, Osaka University

Distribution coefficients measured with noncarrier tracers of Zr-88 and Hf-175 on TBP resin in hydrochloric acid and nitric acid solutions

A. Yokoyama,[*1] S. Kamataki,[*2] K. Morishita,[*2] and H. Haba

Research on the chemical properties of transactinides has gathered considerable attention in spite of experimental difficulties in fulfilling several requirements for measurement such as a quick equilibration at ultralow concentration, that is, in the extreme case, one-atom-at-a-time chemistry, or in other words, single-atom chemistry.[1] Distribution coefficients of rutherfordium, Rf, in liquid-liquid systems are being investigated because of the lack of such data and contradiction between earlier data.[2]

In this study, distribution coefficients, K_{d}, of Zr and Hf that are homologues of Rf, were measured with noncarrier tracers of Zr-88 and Hf-175 on TBP resin in hydrochloric acid and nitric acid solutions in order to present data that can be compared with those of rutherfordium in a solvent extraction system and also to discuss the dependence of the properties on the concentration of the relevant chemical species and the applicability of the rutherfordium experiment.

The TBP resin that an organic solvent of tributylphosphate (TBP) was attached to, aimed at rapid chemical procedures for the rutherfordium experiment, was prepared for this study as follows. The resin was made of MCI GEL CHP20Y, Mitsubishi Chemical Corporation, a styrenedivinylbenzen copolymer of about 30 μm in particle size used as a supporting material, which was washed beforehand with methanol and acetone and dried at 110°C in a vacuum oven for 6 hours and weighed. Then, the resin was suspended in stirred methanol solution, while TBP was added in drops up to 20% of the resin in weight. After stirring and heating under an IR lamp until methanol was removed, the resin was again dried at 110°C in the vacuum oven for 6 hours and weighed.

The carrier-free radiotracers of Zr-88 and Hf-175 were produced in the ^{89}Y(p,2n) and the ^{175}Lu(p,n) reactions, respectively, using 20-MeV protons from the AVF cyclotron of Research Center for Nuclear Physics, Osaka university. In addition, multitracers from a Au target including Hf-175 and multitracers from a Ag target including Zr-88, which are very useful in cross-checking the data because the distribution coefficients are determined simultaneously for many nuclides, were produced at RIKEN. For both cases, the target material was chemically separated to produce carrier-free tracer solutions.

The batch method was applied to the measurement by using the tracers mentioned above. The TBP resin of 5 to 200 mg was placed in a polypropylene tube with a cap and 25 to 200 μL of Zr-88 and Hf-175 tracer solutions with hydrochloric acid or nitric acid were added so as to produce 3 mL of solution in total. The tube was shaken for 10 minutes, centrifuged for 3 minutes, and 1 mL aqueous solution was pipetted into another tube and assayed by γ-ray spectrometry.

In Figs. 1 and 2, it is shown that the measured values are consistent with each other as a general trend except for the Hf data at a high concentration of hydrochloric acid, and they are larger than the data in a previous report[3] at the ordinary concentration of Zr and Hf atoms by one order of magnitude although they have similar tendencies as functions of the acid concentrations of HCl and HNO_3. It was concluded that the solution system of nitric acid in the range from 6 to 8 M may be promising for the measurement of Rf due to K_d values appropriate for the measurement and the interesting discrepancy between Zr and Hf.

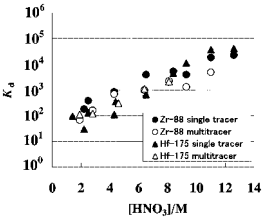

Fig. 1. Distribution coefficients of Zr and Hf (on TBP resin) in nitric acid measured with single tracers and multitracers.

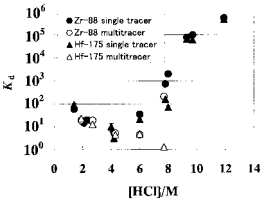

Fig. 2. Distribution coefficients of Zr and Hf (on TBP resin) in hydrochloric acid measured with single tracers and multitracers.

References

1) D. Trubert and C. Le Naour: in *The Chemistry of Superheavy Elements,* edited by M. Schädel (Kluwer Academic Publishers, Dordrecht, 2003), p. 95.
2) H. Haba, K. Tsukada, K. Akiyama, M. Asai, A. Toyoshima, Y. Ishii, S. Enomoto, and Y. Nagame: RIKEN Accel. Prog. Rep. **38**, 107 (2005).
3) M. Takaka and H. Akaiwa: in *Yobai Chushutsu Kagaku* (Shokabo, Tokyo, 2001), pp. 247, 249.

*1 Graduate School of Natural Science and Technology, Kanazawa University
*2 Faculty of Science, Kanazawa University

Effects of milk and soy milk on uptake of trace elements in rats

Y. Nakanishi,* M. Suzuki,* M. Hasama, T. Ando,* M. Ozaki,* H. Haba, S. Enomoto,* and S. Kimura*

The National Nutrition Survey 2002 showed that intakes of calcium and iron are not sufficient in the Japanese population, especially young women. Recent studies suggest that there is a relationship between previous milk consumption and bone mass in young women.[1] Soy milk consumption may be effective in reducing bone loss in postmenopausal women because of the estrogenic properties of soy isoflavone.

Iron absorption may be inhibited by the high intakes of calcium. Since calcium inhibits both heme and non-heme iron absorption, Hallberg et al. suggested that the inhibition is occurring in the intestinal mucosal cells where calcium interferes with iron transport.[2] On the other hand, the components of milk, such as casein phosphopeptides are suggested to enhance mineral absorption. Further studies are necessary to clarify the interaction of milk consumption and iron absorption and storage. Thus, to investigate the effect of milk and soy milk on the absorption of various elements, we determined the uptake rates of trace elements in rats using a multitracer technique.

The multitracer solution was prepared from a Ag target irradiated with a heavy-ion beam of 135 MeV/nucleon accelerated in the RRC. $^{59}FeSO_4$ solution was purchased and added to the multitracer solution. The detailed procedure for preparing the multitracer solution was described previously.[3]

The rats were orally administered multitracer solution and distilled water (DW), milk and soy milk. The rats were kept in cages and sacrificed 3, 7 and 24 h after the administration of test solution. Then, the liver and blood were collected. Serum was separated by centrifugation (3000 rpm for 10 min). The radioactivities of the liver and serum were measured using high-purity Ge detectors and the γ-ray spectra were analyzed. Data were statistically analyzed by two-way ANOVA.

The rate of Fe uptake in serum in rats administered with milk and soy milk was significantly lower than that in rats administered DW ($p < 0.001$ with two-factor interaction) (Fig. 1). The rates of Se, Co and Mn uptakes in serum in rats administered soy milk were significantly lower than those in rats administered DW ($p < 0.01$) There was no significant difference in the rates of trace element uptake in the liver.

The results were consistent with the hypothesis that a high calcium intake inhibits iron absorption. In addition, soy milk was shown to be a strong inhibitor of trace element absorption.

Both milk and soy milk did not influence the uptake of iron in the liver of normal rats. Further studies regarding of the uptake rates of iron and calcium in iron-deficient rats are necessary.

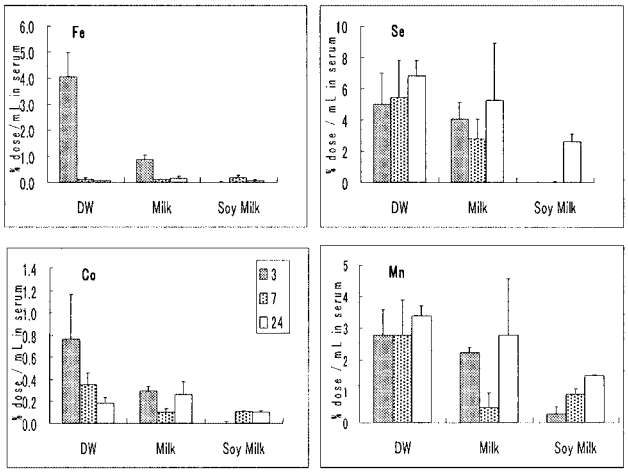

Fig. 1. Incorporation of Fe, Se, Co and Mn into serum.

References

1) D. Teegarden et al.: Am. J. Clin. Nutr. **69**, 1014 (1998).
2) L. Hallberg et al.: Eur. J. Clin. Nutr. **46**, 317 (1992).
3) S. Ambe et al.: Anal. Sci. **7**, 317 (1991).

* Graduate School of Human Life Sciences, Showa Women's University

Influence of dopamine on overaccumulation of copper in LEC rats: A proposal

M. Hasama, S. Kimura,* and S. Enomoto

Wilson's disease (WD)-related neuropathy is characterized by extrapyramidal dysfunction such as involuntary movement and salivation.[1] WD exhibits copper (Cu) overaccumulation in liver with varied clinical manifestations, and many cases with WD have severe extrapyramidal dysfunction. In order to better understand the etiology of this disorder, different animal models of WD have been proposed. Among them, aged Long Evans Cinnamon (LEC) rats have been widely studied because they show several forms of Cu overaccumlation in the brain.

The hepatic Cu accumulation seen in LEC rats also occurs in WD patients. LEC rats also show an iron overload in the liver and the brain.[2] It is well known that Cu and iron accumulations increase the effects of aging, and these accumulations might have deleterious effects on the liver and the brain via oxidative stress. Furthermore, Cu and iron accumulation in the brain may affect the metabolism of other elements. Zinc and manganese may be of particular relevance in LEC rat brain because these elements play a role in reactive oxygen removal from the brain.

For this study, a radioactive multitracer technology, which enables simultaneous tracing of a number of elements, is applicable. The radioactive multitracer technology was developed at RIKEN and is widely used in trace-element studies. A multitracer solution is obtained from a target that has been irradiated with high-energy heavy irons. Using the multitracer prepared from an Ag target irradiated with a ^{14}N beam, it was possible to examine the distributions of 13 trace elements in the brain.

In this study, LEC rats were given unilateral intrastriatal stereotaxic injections of multitracer as part of the microdialysis method. The microdialysis technique is commonly and widely used for the biochemical analysis of interstitial fluids in various tissues. The purpose of this method is to identify several theoretical models that take into account both the diffusional resistances encountered *in vivo* and the effects of various active processes, such as metabolism, release and uptake, and transport across the blood brain barrier.

The microdialysis method is described below. LEC rats were anesthetized and placed in a stereotaxic apparatus. The skull was exposed, and a small hole was drilled on one side. The microdialysis probe, an intercellular lymph dialyzer, is implanted vertically in the striatum (coordinates: anterior: +1.0 mm from bregma, lateral: +3.0 mm from midline and vertical: −3.6 mm from dura), according to the atlas of Paxinos and Watson.[3] After the recovery phase, artificial cerebrospinal fluid (ACSF) in which multitracer was dissolved is injected into the striatum. In addition, striatal dopamine is quantified in time. Finally, the probes are removed and the brains are cut on a Vibratome in serial coronal slices. The sliced samples are subjected to γ-ray spectrometry with pure Ge detectors, set in reference to an appropriate standard, to determine the percentage of different tracers in the injected dose.

This method is discussed in relation to the trace-element metabolism in each brain area, together with a discussion of the striatal dopamine concentration.

The extrapyramidal dysfunction, WD-related neuropathy, stems from an abnormal striatal dopamine system.[4] We also investigate the change of striatal dopamine concentration induced by nerve stimulus, such as high K^+.

References

1) H. Shim et al.: J. Nutr. **133**, 1527S (2003).
2) D. W. Kim et al.: Neurochem. Res. **30**, 475 (2005).
3) G. Paxinos et al.: *The Rat Brain Stereotaxic Coordinates* (Academic Press, New York, 1987).
4) H. Barthel et al.: Eur. J. Nucl. Med. Mol. Imaging. **28**, 1656 (2001).

* Graduate School of Human Life Science, Showa Women's University

Investigation of Cu dynamics in Long-Evans Cinnamon rats

A. Nakayama,[*1] H. Yasui,[*2] H. Sakurai,[*2] H. Haba, and S. Enomoto

Long-Evans rats with a cinnamon-like coat color (LEC rat) develop hepatitis at approximately 4 months after birth due to an unusual accumulation of Cu in their liver.[1] An excess of Cu exhibits leads of cytotoxity and usually induces the production of some metal-binding proteins such as metallothionein (MT) to protect organs against Cu-induced cell damage. MT binds to metals to maintain homeostasis or to detoxify heavy metals, but Cu-binding MT reacts with hydrogen peroxide to generate hydroxyl radicals, which in turn leads to hepatic disorders.[2] On the other hand, it has been reported that organisms have developed sophisticated mechanisms of maintaining the balance between essential and toxic Cu levels.[3] Within cells, Cu is distributed to specific subcellular components or proteins by Cu chaperones that include Rah1 and ATP7A/B, which delivers Cu to ceruloplasmin, Cox17, which delivers Cu to mitochondrial CCO, and CCS, which inserts Cu into Cu, Zn-SOD.

However, Cu kinetics in the body and cells of LEC rats has not yet been clarified sufficiently. One of the solution for this is the evaluation of copper kinetics using a radioactive tracer, because the utilization of a radioactive Cu isotope is generally difficult. Thus, Nakayama et al. attempted to produce ^{67}Cu with the longest half-life ($t_{1/2} = 61.7$ h) among radioactive Cu isotopes and to investigate the intracellular Cu kinetics using ^{67}Cu.

^{67}Cu was produced via the ^{70}Zn(p, α) reaction.[4] In brief, an enriched ^{70}Zn target (80%) was irradiated with a 0.96 μA proton beam (proton energy: 12.8 MeV) for 1 h and ^{67}Cu was separated from the unreacted target and by-products, ^{67}Ga and ^{56}Co, by anion-exchange chromatography. The resulting solution containing ^{67}Cu was heated to dryness and stored until use. The dried ^{67}Cu was completely dissolved in a small amount of 1 M HCl and diluted with PBS. The ^{67}Cu-containing solution was intravenously (iv) and intraperitoneally (ip) injected into 9-, 15-week-old, and aged LEC rats and 10-week-old Wistar (used as control) rats. After 2 h, we collected the liver, kidney, and blood, and then measured in the radioactivities. A portion of each liver was used to produce cytosol, which was subjected to SDS-PAGE and analyzed for the intracellular distribution of ^{67}Cu using a bioimaging analyzer.

Figure 1 shows organ (A) and intracellular (B) ^{67}Cu distribution after iv administration. The results of ip administration were similar to those of iv administration. The ^{67}Cu distribution was approximately four fold higher in the liver and two fold lower in the blood of LEC rats than in those of Wistar rats. These results suggest that the administrated Cu was immediately distributed from the blood and accumulated in the liver of LEC rats. The intracellular ^{67}Cu distribution showed that the ^{67}Cu distribution for MT was significantly higher and that for Rah1 was significantly lower in the hepatic cells of LEC rats than in those of Wistar rats. These results were consistent with previous reports.[5,6] The distribution for CCS was lower in the livers of 9-week-old LEC rats than in those of the other rats, whereas the distribution for SOD was almost the same. Although the reason and role of the decreased distribution for CCS are unknown at present, this might be related to the development of hepatitis.

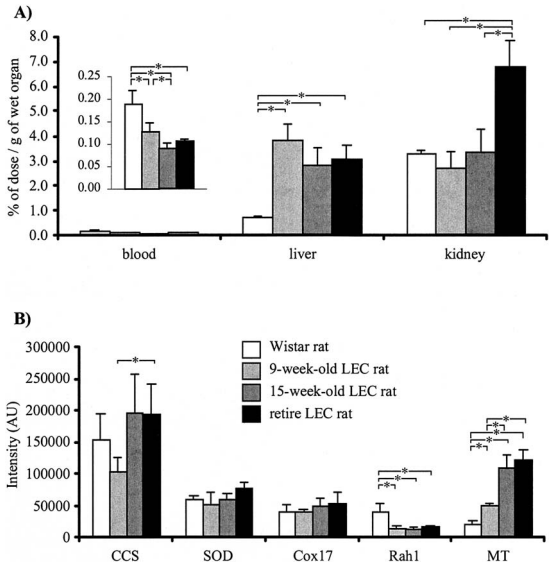

Fig. 1. ^{67}Cu distribution (A) to the blood, liver and kidney of the 9-, 15-week-old and retired LEC and Wistar rats and (B) to the intracellular Cu-containing proteins in the liver cells of 9-, 15-week-old and retired LEC and Wistar rats. The insert is the expanded figure of the distribution to blood. $*$ means significant difference at the level of $p < 0.05$.

*1 Devision of Medicine, Vanderbilt University Medical Center, USA
*2 Department of Analytical and Bioinorganic Chemistry, Kyoto Parmaceutical University

References

1) M. Sasaki et al.: Rat News Lett. **14**, 4 (1985).
2) H. Sakurai et al.: Biochem. Biophys. Res. Commun. **184**, 1393 (1992).
3) M. Marjorette et al.: J. Biol. Chem. **275**, 33244 (2000).
4) D. J. Jamriska et al.: J. Radioanal. Nucl. Chem. **195**, 263 (1995).
5) A. Nakayama et al.: J. Trace Elem. Exp. Med. **15**, 31 (2002).
6) J. Wu et al.: Nat. Genet. **7**, 541 (1994).

Difference in property of skin penetration between ^{65}Zn(II) ion and its complex topically applied on skin of live hairless mice

H. Yasui,* H. Nishimura,* H. Haba, S. Enomoto, and H. Sakurai*

Zinc (Zn), with an atomic number of 30 and an atomic weight of 65.37, is one of the most important essential trace elements found in all living systems. This metal is necessary as a catalytic component for more than 200 enzymes and is also a structural component of many proteins, hormones, neuropeptides, and hormone receptors.[1] Among the many pharmacological and nutritional roles of Zn(II), its anti-inflammatory activity has been well known for a long time.[2] Zinc oxide (ZnO) is clinically used in many countries as an anti-inflammatory agent for the treatment of wounds. Recently, we have found that the supplementation of oral Zn(II) and its complex to alive hairless mice exposed to UVA prevents skin damage.

On the basis of these results, we examined whether Zn(II) applied topically on the skin of alive hairless mice exhibits antioxidative activity against reactive oxygen species (ROS) generated in UVA-exposed skin.[3] When $ZnCl_2$ was topically applied on the skin surface of mice at a dose of 40 μg Zn/5 cm^2 before UVA exposure (18 J/cm^2), ROS level in UVA-exposed skin significantly decreased. However, when $ZnCl_2$ was applied at the same dose for 30 min and then removed immediately before UVA exposure, the effect of $ZnCl_2$ application disappeared. We then prolonged the application time from 30 to 60 and 180 min and observed the effects of Zn(II). Even after the removal of $ZnCl_2$ applied $ZnCl_2$ for 60 and 180 min, ROS levels further decreased to the level of the control. These results indicate that (1) $ZnCl_2$ does not act as a filter for UVA light and that (2) $ZnCl_2$ might induce some antioxidative enzymes or proteins that were synthesized for a short time such as 60 or 180 min. On the basis of the finding of the protective effect of $ZnCl_2$ against skin damage in regard to the ROS suppressive effect in alive UVA-exposed mice, we topically applied $Zn(pic)_2$ (bis(picolinato)Zn(II) complex), with a partition coefficient of 0.02 in an octanol-saline system at 37°C,[4] at the same dose as that of $ZnCl_2$; however, its antioxidative effect significantly decreased in comparison with $ZnCl_2$. Thus, it is necessary to find the causative factors for the difference in antioxidative activity between $ZnCl_2$ and $Zn(pic)_2$. First, we examined in this study the features of skin penetration of $ZnCl_2$ and $Zn(pic)_2$ by monitoring ^{65}Zn(II) level after the topical application of ^{65}Zn-labeled compounds.

^{65}Zn in the chemical form of $ZnCl_2$ in 0.5 mol/L HCl, was obtained from RIKEN. ^{65}Zn solution was slowly dried and then the residue was redissolved in a saline (activity = 370 kBq/mL). $ZnCl_2$ dissolved in distilled water was mixed with 37 kBq of ^{65}Zn to a final volume of 1 mL. While $Zn(pic)_2$ and picolinic acid (2% of complex) dissolved in phosphate buffer (pH 7.8) were mixed with 37 kBq of ^{65}Zn, the buffer was added to the preparation to a final volume of 1 mL. The preparation was then labeled with ^{65}Zn by allowing the preparation to stand at 25°C overnight. The next day, 1 mL of ethanol was added to 1 mL of each ^{65}Zn-labeled solution to a final volume of 2 mL with 50% ethanol-water solution. The radioactivity applied to each mouse was 0.925 kBq of ^{65}Zn/2.5 cm^2. Female hairless mice (10–12 weeks old), weighing 25 g, were administered 50 μL of 50% ethanol-water solution of $^{65}ZnCl_2$ or $^{65}Zn(pic)_2$ by a single topical application at a dose of 20 μg Zn/2.5 cm^2. After the treatment (30–180 min), the mice were sacrificed under anesthesia with ether and the applied area of the skin was removed. The stratum corneum was immediately removed by tape-stripping 5 times using Scotch mending tape, and the remaining skin as the sum of the epidermis and dermis was weighed and transferred to polyethylene tubes for analysis using a gamma counter. Radioactivity due to ^{65}Zn incorporated in the epidermis and dermis was counted with an Aloka ARC-360 autowell gamma system using the peak area of 1115.5 keV due to the ^{65}Zn nucleus as reference. Consequently, $^{65}ZnCl_2$ was found to penetrate more efficiently into the skin tissue than $^{65}Zn(pic)_2$ at 1% significant difference level (see Fig. 1). This feature seems to be due to the higher contribution of the polar route to transporting a ^{65}Zn-labeled compound through the stratum corneum layer, providing a new approach to treatment with Zn compound.

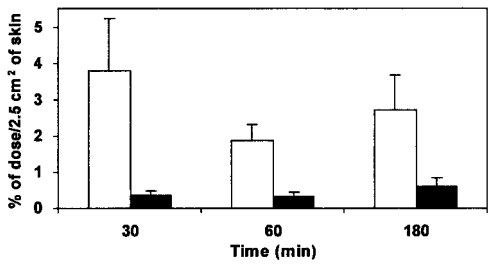

Fig. 1. Penetration of $^{65}ZnCl_2$ (open bar) and $^{65}Zn(pic)_2$ (closed bar) into epidermis and dermis of hairless mice.

References

1) A. S. Prasad: Nutr. Rev. **41**, 197 (1983).
2) M. S. Ågren: Acta Derm. –Venereol. **71**, 153 (1991).
3) H. Sakurai, H. Yasui, K. Mishina, and H. Nishimura: Biomed. Res. Trace Elem. **14**, 27 (2003).
4) Y. Yoshikawa, E. Ueda, K. Kawabe, H. Miyake, T. Takino, H. Sakurai, and Y. Kojima: J. Biol. Inorg. Chem. **7**, 68 (2002).

* Department of Analytical and Bioinorganic Chemistry, Kyoto Pharmaceutical University

Behavior of trace elements and protein contents in livers of zinc-deficient mice

R. Minayoshi,[*1] T. Ohyama,[*1] N. Kinugawa,[*1] J. Kamishima,[*1] M. Noguchi,[*2] K. Ishikawa,[*2] H. Suganuma,[*1] K. Takahashi, S. Enomoto, and M. Yanaga[*1]

Previously, the concentrations of zinc and other trace elements in various tissues of Zn-deficient mice were determined by INAA to investigate the physiological effect of Zn deficiency on the concentrations of other elements in mice.[1)] No significant differences between Zn-deficient and normal mice were found in the zinc concentration of liver. On the other hand, the concentration of Co increased in all the tissues of Zn-deficient mice. Then, the following two studies were carried out to investigate the behavior of trace metallic elements bound to proteins. One is the determination of the concentrations of trace elements and proteins after gel filtration chromatography for cytosolic fraction of hepatocytes. The other is the investigation of affinities between metals and proteins, which are contained in these fractions.

Eight-week-old male mice of ICR strain were divided into two groups; one group was fed a Zn-deficient diet and ultrapure water (Zn-def. mice), and the other one fed a control diet and the same water (control mice). After three weeks, their livers were removed and immediately weighed. Every eight livers of each group was together homogenized and separated into two subcellular fractions, such as supernatant (cytosolic fraction) and other fractions, by ultracentrifugation. The cytosolic fraction was further divided into forty fractions (2 ml per fraction) by gel filtration chromatography (Sephadex G-100) using Tris-HCl buffer (pH 7.4) as eluent, at a flow rate of 10 ml/h, at 4°C. Then, the concentrations of the metallic elements and proteins in each fraction were determined by ICP-MS and BCA protein assay, respectively. In accordance with the results of ICP-MS, the 12th–19th fractions, in which the concentrations of zinc decreased, were used for the following experiments. Proteins in these fractions were further separated with SDS-PAGE. The gel was stained with silver stain. Multitracer solution was added to the 14th–16th fractions to investigate the affinities between the trace elements and metalloproteins, and incubated for 1 h at 4°C to prevent denaturation and decomposition of proteins. Each solution was poured into several centrifugal filter tubes, such as Micron YM-3, -10, -30, and -50 (Millipore Co.), and centrifuged at $2000 \times g$ for 30 min. The radioactivities in those samples were measured with HPGe detectors. In each examination process, such as gel filtration chromatography, SDS-PAGE, and the multitracer experiment, the amounts of proteins in the samples for two groups were adjusted to be equal to each other.

The zinc concentrations in the 13th–18th, 21st, and 22nd fractions of Zn-def. mice were much lower, and the cobalt concentrations in the 14th, 17th, 18th, 21st, and 22nd fractions were higher than the control ones. On the other hand, the concentrations of proteins in the 13th–15th fractions of Zn-def. mice were low. However, no significant differences between Zn-def. and control mice were found in the positions and numbers of protein bands of lanes on gel for the 12th–21st fractions.

The rates of radioactivities of ^{65}Zn, and ^{56}Co detected from the filters in the 14th fraction are shown in Fig. 1. The radioactivities detected from the filters indicate the amounts of metal elements bound to proteins. The affinities between ^{65}Zn and proteins over 30 kDa in the 14th fraction of Zn-def. mice decreased. On the other hand, these were no differences between two groups on the affinities between ^{56}Co and proteins in the 14th fraction. Furthermore, the result indicates that the size of cobalt affinitic proteins is almost in the vicinity of 10 kDa, because the affinities of over 10 kDa were much lower than 3 kDa of each group.

These results may suggest that the zinc-binding proteins in a range of 10 kDa $\leq$ decreased or zinc replaced by the other metal elements, whereas the results of SDS-PAGE showed that there was neither disappearance of metalloproteins nor induction of other proteins.

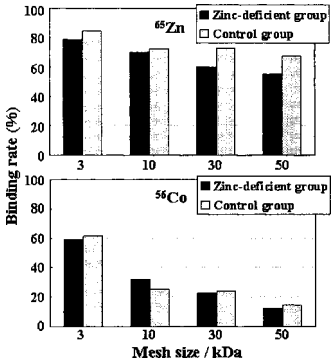

Fig. 1. Affinities between proteins and ^{65}Zn, and ^{56}Co in 14th fraction.

Reference

1) M. Yanaga, H. Wakasa, T. Yoshida, M. Iwama, K. Shinotsuka, M. Noguchi, and T. Omori: J. Radioanal. Nucl. Chem. **245** 255 (2000), and references therein.

*1 Radiochemistry Research Laboratory, Faculty of Science, Shizuoka University
*2 Department of Biology and Geosciences, Faculty of Science, Shizuoka University

Determination of rhenium and technetium in marine algae

T. Ishii,* T. Sakuragi,* H. Haba, and S. Enomoto

The differences of biological and chemical behaviors between Re and Tc belonging to the same group in the periodic table were examined from elemental analyses with various separation procedures and bioaccumulation experiments.

Fifty species of marine organisms including algae (*Bryospsis maxima, Sargassum thunbergii, Fucus vesiculosus, Ascophyllum nodosum etc.*) were collected in Japan, Canada, Norway and UK.

The metallic ^{95}Mo target (Enrichment; 96.8%) with 0.01 mm in thickness from the Oak Ridge National Laboratory was irradiated by a 8.8–14 MeV proton beam using the RIKEN K70 AVF cyclotron, as shown in Fig. 1. ^{95m}Tc was used to obtain the recovery or to examine its behavior while chemical separations were carried out. The radioactivity of ^{95m}Tc produced in the ^{95}Mo (p, n) reaction was 538 kBq/0.0055 g of ^{95}Mo. The specific activity of 1.734 Bq/fg at mass number $A = 99$ in enriched ^{95}Mo was much higher than that (0.035 Bq/fg) of Mo having a natural abundance, as shown in Table 1. If 173.4 Bq of ^{95m}Tc is spiked as a yield monitor, only 5 ppq (100 fg/20 mL) is estimated to enhance the intensity at $A = 99$. It was supposed that an isotope at $A = 99$ mass was ^{99}Tc derived from the reactions such as ^{100}Mo$(p, 2n)$, ^{100}Mo$(n, 2n)^{99}$Mo $\rightarrow$ ^{99m}Tc, ^{98}Mo(p, γ), and ^{98}Mo(n, γ)^{99}Mo $\rightarrow$ ^{99m}Tc.[1)]

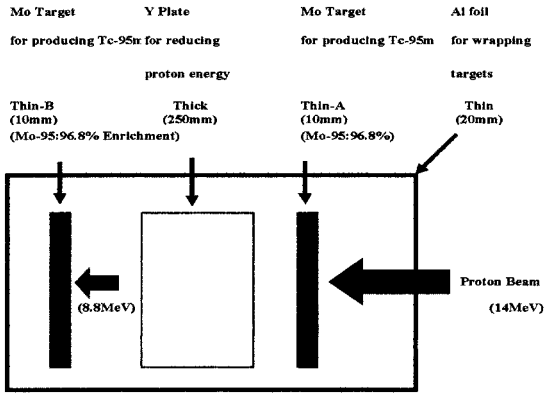

Fig. 1. Mo targets used for producing ^{95m}Tc.

Table 1. Comparison of the specific activity based on differences of proton energy and enrichment of Mo targets.

Target	Proton energy	Specific activity*
Enriched Mo-95	8.8 MeV	1.734 Bq/fg
Enriched Mo-95	14.0MeV	0.126 Bq/fg
Natural Mo	14.0MeV	0.035 Bq/fg

* Specific activity = Activity of Tc-95m/Amount at a mass 99

* Research Center for Radiation Safety, National Institute of Radiological Sciences

Prior to the determination of ^{99}Tc, ^{99}Tc in samples was collected on a 3 M Empore 3292 Tc disk, an anion exchange resin, an Eichrom TEVA resin and disk, and an activated charcoal.

Since the measurements of ^{99}Tc by ICP-MS was supposed to be influenced by ^{98}Mo^{1}H$^+$ and ^{99}Ru, almost all of Mo and Ru were removed by the TEVA resin and the anion exchange resin. The concentrations of ^{99}Tc in final volume of 20 mL were determined by a ThermoFinnigan Element2 HR ICP-MS (Sensitivity; 750,000 cps/ppb, Detection limit; 31.4 fg/mL = 20 μBq/mL).

Beta ray (β_{max}; 293.7 keV) of ^{99}Tc on the Tc disk was also measured by a PICOBETA PBS-1 Low-Background beta-ray spectrometer (Absolute detectable amount; 2 mBq) for 10,000–300,000 sec.

In the case of Re, 0.1–2 g of dry materials were wet-digested by H_2O_2 and HNO_3. The concentrations of Re were measured by ICP-MS using an ACROS ORGANICS Re standard.

^{99}Tc concentrations differed among sampling locations or species of organisms, as shown in Table 2. The concentration of Re in green alga *B. maxima* was more than one hundred timed higher than other species of marine algae.[1)]

Wide differences in biological and chemical behavior were observed between Re and Tc. For example, it was found from the results of elemental analyses and bioaccumulation experiments that the concentration factor of Tc in *F. vesiculosus* was ten times higher than that of Re.[1)]

Furthermore, Tc was not removed from the 3 M Empore 3292 Tc disk and Eichrom TEVA disk although the majority of Re was eluted from collectors by 10 M HCl solution.

Table 2. Comparison of ^{99}Tc concentration in marine algae collected from various sites.

Sample	Country	Area or Location	Reported value	This work
EA2453	UK	Sellafield	61600 ± 13200	59400 ± 5100
EA2454	UK	Sellafield	25520 ± 5280	26800 ± 2180
EA2957	UK	Sellafield	2750 ± 250	2520 ± 150
F. vesiculosus	UK	Sellafield	no data	48690 ± 930
F. vesiculosus	Norway	Hillesøy	no data	84 ± 26
A. nodosum	Canada	Canada-East coast	no data	3.5 ± 1.5
B. maxima	Japan	Chiba and Ibaraki	no data	0.66 ± 0.25
S. thunbergii	Japan	Aomori and Chiba	no data	0.051 ± 0.017

References

1) T. Ishii et al.: Proc. 2nd Int. Conf. on the Radioactivity in the Environment, Nice, France, 2005-10, edited by P. Strand (2005), p. 253.

Search for metal delivery from nose to brain: A multitracer study

Y. Kanayama,* E. Hayashi,* H. Haba, S. Enomoto, and R. Amano*

Because intranasal administration has a possibility to provide a direct delivery route to the brain, it is expected as an effective administration method for certain drugs or metals targeting the brain, in particular when such drugs or metals injected into the blood are hardly delivered through the blood-brain barrier or are toxic. For example, Mn^{2+}, well known as a neurotoxic element, can be delivered into the olfactory bulb (OB) by the axonal transport of the olfactory neuron; therefore, it is considered as an imaging agent of the neural pathway in Mn-enhanced MRI.[1] The axonal transport is slow, so the Mn^{2+} transport takes several days to reach the distant brain regions from OB. On the other hand, we previously found the rapid olfactory transport of Tl^{+}, *i.e.*, it was transported in the OB within 3 h and was eliminated during 48 h after intranasal administration.[2] This result indicates that there are other routes from the nose to the brain aside from the axonal transport of the olfactory neuron. In some cases, the fast delivery, as in Tl^{+}, is desired for diagnosis or therapy by intranasal administration. Therefore, more detailed information concerning the delivery of intranasally administered materials is important. To search for a fast delivery route from the nose to the brain, a preliminary study of the accumulation of several metal ions in nasal-cavity-related tissues using a multitracer was performed.

The multitracer was obtained from a Ag target according to the method of Haba et al.[3] The multitracer solution was administered into Wistar rats (male, 6-week-old) intranasally (i.n.) and intravenously (i.v.). At 6 and 24 hours, rats were sacrificed and the following 15 tissues were sampled: the blood, deep lateral cervical lymph nodes, superficial lateral cervical lymph nodes, axillary lymph nodes, trigeminal nerve, OB, olfactory cortices (piriform cortex, amygdala, and entorhinal area), hippocampus, striatum, cerebral cortex, brainstem (except the hindbrain), cerebellum, pons, medulla oblongata, and spinal cord. After activities were measured, the uptake rates of each sample were given as %dose/g wet weight.

Table 1 shows the uptake rates of ^{46}Sc, ^{48}V, ^{54}Mn, ^{65}Zn, ^{75}Se, ^{83}Rb, ^{88}Y, ^{88}Zr, and ^{103}Ru in each sample 24 h after administration. In i.n. administration, ^{46}Sc, ^{54}Mn, ^{65}Zn and ^{83}Rb showed brain accumulations. It was found that ^{46}Sc was highly accumulated in the trigeminal nerve, brainstem, cerebellum and pons. The higher uptake rates of ^{54}Mn and ^{83}Rb in the OB after i.n. administration than those after i.v. administration are considered to be due to the olfactory nervous transport.

Not to mention, further experimentation is needed to describe the brain delivery route because of the limited number of samples in the present one. However, no fast delivery was observed except for ^{83}Rb at least 6 h after i.n. administration.

References

1) A. P. Koretsky and A. C. Silva: NMR Biomedicine **17**, 527 (2004).
2) Y. Kanayama et al.: Nucl. Med. Biol. **32**, 505 (2005).
3) H. Haba et al.: Radiochim. Acta **93**, 539 (2005).

Table 1. Tissue uptake rates of multitracer containing radionuclides 24 h after intranasal (i.n.) and intravenous (i.v.) administrations in rat. Data are calculated in terms of %dose/g for a rat.

administration method	i.n.									i.v.								
radionuclide	^{46}Sc	^{48}V	^{54}Mn	^{65}Zn	^{75}Se	^{83}Rb	^{88}Y	^{88}Zr	^{103}Ru	^{46}Sc	^{48}V	^{54}Mn	^{65}Zn	^{75}Se	^{83}Rb	^{88}Y	^{88}Zr	^{103}Ru
blood	0.545	0.177	0.473	0.128	1.715	0.254	n.d.	0.095	3.314	0.585	0.288	0.633	0.055	0.939	0.254	0.013	0.394	0.352
deep lateral cervical lymph nodes	0.500	0.157	1.074	0.815	0.617	0.813	0.026	0.019	1.060	1.380	0.310	0.568	0.960	0.803	0.796	0.069	0.423	1.080
superficial lateral cervical lymph nodes	1.174	0.062	0.187	0.254	0.344	0.372	0.006	0.114	0.822	1.667	0.441	0.556	1.228	0.748	0.873	0.128	0.185	n.d.
axillary lymph nodes	0.422	0.074	0.138	0.287	0.291	0.432	n.d.	n.d.	0.182	0.852	0.477	0.445	0.825	0.625	0.694	0.095	0.386	1.116
trigeminal nerve	5.330	0.255	1.350	0.678	0.996	2.006	0.397	0.281	7.623	5.494	0.942	1.276	0.946	1.400	1.929	0.197	0.246	5.963
olfactory bulb	0.069	n.d.	1.904	0.074	0.062	0.248	n.d.	0.044	0.028	n.d.	0.016	0.129	0.015	0.081	0.115	0.008	n.d.	0.019
olfactory cortices	0.155	n.d.	0.158	0.032	0.050	0.217	0.004	n.d.	0.005	0.125	0.022	0.069	0.111	0.069	0.180	0.013	0.018	n.d.
hippocampus	0.033	n.d.	0.032	0.108	0.038	0.108	0.000	0.031	n.d.	0.386	n.d.	0.132	0.102	0.089	0.152	n.d.	0.000	n.d.
striatum	n.d.	n.d.	n.d.	n.d.	0.014	0.081	n.d.	0.047	n.d.	0.108	0.022	0.085	0.189	0.119	0.186	0.015	0.016	n.d.
cerebral cortex	0.039	n.d.	0.042	0.026	0.047	0.129	0.001	n.d.	n.d.	0.084	0.022	0.110	0.186	0.106	0.208	n.d.	0.016	n.d.
brainstem	0.145	0.012	0.047	0.045	0.043	0.127	0.002	0.000	n.d.	0.138	n.d.	0.083	0.106	0.091	0.166	0.008	0.006	n.d.
cerebellum	0.206	n.d.	0.043	0.006	0.044	0.113	n.d.	0.009	n.d.	0.155	0.029	0.085	0.084	0.100	0.191	0.002	0.011	n.d.
pons	0.231	n.d.	0.064	0.154	0.048	0.163	n.d.	n.d.	n.d.	0.208	0.070	0.090	0.082	0.057	0.218	n.d.	0.006	n.d.
medulla oblongata	0.184	0.025	n.d.	0.058	0.033	0.153	0.015	n.d.	n.d.	0.260	n.d.	0.148	0.025	0.065	0.201	n.d.	0.052	n.d.
spinal cord	0.189	0.033	0.141	0.187	0.141	0.364	0.004	0.011	n.d.	0.745	0.070	0.219	0.324	0.235	0.549	0.130	0.116	0.132

* School of Health Sciences, Faculty of Medicine, Kanazawa University

Preliminary study of biodistribution of $^{203}PbCl_2$ and ^{203}Pb-DOTMP in mice

K. Washiyama,* H. Haba, Y. Kanayama,* S. Enomoto, and R. Amano*

Recently, α-particle-emitting nuclides have been found to be promising for targeted radionuclide therapy owing to the high linear energy transfer and short path length of α-particles in tissues.[1] In addition to these physical properties, some α-emitting nuclides that are members of a decay chain release successive α- and β-particles, and are called *in vivo* generators.[2] Cascade α-emission close to the target site is more effective for therapy than single α-emission.

In radionuclide therapy utilizing *in vivo* generators, it is important to maintain the retention of daughter nuclides at the target site after the decay of the parent nuclide in addition to the selective accumulation of the parent nuclide to that site. Otherwise, the released daughter nuclides could be localized to other normal tissues and may cause radiotoxicity. Therefore, the pharmacokinetics of various daughter nuclides is mandatory in predicting and preventing radiotoxicity. However, it is often difficult to determine the accurate biodistribution of daughter nuclides owing to their short half-lives.

In this study, we produced a ^{203}Pb ($T_{1/2}$ = 51.9 h) tracer and evaluated the Pb biodistribution in the development of an alternative pharmacokinetic tracer in mice for ^{211}Pb ($T_{1/2}$ = 36.1 m) and ^{212}Pb ($T_{1/2}$ = 10.64 h), which belong to the *in vivo* generators of ^{223}Ra ($T_{1/2}$ = 11.435 d) and ^{224}Ra ($T_{1/2}$ = 3.66 d), respectively.

Macrocyclic phosphonate chelate 1, 4, 7, 10-tetraazacyclododecane-1, 4, 7, 10-tetramethylenephosphonic acid (DOTMP) is a well-known bone-targeting agent and its application to the treatment of various bone-forming tumors or calcified metastases has been reported.[3,4] DOTMP is excreted rapidly from the whole body into the urine just after administration. Therefore, to prevent the radiotoxicity by Pb isotopes during the use of *in vivo* generators for the treatment of bone metastases, we also prepared a bone-targeting labeled compound, ^{203}Pb-DOTMP, and evaluated its biodistriution.

Lead-203 was produced via the ^{203}Tl (p, n) ^{203}Pb reaction by irradiating $^{nat}Tl_2O_3$ with 14 MeV protons at the RIKEN K70 AVF cyclotron. Irradiation was performed at 4.5 μA for 2 h. After irradiation, the target was left to stand for 4 days to allow the decay of the short half-life radionuclides, ^{204m}Pb ($T_{1/2}$ = 67.2 m) and ^{202m}Pb ($T_{1/2}$ = 3.62 h). The target was dissolved in 2 mL of 8 M HNO_3 and the solution was heated to dryness, and then 1 mL of 1 M HCl was added. The solution was loaded onto an anion exchange column (DOWEX 1 × 8) and ^{203}Pb was passed through the column with 1 M HCl while the target material was retained on the column. The eluate was evaporated to dryness and then 2 mL of 0.1 M HCl was added to prepare a stock solution. One milliliter of the stock solution was evaporated to dryness and 1 mL of saline was added to the residue to prepare a $^{203}PbCl_2$ solution. The residual 1 mL stock solution was mixed with DOTMP and adjusted to pH within 7–8 by adding 1 M NaOH and heated at 80°C for 15 min to prepare a ^{203}Pb-DOTMP solution.

Male 13-week-old ICR mice were administered with 100 μL of $^{203}PbCl_2$ solution (0.9 kBq) or ^{203}Pb-DOTMP solution (1.0 kBq) *via* the tail vein. Each mouse was sacrificed and dissected 15 min, 30 min, 1 h, 3 h, and 6 h after injection of $^{203}PbCl_2$ or ^{203}Pb-DOTMP. The blood, lung, liver, spleen, stomach, large intestine, small intestine, kidney, muscle, cardiac muscle, and femur were excised and weighed. Each tissue sample was subjected to γ-ray spectrometry. The uptake of ^{203}Pb was determined using 279.2 keV γ-ray. The results are expressed as percent injected dose per gram (%ID/g) of tissue.

The uptake rate of $^{203}PbCl_2$ showed the same trend as the already reported results.[5] The skeletal uptake rates of $^{203}PbCl_2$ and ^{203}Pb-DOTMP were comparable and increased with time. On the other hand, the uptake rates of ^{203}Pb-DOTMP in the other excised tissues significantly decreased compared with those of the $^{203}PbCl_2$ at more than 6 h. In the kidney, although the uptake rate 15 min after administration was 30.7%ID/g for the $^{203}PbCl_2$ administration, it was significantly reduced to 3.8%ID/g for the ^{203}Pb-DOTMP administration.

In conclusion, the cyclotron production isotope ^{203}Pb will provide an accurate biodistribution of Pb-mediated radiopharmaceuticals and perhaps give more detailed pharmacokinetic information on ^{211}Pb and ^{212}Pb generated *in vivo*.

References

1) M. R. McDevitt et al.: Eur. J. Nucl. Med. **25**, 1341 (1998).
2) M. R. McDevitt et al.: Science **294**, 1537 (2001).
3) S. P. Hassfjell et al.: Nucl. Med. Biol. **24**, 231 (1997).
4) G. Henriksen et al.: Anticancer Res. **24**, 101 (2004).
5) S. Z. Lever and U. Scheffel: Neurotoxicology **19**, 197 (1998).

* Graduate School of Medical Sciences, Kanazawa University

Comparative study of biotrace elements in bile of rat under oxidative stress

K. Endo, Y. Sakuma,* K. Matsuoka,* C. Honda,* K. Matsumoto,* and S. Enomoto

It was demonstrated in a previous study that the time course of trace elements in the abdomen can be monitored by noninvasive measurement in the combined use of a well-collimated lead slit and a Ge semiconducting detector.[1] In this study, the excretion rates of biotrace elements in the bile of Se-deficient and normal rats were examined using the multitracer (MT) technique to improve reproducibility.[2] We compared the results obtained using MT with those obtained by instrumental neutron activation analysis (INAA).

Wistar female rats that were on the 15th day of pregnancy were fed Se-deficient (SeD) diet (Oriental Yeast Co., Ltd.) and ultrapure water. Newly born rats were remained with their own mothers for four weeks. Four weeks after birth, young rats were weaned, and then fed on SeD diet and ultra-pure water until experiments. Male rats were used for experiments at 8 weeks old as the SeD group. Normal male Wistar rats old as the SeD group were purchased and used as the normal control group. MT solutions were prepared using silver foil irradiated with N-14 beams of 135 MeV/nucleon at the RIKEN–Ring Cyclotron.

The biliary duct of a Wister rat was cannulated with a polyethylene tube under Nembutal-induced anesthesia. A saline solution containing MT was injected intravenously to SeD and normal rats. After the administration of MT solution (200 μL), bile samples were collected in a polyethylene tube every 5 min, the γ-ray spectra of each fraction were measured. To determine the contents of stable elements in the bile samples from normal and SeD rats, the bile samples from normal and SeD rats were analyzed by INAA at JRR-4 in Japan Atomic Energy Research Institute (JAERI).

The excretion rates of Se, Sr, As, Mn, Co, and V in the bile of Se-D and normal rats were estimated from γ-ray spectra. The radioactivity of each nuclide increased and reached a plateau about 20 min after administration. The excretion rate of Se into the bile of Se-D rats was about 1/5 lower than that in normal rats. Although the excretion rates of metal ions into the bile of Se-D and normal rats were measured within 60 min after administration, no radioactivities of Fe and Zn were detected in this time range. This indicates that both elements were absorbed and accumulated in the liver, while other elements were excreted into bile. It is known that Fe(III) binds to transferrin in blood and resulting complex is transferred to the liver, spleen, and/or bone marrow by blood circulation, where Fe ions are stored as ferritin in liver.

Heme metabolism is an important for iron because many proteins contain heme as a prosthetic group. When these hemoproteins turn over, the heme is not recovered, but is degraded. New heme is synthesized for their replacements. In liver, heme-iron is metabolized, and the iron ions are excreted into bile and reabsorbed in duodenum, the effective half-life of Fe is 70 days in animals. Therefore, the radioactivity of ^{59}Fe was not observed within the time range in this study. Nearly 70% of Zn binds to albumin, and 30% of the metal to α-macroglobulin in blood. It is stored as Zn-metallothionein in liver. Zn is used for active centers of many enzymes. Therefore, ^{65}Zn is also not excreted into bile immediately after the administration of MT.

The contents of Fe and Zn in bile were determined by INAA. The results indicated that Fe and Zn were found in the bile of both normal and SeD rats. The contents of Fe in normal and SeD rats were nearly the same (17–20 mg/kg dried bile weight), and those of Zn were 0.4 mg/kg dried bile weight for the normal group, and 1 mg/kg dried bile weight for the SeD group. The comparison of data obtained by the MT technique and those by INAA may lead us to conclude that Fe detected by INAA in the bile of rats is a metabolite of heme-iron, and that stable Zn detected in bile by INAA is also metabolite from the liver.

References

1) K. Matsumoto et al.: Biol. Pharm. Bull. **28**, 2029 (2005).
2) K. Endo et al.: RIKEN Accel. Prog. Rep. **38**, 120 (2005).

* Showa Pharmaceutical University

Efflux study of trace elements in a cisplatin-resistant lung cancer cell line using a multitracer technique

T. Suzuki,[*1] T. Togawa,[*1] A. Yumoto,[*1] M. Takahashi,[*1] K. Nishio,[*2] H. Haba, S. Enomoto, and S. Tanabe[*1]

The molecular mechanism underlying cisplatin resistance has been revealed to be "multi-functional," involving a decreased accumulation, an enhanced intracellular detoxification and an increased DNA repair ability. The decreased accumulation of cisplatin was observed in non-small cell lung cancer (NSCLC) cell lines resistant to cisplatin. There is a good correlation between the intracellular amount of platinum and sensitivity to cisplatin. This observation suggests that intracellular accumulation is a major determinant of cisplatin resistance, at least in NSCLC. Previously, it was reported that cisplatin enters cells in an ATP-dependent manner. Further more it was reported that cisplatin is effluxed by multidrug resistance proteins (MRPs) as a glutathione conjugate.[1)] On the other hand, certain metals, such as arsenite and cadmium, are effluxed from cells in the same ATP-dependent manner. Therefore, the contribution of these transporters is important for metal detoxification analysis. However, the molecular mechanisms underlying metal transport, such as uptake and efflux transporters, are unclear.

In this study, to investigate whether metal transporters are up-regulated in cisplatin resistant cell line, we determined the percentage of efflux of various metals from cisplatin-resistant cell lines using a multitracer (MT) technique.

We developed this new method for efflux analysis and used the human NSCLC cell line PC-9 and its cisplatin-resistant subline, PC-9/CPr. The cells were grown in RPMI1640 supplemented with 10% FBS. A radioactive MT solution was obtained from an Ag target irradiated in the RIKEN Ring Cyclotron, and it was prepared as a physiological saline solution. The MT solution was then added to the cells in a serum-free medium and incubated at 37°C for 2 hr (uptake of MT). After incubation, the MT solution was removed and the cells were washed with the same medium. Then, a medium containing FBS was added and the cells were further incubated at 37°C for 1, 2 or 4 hrs. After incubation, an aliquot of the culture medium was collected and analyzed using a Ge detector. The percentage of efflux of several metals, ^{59}Fe, ^{75}Se, ^{48}V, ^{65}Zn and ^{74}As from PC-9/CPr were higher than those from the parental cell line PC-9. The efflux percentage profile for Zn is shown in Fig. 1. We focused on the Zn transport system and performed RT-PCR analysis of Zn transporters. Total RNAs were prepared from PC-9 and PC-9/CPr cell lines. Reverse transcription and PCR were performed as previously described.[2)] mRNA for one Zn transporter was overexpressed in PC-9/CPr cells as compared with parental cells (Fig. 2).

From these results, one metal transporter gene, which was highly expressed in CPr cells, was identified by the MT technique.

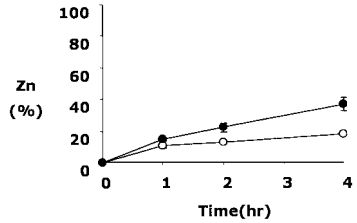

Fig. 1. Efflux of Zn tracer in lung cancer cell lines. Cisplatin-resistant cell line, PC-9/CPr (closed symbol) and parental cell line, PC-9 (open symbol). ^{65}Zn was measured using a Ge detector.

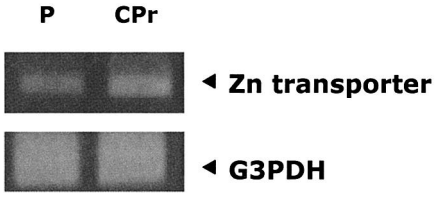

Fig. 2. mRNA expression of Zn transporter in PC-9/CPr and PC-9.

References

1) T. Suzuki et al.: Curr. Drug Metab. **2**, 363 (2001).
2) T. Suzuki et al.: J. Health Sci. **49**, 524 (2003).

*1 Department of Analytical Biochemistry, Meiji Pharmaceutical University
*2 Project Ward, National Cancer Center Hospital

Removal of radionuclides from solution by *Escherichia coli*

N. Ishii,* S. Uchida,* K. Tagami,* S. Enomoto, and H. Haba

Technetium-99 (^{99}Tc) is a radioactive contaminant in marine[1] and terrestrial environments.[2] This radionuclide has a long half-life of 2.1×10^5 y, suggesting the accumulation of ^{99}Tc in the environment every year. In addition, technetium as pertechnetate (TcO_4^-) is readily available to plants.[3] It was our concern that ^{99}Tc may be transferred from plants to humans. Therefore, the removal of ^{99}Tc from the environment is desirable.

The bacterium, *Escherichia coli* is able to remove ^{99}Tc from solution under anaerobic conditions.[4] This ability of *E. coli* cells may also allow the removal of other metal contaminants in the environment. In this study, the removal of various radionuclides from solution by *E. coli* was investigated using a multitracer technique.

A radioactive multitracer solution was obtained from a thin gold foil irradiated with a heavy ion beam of 135 MeV nucleon^{-1} in the RIKEN Ring Cyclotron. Technetium, as $NH_4{}^{99}TcO_4$, was obtained from Isotope Products Laboratories, Valencia, CA. Solutions of a multitracer and ^{99}Tc were both sterilized by passing them through a 0.2-μm-pore-size filter before use. The filter-sterilized multitracer solution contained ^{83}Rb, ^{85}Sr, ^{88}Y, ^{139}Ce, ^{143}Pm, and ^{153}Gd.

E. coli HB101 (ATCC33694) was precultured in LB medium at 37°C for 24 h. Cells were harvested, washed, and then suspended in a fresh LB medium. The abundance of the cells was determined by measuring the turbidity of the suspension at an optical density of 600 nm using a spectrophotometer UV-160 (Shimadzu, Kyoto, Japan). The solutions of the multitracer and ^{99}Tc were separately added to the culture of *E. coli*. The cultures with radioactive tracer elements were incubated at 25°C in the dark under anaerobic condition. For anaerobic incubation, a bag of Anaeropack Kenki (Mitsubishi Gas Chemical Co., Inc., Tokyo, Japan) that absorbs oxygen and emits carbon dioxide was used.

After the incubation, the culture was filtered with a 0.2-μm-pore-size filter. The radioactivities of the multitracer in the culture and its filtrate were measured using a Ge detecting system (Seiko EG & G ORTEC). The radioactivity of ^{99}Tc was measured with the Tri-Carb-25WTR Liquid Scintillation Analyzer (Packard, IL, USA).

The removal of ^{99}Tc from solution by *E. coli* was observed (Fig. 1 (a)). The initial concentration of ^{99}Tc was maintained for 1 d. This radionuclide was gradually removed from day 2 of incubation and then approximately 60% of the total ^{99}Tc added was removed on day 7 of incubation.

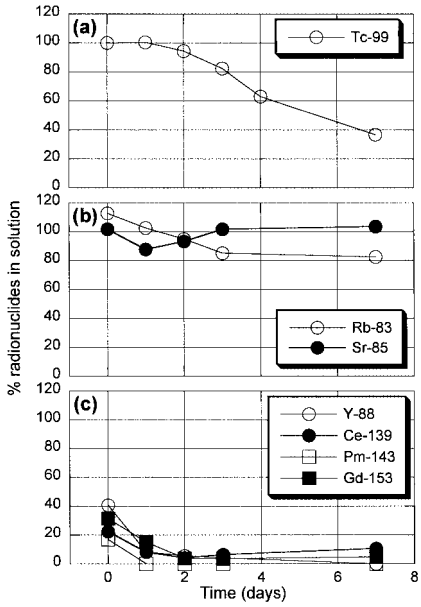

Fig. 1. Removal patterns of radionuclides from *E. coli* culture. The plots indicate the mean ($n = 3$).

For radionuclides in the multitracer solution, two types of removal pattern were observed; these patterns differed from that of ^{99}Tc. As shown in Fig. 1 (b), ^{83}Rb and ^{85}Sr were hardly removed during the experimental periods. On the other hand, ^{88}Y, ^{139}Ce, ^{143}Pm, and ^{153}Gd were immediately removed from the solution (Fig. 1 (c)). From these results, it was found that *E. coli* cells are able to remove the latter four radionuclides as well as ^{99}Tc from solution.

In the case of ^{99}Tc, *E. coli* removes it metabolically.[4] but it seems that the removal mechanisms for ^{88}Y, ^{139}Ce, ^{143}Pm, and ^{153}Gd are different from that for ^{99}Tc. For instance, approximately 75% of total ^{143}Pm added was removed even on day 0 of incubation (Fig. 1 (c)), although the measurement of radioactivities on day 0 was carried out within 1 h from the addition of the multitracer solution. The rapid removal of ^{88}Y, ^{139}Ce, ^{143}Pm, and ^{153}Gd could be a result of the electrochemical adsorption of these elements on the surface of *E. coli* cells if those radionuclides are charged positively, since the *E. coli* cell surface has a negative charge. It is necessary to determine the chemical forms of those nuclides in the culture in the next step.

* National Institute of Radiological Sciences

References

1) V. Smith et al.: J. Environ. Radioact. **56**, 269 (2001).
2) K. Tagami and S. Uchida: J. Nucl. Radiochem. Sci. **3**, 1 (2002).
3) R. E. Wildung et al.: Health Phys. **32**, 314 (1977).
4) J. R. Lloyd et al.: J. Bacteriol. **179**, 2014 (1997).

Effects of microorganisms on uptake of radionuclides by plants

T. Soshi,* I. Yamaguchi, and S. Enomoto

Radionuclides released by nuclear power plants into the environment are a potential risk to human health. Phytoremediation is an efficient method of removing radionuclides and other harmful pollutants from the soil. We showed the effects of microorganisms on the uptake of radionuclides by host plants, such as perennial ryegrass for the endophyte *Neotyphodium lolii*, rice pathogenic fungus *Gibberella fujikuroi*. The Fusarium species symbiotic to tomato was monitored using the multitracer technology. Figure 1 shows the uptake rate of several elements. In a noninfected tomato plant, the uptake rates of Na and Tc were high, about 10% for Na and 32% for Tc. For other nuclides, such as Sc, Mn, Co, Se, Rb, and Sr, the uptake rates were relatively low (1% to 8%). The uptake rates of Cs and Zn were less than 1% (0.14% Cs and 0.77% Zn). The perennial ryegrass colonized by the endophyte showed a lower uptake rate than the plant without the endophyte. *G. fujikuroi* was able to enhance the uptake of radionuclides (Cs, Sr, Mn, Zn, and Co) by rice via infection. The uptake rates of Mn and Co in an infected rice plant increased to almost as twice as those in a noninfected rice plant. *G. fujikuroi* is known to produce large amounts of gibberellins. The effect of gibberellin treatment on the radionuclide uptake by plants was almost the same effect as infection of *G. fujikuroi*. We also have analyzed the effects of five nonpathogenic strains, *Fusarium oxysporum*, *Fusarium spio rycopersici* isolated from tomato rhizosphere. Each strain showed uptake enhancement of some radionuclides by plants. Finally, we indicated that the ideal plant for phytoremediation should be fast growing, high in biomass, deep rooted, easy to harvest, tolerant and able to accumulate metals in their aerial part. However, no plant that fulfills all those criteria has been described. In terms of phytoremediation of contaminated soil using long-lived radionuclides such as Sr and Cs, the use of a rhizofungus that can enhance the uptake of radionuclides by plants is expected to increase the clean-up efficiency markedly.

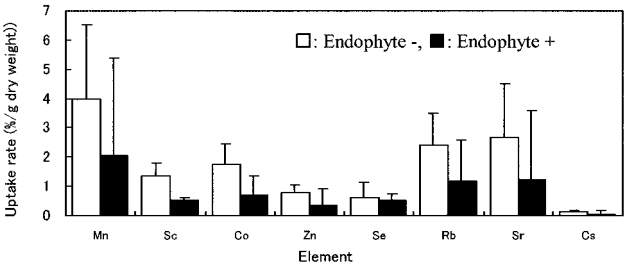

(a)

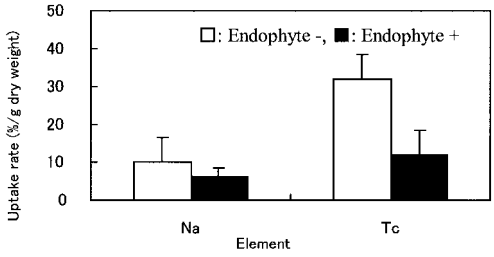

(b)

Fig. 1. Influence of endphyto on the uptake of radionuclides by perennial rygrass. (a) uptake of Sc, Mn, Co, Zn, Se, Rb, Sr, Cs. (b) uptake of Na and Tc by perennial rygrass. Data was expressed as the uptake percentage compared to the control per gram dry weight of the plant. Error bar shows standard deviation.

* Japan Environment Research Corporation

Imaging performance test of prototype model for GREI

S. Motomura, S. Enomoto, H. Haba, Y. Gono, and Y. Yano

We are developing a γ-ray emission imaging (GREI) apparatus that enables simultaneous and nondestructive imaging of multitracer distribution.[1] The current prototype model is a Compton camera consisting of two double-sided orthogonal-strip germanium (Ge) detectors. To reconstruct the distribution image, a simple back-projection (SBP) image is constructed first from the obtained data, then the SBP image is processed with analytical or iterative reconstruction methods.[2]

The quality of the image is affected by the statistics, that is, how many data are obtained for the γ rays specific for the nuclide. We have already estimated the relationship between the spatial resolution and the statistical noise components in the SBP image by Monte Carlo simulation.[3] In this report, we will show an experimental result that shows the imaging performance of the current prototype model.

The γ-ray measurement was performed under the same condition as the simulation. A pointlike γ-ray source of ^{65}Zn, which emits 1116 keV γ-rays, was placed 69 mm apart from the center of the front Ge detector. The measurement was continued until 1.0×10^5 events were collected. After the measurement, SBP images were constructed from the stored data with 1.0×10^4, 5.0×10^4 and 1.0×10^5 events.

Figure 1 shows the Fourier power spectral densities (FPSDs) of the SBP images obtained in the experiment. One can see in Fig. 1 that the statistical noise dominates the high-frequency components because they are significantly dependent on the statistics. The reconstructed images with 1.0×10^4 and 1.0×10^5 events are shown in Fig. 2. A higher spatial resolution was obtained when the number of events was larger. The relationship between the full width at half maximum (FWHM) of the reconstructed image and $(2f_c)^{-1}$ is shown in Fig. 3, where f_c is the spatial frequency that the noise components are beginning to dominate in the FPSD of the SBP image. Figure 3 seems to show that the spatial resolution has the same value as $(2f_c)^{-1}$. These results are in good agreement with those of the simulation.

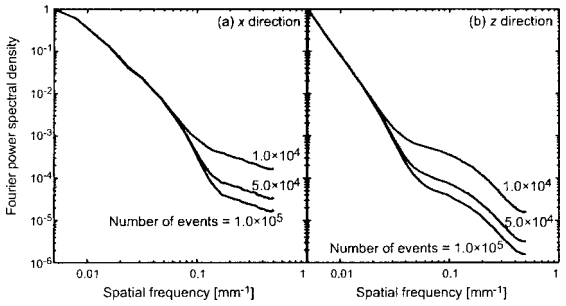

Fig. 1. Fourier power spectral densities of SBP images obtained by experiment.

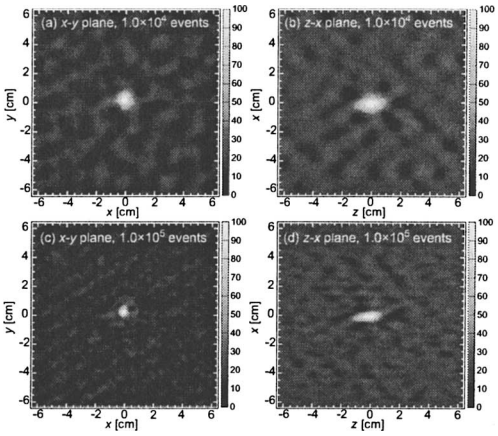

Fig. 2. Reconstructed image of point source with 1.0×10^4 and 1.0×10^5 events.

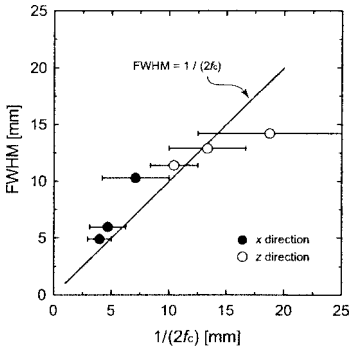

Fig. 3. Relationship between spatial resolution and statistical noise component. The definition of f_c is given in the text.

When we design detectors for use with the apparatus, the imaging performance should be optimized considering the required measurement time and the spatial resolution. However, the image reconstruction method suitable for the apparatus has not been completed yet. In spite of this, we can carry out the optimization of the performance because we have obtained the relationship between the spatial resolution and the statistical noise components in the SBP image.

References

1) S. Motomura and S. Enomoto: J. Clin. Exper. Med. **205**, 884 (2003).
2) S. Motomura et al.: RIKEN Accel. Prog. Rep. **38**, 124 (2005).
3) S. Motomura et al.: RIKEN Accel. Prog. Rep. **38**, 125 (2005).

Reactions of ^{57}Mn implanted into solid oxygen

Y. Kobayashi, H. Nonaka,[*1] J. Miyazaki,[*1] K. M. Kubo,[*2] H. Ueno, A. Yoshimi, H. Miyoshi,[*3] D. Kameda, K. Shimada,[*3] D. Nagae,[*3] K. Asahi, and Y. Yamada[*1]

We have studied novel chemical reactions of ^{57}Mn atoms with oxygen by in-beam Mössbauer spectroscopy using a short-lived radioactive beam, ^{57}Mn ($T_{1/2}$ = 1.45 min). Implantation of particles directly into an appropriate substance produces a variety of novel chemical species and exotic valence states unavailable under normal conditions. In our previous study, a high valence state of Fe(VIII) was obtained from the in-beam Mössbauer spectra of ^{57}Fe/^{57}Mn implanted into $KMnO_4$ at low temperatures.[1)] In this study, we report the in situ characterization of the reaction products between Fe and oxygen by ^{57}Fe/^{57}Mn implantation Mössbauer spectroscopy. The oxidation of Fe is a fundamentally interesting subject from the viewpoint of the corrosion of materials and catalytic reactions.

^{57}Mn particles were produced as a secondary RI beam following a nuclear projectile fragmentation of ^{58}Fe^{21+} beams (E = 63 MeV/nucleon, I = 40 pnA) accelerated by a linac and a ring cyclotron with a Be production target. The ^{57}Mn was separated and focused by the in-flight isotope separator using RIPS. Subsequently, the ^{57}Mn was implanted into a solid O_2 sample after passing through an Al plate with an appropriate thickness to suppress the beam energy down to about 26 MeV/nucleon. The stopping range of ^{57}Mn in the solid O_2 was calculated to be 180 μm from the surface with the straggling range of $\pm$100 μm. The beam intensity of ^{57}Mn was typically 5×10^6 particles/s.

The solid O_2 sample was prepared on an Al plate (18 K). The thickness of the sample was estimated to be approximately 1 mm. The 14.4 keV γ-rays emitted from ^{57}Mn were detected by a parallel-plate avalanche counter (PPAC) with an ^{57}Fe-enriched stainless-steel foil.

Solid O_2 appears in α- ($0 \le T \le 24$ K), β- ($24 \le T \le 44$ K), and γ-phases ($44 \le T \le 54$ K). The ^{57}Fe/^{57}Mn in-beam Mössbauer spectra were measured at 18, 32 and 40 K during the implantation of ^{57}Mn. The counting times were 18, 12, and 12 hr, respectively. The total implantation dose of ^{57}Mn was typically 5×10^{11} ^{57}Mn/cm^2 for one spectrum. The spectra obtained at 18 and 32 K are shown in Fig. 1 (a) and (b), respectively. The spectra obtained at 32 and 40 K have two components of Fe in the Al substance, which were a substitutional Fe atom ($I.S.$ = -0.56 mm/s at 30 K) and an interstitial one ($I.S.$ = -0.19 mm/s at 30 K);

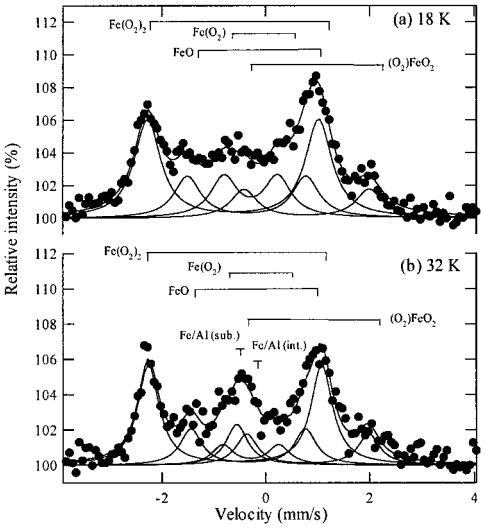

Fig. 1. In-beam Mössbauer spectra of ^{57}Fe/^{57}Mn atoms implanted into solid oxygen at (a) 18 and (b) 32 K.

some of ^{57}Mn particles reached the Al substance when the thickness of solid oxygen became smaller as the O_2 molecules evaporated due to the higher vapor pressure at higher temperatures.

Our present results of in-beam Mössbauer spectra proved to have 4 components of Lorentzian doublets. These components were assigned to FeO (S = 2), $Fe(O_2)$ (S = 1), $(O_2)FeO_2$ (S = 0), and $Fe(O_2)_2$ (S = 0) from the Mössbauer parameters ($I.S.$ and $Q.S.$). The assignments were confirmed by ab-initio molecular orbital calculations using Gaussian 98 and 03 programs. While FeO, $Fe(O_2)$, and $(O_2)FeO_2$ were also produced by the reaction of the laser-evaporated Fe atoms with O_2,[2)] divalent $Fe(O_2)_2$ was newly formed in this ^{57}Mn implantation experiment. $Fe(O_2)_2$ is a major component of resonance areas (49% at 18 K, 45% at 32 K) in the spectra (Fig. 1). Although an energetic ^{57}Mn atom certainly creates defects and decomposes the O_2 molecules until it stops at the suitable final position in solid O_2, the ^{57}Fe atom at the final position is neatly surrounded by O_2 molecules. Therefore, $Fe(O_2)_2$ is obtained as the primary ^{57}Fe product, which has O_2 without breaking O-O bond.

*1 Department of Chemistry, Tokyo University of Science
*2 College of Liberal Arts, International Christian University
*3 Department of Physics, Tokyo Institute of Technology

References

1) Y. Kobayashi, M. K. Kubo, Y. Yamada, T. Saito, H. Ueno, H. Ogawa, W. Sato, K. Yoneda, H. Watanabe, N. Imai, H. Miyoshi, and K. Asahi: J. Radioanal. Nucl. Chem. **255**, 403 (2003).
2) Y. Yamada, H. Sumino, Y. Okamura, H. Shimasaki, and T. Tominaga: Appl. Radiat. Isot., **52**, 157 (2000).

Production of ^{83}Rb for ^{83}Kr Mössbauer spectroscopy

K. M. Kubo,[*1] Y. Kobayashi, Y. Yamada,[*2] and H. Haba

Krypton is one of the rare gas (RG) elements. After xenon was found to form fluorides and is not truly inert to chemical reaction, the first krypton compound KrF_2 was synthesized in 1963.[1] Since then there have been numerous studies on the synthesis of RG compounds and clarification of the nature of their chemical bonds. On the basis of *ab initio* molecular orbital calculations, the nonfluorinated compound HKrCl was prepared in 1995.[2] There have been few attempts to prepare novel RG compounds containing RG-C bonds.[3] In these attempts, the matrix-isolation-laser-excitation (MILE) technique was adopted. A reactant compound, *e.g.*, hydrogen chloride is condensed onto a CsI substrate with a RG to form a reaction matrix. After condensation, the matrix is irradiated with a laser beam to excite the reactant to form a RG compound. RG compounds formed are confirmed by IR spectroscopy. In MILE experiments there is a limitation that one RG atom can form a chemical bond to only one reactant molecule, because the reactant concentration is kept low (molar ratio of RG/reactant $\geq$ 1000). Compounds with xenon and acetylene were prepared in 2003.[4] Krypton compounds with a similar structure are believed to exist on the basis of calculations, but have not been experimentally confirmed.

We have been applying an ion implantation method to generate novel and rare chemical compounds of Fe using the RIKEN cyclotron in combination with emission Mössbauer spectroscopy as a characterization method.[5] By this method, we prepare various solid targets to react with incoming ions. We may observe the reactions of krypton with various solid materials using the RIKEN cyclotron.

Fortunately, krypton has the Mössbauer active nuclide ^{83}Kr. Mössbauer spectroscopy provides information on the valence state and electric field gradient at the Kr nucleus, complementary to IR spectroscopy, which provides atom-atom bond parameters. With the aim of producing compounds consisting of one krypton and two or more reactant molecules beyond the scope of the dilute MILE condition, we have started a new project on ^{83}Kr Mössbauer spectroscopy using the RIKEN cyclotron. As the first, step we are setting up a Mössbauer spectrometer for ^{83}Kr using a radioisotope source, ^{83}Rb ($T_{1/2}$ = 86.2 d).

The Mössbauer level of ^{83}Kr is the first excited state at 9.396 keV. Above this level there is a metastable state, ^{83m}Kr, with a half-life of 1.83 h. There have been ^{83}Kr Mössbauer studies since the 1960's. Most of the previous studies used ^{83}Rb as the radiation source embedded in solid matrices. We chose a ^{83m}Kr source separated from ^{83}Rb to reduce the radiation background from ^{83}Rb. Carrier-free ^{83m}Kr deposited on a cold plate will enable us to obtain Mössbauer spectra of good quality.

A $CaBr_2$ target was irradiated with an α particle beam of 25 MeV. After the irradiation, the target was dissolved in water. $(NH_4)CO_3$ solution was added to precipitate and separate $CaCO_3$. For the isolation of ^{83}Rb, 18-crown-6 and picric acid were added to the solution and extracted with chloroform.[6] With a 2 g molecular sieve, the chloroform solution was evaporated. The molecular sieve containing ^{83}Rb was packed in a glass tube and placed in a gas line. Helium gas was passed through the gas line and the cold trapping of ^{83m}Kr generated from the ^{83}Rb in the molecular sieve was attempted. Measurements using a proportional counter showed no evidence of trapping of ^{83m}Kr. It was supposed that picric acid covered the surface of the molecular sieve and prevented ^{83m}Kr to escape from the molecular sieve. We are now planning to change the separation method using an ion-exchange resin instead of carrying out crown ether extraction.

References

1) J. J. Turner and G. C. Pimentel: Science **140**, 974 (1963).
2) M. Pettersson, J. Lundell, and M. Räsänen: J. Chem. Phys. **102**, 6423 (1995).
3) For example, M. Pettersson, J. Lundell, L. Khriachtchev, and M. Räsänen: J. Chem. Phys. **109**, 618 (1998).
4) L. Khriachtchev et al.: J. Am. Chem. Soc. **125**, 4695 (2003); V. I. Feldman et al.: J. Am. Chem. Soc. **125**, 4698 (2003).
5) For example, Y. Kobayashi et al.: RIKEN Accel. Prog. Rep. **38**, 111 (2005).
6) T. Kimura et al.: Chem. Lett. **1977**, 563.

[*1] Department of Chemistry, International Christian University
[*2] Department of Chemistry, Tokyo University of Science

^{99}Ru Mössbauer and μSR studies of $CaRuO_3$

Y. Kobayashi, T. Taniguchi,* I. Watanabe, T. Suzuki, S. Mizusaki,* H. Haba, T. Okada, Y. Noro,* and Y. Nagata*

A series of ternary Ru oxides, MRuO$_3$ (M = alkali earth metals), have been known to show a wide variety of magnetic properties, where the electron configuration of Ru ions is $4d^4$ in the low-spin state (S = 1). Although both $CaRuO_3$ and $SrRuO_3$ have similar distorted cubic perovskite structures, their magnetic properties are very different. Static magnetic measurement, neutron diffraction, and Mössbauer studies well established that $SrRuO_3$ becomes ferromagnetic below T_c = 165 K. However, the magnetic properties of $CaRuO_3$ at low temperatures are not yet thoroughly understood, as compared with those of $SrRuO_3$. Recent literature contains contradictory results, for example, $CaRuO_3$ is antiferromagnetic, Pauli paramagnetic, exchange-enhanced paramagnetic, weakly ferromagnetic, or in a spin-glass state with long-range ordering. The unconfirmed trigger for the magnetic behavior of $CaRuO_3$, as described above, is that the electronic states of the Ru oxides are very sensitive to the existence of disorder and defects around Ru ions.

In this study, we have applied ^{99}Ru Mössbauer spectroscopy and μSR measurement to a single crystal of $CaRuO_3$ to clarify the magnetic ground state of this sample.

Single crystals of $CaRuO_3$ were prepared by the flux method with powdered polycrystalline samples as the starting material. A polycrystalline $CaRuO_3$ sample was obtained by sintering a stoichiometric composition of RuO_2 and $CaCO_3$ at 1200°C for 48 h. Then, a mixture of a polycrystalline $CaRuO_3$ and a flux of $CaCl_2$ was heated at 1300°C for 5 h and cooled to 1100°C by the slow rate of 1°C/h. The single crystals of $CaRuO_3$ could be collected by washing out the flux. The chemical composition, the X-ray diffraction pattern, the magnetization, and the electrical resistivity were measured. The temperature dependence of the magnetic susceptibility of $CaRuO_3$ follows the Curie-Weiss law in the high-temperature region above about 50 K, but gradually deviates from the law upon lowering the temperature to 1.7 K. The effective paramagnetic moment (p_{eff}) and the paramagnetic Curie temperature (Θ) are 2.82 μ_B and −200 K, respectively. The detailed characterizations of polycrystalline and single-crystalline $CaRuO_3$ have been described in Refs. 1 and 2.

The ^{99}Ru Mössbauer spectra were measured at 5 and 1.6 K, as shown in Figs. 1 (a) and (b), respectively. The Mössbauer source nuclide ^{99}Rh ($T_{1/2}$ = 15.0 d) was prepared by proton irradiation of a 95%-enriched ^{99}Ru metal target in the AVF Cyclotron.[3] The spectra

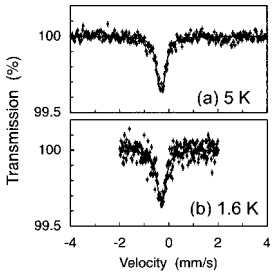

Fig. 1. ^{99}Ru Mössbauer spectra of $CaRuO_3$ at (a) 5 K and (b) 1.6 K.

down to 5 K apparently consist of small doublets with slight asymmetry, as typically observed for an electric quadrupole interaction with no appreciable hyperfine magnetic interaction, and were analyzed satisfactorily under the assumption of a pure electric field gradient with axial symmetry. The derived isomer shift and quadrupole splitting are −0.31 mm/s and 0.22 mm/s, respectively. Our Mössbauer results for $CaRuO_3$ down to 1.6 K are consistent with the absence of an anomaly in the magnetization measurement.

The μSR measurement was carried out at the RIKEN-RAL Muon Facility in the UK, using a pulsed muon beam and a ^{3}He cryostat down to 0.3 K. The ZF-μSR time spectrum (Fig. 2) can be well analyzed using an exponential function, suggesting the existence of dynamically fluctuating internal fields at the muon site. The time spectrum was decoupled by the application of an external field of 100 G, proving that the muon spin depolarized mainly due to nuclear dipole fields from Ru. From these results, we conclude that the electronic moments of Ru are in the paramagnetic state and are still dynamically fluctuating at 0.3 K. Thus, on the basis of our results of the ^{99}Ru Mössbauer and μSR studies, it is concluded that $CaRuO_3$ has no appreciable magnetic ordered state down to 0.3 K.

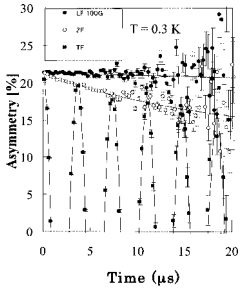

Fig. 2. μSR time spectra of $CaRuO_3$ at 0.3 K.

References

1) A. Koriyama et al.: J. Alloys Compd. **171**, 339 (2003).
2) A. Koriyama et al.: J. Alloys Compd. **372**, 58 (2004).
3) Y. Kobayashi et al.: Inorg. Chem. **31**, 4570 (1992).

* Colledge of Science and Engineering, Aoyama Gakuin University

Effect of heavy-ion-induced DNA damage on response of DNA-dependent protein kinase

M. Tomita,* M. Izumi, T. Tsukada, N. Fukunishi, H. Ryuto, Y. Yano, and K. Sakai*

Ionizing radiations induce DNA double-strand breaks (DSBs). In vertebrate cells, there are two major DSB repair pathways: non-homologous end joining (NHEJ) and homologous recombination (HR).[1] The repair of DSBs by NHEJ requires at least DNA-dependent protein kinase (DNA-PK), XRCC4 and DNA ligase IV. DNA-PK is composed of a catalytic subunit (DNA-PKcs) and DNA end-binding Ku70 and Ku86 heterodimer. DNA-PK is activated to bind to the ends of double-stranded DNA, and phosphorylates XRCC4.[2,3]

Accelerated heavy ions with high linear energy transfer (LET) can induce complex clustered DNA damage involving two or more DSBs. The complexity of clustered DNA damage shows a strong LET dependence, which makes it a good candidate prime determinant of the higher biological effectiveness of high-LET heavy ions than that of low-LET X-rays.[4] We previously reported that DNA-PKcs phosphorylated on Thr2638 is recruited in the vicinity of clustered DNA damage induced by heavy ions.[5] In addition, the relative biological effectiveness (RBE) for cell killing in DNA-PKcs-defective human M059J cells is significantly lower than that in normal M059K cells.[6] To further analyze the response of DSB repair proteins to heavy-ion-induced DSBs in vertebrate cells, we are currently investigating the sensitivity to heavy ions of mutants defective in DSB repair genes generated from the chicken B-cell line DT40. Here, we show the sensitivity of *DNA-PKcs*$^{-/-/-}$[7] cells to high-LET Ar ions.

Figure 1 shows the clonogenic surviving fractions of wild-type and *DNA-PKcs*$^{-/-/-}$ DT40 cells irradiated with 250 kV X-rays or 95 MeV/u Ar ions at 350 keV/μm. The surviving fractions were determined by a colony formation assay. The radiosensitivity of wild-type DT40 cells to Ar ions was higher than that to X-rays (Fig. 1 (A)). The dose leading to 10% cell survival (D_{10}), calculated from the cell survival curve, was 4.9 Gy and 2.8 Gy for X-rays and Ar ions, respectively (Table 1). The RBE relative to X-rays was 1.8. On the other hand, the radiosensitivity of *DNA-PKcs*$^{-/-/-}$ cells to Ar ions was not largely different from that to X-rays (Fig. 1 (B)), although the cell survival curve for X-rays was biphasic. The D_{10} values were 2.8 Gy and 2.5 Gy for X-rays and Ar ions, respectively. Thus, the RBE in *DNA-PKcs*$^{-/-/-}$ cells was 1.1, which is significantly lower than that in wild-type cells (Table 1). Our present and previous results[5,6] suggest that NHEJ cannot efficiently repair DSBs induced by high-LET heavy ions.

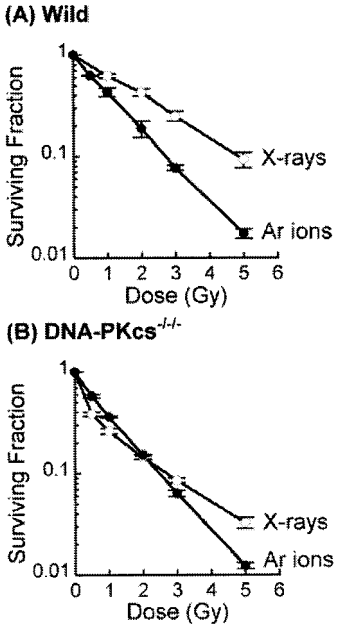

Fig. 1. Cell survival curves for wild-type (A) and *DNA-PKcs*$^{-/-/-}$ (B) DT40 cells. Cells were irradiated with 250 kV X-rays and 95 MeV/u Ar ions (350 keV/μm). Error bars represent standard errors of means (SEM), which were obtained from two to five independent experiments.

Table 1. D_{10} and RBE values.

Cells	D_{10}[a] (Gy)		RBE
	X-rays	Ar ions	
Wild	4.9	2.8	1.8
DNA-PKcs$^{-/-/-}$	2.8	2.5	1.1

[a]The dose leading to 10% cell survival.

* Central Research Institute of Electric Power Industry

References
1) K. K. Khanna and S. P. Jackson: Nat. Genet. **27**, 247 (2001).
2) G. C. M. Smith and S. P. Jackson: Genes Dev. **13**, 916 (1999).
3) Y. Matsumoto et al.: FEBS Lett. **478**, 67 (2000).
4) D. T. Goodhead: J. Radiat. Res. **40**, Suppl. 1 (1998).
5) M. Tomita et al.: RIKEN Accel. Prog. Rep. **38**, 129 (2005).
6) M. Tomita et al.: RIKEN Accel. Prog. Rep. **37**, 145 (2004).
7) T. Fukushima et al.: J. Biol. Chem. **276**, 44413 (2001).

Maximal protection by DMSO in inactivation of mammalian cells exposed to very high LET radiation

R. Hirayama,[*1,*2] A. Ito,[*3] Y. Furusawa,[*2] M. Tomita,[*4] T. Tsukada, M. Izumi, F. Yatagai, and K. Ando[*2]

Interactions between ionizing radiation and biological targets include direct action and indirect action. It has been well known that indirect action is important in the case of low linear energy transfer (LET) radiation including X-rays and γ rays. Chapman et al. reported that the extent of protection by 2 M DMSO against carbon ions with an LET of 180 keV/μm is at least 50% for cell inactivation.[1)] Roots et al. used 1.5–2 M ethylene glycol as an OH radical scavenger in Chinese hamster ovary cell inactivation by very high LET radiation.[2)] They estimated indirect action of approximately 20–25% at LETs higher than 600 keV/μm. Ito et al.[3)] estimated the maximal contribution of indirect action up to an LET of 440 keV/μm using a method proposed by Shinohara et al.[4)] in which protection level is extrapolated to an infinite DMSO concentration. In this study, we have extended the estimation of a maximal protectable fraction by DMSO to a very high LET region of up to 2000 keV/μm. The protectable fraction was estimated from the regression curves for reciprocal plots of DMSO concentration versus degree of protection that was obtained using

$$\text{Degree of protection} = (\ln \mathrm{SF}_0 - \ln \mathrm{SF}_x)/\ln \mathrm{SF}_0 \quad (1)$$

where SF_0 and SF_x are surviving fractions at 0 M and x M DMSO. The formula was calculated from the reciprocal of DMSO concentration

$$y = k \cdot (1/x) + y_\infty \quad (2)$$

where y is a reciprocal of the degree of protection by DMSO and y_∞ is a reciprocal of the degree of protection by DMSO at ultimate concentration. Slope k is an inclination of the regression line.

$$\text{Indirect action } (\%) = (1/y_\infty) \times 100 \quad (3)$$

We have examined the radioprotection effects of various DMSO concentrations on Chinese hamster V79 cells irradiated with iron ions (Fig. 1). DMSO seems to have little toxicity, because plating efficiency was high (0.83) in the presence of 1.0 M DMSO. The contribution of indirect action decreased with increasing LET, and became constant at very high LETs. The contributions of indirect action to cell death were 52, 39 and 32% at LETs of 797, 1298 and 2106 keV/μm, respectively (Fig. 2). We propose the importance of the contribution of indirect action to cell death even at very high LETs.

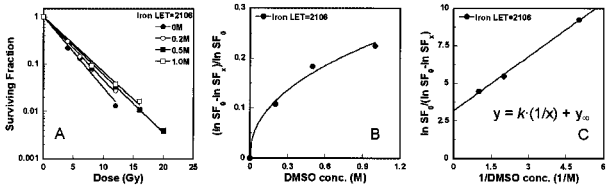

Fig. 1. Panel A: Survival data for V79 cells irradiated with iron ions in presence of various DMSO concentrations. Panel B: The degree of protection was estimated using Eq. (1). Panel C: Reciprocal plots for results shown in panel B.

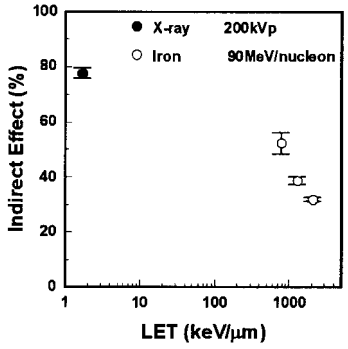

Fig. 2. LET dependence of indirect action (maximal protectable fraction by DMSO) on death of V79 cells. The error bars are SEM for a protectable fraction calculated from a regression line that was drawn for nine or twelve different points.

References

1) J. D. Chapman et al.: Radiat. Environ. Biophys. **16**, 29 (1979).
2) R. Roots et al.: Int. J. Radiat. Biol. Relat. Stud. Phys. Chem. Med. **47**, 157 (1985).
3) A. Ito et al.: Radiat. Res., in press.
4) K. Shinohara et al.: Acta Oncol. **35**, 869 (1996).

*1 Graduate School of Science and Technology, Chiba University
*2 Heavy-ion Radiobiology Research Group, National Institute of Radiological Sciences
*3 Course of Energy Engineering, Department of Applied Science, School of Engineering, Tokai University
*4 Low Dose Radiation Research Center, Nuclear Technology Research Laboratory, Central Research Institute of Electric Power Industry

Mutation induction in frozen human cultured cells by low-dose carbon ion irradiation

Y. Umebayashi, M. Honma,* T. Abe, M. Iwaki, and F. Yatagai

It is important to elucidate the genetic influences of low-dose or low-dose rate ionizing radiation at the cellular level. For the convenience of molecular analysis of mutations located in the gene as well as those extending to the chromosome, we have developed a methodology (Fig. 1) using human lymphoblastoid cell TK6 and succeeded in detecting low-dose carbon ion beam irradiation effects.[1)] Our interest extends to whether we can detect such radiation effects in TK6 after the irradiation of frozen cells. The success of our attempt is reported here.

TK6 cells are functionally heterozygous at their *TK* locus. TK6 cells were treated with HAT medium to eliminate pre-existing TK^- mutants and then frozen and kept in a $-80°C$ freezer. Then, the frozen cells were exposed to 10 cGy of C-ion (135 MeV/u) accelerated by RIKEN Ring Cyclotron, while cooling it with dry ice and ethanol. Then the cells were preserved in a $-80°C$ freezer until the assays. TK^- mutant clones were isolated on the basis of their resistance to 4 μg/ml trifluorothymidine (TFT). The early TK^- mutant clones (EM) and the late ones (LM) were selected after two and four weeks of incubation, respectively (Fig. 1). The selected TK^- mutants were first analyzed in determining the loss of *TK* heterozygosity (LOH) by the PCR analysis of the exons 4 and 7 regions in the *TK* locus. This PCR analysis also provided us the types of LOH, hemizygous and homozygous, considered as a result of the end-joining repair or homologous recombination repair of DNA double-strand breaks (DSBs), respectively. To determine the extension of deleted or replaced parts of the chromosome in the LOH mutants, we analyzed 10 microsatellites on chromosome 17 by multiple PCR.

Figure 2 shows the average values of plating efficiency (PE) and TK^- mutation frequency (MF) of more than three independent experiments. These measurements demonstrated that this level of low-dose irradiation of frozen cells is not toxic for cell viability. No toxic effects were observed after the C-ion irradiation with the same dose under normal incubation of the suspension culture. In both assays performed within a few days and after about one month, total TK^- MFs (EM + LM) were increased by the 10 cGy C-ion irradiation to about 1.6-fold (2.5×10^{-6} to 3.9×10^{-6}) and 2.1-fold (2.5×10^{-6} to 5.3×10^{-6}), respectively. Such increases were statistically significant not in the case of a few days but in the case of one month.

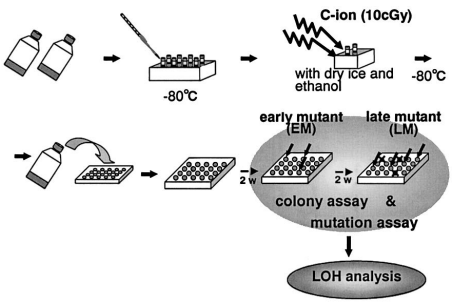

Fig. 1. Schematic illustration of experimental procedures.

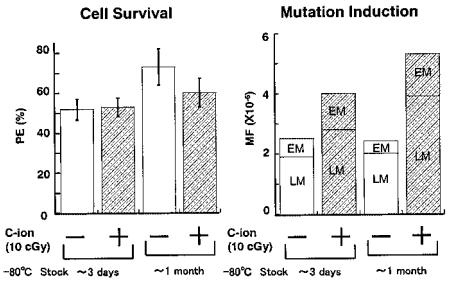

Fig. 2. Plating efficiency (PE) and *TK* mutation frequency (MF).

The PCR analysis of TK^- mutants showed no specific changes in the distribution of mutation classes (non-LOH, hemizygous LOH, and homozygous LOH) by the 10 cGy C-ion irradiation (data, not shown). However, the following characteristic changes in the fine structure of LOHs were observed after this low-dose irradiation level. As observed in the suspension culture irradiation,[1,2)] the special type of hemizygous LOH events, in which the deleted part of the chromosome does not reach the telomere marker, were identified only in the irradiation case. This LOH events can be suggested to reflect the effect of C-ion irradiation, because DSBs created by C-ion traversal through the cell result in this special type of hemizygous event through the nonhomologous end-joining repair of DSBs.

The present results suggest that this mutational analysis can be used for estimating the genetic effects of low-dose ionizing radiation, particularly heavy ions. These results could also provide the possibility of obtaining information about the genetic influences of space environmental radiation using this frozen-cell system in our future experiments at International Space Station.

* Division of Genetics and Mutagenesis, National Institute of Health Sciences

References

1) S. Morimoto et al.: J. Radiat. Res. **43**, 163 (2002).
2) S. Morimoto et al.: Radiat. Res. **157**, 533 (2002).

Study on mutants of *Monascus pilosus* induced by heavy-ion beam

T. Koide,[*1] H. Saito, Y. Miyazawa,[*2] T. Abe, H. Ryuto, and N. Fukunishi

A heavy-ion beam is available for breeding technology and much data has been accumulated, particularly regarding plants.[1)] However, there is no report about the effect of heavy-ion beams in filamentous fungi. *Monascus*, a traditional fermentation fungus, is used as a natural dietary supplement. In this report, *Monascus pilosus* IFO 4520 was exposed to various types of heavy-ion.

The conidia of *M. pilosus* for irradiation were prepared as follows. *M. pilosus* were cultured on PDA medium for 1 week, and the myceria were suspended in distilled water. The suspension was filtered using cotton to remove the myceria and the filtrate including conidia was obtained. The filtrate was irradiated with ^{12}C, ^{20}Ne and ^{40}Ar ions in dose ranges of 50 to 300 Gy, 10 to 200 Gy, and 5 to 100 Gy, respectively. These ions were accelerated up to 135, 135 and 95 MeV/nucleon, and their LETs were approximately 22.5, 61.0 and 281.5 keV/μm, respectively.

After the irradiation, the filtrates were spread on PDA medium. Survival rates were determined on the basis of colony-forming ability (Fig. 1). The lethal dose 50 (LD_{50}) was estimated from dose-response curves and the relationship between LD_{50} and LET is shown in Fig. 2. All of the dose-response curves are of the sigmoidal type. The ^{20}Ne- and ^{40}Ar-ion beams had greater lethal effects than the ^{12}C-ion beam, and this difference is thought to be due to LET. It is impossible to explain the relationship between the lethal effect and LET is impossible since there are few data in Fig. 2. Further investigation is required to reveal that LET has an optimum value or flattens over some value.

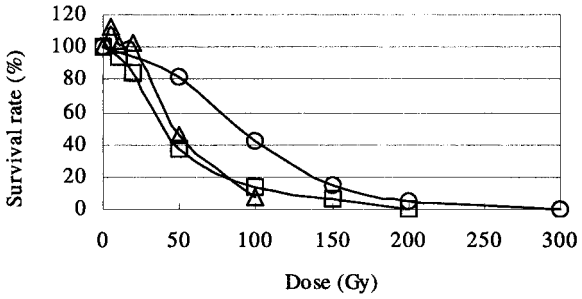

Fig. 1. Dose-response curves of conidia of *M. pilosus* IFO 4520 exposed to ^{12}C (circle), ^{20}Ne (square) and ^{40}Ar (triangle) ion beams.

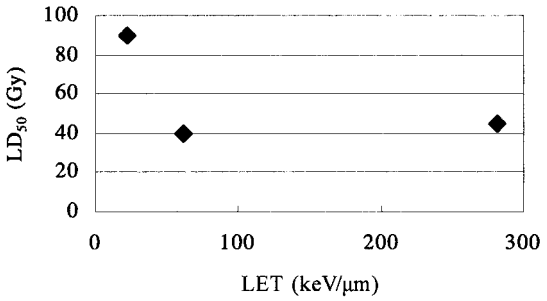

Fig. 2. Relationship between LD_{50} and LET.

Reference

1) H. Saito et al.: RIKEN Accel. Prog. Rep. **37**, 147 (2004).

[*1] Riken Vitamin Co., Ltd.
[*2] Graduate School of Life Sciences, Tohoku University

In situ visible markers of *Arabidopsis* for radiation biology

Y. Y. Yamamoto, M. Saito,* S. Yoshida, and T. Abe

In this study, two molecular markers were used for *in situ* detection of genetic alterations. The two detection markers were applied to heavy-ion biology for the first time.

The first marker is for the detection of mutation at the mutated generation (M_1). Because of the diploid nature of higher plants, a genetic mutation is not detected as a phenotypic alteration until homozygous mutants are identified at the next generation after mutagenesis ($= M_2$). However, we considered it would be possible to detect mutations at M_1, if we focus on a specific locus.

The *Arabidopsis COP9* gene suppresses anthocyanin biosynthesis, and the loss of *COP9* results in a heavy accumulation of anthocyanins, which are red pigments.[1] A null allele of *COP9*, obtained by the insertion of a kanamycin-resistant gene,[1] enables the preparation of its heterozygous seedlings ($COP9^{+/-}$). Grown on a kanamycin-containing medium, wild-type seedlings have kanamycin-sensitive white cotyledons, and heterozygotes have kanamycin-resistant green cotyledons. The homozygote ($COP9^{-/-}$) plants are also resistant to kanamycin, but have red cotyledons due to the loss of *COP9*. If the intact allele of the heterozygote is damaged by mutagens, the affected cell is expected to show red pigmentation. Because different cells undergo different mutations by mutagenic treatments, a mutagenized M_1 plant is expected to show a chimeric feature.

The seeds of *cop9* heterozygotes obtained by self-pollination, which are a mixture of segregated $COP9^{+/+}$, $COP9^{+/-}$, and $COP9^{-/-}$ seeds, were irradiated with a Ne-ion beam. The treated seeds were grown on a medium containing kanamycin, and heterozygote seedlings were selected and grown in soil. About one month after the transfer, the plants were examined for the presence of red cells. As expected, clear red sectors were observed (Fig. 1). Such sectors were not observed among nonirradiated populations of *cop9* heterozygotes (Table 1) or irradiated wild-type populations (data not shown), strongly suggesting that the sectors are caused by the mutation of *COP9*. Our results demonstrate that mutation rate can be monitored at M_1 generation using this "red sector" assay. In addition, this assay might be useful for the analysis of cell lineage, because one continuous sector is the offspring of a single cell at the time of mutagenic treatments.

We also attempted to examine the *COP1* locus[2] using the same assay, but we could not observe any clear red sectors after Ne-ion beam irradiation (data not shown).

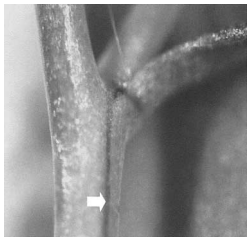

Fig. 1. Red sector on *cop9* heterozygote plant found in population of Ne-ion-beam irradiated plants. The arrow indicates the sector.

Table 1. *cop9* sectors observed on heterozygote plants.

Treatment	Red sectors/examined plants
Control	0/83
Ne-ion beam 100 Gy	6/112

The second marker is for the *in situ* detection of homologous recombination (HR). Swoboda et al. have developed an assay system in which the recombination of neighboring homologous regions results in the recovery of the split *GUS* gene, and the event is detected by GUS staining.[3] Using this assay, their group found that the irradiation with γ ray and UV enhances HR activity.[4,5] Our question is whether HR is also stimulated by irradiation with a heavy-ion beam. Dry seeds carrying the split *GUS* reporter were irradiated with the Ne beam, germinated and grown for two weeks. The seedlings were then subjected to *in situ* GUS staining, and blue areas indicating GUS activity were counted. As shown in Table 2, HR frequency increased threefold following the irradiation. We observed that the blue staining did not form long sectors as shown in Fig. 1, but a spotty staining pattern was observed in tissues that developed after germination, such as the stems and true leaves (data not shown). This observed staining pattern indicates that the stimulation of HR lasts for weeks after the irradiation and the response is systemic.

In summary, our two assays using two visible markers as described above showed reasonable responses to Ne beam irradiations, demonstrating that they are both useful for studies in radiation biology.

Table 2. *In situ* detection of HR by split GUS.

Treatment	Blue spots/examined plants[1]
Control	46/80
Ne-ion beam 150 Gy	130/80

[1]Sum of two independent experiments.

References
1) N. Wei et al.: Cell **78**, 117 (1994).
2) X.-W. Deng et al.: Cell **71**, 791 (1992).
3) P. Swoboda et al.: EMBO J. **13**, 484 (1994).
4) G. Ries et al.: Nature **406**, 98 (2000).
5) O. Kovalchuk et al.: Mutat. Res. **449**, 47 (2000).

* Fukui Agricultural Experiment Station

Einkorn wheat mutant, *mvp* which shows maintained vegetative phase is caused by ion-beam-derived mutation of wheat *APETALA1*

K. Murai,* C. Ikari,* N. Shitsukawa,* S. Shimada,* K. Sakamoto, H. Saito, H. Ryuto, N. Fukunishi, and T. Abe

The timing of the phase transition from vegetative to reproductive growth is related to heading time, which is one of the most important traits in cereal crops. In wheat, heading time is genetically determined by three component characteristics, i.e., vernalization requirement, photoperiodic sensitivity and narrow-sense earliness (earliness *per se*) that is, the autonomous promoting pathway.[1] Vernalization requirement means the sensitivity of the plants to cold temperature which accelerates spike primordium formation; vernalization-insensitive (spring habit) genes, *Vrn-A1*, *Vrn-B1* and *Vrn-D1*, were genetically identified on chromosomes 5A, 5B and 5D, respectively. The photoperiodic (long-day) response is controlled by three genes, *Ppd-A1*, *Ppd-B1* and *Ppd-D1*, located on chromosomes 2A, 2B and 2D, respectively. Narrow-sense earliness is the earliness of fully vernalized plants grown under long-day conditions, and no major genes have been detected for this character. In *Arabidopsis*, a MADS-box gene, *APETALA1*, functions in floral meristem formation as well as floral organ formation, and plays an important role in phase transition.[2] In the previous research, we revealed that the wheat *APETALA1* ortholog, *WAP1* (Wheat *AP*ETALA*1*), is a key gene in the regulatory pathway controlling the phase transition from vegetative to reproductive growth in wheat, and *WAP1* is identical to *Vrn* genes for vernalization insensitiveness, which have been genetically identified.[3] Here, we report an einkorn wheat mutant showing a *maintained vegetative phase* (*mvp*) phenotype after ion-beam treatment, which does not transit from the vegetative to reproductive phase. The *mvp* mutant was caused by the deletion of *WAP1* coding and promoter regions, which indicates that *WAP1* is an indispensable gene for phase transition in wheat.

Einkorn wheat (*Triticum monococcum*) strains KU104-1 and KU104-2 were used for ion-beam (N, 50 Gy) treatment. We obtained two alleles of *mvp* mutation, one from 1326 M_2 lines of KU104-1 and the other from 1921 M_2 lines of KU104-2, *mvp2* and *mvp1*, respectively (Fig. 1). M_3 lines, segregating *mvp* and wild-type (WT) phenotypes, were planted in the field and their phenotypes were analyzed. To confirm that the *mvp* phenotype is caused by the deletion of *WAP1*, we performed PCR analysis of individual M_3 plants. Genomic DNA was isolated from each M_3 plant, and the presence or absence of the *WAP1* gene was assessed using *WAP1*-specific primer. As a result, the *WAP1*-deleted genotype was co-segregated with the *mvp* phenotype. Furthermore, sequence analysis indicated that a deletion of the region that includes *WAP1* occurs in *mvp1* genomic DNA.

Fig. 1. M_3 line segregating *mvp2* (arrow) and WT plants.

Total RNAs were extracted from leaves of WT and *mvp* M_3 plants, and cDNAs were synthesized from the total RNAs. To examine the *WAP1* gene expression in the M_3 plants, RT-PCR analysis was conducted using *WAP1* gene-specific primer.[3] *WAP1* gene expression was started just before the timing of phase transition from the vegetative to reproductive stage, and continued during the vegetative stage in WT plants. On the other hand, no expression of *WAP1* was started in *mvp* mutants. Furthermore, no expression of the wheat *FLOWERING LOCUS T* ortholog, *WFT*, was observed in *mvp* mutants. *FT* is a promoter of the phase transition that acts in the photoperiod-dependent pathway in *Arabidopsis*.[4] Expression analysis of *WFT* indicated that *WFT* functions in the promotion pathway of phase transition after a long-day photoperiod in wheat (unpublished data). We also found that *WFT* was weakly expressed in the *WAP1* cosuppression transgenic line compared with nontransformants (unpublished data). These results, together with those of *WFT* expression analysis in *mvp* mutant, suggest that *WAP1* and *WFT* are up-regulated by each other and function in a coordinated manner. In conclusion, the mutation gene of *mvp* is *WAP1*, which is an indispensable gene for transition from the vegetative to reproductive phase in wheat.

* Fukui Prefectural University

References
1) K. Murai: Wheat Inf. Serv. **100** (2006), in press.
2) Y. Komeda: Annu. Rev. Plant Biol. **55**, 521 (2004).
3) K. Mura et al.: Plant Cell Physiol. **44**, 1255 (2003).
4) P. K. Boss et al.: Plant Cell **16**, S18 (2004).

Isolation of morphological mutants of rice induced by heavy-ion irradiation

T. Abe, H. Takehisa,[*1] M. Yasuda,[*2] Y. Hayashi, H. Saito, H. Ichida,[*3] T. Shirao,[*4] R. Onuma,[*5] H. Ryuto, N. Fukunishi, Y. Miyazawa,[*1] H. Tokairin, H. Nakashita, T. Kudo, and T. Sato[*1]

In a previous paper, we reported the effect of C-ion beams on the induction of rice mutations.[1)] In this paper, aggregate data from 2000 to 2004 represent the mutational effect of heavy ions on rice. We have also isolated a lesion-mimic mutant and a tall mutant from progenies of imbibed seeds irradiated in 2002.

The rice seeds (*Oryza sativa* L. cv. Nipponbare) were soaked for 3 days in water at 30°C without light. The seeds that imbibed water were exposed to C or Ne ions accelerated to 135 MeV/nucleon by the RRC within a dose range of 10 to 160 Gy. LET values of the C and Ne ions corresponded to 22.5 and 63.0 keV/μm, respectively. After irradiation, the seedlings were transplanted to the paddy field. M_2 seeds were harvested separately from each M_1plant approximately 6 months after irradiation. M_2 seeds were sown on seedbeds and grown in a greenhouse under daily conditions of 30°C for 11 h (daytime) and at 25°C for 13 h (night). One month later, chlorophyll-deficient mutants (CDM) were observed.

Sixty M_2 progenies which consisted of 1033 individual lines (C ion) and 13 M_2 progenies in 273 lines (Ne ion) were segregated into green plants and CDM, that is, albina (albino), xanta (yellow leaves), chlorina (pale green leaves), and striata (striped leaves) phenotypes. The optimal CDM induction was obtained for irradiation at 40 Gy for C ions and 10 Gy for Ne ions (Fig. 1). We successfully isolated a bronzing mutant (7-3b) from the 10 Gy Ne-ion irradiation and a tall mutant (6-99t) from the 40 Gy C-ion irradiation (Table 1). These two mutants were selected as homozygous phenotypes in M_3 progenies. The 6-99t strain increased plant height from 87.2 to 101.6 cm. However, the first heading date of M_3 plants was the same as the control on August 24, 2004. The 7-3b strain had brown spots on leaves similar to lesions induced by pathogens (Fig. 2). Brown spots were visible from an early development stage. Some mutants are resistant to rice blast and bacterial blight in this type of lesion-mimic mutants.[2)] Disease resistance of the 7-3b strain was examined by an inoculation test of rice blast disease caused by *Magnaporthe grisea,* one of the most economically important diseases. Four-leaf stage rice plants were inoculated with *M. grisea* race 007, and spreading necrotic lesions caused by the pathogen which appeared on the fourth leaf were counted five days after the inoculation. The number of lesions on the 7-3b strain was significantly less than that of control plants, indicating that the mutant exhibited enhanced resistance against rice blast disease. The mutants of rice induced by ion-beam irradiation could be important as genetic resources for research in plant functional genomics.

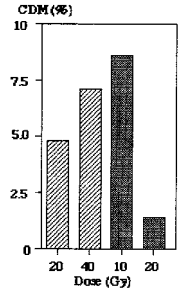

Fig. 1. Frequencies of CDP induced with ion beam irradiation. ▨: C ion and ■: Ne ion.

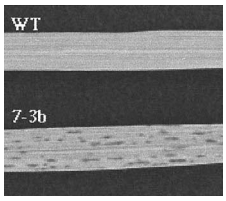

Fig. 2. Leaves of 19-week-old rice plants. WT: wild type (control) and 7-3b.

Table 1. Morphological mutants induced with ion-beam irradiation.

	Plant height (cm)	Panicle weight (g)[§]	No. of grains	Fertile grains (%)[§]	1,000 grains weight (g)
Control	87.2 ± 1.9	2.53 ± 0.13	102 ± 6	95.0 ± 0.8	24.6 ± 0.5
7-3b	80.9 ± 2.0	1.37 ± 0.04	70 ± 3	85.5 ± 2.4	21.2 ± 0.4
6-99t	101.6 ± 1.6	2.63 ± 0.07	109 ± 3	90.9 ± 0.9	25.0 ± 0.2

[§]Measured for the longest panicle.
± SE

[*1] Graduate School of Life Sciences, Tohoku University
[*2] Mayekawa MFG. Co., Ltd.
[*3] Faculty of Horticulture, Chiba University
[*4] Kagoshima Biotechnology Institute
[*5] Faculty of Science, Tokyo University of Science

References

1) T. Abe et al.: RIKEN Accel. Prog. Rep. **38**, 132 (2005).
2) R. Mizobuchi et al.: Plant Sci. **163**, 345 (2002).

Characteristics of glutinous rice mutants induced by nitrogen-ion beam irradiation

K. Ohkoshi,[*1] T. Nagashima,[*1] Y. Nishikawa,[*1] R. Hayashi,[*1] M. Ohara,[*1] Y. Ito,[*1] T. Abe, K. Sakamoto,[*2] N. Fukunishi, and H. Ryuto

Recently, heavy-ion beam mutagenesis has been widely recognized as a highly effective technique for mutation breeding. In this report, characteristics of glutinous rice mutants induced by N-ion beam irradiation on nonglutinous rice seeds are presented.

The 680 grains of dry seeds, nonglutinous rice (*Oryza sativa* L. cv. Chiba No.19), were irradiated by N ions at 135 MeV/nucleon with a dose range of 10 to 200 Gy in 1999. The M_2 seeds harvested from the seeds that had been irradiated by the same dose were mixed, and 400 seeds were selected randomly to obtain M_3 seeds. The grains of the M_3 generation that had a cloudy endosperm were selected to produce a new variety of glutinous rice in 2002. The superior lines from two generations, descendants (M_5) were selected in 2004.

The N-ion irradiation did not decrease the germination rates. The survival rates decreased when the seeds were irradiated with doses higher than 50 Gy. The rates of sterile M_2 plants increased when the doses were higher than 100 Gy. A 200 Gy irradiation produced the highest percentage, shown to be 2.2% of grains with a cloudy endosperm (Table 1). The numbers of selected M_5 lines were 23, 13, 1, 1, and 15, which resulted from 10, 20, 50, 100, and 200 Gy irradiation, respectively. The amylose contents of seeds in selected lines were measured to determine whether the seeds were glutinous or nonglutinous. The resulting amylose content ratios were approximately the same as those of the standard variety of glutinous rice cv. Himenomochi within the range from −0.36% to +0.07%. Therefore, the selected lines are glutinous rice mutants. The characteristics of glutinous rice mutants were observed at 10, 20 and 200 Gy lines. The heading periods of the selected lines were longer than that of the control (Fig. 1). The first heading dates of 10 and 20 Gy lines were earlier than that of the control. On the other hand, that of the 200 Gy line came from 1 to 6 days later than the control. The difference in the mean values of culm length between 20 Gy lines and the control was 5 cm, and 200 Gy lines and the control line was 11.6 cm. The culm length of one of the 200 Gy lines, 70.4 cm, was the longest, and it was approximately 10 cm longer than the mean value of the control (Fig. 2). Many plants that appeared in 10 Gy lines have panicle lengths shorter than the mean value of the control, 18.9 cm. Most of the plants in 20 and 200 Gy lines had longer panicle lengths than the plants in the control. As the dose increased, the culm length and the number of panicles had a tendency to increase. Therefore, we succeeded in producing glutinous rice mutants that have various heading dates and yielding abilities.

Table 1. Percentage of grains with cloudy endosperm in rice seeds irradiated by N-ion beam in 2002 (M_3).

Dose (Gy)	Number of examined grains	Rate of cloudy grains(%)
0	125900	0
10	113603	0.6
20	108497	0.3
50	154729	0.1
100	85395	0.1
200	90299	2.2

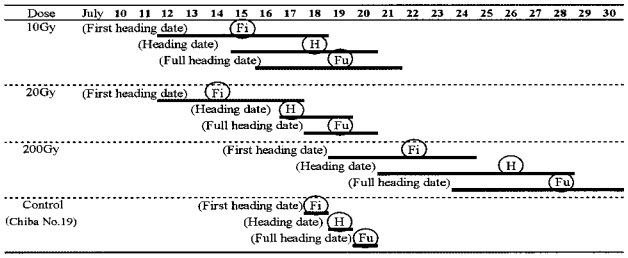

Fig. 1. Days from first to full heading on each dose of glutinous rice mutants in 2004 (M_5). The first heading date means 20% headed, the heading date means 50% headed. Each symbol (Fi)(H)(Fu) shows the date of the means of each growth stage. No. of lines for examination: 23 for 10 Gy, 13 for 20 Gy and 15 for 200 Gy.

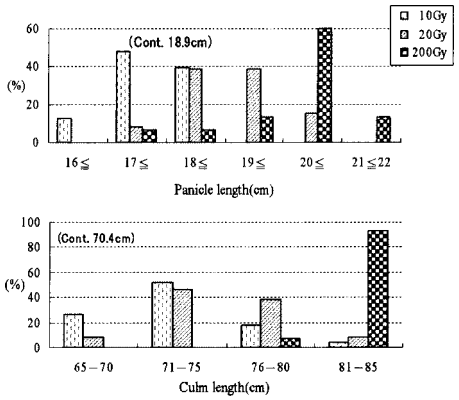

Fig. 2. Rate of panicle length and culm length on each dose glutinous rice mutants in 2004 (M_5).

[*1] Chiba Prefectural Agriculture Research Center
[*2] Japan Atomic Energy Research Institute

Mutation induction by heavy-ion beam irradiation in daylily, *Hemerocallis hybrida*

H. Saito, J. Amano,* S. Mori,* N. Fukunishi, H. Ryuto, M. Nakano,* and T. Abe

Hemerocallis species (daylilies) belonging to the Liliaceous family are very popular garden plants because of their various flower colors and forms, and high resistance to biological and environmental stresses. The breeding of these species has long been carried out by inter- and intra-specific sexual hybridization, sport selection, polyploidization, and hybridization between plants of different ploidy levels.[1] Recently, heavy-ion beams have been frequently utilized for breeding by artificially inducing mutations in various plant species.[2] Therefore, we examined the possibility of applying heavy-ion beam irradiation to the development of daylily mutants.

Adult plants of *H. hybrida* cv. Stella d'Oro were precultured at 25/22°C (day/night) for one week following cold storage at 4°C for 3 months. Sections (ca. 6 cm long), each of which includes the crown, were irradiated with ^{12}C-ion beams (135 MeV/nucleon, LET; 23 keV/μm) at a dose of up to 10 Gy. After the irradiations, sections were planted to pots and were grown at 25/22°C (day/night) under a 16 h/8 h (light/dark) photoperiod for 9 months. All flowers were artificially self-pollinated at anthesis.

All the control non-irradiated crowns sprouted within 2 months after the planting, and all crowns that survived after the irradiations also sprouted within 3-month culturing. The decrease in survival rate was observed with the increase in dose; the 10 Gy-irradiation treatment decreased the survival rate to 65%. In the case of 7.5 Gy-irradiation treatment, flowering rate and the numbers of scapes, flowers and seeds decreased to one-half of those of controls. On the other hand, branching was promoted by the irradiations at 2.5 and 5 Gy, and the number of branchings in plants irradiated at 7.5 Gy was similar to that in the control plants (Table 1).

The effects of irradiation on mutation induction are shown in Table 2. Abnormal flowers and variegated leaves were observed in the lines irradiated at the range from 2.5 Gy to 7.5 Gy. The abnormal flowers were characterized by the distortion or lobation of pistils and tepals, or an increased number of tepals. Variegated leaves partially developed during the sprouting and branching. After branching, three lines consisting of only variegated leaves were obtained by 5 and 7.5 Gy irradiations. Two lines consisting of shorter leaves than those of the control lines with the average length of 38.5 cm were obtained by 2.5 Gy and 7.5 Gy irradiations.

Morphological alterations such as the formation of abnormal flowers, variegated leaves and shorter leaves were observed in several plants at the flowering stage. These mutant lines were transplanted in a field, and their detailed characterization is in progress.

References

1) L. Hill and N. Hill: *Daylilies: The perfect perennial* (Storey Publishing, North Adams, 1991).
2) T. Abe, Y. Miyazawa, H. Saito, S. Yoshida, N. Fukunishi, H. Ryuto, and Y. Yano: Proc. 14th Symp. on Accelerator Science and Technology Tsukuba, 2003-11 (KEK, 2003), p. 578.

Table 1. Effects of C-ion beam irradiation on growth of *Hemerocallis hybrida*.[a]

Irradiation dose (Gy)	No. of plants irradiated	Survival rate (%)	Flowering rate (%)	No. of scapes per line	No. of flowers per line	No. of seeds per line	No. of branchings per line [b]
0	15	100	87	2.0±0.3	10.8±2.1	4.7±0.9	2.4±0.3
2.5	20	100	80	2.0±0.2	8.9±1.4	5.3±1.2	3.9±0.5
5	20	70	60	1.7±0.2	6.9±1.5	3.2±1.3	3.3±1.0
7.5	20	80	30	0.8±0.3	3.8±1.5	2.3±1.6	2.3±0.5
10	20	65	10	0.3±0.2	1.1±0.7	1.5±1.1	1.2±0.1

a: Values represent the mean ± standard error of the lines that survived.
b: Data show the total number of plants after branching in each line.

Table 2. Effects of C-ion beam irradiation on mutation induction in *Hemerocallis hybrida*.

Irradiation dose (Gy)	No. of plants irradiated	No. of lines with abnormal flowers / Total no. of lines flowered	No. of lines with variegated leaves / Total no. of lines survived	No. of lines consisting of only variegated leaves	Distribution of longest leaf length for each line [a]						
					20 -24	25 -29	30 -34	35 -39	40 -44	45 -49	50 -55 (cm)
0	15	1 / 13	0 / 15	0	0	0	4	3	4	1	1
2.5	20	10 / 16	4 / 20	0	0	1	3	3	6	3	0
5	20	6 / 14	3 / 14	2	0	0	2	3	6	2	1
7.5	20	3 / 6	6 / 16	1	1	0	1	0	2	2	0
10	20	0 / 2	0 / 13	0	0	0	0	2	0	0	0

a: Data were recorded in the lines flowered.

* Faculty of Agriculture, Niigata University

Sterile verbena cultivar produced by heavy-ion beam irradiation and wild species *Verbena peruviana* exhibit different self-incompatible phenotypes

H. Saito, Y. Hayashi, N. Fukunishi, H. Ryuto, T. Kanaya,* K. Suzuki,* and T. Abe

Garden verbenas (*Verbena hybrida*) of the Verbenaceae family are one of the most utilized bedding plants because of their beautiful flowers and vigorous growth. They are a result of interspecific hybridization among several species, and most of them frequently produce seeds. Recently, a sterile mutant has been isolated from the cultivar 'Coral Pink' of the Temari® series (Suntory Flowers Ltd., Osaka, Japan) by mutation induction using heavy ions.[1] In our previous study,[2] we described that the sterile mutant line exhibits self-incompatibility (SI) similarly to that in teak (*Tectonia grandis*) of the Verbenaceae family.[3] SI is an important outbreeding mechanism, and is useful to plant breeders as it provides an efficient pollination control system for the commercial production of hybrid seeds. However, it remains to be elucidated whether SI exists in wild *Verbena* species. In this study, therefore, we investigated whether the sterile mutant is a revertant that regained the SI phenotype.

Wild-type *V. peruviana* (VP), one of origins of the Temari® series, and the sterile mutant of 'Coral Pink' (SC) and its original fertile one (FC) were used. Seed set following pollination tests and the behavior of pollen tubes in pistils after self-pollination were investigated as in our previous report.[2]

Although the reciprocal pollination between VP and FC or SC produced many seeds, self-pollinated VP flowers produced no seeds (Table 1). The former result indicates that VP also has functional male and female gametes, the same as SC and FC. The latter result suggests that VP has an SI phenotype similar to that of SC[2] and teak.[3] To clarify the mechanism of SI in *Verbena*, the behavior of pollen tubes in pistils was compared among self-pollinated three lines (Fig. 1).

Table 1. Seed set following self- and cross-pollinations at anthesis.

♀ \ ♂	FC	SC	VP
FC	54 / 102 (52.9) [a]	nt[b]	nt
SC	50 / 107 (46.7)	1 / 156 (0.6)	72 / 126 (57.1)
VP	48 / 105 (45.7)	80 / 136 (59.7)	0 / 113 (0)

a: No. of flowers producing seeds / No. of flowers pollinated (%).
b: Not tested.

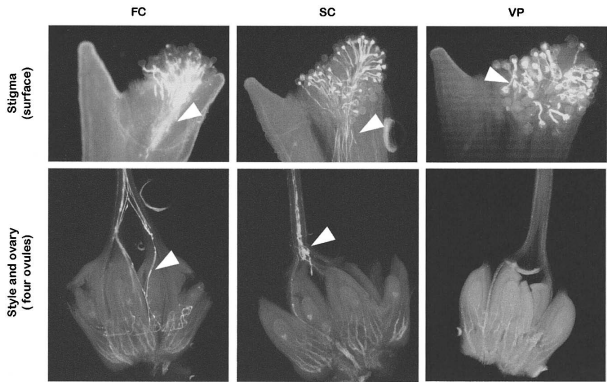

Fig. 1. Fluorescence micrographs of self-pollinated pistils 3 h (stigma) and 24 h (lower part of style and ovary) following pollination. Pistils were stained with decolorized aniline blue to localize callose. Arrowheads show pollen tubes.

Pollen germination in stigma was observed in all lines. However, almost all self-pollen tubes of SC reached the lower region of the style or the upper regions of the ovary; on the other hand, the pollen tube growth of VP was inhibited at the upper part of the style. Interestingly, a distinct difference in reaction in self-pollen rejection was observed between SC and VP. According to observations in the self-pollen-inhibited area, the SI system in SC is late-acting SI as described in teak;[3] on the other hand, that in VP is likely to be gametophytic SI which is described in other families such as Solanaceae and Rosaceae.[4] Detailed characterization and genetic analysis of the SI phenotype in the genus *Verbena* are in progress.

References

1) K. Suzuki et al.: RIKEN Accel. Prog. Rep. **35**, 129 (2002).
2) H. Saito et al.: RIKEN Accel. Prog. Rep. **38**, 137 (2005).
3) S. Tangmitcharoen and J. N. Owens: Ann. Bot. **80**, 401 (1997).
4) K. R. Shivanna: *Pollen Biology and Biotechnology* (Science Publishers, Inc., New Hampshire, 2003).

* Production Department, Suntory Flowers Ltd.

Ion beam sensitivity of ornamental plants

T. Kanaya,* K. Suzuki,* K. Miyazaki,* H. Saito, Y. Hayashi, H. Ryuto, N. Fukunishi, and T. Abe

The heavy-ion beam is known as an effective mutagen for various plants. Riken and Suntory Flowers Ltd. have jointly developed some new ornamental varieties of *Verbena* and *Petunia* using heavy-ion-beam irradiation.[1)] We report here the sensitivity of some ornamental plants to heavy-ion beams.

Plant materials developed by Suntory Flowers Ltd. were used. In vitro nodal culture materials of 'Million Bells Trailing Pink' (MBTP, *Calibrachoa* sp.), 'Senetti Blue' (SNB, *Senecio cruentus* × *S. heritierii*), 'Little Tutu Lemon Mist' (LTLM, *Scoparia* sp.), 'Sun Parasol Red Mini' (SPRM, *Mandevilla* Hybrid) and leaf discs of 'Summer Wave Large Pink & White' (SWLP, *Torenia hybrida*) were irradiated with C-ions. The survival rates of nodal culture materials of MBTP, SNB, LTLM and SPRM were calculated at the time of acclimatization (Fig. 1). All of developed shoots of SWLP were acclimatized after shoot development and counted. SWLP was also irradiated with Ne-ions and the number of shoots was counted in the same way. In the Fe-ion irradiation, leaf discs of 'Summer Wave Blue' (SWB), 'Summer Wave Violet' (SWV) and 'Summer Wave Amethyst' (SWA) were used and developed shoots were acclimatized and counted.

The survival rates of MBTP, SNB, LTLM and SPRM irradiated with C-ions are shown in Fig. 1. The rates of MBTP and LTLM decreased with increasing dosage. SPRM exhibited almost the same tendency of alteration in survival rate. The LD50 of MBTP was between 10 to 20 Gy and that of SPRM was between 20 to 30 Gy. On the other hand, the survival rate of SNB showed no particular alternation in the range of 5 to 50 Gy.

The number of developed shoots from leaf discs of SWLP decreased with increasing dosage in the range of 10 to 50 Gy (Fig. 2). In the case of Ne-ion irradiation, the number of developed shoots of SWLP markedly decreased in the range of 10 to 40 Gy (Fig. 3). When SWB, SWV and SWA were irradiated with Fe-ions, the number of obtained shoots declined in the range of 20 to 50 Gy (Fig. 4).

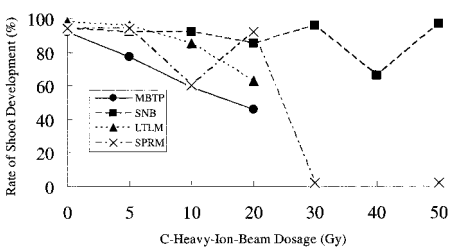

Fig. 1. Survival rates of MBTP, SNB, LTLM and SPRM irradiated with C-ion beam.

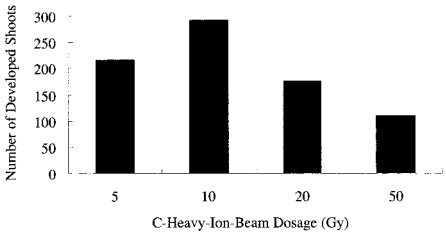

Fig. 2. Number of shoots developed from 25 pieces of leaf discs of SWLP irradiated with C-ion beam.

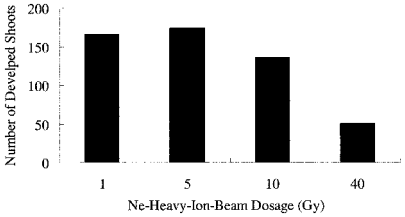

Fig. 3. Number of shoots developed from 25 pieces of leaf discs of SWLP irradiated with Ne-ion beam.

From these results, in C-ion irradiation, we suppose that 10–20 Gy for *Calibrachoa*, 20–30 Gy for *Mandevilla*, over 20 Gy for *Scoparia* and over 50 Gy for *Senecio* are effective dosages in the survival of these genera. In the irradiation for *Torenia*, 10–50 Gy of C-ions, 10–40 Gy of Ne-ions and 20–50 Gy of Fe-ions have effects on the survival. However, we should pay attention to differences in sensitivity among varieties of the same genus.

In addition to the examination of sensitivity to heavy-ion beams, we are also studying the relationship among ion type, dosage and phenotypic mutation.

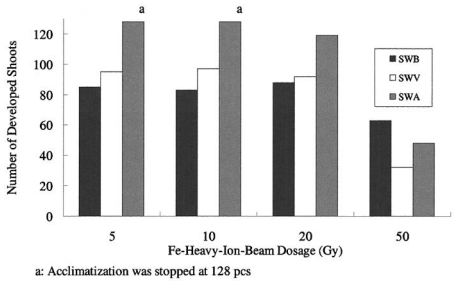

Fig. 4. Number of shoots developed from 25 pieces of leaf discs of SWB, SWV and SWA irradiated with Fe-ion beam.

Reference

1) K. Suzuki et al.: Radiation & Industries **99**, 40 (2003).

* Suntory Flowers Ltd.

Effect of heavy-ion beam irradiation on cyclamen

M. Sugiyama,* T. Terakawa,* H. Saito, Y. Hayashi, N. Fukunishi, H. Ryuto, and T. Abe

Cyclamen (*Cyclamen persicum*) is one of the most popular potted plants in winter in Japan. Thus far, a new variety of cyclamen has been developed mainly by a crossbreeding method. Using this method, it takes a long time to develop this new variety because it requires many crossbreedings to improve the plant. Recently, mutation breeding of ornamental plants and flowers by heavy-ion beam irradiation has been performed. This new method induces mutations in plants at a high frequency, which shortens the breeding process. The sterile mutants of verbena[1] and pelargonium[2] and the flower color mutants of chrysanthemum[3] and carnation[4] were developed by this method. In this study, we examined the effect of heavy-ion beam irradiation on the viability of cyclamen. This is the first step that leads to an establishment of a mutation breeding of this plant.

A callus, a somatic embryo and a plantlet of cyclamen (*cv.* Hokko mini no.1) were irradiated with a ^{12}C ion beam (135 MeV/nucleon, LET 23 KeV/μm), then the effect of the irradiation was examined. 1) A callus was produced by culturing a scape segment for one month on MS medium containing kinetin and 2,4-dichlorophenoxyacetic acid. 15 calli were irradiated at doses of 10, 20, 40, 60, and 80 Gy in each experiment. Three months after the irradiation, the amount of somatic embryo formed on the callus was determined. 2) Somatic embryos were produced by culturing scapes for three months on the same medium as above. Then 210 somatic embryos were irradiated in each experiment in the same way as the callus was. Two months after the irradiation, the survival rate of the somatic embryo was examined. 3) A plantlet was produced by germinating the somatic embryo on MS medium containing benzylaminopurine and naphthylacetic acid, and 70 plantlets were irradiated in each experiment as above. Three months after the irradiation, the survival rate of the plantlet was determined.

Somatic embryogenesis from a callus was suppressed by heavy-ion beam irradiation (Fig. 1). Severer suppression was observed at higher irradiation doses. Only 0.2 g of somatic embryo was produced at a dose of 80 Gy while 1.1 g was obtained in the control that was not irradiated. The somatic embryos and plantlets were injured by the heavy-ion beam irradiation. Only 11% of the embryos irradiated at 60 and 80 Gy survived while 41% of the control survived (Fig. 2). All the plantlets irradiated at 40 Gy and higher died while 67% of the control survived (Fig. 3). These results suggest that the somatic embryo is more resistant to heavy-ion beam irradiation than the plantlet is. We are now identifying the most suitable stage of a cyclamen culture for mutation induction by heavy-ion beam irradiation.

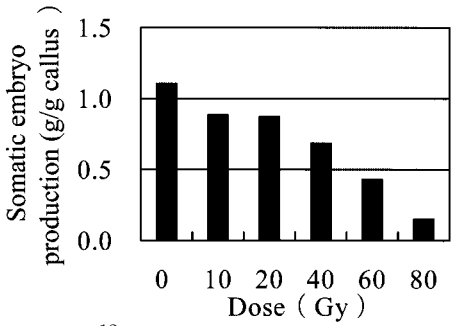

Fig. 1. Effect of ^{12}C ion beam irradiation on somatic embryogenesis. The fresh weight of the somatic embryo produced on a callus was examined.

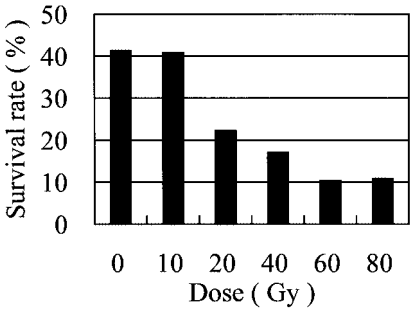

Fig. 2. Effect of ^{12}C ion beam irradiation on survival rate of somatic embryo.

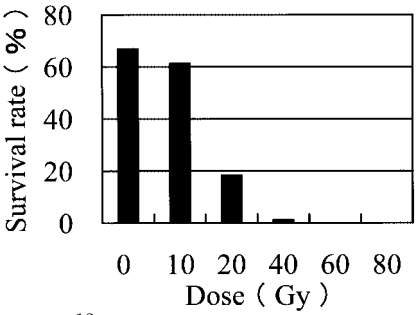

Fig. 3. Effect of ^{12}C ion beam irradiation on survival rate of plantlet.

References

1) K. Suzuki et al.: RIKEN Accel. Prog. Rep. **35**, 129 (2002).
2) M. Sugiyama et al.: RIKEN Accel. Prog. Rep. **38**, 136 (2005).
3) S. Nagatomi et al.: Breed. Sci. **48** Suppl. 1, 220 (1998).
4) M. Okamura et al.: Nucl. Instrum. Methods Phys. Res. B **206**, 574 (2003).

* Hokko Chemical Industry Co., Ltd.

STJ cryogenic detector response to α-particles

S. Bishop, H. Sato, Y. Takizawa, M. Kurakado, H. Shimizu, and T. Motobayashi

The advent of low energy radioactive ion beam facilities will provide unprecedented opportunities to probe the nuclear physics processes that occur within astrophysical events such as super novae, novae, γ-ray and x-ray bursts. A foremost objective of these low energy radioactive ion beam facilities will be to measure the rates of proton and α-particle capture reactions, and thus provide new insights into explosive nucleosynthesis. These reactions occur at sub-Coulomb barrier energies, posing severe experimental constraints on beam-induced backgrounds: at these low energies, particle identification, using gas ionization chambers and silicon detectors, with the standard $\Delta E - E$ methods fails, due to insufficient energy resolution of these detectors.

Low temperature cryogenic detectors have the potential to overcome this problem. The detector reported herein consists of a single crystal sapphire substrate 12 mm×12 mm×0.4 mm in size.[1] Fabricated onto one side of this substrate are 4 independent arrays of 864 series-connected superconducting tunnel junctions (STJ); each STJ is 110 μm in diameter and is constructed from a layering of 200 nm Nb/50 nm Al/$\approx$ 2 nm AlO_x/50 nm Al/150 nm Nb. Figure 1 shows a photograph of the detector, with relevant components labelled. The active detection area of the detector is that region within the 4 rectangular arrays, and it has an area of 8 mm×8 mm.

These detectors are essentially calorimeters and the principle of particle detection is now briefly described. A charged α-particle impinging on the sapphire substrate has its kinetic energy converted into ionization energy loss (30%) and heat (70%). Provided that the detector is cooled to $\approx$ 350 mK, the tiny temperature change of the detector substrate can be directly detected. The heat manifests itself in the form of lattice phonons. Those phonons with energy $E_{\rm p} \geq \Omega$, where Ω is the energy required to break a Cooper pair in Nb, interact with the superconducting Nb base of each STJ producing excited electrons which can then tunnel across the AlO_x barrier,[2,3] thereby creating an electrical signal representative of the incident particle's total energy.

The detector was attached to a gold plated copper mounting plate by applying a small dab of varnish under each corner of the sapphire substrate. This mounting plate, along with a calibrated ^{241}Am α-source, was then attached an "L"-shaped copper holder using common screws for both. Sandwiched between the brass mounting plate and copper holder, and 5 mm away from the α-source, was a thin strip of aluminized mylar with a $\approx$1 mm diameter hole pierced through it, serving as a collimator to prevent α events landing directly above any of the STJ arrays. The distance between the α-source and facing surface of the detector was 7 mm. This geometry allowed a circular area $\approx$ 4 mm in diameter, of the detector active area, to be uniformly irradiated by the source. Figure 2 schematically shows the experimental set-up just described. This arrangement was mounted onto the cold stage of a ^{3}He cryostat and brought to an (unregulated) operating temperature $T \approx 350$ mK. Charge sensitive preamplifiers (Ortec 142 A) were used to indepedently amplify the signals from each of the 4 STJ arrays. These signals were further processed by Canberra spectroscopic shaping amplifiers and fed to peak sensing ADC modules.

A 4-fold software coincidence requirement between the STJ array signals was imposed on the data thus obtained. Event-by-event summation of the 4 array signals results in a total energy measurement of each detected α-particle; however, this quantity is highly dependent[1] on the arrival position of the incident α-particle. This position dependence can be corrected for by using the position information as determined by charge division between the horizontal and vertical pairs of STJ arrays. Referring to Fig. 1, the x position of an event is defined as: $V_C/(V_A + V_C)$, and analogously we have for the y position: $y = V_B/(V_B + V_D)$, where, by these definitions, the coordinate origin is po-

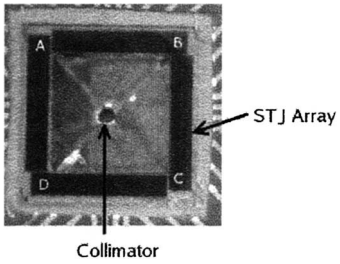

Fig. 1. Schematic side-view of STJ detector mounting on the ^{4}He cold stage.

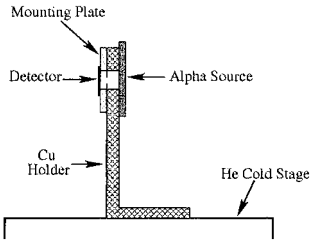

Fig. 2. Schematic side-view of STJ detector mounting on the ^{4}He cold stage.

sitioned in the lower left corner of the detector and V is the voltage signal from an array. The entire span of (X, Y) values is then subdivided into $N \times N$ cells, forming a "virtual" segmentation of the detector's active area, as depicted in Fig. 1. For each cell having sufficient statistics, a total energy spectrum is formed and the *mean* total energy value, $\langle E \rangle$, is stored. The zeroth order position correction to the total energy data involves creating a correction factor R_0, for each cell's energy values, comprised of $R_0 = \langle E \rangle_{\max} / \langle E \rangle$, where $R = \langle E \rangle_{\max}$ is the maximum mean energy value of all cells. Higher order corrections can be performed by taking the corrected R_0 values and doing a 2-dimensional Taylor series expansion in the position coordinates. To first order, the expanded correction factor for any position coordinate (X, Y) is given by:

$$r = R_0 + \frac{R_1 - R_0}{X_1 - X_0}(X - X_0) + \frac{R_2 - R_0}{Y_2 - Y_0}(Y - Y_0) \quad (1)$$

where R_0 is the zeroth order correction factor, previously described, of the cell in which the particular (X, Y) event occurs (the event cell); X_0 and Y_0 are the coordinates defining the centre of the event cell; R_1 and R_2 are the zeroth order correction factors for the nearest neighbouring cells, in the x and y directions, respectively. For these data, $N = 30$ and the minimum statistics required for each cell was 20 events; cells with less than this number of events were omitted from the analysis.

Figure 3 shows the α-particle energy spectrum obtained with this detector after approximately 1 hour of data taking; it is highly non-Gaussian and is ≈ 72 channels wide in FWHM. In contrast, the insert shows the same spectrum after applying the previously described position correction procedure of Eq. (1); the result is a highly Gaussian spectrum ≈ 18 channels wide in FWHM. The FWHM energy resolution obtained is 2.85%. This result contrasts with typical silicon detector energy resultions that are typically $< 1\%$ for ^{241}Am alpha particles. More study is required to understand the performance of the detector in regards to energy resolution. For example, an important parameter to control for future studies will be the heat conduction paths from the detector substrate to the helium cold stage; being able to more precisely control the path locations and their surface contacts with the substrate could be adjusted to optimize phonon losses to the thermal bath and, therefore, presumably improve the energy resolution.

Finally, another source of improvement for future detector design is in the electronics used for data acquisition. Figure 4 shows the corrected mean energy

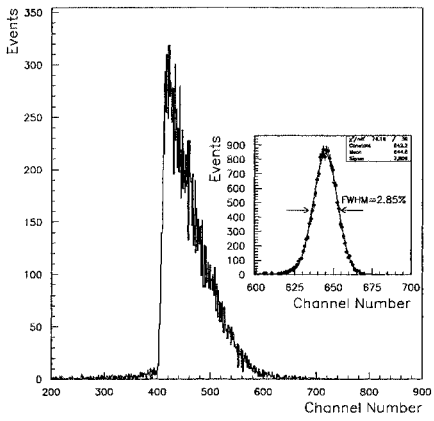

Fig. 3. Uncorrected (solid line) and corrected (insert) α-particle energy spectrum.

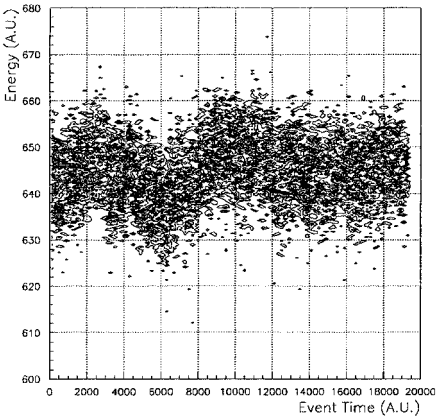

Fig. 4. Time instability of α-particle energy signals.

events as a function of event time (both in arbitrary units) during the course of the experiment. Evident in the figure is a sizable instability in the total energy signals. The source of this instability is not yet known, but one possible source could be the amplifier system used to obtain the signals. Development is now underway to design and construct preamplifiers that will be placed in the cryostat, cooled by the liquid nitrogen cooling jacket, and positioned close to the detector. In this way, electronic noise should be reduced and, perhaps, the instability observed in Fig. 4 will be eliminated.

References

1) M. Kurakado et al.: Nucl. Instrum. Methods Phys. Res. A **506**, 134 (2003).
2) M. Kurakado: X-Ray Spectrom. **28**, 388 (1999).
3) M. Kurakado: X-Ray Spectrom. **29**, 137 (2000).

Mixed-wave RF-application system for Q-moment measurements

M. Takemura,* M. Uchida,* D. Kameda, H. Ueno, G. Kijima,* A. Yoshimi, K. Shimada,* D. Nagae,* T. Haseyama, T. Arai,* S. Suda,* T. Inoue,* K. Takase,* and K. Asahi

By the β-NMR method with spin-polarized RI beams in RIPS, we measured the magnetic moments of ^{30}Al and ^{32}Al.[1] We apply this technique to the measurement of the nuclear quadrupole moments which are interesting from the viewpoint of studying nuclear deformations around "the island of inversion".[2] The Q-moment measurement, however, is more complicated than the β-NMR experiment. This is because we must control $2I$ different resonance frequencies according to quadrupole splitting, where I denotes the nuclear spin. Otherwise, the β-ray asymmetry change would be much smaller than that in the β-NMR experiment. We have developed a new RF-application system to realize spin manipulation[3,4] such that all of the $2I$ transitions between magnetic substates are induced using an RF pulse, the frequency component of which includes the $2I$ resonance frequencies.

Using a crystal sample with an electric field gradient(eq) having cylindrical symmetry about the principal axis, the $2I$ frequencies are given as $f^{m\leftrightarrow m-1} = f_0 - \frac{e^2qQ}{h}\frac{3}{2I(2I-1)}\frac{3\cos^2\theta_c-1}{2}\left(m-\frac{1}{2}\right)$, where m and $f^{m\leftrightarrow m-1}$ denote the quantum number of the magnetic substate and the resonance frequency corresponding to the RF transition between m and $m-1$, respectively. The Larmor frequency and the quadrupole coupling constant are denoted as f_0 and $\frac{e^2qQ}{h}$, respectively, and the angle between the static magnetic field and the crystalline c-axis parallel to the principal axis of eq is denoted as θ_c. In an experiment, a Q-moment region is searched with linear sweeps of the $2I$ frequencies $f^{m\leftrightarrow m-1}$ by the adiabatic fast passage (AFP) method. There are two ways in which to apply the $2I$ frequencies. i) The waveform $w(t)$ is generated by superposing sine waves, such as $w(t) = a(t)\sum_{m=I}^{-I+1}\sin\left(2\pi f^{m\leftrightarrow m-1}t\right)$, where $a(t)$ denotes the amplitude modulation (AM) of the RF field, as shown in Fig. 1 (a). A trapezoidal shape is typically employed for AM. We call the waveform $w(t)$ a mixed-wave RF pulse. The mixed-wave RF pulse is useful for very short-lived nuclei because of the short RF application time. ii) The sine waves are sequentially connected, as shown in Fig. 1 (b). In this case, we can employ a strong RF field for each sine wave. This is advantageous for spin reversal by the AFP method. The RF application time, however, becomes longer. RF applications for $\left(\sum_{n=1}^{2I} n\right)$ repetitions are needed to reverse the direction of spin polarization because the population of the m substate could be exchanged with that of the $m-1$ substate by the sweep over $f^{m\leftrightarrow m-1}$. The waveform $w(t)$ is converted into numerical data for a waveform generator, AWG615 (Tektronix). The time step of the data is determined from the time resolution and the memory length of the device.

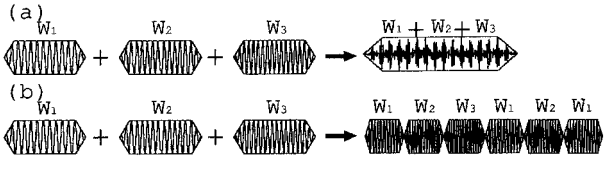

Fig. 1. RF pulse for $I = 3/2$: (a) Mixed-wave (b) Sequential-wave

In order to check this system before the Q-moment measurement of neutron-rich Al isotopes, we compared the magnitude of the change of the β-ray asymmetry of ^{12}B obtained by Q-moment measurement using this new system with the magnitude obtained by β-NMR measurement. Spin-polarized ^{12}B was produced by the projectile fragmentation of 70.0 MeV/nucleon ^{18}O projectiles on a 429 mg/cm^2 thick Nb target. The ^{12}B fragments were separated isotopically in RIPS. In order to induce spin polarization, the emission angle and the outgoing momentum were selected to be 2.1°∼6.5° and 14.2 ± 0.3 GeV/c, respectively. The spin-polarized fragments were implanted in a stopper placed at the end of the RIPS. A stack of thin Pt foils was employed in the β-NMR measurement. In the Q-moment measurement, we employed a stack of single-crystal Mg plates with the c-axis maintained parallel to the static magnetic field $B_0 = 30.5$ mT. The electric field gradient of the Mg sample and the Q-moment value were taken from the literature.[4,5]

The β-asymmetry change obtained using this new system was $A_\beta P = -1.7 \pm 0.1\%$, which was 30% smaller than that obtained by β-NMR measurement, where A_β and P denote the β-ray asymmetry factor and spin polarization, respectively. We consider that the reduction of the β-asymmetry change results from the inhomogeneous broadening of the spectrum due to the position distribution of ^{12}B in the crystal sample. From the results, we conclude that the new RF-application system is available for the Q-moment measurement.

* Department of Physics, Tokyo Institute of Technology

References

1) H. Ueno et al.: Phys. Lett. B **615**, 186 (2005).
2) E. K. Warburton et al.: Phys. Rev. C **41**, 1147 (1990).
3) E. Arnold et al.: Phys. Lett. B **281**, 16 (1992).
4) T. Minamisono et al.: Phys. Rev. Lett. **69**, 2058 (1992).
5) H. Izumi et al.: Phys. Lett. B **366**, 51 (1996).

Development of recoil particle detector system for proton elastic scattering

H. Takeda, H. Sakurai, T. Ichihara, T. Suda, Y. Watanabe, T. Ohnishi, H. Sakaguchi,[*1] T. Murakami,[*1] S. Terashima,[*1] J. Zenihiro,[*1] Y. Iwao,[*1] T. Fukui,[*1] H. Matsumoto,[*1] Y. Matsuda,[*2] and M. Kitayama[*2]

Density distributions of nuclear charge and matter are one of the most fundamental information in nuclear physics. However, unambiguous information about matter and neutron distributions in nuclei is difficult to obtain, since electromagnetic interaction provides little information about neutrons. Among various strongly interacting probes, proton elastic scattering at intermediate energies (200 – 400 MeV) has served as one of the best methods for probing matter density distributions in nuclei. For stable nuclei, we have succeeded in extracting neutron distributions from proton elastic scattering measured at RCNP in Osaka University.[1)] In the case of unstable nuclei, an inverse kinematic method is the only way to perform proton elastic scattering, in which the beam is composed of the nucleus of interest. Scattering angles and energies of recoil protons must be measured to distinguish between elastic and inelastic scattering.

To perform such measurements at the RIBF being constructed in RIKEN, we developed a recoil particle detector system, which consists of a solid hydrogen target (SHT),[2)] multiwire drift chambers (RDCs) for determining scattering angles, a thin plastic scintillator for triggers, and NaI(Tl) scintillators[3)] for measuring total energies of recoil particles. In addition to the recoil particle detectors, another set of multiwire drift chambers (BDCs), a delay-line PPAC with a 150 mm×100 mm active area and 2 mm pitch scintillating fiber (SciFi) detectors with a 120 mm×50 mm active area were developed to measure the incident beam. The BDC will be located just upstream of the target to measure the position and angle of the beam at the target position. The PPAC and SciFi detectors will be installed at the dispersive focal plane of the beam line to select the momentum of the beam.

We performed three experiments this year. The first one was performed at the RIKEN E1C course in June. The recoil particle detectors were fully installed for the first time. A schematic view of the experimental setup is shown in Fig. 1. The BDC was not installed because it was under construction at that time. A 0.5-mm-thick CH_2 target was used instead of the SHT. An ^{40}Ar primary beam at 95 MeV/nucleon was used. We succeeded in observing recoil protons coinciding with the beam events.

To evaluate the performance of the beamline detectors (BDC, PPAC and SciFi) at an intermediate-energy beam, the second experiment was performed

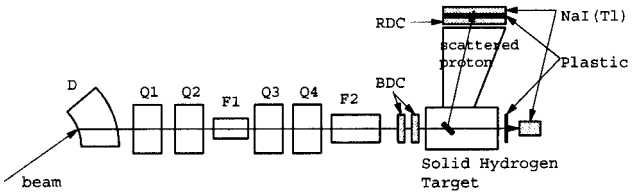

Fig. 1. Schematic view of experimental setup at E1C beam line.

at the SB2 beam line of the Heavy Ion Medical Accelerator in Chiba (HIMAC) in July. A ^{22}Ne primary beam at 390 MeV/nucleon was bombarded on a 30-mm-thick ^{9}Be target to produce an ^{20}O secondary beam at 300 MeV/nucleon, which was directly applied to the detectors. Position resolutions of 150 μm and 500 μm in sigma were achieved for the BDC and PPAC detectors, respectively. The efficiencies of the BDC and SciFi detectors had plateaus at 90–99% even at the maximum beam intensity of 10^6 particles/sec; however, we could not find a plateau for PPAC efficiency. Smaller energy losses at a higher energy region decreased efficiency and higher voltages were required for operation. Discharge occurred before efficiency reached a plateau. More investigations are required for the PPAC detectors to work at an intermediate-energy beam.

Finally we carried out the system integration test again at the E1C course with an ^{40}Ar beam in October. The experimental setup was almost the same as the previous experiment except for BDC installation and the 3-mm-thick SHT target covered with 60 μm kapton windows on both sides. The analysis is now in progress.

We are planning to perform proton elastic scattering off ^{20}O using the fully installed recoil particle detector system at the HIMAC in this coming February.

References

1) H. Takeda et al.: AIP Conf. Proc. **610**, 648 (2002); AIP Conf. Proc. **675**, 720 (2003); Proc. Kyudai-RCNP Int. Mini-Symp. on Nuclear Many-Body and Medium Effects in Nuclear Interactions and Reactions (MEDIUM2002), Fukuoka, 2002-10 (World Scientific, Singapore, 2003), p. 269; S. Terashima et al.: RCNP Ann. Rep. **2002**, p. 43.
2) T. Ohnishi et al.: RIKEN Accel. Prog. Rep. **38**, 150 (2005).
3) H. Takeda et al.: RIKEN Accel. Prog. Rep. **38**, 146 (2005).

*1 Department of Physics, Kyoto University
*2 Department of Physics, Tohoku University

Neutron polarimeter for test of Bell's inequality

K. Yako,[*1] K. Miki,[*1] S. Noji,[*1] H. Kuboki,[*1] T. Kawabata,[*2] and H. Sakai[*1]

In 1935, Einstein, Podolsky, and Rosen (EPR) claimed that quantum mechanics is incomplete in terms of local realism, which is a classical conception of nature.[1)] This argument was developed by Bell quantitatively and he showed that any local hidden variable theory will result in an inequality, which contradicts quantum mechanical prediction.[2)] We have started a series of experiments to test the inequality in a proton-proton system and a proton-neutron system by measuring the spin correlation.

To test Bell's inequality in a proton-neutron system, proton-neutron pairs in $^1S_0$ are produced by the $d(d, pn[^1S_0])pn[^1S_0]$ reaction at $E_d = 135A$ MeV. The polarization of the proton is analyzed using a focal plane polarimeter (EPOL)[3)] installed at SMART in the E4 experimental area. The neutron spin is analyzed using a neutron polarimeter (NPOL). The requirements for NPOL are an energy resolution of < 1 MeV and a figure of merit (FOM $\equiv \epsilon_d A_y^2$) of $> 10^{-5}$, where ϵ_d and A_y are the double scattering efficiency and the effective analyzing power of NPOL, respectively.

NPOL is located 18 m away from the target. A schematic view of NPOL is shown in Fig. 1. NPOL consists of four stacks of three planes of plastic scintillators. Each plane is made of six plastic scintillators (Bicron BC408) with dimensions of $10 \times 60 \times 3\,\mathrm{cm}^3$, which is viewed from both sides using photomultiplier tubes (PMTs) such that the positions are obtained from the timing information derived from the PMTs. The typical position resolution is 3 cm in the longitudinal direction of the scintillator. The neutron polarimetry is based on the scattering asymmetry of events in which two successive stacks are hit. The first stack serves as a neutron polarization analyzer (NA), whereas the next stack placed downstream by 55 cm serves as neutron catcher (NC). The polar angle θ and azimuthal angle ϕ of neutron scattering in NA are determined from the position information in NA and NC. The most useful event is the elastic scattering of a neutron by a proton in NA and its detection in NC. To eliminate signals due to charged particles in the counter planes, three sets of thin plastic scintillators with dimensions of $20 \times 60 \times 0.5\,\mathrm{cm}^3$ are placed in front of each scintillator stack.

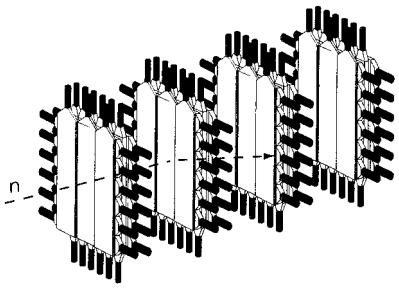

Fig. 1. A schematic view of NPOL.

A_y is measured using the monoenergetic neutron beam produced by polarized neutron beams produced by the $^6\mathrm{Li}(d, n)X$ reaction at 0° at $E_d = 135A$ MeV. The typical polarization of the neutron beam, estimated from the polarization of the deuteron beam p_d, is $p_n = p_d = 0.64 \pm 0.02$.[4)] The efficiency is calibrated using neutrons produced by the $^7\mathrm{Li}(p, n)$ reaction.[5)]

The incident neutron energies are obtained by the time-of-flight (TOF) technique. The intrinsic time resolution is 0.4 ns. The estimated energy resolution including the effect of counter thickness is 0.9 MeV. The sector method was applied to obtain A_y.[4)] The software cuts are optimized, as shown in Table 1, to obtain the maximum FOM. The results are $\epsilon_d = (4.2 \pm 0.1) \times 10^{-4}$, $A_y = 0.28 \pm 0.01$, and FOM $= (3.2 \pm 0.1) \times 10^{-5}$. The systematic uncertainty due to uncertainty in p_d is estimated to be ± 0.01. The FOM value is consistent with similar NPOLs at IUCF[6)] and RCNP[7)] when the FOM value is normalized by the total volume of the plastic scintillators.

Table 1. Optimized cuts[4)] applied to NPOL data.

Quantity	Cut
ϕ	$\Phi = 66.8°$
θ	$(\theta_{\min}, \theta_{\max}) = (16.0°, 36.5°)$
Pulse height	$> 5.0\,\mathrm{MeV}_{ee}$
Velocity ratio	0.77–1.09

References
1) A. Einstein, B. Podolsky, and N. Rosen: Phys. Rev. **47**, 777 (1935).
2) J. S. Bell: Physics **1**, 195 (1964).
3) T. Saito et al.: RIKEN Accel. Prog. Rep. **37**, 45 (2004).
4) K. Yako et al.: RIKEN Accel. Prog. Rep. **38**, 156 (2005), and references therein.
5) T. N. Taddeucci et al.: Phys. Rev. C **41** 2548 (1990).
6) M. Palarczyk et al.: Nucl. Instrum. Methods Phys. Res. A **457**, 309 (2001).
7) T. Wakasa et al.: Nucl. Instrum. Methods Phys. Res. A **404**, 355 (1998).

[*1] Department of Physics, University of Tokyo
[*2] Center of Nuclear Science, University of Tokyo

Improvement of resolving power of multireflection time-of-flight mass spectrometer

Y. Ishida, M. Wada, Y. Yamazaki, and H. Wollnik*

A multireflection time-of-flight mass spectrometer (MR-TOF)[1] has been developed for the precise mass measurement of short-lived nuclei, which will be provided at the slow RI-beam facility (SLOWRI) of RIKEN-RIBF.[2] Bunched slow ions from SLOWRI will be transferred to a linear ion trap to be compressed in phase space. The MR-TOF consists of two coaxially arranged ion mirrors. Ions ejected from the ion trap and injected into the MR-TOF will move back and forth repeatedly between the ion mirrors in an energy-isochronous manner. Thus, ion flight time increases while the ion bunch duration remains constant.

In a previous report[3] a mass resolving power $m/\Delta m$ of more than 60,000 was reported. With sufficient statistics, i.e., more than three hundred ions their masses can be determined at less than 1 ppm. This precision is sufficient for studying the global properties of the nuclear structure and for probing theoretical models. However, further system improvements are desirable because of the small yields of ions in the region far from the β-stability and because it would be advantageous to separate ions of nuclei in the ground state from those in the isomeric state. Also, it is necessary to eliminate the long tails of mass peaks caused mainly by angle and energy straggling events in ion-atom collisions.

By computer simulations using SIMION,[4] it was found that ions with large position deviations from the central axis at the middle between the ion mirrors are responsible for the long peak tails in the mass spectrum. To eliminate such off-axis ions, a 3-mm aperture was placed in front of the ion detector. Figure 1 shows the obtained mass spectrum after a flight time of ≈3 ms using CO ions with a mass of 27.9949 u and N_2 ions with a mass of 28.0061 u. From this spectrum we obtained a FWHM mass resolving power of $m/\Delta m \approx 110{,}000$, which is almost twice that previously reported.[3] Moreover, the tails of the mass peaks markedly decreased compared with those of the previous spectrum, so that the full width at one-tenth maximum in mass unit decreased to one-third of that previously reported.

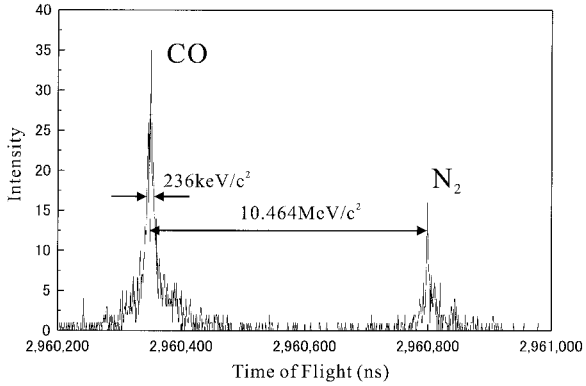

Fig. 1. Mass spectrum of CO-N_2 mass doublet after flight time of ≈3 ms.

Since the back end of the entrance ion mirror through which the ions must be injected is at a positive potential with respect to the drift region between the ion trap and MR-TOF even at the time of ion injection, the ions diverge when entering the ion mirror. To minimize such divergence, it would be advantageous to place round lenses between the ion trap and MR-TOF.

Another method for improving the emittance is to cool the ion trap and He buffer gas. This will reduce not only the ion spacial distribution but also the average ion velocity in the trap. As a result, we expect that shorter ion pulses are extracted from the trap, thus, the mass resolving power is improved. We are preparing to cool the ion trap using a cryogenic refrigerator.

References

1) Y. Ishida et al.: Nucl. Instrum. Methods Phys. Res. B **219/220**, 468 (2004).
2) M. Wada et al.: Nucl. Instrum. Methods Phys. Res. B **204**, 570 (2003).
3) Y. Ishida et al.: RIKEN Accel. Prog. Rep. **38**, 164 (2005).
4) D. A. Dahl: Int. J. Mass Spectrom. **200**, 3 (2000).

* University Giessen, Germany

Development of low-energy muon beam line at the RIKEN-RAL muon facility

Y. Matsuda, P. Bakule, Y. Ikedo,* K. Ishida, M. Iwasaki, S. Makimura,* T. Matsuzaki, Y. Miyake,* K. Nagamine, K. Shimomura,* and P. Strasser*

Spin polarized positive muons (μ^+) have a unique application in condensed matter physics as extremely sensitive magnetic microprobes. Muons implanted into a host material can convey information about the local magnetic field distribution and fluctuations through the rotation or relaxation of their spin. The change of muon spin distribution can be observed by measuring the angular distribution of positrons into which muons decay. This technique is called μSR, and has been used for various materials.

Until now, μSR experiments have been carried out using "surface muons," whose range is approximately 1.4 mm in water and 0.3 mm in iron. To study the magnetic properties of thin films or multi-layered structures with the depth sensitivity on the nanometer scale, muon beams whose kinetic energy can be varied from sub-keV to a few tens keV, with their uncertainty within several percent, are required.

We have been developing a technique[1] that allows us to produce muons with kinetic energy as low as 0.2 eV by resonant laser ionization of thermal muonium atoms (μ^+e^-). Since our first generation of low-energy muons in 2001,[2] we have increased the power of ionizing lasers, and have optimized both the focusing of the incident muon beam and the transport efficiency of low-energy muons after re-acceleration. This has resulted in the yield of low-energy muons being increased by a few hundred fold to 15 μ^+/sec at the sample position. Our measurement shows no saturation of the yield with the power of ionizing laser, suggesting that further increase can be expected as the laser system is improved.

The characteristics of the low-energy muons were measured by a 2-dimensional position sensitive MCP. The observed beam profile at the sample position showed that the muons were tightly focused to a spot of $3 \times 4\,\mathrm{mm}^2$ (FWHM), which is more than 100-fold smaller than the size of the conventional surface muon beam. The temporal width of the low-energy muon was less than 10 nsec, which is 10-fold narrower than that of the surface muon beam. These results demonstrate that our method is ideally suited to pulsed muon sources, including the RIKEN-RAL muon facility.

A compact μSR spectrometer has been installed in the beam line. A solenoid-type magnet can apply a magnetic field of up to 700 Gauss at the sample position. Plastic scintillators cover around 80% of total solid angle from the sample position, maximizing the positron signal from low-energy muons. A GM refrigerator is mounted to the spectrometer, enabling the cooling ofa sample down to 10 K.

As a demonstration of the high time resolution of the low-energy muon beam, we have implanted 15 keV muons into SiO_2 and observed the spin precession signal from triplet muonium in transverse magnetic fields of 50 Gauss and 100 Gauss at room temperature. As shown in Fig. 1, there was no observed reduction in asymmetry between the two measurements, which implies that higher frequencies of up to 30 MHz could be observed without a loss of asymmetry.

For the first application of this low-energy muon beam, we are considering the measurement of the magnetic properties of a thin perovskite manganite film grown on $SrTiO_3$ substrates. Perovskite manganites show various interesting phenomena, such as colossal magneto-resistance effect, which have large potential for device application. However, it is understood that the phase diagram of thin perovskite manganite films are different from that of bulk crystals due to lattice strain from the substrates. The measurement of such a system will be a good demonstration of the capability of low-energy muons as a unique probe of magnetic properties for thin films and multilayer systems.

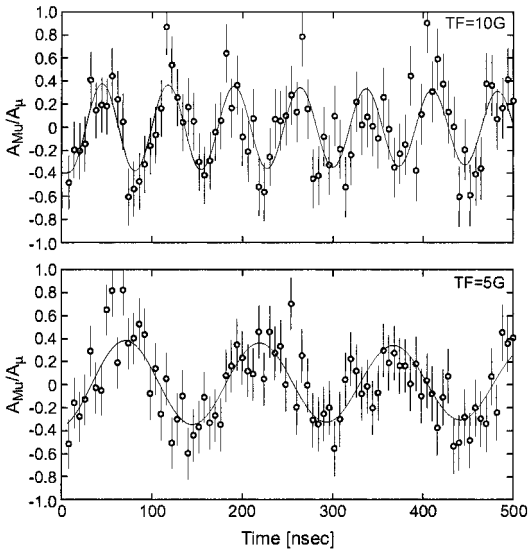

Fig. 1. Muonium spin precession signal in SiO_2. The asymmetry is shown relative to the diamagnetic asymmetry in bulk aluminium of 10.4(3)%.

* High Energy Accelerator Research Organization (KEK)

References

1) P. Bakule et al.: Spectrochim. Acta B **58**, 1019 (2003).
2) Y. Matsuda et al.: Physica B **326**, 217 (2003).

Particle discrimination using pulse shape analysis in Si detector

M. Kurokawa, H. Baba, M. Yamaguchi, S. Nishimura, T. Fukuchi,[*1] A. Ozawa,[*2] and Y. Tagishi

To identify the charge and mass numbers of nuclei, the pulse-shape discrimination of a signal from a Si detector was proposed more than 40 years ago. The technique is based on a monotonic increase in charge collection time with the charge and mass number of nuclei having the same energy. The increase is associated with a longer distance between an electrode on the junction side and the position where an incident particle induces ionization with the highest density. Collection time can be obtained by applying the appropriate analyzing method to a signal pulse from a detector. Since the idea was realized by Pausch et al.[1] for the first time, different analyzing methods have been examined over these ten years to improve the capabilities of the technique. In spite of these efforts, the discrimination in a low energy region has been constrained because of an unexpected phenomenon. Shorter time information has been obtained from the analyis for longer distance. To find an analyzing method which can prevent the constraint, charge collection time should be studied directly. Because the normalized pulse height of the signal from a preamplifier is directly related to the position of the charge carriers generated by the ionization, we recorded the pulse shape at the ouput stage of a preamplifier for light-charged particles with low energy without performing any analysis.

Beam test was performed at the TANDEM accelerator at the University of Tsukuba. The incident energy of a ^{7}Li beam was 20 MeV, and scattered particles by a C_6D_4 target were detected using an ion-implanted Si detector manufactured by Canberra. The specifications are shown in Table 1. The detector was operated at the bias voltage required for the total depletion and was irradiated from the ohmic side. The junction side is divided into 4 strips. To record the pulse shape from a strip, the signal of the preamplifier was coded by a sampling ADC (SIS3301) with a resolution of 14 bit and 100 MSamples/s. The rise time of the preamplifier was 75 ns for a signal from the strip with a capacitance of 250 pF.

Table 1. Specifications of detector used in this study.

type	effective area mm^2	thickness μm	depletion voltage V
n	50×50	320	20

In Fig. 1, the energy dependence of the extracted rise time, which is defined here as the time difference when the magunitude of the pulse reaches 15 and 60% of its maximum height, is shown for the recorded pulse shapes. The energy was obtained by trapezoidal shaping. As shown in the figure, charge discrimination is possible down to a total energy of 3 MeV, which corresponds to the stopping range of 6 μm for a ^{7}Li ion. This is the first result for the ion with an energy lower than 5 MeV showing the possibility of pulse shape discrimination. On the other hand, the present analysis also shows the problem similar to that described previously. For He and Li ions below 8 MeV, rise time is decreasing as a function of energy and each locus merges below 3 MeV.

The present results show that the rise time does not seem to depend on atomic number in such a low energy region. An attempt to extract a timing corresponding to the starting point of the signal is now in progress.

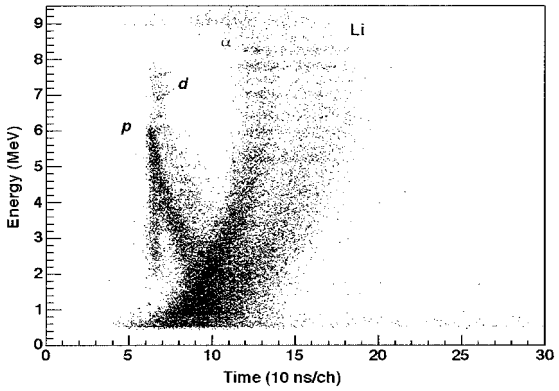

Fig. 1. Relationship between energy and rise time (see in the text).

Reference

1) G. Pausch et al.: IEEE Trans. Nucl. Sci. **43**, 1097 (1996).

[*1] Department of Physics, Rikkyo University
[*2] Department of Physics, University of Tsukuba

Recent development of liquid hydrogen target

K. Tanaka, Y. Kondo,[*1] M. Tamaki,[*2] H. Suzuki,[*2] T. Nakabayashi,[*1] K. Kobayashi,[*3] Y. Yanagisawa, T. Minemura,[*4] H. Ryuto, T. Motobayashi, and H. Sakurai

A liquid hydrogen target[1)] has used in several experiments.[2)] In recent years, we have improved it for application in a reaction cross-section (σ_R) measurement. The main goal is to make the 30 mm thickness of the liquid hydrogen target within 1% error, because the accuracy of the target thickness directly reflects that of σ_R. To achieve this goal, we have tried to precisely control target thickness and the temperature of the liquid hydrogen target, because the density of a liquid depends on temperature.

The target cell consists of an aluminum frame and a thin beam window where a beam from an accelerator passes through. This window film is swelled by a pressure difference between a vacuum outside the cell and the gas or liquid inside. To reduce the thickness error, it is important to lower and control the swelling height of the cell window. Therefore, we employed a Havar-alloy foil as the window for which the tensile strength is very heigh. In the past, we used a Kapton-resin film for the beam window. However, it easily expanded, thus, the swelling height became large and the repeatability of the height was not reliable. However, the wrinkle on the Havar window film increased the swelling height when the cell was filled with hydrogen gas, therefore, we tried to remove it.

The Havar foil was easy to peel at the cryogenic temperature, because the thermal shrinkage due to the lower temperature between a metal and an adhesive agent of a resinous matter is large, although we utilized the Stycast 1266A Epoxy adhesive agent for which the thermal shrinkage is small. On the other hand, the thermal changes of the Kapton-resin film and Epoxy adhesive agent are similar, thus, the Kapton window was stable against the temperature change. Therefore, we glued the ring of the Kapton firm on the boundary between the Havar foil and the aluminum frame of the cell to strengthen the stability of the gluing. The improved cell was tolerant under 2 atm pressure against a vacuum and was stagle for many times phase transitions of the liquid hydrogen.

The wrinkles on the window mainly occurred after heating the adhesive agent up to 93 degree as a second stiffening to strengthen the stability of the glued Havar window. With the Kapton-ring method, the adhesive power was sufficiently strong to make a liquid hydrogen target without the second stiffening. Therefore, we omitted the heating for the second stiffening to reduce the wrinkles. A typical window is shown in Fig. 1.

We measured the shape of the window under several conditions. The distance between the sensor and the surfaces of the beam window and the cell frame was measured using the Laser displacement sensor KEYENCE LK-500 within 0.1 mm accuracy, and scanned in the horizontal and vertical directions from the target center. Table 1 shows the results of the swelling height at the center of the beam window. The error in Havar window height is 0.1 mm. The typical window swelling is shown in Fig. 2.

Temperature control is also important to deduce the thickness of the liquid hydrogen target because the density of a liquid depends on temperature. In the case of liquid hydrogen, the density changes 1% per 0.6 K temperature change.[3)] We used the Si diode thermometer SCIENTIFIC INSTRUMENTS Si410AA in which the accuracy is within 0.1 K. The sensor output was read using the LAKESHORE 331S Temperature Controller, which controls the heater current automatically with proportional-integral-derivative control loops based on the user-set temperature and feedback

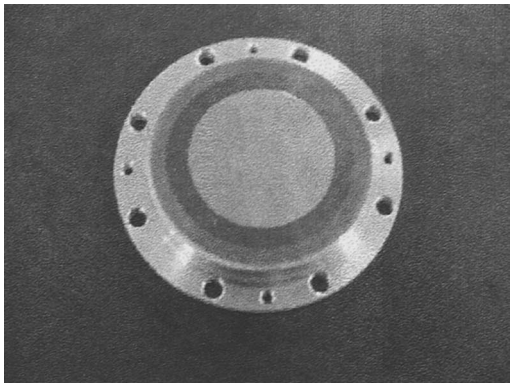

Fig. 1. Typical window parts of target cell. The Havar window is strengthened by the glued Kapton-ring film so as not to peel off after a large temperature change.

Table 1. Swelling height of target cell window. The Havar window was measured at 16 K and the Kapton window at room temperature.

window size	material	pressure 1.0 atm	0.5 atm	0.3 atm
30 ϕ	Kapton 50 μm	2.5∼3 mm		
30 ϕ	Havar 12 μm	0.9 mm	0.8 mm	
40 ϕ	Havar 12 μm	1.2 mm		0.7 mm

[*1] Department of Physics, Tokyo Institute of Technology
[*2] Department of Physics, University of Tokyo
[*3] Department of Physics, University of Saitama
[*4] Institute of Particle and Nuclear Studies, High Energy Accelerator Research Organization (KEK)

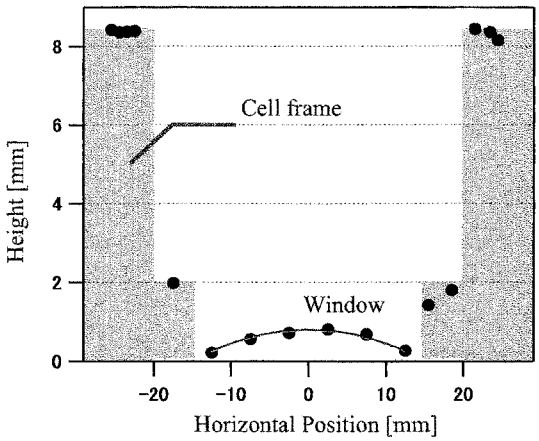

Fig. 2. Typical result of distance measurement. The horizontal axis shows the position along the window. The vertical axis shows the height from the surface of which the window adhered. The shaded area denotes the aluminum frame of the cell. This is the case for a 12 μm-thick Havar window, 0.5 atm pressure, and a 30 ϕ size window.

from the sensor. The stability of the liquid hydrogen temperature with the heater control was less than 0.1 K per day.

We made the liquid hydrogen cell with the Havar window. The swelling height of the window was lower than that of the former cell using the Kapton window. Furthermore, we installed the temperature control system which adjusted the heater current to reduce the fluctuation in liquid hydrogen density depending on the temperature. With these improvements in the window swelling and the density of the liquid hydrogen, we could make the liquid hydrogen target within 1% accuracy of thickness for σ_R measurement.

References

1) H. Akiyoshi et al.: RIKEN Accel. Prog. Rep. **32**, 167 (1999).
2) Y. Yanagisawa et al.: Phys. Lett. B **566**, 84, (2003); S. Kanno et al.: RIKEN Accel. Prog. Rep. **38**, 66 (2005).
3) B. A. Younglove et al.: J. Phys. Chem. Ref. Data **11**, 1 (1982); Webpage of National Institute of Standards and Technology, http://webbook.nist.gov/chemistry/fluid/

Development of Self-Confining Radioactive Ion Target (SCRIT)

M. Wakasugi, T. Emoto, Y. Furukawa,[*1] S. Ito, T. Koseki, K. Kurita,[*2] T. Masuda,[*2] M. Nakamura, T. Suda, T. Tamae,[*1] H. Takeda, and Y. Yano

The self-confining radioactive ion target (SCRIT) technology provides a fixed RI ion target for electron scattering experiment. The RI ions are three-dimensionally confined along the electron beam axis in the storage ring. This confinement is realized by periodic transverse focusing kicks by the electron bunches and additionally applied longitudinal mirror potential at a local position of the electron storage ring. Since the SCRIT is a completely new device, we should study its performance. First we performed a computer simulation on the ion motion in the SCRIT. The results of this calculation indicate that the time-averaged luminosity of more than $10^{27}\,\mathrm{cm}^{-2}\mathrm{s}^{-1}$ is achievable.[1)]

The R&D study to confirm the SCRIT principal is now under way at the KSR in Kyoto University. A prototype of the SCRIT devices is installed in the KSR,[2)] as shown in Fig. 1. The prototype consists of the SCRIT device, an ion source, and an electrostatic transport line for ion injection. The surface ionization ion source of ^{133}Cs is used and the pulsed ion beam is generated by grid action. The ion beam is accelerated to 10 keV and merged with the electron beam axis by the 90-degree deflector. The SCRIT is an electrode system in which 40 thin electrodes are stacked every 11 mm to produce a longitudinal mirror potential. The potential wall is quickly switched off and its timing is synchronized with the ion injection.

Trapping of the ^{133}Cs ions in the SCRIT was confirmed by measuring of the ions released from the SCRIT at a certain trapping time after the injection.

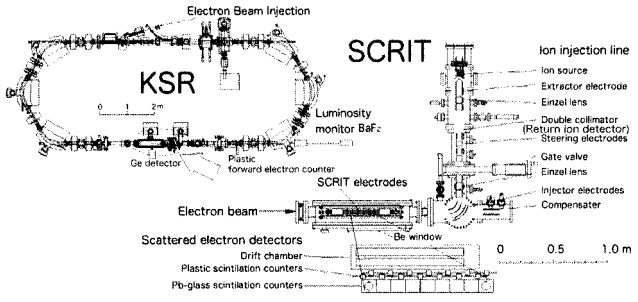

Fig. 1. SCRIT prototype installed in the KSR.

Released ions go back along the injection line and some of them is detected at the return ion detector. Taking transmission efficiency and the estimated average charge state into account, the number of Cs ions trapped in the SCRIT is obtained and then plotted as a function of the trapping time in Fig. 2. The four series plotted in this figure have different number of initially injected ions (N_{inj}). With a large N_{inj}, the number of trapped ions is more quickly decreased. This phenomenon is expected from the calculation.[1)] Assuming that the ions exist transversely inside the electron beam envelope in the SCRIT, the luminosity can be calculated to be $L \sim 10^{24}\,\mathrm{cm}^{-2}\mathrm{s}^{-1}$ in the trapping-time region of 0.1–1 s, $L \sim 10^{25}\,\mathrm{cm}^{-2}\mathrm{s}^{-1}$ in 10–100 ms, and $L \sim 10^{26}\,\mathrm{cm}^{-2}\mathrm{s}^{-1}$ in 1–10 ms.

In the next step, we are preparing the direct determination of the luminosity by measurements of the bremsstrahlung X-ray or foreword-scattering electrons produced by collisions with Cs ions.

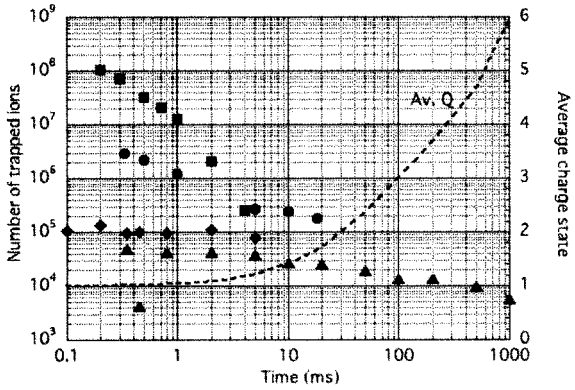

Fig. 2. Observed number of trapped ions as a function of the trapping time.

References

1) M. Wakasugi, T. Suda, and Y. Yano: Nucl. Instrum. Methods Phys. Res. A **532**, 216 (2004).
2) A. Noda et al.: Proc. 5th Int. Conf. of European Particle Accelerator Conference, Barcelona, Spain, 1996-6, (Institute of Physics Publishing, Bristol and Philadelphia, 1996), p. 451.

*1 Laboratory of Nuclear Science, Tohoku University
*2 Department of Physics, Rikkyo University

High-stability current source for EDM experiments

A. Yoshimi, K. Asahi, M. Uchida,* S. Oshima,* and T. Inoue*

The measurement of spin precession is sometimes very important for fundamental physics studies such as the search for T-violating electric dipole moment (EDM). The developments of polarized ^{129}Xe nuclei and the self-sustained nuclear spin maser with the polarized nuclei are in progress aiming at the EDM search.[1] In such experiments, a magnetic field with a good homogeneity and stability is required. The fluctuation of the applied magnetic field B_0 should be as small as possible because the precession frequency of spin is proportional to B_0. A precise magnetometer with magneto-optical rotation effect is being developed for actively stabilizing the magnetic field.[2] In this report, field fluctuation due to a current source which provides a current in a solenoid magnet is discussed.

We have compared the stabilities of two current sources. One is a conventional constant current source (1 A/10 V, minimum range is 1 μA) which we had used for the spin precession measurements. This is commercially available, and its nominal stability is less than 10^{-3}. Another is a low-noise current source, PSE-1101, which has been fabricated to reduce current fluctuation for a long-term period (low-frequency noise). The latter has a maximum current of 30 mA (30 mA/10 V). The general cause of low-frequency noise for commercial current source comes from Zener diode used as a voltage reference.[3] A low-noise battery is used instead as the voltage reference in the PSE-1101. The currents were measured using the setup shown in Fig. 1, where the currents in a solenoid magnet were measured using a precise ammeter DMM-2002, KEITHLEY. The supplied current was set around 3.5 mA, which corresponds to a static field of 2.8 μT.

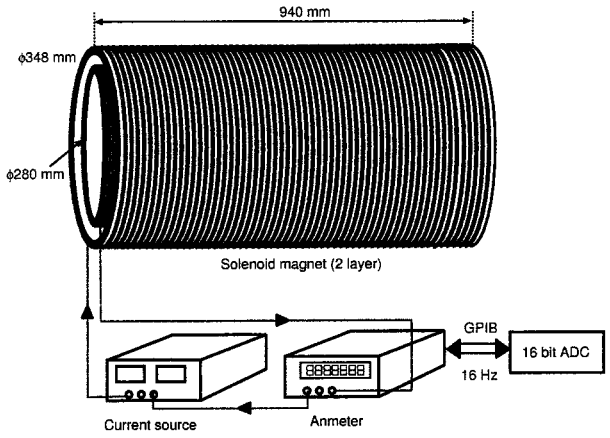

Fig. 1. Setup for measuring current stability in solenoid magnet. Solenoid magnet consists of two layers.

The results are shown in Fig. 2. Figure 2 (a) shows a comparison of the current stabilities of each current source. The fluctuation at a time scale of 10^3 seconds is greatly reduced, and it is estimated to be reduced by less than 1/30 as shown in Fig. 2 (b). In Fig. 2 (b), data points were averaged every 60 seconds. Thus, this fluctuation width is smaller than the ammeter's resolution, and is expected to be further reduced ($\delta I/I < 10^{-6}$). Further stabilization is expected by improving the thermal shield in the circuit. We are now preparing for the frequency measurement of the spin maser which can reveal current stability with higher precision.

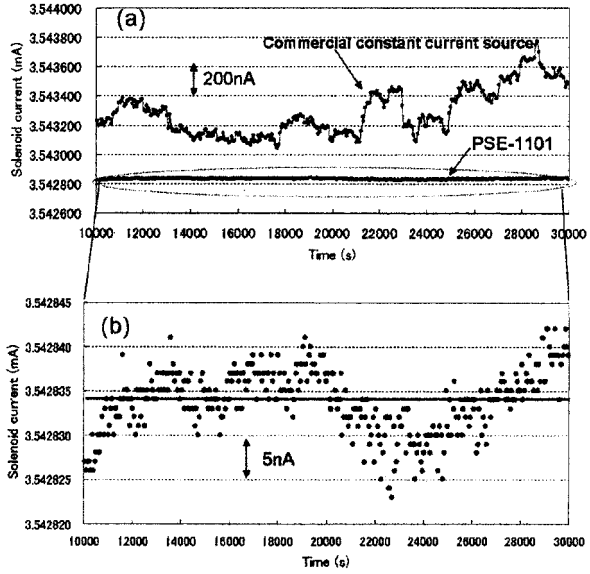

Fig. 2. Measured fluctuations of currents in solenoid magnet. (a) Comparison of stabilities when we use conventional constant current source and low-noise current source PSE-1101 with low-noise battery. (b) Magnified figure (along current axis) for data with PSE-1101.

References

1) A. Yoshimi et al.: RIKEN Accel. Prog. Rep. **36**, 173 (2003).
2) A. Yoshimi et al.: RIKEN Accel. Prog. Rep. **38**, 169 (2005).
3) C. Ciofi et al.: IEEE Trans. Instrum. Meas. **47**, 78 (1998).

* Department of Physics, Tokyo Institute of Technology

RF cavity for spin selection in RIABR

D. Nagae,[*1] K. Asahi,[*1] K. Shimada,[*1] A. Yoshimi, H. Ueno, T. Haseyama, J. Murata,[*2] Y. Kobayashi, D. Kameda, M. Uchida,[*1] G. Kijima,[*1] T. Arai,[*1] M. Takemura,[*1] H. Kawamura,[*2] S. Suda,[*1] T. Inoue,[*1] and K. Takase[*1]

A device that produces a low-energy and largely spin-polarized RI beam based on the atomic beam resonance method (RIABR) has been developed.[1,2] In the RIABR method, the produced RI beam is firstly decelerated and neutralized. RI atoms are then transmitted to a set of hexapole magnets to converge only those atoms with a selected atom spin direction. An rf field at a certain frequency is applied, and according to the Breit-Rabi scheme, a transition is induced when the frequency satisfies a resonance condition. The atoms then enter the region of the quadrupole magnets where only those atoms that have executed the transition are deflected. Thus, a highly spin-polarized slow RI beam is obtained. In the present study, we have fabricated a hyperfine transition system using ^{7}Li and we are testing its performance.

The ground and the first excited atomic levels of ^{7}Li are split into total spin states F = 2 and F = 1 by the hyperfine interaction. In our system, atoms in the state of $^2S_{1/2}$, F = 1 are optically pumped into $^2P_{1/2}$, F = 2 states (D1 transition) by a linearly polarized laser beam upstream an rf cavity. Because the traverse time of the atomic beam across the laser beam is approximately 100 times as large as the spontaneous emission lifetime, the laser beam exceeding the saturation intensity strongly populates the hyperfine state $^2S_{1/2}$, F = 2. Fluorescence is detected by a photodiode (Hamamatsu S2281). The rf cavity is placed following the pumping region to induce a hyperfine transition $^2S_{1/2}$, F = 2 → $^2S_{1/2}$, F = 1 by applying an rf field of hyperfine frequency (803 MHz). A linearly polarized laser beam downstream the rf cavity induces the D1 transition only for atoms that have executed the hyperfine transition in the rf cavity and fluorescence is detected by an another photodiode.

A schematic view of the test experiment setup is shown in Fig. 1. An atomic beam was produced by heating lithium metal in an oven at 500°C. Lithium atoms were extracted through a 1 mm orifice of the oven. The oven and the atomic beam path were enclosed in a vacuum chamber. The pressure was approximately 2×10^{-5} Torr. The lithium atoms were excited using a single-frequency diode laser with a custom-designed external cavity. The typical power was 15 mW at 670.97 nm. The linewidth of the laser was sufficiently narrow to distinguish two hyperfine transitions. We detuned the laser frequency up to 5.2 GHz by sweeping the grating angle with a piezoelectric transducer. As shown in Fig. 2, a fluorescence spectrum with three peaks was obtained using the upstream photodiode. The first peak corresponds to the ^{6}Li D2 line. The second and third peaks correspond to the transitions $^2S_{1/2}$, F = 2 → $^2P_{1/2}$ and $^2S_{1/2}$, F = 1 → $^2P_{1/2}$ hyperfine lines of ^{7}Li, respectively, separated by about 800 MHz. The resonance widths were predominantly determined by the Doppler broadening due to beam divergence. The hyperfine splittings of the excited states were not resolved due to the Doppler broadening.

A measurement of the spin transition will be performed soon.

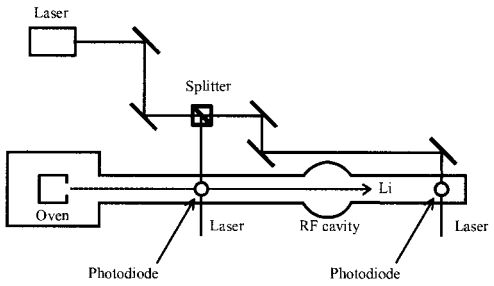

Fig. 1. Schematic view of RF test cavity.

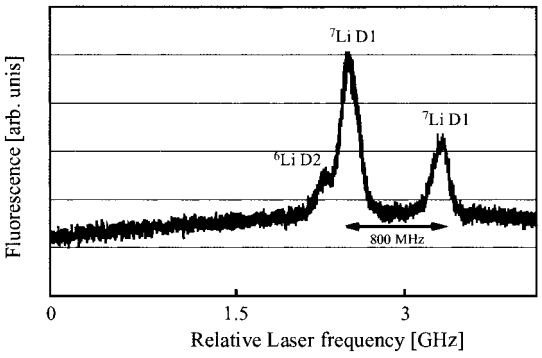

Fig. 2. Fluorescence taken during laser detuning. The first peak corresponds to the ^{6}Li D2 line and the second and third peaks to the ^{7}Li D1 lines.

References

1) D. Nagae et al.: Physica E **29**, 580 (2005).
2) K. Shimada et al.: RIKEN Accel. Prog. Rep. **39**, 156 (2006).

*1 Department of Physics, Tokyo Institute of Technology
*2 Department of Physics, Rikkyo University

Development of gas degrader and gas scintillation beam monitor

K. Shimada,[*1] K. Asahi, D. Nagae,[*1] A. Yoshimi, H. Ueno, Y. Kobayashi, T. Haseyama, J. Murata,[*2] M. Uchida,[*1] D. Kameda,[*1] G. Kijima,[*1] H. Kawamura,[*2] T. Arai,[*1] M. Takemura,[*1] S. Suda,[*1] T. Inoue,[*1] K. Takase,[*1] and H. Miyoshi[*1]

We have developed a method of a producing slow radioactive isotope (RI) beam for the RI atomic beam resonance method (RIABR).[1)] In this paper, we report on the development of an energy degrader that is to be used when the beam is stopped in a gas to produce a slow RI beam. In addition, it can be useful for monitoring the incoming beam intensity on the basis of the scintillation of Ar atoms excited by the incident beam.

When a beam is stopped at an arbitrary position in a gas-filled chamber, the beam is passed through some material to reduce its energy. Very fine control of the thickness of the material for energy reduction is required because of the limited stopping power of the gas. Earlier, we had been using Al foil whose angle to the beam axis could be controlled in order to change the thickness of the energy degrader.[2)] For finer thickness control, we tried another approach of using on Ar gas volume as the energy degrader, since the density of the gas is extremely smaller than that of the solid. On the other hand, when a charged particle passes through a volume of Ar gas, it leaves a population of excited Ar atoms in its wake. When these excited Ar atoms return to their ground state, photons are emitted. The number of excitated Ar atoms is proportional to the incident beam intensity. Therefore, the beam intensity can be estimated by counting the emitted photons. The main wavelength of scintillation is around 250 nm.[3)] The emitted scintillation photons are detected by a UV photomultiplier tube (Hamamatsu R2809U-06), which is sensitive to wavelengths between 160 and 320 nm.

Test experiments of the gas degrader and the beam monitor were carried out at Tohoku University Cyclotron and Radioisotope Center (CYRIC) (Fig. 1). The incident beam was $^{14}N^{5+}$ of 130 MeV. The pressure of Ar gas was controlled by a mass flow controller (MKS M100B) and a needle valve located between the chamber and a scroll pump. The accuracy of the pressure was typically ± 0.1 Torr at 218.0 Torr, which corresponded to $\pm 1.4 \times 10^{-5}$ g/cm^2. A Faraday cap (F. C.) with 60 mm i.d. was placed at 220 mm from the Al window. The two grounded electrodes were attached to the inside wall of the duct to quench the space charge generated far from the F. C. by collisions between the beam and Ne atoms. The currents at the F. C. were not the same as the beam current because the remaining space charge was added, which is typically 40 times larger than the beam current.

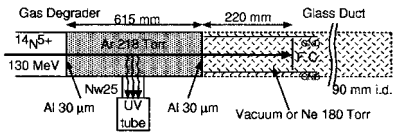

Fig. 1. Setup of the experiments.

The currents at the F. C. against the pressure of the Ar are shown in Fig. 2. The curves of the current should be constant until the thickness of the degrader becomes comparable to the range of the particle, however, they increase with increasing intensity. One of the reasons behind this is the secoundary electron emission effect. On the other hand, each decreasing part of the curves is fitted with a Woods-Saxon curve. When the glass chamber was a vacuum, the mean pressure was 302 Torr and the width was 0.66%, which corresponds to 39.7(9) mg/cm^2. Meanwhile, when the glass chamber was filled with 180 Torr Ne gas, the mean pressure was 266 Torr and the width was 1.0%, which corresponds to 34.9(6) mg/cm^2. Therefore we can make the incident beam stop in the Ne gas volume by adjusting the Ar pressure to between 266 Torr and 302 Torr. Figure 3 shows a plot of the scintillation current vs. the incident beam current. It shows good linearity. So far, the accurary of the beam current is evaluated to be 10% but is making limited by the calibration process. The incident beam current read by the F. C. fluctuated due to the improper shape of the F. C.

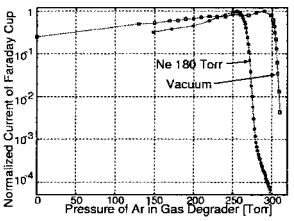

Fig. 2. Normalized current at Faraday Cup as a function of Ar gas pressure.

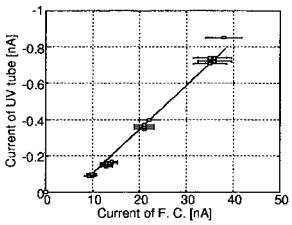

Fig. 3. Currents at the UV multiplier tube and F. C. were changing beam intensity.

*1 Department of Physics, Tokyo Institute of Technology
*2 Department of Physics, Rikkyo University

References

1) K. Shimada et al.: RIKEN Accel. Prog. Rep. **38**, 163 (2005).
2) H. Miyoshi et al.: RIKEN Accel. Prog. Rep. **37**, 171 (2004).
3) G. F. Knoll: in *Radiation Detection and Measurement* (John Wiley & Sons, Inc., Hoboken, 2000), p. 246.

Trapping radioactive Be isotopes using rf ion guide

A. Takamine,[*1] M. Wada, Y. Ishida, T. Nakamura, K. Okada,[*2] S. Shiba,[*3] Y. Yamazaki, T. Kambara, Y. Kanai, T. M. Kojima, Y. Nakai, N. Oshima,[*4] A. Yoshida, T. Kubo, S. Ohtani,[*3] K. Noda,[*5] I. Katayama,[*6] G. Jegou, V. Lioubimov,[*7] H. A. Schuessler,[*7] V. Varentsov,[*8] and H. Wollnik[*9]

A universal facility for SLOW Radioactive Ion beams (SLOWRI) is being developed[1)] as part of the RIKEN Radioactive Ion Beam Factory (RIBF).[2)] SLOWRI aims at providing universal slow RI-beams of high purity and small emittance by slowing down and cooling energetic RI ions using an rf ion guide. We achieved a high overall efficiency of ∼5% and a maximum intensity of ∼24 kcps for ∼100 MeV/nucleon ^{8}Li ions from the RIKEN projectile fragment separator RIPS. Although the efficiency decreases as the beam intensity increases, this is found to be due to the space charge produced during the stopping process of incoming energetic ions.[3)] Several hypotheses to overcome the problem are proposed and they are to be tested soon.

Because the present performance of the rf ion guide is already sufficient for performing a precise spectroscopy of the hyperfine structure of stored Be^{+} ions in a trap, we connected a cryogenic linear Paul trap following the long SPIG as shown in Fig. 1. A schematic diagram of the setup is also shown in Fig. 2.

In off-line tests, we used stable $^{9}Be^{+}$ ions, which are produced by Nd:YAG laser ablation in the gas cell, to optimize the trapping condition of Be ions. The ablated ^{9}Be ions are extracted from the gas cell through the exit nozzle. The ^{9}Be ions are transported by a rf six-pole beam guide (SPIG)[4)] through differential pumping sections into a high vacuum chamber. Because the beam transported from the gas cell contains many impure molecular ions, we used a quadrupole mass filter to select the ions of interest, and the selected ions were injected into the cryogenic linear Paul trap where laser spectroscopy was performed. The selected Be^{+} ions were continuously accumulated in the linear Paul trap by buffer gas cooling. A schematic drawing of the linear trap and axial potential produced by the electrodes are shown in Fig. 3. We measured the in-

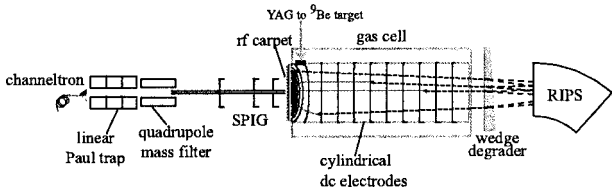

Fig. 2. Schematic of experimental setup. Refer to Refs. 1 and 3 for details. Ions thermalized in the gas cell filled with 13 mbar of He are transported by dc fields and rf fields to the exit nozzle and transported by SPIG.[1)] SPIG consists of two segments, an upstream section of 10 cm and a downstream section of 50 cm. These two segments are applied rf voltages of 120 $V_{p.p.}$ with 24 MHz and 120 $V_{p.p.}$ with 20 MHz, respectively. The frequency of the quadrupole mass filter is 3.36 MHz and the mass resolving power is 22.

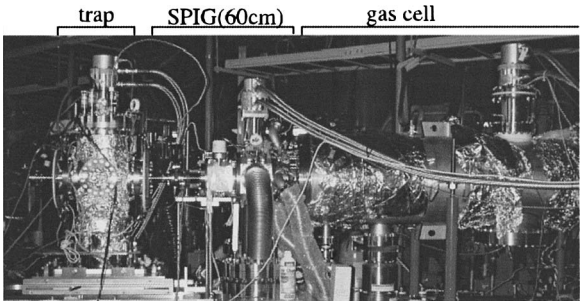

Fig. 1. Photo of experimental setup.

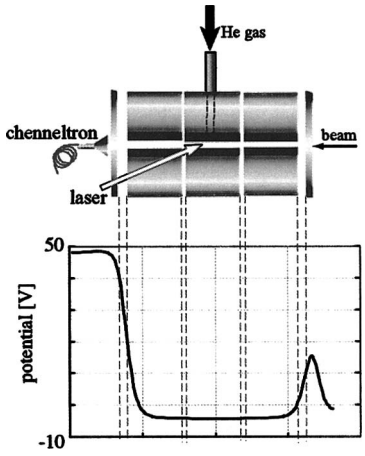

Fig. 3. Cryogenic linear Paul trap for laser spectroscopy. The trap electrode is segmented into three sections. Each 4-cm-long segment consists of four hyperbolical electrodes of $r_0 = 8$ mm. A rf voltage of 250 $V_{p.p.}$ with 3.7 MHz is applied to the trap, which radially confines ions. The static potential as shown in this figure is also applied, which axially confines ions.

*1 Graduate School of Arts and Sciences, University of Tokyo
*2 Department of Physics, Sophia University
*3 Institute for Laser Science, University of Electro-Communications
*4 Research Institute of Instrumentation Frontier, Advanced Industrial Science and Technology (AIST)
*5 National Institute for Radiological Science
*6 Institute of Particle and Nuclear Studies, High Energy Accelerator Research Association (KEK)
*7 Department of Physics, Texas A&M University, USA
*8 Kholopin Radium Institute, Russia
*9 II. Physikalisches Institute, Justus-Liebig-Universitaet, Germany

tensity of slow ion beams and the number of trapped ions using a channeltron located behind the linear Paul trap.

Figure 4 shows the number of trapped ions and trapping efficiency as a function of trapping time. We trapped 1.6×10^6 ions at maximum and achieved a maximum trapping efficiency of 43%. The kinetic energy of ions transported was $\sim$6 eV, which is determined by the potential of the upstream SPIG. The He gas pressure in the trap was approximately 6.0×10^{-3} mbar.

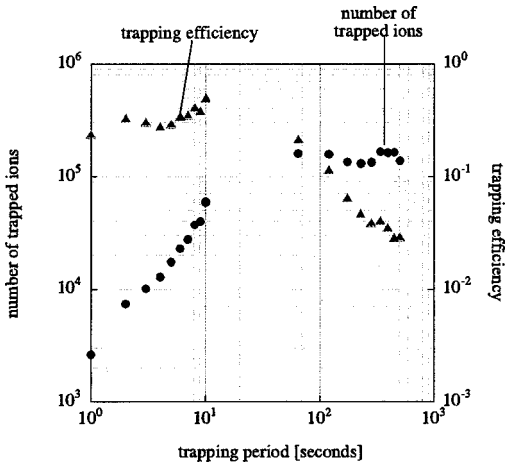

Fig. 4. The number of trapped ions and trapping efficiency were plotted for different trapping periods. The beam intensity was 10 kcps.

In an on-line experiment, we injected 100 MeV/nucleon ^{10}Be beams provided by RIPS into our setup. Although the intensity of slow ^{10}Be ions was as low as 10 cps due to a problem in the SPIG, we succeeded in trapping several hundreds $^{10}Be^+$ ions in the linear trap and measured the isotope shift of $^{10}Be^+$.[5)]

References

1) M. Wada et al.: Nucl. Instrum. Methods Phys. Res. B **204**, 570 (2003).
2) M. Motobayashi: Nucl. Instrum. Methods Phys. Res. B **204**, 737 (2003).
3) A. Takamine et al.: Rev. Sci. Instrum. **76**, 103503 (2005).
4) H. Xu et al.: Nucl. Instrum. Methods Phys. Res. A **333**, 274 (1993).
5) T. Nakamura et al.: RIKEN Accel. Prog. Rep. **39**, 41 (2006).

Network and computing environment for RIKEN accelerator research facility

T. Ichihara, Y. Watanabe, K. Yoshida, and A. Yoshida

The advanced computer network[1] started operation in 2002 at the RIKEN Accelerator Research Facility (RARF). The major updates undertaken this year are summarized as follows.

1) Replacement of LAN Hardware

The hardwares of the local area network (LAN) of RIKEN Wako campus have been updated in April 2005. Concerning this update, all LAN equipments of RARF have also been updated to a new system. Moreover, new LAN equipment has been installed in the new buildings of RI Beam Factory (RIBF) accelerators and experiments in June 2005.

Figure 1 shows the current configuration of RARF/RIBF network. The new network equipment of RARF/RIBF consists of Catalyst 4507R regional routers located at the Nishina and RIBF buildings and Catalyst 3750 floor switches located at each floor of the buildings.

Each Catalyst 4507R router is equipped with a redundant dual control unit for reliable operation. The Catalyst 4507R routers of the Nishina building are connected to Catalyst 6509 RIKEN Wako backbone router by 8 pairs of optical fibers with bandwidth of 8 Gbps. Moreover, the Catalyst 4507R routers of RIBF building are connected to the Catalyst 4507 router of the Nishina building at 8 Gbps. The Catalyst 6509 backbone routes are connected to the Internet (Super Sinet) via Inkra 1504 firewall at the speed of 1 Gbps. This bandwidth of the Internet connection is expected to be expanded from 1 to 10 Gbps in 2006.

The current RARF network consists of 26 private networks and two global networks. Each private network is basically related to each research laboratory or each floor of the buildings. The routing of IP and Appletalk between the private networks is carried out for convenience.

All computers connected to the RARF private LAN are assigned private addresses statically or dynamically. To access the Internet, these private addresses are translated dynamically to global addresses by Inkra 1504 firewall. The utilization of the Virtual Private Network (VPN) enables the access of private networks from outside of RIKEN using secure encrypted channel over the Internet.

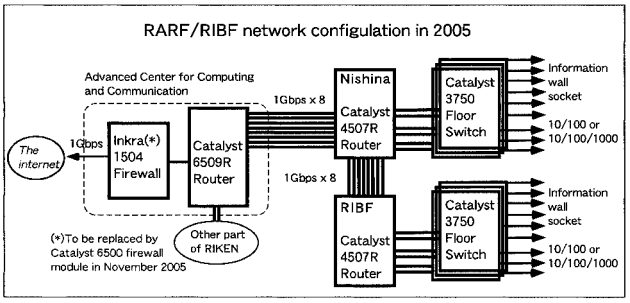

Fig. 1. Configuration of RARF/RIBF network.

2) Wireless LAN Access point of RARF

Recently, most laptop computers have been equipped with wireless network interface. This year, 35 units of wireless LAN access point of 802.11g/802.11b (54 Mbps/11 Mbps) standard have been installed in RARF/RIBF LAN. Table 1 shows the summary of the number of wireless LAN access points in RARF/RIBF area. The details of the RARF/RIBF wireless LAN access points can be found elsewhere.[2] Wi-Fi Protect Access authentication is used for most wireless LAN access points for establishing secure connections.

3) New 10 TB RAID File System

Currently 2.8 TB SCSI Redundant Arrays of Inexpensive Disks (RAIDs) are connected to RARFNFS0 file server and they are utilized as work area for experimental data analysis and simulation. However, more than six years have passed since the installation and the replacement of the SCSI RAID system is still requited for the sake of maintenance and security of the file contents. We have installed a new 10 TB Fiber-Channel RAID to update this SCSI RAID system. Moreover, the new file server of SUN Fire V40z with dual Opteron 880 CPU (dual core of 2.4 GHz) has been installed to serve the 10 TB file systems.

Most of the RARF users have e-mail addresses of the following patterns:

username@rarf.riken.jp or *username@riken.jp*

The first represents the e-mail address of the RARF mail server (RARFAXP) and the second represents the e-mail address of the RIKEN mail server (postman).

Table 1. Number of wireless access points (WAPs) of RARF/RIBF.

Building	Number of WAPs
RIBF	36
Nishina	14
Linac	3
Mail Bldg.	3

References

1) T. Ichihara et al.: RIKEN Accel. Prog. Rep. **36**, 199 (2002).
2) http://rarfaxp.riken.jp/comp/net/wireless.html

Hydrogen depth profile analysis of silicone modified by plasma ion implantation

T. Kobayashi, T. Yokota,* A. Nakao, and K. Ogiwara

Medical catheters are made of biologically inert materials such as silicone, polytetra-fluoroethylene (PTFE) and polyurethane. Due to their poor tissue adhesion, the interface of the catheter and the tissue tends to be a path for bacteria when it is set in place for a long period.[1] If the tissue adheres well to the catheter surface, exit-site and tunnel infections will be suppressed. We irradiated silicone sheets and tubes with inert gas ions by plasma-based ion implantation (PBII). The cell attachment and the adhesion strength of the fibrin glue (biological tissue adhesive) were markedly improved.[2] In this study, depth profiles of elements at the surface of irradiated silicones were investigated by Rutherford backscattering spectrometry (RBS) and elastic recoil detection analysis (ERDA) using a pelletron accelerator.

Silicone sheets (THE740-8U, 1 mm thick, GE Toshiba Silicones) and tubes (catheters for peritoneal dialysis, 4 mmϕ × 1 mm thick, Medionics International Inc.) were irradiated with Ar ions by PBII for 30 minutes at a pressure 1×10^{-1} Pa. PBII was performed by applying a pulsed RF (13.56 MHz, 500 W, 30 μs) and a pulsed DC (from 0 to –10 kV, 10 μs) alternately to the electrically floated sample holder at a cycle of 2 kHz. The sheet samples were fixed with a conductive adhesive tape on the flat sample holder. The tubular samples were penetrated with bar-type holders and only the outside was irradiated. During irradiation, the temperature of the sample surface was not observed; however, the temperature on the rear side of the specimens below 95°C was observed using a sticker-type temperature indicator. After irradiation, the samples were cooled in vacuum for 60 minutes.

Figure 1 shows the RBS spectra of silicones obtained using a 2.28 MeV He^+ beam. The distribution of the implanted Ar atoms became broad with increasing voltage. Using HYPRA simulation code, the mean range of Ar atoms was estimated to be less than 6.5 nm for 5 kV and 6.5–19.5 nm for 10 kV. The broad peak observed around 340 ch corresponds to Fe atoms from the chamber or the electrode made of stainless steel. In our case, the distance between the sample holder and the chamber wall is about 20 cm. The size and material of a chamber, an electrode and sample holders should be carefully designed to avoid unexpected contamination. Enrichment of carbon atoms due to a gas detachment is clearly observed in the sample irradiated with 10 kV. The deposition of amorphous carbon will also occur by attracting emitted hydrocarbon.

Figure 2 shows the ERDA spectra obtained using the 2.28 MeV He^+ beam at an incident angle of 15° with respect to the surface. The hydrogen distribution is estimated by comparing each spectrum with the unirradiated one. At the surface, hydrogen atoms detached due to a bond scission caused by incident ions and thermal decomposition. On the other hand, the hydrogen density increased in the interior region. This is not observed in conventional ion implantation using accelerators. The detached hydrogen in plasma will be accelerated and implanted again.

The thus-formed carbon-rich surface showed good affinity with cells and proteins and a test using animals has been started.

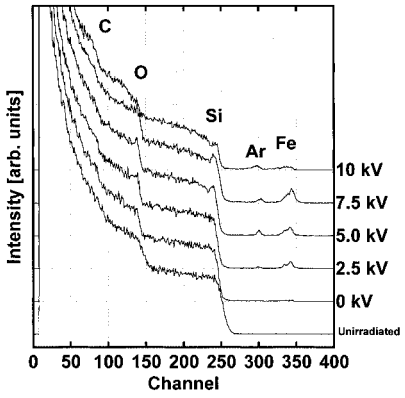

Fig. 1. RBS spectra of silicone specimens irradiated with Ar by PBII.

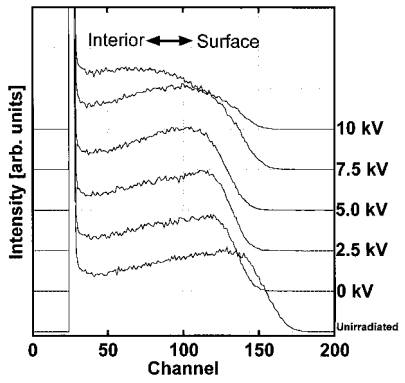

Fig. 2. ERDA spectra of silicone specimens irradiated with Ar by PBII.

References

1) W. F. Kean, S. R. Alexander, and G. R. Balite: Perit. Dial. Int. **16**, 557 (1996).
2) T. Kobayashi et al.: submitted to Surf. Coat. Technol.

* School of Engineering, University of Tokyo

Q_T resummation in transversely polarized Drell-Yan process

H. Kawamura, J. Kodaira,[*1] H. Shimizu,[*1] and K. Tanaka[*2]

Transversely polarized Drell-Yan process (tDY) is one of the processes where we can measure the transversity distribution $\delta q(x)$, the distribution of transversely polarized quarks inside transversely polarized nucleon. $\delta q(x)$ can not be measured in inclusive DIS due to its chiral-odd nature,[1] and remains as the last unknown distribution at the leading twist.

The spin dependent part of tDY cross section is proportional to $\cos(2\phi)$ where ϕ is the azimuthal angle of the produced lepton. Therefore the calculation of QCD corrections to this process is cumbersome compared with unpolarized and longitudinally polarized cases. So far, Q_T-integrated cross section at $\mathcal{O}(\alpha_s)$ has been calculated by several authors in various schemes,[2–4] while Q_T distribution of the DY-pair is given by Vogelsang and Weber in massive gluon scheme only.[3] Here we present Q_T dependent cross section in $\overline{MS}$ scheme.

We consider $\mathcal{O}(\alpha_s)$ corrections to tDY: $h_1(P_1, s_1) + h_2(P_2, s_2) \to l(k_1) + \bar{l}(k_2) + X$, where h_1, h_2 denote nucleons with momentum P_1, P_2 and transverse spin s_1, s_2, and $Q = k_1 + k_2$ is the 4-momentum of DY pair. The spin dependent cross section $\Delta_T d\sigma \equiv (d\sigma(s_1, s_2) - d\sigma(s_1, -s_2))/2$ is given as a convolution

$$\Delta_T d\sigma = \int dx_1 dx_2 \, \delta H(x_1\,,\, x_2)\, \Delta_T d\hat{\sigma}(s_1\,,\, s_2), \quad (1)$$

where $\delta H(x_1\,,\, x_2) = \sum_i e_i^2 [\delta q_i(x_1)\delta\bar{q}_i(x_2) + (1 \leftrightarrow 2)]$ and $\Delta_T d\hat{\sigma}$ is the corresponding partonic cross section. We compute the one-loop corrections to $\Delta_T d\hat{\sigma}$, which involve the virtual gluon corrections and the real gluon emission contributions, e.g., $q(p_1, s_1) + \bar{q}(p_2, s_2) \to l(k_1) + \bar{l}(k_2) + g$, with $p_i = x_i P_i$. We regularize the infrared divergence in $D = 4 - 2\epsilon$ dimension, and employ naive anticommuting γ_5 which is a usual prescription in the transverse spin channel.[4] In the $\overline{\rm MS}$ scheme, we eventually get to NLO accuracy,

$$\frac{\Delta_T d\sigma}{dQ^2 dQ_T^2 dy d\phi} = N \cos(2\phi) \left[X(Q^2, Q_T^2, y) + Y(Q^2, Q_T^2, y)\right], \quad (2)$$

where $N = \alpha^2/(3\, N_c\, S\, Q^2)$ with $S = (P_1 + P_2)^2$, y is the rapidity of virtual photon, and ϕ is the azimuthal angle of one of the leptons with respect to the initial spin axis. The cross section is decomposed into two parts. The function X contains singular terms: $\delta(Q_T^2), 1/(Q_T^2)_+, (\ln(Q^2/Q_T^2)/Q_T^2)_+$, etc., while Y is finite at $Q_T = 0$. The analytic expressions of X and Y can be seen in Ref. 5.

As is well-known, the singular terms $\alpha^n \ln^m(Q^2/Q_T^2)/\, Q_T^2$ $(m \le 2n-1)$ appear at each order of α_s due to the soft gluon effects, and resummation of these logarithmic terms are needed to obtain a reliable prediction of Q_T distribution. Figure 1 shows the Q_T distribution of tDY at $\sqrt{S} = 100\,\text{GeV}$, $Q = 10\,\text{GeV}$, $y = \phi = 0$ with a model for $\delta q(x)$ given by Martin et al.[6] We implement the integration in impact parameter space[7] by "contour deformation prescription".[8] We also take the non-perturbative function as $F^{NP}(b) = \exp(-gb^2)$ where b is the impact parameter conjugate to Q_T. Solid line shows the $\mathcal{O}(\alpha_f)$ result, while the dashed and dot-dashed lines show the resummed results at the next to leading log (NLL) level, with $g = 0.5\,\text{GeV}^2$ and $g = 0$, respectively.

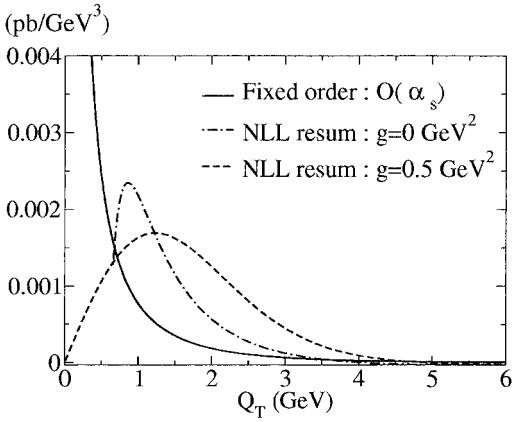

Fig. 1. Q_T distribution: $\Delta_T d\sigma/dQ^2 dQ_T dy d\phi$ at $\sqrt{S} = 100\,\text{GeV}$, $Q = 10\,\text{GeV}$, $y = \phi = 0$.

*1 Theory Division, High Energy Accelerator Organization (KEK)
*2 Department of Physics, Juntendo University

References

1) J. P. Ralston and D. Soper: Nucl. Phys. B **152**, 109 (1979).
2) A. Mukherjee, M. Stratmann, and W. Vogelsang: Phys. Rev. D **67**, 114006 (2003), and references therein.
3) W. Vogelsang and A. Weber: Phys. Rev. D **48**, 2073 (1993).
4) W. Vogelsang: Phys. Rev. D **57**, 1886 (1998).
5) H. Kawamura et al.: Nucl. Phys. B (Proc. Suppl.) **135**, 19 (2004); H. Kawamura, J. Kodaira, H. Shimizu, and K. Tanaka: hep-ph/0512137.
6) O. Martin et al.: Phys. Rev. D **57**, 3084 (1998); Phys. Rev. D **60**, 117502 (1999).
7) J. C. Collins, D. Soper, and G. Sterman: Nucl. Phys. B **250**, 199 (1985).
8) S. Kulesza, G. Sterman, and W. Vogelsang: Phys. Rev. D **66**, 014001 (2002).

Soft-gluon resummation for prompt photons†

W. Vogelsang

Prompt-photon production at high transverse momentum, $pp, p\bar{p}, pN \to \gamma X$, has been a classic tool for constraining the nucleon's gluon density, because at leading order a photon can be produced in the Compton reaction $qg \to \gamma q$. The "point-like" coupling of the photon to the quark provides a potentially clean electromagnetic probe of QCD hard scattering. However, a pattern of disagreement between theoretical next-to-leading order (NLO) predictions[1,2] and experimental data in the fixed-target regime[3,4] has been observed in recent years, NLO theory showing a shortfall.

In a recent paper,[5] we have shown that the theoretical description of single-inclusive photon production in the fixed-target regime is improved by taking into account large perturbative contributions to the partonic hard-scattering cross sections to all orders in perturbation theory. These terms, known as threshold logarithms, arise when the initial partons have just enough energy to produce a high-transverse momentum photon and a massless recoiling jet. The phase space available for gluon radiation vanishes then, resulting in large logarithmic corrections to the partonic cross section. For the cross section integrated over all rapidities, the most important logarithms are of the form $\alpha_s^k \ln^{2k}\left(1-\hat{x}_T^2\right)$ at the kth order in perturbation theory, where $\hat{x}_T \equiv 2p_T/\sqrt{\hat{s}}$, with p_T the photon transverse momentum and $\sqrt{\hat{s}}$ the partonic center-of-mass energy. Sufficiently close to threshold, NLO, which captures only the term for $k = 1$, will not be adequate, and all logarithmic terms will become relevant.[5]

High-p_T photons are not only produced by the "direct" contributions from the partonic hard processes $ab \to \gamma c$, but also in jet fragmentation. Despite the fact that according to the NLO calculation this fragmentation contribution is only a subdominant part of the cross section, it receives larger threshold corrections, due to the structure of the underlying hard-scattering cross sections.[6] Figure 1 shows the ratios direct/(direct+fragmentation) and fragmentation/(direct+fragmentation) as functions of the photon transverse momentum p_T, for pp collisions at $\sqrt{S} = 31.5\,\text{GeV}$. One can see that the NLO fragmentation component contributes about 40% of the cross section at the lowest p_T shown and then rapidly decreases, becoming lower than 10% at $p_T \approx 11\,\text{GeV}$. After resummation, however, the fragmentation contribution yields almost 60% of the cross section at smaller p_T and still more than 20% at $p_T = 11\,\text{GeV}$.

Figure 2 shows a comparison with the data for $pp \to \gamma X$ from UA6[4] at $\sqrt{S} = 24.3\,\text{GeV}$. The resummed calculation, which shows a very small scale dependence, is in very good agreement with the data. Resummation of the fragmentation component leads to a non-negligible enhancement of the cross section.

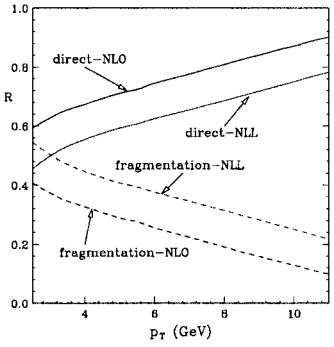

Fig. 1. Relative contributions of direct and fragmentation photons to the cross section for pp collisions at $\sqrt{S} = 31.5\,\text{GeV}$.

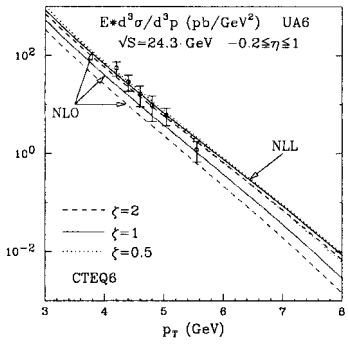

Fig. 2. Comparison to data from UA6[4] for $pp \to \gamma X$ at $\sqrt{S} = 24.3\,\text{GeV}$ and photon rapidities $-0.2 \le \eta \le 1$.

References

1) P. Aurenche et al.: Phys. Lett. B **140**, 87 (1984); Nucl. Phys. B **297**, 661 (1988); H. Baer et al.: Phys. Lett. B **234**, 127 (1990); Phys. Rev. D **42**, 61 (1990); L. E. Gordon and W. Vogelsang: Phys. Rev. D **48**, 3136 (1993); Phys. Rev. D **50**, 1901 (1994).
2) F. Aversa et al.: Nucl. Phys. B **327**, 105 (1989); D. de Florian: Phys. Rev. D **67**, 054004 (2003); B. Jäger et al.: Phys. Rev. D **67**, 054005 (2003).
3) L. Apanasevich, E706 Collaboration et al.: Phys. Rev. Lett. **81**, 2642 (1998); Phys. Rev. D **70**, 092009 (2004).
4) G. Ballocchi, UA6 Collaboration et al.: Phys. Lett. B **436**, 222 (1998).
5) D. de Florian and W. Vogelsang: Phys. Rev. D **72**, 014014 (2005).
6) D. de Florian and W. Vogelsang: Phys. Rev. D **71**, 114004 (2005).

† Condensed from the article Phys. Rev. D **72**, 014014 (2005)

Thermal phase transition of color superconductivity with Ginzburg-Landau action on the lattice

M. Ohtani, S. Digal,* and T. Hatsuda*

In dense cold quark matter, the color-superconducting phase is expected to be realized due to diquark pairing. Since the most attractive channel is found to be in the color anti-triplet and $J^P = 0^+$, the diquark field in this channel, Φ_{cf}, is most relevant for color superconductivity. A three-dimensional Ginzburg-Landau (GL) action written in terms of Φ_{cf} was proposed[1] to study the thermal transition of color superconductivity. It was realized that thermal gluons convert the second-order transition in the mean-field theory to the first-order transition.[2,3] Such a weak-coupling study, however, is valid only at an extremely high density. Furthermore, thermal fluctuations in Φ_{cf} become crucial as density decreases.[2]

Motivated by this, we carry out Monte-Carlo simulations of the GL action.[4] In our simulation, we extend the GL action[1] to a *four-dimensional* action to define the Polyakov loop. The discretization of the extended action and rescaling of the fields lead us to the action

$$S = \sum_x \Big\{ \mathrm{Tr}(\Phi_x^\dagger \Phi_x) + (\lambda_1 + \lambda_2) \left(\mathrm{Tr}(\Phi_x^\dagger \Phi_x) - 1\right)^2 + \lambda_2 \left(\mathrm{Tr}(\Phi_x^\dagger \Phi_x)^2 - \left[\mathrm{Tr}(\Phi_x^\dagger \Phi_x)\right]^2 \right) - 2\kappa \sum_\mu \mathrm{Re}\ \mathrm{Tr}(\Phi_{x+\mu}^\dagger U_\mu^* \Phi_x) + S_\mathrm{g} \Big\}, \quad (1)$$

where S_g is the standard plaquette action. Taking several sets of λ_i, we carry out simulations by scanning κ with a lattice volume of 2×12^3. We use the pseudo heat-bath method to update link variables and generalize the update algorithm of SU(2) Higgs.

The color-superconducting and normal phases are distinguished by the gauge invariant operator $\sum_x \mathrm{Tr}\ \Phi_x^\dagger \Phi_x$. We can observe a discontinuous change in expectation value with κ. We confirm the discontinuity of other gauge-invariant operators at the same κ. This is evidence of the first-order phase transition.

Moreover, we can differentiate different color-superconducting states by diagonalizing $\sum_x \Phi_x^\dagger \Phi_x$ in the flavor space to extract its eigenvalues. We observe one large and two degenerate small eigenvalues in a particular set of couplings. In this case, we regard the state as the 2SC phase in which the quarks pair in one specific color-flavor channel. We also observe three degenerate eigenvalues, which correspond to the CFL phase where all channels are involved equally in the pairing. As we scan κ, we find rapid changes in the eigenvalues of $\sum_x \Phi_x^\dagger \Phi_x$ at κ_c. When we simulate around this point, we observe the hysteresis loops of the observables. This is also evidence of the first-order transition.

* Department of Physics, University of Tokyo

To determine the most stable state near the critical point, we divide the lattice volume into domains and place different phases of the hysteresis loop into different domains. Starting from such a mixed configuration, a state with the highest pressure pushes away the other states after many update steps. In this way, we can determine the most favorable state for each κ.

We find three types of transition depending on the value of couplings as shown in Fig. 1: for large λ_2, a transition from the normal phase to CFL occurs. For small or negative λ_2, a transition from the normal phase to 2SC occurs. For intermediate λ_2, successive transitions, normal→2SC→CFL, occur.

The global feature of the phase diagram in Fig. 1 is qualitatively similar to that of the weak-coupling analysis. Note that, near the phase boundary between 2SC and CFL, we find that metastable 2SC survives, even when the global minimum of free energy transfers directly from the normal phase to CFL.

To obtain a realistic phase diagram of color superconductivity on the temperature (T) and chemical potential (μ) plane, it is necessary to relate our couplings to T and μ. Quark masses and color and charge neutralities become crucial at a low baryon density and lead to a more complex phase structure. Further studies are needed to solve these problems.

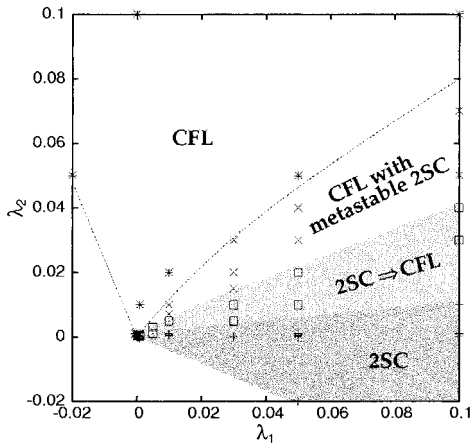

Fig. 1. Phase diagram in coupling space obtained by simulation.

References

1) K. Iida and G. Baym: Phys. Rev. D **63**, 074018 (2001); Phys. Rev. D **66**, 014015 (2002).
2) T. Matsuura, K. Iida, T. Hatsuda, and G. Baym: Phys. Rev. D **69**, 074012 (2004).
3) I. Giannakis, D. F. Hou, H. C. Ren, and D. H. Rischke: Phys. Rev. Lett. **93**, 232301 (2004).
4) S. Digal, T. Hatsuda, and M. Ohtani: hep-lat/0511018.

Magnetic vortex in color-flavor locked quark matter†

K. Iida

The possibility that dense quark matter occurs in neutron stars has been considered for the past three decades. The possible presence of a diquark condensate in such quark matter has generated new interest in such matter. Among various condensates, a color-flavor locked (CFL) state,[1] in which all three color and flavors are gapped, has been studied most intensively, along with a two-flavor pairing state. In the weak coupling (high density) and massless limit the CFL state is most stable at zero temperature and near the transition temperature, a feature ensured by the quark-quark attraction in the color antitriplet channel due to one-gluon exchange. Although the massless, weak coupling results for diquark condensation are modified by effects of strong coupling and nonzero quark masses in a regime as might be encountered in possible quark matter in neutron star interiors, the CFL phase has to be reckoned with as a reference state in such a regime.

Response of the CFL condensate to magnetic fields, as would be experienced by quark matter if present in neutron stars, was considered in Refs. 2–4. Because of nonvanishing color and electric charge carried by diquark pairs, electromagnetic superconductivity and color superconductivity occur in the CFL phase. These two phenomena are not independent in the sense that transverse photon and gluon fields are mixed with each other. One of the resultant mixed fields is freely propagating, while the other is Meissner screened and thus massive. The massive mixed field and the winding of the $SU(3)$ phase in color-flavor space are essential to the structure of a magnetic vortex in the CFL phase. This point was not taken into account in Ref. 3. The criterion of whether or not the CFL state can allow magnetic vortices to form (type II or type I) has been described by Giannakis and Ren[4] in terms of the energy needed to form a planar surface separating the normal and superconducting material, but the detailed structure of the magnetic vortex has yet to be determined.

In this work we examine the properties of magnetic vortices in the CFL phase within the framework of Ginzburg-Landau theory. These vortices are characterized by three different fields: the CFL diquark field, the massive photon-gluon mixed field, and a color-flavor unlocked diquark field coupled to the mixed field.[4] In the London limit where the wavelengths of distortions of the condensate are long compared with the size of the vortex core, the supercurrents surrounding the core can be written in terms of the color-flavor $SU(3)$ phase of the CFL condensate and the mixed field. From such supercurrent structures we derive the lower critical field, H_{c1}. We next examine the vortex structure near the core, in which the color-flavor unlocked condensate plays a role as shown in Fig. 1, and derive the upper critical field, H_{c2}. Finally we revisit how to distinguish between type I and type II superconductors from the viewpoint of the intervortex interactions. We have found that the nature of the intervortex interaction, controlled by the color-flavor unlocked condensate, provides a stringent constraint on the type II regime.

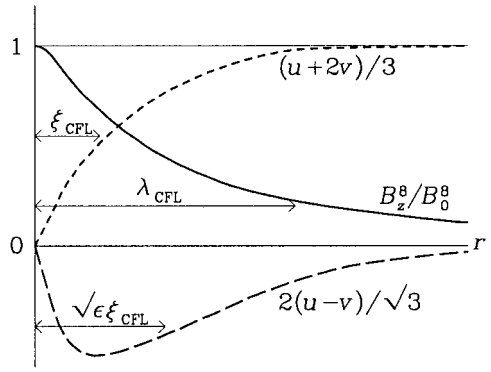

Fig. 1. Schematic variation of the massive photon-gluon mixed field $\mathcal{B}_z^8$ (solid line), the CFL condensate $(u + 2v)/3$ (dotted line), and the color-flavor unlocked condensate $2(u - v)/\sqrt{3}$ (dashed line) for a singly quantized vortex ($\lambda_{\rm CFL} > \sqrt{\epsilon}\xi_{\rm CFL} > \xi_{\rm CFL}$ with the London penetration depth $\lambda_{\rm CFL}$, the Ginzburg-Landau coherence length $\xi_{\rm CFL}$, and the parameter ϵ characterizing the scale of the spatial variation of the color-flavor unlocked condensate).

References
1) M. Alford, K. Rajagopal, and F. Wilczek: Nucl. Phys. B **537**, 443 (1999).
2) M. Alford, J. Berges, and K. Rajagopal: Nucl. Phys. B **571**, 269 (2000).
3) K. Iida and G. Baym: Phys. Rev. D **66**, 014015 (2002).
4) I. Giannakis and H.-C. Ren: Nucl. Phys. B **669**, 462 (2003).

† Condensed from the article in Phys. Rev. D **71**, 054011 (2005)

Quarkonia correlators and spectral functions on anisotropic lattices

A. Jakovác,[*1] P. Petreczky, K. Petrov,[*2] and A. Velytsky[*3]

Temporal meson correlation functions in Euclidean time can be related to meson spectral functions by analytic continuation. Furthermore using the Maximum Entropy Method (MEM) one can extract the spectral functions from meson correlators calculated on a finite lattice.[1)] The method was applied at zero[1)] as well as non-zero temperatures.[2–5)] In particular, in Refs. 3–5 the charmonium spectral functions have been calculated and the calculations have shown that 1S charmonium states (η_c and J/ψ) can exist in the Quark Gluon Plasma up to temperatures as high as $1.5T_c$ while the 1P states (χ_{c0} and χ_{c1}) are dissociated at $1.1T_c$. The statistical and systematic errors in this calculations, however, are not fully under control. In Refs. 4, 5 calculation were done with limited statistics, while in Ref. 3 a different kind of meson operator was used and calculations were done only at one lattice spacing.

We have calculated the temporal correlators of local quarkonium operators in the pseudo-scalar, scalar and vector channels which correspond to η_c, χ_c and J/ψ states respectively. Calculations were done using anisotropic quenched lattices and Fermilab formulation.[6)] Numerical investigation have been done using the Wilson action at $\beta = 6/g^2 = 5.7,\ 5.9,\ 6.1,\ 6.3$ and 6.5 and the anisotropies $\xi = a_s/a_t = 2$ and 4. These values of β correspond to lattice spacings $a_t^{-1} = 1.91,\ 2.91,\ 8.18,\ 14.12\,\mathrm{GeV}$. The parameters of the quark action we fixed non-perturbatively using the velocity of sound. Typically we calculated the quarkonia correlators on 1000 gauge configurations.

The spectral functions were reconstructed from the temporal correlators calculated on the lattice using MEM. At zero temperature we also parameterize the spectral functions as a sum of delta functions $\sigma(\omega) = \sum_i F_i \delta(\omega^2 - m_i^2)$ and determine the parameters F_i and m_i using constrained curve fitting techniques.[7)] We find that the analysis of the spectral functions with MEM and constrained curve fitting give consistent results for quarkonia masses m_i and decay constants F_i.

Next we have investigated the correlation functions of charmonia at different temperatures in the pseudo-scalar and scalar channels. We have found that in the pseudo-scalar channel the correlators do not show significant temperature dependence up to temperatures $T \sim 2T_c$, while the correlation function in the scalar channel were found to be significantly different from the zero temperature correlator already at temperatures $T \geq 1.1T_c$. While this is qualitatively consistent with finding of Ref. 5 we have also found that there are small differences in the temperature dependence of the charmonium correlators relative to the results in Ref. 5. This possibly means that cutoff effects in the temporal correlators are not completely under control. The spectral functions reconstructed at finite temperature using MEM confirmed the expectations based on the temperature dependence of the correlators: the η_c state survives till temperatures as high as $1.5T_c$, while the χ_c state is dissociated at $T \sim 1.1T_c$. This is in complete agreement with the results of earlier studies.

The temperature dependence of the vector correlators is qualitatively different from that in the pseudo-scalar channel. This is quite unexpected as both J/ψ and η_c are 1S state and differ by hyperfine splitting. We expect that their properties should be also very similar in the medium. It turns out that there is an extra contribution to the vector spectral function at very low energies $\omega \sim 0$ due to transport of heavy quark in Quark Gluon Plasma. It can be shown that this contribution causes the different temperature dependence of the correlators in vector and pseudo-scalar channels. A more detailed discussion of this issue can be found in Ref. 8.

We also studied bottomonia correlators and spectral functions at finite temperature. Because of the significantly larger quark mass bottomonia states are smaller in size and thus expected to dissolve at higher temperatures than the corresponding charmonia states. The pseudo-scalar correlator which corresponds to $\eta_b(1S)$ state show no temperature dependence till temperatures as high as $2.6T_c$. The spectral function also indicate the existence of this state for $T > T_c$ as expected. The correlator in the scalar channel which corresponds to χ_b on the other hand show strong temperature dependence already for $T \geq 1.15T_c$ and the spectral function is strongly modified at these temperatures.[9)]

*1 Budapest Technical University, Hungary
*2 Niels Bohr Institute, Denmark
*3 Department of Physics and Astronomy, University of California, Los Angeles, USA

References
1) M. Asakawa et al.: Prog. Part. Nucl. Phys. **46**, 459 (2001); T. Yamazaki et al.: Phys. Rev. D **65**, 014501 (2002).
2) F. Karsch et al.: Phys. Lett. B **530**, 147 (2002).
3) T. Umeda et al.: hep-lat/0211003.
4) M. Asakawa and T. Hatsuda: Phys. Rev. Lett. **92**, 012001 (2004).
5) S. Datta et al.: Phys. Rev. D **69**, 094507 (2004).
6) P. Chen: Phys. Rev. D **64**, 034509 (2001).
7) G. P. Lepage et al.: Nucl. Phys. B (Proc. Suppl.) **106**, 12 (2002).
8) P. Petreczky et al.: hep-lat/0510021.
9) K. Petrov et al.: hep-lat/0509138.

Recent results from unquenched light sea quark simulations†

T. Izubuchi*

Among the developments in the year of 2005 including the finalization of the projects of two flavor dynamical domain wall fermion ($N_F = 2$ DWF),[1] flavor singlet meson (η') spectrum on $N_F = 2$ DWF configuration,[2] the analysis of effective theory in the case of mixed actions,[3] the development of mythology for light-by-light contribution in muon anomalous magnetic moment, $g-2$,[4] and the new challenge for $N_F = 2+1$ dynamical simulation,[5] an investigation of the electromagnetic (EM) properties[6] of hadrons is described in this article.

As the electric charge of up quarks and that of down quarks differ, isospin symmetry among hadrons is broken at the order of fine structure constant, $\mathcal{O}(\alpha_{\rm em}) \sim \mathcal{O}(1\%)$, on top of the breaking effect due to the mass difference between quarks, $m_- = (m_u - m_d)/2$. The latter turns out to be very small, $\mathcal{O}\Big((m_-^2/\Lambda_{\rm QCD})^2\Big)$, and the EM effects are dominant in mass difference between charged, $\pi^\pm$, and neutral, π^0, mesons.

In fact, at leading order of chiral perturbation theory including EM effect, pion masses are given by

$$m^2_{\pi^\pm} = \alpha_{\rm em}\,\Delta^{(0)}_+ + 2\,(B_0 + \alpha_{\rm em}\,\Delta^{(m)}_+)\,m_+, \qquad (1)$$

$$m^2_{\pi^0} = 2\,(B_0 + \alpha_{\rm em}\,\Delta^{(m)}_0)\,m_+, \qquad (2)$$

$m_\pm = (m_d \pm m_u)/2$ and unknown low energy constants B_0, $\Delta^{(0,m)}_{+,0}$. The difference between the second terms of Eqs. (1) and (2), proportional to $\Delta^{(m)}_+ - \Delta^{(m)}_0$, expresses the correction to the Dashen's theorem.

To investigate the EM properties of hadrons nonperturbatively, we carried out QED+QCD simulation by generating photon field, $A_{{\rm em},\mu}(x)$, with SU(3) gauge field, $U_{{\rm qcd},\mu}(x)$ from the $N_F = 2$ DWF project.[1] Two gauge interactions are incorporated into the Dirac operator of charge Q_q quark, $D[U_\mu]$, substituting $U_\mu(x) = U_{{\rm qcd},\mu} \times \exp\left(iQ_q A_{{\rm em},\mu}\right)(x)$, from which the propagator Hadrons are then constructed using a wall source and a point sink. In this article, we focus on the results of EM mass splitting in the pseudoscalar sector.

In Fig. 1, the left panel shows the $\alpha_{\rm QED}$ dependence of a measure of EM splitting defined as the difference of squared masses by the box symbols. Although the size of signal is small, the correlation between π^0 and $\pi^\pm$ sharing the same SU(3) ensemble helps in the disentanglement of the signal of splitting from statistical noise. The approximate linearity of points indicates merely a small contribution from the higher order terms. The splitting at physical EM charge, $\alpha_{\rm QED} = 1/137$, as a function of averaged quark mass m_+ is plotted in the right panel of Fig. 1. The meson interpolation fields employed are the time components of axial vector current (circle) and pseudoscalar density (box). From these results, we determine B_0 and $\Delta^{(0,m)}_{+,0}$ omitting the higher order terms, $\mathcal{O}(\alpha_{\rm em} m_\pm)$.

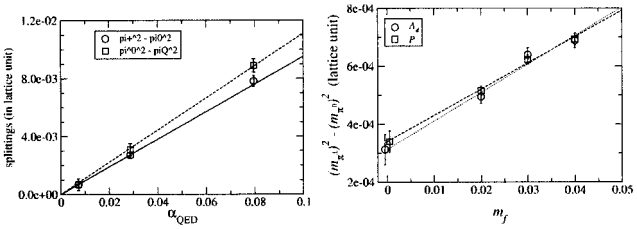

Fig. 1. Dependence of EM splitting to $\alpha_{\rm QED}$ (left) and m_+ (right). Left panel shows squared mass differences of $\pi^\pm$ compared with charge neutral pion π^0 (circle), and that to pure QCD pion π_Q (square).

Using the experimental values of pion and kaon masses as input to Eqs. (1) and (2) and also their counterparts for kaon masses, multiplying the non-perturbative quark mass renormalization factor $1/Z_m = 0.62$,[1] we evaluate light quark masses as

$$m_u^{\overline{\rm MS}}(2\,{\rm GeV}, {\rm ref}) = 2.84(23)\ {\rm MeV}\ (A_4),\ 2.89(8)\ {\rm MeV}\ (P),$$

$$m_d^{\overline{\rm MS}}(2\,{\rm GeV}, {\rm ref}) = 5.41(24)\ {\rm MeV}\ (A_4),\ 5.49(13)\ {\rm MeV}\ (P),$$

$$m_s^{\overline{\rm MS}}(2\,{\rm GeV}, {\rm ref}) = 106.8(8)\ {\rm MeV}\ (A_4),\ 106.5(5)\ {\rm MeV}\ (P),$$

from each data of interpolation fields, A_4 and P, used.

There are several sources of systematical errors: such as omissions of photon's vacuum polarization, non degenerate quark masses, and disconnected diagram, and fnite volume effects. The numbers quoted should be considered preliminary; however these are encouraging results and we will extend this study to other hadrons particularly for splitting between proton and neutron,[7] $g-2$ light-by-light project,[4] and $N_F = 2+1$ QCD configuration.

† Condensed from two articles[1,6]

* Institute for Theoretical Physics, Kanazawa University

References

1) T. Izubuchi: Talk at 23th Int. Symp. on Lattice Field Theory, Dublin, Ireland, 2005-7.
2) K. Hashimoto and T. Izubuchi: RIKEN Accel. Prog. Rep. **39**, 169 (2006).
3) M. Golterman, T. Izubuchi, and Y. Shamir: Phys. Rev. D **71**, 114508 (2005); hep-lat/0504013.
4) M. Hayakawa, T. Blum, T. Izubuchi, and N. Yamada: hep-lat/0509016.
5) K. Hashimoto and T. Izubuchi: hep-lat/0510079.
6) N. Yamada, T. Blum, M. Hayakawa, and T. Izubuchi: hep-lat/0509124.
7) T. Doi et al.: in progress.

Flavor-singlet pseudoscalar meson in two-flavor domain wall QCD†

K. Hashimoto* and T. Izubuchi*

We report our ongoing calculation of the flavor-singlet pseudoscalar meson (η') spectrum in two-flavor domain wall QCD. η' meson study is one of the most important areas of physics for explaining the quantum anomaly of $U(1)_A$ symmetry and its relation to the nontrivial topology of the QCD vacuum. The breaking of flavor-singlet axial vector current conservation alters the properties of η' *nonperturbatively* from that of flavor nonsinglet mesons, i.e., η' is not an NG boson.

A domain wall fermion[1] is one of the lattice chiral fermions that have exact flavor and almost exact chiral symmetries, even at a finite lattice spacing ($a > 0$), and is thus suitable for investigating the nonperturbative physics of chiral anomaly. We use the $N_f = 2$ QCD ensemble of the domain wall fermion and the DBW2 gauge[2] actions, in which m_π/m_ρ is from 0.53 to 0.65, the lattice size is $16^3 \times 32$, the lattice spacing is $a^{-1} \approx 1.7\,\mathrm{GeV}$, and the measure of residual chiral symmetry breaking is $m_{\mathrm{res}} \sim 0.1 \times m_f$.[3]

The η' propagator is calculated from two parts: $\langle \eta'(t)\eta'^{\dagger}(0)\rangle = C(t) - 2D(t)$, in $N_f = 2$, in which $C(t)$ is the connected quark loop, the same as the pion propagator, and $D(t)$ is the correlator of disconnected loops. Although $D(t)$ is suppressed by the OZI rule, it is propagated picking $U(1)_A$ anomaly, $m_0^2 \sim (\int F\tilde{F})^2$.

To improve the η' signal, we smear quark operators in a gauge-invariant manner (Wuppertal smearing):[4]

$q_L \to q_S = \left[1+\frac{\omega^2}{4N}\sum_{i=1}^{3}(\nabla_i+\nabla_i^{\dagger})\right]^N q_L$, with the parameters $N = 40$ and $\omega = 4.35$. Correlators $\langle \eta'_I \eta'_J\rangle$ are calculated by contracting local ($I, J = L$) and smeared ($I, J = S$) propagators using the Kuramashi method[5] on ~ 2 TFlops QCDOC machines at BNL.

The left panel of Fig. 1 (a) shows a comparison of smearing effect for effective η' mass for $m_f = 0.04$. Because we found that $\langle \eta'_S \eta'_S\rangle$ derives the earliest and optimum plateau, we mainly analyze the $I, J = S$ channel.

$m_{\eta'}$ is obtained by the following methods:

(A) Fit the $\langle \eta'_S \eta'_S\rangle$ propagator using a single exponential function.

(B) Fit the ratio of $C(t)$ to $D(t)$ using m_π:

$$2D(t)/C(t) = 1 - Be^{-(m_{\eta'}-m_\pi)t}, \quad (1)$$

$$\langle \pi_S(t)\pi_S^{\dagger}(0)\rangle = A_\pi\left[e^{-m_\pi t} + e^{-m_\pi(N_t-t)}\right]. \quad (2)$$

(C) Diagonalize[6] the 2×2 matrix using:

$$X(t) = \begin{pmatrix} \langle \eta'_L(t)\eta'^{\dagger}_L(0)\rangle & \langle \eta'_L(t)\eta'^{\dagger}_S(0)\rangle \\ \langle \eta'_S(t)\eta'^{\dagger}_L(0)\rangle & \langle \eta'_S(t)\eta'^{\dagger}_S(0)\rangle \end{pmatrix}, \quad (3)$$

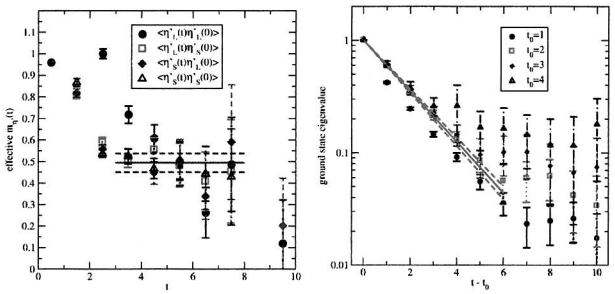

(a) (b)

Fig. 1. (a) Comparison of smearing effect of effective $m_{\eta'}$ as function of t for $m_f = 0.04$. (b) Ground state eigenvalue Eq. (4) vs $t-t_0$ for $m_f = 0.04$. Lines show fit ranges and fit results by a single exponential function and Eq. (4) respectively.

which is to be diagonalized as

$$X^{-1/2}(t_0)X(t)X^{-1/2}(t_0) \xrightarrow{\text{diag.}} \begin{pmatrix} \frac{e^{-m_{\eta'}t}+e^{-m_{\eta'}(N_t-t)}}{e^{-m_{\eta'}t_0+e^{-m_{\eta'}(N_t-t_0)}}} & 0 \\ 0 & \text{excited state} \end{pmatrix}. \quad (4)$$

Thus, $m_{\eta'}$ is obtained by the fit.

The effect of finite N_t in Eq. (4) turns out to be negligible and the eigenvalue behaves as a single exponential function as shown in the right panel of Fig. 1 (b) for $t_0 \geq 2$.

Our preliminary results are shown in Table 1. We find that the methods are consistent with each other within $\sim 20\%$ errors, and method (C) reduces statistical error by up to 50%, which is encouraging.

Table 1. Preliminary results of m_π and $m_{\eta'}$ from different fits. Only statistical errors are quoted.

m_f	$m_\pi a$	$m_{\eta'}a$ (A)	$m_{\eta'}a$ (B)	$m_{\eta'}a$ (C)
0.02	0.2955(14)	0.575(98)	0.541(88)	0.540(68)
0.03	0.3587(12)	0.710(82)	0.686(81)	0.695(69)
0.04	0.4079(12)	0.492(44)	0.475(43)	0.522(22)

† Work done under RBC Collaboration

* Institute for Theoretical Physics, Kanazawa University

References

1) D. B. Kaplan: Phys. Lett. B **288**, 342 (1992); Y. Shamir: Nucl. Phys. B **406**, 90 (1993); V. Furman et al.: Nucl. Phys. B **439**, 54 (1995).
2) T. Takaishi: Phys. Rev. D **54**, 1050 (1996); P. de Forcrand, QCD-TARO Collaboration et al.: Nucl. Phys. B **577**, 263 (2000).
3) Y. Aoki, RBC Collaboration et al.: hep-lat/0411006; T. Izubuchi, RBC Collaboration: Nucl. Phys. B Proc. Suppl. **140**, 237 (2005); K. Hashimoto and T. Izubuchi, RBC Collaboration: Nucl. Phys. B Proc. Suppl. **140**, 341 (2005).
4) S. Güsken: Nucl. Phys. B Proc. Suppl. **17**, 361 (1990).
5) Y. Kuramashi et al.: Phys. Rev. Lett. **72**, 3448 (1994).
6) M. Lüscher and U. Wolff: Nucl. Phys. B **339**, 222 (1990).

Bound state spectrum in finite volume

S. Sasaki and T. Yamazaki

The signature of bound state formation on the lattice is of particular interest. In the infinite volume, the bound state is well defined because there is no continuum state below threshold. However, in a finite box on the lattice, all states have discrete energies. Moreover, the lowest level of elastic scattering states appears below threshold if an interaction is attractive between two particles.[1] Therefore, it is hard to clearly distinguish between the "loosely bound state" and the scattering state in this sense.

To study bound states in the finite volume, we calculate the positronium spectra in the Higgs phase of $U(1)$ gauge dynamics, where photons are massive and then massive photons give rise to short-ranged interparticle force. We try to identify bound state formation by the Lüscher's finite size method,[1] which suggests specific volume dependences of the energy gap/shift from the threshold energy for either bound states or scattering states.

We perform numerical simulations for positronium spectra ($^1S_0$ and $^3S_1$ states) in the Higgs phase of $U(1)$ gauge dynamics ($\beta = 2.0$ and $h = 0.6$) on $L^3 \times 24$ lattices with several spatial sizes, $L = 8$, 10, 12, 16, 20, 24.[2] The two-point functions of $^1S_0$ and $^3S_1$ states are constructed from the bilinear pseudo-scalar operator $\overline{\Psi}_x \gamma_5 \Psi_x$ and vector operator $\overline{\Psi}_x \gamma_\mu \Psi_x$, respectively. To evaluate the threshold energy, we also calculate the electron mass in the Landau gauge.

Figure 1 shows the masses of $^1S_0$ and $^3S_1$ positronium states as functions of the electron mass. The left (right) panel corresponds to results with charge-three (four) electron fields. The certain energy gap from the threshold energy appears in the simulations with charge-four electron fields. It is natural to expect that higher charged electrons provide larger energy gaps because the interparticle force is proportional to (charge q)^2. For $q = 4$, the hyperfine mass splitting of positronium states is also clearly observed.

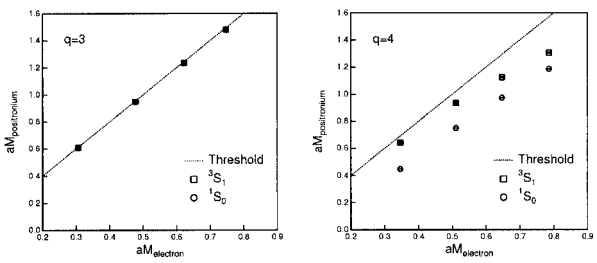

Fig. 1. Masses of $^3S_1$ and $^1S_0$ positronium states as functions of electron mass.

The volume dependences of energy gaps at $aM_{\rm electron} \simeq 0.5$ are shown in Fig. 2. All data that points in the right panel ($q = 4$) are clearly below the lower bound for the asymptotic solution of the scattering state in the Lüscher's formula.[3] The volume dependence is drastically changed around $L \simeq 12$–16. Data for the larger lattice sizes are well fitted by the form $\Delta E_L = \Delta E_\infty + \frac{a}{L} e^{-bL}$, which is inspired by the asymptotic solution of the bound state in the Lüscher's formula.[4] The energy gaps for either $^1S_0$ or $^3S_1$ states should remain finite in the infinite volume limit. Therefore, the bound states of electron-positron are certainly formed in the simulations with charge-four electrons even in the Higgs phase, where interparticle forces are short-ranged.

Although an upward tendency of the L dependence is observed as spatial size L increases in the left panel ($q = 3$), all data points are located near the lower bound for the asymptotic solution of the scattering state. Also, that the L dependence seems to become opposite around $L \simeq 20$–24. These observations suggest that the observed states are unlikely the lowest level of elastic scattering states, rather they are likely a "loosely bound state." However, to draw firm conclusions, more detailed studies and additional data for larger L are required.

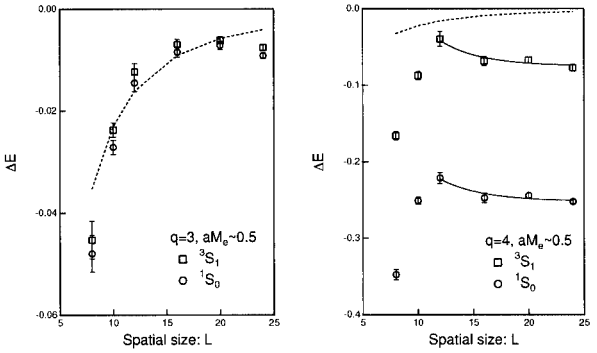

Fig. 2. Mass gaps from threshold energy as functions of spatial lattice size L in lattice units. Dashed lines represent a lower bound for the asymptotic solution of the scattering state.

References

1) M. Lüscher: Commun. Math. Phys. **104**, 177 (1986); Nucl. Phys. B **354**, 531 (1991).
2) S. Sasaki and T. Yamazaki: hep-lat/0510032.
3) K. Yokokawa, S. Sasaki, A. Hayashigaki, and T. Hatsuda: hep-lat/0509189.
4) S. R. Beane et al.: Phys. Lett. B **585**, 106 (2004).

Study of spin 3/2 pentaquarks in anisotropic lattice QCD†

T. Doi, N. Ishii,*1 Y. Nemoto,*2 M. Oka,*1 and H. Suganuma*3

The announcement[1] of the discovery of the new particle Θ^+ (1540), whose minimal configuration is $uudd\bar{s}$, has triggered numerous studies thus far. Experimentally, several groups confirmed the existence of Θ^+, whereas other groups reported null results.[2] Note that even positive results have determined neither spin nor parity. Theoretically, one of the central issues is to realize the mechanism for the extremely narrow decay width of $\Gamma \lesssim 1\,\mathrm{MeV}$. In this report, we investigate $J = 3/2$ possibility. In fact, if $\Theta^+$is a $J^P = 3/2^-$ state, the decay to the KN state is of d-wave, leading to a highly suppressed decay width due to the large centrifugal barrier as well as the wave function factor.[3] On the other hand, $J^P = 3/2^+$ possibility attracts another interest because such a state may appear as a spin partner of $J^P = 1/2^+$ pentaquark (5 Q).

In this report, we present the analysis of 5 Q in $J^P = 3/2^\pm$ channels using quenched anisotropic lattice QCD. Note that the lattice QCD studies of 5 Q thus far[4,5] are restricted to $J^P = 1/2^\pm$ channels, except for a very recent one.[6] To perform a high-precision analysis, we generate 1000 gauge configurations using the Wilson gauge action at $\beta = 5.75$ ($a_s^{-1} = 1.1\,\mathrm{GeV}$) on the $12^3 \times 96$ lattice with the renormalized anisotropy $a_s/a_t = 4$. The $O(a)$-improved Wilson quark action is employed with hopping parameters as $\kappa = 0.1210$–0.1240 for u, d-quarks ($m_\pi/m_\rho = 0.81$–0.66) and $\kappa_s = 0.1240$ fixed for s-quark. To enhance the low-lying spectra, we adopt gaussian smeared sources. The two-point correlator is studied using the three types of Rarita-Schwinger fields with $I = 0$: (a) NK*-type, $\epsilon_{abc}\left(u_a^T C\gamma_5 d_b\right) u_c \cdot (\bar{s}_d\gamma_\mu d_d) + (u \leftrightarrow d)$, (b) (color-)twisted NK*-type, $\epsilon_{abc}\left(u_a^T C\gamma_5 d_b\right) u_d \cdot (\bar{s}_d\gamma_\mu d_c) + (u \leftrightarrow d)$ and (c) diquark-type, $\epsilon_{abc}\epsilon_{def}\epsilon_{cfg}\left(u_a^T C\gamma_5 d_b\right)\left(u_d^T C\gamma_5\gamma_\mu d_e\right) C\gamma_5\bar{s}_g$.

We analyze the effective mass of the correlator, and observe plateaux except for the result of the diquark-type field in $J^P = 3/2^-$. In Fig. 1, we show 5 Q masses that are determined by single-exponential fits. In $J^P = 3/2^-$ channel, we find that none of the 5 Q states appear below the NK d-wave threshold, although this threshold is raised by 200–250 MeV due to the finite extent of the spatial lattice. We perform the linear chiral extrapolation and obtain $m_{5\,\mathrm{Q}} = 2.17(4)$ and $2.11(4)\,\mathrm{GeV}$ from NK*- and twisted NK*-type fields, respectively, which are too heavy to be identified with Θ^+. In $J^P = 3/2^+$ channel, we obtain $m_{5\,\mathrm{Q}} = 2.64(7)$, $2.48(10)$ and $2.42(6)\,\mathrm{GeV}$ in the chiral limit from NK*-, twisted NK*- and diquark-type fields, respectively, which are again too heavy to be identified with Θ^+.

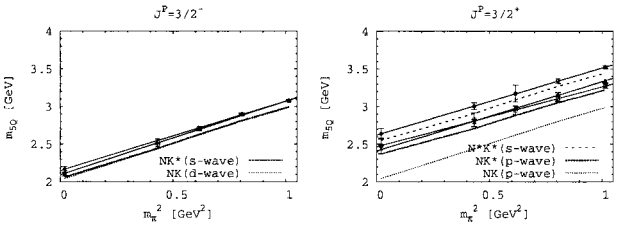

Fig. 1. $m_{5\,\mathrm{Q}}$ against m_π^2 in $J^P = 3/2^\pm$ channels. Open circle, box, triangle symbols denote the results for NK*, twisted NK*, and diquark-type fields, respectively, and the solid lines represent the chiral extrapolations.

To understand the nature of the observed plateaux, we perform the hybrid boundary condition (HBC) analysis,[5] in which we impose the spatially antiperiodic BC (APBC) on u and d-quarks and the periodic BC (PBC) on s-quark. With HBC, N, K and K* are subject to APBC, whereas Θ^+ is still subject to PBC. Therefore, we expect the energy shift with HBC for NK and NK* states because of the difference in momentum quantization, whereas the energy shift for $\Theta^+$is expected to be marginal. In this way, we identify the observed plateaux as follows. In $J^P = 3/2^-$ channel, both plateaux from NK*- and twisted NK*-type fields are regarded as s-wave NK* states. In $J^P = 3/2^+$ channel, the plateau from an NK*-type field is most likely to be an s-wave N*K* state, whereas the other plateaux from twisted NK*- and diquark-type fields are p-wave NK* states. In conclusion, we do not observe any relevant signals of compact 5 Q states.

† Condensed from the article in Phys. Rev. D **72**, 074503 (2005)
*1 Department of Physics, Tokyo Institute of Technology
*2 Department of Physics, Nagoya University
*3 Department of Physics, Kyoto University

References

1) LEPS Collaboration, T. Nakano et al.: Phys. Rev. Lett. **91**, 012002 (2003).
2) For a review, K. H. Hicks: Prog. Part. Nucl. Phys. **55**, 647 (2005), and references therein.
3) A. Hosaka: Phys. Lett. B **571**, 55 (2003).
4) F. Csikor et al.: JHEP **0311**, 070 (2003); S. Sasaki: Phys. Rev. Lett. **93**, 152001 (2004); T. W. Chiu and T. H. Hsieh: Phys. Rev. D **72**, 034505 (2005); N. Mathur et al.: Phys. Rev. D **70**, 074508 (2004); T. T. Takahashi, T. Umeda, T. Onogi, and T. Kunihiro: Phys. Rev. D **71**, 114509 (2005); B. G. Lasscock et al.: Phys. Rev. D **72**, 014502 (2005); C. Alexandrou and A. Tsapalis: hep-lat/0503013; F. Csikor et al.: hep-lat/0503012; K. Holland and K. J. Juge: hep-lat/0504007.
5) N. Ishii, T. Doi, H. Iida, M. Oka, F. Okiharu, and H. Suganuma: Phys. Rev. D **71**, 034001 (2005).
6) B. G. Lasscock et al.: Phys. Rev. D **72**, 074507 (2005).

$\Delta I = 3/2$ kaon weak matrix elements with non-zero total momentum

T. Yamazaki for RIKEN-BNL-Columbia Collaboration

The calculation of the $K \to \pi\pi$ weak matrix element is one of the challenging studies in lattice QCD, because it is difficult to calculate directly on a lattice due to the difficulty in the calculation of the two-pion state in finite volume. To address the problem, many groups employed an indirect method,[1] where the $K \to \pi\pi$ process is reduced to the $K \to \pi$ and $K \to 0$ processes. However, the reduction may cause systematic errors, because in the decay process the final state interaction effect of the two-pion state is expected to play an important role.

The extraction of the two-pion state with non-zero relative momentum $p \neq 0$ requires complicated calculations and analyses. However, using the non-zero total momentum (Lab) system, $|\vec{P}| \neq 0$, we can extract the two-pion state with $p \neq 0$ without complicated calculations and analyzes, because the ground state of the two-pion is $|\pi(0)\pi(\vec{P})\rangle$, which relates to the two-pion state with $p \neq 0$ in the center-of-mass (CM) system.

In the Lab system, however, we cannot naively apply the formula proposed by Lellouch and Lüscher (LL),[2] which converts the on-shell decay amplitude on finite volume to that in the infinite volume, because the formula is derived in the CM system. Before the simulation, we have to extend the LL formula to the Lab system calculation. Very recently, Kim et al.[3] and we[4] have proposed the extension of the formula. Here, we apply the extended formula in the calculation of the $\Delta I = 3/2$ kaon weak matrix elements.

We employ the quenched lattice QCD using the DBW2 gauge gluon action with $\beta = 0.87$, and the domain wall fermion action with the domain wall height $M = 1.8$, and the fifth dimension length $L_s = 12$. In the parameters, the lattice spacing corresponds to $a^{-1} = 1.31(1)\,\mathrm{GeV}$. The lattice size is $L^3 \cdot T = 16^3 \cdot 32$, where the spatial volume is about 2.4 fm. The number of configuration is 111. Our calculation is carried out with four pion masses, whose range is $m_\pi = 350$–$600\,\mathrm{MeV}$, for the chiral extrapolation of the decay amplitudes. We calculate decay amplitude in the CM and Lab $|\vec{P}| = 2\pi/L$ systems, where the typical relative momenta of the pions are 80 and 260 MeV in each system. Then, we interpolate the decay amplitudes to the physical momentum 206 MeV.

We calculate the physical quantity of the final state interaction, the $I = 2$ $\pi\pi$ scattering phase shift δ, from the two-pion energy in each system calculation using the finite volume method.[5] Figure 1 shows the results of δ in each pion mass, and those obtained using the chiral perturbation theory (ChPT).[6] We also obtain the scattering length $a_0/m_\pi = -1.91(12)\,\mathrm{GeV}^{-2}$ at the physical pion mass, which is comparable with that of ChPT,[6] $a_0/m_\pi = -2.265(51)\,\mathrm{GeV}^{-2}$.

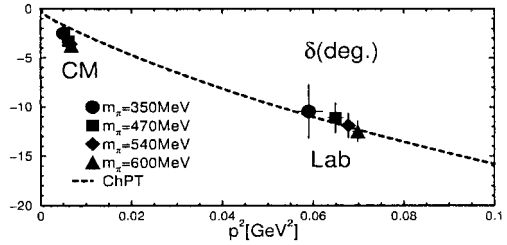

Fig. 1. Measured scattering phase shift and result of ChPT.

We calculate ReA_2 from the measured weak matrix elements. The ReA_2 obtained from the CM and Lab system calculations are shown in Fig. 2. We also plot the results previously obtained in several works.[7–10] We estimate ReA_2 at the physical point, $m_\pi = 140\,\mathrm{MeV}$ and $p = 206\,\mathrm{MeV}$, with the fitting form $A_{00} + A_{10}m_\pi^2 + A_{11}m_\pi^2 p^2 + A_{01}p^2$. The dashed line in the figure denotes the extrapolation of the result with $p = 206\,\mathrm{MeV}$ to the physical pion mass. We obtain Re$A_2 = 2.55(43) \times 10^{-8}\,\mathrm{GeV}$ at the physical point, which is 1.70(28)-fold larger than the experimental ReA_2. To understand the difference from the experiment ReA_2, we need a more detailed investigation of the systematic errors.

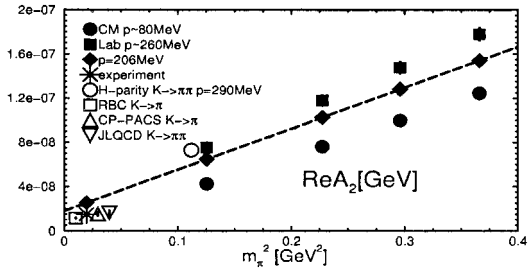

Fig. 2. Measured ReA_2 and results of previous works.

References

1) C. W. Bernard et al.: Phys. Rev. D **32**, 2343 (1985).
2) L. Lellouch and M. Lüscher: Commun. Math. Phys. **219**, 31 (2001).
3) C. Kim et al.: Nucl. Phys. B **727**, 218 (2005).
4) N. H. Christ, C. Kim, and T. Yamazaki: Phys. Rev. D **72**, 114506 (2005).
5) K. Rummukainen and S. Gottlieb: Nucl. Phys. B **450**, 397 (1995).
6) G. Colangelo et al.: Nucl. Phys. B **603**, 125 (2001).
7) C. Kim: Nucl. Phys. B (Proc. Suppl.) **140**, 381 (2005); his doctoral thesis.
8) J. Noaki, CP-PACS Collaboration, et al.: Phys. Rev. D **68**, 014501 (2003).
9) T. Blum, the RBC Collaboration, et al.: Phys. Rev. D **68**, 114506 (2003).
10) S. Aoki, JLQCD Collaboration, et al.: Phys. Rev. D **58**, 054503 (1998).

Neutron electric dipole moment from lattice QCD

E. Shintani,[*1] S. Aoki,[*1] N. Ishizuka,[*1,*2] K. Kanaya,[*1] Y. Kikukawa,[*3] Y. Kuramashi,[*1,*2] M. Okawa,[*4] Y. Taniguchi,[*1,*2] A. Ukawa,[*1,*2] and T. Yoshié[*1,*2]

One of the most stringent constraints on the possible violation of the CP symmetry in the strong interaction comes from the measurement of the neutron electric dipole moment (NEDM) $\vec{d}_n$. The current upper bound is given by $|\vec{d}_n| < 6.3 \times 10^{-26}\ e \cdot \mathrm{cm}\,(90\%\ \mathrm{C.L.})$.[1] On the other hand, QCD allows a gauge invariant renormalizable CP-odd θ term in the Lagrangian. Crude model estimations[2,3] and the experimental bound on $|\vec{d}_n|$ yield a very stringent bound $\theta \leq O(10^{-10})$.

Current model estimates give not only an order of magnitude different results on $\vec{d}_n$ but also differ even in its sign. Clearly, the first-principles determination of $\vec{d}_n$ from lattice QCD is required to determine θ, if a nonzero value is found for NEDM in future experiments. In this report, we present our result of a feasibility study for the lattice QCD calculation of NEDM.[4]

We consider the electromagnetic form factor of the nucleon defined as

$$\langle N(\vec{p},s)|J_\mu^{\mathrm{EM}}|N(\vec{p'},s')\rangle = \bar{u}(\vec{p},s)\left[\frac{F_3(q^2)}{2m_N}q_\nu\sigma_{\mu\nu}\gamma_5 + \cdots\right]u(\vec{p'},s'), \quad (1)$$

where J_μ^{EM} is the electromagnetic current, $q = p - p'$ is the momentum transfer, $|N(\vec{p},s)\rangle$ is the on-shell nucleon state with momentum $\vec{p}$, energy $p_0 = \sqrt{m_N^2 + \vec{p}^2}$ and helicity s. On the right-hand side, we explicitly write the form factor F_3 only, which is related to NEDM as $|\vec{d}_n| = \lim_{q^2\to 0} F_3(q^2)/2m_N = F_3(0)/2m_N$.

The electromagnetic form factor can be extracted from the three-point correlation function

$$G^Q_{NJ_\mu N}(q,t,\tau) = \langle N(\vec{p},t)J_\mu^{\mathrm{EM}}(\vec{q},\tau)\bar{N}(\vec{p'},0)Q\rangle, \quad (2)$$

calculated in the presence of the topological charge Q. We can extract F_3 in two independent ways, using tr $[G^Q_{NJ_4N}(q,t,\tau)\Gamma_4\gamma_5]$ and tr $[G^Q_{NJ_4N}(q,t,\tau)i\Gamma_4\gamma_5\gamma_i]$, where $\Gamma_4 = (1+\gamma_4)/2$. In addition to the three-point function, the two-point function is calculated to extract the mixing coefficient f_N^1 as

$$\langle N(p,s)\bar{N}(p,s)Q\rangle = |Z_N|^2 e^{-E_N t}\frac{f_N^1 m_N}{2E_N}\gamma_5. \quad (3)$$

We calculate two- and three-point functions on 730 quenched gauge configurations generated with the RG-improved gauge action at $\beta = 2.6$, corresponding to $a^{-1} = 1.81(4)\,\mathrm{GeV}$ determined from ρ meson mass, on a $16^3 \times 32$ lattice. For the quark action, we employ the domain-wall fermion with the fifth dimension length $N_s = 16$ and the domain-wall height $M = 1.8$, taking the quark mass of $m_f = 0.03$ corresponding to $m_{PS}/m_V = 0.63$. The topological charge Q is calculated by the cooling method with an $O(a^2)$ improved definition. As shown in Ref. 4, 730 configurations are sufficient to extract the CP-odd phase parameter f_N^1 from the two-point correlation function, and we obtain $f_N^1 = -0.247(17)$.

After subtracting the mixing contribution, we obtain two independent estimates for F_3, which are plotted in Fig. 1 as a function of t for $\tau = 6$. The two estimates agree at a sufficiently large t, demonstrating the correctness of our formulae. After fitting the results at $12 \leq t \leq 15$, we obtain

$$F_3(q^2 \simeq 0.58\,\mathrm{GeV}^2)/2m_N = \begin{cases} -0.024(5)\ e\cdot\theta\cdot\mathrm{fm} & \text{neutron} \\ +0.021(6)\ e\cdot\theta\cdot\mathrm{fm} & \text{proton} \end{cases}. \quad (4)$$

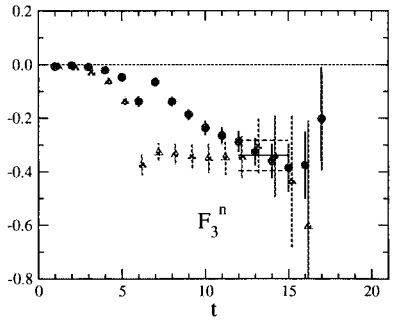

Fig. 1. F_3 for neutron as function of t with current inserted at $\tau = 6$. Circles represent the result with $\Gamma_4\gamma_5$ projection, while triangles represents that with $\Gamma_4\gamma_5\gamma_j$, averaged over $j = 1, 2, 3$. Straight lines show the fitting results for the former.

*1 Graduate School of Pure and Applied Sciences, University of Tsukuba
*2 Center for Computational Sciences, University of Tsukuba
*3 Department of Physics, Nagoya University
*4 Department of Physics, Hiroshima University

References

1) P. G. Harris et al.: Phys. Rev. Lett. **82**, 904 (1999).
2) R. J. Crewther, P. Di Vecchia, G. Veneziano, and E. Witten: Phys. Lett. B **88**, 123 (1979); erratum, Phys. Lett. B **91**, 487 (1980); P. Di Vecchia: Acta Phys. Austriaca Suppl. **22**, 341 (1980).
3) M. Pospelov and A. Ritz: Nucl. Phys. B **558**, 243 (1999); Nucl. Phys. B **573**, 177 (2000); C.-T. Chan, E. M. Henley, and T. Meissner: hep-ph/9905317; M. Pospelov and A. Ritz: Phys. Rev. Lett. **27**, 2526 (1999); Phys. Rev. D **63**, 073015 (2001); B. Borasoy: Phys. Rev. D **61**, 114017 (2000).
4) E. Shintani, et al.: Phys. Rev. D **72**, 014504 (2005).

Status of QCDOC (QCD On a Chip) computer project

P. A. Boyle,[*1] D. Chen,[*2] N. H. Christ,[*3] M. Clark,[*1] S. D. Cohen,[*3] C. Cristian,[*3] Z. Dong,[*3] A. Gara,[*2] B. Joó,[*1] C. Jung,[*3,*4] C. Kim,[*3] L. Levkova,[*3] X. Liao,[*3] G. Liu,[*3] R. D. Mawhinney,[*3] S. Ohta,[*5,*6] K. Petrov,[*3,*4] T. Wettig,[*7] and A. Yamaguchi[*1,*8]

QCDOC (QCD On a Chip) computer project[1–7] was started in 1999 as a joint project of RIKEN, Columbia University and IBM Research. The UKQCD Collaboration joined later. The project aimed at providing a computational power in the range of tens of TFlops optimized for numerical investigations of lattice QCD (Quantum Chromodynamics). QCD is the fundamental theory of the strong interaction of elementary particles. Based on the SU(3) quantum gauge field theory of quarks and gluons, QCD describes the dynamics of strongly interacting elementary particles such as proton, neutron, pion, kaon and various atomic nuclei. Lattice QCD provides both the definition of QCD and a method of exactly and accurately extracting the outcome of the theory.

Each QCDOC configuration involves tens of thousands of computational nodes each communicating with its twelve nearest neighbors in a six-dimensional hypercubic network. A single QCDOC computational node consists of a single application specific integrated circuit (ASIC) with a) a 500 MHz, 32-bit PowerPC 440 processor core, b) a 64-bit, 1 GFlops floating-point unit, c) 4 MBytes of embedded-DRAM memory, d) controllers for embedded and external memories, e) a nearest-neighbor serial communication unit (SCU) with latencies of 350 ns (550 ns) for supervisor (regular) transfers that occur simultaneously in 12 independent directions and an aggregate bandwidth of 12 Gbit/s, and f) other components such as an Ethernet controller. Two such ASICs are mounted on a daughterboard. Thirty-two daughterboards are mounted on a motherboard, and eight motherboards are mounted in a crate with two backplanes. The final machine consists of a certain number of such crates.

Last year, we reported the completion of the design and the start of the construction. Before the end of the Japanese fiscal year 2004, two 10-TFlops configurations were completed (see Fig. 1): one for the RIKEN-BNL Research Center (RBRC) and another for the UKQCD Collaboration. Both configurations were immediately provided for lattice QCD research.

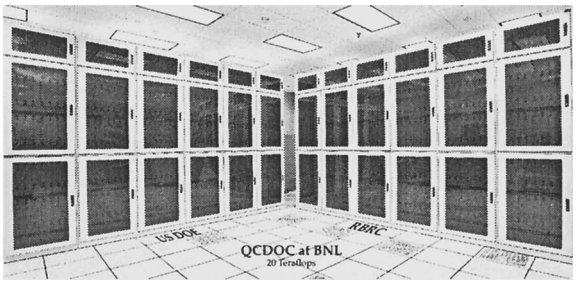

Fig. 1. Two 10-TFlops configurations of QCDOC computer for RIKEN-BNL Research Center and US DOE, at Brookhaven National Laboratory.

At the same time, the RIKEN-BNL-Columbia QCD Collaboration, which had been collaborating in lattice QCD research using the QCDSP computer, and a part of the UKQCD Collaboration, started a joint collaboration on lattice QCD using three light flavors (very light and degenerate up and down, and about 100 MeV strange) of dynamical domain-wall fermions (DWF) quakrs. This joint collaboration is now carrying out the calculation of observables regarding nucleon form factors and structure functions and the $\Delta I = 1/2$ rule and CP-violating amplitudes of kaon decay. About 2/3 of the RBRC and UKQCD QCDOC computers are dedicated to this effort. In addition, another 10-TFlops configuration of QCDOC was completed this year at the request of the US Department of Energy. This configuration is provided for the use of the US lattice QCD community at large.

*1 Department of Physics and Astronomy, University of Edinburgh, Scotland
*2 IBM T. J. Watson Research Center, USA
*3 Department of Physics, Columbia University, USA
*4 Department of Physics, Brookhaven National Laboratory, USA
*5 Institute of Particle and Nuclear Studies, KEK
*6 Physics Department, Sokendai
*7 Department of Physics, Yale University, USA
*8 Department of Physics and Astronomy, University of Glasgow, Scotland

References

1) P. A. Boyle et al.: J. Phys. Conference Series **16**, 129 (2005).
2) P. A. Boyle et al.: Nucl. Phys. Proc. Suppl. **140**, 169 (2005).
3) P. A. Boyle et al.: Nucl. Phys. Proc. Suppl. **129**, 838 (2004); hep-lat/0309096.
4) P. A. Boyle, C. Jung, and T. Wettig, QCDOC Collaboration: hep-lat/0306023.
5) P. A. Boyle et al.: Nucl. Phys. Proc. Suppl. **119**, 1041 (2003); hep-lat/0210034.
6) P. A. Boyle, et al.: Nucl. Phys. Proc. Suppl. **106**, 177 (2002); hep-lat/0110124.
7) D. Chen et al.: Nucl. Phys. Proc. Suppl. **94**, 825 (2001); hep-lat/0011004.

Measurement of double helicity asymmetry (A_{LL}) in π^0 production in proton-proton collisions at RHIC-PHENIX experiment

Y. Fukao,* for the PHENIX Collaboration

One of the goals of the RHIC-Spin program is to measure gluon polarization in the proton. Double-longitudinal-spin asymmetry (A_{LL}) in high-transverse-momentum (p_T) particle production in polarized proton-proton collisions is a good probe. During the run in 2005 (Run 5), RHIC was operated using longitudinally polarized proton beams with a center of mass energy of 200 GeV. The average beam polarization (P) was 47% and the integrated luminosity (L) accumulated at PHENIX[1] was 3.8 pb^{-1}, which are 40 times larger than those in the past years in terms of figure of merit (P^4L). In this report, we present the preliminary results of A_{LL} in the π^0 production of the p_T range from 1 GeV/c to 9 GeV/c and at the midrapidity using approximately 50% of the data obtained in Run 5.

A_{LL} can be calculated using the formula

$$A_{LL} = \frac{1}{|P_B||P_Y|}\frac{N_{++} - RN_{+-}}{N_{++} + RN_{+-}}, \quad R = \frac{L_{++}}{L_{+-}},$$

where $P_{B(Y)}$ is the polarization of the beam rotating (anti)clockwise, N is the yield of π^0, L is the integrated luminosity and $++$ ($+-$) denotes identical (opposite) helicity beams. We adopted a beam-beam counter (BBC) to measure R.[2] Its error was evaluated by comparing the BBC counts with those obtained using a zero-degree calorimeter to be $\delta R = 1.0 \times 10^{-4}$. This corresponds to $\delta A_{LL} = 2.3 \times 10^{-4}$ for a beam polarization of 47%, which is sufficiently small compared with the uncertainty from the statistics of π^0.

Beam polarization was measured using a proton-carbon CNI polarimeter.[3] The CNI polarimeter assigned 20% to the error of the beam polarization in Run 5, which affected the scaling error of double helicity asymmetry by 40%. The PHENIX local polarimeter[4] confirmed that the direction of the proton spin in the PHENIX collision point was more than 98% longitudinal and this effect is fully absorbed in the uncertainty of the absolute polarization.

High p_T π^0's were collected using a high-p_T photon trigger[5] based on an electromagnetic calorimeter with an energy threshold of 1.4 GeV. A charged particle veto was applied to purify photons and to reduce background to the π^0 signal utilizing a pad chamber in front of the calorimeter. Roughly π^0's of 3×10^7 counts are obtained within a ± 25 MeV mass window in the p_T range of 1–9 GeV/c after the cut for particle identification. The background fractions in this mass window are 32%, 14% and 7% for 1–2, 2–3 and 3–4 GeV/c $\pi^0 p_T$ bins, respectively, and 5% for a p_T of more than 4 GeV/c.

The systematic error of A_{LL} can be evaluated by the bunch shuffling technique. In each shuffle, we randomly assigned a beam helicity sign to each bunch crossing. This can mimic many experimental data. The fluctuation of A_{LL} generated by a sufficient number of shuffles should be a result of the statistics of π^0 and systematics, which depends on bunch and fill. By comparing the statistical error of A_{LL} with the width of the A_{LL} distribution obtained by bunch shuffling, we found that systematic error is negligible compared with statistical uncertainty. Note that the systematic error correlated over all bunches or all fills cannot be evaluated by this bunch shuffling method. The main contributors to these errors are the uncertainty of beam polarization.

Figure 1 shows the Run 5 results of π^0 A_{LL}. Four theoretical curves[6] based on perturbative quantum chromodynamics (pQDC) are also shown in the figure. Our results reject the case that gluon spin aligns with proton spin maximally (GRSV-max). Note that the sensitivity of the data to the theoretical curves is dominated by lower-p_T bins at present. More statistics in a higher-p_T region would be helpful to further our knowledge of gluon polarization, where pQCD is expected to describe the data better. It is also important to study a lower-p_T region using other probes, where soft processes can participate.

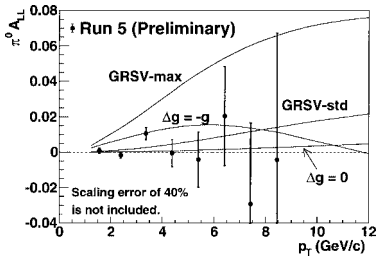

Fig. 1. π^0 A_{LL} as a function of p_T. The error bars denote only statistical uncertainty.

References

1) K. Adcox et al.: Nucl. Instrum. Methods Phys. Res. A **499**, 469 (2003).
2) K. Boyle et al.: RIKEN Accel. Prog. Rep. **39**, 197 (2006).
3) O. Jinnouchi et al.: RHIC/CAD Accel. Phys. Note, 171 (2004).
4) M. Togawa et al.: RIKEN Accel. Prog. Rep. **39**, 198 (2006).
5) K. Okada et al.: RIKEN Accel. Prog. Rep. **36**, 248 (2003).
6) B. Jäger et al.: Phys. Rev. D **67**, 054005 (2003).

* Kyoto University

Measurement of direct photons in $\sqrt{s} = 200\,\mathrm{GeV}$ $p+p$ collisions

K. Okada, Y. Akiba, Y. Goto, H. Hiejima,[*1] T. Horaguchi,[*2] M. Togawa,[*3] H. Torii, and A. Bazilevsky[*4]

Direct photon production in $p+p$ collisions is one of the simplest processes in QCD. At the RHIC energy, the dominant process is quark-gluon Compton scattering ($q+g \to q+\gamma$). The cross section measurement of such a process provides us information on gluon distributions in proton, both unpolarized and polarized.

The analysis is performed with 240 nb^{-1} of the $p+p$ data taken in 2003 with the PHENIX central arm detectors.[1)] We published measurements of direct photon in $5.5 < p_T < 7\,\mathrm{GeV}/c$ from the 2002 run period.[2)] The present data have much higher statistics, and the measured p_T range is extended to $3 < p_T < 17\,\mathrm{GeV}/c$. Photons are detected by the electromagnetic calorimeters (EMCal) and the charged tracking system is used to reject backgrounds. Photons are selected from clusters in the EMCal by a shape cut, a timing cut and a charged hadron veto cut.

Background photons, mainly from $\pi^0 \to \gamma\gamma$ decay, are subtracted by the following π^0 tagging method. From the invariant mass distribution of any two photons in an event, the number of photons from π^0 decay is measured statistically in each photon p_T bin. This number of photons from π^0 is then corrected for π^0 detection efficiency due to the acceptance, the detector dead area, and the minimum photon energy threshold. The efficiency is estimated by a Monte Carlo simulation. The contributions of other hadronic decays are estimated by multiplying a factor, which is obtained from the production ratio to π^0's and their decay branching ratio to photons. Of all photon clusters, 50(20)% are tagged as photons from π^0, and 85(30)% are estimated as photons from hadrons at $p_T = 5(16)$GeV/c.

Figure 1 shows the invariant cross section of the direct photon obtained from this analysis together with a next to leading order (NLO) pQCD calculation. In general, the NLO pQCD calculation describes our data well. Although the systematic error is large, some excess may exist in the low p_T region. One of the possible explanations is higher-order contributions.

A direct photon is isolated, while a photon from hadronic decay is accompanied with other jet activities. Thus, when we require little activity around the photon, photons from hadronic decay are expected to be suppressed more than direct photons. In Fig. 2, the filled circles show the ratio of direct photons with and without an isolation cut. In the same figure, the ratio of π^0 decay photons is also shown with open circles. Here, the isolation cut required that less than 10% of the photon energy is observed within a cone of 0.5 [rad] around the photon. As expected, the isolation cut rejects a larger fraction of π^0 decay photons than direct photons. The direct photons are isolated especially in the high-p_T region. NLO pQCD predictions[3,4)] for direct photons are also plotted in the figure. The theory predictions are consistent with the data.

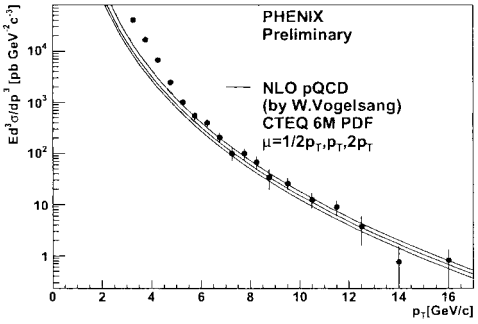

Fig. 1. Direct photon spectra from subtraction method with NLO pQCD calculation.[3)] Boxes represent the systematic errors. Three lines represent calculations with 3 different factorization scales.

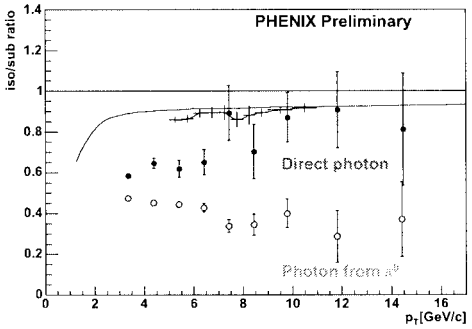

Fig. 2. Ratio of result of isolation method to result of subtraction method. Lines represent NLO pQCD calculations.[3,4)]

In summary, we have measured direct photon production in $p+p$ collisions at $\sqrt{s} = 200\,\mathrm{GeV}$. In general, a NLO pQCD calculation describes well both cross section and isolation behaviors. In the lower-p_T region, as our data can not lead to a conclusion with systematic uncertainties, it is interesting to know whether there are higher-order contributions.

References

1) K. Adcox et al.: Nucl. Instrum. Methods Phys. Res. A **499**, 469 (2003).
2) S. S. Adler et al.: Phys. Rev. D **71**, 071102 (2005).
3) Private communication with Werner Vogelsang (RBRC).
4) Private communication with Monique Werlen (LAPTH).

*1 University of Illinois, USA
*2 Kyoto University
*3 Tokyo Institute of Technology
*4 Brookhaven National Laboratory, USA

Measurement of transverse single-spin asymmetries with muons in polarized p+p collisions at $\sqrt{s} = 200\,\mathrm{GeV}$

H. M. Albataineh,[*1] M. X. Liu,[*2] and X. Wang[*1]

The spin structure of the proton has revealed itself to be extremely complex and is an active area of ongoing research. Large transverse single-spin asymmetries in inclusive particle production at fixed target energies[1,2] were observed in forward pion production by the E704 collaboration at Fermi Lab ($\sqrt{s} = 19.4\,\mathrm{GeV}$). Such large asymmetries were initially surprising due to the prediction of pQCD of the leading twist that these asymmetries should be small. The interest has recently grown with the discovery by PHENIX, STAR and BRAHMS collaborations that these asymmetries persist even to RHIC energies.[3] Transverse single-spin asymmetries (SSAs) A_N have the potential to be an important tool in understanding the quark spin distributions in a polarized proton. Precision measurement of SSAs in different regions of x_F and p_T with various particles and their QCD analysis may serve to quantify contributions from different mechanisms.

We measure the production of single muons using the PHENIX muon arms which cover the forward rapidity range of ($1.2 < |\eta| < 2.4$). The muon candidates are a mix of decay products of light charged mesons ($\pi^{\pm}, K^{\pm}$) and heavy quarks (c,b) which can be identified and separated by an experimental methods. In general, yields of ($\mu^{\pm}$) from ($\pi^{\pm}, K^{\pm}$) decay strongly depend on the collision Z vertex: the farther away the collision vertex from the absorber, the more likely ($\pi^{\pm}, K^{\pm}$) will decay. On the other hand, ($\mu^{\pm}$) from heavy flavor decay is independent of the collision vertex. Figure 1 shows the Z vertex dependance of muon yields with different origins.

Here, we report our inclusive analysis with single muons ($\mu^{\pm}$). The left-right single-spin asymmetry A_N can be extracted using

$$A_N = \frac{1}{P_b}\frac{\sigma^{\uparrow} - \sigma^{\downarrow}}{\sigma^{\uparrow} + \sigma^{\downarrow}} = \frac{1}{P_b}\frac{N^{\uparrow} - RN^{\downarrow}}{N^{\uparrow} + RN^{\downarrow}}\,, \qquad (1)$$

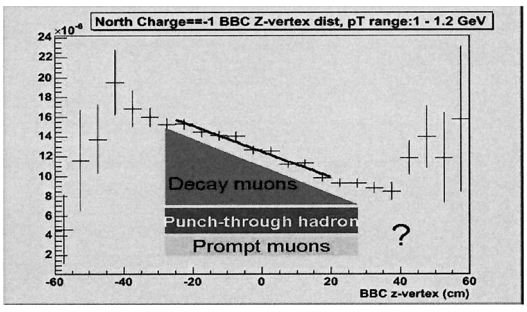

Fig. 1. Normalized muon event Z vertex.

where P_b is the beam polarization, $\sigma^{\uparrow}$ ($\sigma^{\downarrow}$) the production cross section when the proton in the bunch is polarized up (down), $N^{\uparrow}(N^{\downarrow})$ the experimental yield of muons from such collisions, and $R = L^{\uparrow}/L^{\downarrow}$ the relative integrated luminosity. In our analysis, we measure the asymmetry

$$A_N \approx \frac{1}{P_b}\frac{\sqrt{N_L^{\uparrow}N_R^{\downarrow}} - \sqrt{N_L^{\downarrow}N_R^{\uparrow}}}{\sqrt{N_L^{\uparrow}N_R^{\downarrow}} + \sqrt{N_L^{\downarrow}N_R^{\uparrow}}}\,, \qquad (2)$$

which is a good experimental approximation of measuring A_N defined in Eq. (1), where most of the detector-related acceptance and efficiency uncertainties are canceled out.[4] The expected statistical uncertainties for the single-spin asymmetries measured in run5 estimated from the collected data ($L = 0.16\,\mathrm{pb}^{-1}$, $P_b \sim 48\%$ average polarization), are shown in Fig. 2 for both positively (top) and negatively (bottom) charged muon candidates. Roughly speaking, half of the muon candidates are muons from light hadron ($\pi^{\pm}, K^{\pm}$) decays and the other half are punch-through light hadrons ($\pi^{\pm}, K^{\pm}$); the fraction of muons from heavy quark decays is very small in this inclusive low-p_T muon sample.

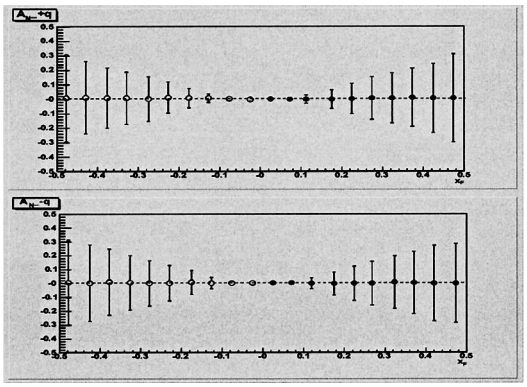

Fig. 2. Expected accuracy for A_N (the top is μ^+ and the bottom is μ^-).

*1 New Mexico State University, USA
*2 Los Alamos National Laboratory, USA

References

1) D. L. Adams et al.: Phys. Lett. B **264**, 462 (1991).
2) D. L. Adams et al.: Phys. Rev. D **53**, 4747 (1996).
3) S. S. Adler et al. The PHENIX Collaboration: Phys. Rev. Lett. **94**, 202001 (2005).
4) H. Spinka: ANL-HEP-TR99-133 (1999).

Double-spin asymmetry of $J/\psi \to \mu^+\mu^-$ in longitudinally polarized $p+p$ collisions at $\sqrt{s} = 200\,\mathrm{GeV}$

I. Younus,[*1] M. Liu,[*2] M. Brooks,[*2] and K. Boyle,[*3] for the PHENIX Collaboration

The heavy quark production in polarized $p+p$ collision at RHIC energy is dominated by gluon-gluon fusion, and thus provides direct access to the polarized gluon distribution in the proton. The double longitudinal spin asymmetry in heavy quarkonium production is sensitive to polarized gluon distribution in the nucleon:

$$A_{LL} = \frac{\sigma^{++} - \sigma^{+-}}{\sigma^{++} + \sigma^{+-}} \approx \frac{\Delta g(x_1)}{g(x_1)} \frac{\Delta g(x_2)}{g(x_2)} a_{LL}^{gg \to Q\bar{Q}}$$

where 'a_{LL}' is the partonic level asymmetry.

In this report, we present the results for double-longitudinal spin asymmetry in J/ψ production in polarized $p+p$ collisions at RHIC. The J/ψ has the largest production cross section among all heavy quarkonia. The PHENIX experiment at RHIC is capable of measuring J/ψ yields through $J/\psi \to \mu^+\mu^-$ channel at forward rapidities ($1.2 < |\eta| < 2.4$). Experimentally, A_{LL} is measured as:

$$A_{LL} = \frac{1}{P_B P_Y} \frac{N_{J/\psi}^{++} - R \cdot N_{J/\psi}^{+-}}{N_{J/\psi}^{++} + R \cdot N_{J/\psi}^{+-}},\ R = \frac{L^{++}}{L^{+-}}$$

where $N^{++}(N^{+-})$ is the number of J/ψ produced in the same (opposite) helicity state $p+p$ collisions, and P_B and P_Y are the polarization values of the colliding beams. R is the relative luminosity of different helicity configurations.[1)]

During the RHIC run in 2005, PHENIX accumulated $3.8 pb^{-1}$ of integrated luminosity with an average beam polarization of 47%. For this analysis, we used the local level-1 di-muon triggered data sample ($3.2 pb^{-1}$) obtained using the PHENIX muon spectrometer.[2)]

A single Gaussian fit to $\mu^+\mu^-$ invariant mass spectrum from the entire data set is shown in Fig. 1. An exponential background under the J/ψ mass peak is assumed in this fit. The total number of J/ψ in the selected sample is 7319 ± 102.0. For A_{LL} calculation, J/ψ yield was extracted for each RHIC store of the beam as the relative luminosity varied significantly in each store, but remained constant within a store. Most of the combinatoric background for $\mu^+\mu^-$ pairs in the J/ψ mass region was removed using like-sign muon pairs:

$$N_{J/\psi} = N(\mu^+\mu^-) - N(\mu^+\mu^+,\ \mu^-\mu^-).$$

The purity of the J/ψ sample after this subtraction is above 90%. A global collision vertex range and muon track quality cuts were applied for event selection. Asymmetry was calculated for each RHIC store for two p_T bins. The average asymmetry values over all stores for each p_T bin are:

$A_{LL}(< p_T >= 0.82) = +0.006 \pm 0.088$

$A_{LL}(< p_T >= 2.30) = -0.073 \pm 0.091.$

The background asymmetry was estimated using the $\mu^+\mu^-$ pairs within $2 < M_{mm} < 2.5\,\mathrm{GeV}$ from the invariant mass spectrum in Fig. 1, and $\mu^+\mu^+, \mu^-\mu^-$ pairs within $2.6 < M_{mm} < 3.6\,\mathrm{GeV}$. The average background contribution is estimated to be -0.0041 ± 0.018. Currently, the dominant systematic error comes from the extraction of J/ψ yield and asymmetry with different mass windows and is expected to improve significantly with high statistics data in the future.

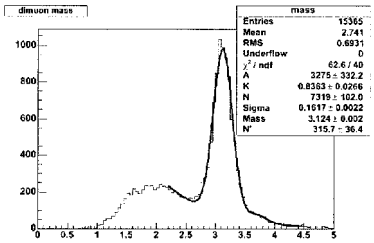

Fig. 1. Di-muon invariant mass distribution.

Figure 2 shows the final A_{LL} results for the two p_T bins along with the theoretical prediction[3,4)] from different J/ψ production models. The p_T averaged asymmetry is $-0.032 \pm 0.065(stat)$. In the future, the expected $320 pb^{-1}$ delivered luminosity with improved beam polarization of 70%, will improve the statistical figure of merit ($P^4 \times L$) of the double spin asymmetry by a factor of ~ 100.

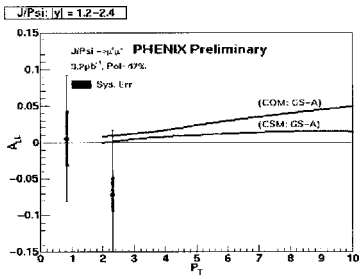

Fig. 2. PHENIX preliminary results for J/ψ asymmetry.

*1 University of New Mexico, USA
*2 Los Alamos National Laboratory, USA
*3 State University of New York, USA

References
1) K. Boyle et al.: RIKEN Accel. Prog. Rep. **39**, 197 (2006).
2) H. Akikawa et al.: Nucl. Instrum. Methods Phys. Res. A **499**, 537 (2003).
3) A. Tkabladze and O. Teryaev: Phys. Rev. D **56**, 7331 (1997).
4) M. Klasen et al.: hep-ph/0306080.

Spin transfer to inclusive $\overline{\Lambda}^0$ hyperons from longitudinally polarized protons at $\sqrt{S} = 200\,\mathrm{GeV}$

V. L. Rykov, K. Aoki,* H. Torii, and PHENIX Collaboration

Correlations between spins of initial and final state hadrons provide the valuable information on the both, polarized parton distributions of initial projectiles as well as the spin-dependent fragmentation functions of the produced jets into spin-nonzero hadrons. Since spin-transfer studies require knowledge of final state polarization, at high energies they are limited almost exclusively to final states with weakly decaying hyperons.[1] Spin-transfers from an initial polarization component S_i to a final polarization component S_f (Fig. 1) are defined in terms of spin-correlation parameters $D_{S_iS_f}$.

During RHIC runs 3–5 (2003-05) with longitudinally polarized protons, about (1.5–2)$\times 10^5$ of reconstructible $\Lambda \to p\pi^-$ and $\overline{\Lambda} \to \overline{p}\pi^+$ decays have been accumulated in the PHENIX Central Arm detectors.[2] Here, we present the analysis on the spin-transfer to $\overline{\Lambda}$-hyperons, using PHENIX run 3 (2003) data. The analyzed sample corresponds to the integrated luminosity of 206 nb^{-1} and average beam polarization 34%.

In run 3, the largest statistics of Λ and $\overline{\Lambda}$ decays have been accumulated in the EMCAL[a] triggered events with the nominal threshold of 1.4 GeV photon energy. This trigger is by a factor of ~ 4 more sensitive to $\overline{\Lambda}$- than to Λ-decays, because of antiproton "self-triggering" due to annihilations in the EMCAL. Such "self-triggering" also allows to select a truly inclusive $\overline{\Lambda}$ sample by requiring matching antiproton tracks and trigger clusters in the EMCAL. For the reasons above, we concentrated spin-transfer analysis of run 3 data on $\overline{\Lambda}$-hyperons only.

Candidates to $\overline{\Lambda}$ decays have been selected from identified $\overline{p}\pi^+$ pairs (Fig. 2) within the invariant mass window: $1.109 < M_{\overline{p}\pi^+} < 1.125\,\mathrm{GeV/c^2}$. Charged particle identification[2] was based on the reconstructed momenta and time-of-flight measurements with EMCAL. Pairs within the "side-band" mass window of 1.080–1.095 and 1.160–1.176 GeV/c^2 have been used for evaluating spin-asymmetry correction due to combinatorial background.

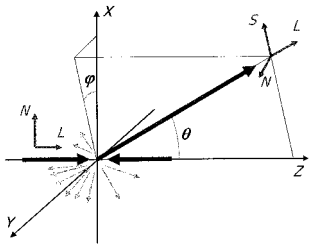

Fig. 1. Kinematics of inclusive production of polarized fermion. L is spin component along momentum; two other are perpendicular to momentum: S in production plane and N normal to production plane.

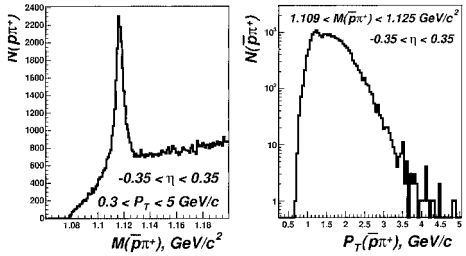

Fig. 2. Invariant mass spectrum for $\overline{p}\pi^+$ pairs (left frame) and P_T distribution of analyzed pairs within $\overline{\Lambda}$ mass window (right frame).

Spin-transfer parameters D_{LL} and D_{LS} have been reconstructed, using parity-violating $\overline{\Lambda}$ decay asymmetry for measuring its polarization. We also measured the double-spin asymmetry A_{LL} for inclusive $\overline{\Lambda}$, which characterizes the cross-section difference between collisions of protons of same and opposite helicities.

Statistical errors for spin-transfer parameters achieved with run 3 data are shown in Fig. 3 along with the error estimates for run 5. Run 3 analysis is essentially completed, and its results are expected to be made public soon. Run 5 analysis is currently at the preparation stage.

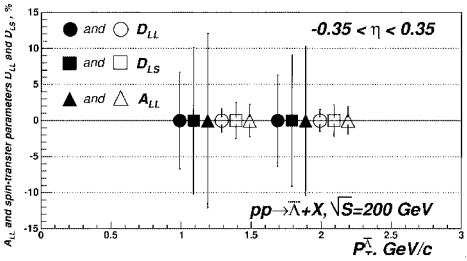

Fig. 3. Statistical errors for spin-transfer parameters and A_{LL} in run 3 (solid markers) and error estimates for run 5 (open markers). The errors are for two bins of P_T distribution in Fig. 2: $P_T < 1.5\,\mathrm{GeV/c}$ ($< P_T >= 1.24\,\mathrm{GeV/c}$) and $P_T > 1.5\,\mathrm{GeV/c}$ ($< P_T >= 1.94\,\mathrm{GeV/c}$). Points are shifted from each other for the better visibility.

* Kyoto University

a) PHENIX Electromagnetic Calorimeter.

References

1) A. Bravar et al.: Phys. Rev. Lett. **78**, 4003 (1997); M. R. Adams et al.: Eur. Phys. J. C **17**, 263 (2000); A. Airapetian et al.: Phys. Rev. D **64**, 112005 (2001).
2) K. Adcox et al.: Nucl. Instrum. Methods Phys. Res. A **499**, 469 (2003).

Measurement of the mid-rapidity helicity asymmetry of η mesons in pp collisions at $\sqrt{s} = 200\,\mathrm{GeV}$

F. Ellinghaus* and J. Seele* for the PHENIX Collaboration

The contribution of gluons to the nucleon's spin remains poorly constrained by existing data. Longitudinal double spin asymmetries, A_{LL}, measured for inclusive hadron production in polarized proton-proton collisions at high energies have been shown[1] to be sensitive to the gluon helicity distribution in the nucleon, Δg.

Polarized proton-proton collisions at the Relativistic Heavy Ion Collider (RHIC) allow for measurements of A_{LL}.[2] This study focuses on A_{LL} in η production ($\vec{p}+\vec{p} \rightarrow \eta + X$), where the η subsequently decays into two photons. The data was taken at the PHENIX experiment in 2005. The electromagnetic calorimeter is the primary detector used in this analysis, allowing for reconstruction of the position and energy of the photons. Using all possible photon pairs, the invariant mass is calculated and shown in Fig. 1. Besides the prominent π^0 peak between about 0.1 and 0.2 $\mathrm{GeV/c^2}$, the η peak (grey region) can also be clearly seen.

A longitudinal spin asymmetry can be written as

$$A_{LL} = \frac{\sigma^{++} - \sigma^{+-}}{\sigma^{++} + \sigma^{+-}} = \frac{\Delta\sigma}{\sigma},$$

where the cross section σ^{++} (σ^{+-}) describes the reaction where both protons have the same (opposite) helicity. The spin dependent term can be written as

$$\Delta\sigma \propto \sum_{abc} \Delta f_a(x_1) \otimes \Delta f_b(x_2) \otimes \Delta\hat{\sigma}^{ab\rightarrow cX'}(\hat{s}) \otimes D_c^{\eta}$$

where Δf is a spin dependent parton distribution function (this includes both quarks and gluons) which is the quantity of interest, $\Delta\hat{\sigma}$ is a hard scattering cross section and is calculable in perturbative QCD, and D_c^{η} is a fragmentation function which can be determined from existing data, e.g., from BELLE. By measuring this asymmetry and knowing the fragmentation functions and hard cross sections, one can obtain the spin dependent parton distribution function for the gluon, i.e. the gluon helicity distribution Δg.

Experimentally, the double helicity asymmetry is defined as

$$A_{LL} = \frac{1}{|P_B||P_Y|}\frac{N_{++} - RN_{+-}}{N_{++} + RN_{+-}}, \quad \text{with} \quad R \equiv \frac{L_{++}}{L_{+-}},$$

where N_{++} (N_{+-}) and L_{++} (L_{+-}) are the experimental yield and the luminosity for the case where the beams have the same (opposite) helicitiy. The achieved uncertainty on the relative luminosity R is on the order of 10^{-4}. The polarizations of the two colliding beams at RHIC are denoted by P_B and P_Y. The preliminary average polarization value is 47% with an uncertainty of 20% per beam.

Calculating the asymmetry in the grey region, consisting of signal (namely the true η's) and background, and in regions with only background (e.g. the hatched regions in Fig. 1), the η asymmetry can be extracted by

$$A_{LL}^{\eta} = \frac{A_{LL}^{\eta+BG} - rA_{LL}^{BG}}{1-r}, \quad \text{with} \quad r \equiv \frac{N^{BG}}{N^{\eta} + N^{BG}}.$$

Based on the data taken in 2005 by the PHENIX collaboration, the expected statistical uncertainty for the longitudinal double spin asymmetry of the η meson as a function of p_T is shown in Fig. 2.

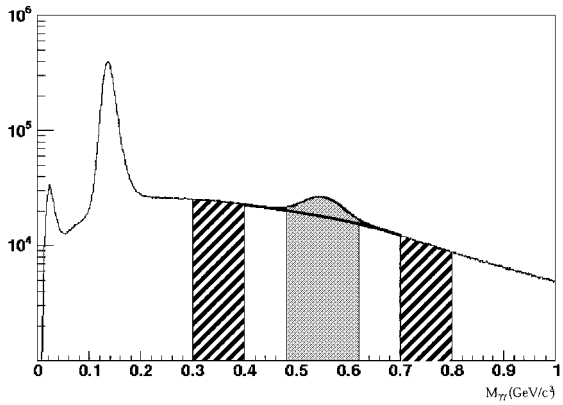

Fig. 1. Two photon invariant mass for $p_T > 2\,\mathrm{GeV/c}$.

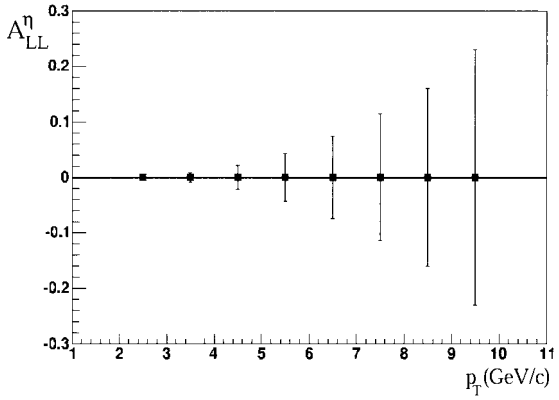

Fig. 2. Expected accuracy for A_{LL}^{η} as a function of p_T.

* University of Colorado, USA

References

1) G. Bunce et al.: Annu. Rev. Nucl. Part. Sci. **50**, 525 (2000).
2) PHENIX Collaboration, S. Adler et al.: Phys. Rev. Lett. **93**, 202002 (2004).

Charged pion longitudinal double-spin asymmetry $A_{LL}^{\pi^{\pm}}$

K. N. Barish,* W. S. Emam,* and A. Morrealé*

Charged hadron and pion production in longitudinally polarized proton proton collisions can be used as a probe of the gluon contribution to the proton spin, ΔG, and promise to be the first measurement sensitive to the sign of ΔG.[1] Pions are produced through a combination of gluon-gluon, quark-gluon, and quark-quark subprocesses, which change in relative strength as a function of transverse momentum, e.g., as shown in Fig. 1 for neutral pions.

As the quark-gluon contribution becomes sizable, A_{LL} can become negative if ΔG is negative (see Fig. 2). π^+, π^-, and π^0 have different quark compositions; thus, A_{LL} is also expected to vary. The measurement of charged and neutral pions will be sensitive to both ΔG(x) and the sign of ΔG.

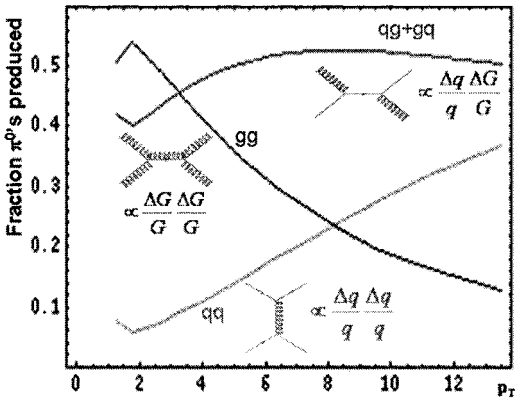

Fig. 1. Relative contributions of gg, qg, and qq for π^0 production.

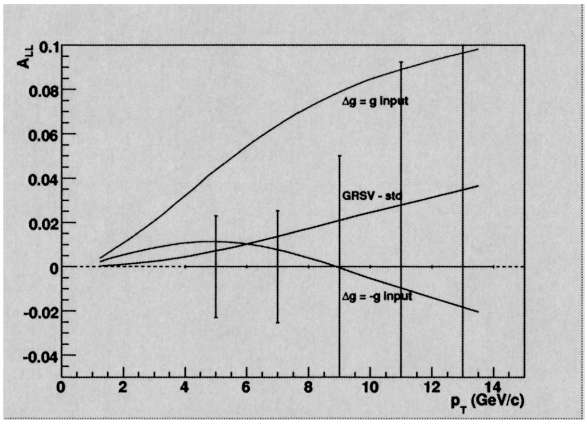

Fig. 2. $A_{LL}^{\pi^+}$ projections for different parameterizations of ΔG for the 2005 Run ($L = 3.8\,\mathrm{pb}^{-1}$ and $P = 47\%$).

In 2005, PHENIX had a significant polarized proton run, recording $3.8\,\mathrm{pb}^{-1}$ with $\approx$47% polarization. This will allow us to measure $A_{LL}^{\pi^{\pm}}$ up to intermediate p_T, where A_{LL} can start to turn over if ΔG is negative. In addition to providing an important complimentary measurement to the π^0 measurement, we are developing the analysis techniques for future high luminosity and polarization runs.

High-p_T pions can be triggered in PHENIX with the use of the EMCal-RICH trigger (ERT), which can select events with correlated RHIC and EMCal hits. Charged pions above 5.5 GeV fire the RICH detector and deposit energy in the EMCal. To have a reasonable efficiency, a low threshold is required for deposted energy in the EMCal. The expected loss of efficiency was taken into account for the projected sensitivities shown in Fig. 2. Photon-triggered events, which require only an EMCal energy deposit but with a higher threshold, and minimum-bias events are also used to enhance the data-set and to study charged hadrons at a lower transverse momentum. We studied the EMCal and RICH responses for the analysis.

In addition to trigger considerations, pion identification and background issues have been investigated. Backgrounds come from e^- and e^+ from γ-conversion, and from weak decays, mostly from $K^{\pm}$ (see Fig. 3). With appropriate cuts, the background can be minimized.

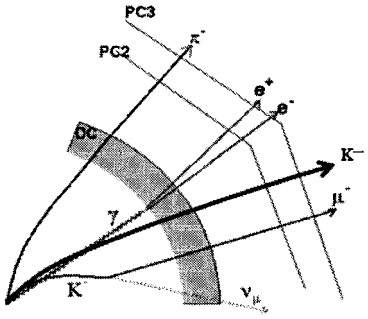

Fig. 3. Charged pion background sources.

Reference

1) B. Jager, A. Schafer, M. Stratmann, and W. Vogelsang: Phys. Rev. D **67** 054005 (2003).

* University of California, Riverside, USA

k_T asymmetry in longitudinally polarized pp collisions at PHENIX

D. E. Fields, J. Rak,* I. Younus,* and R. Hobbs*

Researchers in the PHENIX experiment at RHIC have developed a method for measuring the average net pair transverse momentum of hard scattered jets at central rapidity.[1] This method utilizes the azimuthal correlation between a leading high p_T π^0 and another charged hadron. The widths of the resulting near- and far-side peaks can then be related to the fragmentation transverse momentum, j_T (the transverse momentum of the fragmented hadron relative to the hard-scattered parton) and the net pair transverse momentum, k_T in a straightforward manner. The net pair transverse momentum can be produced from parton intrinsic transverse momentum inside the proton, from soft gluon emmission, or from next-to-leading order processes of the perturbative QCD. In addition, one can consider the possibility that spin-correlated transverse momentum (orbital angular momentum) may contribute to k_T, as discussed in Ref. 2. Coherent spin-dependent parton transverse momentum adds to k_T an amount dependent upon the helicity combination of the colliding protons, and upon the impact parameter of the collision. However, an integration over impact parameter will likely leave a residual effect that is dependent only on the helicity combination, a signal that could be examined in the present data from past RHIC runs.

We have examined this k_T asymmetry in the 2003 RHIC run. Figure 1 shows the azimuthal angle distribution between triggered π^0 in the transverse momentum range of ($3.0\,GeV/c < p_{Tt} < 7.0\,GeV/c$) and an associated charged hadron in the ($0.5\,GeV/c < p_{Ta} < 2.5\,GeV/c$) range for opposite (a) and same (b) helicities for the colliding protons. From these correlation functions, the widths of the near-side peak (around $\Delta\phi = 0$) and the far-side peak (around $\Delta\phi = \pi$) are exctracted. From these, the corresponding values of fragmentation transverse momentum j_T, and root-mean-squared (RMS) transverse momentum fraction weighted by a momentum fraction (z) of the fragmented hadron to the scattered parton, $(zk_T)_{RMS}$, are determined.

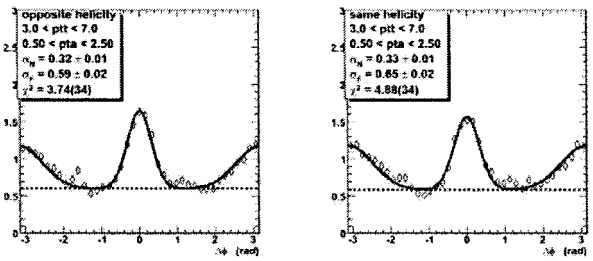

(a) (b)

Fig. 1. Azimuthal correlation functions for opposite (a) and same (b) helicities in the ($3.0\,GeV/c < p_{Tt} < 7.0\,GeV/c$) range of triggered π^0 transverse momentum.

The difference in the extracted $(zk_T)_{RMS}$ for the same helicity minus the opposite helicity events is shown in Fig. 2. The 2003 RHIC run data set does not show a significant effect. A bunch shuffling technique[3] was used to test the errors on the points by randomly assigning helicity combinations to each RHIC bunch crossing and then resorting. The distribution of differences in the extracted $(zk_T)_{RMS}$ for many sets of randomized "shuffles" was centered on zero and had widths (shown as dotted lines in Fig. 2) which were consistent with the statistical uncertainties (solid lines in Fig. 2).

The PHENIX data set from polarized proton running during the 2005 RHIC run has approximately ten times higher luminosity, and has almost twice the polarization as that of the 2003 RHIC run. Analysis of this data set is on-going and should be completed soon.

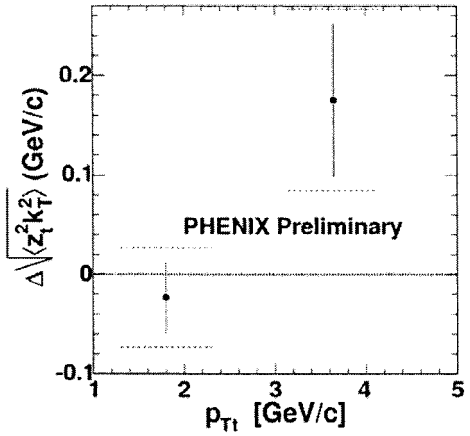

Fig. 2. Difference in $(zk_T)_{RMS}$ for the same helicity minus opposite helicity events as a function of triggered π^0 transverse momentum p_{Tt}.

References

1) J. Rak: J. Phys. G **30**, S1309 (2004).
2) T.-C. Meng et al.: Phys. Rev. D **40**, 769 (1989).
3) S. S. Adler et al.: Phys. Rev. Lett. **93**, 202002 (2004).

* University of New Mexico, USA

Double helicity asymmetry in multiparticle production for polarized proton-proton collisions at PHENIX

K. Nakano*, Y. Akiba, and Y. Goto

One of the goals of the PHENIX experiment is to obtain a polarized gluon distribution function in a proton, $\Delta g(x)$. $\Delta g(x)$ is evaluated by measuring the double helicity asymmetry A_{LL} of reactions in longitudinally-polarized proton-proton collisions, for example, jet production, π^0 production and direct photon production. A jet is measured as a cluster of multiple particles. The multiparticle measurement gives higher statistics than single particle measurements such as π^0. The A_{LL} is defined as

$$A_{LL} = \frac{1}{|P_B||P_Y|}\frac{N_{++} - RN_{+-}}{N_{++} + RN_{+-}}. \quad (1)$$

Here, N_{++} and N_{+-} are the number of measured multiparticle clusters with the same and opposite beam helicities, respectively; $R \equiv L_{++}/L_{+-}$ is the relative luminosity; and P_B and P_Y are the beam polarizations.

We used proton-proton collision data at $\sqrt{s} = 200\,\mathrm{GeV}$ in 2003 with an average beam polarization of ∼26%. The integrated luminosity of the analyzed data is $0.25\,\mathrm{pb}^{-1}$. The PHENIX Central Arm detectors were used in the analysis. The two arms are positioned almost back to back, and each arm covers the pseudorapidity region $|\eta| < 0.35$ and the 90-degree azimuthal angle. Photons were measured with electromagnetic calorimeters, and charged particles were measured with drift chambers and pad chambers. We required that $p_T > 0.4\,\mathrm{GeV}/c$ for photons and $0.4 < p_T < 4\,\mathrm{GeV}/c$ for charged tracks. For each event a high-p_T ($> 2\,\mathrm{GeV}/c$) photon was required to exist.

Particles that satisfied the experimental selections were clustered by a cone method. Starting from each particle in an event as a seed, an interative procedure was used to define a cone around a cluster of particles. The cone radius R ($= \sqrt{(\Delta\phi)^2 + (\Delta\eta)^2}$) was set to 0.3. The transverse momentum of the cone, p_T^{cone}, was defined as the vector sum of the transverse momenta of the particles in the cone.

$$p_T^{\mathrm{cone}} \equiv \left| \sum_{i \in \mathrm{cone}} \vec{p}_{Ti} \right| \quad (2)$$

The cone that gives the largest p_T^{cone} in an event was used as a cone in the event.

The relationship between p_T^{cone} and p_T^{jet} was evaluated with PYTHIA and GEANT simulations.[1] To study the influence of the "underlying event",[2] we used PYTHIA version 6.220 with both the default setting and the "Rick Field MPI tune A" setting.[3] By comparing the simulated events with the real events, we confirmed that the simulation reproduced the event shape reasonably well.[1] The requirement of a high-p_T photon causes a bias on jet production subprocesses (quark-quark, quark-gluon and gluon-gluon reactions). This effect was estimated using PYTHIA. In general, the gluon-gluon reaction is suppressed particularly at low p_T.

Figure 1 shows the A_{LL} of the multiparticle production as a function of p_T^{cone}. Theory predictions with two assumptions on gluon polarization, GRSV-std and $\Delta g = g$ input,[4] are also shown. The dot curve in each theory prediction is the original, which corresponds to the case of $p_T^{\mathrm{cone}} = p_T^{\mathrm{jet}}$. Other curves in each theory prediction have been scaled by the ratio $p_T^{\mathrm{cone}}/p_T^{\mathrm{jet}}$ evaluated with the simulations. The ratio applied to the thin solid/dash curves was estimated using the PYTHIA default setting, and the ratio applied to the thick solid/dash curves was estimated using the PYTHIA MPI setting. In addition, the thin/thick solid curves have been corrected for the trigger bias effect. The scale uncertainty in p_T^{cone} has hardly any effect on A_{LL} because of its gradual slope, and it will be reduced with further studies. The statistical error will be also reduced by a factor of ∼ 20 in Run 2005 data, and we will be able to distinguish the two models.

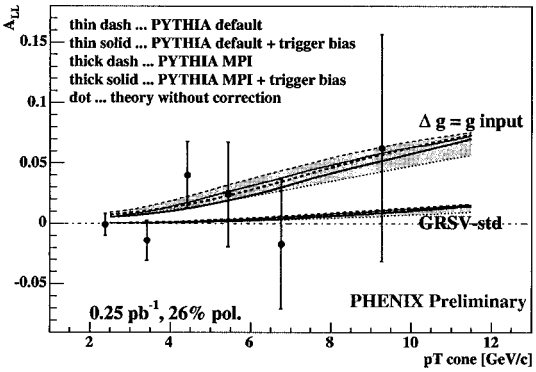

Fig. 1. Double helicity asymmetry (A_{LL}) of multiparticle production as function of p_T^{cone}.

* Department of Physics, Tokyo Institute of Technology

References

1) K. Nakano: Master Thesis, Tokyo Institute of Technology (2004).
2) T. Affolder et al.: Phys. Rev. D **65**, 092002 (2002).
3) R. Field, CDF Collaboration: Acta Phys. Pol. B **36**, 167 (2005).
4) M. Gluck, E. Reya, M. Stratmann, and W. Vogelsang: Phys. Rev. D **63**, 094005 (2001).

Transverse single spin asymmetries at mid-rapidity at $\sqrt{s} = 200\,\mathrm{GeV}$ in p+p collisions

M. Chiu,[*1] K. O. Eyser,[*2] and R. Seidl[*1]

Large single spin asymmetries have been observed in different high energy p+p collisions in the past,[1,2] although they were expected to vanish in perturbative QCD calculations at large transverse momenta (p_T). The spin structure of the nucleon includes a term called transversity distribution δq, which is different from the longitudinal quark distribution Δq because relativistic boosts and rotations do not commute. Transversity therefore probes the relativistic nature of the nucleon and can be determined from transversely polarized scattering processes

$$A_{TT} \propto (\delta q)^2, \qquad A_N \propto \delta q. \tag{1}$$

The analyzing power A_N poses a direct measure of transversity in combination with another chiral odd function. Proposed models include spin dependent fragmentation functions (Collins effect),[3] asymmetries in the intrinsic transverse momentum distributions of partons (Sivers effect),[4] and quark gluon field interference in higher twist calculations.[5] The last one might have a major impact in the RHIC energy regime, especially at lower p_T.

The PHENIX experiment has measured the analyzing power of charged hadrons and neutral pions in the first polarized p+p run and results have been published.[6] Within the polarized run in 2005, a short period was devoted to transverse polarization to estimate A_{TT} as a systematic uncertainty in A_{LL}. The integrated luminosity collected in a significantly shorter period is comparable to the first measurement ($0.15\,\mathrm{pb}^{-1}$) with roughly three times the beam polarization.

Single spin asymmetries in the scattering frame lead to an azimuthal cosine modulation of the differential cross section in the laboratory frame. The yields N_l and N_r in the detector arms (l left and r right)

$$N_l \propto L \cdot \Delta\Omega_l \cdot E_l \cdot (1 + A_N \cdot P \cdot c_l) \tag{2}$$

$$N_r \propto L \cdot \Delta\Omega_l \cdot E_r \cdot (1 - A_N \cdot P \cdot c_r) \tag{3}$$

are dependent on the luminosity L, the detector acceptances $\Delta\Omega_l$ and $\Delta\Omega_r$ and their corresponding efficiencies E_l and E_r, and the modulation arising from the analyzing power A_N and the beam polarization P. The mean values c_l and c_r of the cosine modulation in the respective detector arm is also charge (q) and p_T dependent. The symmetry of the detector with respect to the cosine modulation causes $c_l(q, p_T) \neq c_r(q, p_T)$.

Event quality is based on certain cuts including a global vertex cut and track quality. Conversion electrons and decay particles with short lifetimes are removed by ring imaging Cherenkov information and track matching in the outer detector layers.

In order to remove efficiency and relative luminosity from the asymmetries, an extended square root formula has been calculated $\epsilon = A_N \cdot P$:

$$\epsilon = \frac{N_+(c_l + c_r) - \sqrt{N_+^2(c_l + c_r)^2 - 4c_l c_r N_-^2}}{2c_l c_r N_-}. \tag{4}$$

Here, $N_+ = (N_\uparrow^2 + N_\downarrow^2)$ and $N_- = (N_\uparrow^2 - N_\downarrow^2)$, where $N_\uparrow^2 = N_{\uparrow,l} \cdot N_{\downarrow,r}$, and $N_\downarrow^2$, respectively. The arrows indicate the polarization direction.

Results have been cross checked with simple asymmetries, i. e. asymmetries between detector arms with the same polarization direction and asymmetries between opposite polarization directions in a single detector arm. The simple asymmetries have therefore been cleaned of remaining efficiencies and luminosities.

Figure 1 shows the results of the analyzing power for charged hadrons and a comparison of the published results with the new data set. New mean values have been calculated and are displayed p_T-shifted. For charged hadrons, no evidence of finite single spin asymmetries can be observed in the considered p_T-range.

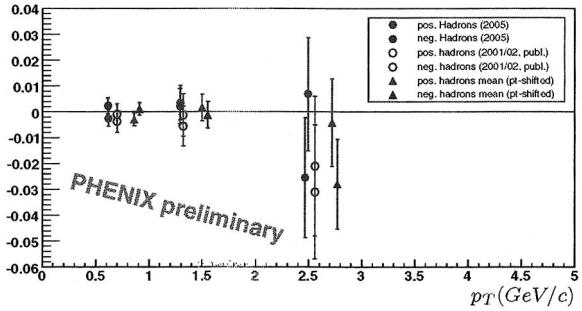

Fig. 1. Results and statistical errors of the analyzing power A_N for charged hadrons from the year 2005 run compared to the already published data from 2001/02.[6] Additional scaling uncertainties of 20% to 30% have to be included from the beam polarization.

*1 University of Illinois, USA
*2 University of California, USA

References
1) D.L. Adams et al.: Phys. Lett. B **264**, 462 (1991).
2) J. Adams et al.: Phys. Rev. Lett. **92**, 171801 (2004).
3) J. Collins: Nucl. Phys. B **396**, 161 (1993).
4) D. Sivers: Phys. Rev. D **43**, 261 (1991).
5) Y. Koike: hep-ph/0210396.
6) S. Adler et al.: Phys. Rev. Lett. **95**, 202001 (2005).

Spin-dependent fragmentation function measurements at Belle experiment

R. Seidl,[*1] D. Gabbert,[*1] M. Grosse-Perdekamp,[*1] K. Hasuko, and A. Ogawa[*2]

The Belle experiment[1] at the asymmetric e^+e^- collider KEKB[2] at Tsukuba, Japan, is mainly dedicated for studying CP violation in B meson decays. It is tuned to the $\Upsilon(4S)$ resonance at 10.58 GeV, whereas background studies are performed at 10.52 GeV. These continuum events are studied to measure spin-dependent and precise spin-independent fragmentation functions (FFs). Here, the first results on the fragmentation of polarized light quarks into pions obtained on a data set of 29.1 fb^{-1} are presented.

The Collins effect[3] occurs in the fragmentation of a transversely polarized quark with polarization $\mathbf{S_q}$ transverse to its 3-momentum $\mathbf{k}$ into an unpolarized hadron of transverse momentum $\mathbf{P}_{h\perp}$ with respect to the original quark direction. The number density for finding an unpolarized hadron h produced from a transversely polarized quark q contains a spin-dependent term:

$$H_1^{\perp q}(z, P_{h\perp}^2)(\hat{\mathbf{k}} \times \mathbf{P}_{h\perp}) \cdot \mathbf{S}_q / z M_h, \qquad (1)$$

where $z \overset{CMS}{=} \frac{2E_h}{Q}$ is the fractional energy the hadron carries in the center of mass system (CMS). The Collins function $H_1^{\perp q}(z, P_{h\perp}^2)$ causes a $\sin(\phi)$ modulation in the azimuthal distribution of the hadron yields around the original quark momentum axis. ϕ is the azimuthal angle between the transverse momentum of the hadron and the plane defined by the quark spin and its momentum. In e^+e^- hadron production, the Collins effect can be observed by correlating the fragmentations of quark and anti-quark in opposing hemispheres. The combination of two hadrons from different hemispheres in two-jetlike events, with azimuthal angles ϕ_1 and ϕ_2, results in a $\cos(\phi_1 + \phi_2)$ modulation of the observed di-hadron yield. In the CMS, these azimuthal angles are defined between the transverse component of the hadron momenta with regard to the jet axis $\hat{n}$ and the plane spanned by the lepton momenta and $\hat{n}$. Following Ref. 4 one either computes the azimuthal angle of each pion relative to the jet axis which results in a $\cos(\phi_1 + \phi_2)$ modulation or one calculates the azimuthal angle (ϕ_0) relative to the axis defined by the 2nd pion which results in a $\cos(2\phi_0)$ modulation. We measure the normalized yields $N(2\phi)/N_0$, where $N(2\phi)$ denotes the number of hadron pairs in the bins of either $2\phi_0$ or $\phi_1 + \phi_2$ and N_0 is the average number of hadron pairs in the whole angle interval. The main background, producing similar azimuthal asymmetries as the Collins effect, is the radiation of soft gluons. This gluonic contribution is proportional to the unpolarized FF and is independent of the charge of the hadrons. Consequently, taking the ratio of the normalized distributions for unlike-sign over like-sign pairs the gluonic distributions drop out in leading order:

$$R := \frac{N(2\phi_0)}{N_0}\Big|_{\text{unlikesign}} \Big/ \frac{N(2\phi_0)}{N_0}\Big|_{\text{likesign}} \quad . \qquad (2)$$

These double ratios are then fit by the sum of a constant term and a $\cos(2\phi_0)$ or $\cos(\phi_1 + \phi_2)$ modulation. The reconstruction of azimuthal asymmetries was tested by a Monte Carlo simulation. The preliminary results of the cosine fits to the double ratios are shown in Fig. 1 for charged pion pairs, where the combined z-bins are obtained by adding the symmetric bins of the 4×4 $z \in [0.2, 0.3, 0.5, 0.7, 1.0]$ bins. A clear nonzero asymmetry is visible. Additionally, the data shows a rising behavior with rising fractional energy z.

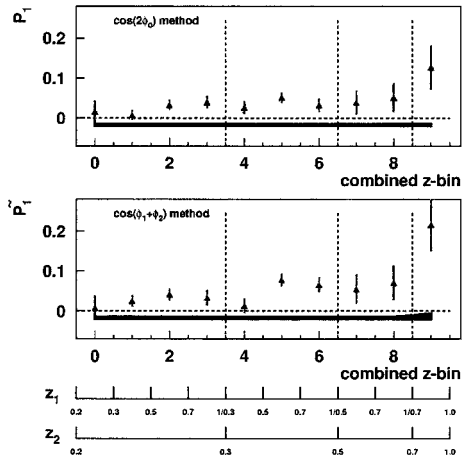

Fig. 1. Double ratio results for $\cos(2\phi_0)$ and $\cos(\phi_1 + \phi_2)$ methods.

References

1) A. Abashian et al.: Nucl. Instrum. Methods Phys. Res. A **479**, 117 (2002).
2) S. Kurokawa and E. Kikutani: Nucl. Instrum. Methods Phys. Res. A **499**, 1 (2003).
3) J. C. Collins: Nucl. Phys. B **396**, 161 (1993).
4) D. Boer, R. Jakob, and P. J. Mulders: Phys. Lett. B **424**, 143 (1998).

*1 University of Illinois, USA
*2 Brookhaven National Laboratory, USA

Polarization measurements of 100 GeV proton beams at RHIC by elastic proton-proton and proton-carbon scattering

I. Nakagawa, I. Alekseev,[*1] A. Bravar,[*2] G. Bunce,[*2] S. Dhawan,[*3] R. Gill,[*2] H. Huang,[*2] W. Haeberli,[*4] G. Igo,[*5] O. Jinnouchi, V. P. Kanavets,[*1] A. Khodinov,[*6] K. Kurita,[*7] Z. Li,[*2] Y. Makdisi,[*2] A. Nass,[*2] W. Lozowski,[*8] W. W. Mackay,[*2] H. Okada,[*9] S. Rescia,[*2] T. Roser,[*2] N. Saito,[*9] H. Spinka,[*10] D. N. Svirida,[*1] D. Underwood,[*10] C. Whitten,[*5] T. Wise,[*4] J. Wood,[*5] and A. Zelenski[*2]

The two types of polarimeter have been developed to measure polarizations of proton beams at relativistic heavy-ion collider (RHIC). A pC polarimeter[1)] provides a relative polarization by measuring asymmetries in left-right yields $(N_{\rm L}, N_{\rm R})$ of recoil carbon events through elastic proton-carbon reaction. The absolute beam polarization $P_{\rm beam}$ is given by normalizing the measured asymmetries by the analyzing power for the elastic pC process $A_{\rm N}^{pC}(t)$

$$P_{\rm beam} = \frac{1}{A_{\rm N}^{pC}(t)} \frac{N_{\rm L} - N_{\rm R}}{N_{\rm L} + N_{\rm R}}, \tag{1}$$

where t is 4-momentum transfer. The silicon strip detectors were implemented around 90° to select the elastic process to be very peripheral ($0.005 < |t| < 0.035$ $(\mathrm{GeV/c})^2$). This is because the t dependent analyzing power is expected to be maximum due to the interference between the electromagnetic and the nuclear strong force amplitudes. This kinematic region is known as Coulomb Nuclear Interference (CNI) region. However, because of the poorly known hadronic spin-flip mechanism at the energy as high as 100 GeV,[2)] the A_N^{pC} is not exactly predictable. Thus the relative A_N^{pC} is experimentally determined from the measured t dependence of the asymmetries and its absolute calibration is obtained from a polarized hydrogen gas jet polarimeter[3)] data which was operated in parallel with the pC polarimeter. Since the target polarization $P_{\rm target}$ is accurately monitored by a Breit-Rabi polarimeter, it can be translated into the absolute beam polarization using a following ratio:

$$\frac{P_{\rm target}}{P_{\rm beam}} = \frac{\epsilon_{\rm target}}{\epsilon_{\rm beam}} \tag{2}$$

where $\epsilon_{\rm target}, \epsilon_{\rm beam}$ are left-right asymmetries $(N_{\rm L} - N_{\rm R})/(N_{\rm L} + N_{\rm R})$ observed when either the target or the beam is polarized, respectively. The A_N^{pC} employed for Run5 online polarization measurements (see Fig. 1) was calibrated by the preliminary analysis result of the Run4 hydrogen polarimeter data with 8.5% uncertainty. This uncertainty is currently dominated by the statistics and it will be improved cumulatively as increasing data in Run5 and future runs. During Run5, it was attempted for the first time to perform measurements on both blue and yellow beams simultaneously/sequentially and as a consequence the accumulated statistics amounted about factor of 4 of the Run4 data. On the other hand, the signal was somehow suffered from more backgrounds and S/N ratio was deteriorated by factor of 2. The cause of this is under investigation.

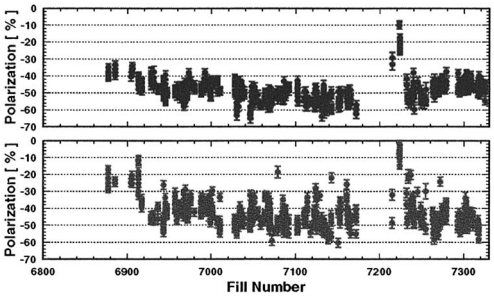

Fig. 1. Results of online (PHENIX physics store) polarization measurements plotted as a function of the fill number for the blue (top) and the yellow (bottom) beams, respectively.

The uncertainty of each pC polarization measurement was estimated to be 12 to 19% as a result of Run3 and Run4 analyses. The RHIC-spin program requires to measure the beam polarization within 5% accuracy. In order to achieve this goal, continuous efforts to improve the polarization measurements have been spent also for Run5. One of the major modifications is in the strip detector of the pC polarimeter. A beam induced pickup noise was significantly suppressed by improving the grounding design of silicon strips. The signal baseline so stabilized is then expected to reduce the uncertainty introduced in the ADC to energy conversion which was one of the largest error sources of Run3 and Run4 data.

*1 Institute for Theoretical and Experimental Physics, Russia
*2 Brookhaven National Laboratory, USA
*3 Yale University, USA
*4 University of Wisconsin, USA
*5 University of California, Los Angeles, USA
*6 Stony Brook University, USA
*7 Rikkyo University
*8 Indiana University Cyclotron Facility, USA
*9 Kyoto University
*10 Argonne National Laboratory, USA

References

1) O. Jinnouchi et al.: RIKEN Accel. Prog. Rep. **38**, 226 (2005).
2) B. Z. Kopeliovich and T. L. Trueman: Phys. Rev. D **64**, 034004 (2001).
3) H. Okada et al.: RIKEN Accel. Prog. Rep. **38**, 224 (2005).

Mid-rapidity neutral pion production in proton-proton collisions at $\sqrt{s} = 200\,\mathrm{GeV}$

A. Bazilevsky,[*1] A. Deshpande,[*2] Y. Fukao,[*3] and I. Younus[*4]

Particle production at large transverse momenta, p_T, in hadronic reactions provides an important testing ground for perturbative Quantum Chromodynamics (pQCD). Successful description of measured particle p_T spectra with pQCD is necessary for interpretation of spin asymmetries in terms of polarized gluon and polarized quark distributions in the nucleon.[1)] It also provides a reference needed to quantify nuclear effects in hadron production in heavy ion collisions.[2)]

First PHENIX results on inclusive π^0 production from proton-proton collisions at $\sqrt{s} = 200\,\mathrm{GeV}$ in the 1–13 GeV/c π^0 p_T range from Year-2002 RHIC run (Run2) has been published.[3)] The analyzed data corresponded to $\sim 40\,\mathrm{nb}^{-1}$ integrated luminosity. In this paper we present an update of PHENIX π^0 cross section measurements based on $\sim 2\,\mathrm{pb}^{-1}$ data accumulated by PHENIX during the Year-2005 RHIC run (Run5). It enabled to extend the p_T range and to significantly decrease the statistical uncertainties of the measurements.

Analysis method for π^0 cross section measurement is described in details in ref.[3)] $\pi^0 \to \gamma\gamma$ decays were detected using the electromagnetic calorimeter (EMCal).[4)] EMCal locates at a radial distance of $\sim 5\,\mathrm{m}$ from the beam line. Each of the towers in the calorimeter subtends $\Delta\phi \times \Delta\eta \sim 0.01 \times 0.01$, thus ensuring that the two photons from a decayed π^0 were clearly resolved up to a p_T of $12\,\mathrm{GeV}/c$. At higher p_T the measured π^0 yields should be corrected for two photon merging probability, which was carefully studied with EMCal Monte Carlo simulation and cross checked vs Test Beam data results. The raw π^0 yields were also corrected for the p_T smearing arising from the EMCal resolutions and the steeply falling spectrum; and for the losses due to the disabled towers and the incomplete azimuthal coverage.

Low p_T part of π^0 spectrum was obtained from "minimum bias" (MB) data sample triggered by beam-beam counters (BBC).[5)] BBCs locate along the beam line at ± 1.44 m from the nominal interaction point and subtended the pseudorapidity range $\pm(3.0$–$3.9)$ with full azimuthal coverage. The BBC trigger cross section in Run5 was traced from Run2 and was found to be $22.9 \pm 2.2\,\mathrm{mb}$. Higher p_T π^0 measurements were done using EMCal based high p_T photon trigger[3)] in coincidence with MB trigger. Its efficiency reached a plateau of $\sim 90\%$ at π^0 p_T of $\sim 4\,\mathrm{GeV}/c$. Since only a fraction of inelastic proton-proton collisions produce particles which enter BBCs, the MB trigger condition biases the recorded data sample, so only a fraction of the inclusive π^0 yield was detected. This fraction was determined with another photon trigger, which was formed without MB trigger requirements. This fraction was found to be ~ 0.78, independent of π^0 p_T.

Figure 1 shows the π^0 cross section results in the p_T range from 1 to 20 GeV/c. NLO pQCD calculations[6,7)] are consistent with the data over the full range of p_T.

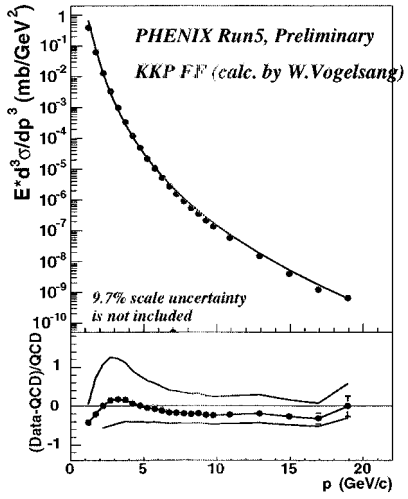

Fig. 1. Upper: The invariant differential cross section for inclusive π^0 production (points) and the results from NLO pQCD calculations[6)] with equal renormalization and factorization scales of p_T using the "Kniehl-Kramer-Pötter" sets of fragmentation functions.[7)] Bottom: The relative difference between the data and the theory with scales of $p_T/2$ (lower curve), p_T, and $2p_T$ (upper curve). In all figures, the normalization error of 9.7% is not shown.

*1 Brookhaven National Laboratory, USA
*2 Stony Brook University, USA
*3 Kyoto University
*4 University of New Mexico, USA

References

1) S. S. Adler et al.: Phys. Rev. Lett. **93**, 202002 (2004).
2) S. S. Adler et al.: Phys. Rev. Lett. **91**, 072301 (2003).
3) S. S. Adler et al.: Phys. Rev. Lett. **91**, 241803 (2003).
4) L. Aphecetche et al.: Nucl. Instrum. Methods Phys. Res. A **499**, 521 (2003).
5) M. Allen et al.: Nucl. Instrum. Methods Phys. Res. A **499**, 549 (2003).
6) F. Aversa et al.: Nucl. Phys. B **327**, 105 (1989); B. Jäger et al.: Phys. Rev. D **67**, 054005 (2003); D. de Florian: Phys. Rev. D **67**, 054004 (2003).
7) B. A. Kniehl et al.: Nucl. Phys. B **597**, 337 (2001).

Selection criteria of dimuon decay from J/ψ in $\sqrt{s} = 200\,\mathrm{GeV}$ proton-proton collisions

N. Kamihara, for the PHENIX Collatoration

Measuring the J/ψ differential cross sections in p+p as a function of the transverse momentum and a function of the rapidity can be a good test that aids in the understanding of the J/ψ mechanism.

There are two muon spectrometers (Muon Arm) in the PHENIX. A Muon Arm consists of a magnet, a muon tracker (MuTr) and a muon identifier (MuID).[1] A MuID is divided into four quadrants in the azimuthal direction. Each quadrant is used as a trigger counter for muons.[2]

The yield of J/ψ is extracted from dimuon mass spectra. The mass spectra are obtained from a triggered dataset. The trigger requires two muon-associated tracks in different quadrants of the MuID.

The event selection criteria are categorized by three steps. The first step is confirming that the event satisfies the trigger requirement (collision vertex position and the muon trigger). The second step is selecting good muon tracks (vertex-matching cuts, the muon reconstruction, and requirement of a hit in the last muon gap). The third step is counting the J/ψ signal from the unlike-sign muon mass spectra.

Collision Vertex: The free space along the beam direction around the interaction point is $\pm 40\,\mathrm{cm}$. Since the collision vertex resolution of the Beam-Beam-Counter (BBC)[3] is 2 cm, the z position of event vertex should be within $\pm 38\,\mathrm{cm}$.

Muon Trigger: Due to the trigger hardware limitation, the dimuon trigger requires each muon to pass through different quadrants of the MuID. Thus the reconstructed muon tracks should penetrate different quadrants. Also, the muon track should reach the last gap of the MuID.

Vertex Matching: Muons from J/ψ decay point to the collision vertex. We compare the collision vertices using the BBC and using tracks. The later one is obtained as follows.

(1) Each muon trajectory at the MuTr is extrapolated to the collision vertex.
(2) Each muon vertex position is determined as the position closest to the beam orbit on the muon trajectory of (1).
(3) The vertex position is determined as the midpoint between two muon vertex points.

The vertex position of a muon trajectory is smeared by the multiple scattering in the hadron absorbers in front of the MuTr. The vertex point using the BBC and the muon track should be consistent with the expected vertex resolution, which is mainly governed by the multiple scattering.

The effect of the multiple scattering is estimated by GEANT simulation. The vertex matching is shown in Fig. 1. Points with error bars are from real muon events and the solid line is the result of the GEANT simulation. The simulation reproduces the real data reasonably well, and the width of vertex matching is 9 cm. Therefore, we applied ± 2 sigma cuts ($\pm 18\,\mathrm{cm}$) for this selection.

Unlike Sign Pair: J/ψ decays into an opposite-charge muon pair. The unlike-sign pair is required.

The three steps of the selection criteria of the dimuon from J/ψ are established.

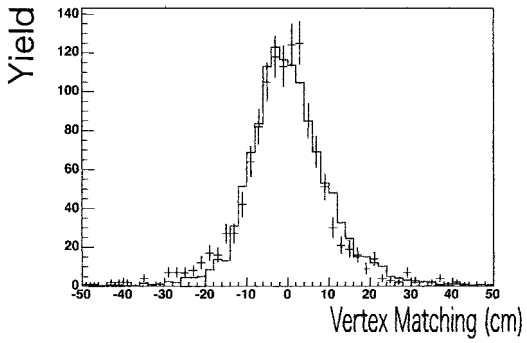

Fig. 1. The vertex matching. The line and the points with error bars are the result of simulation and the real data, respectively.

References

1) H. Akikawa et al.: Nucl. Instrum. Methods Phys. Res. A **499**, 537 (2003).
2) N. Kamihara et al.: RIKEN Accel. Prog. Rep. **37**, 224 (2004).
3) M. Allen et al.: Nucl. Instrum. Methods Phys. Res. A **499**, 549 (2003).

Measurement of single electron spectrum in $\sqrt{s} = 200\,\mathrm{GeV}$ *p*-*p* collisions at RHIC-PHENIX

M. Togawa,[*1] Y. Akiba, R. Averbeck,[*2] S. Butsyk,[*2] F. Kajihara,[*3] T. Tabaru, Y. Tsuchimoto,[*4] and W. Xie, for the PHENIX Collaboration

Heavy quarks (charm and beauty) are generated mainly through gluon-gluon fusion in $\sqrt{s} = 200\,\mathrm{GeV}$ proton-proton collisions at RHIC. Thus, perturbative QCD can be tested and the gluon distribution function can be determined by measuring heavy quark production. However, the production mechanism for heavy quarks remains to be elucidated. At Tevatron ($\sqrt{s} = 1.8\,\mathrm{TeV}$ and $1.96\,\mathrm{TeV}$ p-$\bar{p}$ collisions), the prediction of pQCD is consistent with the measured D meson cross-section data. However, the theory has large uncertainty in the fragmentation function and distribution function, and the data are 2 times larger than the central value obtained on the basis of the theory.[1)]

In the PHENIX experiment, heavy quark production can be measured precisely with single electrons from the semi-leptonic decays of charm and beauty mesons. These measurements can shed new light to our understanding of the production mechanism of heavy quarks.

Electrons are detected by the two central arms of PHENIX.[2)] The yield of electrons can be categorized into *nonphotonic* and *photonic* sources. *Nonphotonic* electrons are mainly from semi-leptonic decays of charm and beauty. *Photonic* electrons include electrons from the photon conversion and Dalitz decays of neutral mesons such as π^0 and η. These two components can be decomposed by cocktail subtraction[3)] and converter subtraction[2)] methods. We analyzed about 300 nb^{-1} of p-p data (in various trigger settings and configurations) taken in the 2003 run of RHIC.

Figure 1 shows the invariant p_{T} spectra of electrons from the semi-leptonic decays of charm and beauty by the cocktail and converter subtraction methods. These independent analyses are consistent with each other. The combination of these results and theoretical calculation are shown in Fig. 2. The data is about 2.5 times larger than that obtained by the Fixed Order plus Next to Leading Log (FONLL) pQCD calculation.

In future analysis, the spectrum can be extended to a higher-p_{T} region with high statistics. The FONLL calculation predicts that beauty decay dominates over charm decay as the source of *nonphotonic* electrons above $4\,\mathrm{GeV/c}$ in $\mathrm{p_T}$. Measurement in the high-$\mathrm{p_T}$ region is sensitive to beauty production. We can discuss what type of process contributes to the large cross section by measuring electrons not only from the charm-dominant region but also from the beauty-dominant region.

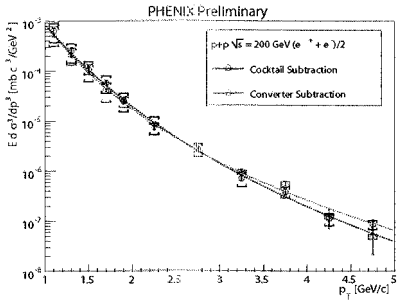

Fig. 1. Invariant p_{T} spectra of electrons from charm and beauty mesons by cocktail and converter subtractions.

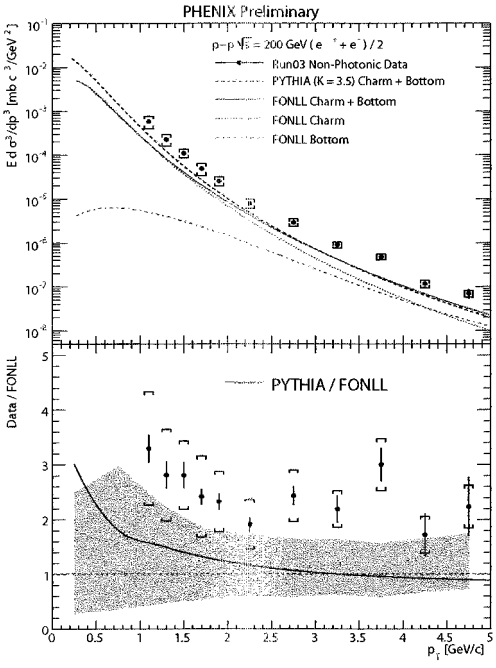

Fig. 2. Invariant p_{T} spectra of electrons from charm and beauty combined cocktail and converter subtraction results. The PYTHIA calculation[4,5)] is tuned to reproduce charm production at SPS and FNAL.[6)]

*1 Department of Physics, Kyoto University
*2 Department of Physics, Stony Brook University, State University of New York, USA
*3 Center for Nuclear Study, Graduate School of Science, University of Tokyo
*4 Graduate School of Science, Hiroshima University

References

1) D. Acosta et al.: Phys. Rev. Lett. **91**, 241804 (2003).
2) M. Togawa et al.: RIKEN Accel. Prog. Rep. **38**, 213 (2005).
3) S. S. Adler et al.: hep-ex/0508034.
4) T. Sjostrand: Comput. Phys. Commun. **82**, 74 (1994).
5) K. Adcox et al.: Phys. Rev. Lett. **88**, 192303 (2002).
6) G. A. Alves et al.: Phys. Rev. Lett. **77**, 2388 (1996).

Measurement of virtual photons at intermediate p_T in Au+Au collisions at $\sqrt{s_{NN}} = 200\,\mathrm{GeV}$

Y. Akiba, for the PHENIX collaboration

High energy collisions of heavy nuclei at RHIC produce high-density partonic matter.[1] A direct photon is an important penetrating probe of the dense matter and its time evolution. There are many possible sources of direct photons in Au+Au collisions at RHIC: pQCD hard scattering, the collision of high-p_T scattered quarks in the dense matter, thermal radiation in the partonic phase, and thermal radiations from the hadronic phase. There are theoretical predictions that thermal photons from the partonic phase are the dominant source of direct photons in the intermediate p_T range $(1 < p_T < 5)$ GeV/c. The observation of thermal photons in this p_T range is therefore direct evidence of the formation of a thermalized partonic matter at RHIC. The initial temperature of the matter can be directly measured from the emission rate of the thermal photons. The measurement of direct photons in the intermediate p_T range is, however, notoriously difficult due to a large background from hadronic decay photons: its expected yield is only 10% of that of background photons.

We obtained the first promising results of direct photon measurement at the intermediate p_T range.[2] To overcome a small signal-to-background ratio, we measured low-mass e^+e^- pairs with $p_T \gg m_{ee}$ instead of real photons. These low-mass pairs are almost real virtual photons, and their emission rates and mass distributions are related to those of real photons.[3] An advantage of this method is that the background contribution from $\pi^0 \to \gamma\gamma$ decay is strongly suppressed by requiring that the mass of the pair is close to or larger than π^0. Since approximately 80% of the background photons are from π^0, the signal-to-background ratio is improved by a factor of 5 or more.

The results are shown in Fig. 1. What we actually measured in this analysis are the ratios of the yield of virtual direct photons and virtual inclusive photons $(\gamma^*_{direct}/\gamma^*_{incl})$ in $90 < m_{ee} < 300\,\mathrm{MeV}$ as a function of p_T. The ratios are then converted to the invariant yields of real direct photons using the yields of the real inclusive photons γ_{incl} measured by PHENIX with the assumption that the (direct/real) ratio is the same for real photons.

Are these thermal photons? The rate is higher than a pQCD calculation[4] scaled by the number of binary $N + N$ collisions. In higher p_T $(p_T > 5)$ GeV/c the pQCD calculation is in good agreement with direct photon data in $p + p$,[5] but there is no $p + p$ data in $p_T < 3\,\mathrm{GeV}/c$. We need reference measurements in

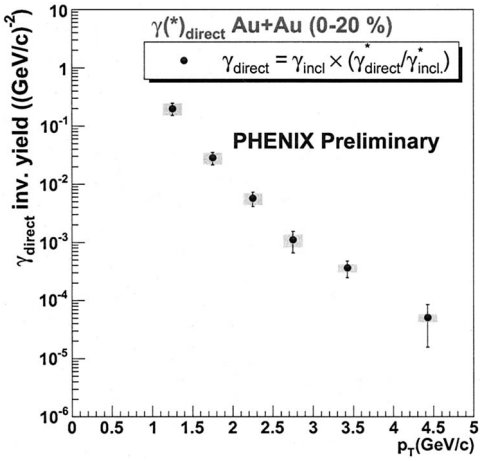

Fig. 1. Invariant yield of direct photons in the 0–20% central Au+Au collisions at $\sqrt{s_{NN}} = 200\,\mathrm{GeV}$ obtained from the analysis of low mass e^+e^- pair.

p+p and d+Au to be able to draw a definite conclusion on the nature of direct photons in the intermediate p_T range. The same analysis method can be used in $p + p$ to test the validity of pQCD in this low-p_T region, and in $d + \mathrm{Au}$ to examine cold nuclear matter effects such as the Cronin effect.

If the direct photon yield is due to thermal radiation, the data can enable the first direct measurement of the initial temperature of the matter by comparison between the data and theoretical calculations. Comparison with a model prediction[6] yields the values from 500 to 600 MeV for T_{max}, where T_{max} is the maximum temperature at the center of the fireball. Averaging over the entire volume leads to smaller values from 300 to 400 MeV. These values are only meaningful if these photons are indeed thermal photons; nevertheless, these results are quite intriguing.

References

1) K. Adcox et al.: Nucl. Phys. A **757**, 184 (2005).
2) S. Bathe for the PHENIX collaboration: Proc. Quark Matter 2005, Budapest, Hungary 2005-8, to be published; nucl-ex/0511042.
3) N. M. Kroll and W. Wada: Phys. Rev. **98**, 1355 (1955).
4) L. E. Gordon and W. Vogelsang: Phys. Rev. D **48**, 3136 (1993).
5) K. Okada et al.: RIKEN Accel. Prog. Rep. **39**, 176 (2006).
6) D. d'Enterria and D. Peressonko: nucl-th/0503054.

Prompt photon production in $\sqrt{s_{NN}}$=200 GeV d+Au collisions at RHIC-PHENIX

H. Torii, Y. Akiba, A. Bazilevsky, K. Okada for the PHENIX Collaboration

Prompt photon is a good probe for investigating gluon distribution because the leading subprocess is gluon-quark Compton scattering. In the E706[1] experiment, a small excess of photon yield in p+N collisions compared with p+p collisions was reported. It implies that the nuclear effect of the N-nucleus affects the initial parton distribution. The PHENIX[2] detector constructed at Relativistic Heavy Ion Collider (RHIC) is designed for studying collisions ranging from p+p to Au+Au. Here, the measurement of prompt photon in d+Au collisions at $\sqrt{s_{NN}} = 200\,\mathrm{GeV}$ is reported.

The PHENIX EMCal[3] covers the mid-rapidity region , $|\eta| < 0.35$, with granularity fine enough to identify individual photons from π^0 decays. The PHENIX EMCal-RICH trigger (ERT) was used to select events with high-energy photons or electrons. Because the trigger efficiency of ERT plateaued at $> 5\,\mathrm{GeV}$ for photons during run 2003, here, only the photons with $p_T > 5\,\mathrm{GeV}$ are selected.

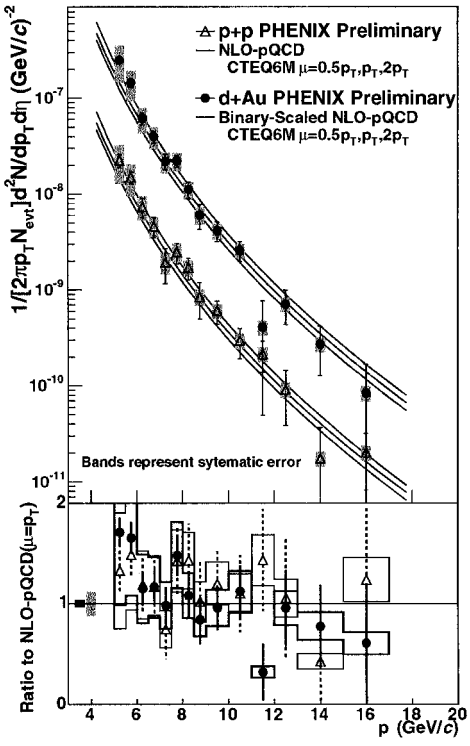

Fig. 1. (Top)Cross section of prompt photon production in $\sqrt{s_{NN}} = 200\,\mathrm{GeV}$ d+Au collisions and in p+p collisions compared with NLO pQCD calculation. An averaged number of nucleon collisions calculated by the Glauber model is used to compare the pQCD calculation in d+Au collisions. (Bottom) Ratio of cross section in d+Au and p+p collisions to NLO pQCD calculation.

The largest background of the prompt photon production is photons from hadron decay, particularly π^0. The fine granularity of EMCal enabled us to identify photons from $\pi^0 \to \gamma + \gamma$ decay from two photon invariant mass spectra. Although the identification was imperfect, 80% of the background could be rejected. The other background contributions were evaluated in a statistical way on the based of our measurement of other hadrons and a Monte-Carlo simulation.

Figure 1 shows the obtained result in d+Au collisions and in p+p collisions. A next-to-leading order pQCD calculation in p+p is shown in the figure for comparison; the calculation is scaled with the mean number of collisions calculated by the Glauber model in d+Au collisions.

To evaluate the nuclear effect, we calculated a nuclear modification factor, $(\sigma_{d+Au})/(\sigma_{pp} \times N)$, where N is the mean number of collisions. The obtained factor shown in Fig. 2 is consistent to the unity within their systematic and statistical errors. It indicates that the nuclear effect of Au nuclei is small.

In summary, although statistical and systematic errors are large, we conclude that the measured nuclear modification in Au nuclei is small.

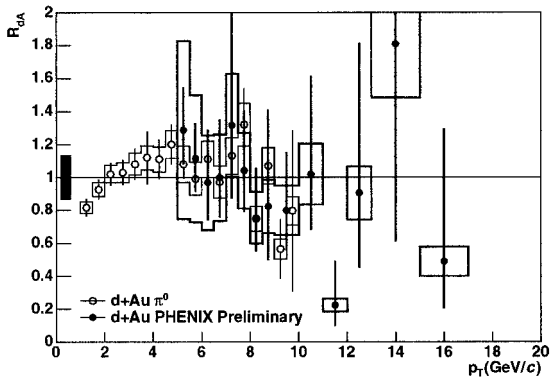

Fig. 2. Nuclear modification factor of prompt photon production in $\sqrt{s_{NN}} = 200\,\mathrm{GeV}$ d+Au collisions compared with π^0 production. An averaged number of nucleon collisions calculated by the Glauber model is used to normalize the result in p+p data in comparison with d+Au data.

References

1) L. Apanasevich et al.: Phys. Rev. D **72**, 032003 (2005).
2) K. Adcox et al.: Nucl. Instrum. Methods Phys. Res. A **499**, 469 (2003).
3) L. Aphecetche et al.: Nucl. Instrum. Methods Phys. Res. A **499**, 521 (2003).

Measurement of neutral pion in $\sqrt{s_{\rm NN}} = 200\,{\rm GeV}$ Au+Au collisions at RHIC-PHENIX

T. Isobe,[*1] H. Hamagaki,[*1] T. Sakaguchi,[*2] G. David,[*2] S. Mioduszewski,[*3] M. L. Purschke,[*2] D. Winter,[*4] B. Sahlmueller,[*5] in collaboration with PHENIX

The PHENIX experiment[1)] has been carried out at the Relativistic Heavy Ion Collider (RHIC) at Brookhaven National Laboratory (BNL) to find evidence of phase transition from normal nuclear matter to Quark Gluon Plasma (QGP). QGP is a new phase of matter consisting of deconfined quarks and gluons. One of the most intriguing observations at RHIC is that the yield of π^0 at high transverse momentum ($p_{\rm T}$) in central $\sqrt{s_{\rm NN}} = 200\,{\rm GeV}$ Au+Au collisions compared with the yield of p+p collision scaled by the number of underlying nucleon-nucleon collisions is suppressed.[2,3)] The observed suppression is interpreted as a consequence of the jet-quenching effect, that is, hard-scattered partons produced in the initial stage suffer a large energy loss while traversing the hot and dense matter.

The amount of suppression can be quantified by a nuclear modification factor ($\rm R_{AA}$). $\rm R_{AA}$ is the ratio between the measured yield and the expected yield from the p+p result, and is defined as

$$R_{\rm AA}(p_{\rm T}) = \frac{d^2N_{\rm AA}/dp_{\rm T}d\eta}{T_{\rm AA}(b)d^2\sigma_{\rm NN}/dp_{\rm T}d\eta}, \qquad (1)$$

where the numerator is the invariant π^0 yield in unit rapidity and the denominator is the expected yield in p+p collision binary scaled by the number of underlying nucleon-nucleon collisions ($T_{\rm AA}(b)$) in Au+Au. $T_{\rm AA}(b)$ is defined as

$$T_{\rm AA}(b) = N_{\rm coll}(b)/\sigma_{\rm NN}, \qquad (2)$$

where $N_{\rm coll}(b)$ is the average number of binary nucleon-nucleon collisions determined by distance (b) between the two nucleons with an inelastic cross section σ_{NN}. If a hard-scattered parton penetrates the bulk matter without any nuclear effects, the $\rm R_{AA}$ is unity.

There are several models that provide quantitative predictions of the amount of suppression. Each model has various effects: initial state effects, Cronin effect[4)] and nuclear shadowing, or strong hadronic final state effects, and energy loss in a dense matter. The systematic study of π^0 production is important to clarify the parton energy loss mechanism in the dense matter.

In RHIC Year-4 run, PHENIX recorded the integrated luminosity of $0.24\,{\rm nb}^{-1}$ in $\sqrt{s_{\rm NN}} = 200\,{\rm GeV}$ Au+Au collisions. π^0s were detected with the PHENIX electromagnetic calorimeter (EMCal) via the two-photon decay mode. To correct the raw π^0 yield, the geometrical acceptance correction, particle identification efficiency, and overlapping effect in high multiplicity were estimated using computing clusters at RIKEN-CCJ.

The large amount of data obtained in RHIC Year-4 has made it possible to measure π^0 up to $\rm p_T \sim 20\,GeV/\mathit{c}$ for the central collisions. $\rm R_{AA}$ as a function of $\rm p_T$ was obtained from corrected $\rm p_T$ spectra. π^0 data obtained in PHENIX Year-3 run was used as the p+p reference. Figure 1 shows the $\rm R_{AA}$ for most central events (0–10%) together with a theoretical prediction which employs the GLV model.[5)] The suppression is very strong, and it is almost constant at $\rm R_{AA} \sim 0.2$ up to a very high $\rm p_T$. The GLV model describes the strong suppression well and it indicates the existence of bulk matter where initial gluon density ($\rm dN^{\mathit{g}}/dy$) is more than 1100 in Au+Au collisions at $\sqrt{s_{\rm NN}} = 200\,{\rm GeV}$.

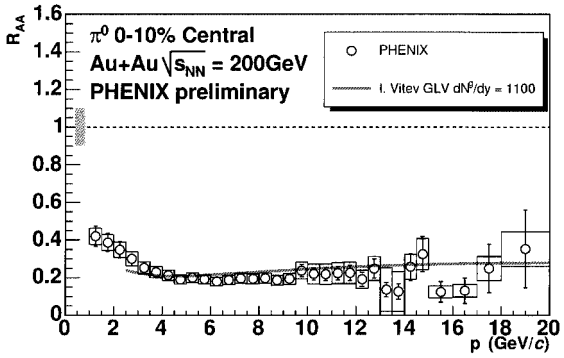

Fig. 1. Comparison of π^0 $\rm R_{AA}$ with prediction of $\rm R_{AA}$ using GLV model in $\sqrt{s_{\rm NN}} = 200\,{\rm GeV}$ Au+Au central (0-10%) collisions. In addition to the statistical and pT-uncorrelated errors, point-to-point varying systematic errors are shown on the data points as boxes. An overall systematic error of $T_{\rm AA}$ normalization is shown at 1.

[*1] Center for Nuclear Study, Graduate School of Science, University of Tokyo
[*2] Brookhaven National Laboratory, USA
[*3] Texas A&M University, USA
[*4] Columbia University, USA
[*5] University of Muenster, Germany

References
1) K. Adcox et al.: Nucl. Instrum. Methods Phys. Res. A **499**, 469 (2003).
2) S. S Adler et al.: Phys. Rev. Lett. **91**, 072301 (2003).
3) S. S Adler et al.: Phys. Rev. Lett. **91**, 072303 (2003).
4) J. W. Cronin et al.: Phys. Rev. D **11**, 3105 (1975).
5) I. Vitev et al.: Phys. Rev. Lett. **89**, 252301 (2002).

Single electron measurement in PHENIX Run-3 *d*+Au experiment

F. Kajihara,[*1] Y. Akiba, R. Averbeck,[*2] S. Butsyk,[*3] H. Hamagaki,[*1] K. Ozawa,[*1] and M. Togawa,[*4]
for the PHENIX Collaboration

Charm production in high-energy nuclear collision provides information on the initial stage of the reaction. Most of midrapidity charm quarks are produced via gluon fusion ($gg \rightarrow c\bar{c}$).[1] Hence, there have been several attempts to use charm production as a probe of the initial-state gluon density in $p+A$ and $A+A$ collisions.[2,3] Observation of gluon shadowing in heavy nuclei is of fundamental interest. In addition, charm measurement in $p+A$ or $d+A$ collisions provides the baseline to study pre-equilibrium charm enhancement and jet quenching in $A+A$ collisions.[4] Open-charm production can be measured through single leptons from semileptonic decays of charmed hadrons ($D\bar{D}$). The semileptonic decays have considerably larger cross sections than the other sources of single leptons such as the dilepton productions.

In the PHENIX experiment at RHIC, single electrons (e^+ or e^-) have been measured at midrapidity ($|y| < 0.35$) for d+Au collisions at $\sqrt{s_{NN}} = 200\,\mathrm{GeV}$. Inclusive electrons can be categorized into two groups. The first group consists of "*photonic*" electrons mainly from the (1) Dalitz decays of mesons (π^0, η, etc) and (2) external photon conversions. The second group consists of "*nonphotonic*" electrons. The signal electron from semileptonic decays of open charm is the dominant source of the second group. In this report, we present the status of *nonphotonic* electron measurement.

To extract *nonphotonic* electron yield $N(p_\mathrm{T})$ by subtraction of *photonic* yield $P(p_\mathrm{T})$ from the total, a "converter subtraction" method is applied.[5] In the experiment, special runs were performed with a photon converter, a brass sheet (1.68% radiation length) around the MVD detector.[6] The photon converter enhances $P(p_\mathrm{T})$ by a certain factor, R_γ, which is the ratio of *photonic* electron yield with to that without the converter. The measured inclusive electron yield $I(p_\mathrm{T})$ is given as $I(p_\mathrm{T}) = P(p_\mathrm{T}) + N(p_\mathrm{T})$ without the converter and $I'(p_\mathrm{T}) = R_\gamma P(p_\mathrm{T}) + N(p_\mathrm{T})$ with the converter. $N(p_\mathrm{T})$ is obtained by solving these two equations.

In the converter subtraction method, the evaluation of R_γ is most important. A GEANT-based Monte Carlo simulation was used to evaluate how much the *photonic* electron yield is increased by the photon converter and to determine R_γ. The simulation was performed using the PHENIX-CCJ (Computing Center in Japan) and RIKEN Super Combined Cluster (RSCC).

*1 Center for Nuclear Study, University of Tokyo
*2 Department of Physics and Astronomy, Stony Brook University, State University of New York, USA
*3 Los Alamos National Laboratory, USA
*4 Department of Physics, Kyoto University

The source of *photonic* electrons in real data is a mixture of mesons (π^0, η, η', ω and ϕ) decaying into real or virtual photons. However, contributions from π^0 and η account for almost all of *photonic* electrons. Therefore, *photonic* electrons from only π^0 and η were studied in the simulation. R_γ of π^0 ($R_\gamma^{\pi^0}$) and R_γ of η (R_γ^{η}) were determined separately, and R_γ was determined by combining $R_\gamma^{\pi^0}$ and R_γ^{η}. For the original π^0 and η spectra, we used the p_T distributions measured in the same experiment.

Figure 1 shows $N(p_\mathrm{T})$ in $\sqrt{s_{NN}} = 200\,\mathrm{GeV}$ d+Au collisions (close square) which is calculated with the new result of *photonic* electron simulation. The error bars indicate statistic errors only and the squares in the background indicate systematic errors. The data are fully corrected for trigger efficiency, geometrical acceptance, reconstruction and eID efficiency.[7] The spectrum is normalized with the binary collision cross section by scaling with $\sigma_{pp}/(Ncoll = 8.5)$ to compare with the *nonphotonic* electron spectrum in the Run-2 p+p. Both spectra seem to match well, and no strong nuclear modification is observed in d+Au collisions.

The analysis of *nonphotonic* electrons in the high-p_T region ($\geq 5\,\mathrm{GeV}/c$) is in progress, which is important for the study of the behavior of b quarks.

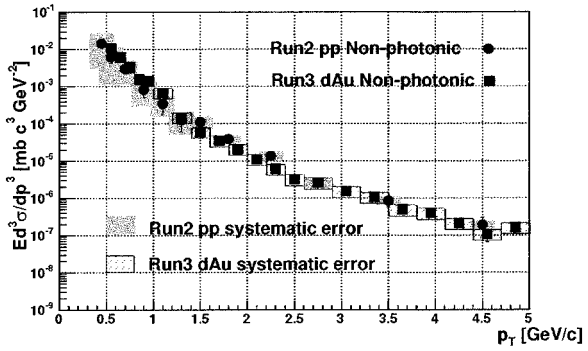

Fig. 1. *Nonphotonic* invariant cross section in $\sqrt{s_{NN}} = 200\,\mathrm{GeV}$ d+Au collisions (close square), which is normalized with the binary collision cross section.

References
1) S. J. Brodskey et al.: Nucl. Phys. B **369**, 519 (1992).
2) Z. Lin and M. Gyulassy: Phys. Rev. Lett. **77**, 1222 (1996).
3) K. Geiger: Phys. Rev. D **48**, 4129 (1993).
4) B. Müller and X. N. Wang: Phys. Rev. Lett. **68**, 2437 (1992).
5) S. S. Adler et al.: Phys. Rev. Lett. **94**. 082301 (2005).
6) K. Adcox et al.: Nucl. Instrum. Methods Phys. Res. A **499**, 469 (2003).
7) F. Kajihara et al.: CNS Annu. Rep. **2003**, 51 (2004).

Single electron measurement in PHENIX Run-4 Au+Au experiment

F. Kajihara,[*1] Y. Akiba, R. Averbeck,[*2] S. Butsyk,[*3] A. Dion,[*2] H. Hamagaki,[*1] and K. Ozawa,[*1]
for the PHENIX Collaboration

A strong suppression of light flavor mesons at a high p_{T} was observed[1,2] in high-energy heavy-ion collisions at RHIC. The leading explanation of this suppression is that high-p_T-scattered partons suffer a significant energy loss in an extremely hot and dense QCD matter.[3] This effect is considered as strong evidence of quark-gluon plasma (QGP) formation. The energy loss for heavy quarks (charm or bottom) was predicted to be smaller than that of light quarks due to larger quark masses.[4] The measurement for heavy quarks will extend our knowledge of the mechanism underlying medium-induced parton energy loss.[5]

In the RHIC-PHENIX experiment in 2004, we measured the Au+Au collisions at $\sqrt{s_{NN}} = 200\,\mathrm{GeV}$. The measurement of single electrons (e^+ or e^-) from semileptonic decays of open charm/bottom is useful for investigating heavy-quark production. Inclusive electrons can be categorized into two groups. The first group consists of "*photonic*" electrons mainly from the (1) Dalitz decays of mesons (π^0, η, etc) and (2) photon conversion. The second is termed "*nonphotonic*" electrons. The decays of charm/bottom are the dominant sources of the second group. To extract *nonphotonic* electron yield by subtracting the *photonic* electron background, we used the so-called "cocktail subtraction" method. This method is used to reconstruct all possible *photonic* electron components, that is cocktail, using a hadron-decay simulator on the basis of published pion spectra[1,2] and to subtract them from the inclusive electron spectrum.[6]

Figure 1 shows the *nonphotonic* electron yield for each centrality, scaled with the corresponding number of binary collisions (N_{col}). The brackets and bars indicate the systematical and statistical errors, respectively. The curves are the best fit curves for the Run-3 p+p *nonphotonic* electron spectrum.[6] In central collisions, a strong suppression at a high p_T is observed. To quantify the suppression, the nuclear modification factors (R_{AA}) for each centrality are shown in Fig. 2. The systematic errors include those of the nuclear thickness function (T_{AB}), $p+p$ data, and Au + Au data.

This is a very interesting result: a clear suppressive effect exists even for *nonphotonic* electrons from the most central to the midcentral. It indicates that the matter is so dense that even heavy quarks are stopped. Presently, we are working to improve the error calculations. We use another method (a "converter subtraction" method) of measuring low $p_T (< 1\,\mathrm{GeV}/c)$.

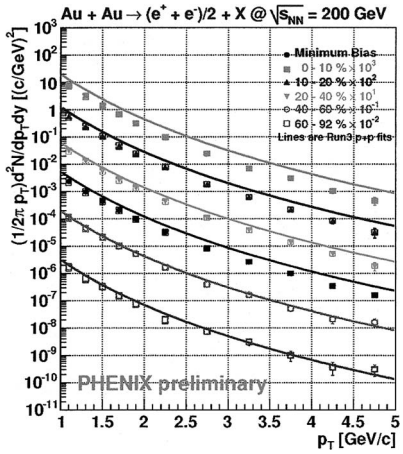

Fig. 1. p_{T} distribution of *nonphotonic* electron invariant yield for each centrality in Run-4 Au + Au compared with Run-3 $p+p$ best fit, scaled by N_{col}.

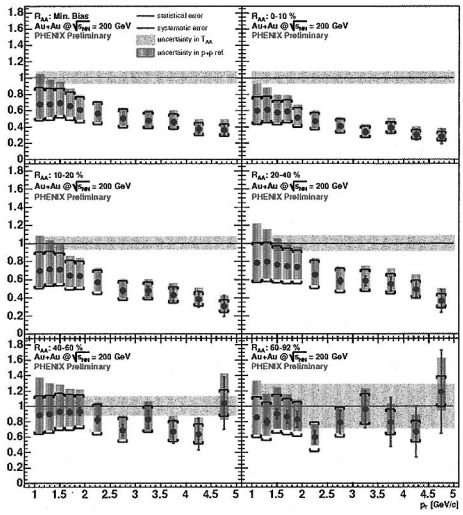

Fig. 2. p_{T} distribution of nuclear modification factor (R_{AA}) for each centrality in Run-4 Au + Au.

The measurement will be also extended to the high-p_{T} region ($\geq 5\,\mathrm{GeV}/c$), where a large b quark decay contribution is expected.

References

1) K. Adcox et al.: Phys. Rev. Lett. **88**, 022301 (2002).
2) S. S. Adler et al.: Phys. Rev. Lett. **91**, 072301 (2003).
3) M. Gyulassy and X. N. Wang: Nucl. Phys. B **420**, 583 (1994).
4) Y. L. Dokshitzer et al.: Phys. Lett. B **519**, 199 (2001).
5) N. Armesto et al.: Phys. Rev. D **71**, 054027 (2005).
6) M. Togawa et al.: RIKEN Accel. Prog. Rep. **39**, 189 (2006).

*1 Center for Nuclear Study, University of Tokyo
*2 Department of Physics and Astronomy, Stony Brook University, State University of New York, USA
*3 Los Alamos National Laboratory, USA

Measurement of low-mass vector mesons in nuclear collisions at PHENIX

Y. Tsuchimoto* and Y. Akiba, for the PHENIX Collaboration

It is predicted that in nuclear matter at high baryon density and/or high temperature, chiral symmetry will be restored and consequently, the masses and widths of low-mass vector mesons (ρ, ω and ϕ) will be modified. Some interesting results that suggest modification of the properties of hadrons in ordinary nucleus matter have been reported.[1,2)]

The Relativistic Heavy Ion Collider at Brookhaven National Laboratory provides a great opportunity to study the properties of mesons in hot and dense matter. We have programs of p+p, d+Au, Cu+Cu and Au+Au collisions at $\sqrt{s_{NN}} = 200\,\mathrm{GeV}$.

The PHENIX central spectrometer[3)] can measure low-mass vector mesons in both leptonic and hadronic decay channels within the same acceptance at midrapidity. The lepton carries information on mesons deep inside the hot and dense matter because an electron does not interact by strong force. The branching ratio of $\phi \to e^+e^-$ to K^+K^- may be sensitive to the medium effect. In this report, we present the measurement of low-mass vector mesons in the dielectron channels in $d + Au$ collisions at $\sqrt{s_{NN}} = 200\,\mathrm{GeV}$.

The PHENIX experiment at RHIC recorded approximately 1 nb^{-1} of d+Au collisions in the 2003 run period. Charged particle tracks were reconstructed using drift chambers and pad chambers. Magnetic field is applied inside the chamber. Then, momentum is calculated by the tracks assuming at charged particles come from a collision vertex.

Ring Imaging Cerenkov detectors (RICHs) and electromagnetic calorimeters (EMC) were used as online triggers for an electron (ERT electron trigger). Detailed off-line identification was applied. We required at least 1 PMT hit of RICH, and energy and timing measured by EMC are equal to its momentum and light speed within 3 σ of this resolution, respectively.

Data were taken in two running periods with different thresholds of EMC energy, that is, 600 MeV and 800 MeV for the single electron. The integrated luminosity of the two periods was approximately the same.

Figure 1 shows the dielectron invariant mass distribution. Data from the two running periods are combined in this figure. A high background due to the random combination of unrelated e^+ and e^- was subtracted by an event mixing method. The background is normalized using a like-sign method. One can clearly observe narrow peaks of ϕ (at 1020 MeV) in the mass distribution. Its mass and width are consistent with known values in vacuum and our simulation. This width is predominated by the experimental resolution

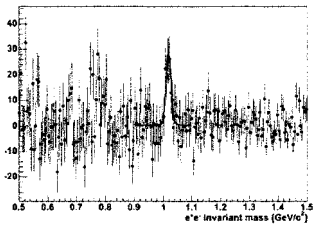

Fig. 1. Low-mass dielectron mass distribution in d+Au collision at $\sqrt{s_{NN}} = 200\,\mathrm{GeV}$.

$\sim 15\,\mathrm{MeV/c^2}$ depending on momentum.

To determine the production cross section of vector mesons, the observed ϕ yields have to be corrected for detector acceptance, electron ID efficiency, and trigger efficiency. A simulator of the ERT has been developed and incorporated into the GEANT-based PHENIX simulation program. Its efficiency and trigger mask were tuned for each 5 period of Run3 d+Au run. We calculated the trigger efficiency of ϕ for each period. In this simulation, the variables of EMC energy, matching and timing are tuned using real detector responses to reduce systematic error of electron identification.

We counted signals within 3 sigma of detector resolution calculated by simulation. The count of normalized mixed events within the same range was subtracted as background. We calculated combined acceptance and efficiency using the simulation program. The corrected ϕ spectra are shown in Fig. 2 where vertical bars indicate systematic errors and red boxes indicate systematic errors of only eID, background normalization and signal counting.

We obtained the corrected transverse energy spectra of ϕ mesons at $\sqrt{s_{NN}} = 200\,\mathrm{GeV}$ d+Au collisions in the PHENIX experiment. Systematic errors need to be considered more.

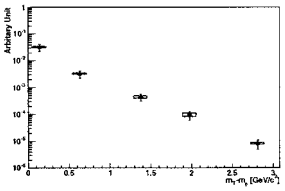

Fig. 2. Corrected m_T spectra of $\phi \to e^+e^-$, where vertical bars indicate statistical errors, and red boxes indicate preliminary systematic error.

References

1) K. Ozawa et al.: Phys. Rev. Lett. **86**, 5019 (2001).
2) K. Suzuki et al.: Phys. Rev. Lett. **92**, 072302 (2004).
3) K. Adcox et al.: Nucl. Instrum. Methods Phys. Res. A **499**, 469 (2003).

* Department of Physics, Hiroshima University

Relative luminosity measurements in a high rate environment

D. M. Kawall

The Relativistic Heavy Ion Collider (RHIC) at Brookhaven National Laboratory has the unique ability to collide beams of high energy polarized protons.[1] This ability presents a significant opportunity for physicists interested in unraveling mysteries associated with the spin of the proton.[2]

To this end, the PHENIX experiment at RHIC has made measurements of the double longitudinal spin asymmetry in the production of π^0 from collisions of like- and unlike-helicity protons at $\sqrt{s} = 200\,\mathrm{GeV}$.[3] The asymmetry, which is sensitive to the polarized gluon density in the proton, is determined from:

$$A_{LL}^{\vec{p}\vec{p}\to\pi^0 X} = \frac{\sigma_{++} - \sigma_{+-}}{\sigma_{++} + \sigma_{+-}} = \frac{1}{|\langle P_1 P_2 \rangle|} \frac{N_{++}/L_{++} - N_{+-}/L_{+-}}{N_{++}/L_{++} + N_{+-}/L_{+-}}$$

where $+,-$ refer to the helicities of the colliding bunches of protons, P_i refers to the polarization of beam i, L_{ab} is the luminosity of beams colliding with helicities a and b, and N_{ab} refers to the helicity-sorted yield of π^0. Thus, in addition to measuring the polarizations of the beams and yields of the final state of interest, we must also measure the relative luminosity $R = L_{++}/L_{+-}$ to much better accuracy than the uncertainties on the yields (a reasonable goal would be $\delta R \approx$ few $\times 10^{-4}$).

Currently R is measured[4] with the two beam-beam counters (BBCs) of PHENIX.[5] Each BBC surrounds the beam pipe 1.44 m upstream or downstream of the nominal interaction point, and covers a pseudorapidity interval $3.0 < |n| < 3.9$. Proton collisions yielding a coincidence of signals in the two BBCs are insensitive to the polarization of the colliding beams at or below the level of 10^{-3}. Counting such coincidences in a scaler is a good measure of the luminosity, so we construct R from the ratio of scaler counts for like-helicity to unlike-helicity bunch pairs.

Systematic corrections to R as constructed above are required when the collision probability per bunch crossing gets above 5 or 10% to keep the uncertainty $\delta R < 10^{-3}$. The correction is required because some crossings will have 2 or more pp collisions, but the scalers only count 1. Consider an extreme case where the $++$ bunch crossings have on average 10 pp interactions/crossing, whereas the $+-$ crossings have 8. Then we would measure 1.0003 with the scaler ratio, whereas the true $R = 1.25$. At the design luminosity of $2 \times 10^{32}\,\mathrm{cm}^{-2}\mathrm{s}^{-1}$, we only expect about 1 pp collision per crossing, but the correction to R from this "saturation" will be too hard to know with the required accuracy. To overcome this problem we have started to count the number of BBC phototubes hit/crossing. Multiple pp interactions/crossing lead to a linear increase in phototubes hit, and the "saturation" problem is lessened.

A second (and worse) problem occurs because the PHENIX central arm acceptance requires that the pp interaction occurs within 30 cm of the nominal interaction point. Since the bunches delivered by RHIC are significantly wider than this, almost 50% of the events occur outside this range. Currently the vertex position is determined from the difference in arrival times of secondary particles at the two BBCs. In a high rate environment with multiple collisions/crossing, the vertex can be reconstructed improperly and we make mistakes deciding which collisions to add to our scaler counts. Since the vertex profiles for $++$ and $+-$ are different, ambiguities in the vertex determination will lead to a large, intractable uncertainty in R.

To overcome this problem, we used data from the wall current monitor in the RHIC ring.[6] This device measures the charge profile of the colliding bunches, from which one can predict the vertex shape for $++$ and $+-$ separately (see Fig. 1), free from rate effects. The observed vertex profile can then be predicted with sufficient accuracy (the RMS width is predicted to within a few mm for instance) that it seems plausible we can make the required vertex shape dependent corrections to determine R with high accuracy at high rates.

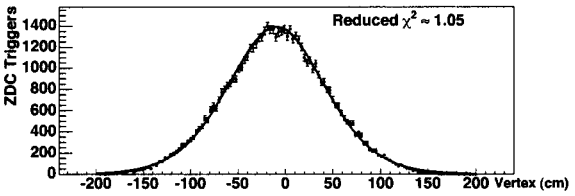

Fig. 1. Predicted and observed vertex profile.

References

1) I. Alekseev et al.: Nucl. Instrum. Methods Phys. Res. A **499**, 392 (2003).
2) G. Bunce et al.: Annu. Rev. Nucl. Part. Sci. **50**, 525 (2000).
3) S. S. Adler et al.: Phys. Rev. Lett. **93**, 202002 (2004).
4) K. Boyle et al.: RIKEN Accel. Prog. Rep. **39**, 197 (2006), and references therein.
5) M. Allen et al.: Nucl. Instrum. Methods Phys. Res. A **499**, 549 (2003).
6) M. Bei et al.: Nucl. Instrum. Methods Phys. Res. A **499**, 372 (2003).

Relative luminosity studies with polarized protons in RHIC Run5 at PHENIX

K. Boyle,[*1] A. Bazilevsky,[*2] A. Deshpande,[*1] Y. Fukao,[*3] Y. Goto, D. Kawall,[*4] and K. Tanida

One of the main goals of the Relativistic Heavy Ion Collider (RHIC) is to constrain the gluon contribution to the proton's spin using longitudinally polarized protons by measuring the double longitudinal spin asymmetry in different production channels. To properly calculate any asymmetry, we must take into account the relative luminosity of bunches with different helicities (++ and −− vs. +− and −+). At PHENIX, we use two beam-beam counters (BBCs) to measure relative luminosity. A second set of detectors, zero-degree calorimeters (ZDCs), is used in conjunction with the BBCs, to estimate uncertainty in relative luminosity. This uncertainty is directly related to the final uncertainty in our asymmetry measurement.

The BBCs are 1.44 m from the center of the interaction point at $|\eta| = 3.0$ to 3.9. A coincidence between the two BBCs is used to trigger events. The vertex point is reconstructed, and a ±30 cm cut is imposed.

The ZDCs are 18 m from the interaction point, and cover ±2.8 mrad in the forward and backward directions. We use the ZDCs to trigger events with two online vertex cuts: ZDCnarrow has a ±30 cm cut, and ZDCwide has a ±150 cm cut.

The number of live events triggered by the BBCs and ZDCs are recorded by a set of scaler boards. To measure relative luminosity, BBC live counts are used. We simply divide the sum of the counts from like helicity collisions by the sum of counts from unlike helicity collisions.

The BBCs are high-statistic detectors, and thus we expect systematic uncertainty to be an important issue. To estimate the accuracy of our result, we compare the values obtained by the BBCs and a second detector system–the ZDCs. We would expect the ratio of the counts in the two detectors, $r(i) = N_{BBC}(i)/N_{ZDCnarrow}(i)$, to be constant independent of bunch crossing i. As there may be some asymmetry in either detector, we actually fit $r(i)$ to

$$r(i) = C[1 + \epsilon_{LL} S_1(i) S_2(i)]. \quad (1)$$

Here, $S_j(i)$ is the sign of the helicity of bunch i in beam j. $\epsilon_{LL} = A_{LL}/P_1P_2$ with P_j the polarization of beam j, and A_{LL} is related to the relative sensitivity of the BBCs and ZDCs to the beam polarization.

A correction is applied to this ratio due to the poor resolution (±30 cm) of the online ZDC reconstructed vertex position. A correlation between $N_{BBC}(i)/N_{ZDCnarrow}(i)$ and the ratio of ZDCnarrow counts to ZDCwide−ZDCnarrow (defined as ZDCout) counts can clearly be seen (Fig. 1). As this effect is due to the ZDCs, we do not correct our relative luminosity.

With this correction applied, we fit Eq. 1 as described above. We do this on a fill-by-fill basis. (A fill is one store in RHIC, injection to dump). Figure 2 shows ϵ_{LL} vs fill number. Fitting this with a constant gives $\delta\epsilon_{LL} = 2.7 \times 10^{-5}$. As the χ^2/NDF is greater than unity (371.1/103), we may be underestimating our uncertainty. Therefore, we enlarge our error by $\sqrt{\chi^2/NDF}$, giving us a final $\epsilon_{LL} = (1.02 \pm 0.52) \times 10^{-4}$. Thus, we conclude that the uncertainty of R in the 2005 data set is $\delta R = 1.0 \times 10^{-4}$. With an average polarization of 47%, this contributes an uncertainty in our measured double spin asymmetry of 2.3×10^{-4}.

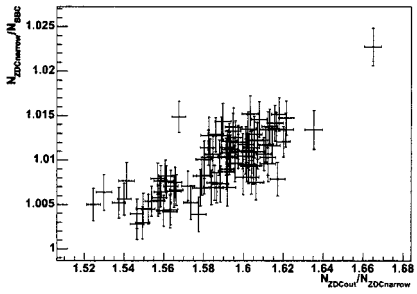

Fig. 1. A clear correlation is seen between $N_{ZDCnarrow}/N_{BBC}$ vs $N_{ZDCnarrow}/N_{ZDCout}$. This is due to poor ZDC resolution (±30 cm) and is corrected for in our final relative luminosity uncertainty.

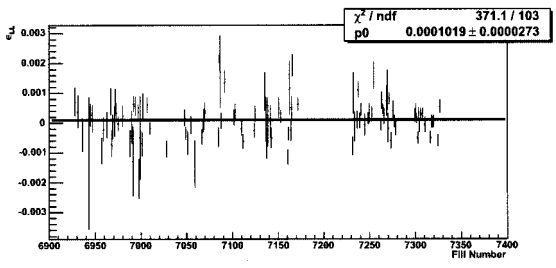

Fig. 2. ϵ_{LL} vs. fill number after correction for poor ZDC resolution.

*1 Department of Physics, Stony Brook University, USA
*2 Brookhaven National Laboratory, USA
*3 Department of Physics, Kyoto University
*4 Department of Physics, University of Massachusetts, USA

PHENIX local polarimeter in 2005

M. Togawa,[*1] K. Aoki[*1], K. Boyle,[*2] A. Deshpande,[*2] Y. Fukao,[*1] Y. Goto, N. Saito,[*1] J. Seele,[*3] and K. Tanida, for the PHENIX Collaboration

One of the main programs of the Relativistic Heavy Ion Collider (RHIC) experiment is a determination of the polarized gluon distribution function in the proton by using longitudinally polarized proton collisions at $\sqrt{s} = 200$ and 500 GeV.[1)] In the RHIC ring, the stable direction of the proton polarization is vertical. The spin rotator magnets, which are located around the experimental area, rotate the spin vector by 90 degrees to enable longitudinal collisions in the PHENIX Interaction Region (IR). The motivation of the PHENIX local polarimeter is to confirm that the proton is longitudinally polarized in the IR during a run by measuring a remaining transverse neutron asymmetry.[2)]

The local polarimeter system consists of a Zero-Degree Calorimeter (ZDC) with position-sensitive Shower-Max Detector (SMD).[3,4)] They cover ±2.8 mrad of the forward and backward directions. The analysis method is the same as that of previous runs.[4)] Since improvements in the data acquisition bandwidth ($3 \sim 5$ kHz), the trigger for the local polarimeter was allowed to operate at a high rate (∼200 Hz) in 2005. This enabled a precise measurement of remaining transverse asymmetries as well as zero backward asymmetries. Finite backward asymmetries have not been seen and can be used as a cross check on analysis by requiring that the analysis reproduce this zero asymmetry.

The basis of the hit position measured by the SMD, left/right and up/down asymmetries were calculated and plotted against the azimuthal angle. Figure 1 shows the raw transverse spin asymmetries during the commissioning period with the spin rotators off (transverse commissioning period) and the normal operation with the spin rotators on (longitudinal period). Finite asymmetries were seen during the transverse period and vanished during the longitudinal period.

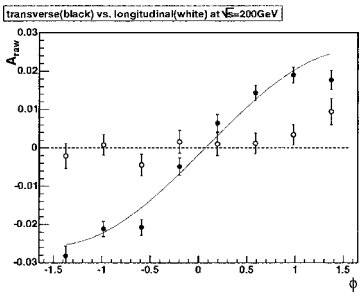

Fig. 1. Raw transverse asymmetries during commissioning period at $\sqrt{s} = 200$ GeV with transverse polarization (black circle) and longitudinal polarization (white circle). The polarization of both beams was almost the same during this period.

The local polarimeter can allow us to measure how much the proton beams are longitudinally polarized using the following formulas.

$$\frac{P_{\rm L}}{P} = \sqrt{1-\left(\frac{P_{\rm T}}{P}\right)^2}, \frac{P_{\rm T}}{P} = \sqrt{\left(\frac{A_{\rm LR}}{A_{tra.}}\right)^2+\left(\frac{A_{\rm UD}}{A_{tra.}}\right)^2},$$

where $P_{\rm L}/P$ and $P_{\rm T}/P$ are the longitudinal and transverse components of the absolute polarization, respectively. $A_{\rm LR}$ and $A_{\rm UD}$ are the left/right and up/down asymmetry values, normalized by beam polarization, during the longitudinal period, respectively. $A_{tra.}$ is the left/right value, normalized by beam polarization, during the transverse commissioning period.

In 2005, the values of $P_{\rm L}/P$ obtained for the two beams were 0.995±0.001 and 0.989±0.002. This confirms the beams were fully longitudinally polarized.

Polarized proton collisions at $\sqrt{s} = 410$ GeV were also performed in 2005. Figure 2 shows the raw transverse spin asymmetries during the $\sqrt{s} = 410$ GeV running period. Transverse asymmetries were clearly seen at this high energy. Since similar neutron asymmetries were found at $\sqrt{s} = 200$ and 410 GeV, similar asymmetries are expected at higher energies. This result is promising for the transverse and longitudinal spin component measurements at $\sqrt{s} = 500$ GeV in the future.

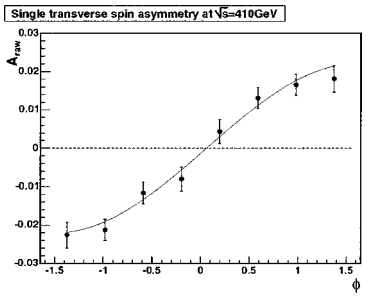

Fig. 2. Raw transverse asymmetries at $\sqrt{s} = 410$ GeV. The neutron asymmetry is expected to persist to 500 GeV.

*1 Department of Physics, Kyoto University
*2 Department of Physics, State University of New York at Stony Brook, USA
*3 Department of Physics, University of Colorado, USA

References

1) G. Bunce et al.: Annu. Rev. Nucl. Part. Sci. **50**, 525 (2000).
2) Y. Fukao et al.: RIKEN Accel. Prog. Rep. **36**, 232 (2003).
3) C. Adler et al.: Nucl. Instrum. Methods Phys. Res. A **470**, 488 (2001).
4) A. Deshpande et al.: RIKEN Accel. Prog. Rep. **37**, 246 (2004).

PHENIX silicon vertex detector upgrade project

Y. Akiba, J. Asai, A. Deshpande,[*1] D. E. Fields,[*2] H. En'yo, K. Fujiwara,[*3] Y. Goto, H. Kano, Z. Li,[*4] H. Ohnishi, Y. Onuki, V. L. Rykov, A. Taketani, M. Tanaka,[*5] J. Tojo, and PHENIX VTX Collaboration

We propose the construction of a silicon vertex tracker (VTX) for the PHENIX experiment at RHIC. The VTX will substantially enhance the physics capabilities of the PHENIX central arm spectrometer. Our primary aim is to carry out precise measurements of heavy-quark production (charm and beauty) in $A+A$, $p(d)+A$, and polarized $p+p$ collisions. These are key measurements that are required for future RHIC programs, both for studies of the dense partonic matter created in heavy-ion collisions and for the measurements of the nucleon spin-structure function.

The main physics topics addressed by the VTX are as follows.

- Probing high-density partonic matter
  - Open heavy-quark production
  - Energy loss of charm in dense matter
  - Thermal dileptons from dense matter
- Measurements of gluon spin structure of nucleon
  - $\Delta G/G$ with heavy-quark production
  - $\Delta G/G$ with γ-jet measurement
- Nucleon structure in nuclei
  - Gluon shadowing over broad x-range

The proposed VTX detector is shown in Fig. 1. The detector consists of two inner layers of silicon pixel detectors and two outer layers of silicon strip detectors. The pixel detector[1)] has been developed in collaboration with the ALICE group at CERN (RIKEN–ALICE collaboration). The pixel chips were used and they worked very well in the NA60 experiment. The silicon strip detector uses a novel "stripixel" sensor developed at BNL. The sensor is read out using the SVX4 chip developed at FNAL.

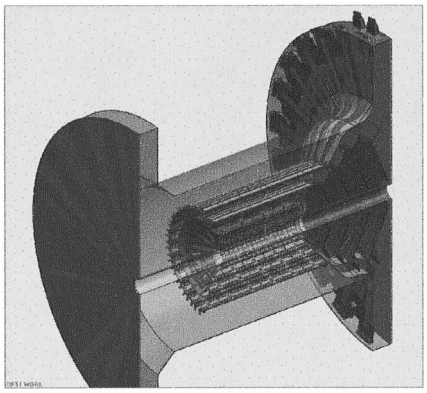

Fig. 1. The PHENIX VTX detector.

The main points of progress this year are as follows.

- We have a successful review of the project by BNL in January 2005. The review recommended the construction of the detector.
- New collaborators from Ecole Polytechnique, France, joined the project. They take responsibility of the Silicon PIxel Read-Out (SPIRO) board.
- Quality Assurance (QA) of the pixel chips at CERN and RIKEN[2)]: Many pieces of pixel sensor assemblies have been produced and being tested at RIKEN.
- Development of "pilot" ASIC for the pixel layers[3)]: The first version of the ASIC worked as designed. The second version has been fabricated.
- Development of a thin data bus for the pixel layers[4)]: A prototype bus has been fabricated.
- Development of a pixel detector assembly system[5)]: The assembly system will be used to fabricate the first prototype ladder.
- An extensive QA of the pre-produciton strip sensor was carried out at BNL[6)] and at U. New Mexico.[7)]
- The first prototype strip detector was fabricated. The detector was successfully read-out by a prototype Read Oout Card using SVX4.[8)]
- The mechanical design work of the VTX detector by LANL collaborators and an engineering company (HYTEC) has started.

*1 Stony Brook University, USA
*2 University of New Mexico, USA
*3 Niigata University
*4 Brookhaven National Laboratory, USA
*5 High Energy Accelerator Research Organization (KEK)

References

1) H. Ohnishi et al.: RIKEN Accel. Prog. Rep. **39**, 200 (2006).
2) K. Fujiwara et al.: RIKEN Accel. Prog. Rep. **39**, 207 (2006).
3) H. Kano et al.: RIKEN Accel. Prog. Rep. **39**, 211 (2006).
4) A. Taketani et al.: RIKEN Accel. Prog. Rep. **39**, 209 (2006).
5) Y. Onuki et al.: RIKEN Accel. Prog. Rep. **39**, 205 (2006).
6) J. Asai et al.: RIKEN Accel. Prog. Rep. **39**, 203 (2006).
7) D. E. Fields et al.: RIKEN Accel. Prog. Rep. **39**, 201 (2006).
8) J. Tojo et al.: RIKEN Accel. Prog. Rep. **39**, 212 (2006).

Development of the silicon pixel detector for PHENIX at CERN

H. Ohnishi, Y. Akiba, J. Asai, H. En'yo, K. Fujiwara, H. Kano, Y. Onuki, and A. Taketani

The relativistic Heavy Ion Collider (RHIC) at Brookhaven National Laboratory is a machine devoted to the investigation of two physics topics: highly dense nuclear matter created by relativistic heavy-ion collisions that may undergo a phase transition from normal nuclear matter to a new state of matter, i.e., quark gluon plasma (QGP); and the spin structure of the nucleon using polarized proton-proton collisions. Heavy-quark measurement (c and b quark) is a key measurement for investigating not only QGP formation but also nucleon spin structures because heavy quarks are mainly produced via gluon-gluon fusion at the collision energy at RHIC. Heavy-quark production is investigated by measuring single electrons using the present PHENIX detectors.[1] However, this measurement is limited by systematic uncertainties caused by large background contributions such as those from Dalitz decay of π^0 and η photon conversions; moreover, it is not possible to separate the charm and beauty contribution models. Therefore, a new vertex tracker, the silicon vertex tracker (VTX), that enables the precise measurement of heavy-quark production is proposed.

Various possibilities are investigated carefully in light of the following requirements.

- Detector should be working under the condition of a few tracks for proton-proton collisions to several hundreds of tracks in central heavy-ion collisions.
- All data in the detector should be read out within $40\,\mu$s, which is required by the PHENIX data acquisition system.
- Electrons from heavy-quark decay should have an offset on the order of $100\,\mu$m from the primary vertex position due to the short lifetime of heavy quarks. To separate such electrons from the major background, those coming mainly from the primary vertex position, the detector should have a tracking resolution of less than $50\,\mu$m.

To satisfy these requirements, the VTX will be built with four layers of the silicon detector, consisting of two inner layers with a silicon pixel detector and two outer layers with a silicon strip detector.

For the two inner layers, we decided to use the silicon pixel detector technology developed for the ALICE experiment at the Large Hadron Collider (LHC) at CERN. This silicon pixel detector is composed of two elements: One is a silicon pixel sensor ladder, consisting of four sensor arrays implemented in a linear arrangement on a single substrate, in which each sensor array consists of 32×256 matrixes with an area of $425 \times 50\,\mu\text{m}^2$ defined by p^+ implants on one side of n-type silicon. The other component is a silicon pixel readout chip that has 32×256 matrixes of readout electronics containing a preamplifier, shapers, a discriminator, a programmable delay and event buffers in each $425 \times 50\,\mu\text{m}^2$ cell. This readout chip is processed using radiation tolerant technology which stands up to 30 Mrad of radiation doses.

The final product pixel ladder has four readout chips interconnected with a pixel sensor via micro-interconnections with small balls of solders, which is known as "bump-bonding". A PHENIX full ladder consists of four 4-pixel-chip ladders in a linear arrangement. The first layer of the VTX consists of ten full pixel ladders and the second layer consists of twenty full pixel ladders surrounding a beam pipe. In total 120 4-chip ladders that consist of 480 pixel readout chips are required to fabricate full pixel detector layers.

The production of the silicon pixel ladder for PHENIX is in progress. Figure 1 shows the four bump-bonded ladders produced in our first batch of production.

Thirteen bump-bonded ladders have been produced and delivered to RIKEN thus far. Five more ladders are now being produced. According to our production schedule, all necessary bump-bonded ladders (150 ladders including spares) will be delivered by May-June 2006.

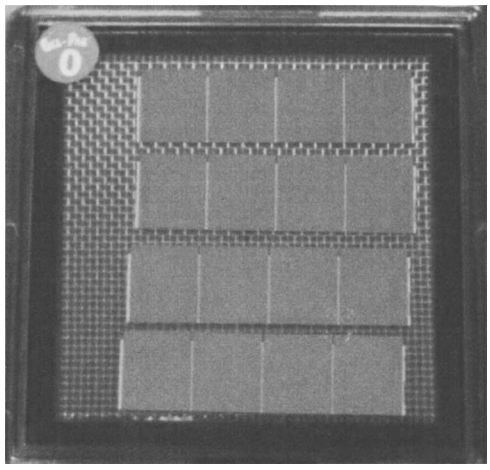

Fig. 1. First four delivered bump-bonded ladders.

Reference

1) S. S. Adler et al.: nucl-ex/0510047.

Evaluation of novel strip-pixel detectors for the silicon vertex tracker at PHENIX

C. Hægemann,* M. Hoeferkamp,* A. Zimmerman,* J. Turner,* M. Malik,* and D. E. Fields,*
for PHENIX VTX Collaboration

As a part of the upgrades for the PHENIX detector at RHIC, a silicon vertex tracking detector is planned. This detector will consist of two pixel layers followed by two strip-pixel layers in the barrel region, and four ministrip layers in the end-cap region. As a part of the development phase of the vertex detector, we have set up three sensor testing facilities at Brookhaven National Laboratory, at the State University of New York, Stonybrook, and at the University of New Mexico to characterize the preproduction sensors, and to develop our testing and quality assurance plans. Preliminary results from these tests are presented here.

The PHENIX experiment at RHIC consists of four spectrometer arms (two in the central rapidity region, and two in the forward rapidity regions), plus several global, event characterization detectors.[1] The two main physics motivations of the experiment are 1) to characterize the QCD state created in the collisions of heavy-ions and 2) to characterize the QCD state in the collisions of polarized protons.

Lacking presently in the PHENIX configuration is the ability to distinguish between particles coming from the primary vertex, and those coming from decay products of heavy-flavor mesons. To add this capability, PHENIX is currently building a silicon vertex tracking (SVT) detector,[2] schematically shown in Fig. 1. The design consists of a four-layer barrel, built from two layers of pixel detectors at 2.5 cm and 5 cm radii, plus two layers of projective "strip-pixel" detectors at 10 cm and 14 cm radii. The coverage of the barrel section of the detector is $-1.2 < \eta < 1.2$ and $\phi \cong 2\pi$. End-cap extensions with silicon ministrip detectors assembled into cones will add vertex tracking capabilities to the forward spectrometers with a coverage of $1.2 < \eta < 2.2$ and $\phi \cong 2\pi$.

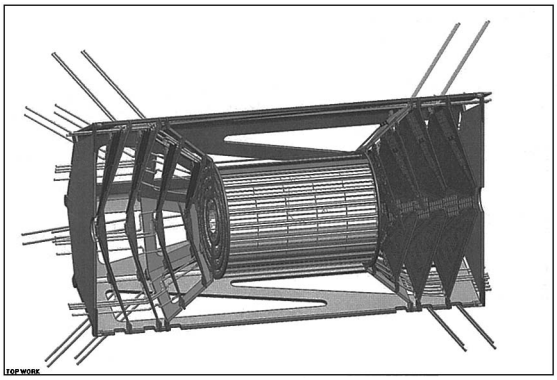

Fig. 1. Schematic layout and dimensions of the SVT, equipped with two pixel detector, and two strip-pixel detector barrel layers. Its end-cap extensions will be built from four ministrip detector cones per side.

Performance requirements for the SVT include a) high-precision tracking for displaced vertex measurement (40 μm DCA resolution) for heavy-flavor tagging; b) large-coverage tracking capability with adequate momentum resolution for jet studies; c) tracking capability in a high charged particle density $dN/d\eta = 700$ at $\eta = 0$ for heavy-ion physics; d) ability to withstand a high radiation dose of approximately 100 KRad over 10 years; e) read-out in high luminosity p+p running; and f) a low material budget to avoid multiple scattering and photon conversion for electron measurement by outer detectors. These factors drove the design to "strip-pixel" detectors in the outer two layers of the barrel detector.

The outer two layers of the silicon barrel require less precise position resolution, and in order to keep the channel count as low as possible, two-dimensional readout silicon strip detectors will be employed. The sensors currently proposed are based on a novel "strip-pixel" design developed at BNL.[3] The design uses 80 μm × 1 mm "pixels" formed by pairs of interleaved electrode spirals in a p-on-n material. The pixels are connected through 3 cm long lines in first and second metal layers, such that a strip-like projective read-out in two stereo coordinates is realized (see Fig. 2). Two strip-pixel arrays, each with 384 + 384 channels on $3 \times 3\,\mathrm{cm}^2$, are implemented on a single-sided 600 μm sensor. The read-out chips are placed on a flexible printed circuit board mounted on top of the sensor and are wire-bonded to the end contacts of the read-out lines on the periphery of the sensors.

As a part of the development phase of the vertex detector, we have set up three sensor testing facilities at Brookhaven National Laboratory, at the State University of New York, Stonybrook, and at the University of New Mexico to characterize the preproduction "strip-pixel" sensors, and to develop our testing and quality assurance plans. Initial tests that are performed on the sensor are as follows: a) measure current versus voltage on the test diodes and on 5% of the strips in order to identify the breakdown voltage of the p-n junction; b) measure capacitance versus voltage on the test diodes and on 5% of the strips in order to identify the full depletion voltage of the p-n-junction; c) measure the leakage current for each strip at full depletion voltage plus 100 V; and d) measure the capacitance for each

* University of New Mexico, USA

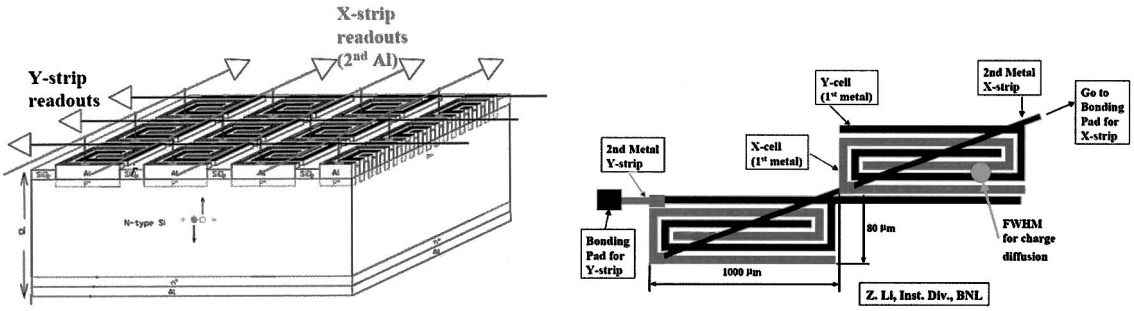

(a) (b)

Fig. 2. (a) Schematic drawing of the p^+ cathode structure of the strip-pixel sensor and its two-dimensional projective readout through lines on two metal layers. (b) Final design of the strip-pixel plaquette. All readout lines of the second metal layer are routed to the long edges of the sensor.

strip at full depletion voltage plus 100 V. These tests are necessary to determine the expected leakage current of the detectors and their expected behavior with radiation damage.

These "standard" tests were performed both before and after the sensor was diced from the wafer (containing three sensors). Figure 3 (a) shows the leakage current as a function of bias voltage for a single strip of a 500 μm thick preproduction sensor. The two curves are the raw (solid line) and temperature-normalized to 20 C (filled diamonds) curves for the same channel. The breakdown voltage was not reached at our limit of 500 V and the full depletion voltage was found to be $\approx$ 70 V. This was confirmed by the measurement of capacitance with bias voltage.

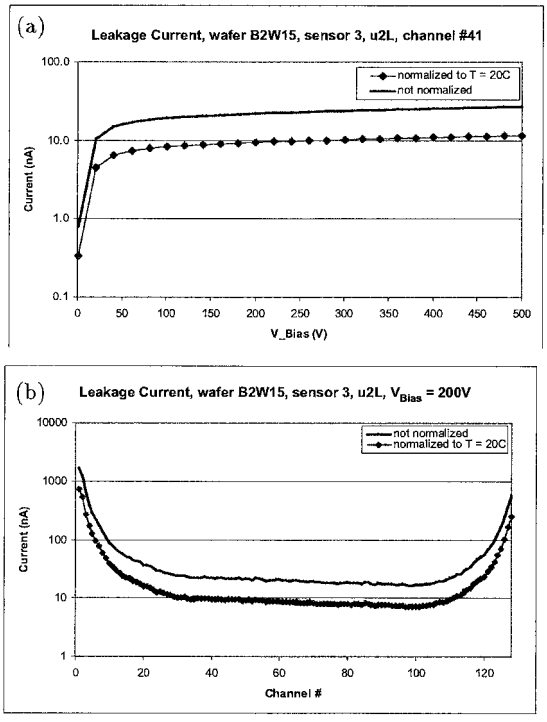

Fig. 3. (a) Leakage current as a function of bias voltage for a particular strip of a 500 μm thick preproduction sensor. The two curves are the raw (solid line) and temperature-normalized (filled diamonds) curves for the same channel. (b) Leakage current for 128 neighboring strips at constant bias voltage of 200 V. for the same 500 μm thick preproduction sensor. The two curves are againthe raw (solid line) and temperature normalized (filled diamonds) curves for each channel. The rise of the leakage current at the beginning and end of the set is explained in the text.

Figure 3 (b) shows the leakage current for a full set of 128 strips at a constant bias voltage of 200 V. The rise of the leakage current at the beginning and end of the set is due to the surface currents from neighboring strips not being grounded and is currently being studied by grounding groups of other strips.

In addition to these tests, we plan to conduct a radiation damage test by exposing the sensor to 200 MeV protons of known dose and repeating the previous tests to better understand the leakage current change with radiation dose. We will also conduct a laser charge sharing study, that will enable us to verify whether the preproduction design of the sensors meets the design requirements.

References

1) K. Adcox et al.: Nucl. Instrum. Methods Phys. Res. A **499**, 469 (2003).
2) C. Woody: Proc. 18th Winter Workshop on Nuclear Dynamics, Nassau, The Bahamas 2002-1 (EP Systema, 2002); J. M. Heuser: Nucl. Instrum. Methods Phys. Res. A **511**, 210 (2003); Y. Akiba: AIP Conf. Proc., **698**, 785 (2003); K. Tanida: Nucl. Instrum. Methods Phys. Res. A **549**, 75 (2005); A. Taketani: Nucl. Instrum. Methods Phys. Res. A **541**, 137 (2005).
3) J. Tojo et al.: IEEE Trans. Nucl. Sci. **51**, 2337 (2004); Z. Li et al.: Nucl. Instrum. Methods Phys. Res. A **541**, 21 (2005); Nucl. Instrum. Methods Phys. Res. A **535**, 404 (2004).

Silicon stripixel sensor test and fabrication of support frame for silicon pixel detector

J. Asai, Y. Akiba, A. L. Deshpande, D. E. Fields, H. En'yo, K. Fujiwara, Y. Goto, H. Kano, H. Ohnishi, Y. Onuki, A. Taketani, and J. Tojo

We are studying the characteristics of quark gluon plasma (QGP) and the spin structure of protons using the Relativistic Heavy Ion Collider (RHIC) at Brookhaven National Laboratory (BNL). PHENIX is a detector for measuring particles in $A + A$, $p(d) + A$, and polarized $p + p$ collisions. A silicon vertex tracker (VTX) will be installed to upgrade PHENIX.[1] The VTX can identify the decay of heavy quarks by the precise measurement of decay vertex and works as a large-solid-angle detector. It consists of a barrel detector and a forward detector. In the barrel detector, the inner two cylindrical layers use a silicon pixel detector and the outer two cylindrical layers use a silicon stripixel detector. Four layers use a ministrip detector in the forward detector. In this article, we report the establishment of a quality assurance (QA) station for the silicon stripixel detector and the development of a test prototype support frame for the silicon pixel detector.

We established the QA station for the silicon stripixel sensor[2] at RIKEN BNL Research Center as shown in Fig. 1.[3] The main procedures of the QA program are the visual inspection and characterization measurement of each silicon sensor using a semiautomatic probe station in a clean room. The probe station uses a probe card with 128 needles to touch the readout pads of the strip sensor. The bias-voltage dependences of the leakage current (I-V) and capacitance (C-V) of all 1,536 readout pads on a single sensor are measured. The preproduction sensors[4] of two companies, SINTEF in Norway and Hamamatsu Photonics in Japan were tested. In the visual inspection, there were bad alignments of through holes in some sensors of SINTEF. The sensors of Hamamatsu Photonics passed the visual inspection. The I-V and C-V of a single strip were measured as shown in Figs. 2 and 3, respectively, while the adjacent 127 strips were grounded to simulate realistic operation of the sensors. The typical leakage current at full depletion voltage was 1.5 nA and the capacitance was 1 pF. Breakdown did not occur at 450 V. After the test, the sensor wafers were diced with a laser dicer at BNL Instrumentation Division and were sent to RIKEN Wako to be connected to an SVX4 readout chip[5] by wire bonding. The charge-sharing property was studied by irradiating infrared (1060 nm wavelength) pulsed laser lights to the detector and reading out signals for the simulation of incident charged particles.[6] The QA of 400 mass production sensors will be carried out at BNL, University of New Mexico[7] and Stony Brook University.

We have begun production of the first silicon pixel detector. The pixel detector consists of a silicon sensor, a readout chip, a readout bus,[8] a support frame,

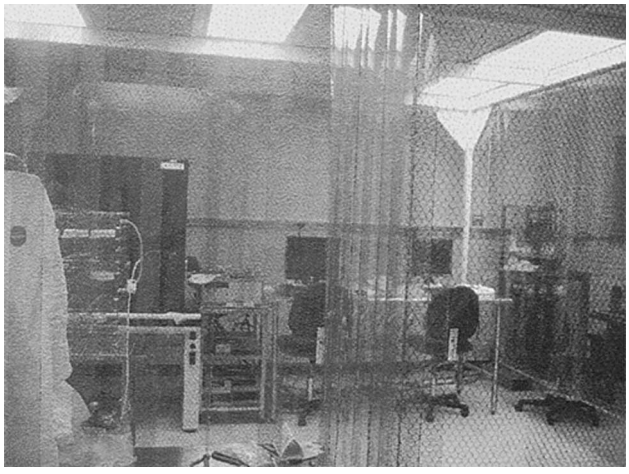

Fig. 1. QA station in clean room at RIKEN BNL Research Center.

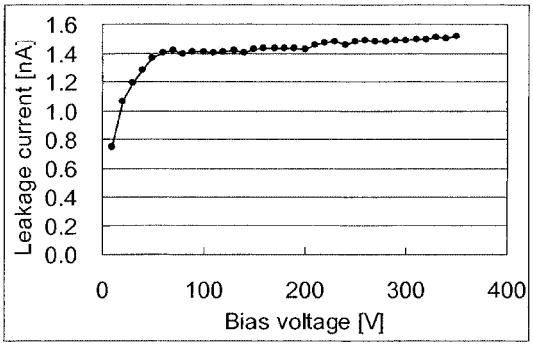

Fig. 2. Bias-voltage dependences of leakage current.

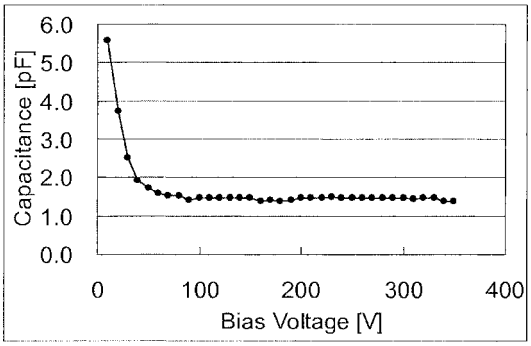

Fig. 3. Bias-voltage dependences of capacitance.

and a readout card. One readout unit of a half stave uses a four-readout-chip ladder with a bump bonded to each silicon sensor. The four-sensor ladder is mounted on the support frame.[9] To minimize multiple scattering, the support frame should have a low material budget. On the other hand, a high thermal conductivity is necessary, because the cooling pipe is designed to run under the support frame. We selected carbon-carbon (C-C) material. For the test of the prototype structure, we made a C-C frame with a thickness of 500 μm, and a size of $15 \times 200\,\mathrm{mm}^2$, and the directions of the carbon fiber intersect the plane shown in Fig. 4 (a). The readout chip consumes approximately 0.8 W/chip. The omega board, whose cross section is shown as the character "Ω" (Fig. 4 (b)) and the cooling aluminum duct for water cooling are placed on the C-C frame. The omega board is made of isotropic graphite material and formed by cold isostatic pressing (CIP); it has a thickness of 500 μm, a size of $15 \times 200\,\mathrm{mm}^2$, and a radius of 5 mm as shown in Fig. 4 (b). A CIP material is also necessary as a high thermal conduction material. Carbon powder may be emitted from the surface of C-C and CIP materials, in which case lamination is required. We selected a parylene coating of 5 μm thickness. The coating is produced by chemical vapor deposition using poly-para-xylylene resin.

Fig. 4. C-C support frame (a) and omega structure (b).

We will test the first production pixel detector with a beam or beta-ray source to measure the efficiency at the beginning of 2006.

References

1) Y. Akiba et al.: RIKEN Accel. Prog. Rep. **39**, 199 (2006).
2) Z. Li et al.: Nucl. Instrum. Methods Phys. Res. A **518**, 300 (2004).
3) J. Asai et al.: RIKEN Accel. Prog. Rep. **38**, 235 (2005).
4) J. Tojo et al.: RIKEN Accel. Prog. Rep. **38**, 231 (2005).
5) http://www-cdf.lbl.gov/users/mweber/svx4.
6) J. Tojo et al.: RIKEN Accel. Prog. Rep. **39**, 212 (2006).
7) D. E. Fields et al.: RIKEN Accel. Prog. Rep. **39**, 182 (2006).
8) A. Taketani et al.: RIKEN Accel. Prog. Rep. **39**, 209 (2006).
9) Y. Onuki et al.: RIKEN Accel. Prog. Rep. **39**, 205 (2006).

Silicon pixel detector assembly for PHENIX upgrade

Y. Onuki, Y. Akiba, J. Asai, H. En'yo, K. Fujiwara,* H. Kano, H. Ohnishi, A. Taketani, and PHENIX VTX Collaboration

The Relativistic Heavy Ion Collider (RHIC) has been constructed at Brookhaven National Laboratory (BNL) to provide collisions of polarized proton-proton $\sqrt{s}$ up to 500 GeV and heavy-ion $\sqrt{s_{NN}}$ up to 200 GeV. The RHIC ring consists of two storage rings and 6 intersection points. The RHIC ring has a circumference of 3.8 km. The designed luminosity is 2×10^{32} cm^{-2}s^{-2} in the 500 GeV proton collisions, and the maximum number of bunches is 120.

The Pioneering High Energy Nuclear Interaction eXperiment (PHENIX) detector has been installed at one of the 6 intersection points. The PHENIX detector consists of 2 central arms and 2 muon arms. Central arms have charged particle and photon detection systems. Muon arms have a muon detection system.

The silicon vertex tracker (VTX) for the PHENIX is planned to be installed in summer 2009. VTX will substantially enhance the physics capabilities of the PHENIX central arm detectors. The purpose of the upgrade is to enable the precise measurement of heavy quarks, which carry direct signals from a Quark Gluon Plasma in heavy ion collisions, and fundamental information on gluon polarization in polarized proton-proton collisions. The VTX will surround the beam pipe, where the collisions occur. VTX consists of two major parts; the inner two layers are pixel-type sensors and the outer two layers are strip-type sensors. The radii of the four layers are 25 mm, 50 mm, 100 mm and 140 mm, respectively.

The inner two pixel layers have 10 and 20 pixel sensor modules (staves) in the ϕ direction. RIKEN is assigned to fabricate all staves. A stave is formed of 4 sensor ladders,[1,2] each consisting of a silicon pixel sensor matrix of 256 × 128 pixels and 50 × 425 μm^2 in size as a unit. A sensor ladder is a hybrid device consisting of a pixel sensor matrix and 4 readout chips interconnected by bump bonding with micro-solder balls.

A stave can be separated into 4 components: a bus[3] which is a flexible circuit board made of aluminum and kapton, 4 sensor ladders, a support[4] made of carbon/carbon (C/C) composite, and a cooling pipe, as shown in Fig. 1. Each component is glued by two-component epoxy paste adhesive, Araldite AW106/HV953U, which is known to be a radiation-hard adhesive and commonly used in high-energy physics. Boron-nitride (BN) powder, obtained from Denka Co., is added to the glue to improve the thermal contductivity between the sensor ladder and the support. The details of cooling are under investigation.

The pixel sensor adopts a binary readout method.

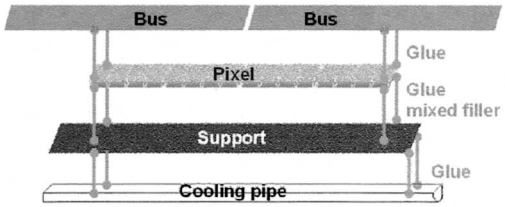

Fig. 1. Stave components.

The general intrinsic resolution of the binary sensor is known to be $L/\sqrt{12}$, where L is pixel size. It can be applied to our pixel sensors, and the resolution is about ∼15 μm. In order to minimize off-line alignment by using real tracks, precise alignment of the assembly is required. We took into account a safety margin and aimed for an assembly precision of 10 μm. A stave fabrication method with high assembly precision and stable quality control should be established before actual production of the stave. In particular, we considered the alignment of 4 sensor ladders arranged in a line and to glue the aligned sensor ladders and support. It is difficult to align sensor ladders as there is no reliable alignment mark on the sensor ladder except for the bonding pad for bus connection. Also, we can't use the edge of the sensor ladder because the dicing position varies about ∼40 μm from lot to lot. The only way to confirm that the 4 sensor ladders are well aligned at 10 μm is to use the pad as an alignment mark because it has sufficient position precision relative to the pixel sensor matrix. We need specific jigs equipped with a high-magnification microscope, precise moving stage with a gauge, a vacuum chucking mechanism for the sensor ladder, and a glue dispenser robot. We have consulted with Daiya Seiki Co., a precision engineering company in Nagano, to make the jigs for alignment and assembly of the stave.

Figure 2 shows the alignment jig which aligns the

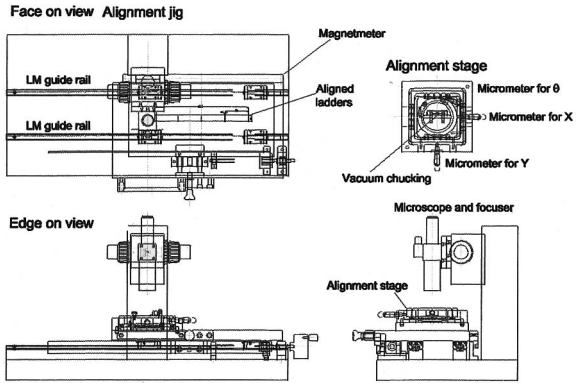

Fig. 2. Alignment jig design.

* Science and Technology, Niigata University

sensor ladder along a straight line. The jig has a microscope and precise X-Y-θ stage with vacuum chucking and linear motion (LM) rails with a high-accuracy running parallelity of $< 10\,\mu$m/m. The sensor ladder is chucked by the stage and moved to the proper position while viewing the pad through the microscope, one by one. Figure 3 shows the aligned sensor ladder positions. The space between sensor ladders, Δx in Fig. 4, is observed to be of μm order using the magnetometer equipped with LM rails. The precision of the space is permitted to be within $\Delta x < 50\,\mu$m at minimum in Fig. 3, The offset between sensor ladders, Δy, is observed with the microscope by running the stage along the LM rails. Aligned sensor ladders are checked using the Mitsutoyo 3D vision measuring machine shown in Fig. 4, and are confirmed to be aligned within the permissible range before gluing.

After alignment, the 4 sensor ladders are glued to the C/C support. The glue, Araldite AW106/HV953U, is added with BN filler to improve the coefficient of thermal conductivity (CTC) and is dispensed uniformly by a programmable automatic dispenser robot made by Musashi Engneering Co. and shown in Fig. 5. Each base laid on the aligned sensor ladders and support

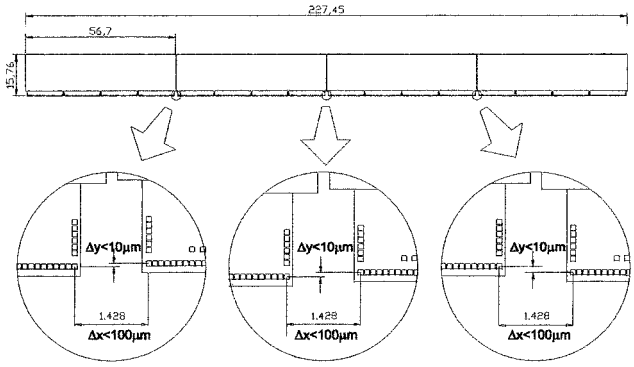

Fig. 3. Position of sensor ladders in a stave.

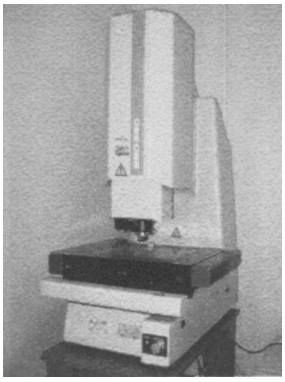

Fig. 4. Mitsutoyo 3D vision measuring machine.

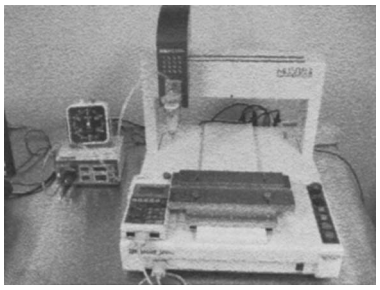

Fig. 5. Musashi glue dispenser robot.

has a linear bush and linear bush pin. Two bases are glued together. The glued position of sensor ladders and support is determined from the difference between the bush and pin radii, which is typically on the $\sim$5 μm level.

The bus is also glued onto the top of the sensor ladders. The gluing procedure is basically the same as that for the support. The bus has several alignment holes. The position accuracy for gluing the bus is determined by the manufacturing precision of the holes. The precision is 50 μm. The accuracy is sufficient to perform wire bonding between sensor ladders and the bus.

These stave components are made of various materials. Therefore we must consider the properties, thermal conductivity, thermal expansion and Young's modulus, shown in Table 1, to maintain a constant temperature of the assembly room. We are commissioning Hayashi Seimitsu Co. to assemble the stave in their highly controlled clean room kept at 24 ± 1 degrees.

In summary, the assembly of the PHENIX/VTX detector has been discussed and is now in progress under the cooperation of researchers and companies. The first trial of manufacturing the stave will be accomplished in December 2005. Furthermore, we are planning to perform the beam test in the spring of 2006.

Table 1. Material properties.

	density [g/cm^3]	CTC [W/m/K]	CTE [ppm/K]	Radation length[cm]	Young's modulus[GPa]
Si	2.34	126	2.6	9.36	113
Al	2.7	200	23	8.9	70
BN	2.08	23	3.0	20.8	55
Cu	8.96	400	17	1.43	117
C/C	1.95	$\parallel$700$\perp$20	$\parallel$-0.8$\perp$10	21.8	$\parallel$294
Kapton	1.42	0.2	10$\sim$20	28.7	$\sim$30
Epoxy	1$\sim$4	0.2$\sim$3	20$\sim$100	4$\sim$28.6	0.4$\sim$10

References

1) K. Fujiwara: RIKEN Accel. Prog. Rep. **38**, 228 (2005).
2) H. Ohnishi: RIKEN Accel. Prog. Rep. **38**, 230 (2005).
3) A. Taketani: RIKEN Accel. Prog. Rep. **38**, 233 (2005).
4) J. Asai: RIKEN Accel. Prog. Rep. **38**, 235 (2005).

Evaluation of pixel readout chip and sensor hybrid for PHENIX upgrade

K. Fujiwara,* Y. Akiba, J. Asai, J. M. Heuser, H. En'yo, H. Kano,
T. Kawasaki,* H. Ohnishi, Y. Onuki, and A. Taketani

The PHENIX experiment at Relativistic Heavy Ion Collider (RHIC) of Brookhaven National Laboratory will be upgraded with a novel four-layer silicon vertex tracker (VTX) by summer, 2009. The detector can enhance experimental capabilities in both the heavy-ion and the polarized proton-proton programs at RHIC. The silicon vertex tracker will identify heavy quark productions by measuring displaced decay vertices, and will reconstruct jets with the acceptance of almost full azimuthal coverage over the rapidity of $|\eta| < 1.2$. It has a high spatial resolution of 30–50 μm for the distance to the closest approach.[1] Here, we report the status of the evaluations of the readout chips and the silicon pixel sensor ladder in the PHENIX Silicon Pixel Detector.

The inner two layers are built from 30 staves with pixel sensors placed cylindrically covering approximately 22 cm along the beam direction. The first layer has a 2.5 cm radius consisting of 10 staves and the second layer has a 5 cm radius consisting of 20 staves. One stave is divided into two half-staves and a half-stave has two sensor ladders. The sensor ladder shown in Fig. 1 consists of a single sensor and four readout chips, which are bump-bonded to each other using microscopic solder balls of 15 μm diameter. The size of the sensor ladder is 15.6 mm $\times$ 57 mm and the total thickness is $\sim$ 350 μm. For the two layers, 120 sensor ladders will be installed.

Because the sensor ladders will be used under a high-level-radiation environment in the experiment, the radiation hard devices developed by the CERN Micro Electronics Group for the ALICE experiment were chosen. (The expected total dose is between 100 krad and 1 Mrad in 10 years.) The sensor chip is based on the $P^+/N/N^+$ silicon with the thickness of 200 μm fabricated by CANBERA.[2] It is partitioned into four active areas, each of which has 32 columns (z) $\times$ 256 rows (ϕ) with pixels of 425 μm (z) $\times$ 50 μm (ϕ). For the readout chip, the ALICE1LHCb readout chips are used, which is designed using the IBM 0.25 μm CMOS process of the radiation hardened technology and has a maximum radiation tolerance of up to 30 Mrad. The size of the chip is 15.6 mm $\times$ 13.7 mm with 150 μm thickness. One chip has 8,192 (32 $\times$ 256) input channels, each of which processes an input signal individually. A raw signal from each pixel is preamplified and discriminated with configurable threshold level. The discriminated binary signal is delayed with programmable duration, and then, stored to be read out by a downstream data acquisition system. The chip has 42 internal 8-bit Digital-to-Analog Converters (DACs) for controlling the threshold of discriminators and various timings. All configurations are set via the JTAG serial interface (IEEE std. 1149.1-1990). The chip is operated using a 10 MHz clock; therefore, the maximum readout speed is 25.6 μsec/chip with a 32-bit line.[3]

Four hundred and eighty ALICE1LHCb readout chips will be used for the construction of the PHENIX silicon pixel detector. Because the yield rates of the chips are less than 50%, we have carried out tests to select fully functional readout chips in the state of wafer.[4] Then, a single sensor and four selected readout chips are interconnected by bump-bonding, and the same testing procedure is performed. Additionally, functionality tests of the sensor ladder with real signals from the sensors induced by β-rays are performed to check the total functionalities of the sensor ladder. These functionality tests are performed at the semi-automatic probe station (SUSS MicroTec Co., Ltd., type PA200) at RIKEN (Fig. 2). In these tests, control signals and test pulses are injected into the chip

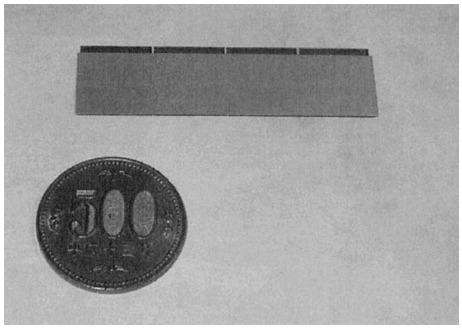

Fig. 1. Silicon pixel sensor ladder.

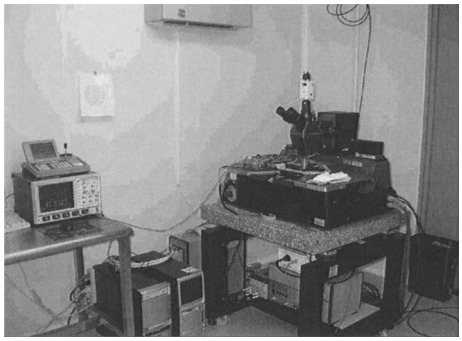

Fig. 2. Semiautomatic probe station at RIKEN.

* Graduate school of Science and Technology, Niigata University

and digital information is read through thin needles touching the bonding pads on the readout chip.

Firstly, all chips are classified according to the following five conditions to select fully functional chips. 1) The current consumed by the analog circuit must be less than 350 mA. The current consumed by the digital circuit must be less than 270 mA. 2) JTAG must be functional. 3) The DACs must be sufficiently linear; the linearities are confirmed by plotting the responses. 4) The global threshold of the 8,192 channels must be less than 2,000 e^-, which is 1/7 of the typical signal caused by a minimum ionizing particle; global threshold on a chip is adjusted so that the counting rate without input signal will be sufficiently low (≤ 1 count/min). Then, output rates are measured by increasing the amplitude of calibrated input pulses. Output rate increases at the threshold level with a finite slope. From the central position and slope of the rise, threshold and noise levels are obtained in the unit of e^-. 5) The number of defect pixels must be less than 82; defect is pixels are pixels having no output even though a sufficiently large test signal is injected into the input.

From the result of the test of the readout chips, the chips are classified into three classes (Classes 1, 2, 3). Class-1 chips are defined as chips which satisfy all the above conditions. They are of good quality for the construction of sensor ladders. Class-2 chips satisfy conditions 1, 2 and 3 only. They can be used for an electrical test for prototypes. The other chips are classified as Class-3 chips. At present, 1,720 chips (20 wafers) have been probed. The results are shown in Table 1. We obtained 605 Class-1 chips (35% of the tested chips), which is sufficient for the construction of the VTX. A readout chip without a sensor chip has a typical global threshold of 1,700 e^- and a typical noise level of 120 e^-.

Secondly, using the Class-1 chips, sensor ladders are assembled and the same test is performed. Typically, the global threshold is 2,700 e^- and the standard deviation of the 8,192 channels on one chip is 220 e^-. The mean noise level is 160 e^-. It seems that the increase in noise level is due to additional noise from a sensor chip. The number of electrons induced by the minimum ionizing particles in the silicon sensor with the thickness of 200 μm is approximately 14,000 e^-. Consequently, the signal-to-noise ratio is approximately 90.

Table 1. The result of wafer probing.

Class-1	35 %	605 chips
Class-2	10 %	168 chips
Class-3	55 %	947 chips

Finally, total functionality, including electrical functionality between a sensor and readout chips is tested by a β-ray source. An inverse bias of 50 V, which is well more than the full depletion voltage ($\sim$ 10 V), is applied to the surface of the sensor using a thin needle. Then, the sensor is irradiated with β-rays from a ^{90}Sr checking source and its signals are processed by electrical circuits in a readout chip. The results are shown in Fig. 3. White dots are caused by pixel defects, the corresponding channels of the readout chips, or the interconnection between readout chip and sensor. More than 99% pixels work on the sensor ladder. Currently, 18 sensor ladders have been assembled. Four sensor ladders have been probed at CERN and 7 sensor ladders have been probed at RIKEN. One sensor ladder of the probed sensor ladders has one broken readout chip. One sensor ladder of the probed sensor ladders has more than 1% of missing bump-bondings. Two sensor ladders of the probed sensor ladders always have noisy pixels on the chips.

In summary, we have tested the performance of 1,720 chips for the VTX construction. As a result, 605 Class-1 chips were obtained. Eighteen sensor ladders have been assembled. Eleven sensor ladders have been probed. Four sensor ladders of the probed 11 sensor ladders have defects. By the end of March 2006, we will obtain 36 sensor ladders. Early in 2006, we will perform the prototype half-stave[5] test. Data-taking performance and detection efficiency will be checked in the test.

References

1) Y. Akiba et al.: RIKEN Accel. Prog. Rep. **39**, 199 (2006).
2) V. Manzari et al.: J. Phys. G **30**, S1091 (2004).
3) W. Snoeys et al.: Nucl. Instrum. Methods Phys. Res. A **466**, 355 (2001).
4) P. Riedler et al.: Nucl. Phys. A **501**, 111 (2003).
5) Y. Onuki et al.: RIKEN Accel. Prog. Rep. **39**, 205 (2006).

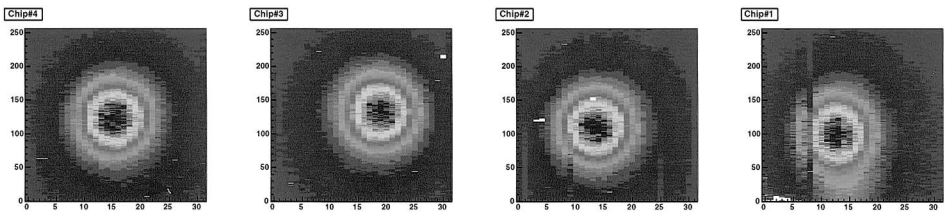

Fig. 3. Inter-connection test result of sensor ladder.

Development of PHENIX PIXEL bus

A. Taketani, Y. Akiba, J. Asai, H. En'yo, K. Fujii,[*1] K. Fujiwara,[*2] Y. Goto, J. M. Heuser, H. Kano, M. Kogo,[*3] T. Kawasaki,[*2] H. Maeta,[*1] H. Ohnishi, Y. Onuki, M. Tanaka,[*4] M. Sekimoto,[*4] and S. Watanabe[*2]

A silicon tracker will be implemeted in the RHIC PHENIX experiment. The main purpose of this new detector is to identify heavy flavor quark production in polarized proton collisions and heavy ion collisions by measuring the distant closest approach, since heavy flavored mesons have a longer lifetime than light mesons, which are 100 to 500 μm. We use two different sensors in this detector[1]: the inner two layers are pixel sensors and the outer two layers are strip sensors.

The detailed structure of the pixel part is described in Ref. 2. The signals from the pixel sensor are digitized at readout chips[3] and then propagate to the SPIRO board, which multiplexes 8 readout chips to the next stage of the DAQ system. The SPIRO board will be located at the endcap part of the PHENIX detector, which is 40 cm to 60 cm away from the pixel sensors. Hence, fine-pitch flexible printed circuit boards are used in these connections as readout buses.

The detector is located at the innermost part of the PHENIX central arm. The material thickness of the detector should be minimized to avoid electron generation upon photon conversion, and to attain better resolution for distant closest approach mesurements. Also, the PHENIX DAQ system requires a 20 kHz readout speed for each subsystem. The pixel part has a total of 3.9 M channels. Therefore, the readout bus has 196 lines, including 128 parallel data lines, control lines, reference voltage lines, and sensor bias voltage lines. The sensor size is 1.55 cm $\times$ 5.7 cm, so the bus should be the same width. The thinner part part of the bus is 25 cm to minimize the material budget in the central detector acceptance region. The reminder of the bus can be slightly thicker, so we can use the industry-standard Cu-polyimide bus, the Cu-extender. These two types of bus will be connected by wire bonding. High-density connectors will be used as the connection between the Cu-extender and the SPIRO board.

In order to satisfy the above requirements, we have been developing an Al-polyimide-based bus, because the radiation length per unit thickness of Al is about 1/6 that of Cu. We established a basic technique of fabricating the bus and discussed the detailed design rules[4] last year. Then the layout of a 1.5-cm-wide bus was designed. Unfortunately, the manufacturing company became bankrupt before the Al-polyimide based bus could actually be fabricated.

For a total electronics test of connecting the sensor hybrid with bump-bonded readout chips, readout bus, Cu-extender, and SPIRO board, we fabricated a 3 cm Cu-polyimide bus instead of the 1.5 cm Al-polyimide bus. The Cu-polyimide bus can be fabricated by industry-standard technology without R&D effort. The layout was designed on the basis of the existing 1.5-cm-wide design. Figure 1 shows the fabricated 3-cm-wide Cu-polyimide bus.

The SPICE model[5] is used to evaluate the bus peformance, such as signal propagation, bus impedance, and crosstalk. In this simulation, the bus length is 25 cm, signal lines are 70 μm wide with a 50 μm space, and polyimide films among the layers are 50 μm thick. Figure 2 represents the propagation performance and cross talk. The signal shape at the receiving end is good enough for GTL-level operation and crosstalk to adjacent lines is 50 mV, which is much smaller than the 0.8 V of GTL H/L logic level difference. The characteristic impedance is calculated to be 15 to 100 Ω.

We have been developing a readout bus for the PHENIX pixel detector. It is required to be of fine pitch and low material budget. We fabricated 3-cm-wide bus with Cu and polyimide for electrical test purposes. An Al-polyimide bus has been developed and its performance has been evaluated on the basis of a simulation.

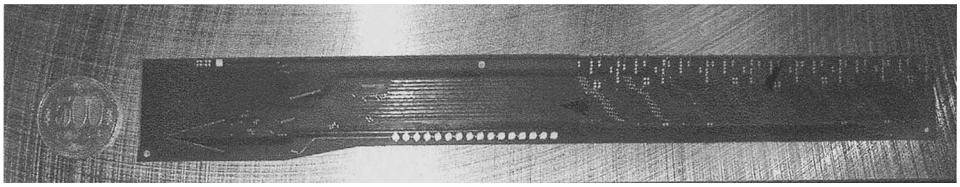

Fig. 1. A 3-cm-wide Cu-polyimide bus.

*1 Hiroshima Kokusai Gakuin University
*2 Niigata University
*3 Tokyo Metropolitan College of Aeronautical Engineering
*4 High Energy Accelerator Research Organization

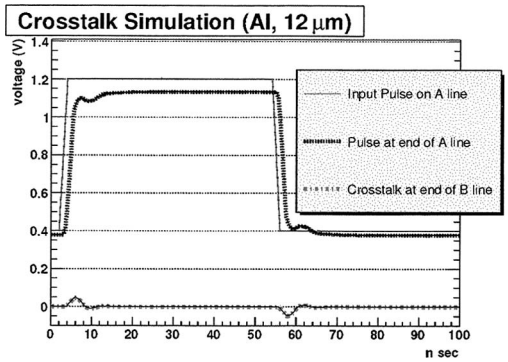

Fig. 2. Propagation and crosstalk for Al-polyimide bus.

References

1) Y. Akiba et al.: RIKEN Accel. Prog. Rep. **38**, 227 (2005).
2) J. M. Heuser et al.: RIKEN Accel. Prog. Rep. **37**, 250 (2004).
3) K. Fujiwara et al.: RIKEN Accel. Prog. Rep. **38**, 228 (2005).
4) A. Taketani et al.: RIKEN Accel. Prog. Rep. **38**, 233 (2005).
5) Avant! Corporation: Star-HSPICE Manual (1988).

Developments and tests of PHENIX pixel detector readout system

H. Kano, A. Taketani, H. Ohnishi, Y. Akiba, K. Fujiwara,* Y. Onuki, J. Asai, and H. En'yo

The PHENIX experiment is expected to be upgraded in 2009. Several new detector systems will provide extended detection capabilities in heavy-ion and polarized proton-proton collisions when RHIC reaches full operation at the designed luminosity in the next few years. The main PHENIX upgrade involves a new silicon vertex tracker installed between the pole faces of the central magnet. The silicon vertex tracker consists of pixel and novel microstrip sensors. The pixel detectors in the inner layer are essential for resolving the high track densities in heavy-ion collisions.

The block diagram of the PHENIX pixel detector readout system is shown in Fig. 1. The right-hand side shows the electronics located in the control room, whereas the left-hand side shows the on-detector electronics. Communication between the control room and the detector is via two optical fibers, one carrying the clock signal, the other carrying trigger, configuration, and control signals. Data transmission from the detector to the control room is performed via a 1.6 Gbps optical-fiber link.

The main components of the on-detector readout electronics are ASICs. All the ASICs have been developed by IBM 0.25μ CMOS technology using radiation-hardening techniques. Precautions have been taken to reduce malfunction due to single-event upsets. The digital-pilot ASIC performs the optical-to-electrical conversion of the incoming clock and data signals, initiates the readout sequence in the readout chips, and sends data to the 1.6 Gbps Ethernet-like serializer chip GOL.[a] We have modified the digital-pilot ASIC[1] based on the ALICE chip architecture,[2,3] which has an extended data bus width (16-bit to 32-bit) for PHENIX. The first version of the chip successfully worked well. Then second version of the chip is designed and fabricated with new features that include parity check, trigger counter, and additional power/ground pins for stable operation.

The test system for the digital-pilot ASIC is shown in Fig. 2. The PC sends dummy hit patterns and control signals to the digital-pilot ASIC via a pulse pattern generator module, and compares between a dummy hit pattern and the output of the ASIC using a FIFO module. In this test for the first version of the chip, all the functions of the modified digital-pilot ASIC worked well.

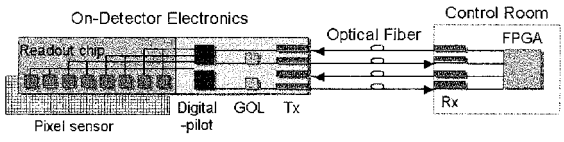

Fig. 1. Block diagram of PHENIX pixel detector readout system.

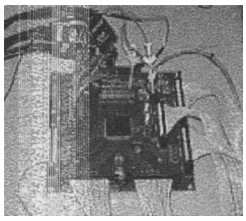

Fig. 2. Picture of PHENIX digital-pilot chip test board.

In the PHENIX pixel optical link between the control room and on-detector electronics, a serializer is used to encode 32-bit words in a serial stream. The stream rate is up to 1.6 Gbps. We developed the test system with GOL and a Vertex-2 pro FPGA with 8b/10b or CIMT[4] encoding (shown in Fig. 3). This system shows a low error rate ($< 10^{-15}$) at 1.6 Gbps (8b/10b and CIMT). This is the first CIMT link system to be realized at the 1.6 Gbps data rate.

We have been developing the PHENIX pixel readout system. The first version of the digital-pilot chip was fabricated and confirmed to work. The second version was fabricated to achieve stable operation.

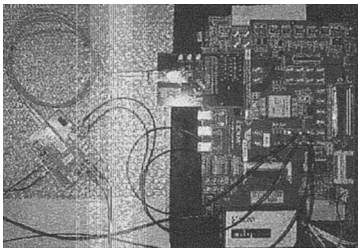

Fig. 3. Picture of test system for optical link system.

* Niigata University

a) http://proj-gol.web.cern.ch/proj-gol/

References

1) H. Kano et al.: RIKEN Accel. Prog. Rep. **38**, 237 (2005).
2) P. Chochula et al.: Nucl. Phys. A **715**, 849 (2003).
3) A. Kluge et al.: CERN 2001-005, 95 (2001).
4) C. Yen et al.: Hewlett-Packard J. Oct. 1992, 736 (1992).

Development of silicon stripixel detector for PHENIX experiment

J. Tojo, Y. Akiba, J. Asai, A. Deshpande,[*1] H. En'yo, D. E. Fields,[*2] Y. Goto, Z. Li,[*3] and M. Sekimoto[*4]

A silicon vertex tracker (VTX) for the PHENIX experiment in the Brookhaven National Laboratory (BNL) has been proposed for enhancing the physics capabilities of the baseline detector system. An overview of the PHENIX detector and the VTX upgrade project is given in Ref. 1 and Ref. 2, respectively. In this article, we report the development of a silicon stripixel detector for the two outer barrel layers of the VTX.

The silicon stripixel detector has an outstanding feature of two-dimensional position sensitivity only for single-sided processing.[3] A combined structure of both pixels and strips is formed on one side of the detector. The two-dimensional position sensitivity is achieved by charge-sharing between two interleaved electrodes arranged in each pixel. Collected charges in interleaved electrodes are projectively read out by strips.

The stripixel detector for the PHENIX experiment has been designed and prototyped in collaboration with the BNL Instrumentation Division. We have studied in detail the performance of the prototype sensors in static electrical tests[4] and beam/source tests.[5] On the basis of those studies, we have carried out the preproduction of the sensors.[6] The important developments are the construction of a prototype detector with the preproduction sensor and a readout electronics with the SVX4 chip[7] used in the VTX and the evaluation of detector leakage current, signal-to-noise ratio (S/N) and the charge-sharing property.

Figure 1 shows the prototype detector fabricated for this evaluation. The preproduction sensor integrated in the detector was processed by Hamamatsu Photonics in Japan. The sensor thickness was 625 μm. The static electrical test of the sensor was performed at the RIKEN BNL Research Center.[8] The sensor was mounted on a printed circuit board of 2 mm thickness. A part of the sensor backplane was glued to the base board using a room-temperature curing conductive epoxy (Loctite 3888) to apply a bias voltage. Two electronic hybrids, each of which contained three SVX4 chips, were used to read out one-half of the sensor and were mounted on the base board. The hybrid backplane was glued to the base board with a room-temperature curing nonconductive epoxy (Araldite 2011). The readout pads on the sensor were electrically connected to SVX4 chips by wire-bonding with a 25-μm-diameter aluminum wire. The electronic hybrids were connected to a prototype control card and a front-end module compatible with the PHENIX DAQ system.

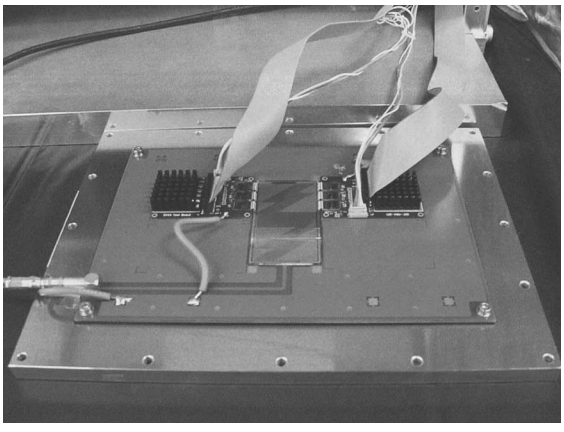

Fig. 1. Photograph of prototype silicon stripixel detector.

Total leakage current in the detector with 768 strips wire-bonded to SVX4 chips was measured to be 0.31 μA at an operating temperature of 19.4°C and the full depletion voltage was 120 V, which corresponded to 0.40 nA per strip on average. The maximum leakage current per strip acceptable in the PHENIX detector operation was estimated to be 15 nA, at which leakage current did not saturate the preamplifier of the SVX4 chip with a dynamic range of 200 fC. The measured leakage current was sufficiently small to operate the detector without the preamplifier saturation.

The noise performance of the detector was evaluated by adjusting the preamplifier rise time and FET bias current in SVX4 chips. The gain in SVX4 chips was calibrated by externally injecting charges to the preamplifier. Figure 2 shows a preliminary result for noise measured in one of the SVX4 chips in the detector. There was a function of real-time pedestal subtraction (RTPS) implemented in the SVX4 chip to suppress common mode noise.[7] The effect of RTPS is also presented in Fig. 2. The equivalent noise charges defined by the root-mean-square of the noise, were determined to be $\sim$1,050 e^- rms with RTPS off and $\sim$800 e^- rms with RTPS on. To estimate S/N for minimum ionizing particle (MIP), it was assumed that the signal readout by each strip consisted of 22,500 electron-hole pairs, in which a factor of 1/2 due to charge-sharing was included. Assuming one MIP signal, S/N values were estimated to be $\sim$21 with RTPS off and $\sim$28 with RTPS on. The results showed an excellent noise performance of the detector.

The charge-sharing property was studied by injecting infrared (1060 nm wavelength) pulsed laser light to the detector. Figure 3 shows a preliminary result of

*1 Department of Physics and Astronomy, State University of New York-Stony Brook, USA
*2 Department of Physics and Astronomy, University of New Mexico, USA
*3 Brookhaven National Laboratory, USA
*4 High Energy Accelerator Research Organization (KEK)

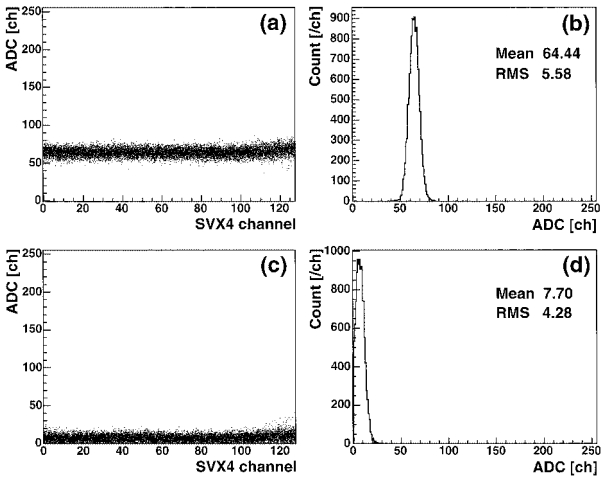

Fig. 2. (a) Noise value (ADC [ch]) as function of SVX4 channel number with RTPS off, (b) Noise distribution for all SVX4 channels in (a), (c) Noise value (ADC [ch]) as function of SVX4 channel number with RTPS on, (d) Noise distribution for all SVX4 channels in (c).

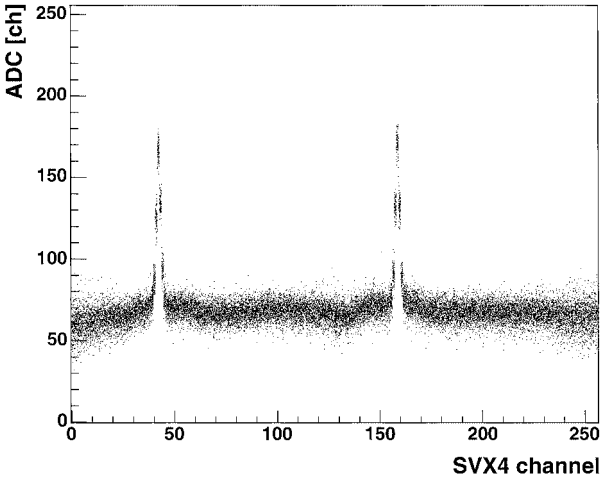

Fig. 3. Collected charges (ADC [ch]) as a function of channel number of two SVX4 chips.

collected charges as a function of channel number of two SVX4 chips. The channel numbers 1–128 correspond to one projective direction of strips (X-strips) and the channel numbers 129–256 correspond to the other projective direction of strips (U-strips). Two-dimensional position sensitivity by charge-sharing is supposed to be observed as one peak in the X-strip range and the other peak in the U-strip range. In the present laser-fiber optic setup, the laser spot size in the detector was too large to study the charge-sharing property in detail. A conclusive result for the charge-sharing property will be obtained by optimizing laser spot size or using a radioactive source.

In summary, we developed the prototype silicon stripixel detector with the preproduction sensor and the SVX4 chip for the PHENIX experiment. We carried out the detector performance tests of leakage current, noise and the charge-sharing property. The preliminary results showed an excellent performance of the detector in terms of leakage current and noise. Detailed studies including the charge-sharing property will be performed using an optimized laser setup and a radioactive source.

References

1) K. Adcox et al.: Nucl. Instrum. Methods Phys. Res. A **499**, 469 (2003).
2) Y. Akiba et al.: RIKEN Accel. Prog. Rep. **39**, 199 (2006).
3) Z. Li: Nucl. Instrum. Methods Phys. Res. A **518**, 738 (2004).
4) Z. Li et al.: RIKEN Accel. Prog. Rep. **36**, 250 (2003); Nucl. Instrum. Methods Phys. Res. A **518**, 300 (2004).
5) J. Tojo et al.: RIKEN Accel. Prog. Rep. **36**, 252 (2003); RIKEN Accel. Prog. Rep. **37**, 251 (2004); IEEE Trans. Nucl. Sci. **51**, 2337 (2004).
6) J. Tojo et al.: RIKEN Accel. Prog. Rep. **38**, 231 (2005).
7) B. Krieger et al.: IEEE Trans. Nucl. Sci. **51**, 1968 (2004).
8) J. Asai et al.: RIKEN Accel. Prog. Rep. **38**, 235 (2005); RIKEN Accel. Prog. Rep. **39**, 203 (2006).

Development of low voltage power supply for PHENIX PIXEL detector

A. Taketani, Y. Akiba, J. Asai, S. Boose,* H. En'yo, K. Fujiwara, H. Kano, H. Ohnishi, and Y. Onuki

The PHENIX experiment at the Relativistic Heavy Ion Collider will be upgraded with a silicon vertex track to enhance the heavy flavor identification capability.[1] The inner two layers will consist of pixel sensors. Signals will be read by bump-bonded readout chips,[2] which include the preamplifier, shaper, discriminator, and digital event buffers. The thickness of the pixel sensor is 200 μm. The amount of signal charge deposited by the typical minimum ionizing particle is about 2 fc and is integraded over 30 nsec. Hence, the readout system must have a low-noise low-voltage power supply. Because a similar pixel detector at the NA60 experiment has been operated with a power supply with 5 mVrms noise, our tentative target is the same level. There are 60 electrically independent half staves, which consist of two sensor hybrids and a readout bus.[3] Half staves are operated at 1.8 V and 3.1 A. We can adjust the voltage supplied to each individual half stave, and turn them on/off in the case of resetting/removing the individual half staves. Therefore, we need 60 individual power supplies for the PIXEL low-voltage power supply. We specified the requirements of the PIXEL low-voltage power supply, fabricated a trial working power supply and then evaluated the performance.

In addition to the number of channels, supply voltage, current, and noise figure, this power supply has various other requirements, because it will be installed 2 to 4 m away from the pixel detectors. Because the voltage drop along the long supply conductor is not appreciable, voltage sensing using another smaller wire should be implemented to stabilize the voltage.

Figure 1 shows a block diagram of the power supply. A Base Power Supply (BPS) feeds DC 5 V to individual Unit Power Modules (UPMs). Then the UPMs will convert 5 V to 1.8 V using a 3-terminal regulator with voltage sensing, which is connected to the load. A PC is connected to a Control and Monitor Unit (CMU) and controls the turning on/off of the BPS and each UPM. The drawing current can be monitored. These control and monitor functions will be implemented using ADAM 5000 remote I/O modules,[4] which are currently used for the PHENIX low-voltage power supply control and monitoring system.[5] The turning on/off will be controlled by the relay, and the current will be monitored by the voltage across the shunt register at the UPM output circuit. The UPM should be a card module with connectors at the front and back for easy maintenance.

A trial power supply is built and tested. The

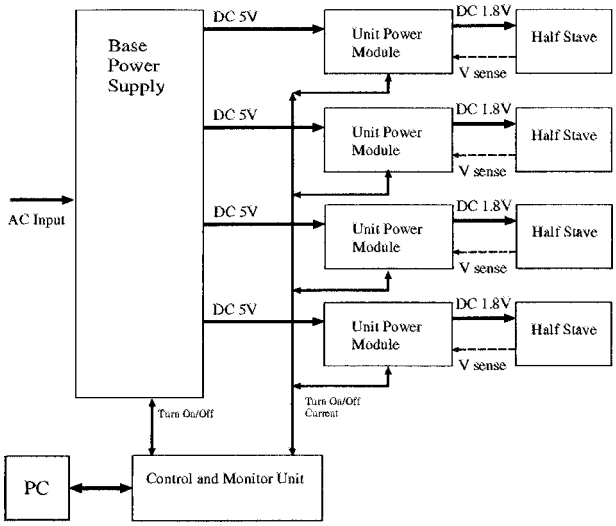

Fig. 1. Block diagram of power supply.

Blenix[6] BLN ultra low-noise AC/DC switching power supply is used as the BPS. Figure 2 shows a photograph of the UPM. The noise is at the 3 mVp-p level. Remote control and monitoring functions are implemented and tested. The UPM size is 15 cm × 10 cm per output, which is sufficiently small.

The low-voltage power supply for the PHENIX PIXEL detector is designed and fabricated for trial. It is found to satisfy the initial requirements.

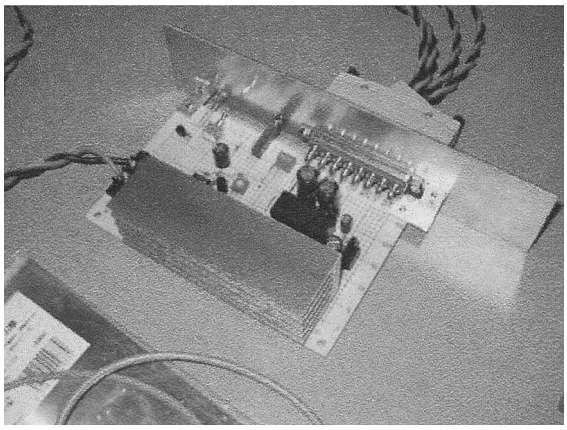

Fig. 2. Photograph of power supply.

References

1) Y. Akiba et al.: RIKEN Accel. Prog. Rep. **38**, 227 (2005).
2) K. Fujiwara et al.: RIKEN Accel. Prog. Rep. **38**, 228 (2005).

* Brookhaven Natinal Laboratory, USA

3) A. Taketani et al.: RIKEN Accel. Prog. Rep. **38**, 233 (2005).
4) ADVANTECH, http://www.advantech.com/
5) S. S. Adler et al.: Nucl. Instrum. Methods Phys. Res. A **499**, 560 (2003).
6) Bellnix Co., Ltd.: http://www.bellnix.com/

Optical alignment system for PHENIX muon tracker

H. Kanoh,[*1] A. Taketani, T.-A. Shibata,[*1] N. Kamihara,[*1] and M. J. Kweon[*2]

The muon tracker of PHENIX is placed in the muon magnet and it has three layers of tracking chambers called stations. By tracking a muon that is bent with a magnetic field, the momenta of muons are measured. The momentum resolution of the muon tracker is determined by the chamber spatial resolution and accuracy of the relative position among stations. The spatial resolution is approximately 70 μm to 100 μm per station. This value is required to separate ψ' mesons from J/ψ mesons in dimuon events. We align the position among the three stations using the field-off event data at the beginning of the run period. However, each station was moved 100–300 μm by the magnetic field and temperature fluctuation during the experiment period. To improve the momentum resolution, we should correct these relative movements. The purpose of the optical alignment system (OASYS)[1] is the real-time monitoring of the relative alignment among the stations. In the present data analysis, the data from the OASYS was not taken into consideration for the position aligment of the tracking chamber, and mass resolution does not yet have a design value.

The OASYS consists of a light source at station 1, a convex lens at station 2, and a CCD camera at station 3. When an individual station moves, the image on the CCD camera moves, reflecting the station movement. A similar alignment system was used in the L3 experiment at LEP.[2] Each station is separated into eight segments called an "octant", and there are 7 sets of optics on each octant. There are 7 (optics/octant) $\times$ 8 (octant/arm) $\times$ 2 (arm) = 112 optics in total. By observing the position of the light spot on the image of the CCD camera, we can monitor each station's movement.

To establish a relative alignment method using the OASYS, we studied the tracking chamber's relative movement. We assume that the tracking chamber is a rigid body, and we model the movement of the tracking chamber with parallel translation and rotation. It is impossible to calculate all of the movements of the three stations from only the information of the OASYS. However, we can assume that station 1 does not change its position, because only the relative position among stations is essential for absolute measurement. Station 1 is chosen as the relative position reference.

We define the octant local coordinate system. The origin is defined as the collision point. The z-axis is defined along the beam, and the north arm is selected as the positive direction. The y-axis is defined along the centerline of the octant, and the x-axis is defined as perpendicular to the y-axis.

First, we discuss the relationships of image movement and optics movement. The movement of the image on the CCD camera $\delta\boldsymbol{x_{img}}$ is described by the movements of station 2 and station 3, $\delta\boldsymbol{x_2^{total}}$ and $\delta\boldsymbol{x_3^{total}}$:

$$\delta\boldsymbol{x_{img}} = \frac{1}{l_1}\left\{(l_1+l_2)\delta\boldsymbol{x_2^{total}} - l_1\delta\boldsymbol{x_3^{total}}\right\}, \tag{1}$$

where l_1 and l_2 are intervals between the stations, as shown in Fig. 1. Next, we will describe the octant's movement with parallel translation and rotation. We define three component vectors $\boldsymbol{\delta x_s}$, which express the octant's parallel translation.

$$\delta\boldsymbol{x_s} = (\delta x_s, \delta y_s, \delta z_s) \tag{2}$$

Here, "s" denotes the index number of the stations ($s = 1, 2, 3$). Then, we also define matrix $\boldsymbol{R_s}$, which expresses the rotation of the chamber around x, y and z axes using three parameters $\delta\phi_{x,s}$, $\delta\phi_{y,s}$ and $\delta\phi_{z,s}$. Actually, $\delta\phi_{i,s}$ $(i = x, y, z)$ is on the order of 10^{-3} to 10^{-4}[rad] and is much smaller than 1, because the interval between the stations is on the order of meters and the movement of the tracking chamber is on the order of several hundreds of micrometers. Therefore, we give the following approximation.

$$\cos\delta\phi_{i,s} \simeq 1, \sin\delta\phi_{i,s} \simeq \delta\phi_{i,s} \ (i = x, y, z) \tag{3}$$

Then, rotation matrix $\boldsymbol{R_s}$ is defined as follows.

$$\boldsymbol{R_s} \equiv \mathbf{1} + \boldsymbol{\varepsilon_s} \tag{4}$$

$$\boldsymbol{\varepsilon_s} \equiv \boldsymbol{\varepsilon(\delta\phi_s)} \equiv \begin{pmatrix} 0 & -\delta\phi_{z,s} & \delta\phi_{y,s} \\ \delta\phi_{z,s} & 0 & -\delta\phi_{x,s} \\ -\delta\phi_{y,s} & \delta\phi_{x,s} & 0 \end{pmatrix} \tag{5}$$

We select the cross point of the octant plane and beam pipe as rotation center $z_{0,s} = (0, 0, z_{0,s})$. The movement due to the rotation of station "s" $\boldsymbol{\delta x_{rotate,s}}$ at position $\boldsymbol{x_s}$ is expressed as

$$\begin{aligned}\delta\boldsymbol{x}_{rotate,s} &= \boldsymbol{R_s}\hat{\boldsymbol{x}}_{\boldsymbol{s}} - \hat{\boldsymbol{x}}_{\boldsymbol{s}} \\ &= \boldsymbol{\varepsilon_s}\hat{\boldsymbol{x}}_{\boldsymbol{s}},\end{aligned} \tag{6}$$

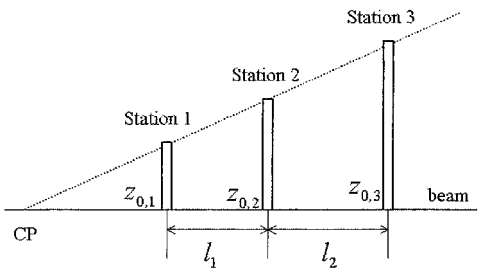

Fig. 1. Cross section of the muon tracker.

[*1] Department of Physics, Tokyo Institute of Technology
[*2] Department of Physics, Korea University, Korea

where $\hat{\boldsymbol{x}}_{\boldsymbol{s}} \equiv \boldsymbol{x}_{\boldsymbol{s}} - \boldsymbol{z}_{\boldsymbol{0,s}}$. From Eqs. (2) and (6), total optics' movement is written as

$$\delta \boldsymbol{x}_{\boldsymbol{s}}^{\boldsymbol{total}} \equiv \delta \boldsymbol{x}_{\boldsymbol{s}} + \boldsymbol{\varepsilon}_{\boldsymbol{s}} \hat{\boldsymbol{x}}_{\boldsymbol{s}}. \tag{7}$$

Then, the movement of the image is written as follows using Eqs. (1) and (7).

$$\begin{aligned} \delta \boldsymbol{x}_{\boldsymbol{img}} &= \frac{1}{l_1} \left\{ (l_1 + l_2) \boldsymbol{\delta x}_{\boldsymbol{2}}^{\boldsymbol{total}} - l_1 \boldsymbol{\delta x}_{\boldsymbol{3}}^{\boldsymbol{total}} \right\} \\ &= \frac{1}{l_1} \left\{ (l_1 + l_2) \delta \boldsymbol{x}_{\boldsymbol{2}} - l_1 \delta \boldsymbol{x}_{\boldsymbol{3}} \right\} \\ &\quad + \frac{1}{l_1} \left\{ (l_1 + l_2) \boldsymbol{\varepsilon}_{\boldsymbol{2}} \hat{\boldsymbol{x}}_{\boldsymbol{2}} - l_1 \boldsymbol{\varepsilon}_{\boldsymbol{3}} \hat{\boldsymbol{x}}_{\boldsymbol{3}} \right\} \end{aligned} \tag{8}$$

Optics are aligned in a straight line. Therefore, vector $\hat{\boldsymbol{x}}_{\boldsymbol{3}}$ is approximately proportional to vector $\hat{\boldsymbol{x}}_{\boldsymbol{2}}$, because of their geometrical relationships:

$$\hat{\boldsymbol{x}}_{\boldsymbol{3}} = \alpha \hat{\boldsymbol{x}}_{\boldsymbol{2}}, \tag{9}$$

where $\alpha = z_{0,3}/z_{0,2}$. Using Eqs. (8) and (9), $\delta \boldsymbol{x}_{\boldsymbol{img}}$ is witten as

$$\begin{aligned} \delta \boldsymbol{x}_{\boldsymbol{img}} &= \frac{1}{l_1} \left\{ (l_1 + l_2) \delta \boldsymbol{x}_{\boldsymbol{2}} - l_1 \delta \boldsymbol{x}_{\boldsymbol{3}} \right\} \\ &\quad + \frac{1}{l_1} \left\{ (l_1 + l_2) \boldsymbol{\varepsilon}_{\boldsymbol{2}} - \alpha l_1 \boldsymbol{\varepsilon}_{\boldsymbol{3}} \right\} \hat{\boldsymbol{x}}_{\boldsymbol{2}}. \end{aligned} \tag{10}$$

Here, we define $\boldsymbol{x}'_{\boldsymbol{2}}$ and $\delta\phi'_{i,2}$ from $\boldsymbol{x}_{\boldsymbol{i}}$ and $\delta\phi_{i,s}$,

$$\delta \boldsymbol{x}'_{\boldsymbol{2}} \equiv \delta \boldsymbol{x}_{\boldsymbol{2}} - \frac{l_1}{l_1 + l_2} \delta \boldsymbol{x}_{\boldsymbol{3}} \tag{11}$$

$$\delta\phi'_{i,2} \equiv \delta\phi_{i,2} - \alpha \frac{l_1}{l_1 + l_2} \delta\phi_{i,3} \quad (i = x, y, z), \tag{12}$$

and $\delta \boldsymbol{x}_{\boldsymbol{img}}$ becomes

$$\delta \boldsymbol{x}_{\boldsymbol{img}} = \frac{l_1 + l_2}{l_1} \left\{ \delta \boldsymbol{x}'_{\boldsymbol{2}} + \boldsymbol{\varepsilon} (\boldsymbol{\delta \phi}'_{\boldsymbol{2}}) \hat{\boldsymbol{x}}_{\boldsymbol{2}} \right\}. \tag{13}$$

In Eqs. (11) and (12), we cannot distinguish the movement of station 2 from that of station 3 using OASYS, and they are mixed. However, only station 2 appears to be moving in Eq. (13). This means that we can approximate that only the central station (station 2) moves. The movement of the image on the CCD camera and the movement of the tracking chamber correspond one to one in Eq. (13), and we can calculate the movement of the tracking chamber from the movement of the image analytically.[3)]

As a result of analysis with data obtained in the run 3 experiment period, we calculate the movement of the tracking chamber in the north muon arm. For example, the result of octant 3 is shown in Fig. 2. The vertical axis is the displacement from the initial value and the horizontal axis is time. Each tracking chamber has moved by 50 μm to 300 μm during the experiment period. We can correct the relative movement of the tracking chamber using our model, and the accuracy of alignment has become less than 40 μm. This value is better than the required accuracy.

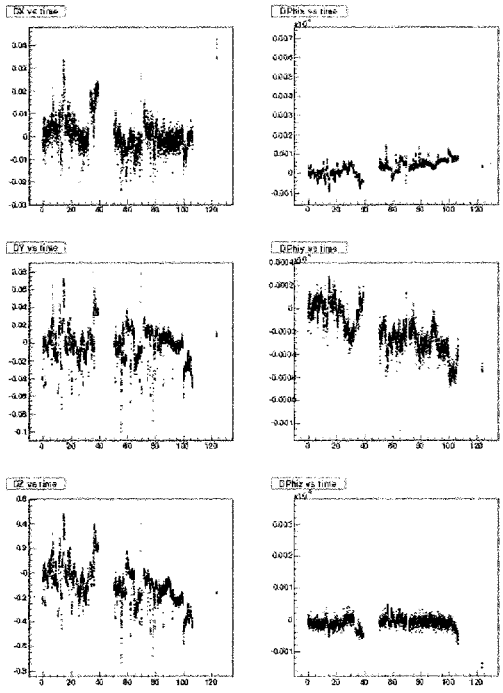

Fig. 2. Time-dependent movement during run 03. δx (left upper), δy (left middle), δz (left lower) and $\delta\phi_x$ (right upper), $\delta\phi_y$ (right middle), $\delta\phi_z$ (right lower).

The correlation of the mass resolution of J/ψ mesons and the accuracy of alignment by OASYS was estimated using Monte Carlo simulation, as shown in Fig. 3. The horizontal axis is the accuracy of alignment in micrometers and the vertical axis is the mass resolution in MeV. The accuracy of better than 50 μm is required to separate ψ' well and it is achieved in our analysis method.

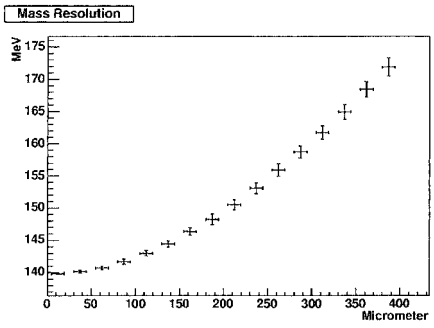

Fig. 3. Alignment accuracy dependence of J/ψ mass resolution, estimated by MC simulation.

References

1) J. Murata et al.: Nucl. Instrum. Methods Phys. Res. A **500**, 309 (2003).
2) B. Adeva et al.: Nucl. Instrum. Methods Phys. Res. A **289**, 335 (1990).
3) H. Kanoh: Master thesis, Tokyo Institute of Technology (2004).

Experimental status of penta quark search via $K^+p \to \pi^+X$ reaction at KEK-PS E559

K. Miwa,* for the E559 Collaboration

Since the report on the evidence of an exotic baryon Θ^+,[1] many studies from both theoretical and experimental aspects have been conduced. The observation at SPring-8/LEPS was immediately confirmed by several experiments.[2] Recently, however, null results have been reported from several high-energy experiments where investigators searched for Θ^+ using higher statistics.[2] Therefore, in such a situation, the confirmation of Θ^+ is urgent and crucial.

We have performed an experiment to search for Θ^+ via the $K^+p \to \pi^+X$ reaction at the K6 beam line with high statistics and good missing mass resolution using the SKS spectrometer at KEK 12 GeV Proton Synchrotron (KEK-PS E559). The best missing mass resolution of 2.35 MeV/c^2 (FWHM) is expected. One of the most important purposes is the determination of the width of Θ^+, if we observe Θ^+. As a target, a 12.5-cm-long liquid hydrogen was used. We used the K^+ beam of 1.2 GeV/c. The typical intensity was 14k counts during the 2 seconds of spill. K^+ was selected using an aerogel cherenkov counter at a trigger level. In the offline analysis, K^+ was selected using the time-of-flight information. The momentum of each beam particle was analyzed using the K6 beam line spectrometer of which the resolution is expected to be $\Delta p/p = 0.047\%$ (FWHM). Scattered particles were detected using the SKS spectrometer.

The setup around the target is shown in Fig. 1. The main background of the measurement is the 3 body decay of K^+ such as $K^+ \to \pi^+\pi^+\pi^-$ or $K^+ \to \pi^+\pi^0\pi^0$. The rejection of these decay backgrounds is essential for the Θ^+ search. In decay events, one or three charged particles are emitted to a forward angle, whereas in a hadoronic reaction such as Δ production or Θ^+ production, two charged particles are emitted with a large scattered angle. Therefore, we installed a large acceptance chamber after the target to detect the charged particles. We selected two charged particle events to reject decay events. To improve S/N ratio by detecting K^+, we also installed a range counter system at the downstream of this chamber.

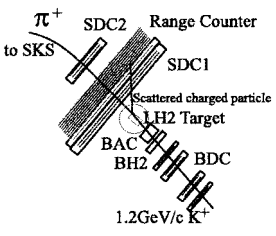

Fig. 1. Experimental setup around the LH_2 target.

The analysis was done using RIKEN-CCJ. For the calibration of the system, we analyzed $H(\pi^+, K^+)$ data to measure Σ^+. We checked the missing mass resolution from the Σ^+ peak width and the efficiencies of detectors and offline analysis from the yield of Σ^+. The yield of Σ^+ is approximately 1050, which is 70% of the expected yield. The width of Σ^+ obtained from the missing mass spectrum is 2.35 MeV/c^2 (FWHM) which is worse than the expected resolution of 1.57 MeV/c^2. This might be caused by an insufficient field map. For Θ^+ search, the missing mass resolution is evaluated to be 3.22 MeV/c^2 in the present analysis.

Let me now describe the present analysis status of (K^+, π^+) data. The vertex distribution after the rejection of decay events is shown in Fig. 2 with the distribution of the empty target data (hatched histogram). The 125 mm liquid hydrogen image is clearly observed. We took approximately 14,000 reaction events of $K^+p \to \pi^+X$. The cross section of this reaction is 5.3 mb[3] and the present yield is about 85% of the expected one. Therefore our analysis is going well. However, there are many background events which is shown in the hatched histogram in Fig. 2. These events might be the contaminations of the K^+ decay events and reaction events at the timing counter upstream of the target (BH2). For example, π^+ from the decays of K^0_S produced by the $K^+n \to K^0p$ reaction can make such broad distribution. We will compare the vertex distribution attributed to these background events with a simulation in future studies.

The analysis of (K^+, π^+) reaction is still preliminary and the analysis of the missing mass is in progress.

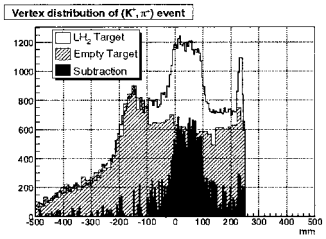

Fig. 2. Vertex distribution of $K^+p \to \pi^+X$ reaction.

* Department of Physics, Kyoto University

References
1) T. Nakano et al.: Phys. Rev. Lett. **91**, 012002 (2003).
2) K. H. Hicks: Prog. Part. Nucl. Phys. **55**, 647 (2005).
3) R. W. Bland et al.: Nucl. Phys. B **13**, 595 (1969).

Vector meson measurements at J-PARC 50-GeV PS

S. Yokkaichi

The spontaneous braking of chiral symmetry plays an essential role in QCD. The constituent light quark mass in hadrons is due to this symmetry braking. In hot/dense matter, the symmetry is expected to be restored and the spectral properties of hadrons such as the mass and the decay width are also expected to be modified in consequence of this restoration. There have been many theoretical approaches to this subject[1] and some experiments have already suggested the modification of hadrons in nuclear matter. The KEK-PS E325 experiment, performed by a group including the author, is one of such experiments. We have reported the spectral modification in a e^+e^- decay channel, ρ/ω mesons[2] and even ϕ meson[3] for the first time.

We intend to perform a next-generation experiment, the measurement of electron pairs from the decay of low-mass vector mesons ($\rho/\omega/\phi$) in nuclear matter at the J-PARC[4] 50-GeV proton synchrotron. The first beam of the 50-GeV PS will be available in JFY 2008. Around 30 Letters of Intent to use the 50-GeV PS including ours were already submitted. Our proposal[5] was selected as one of the Phase-1 experiments.

The goal of our new experiment is to collect the ϕ mesons in ∼100 times as high statistics as that of the E325 experiment in 30 days of operation with comparable (∼10 MeV/c^2) or improved mass resolution. Such measurements enable us to discuss whether the origin of the observed spectral modification is due to the chiral symmetry restoration or not, by qualitative comparison with many of the theoretical predictions.

Several experimental characteristics of E325 are also followed and/or broadened in the new experiment; these are essential in measuring the modification:

- Production of vector mesons in the target nuclei and observation of the decay of mesons in the target nucleus itself, at the normal nuclear density.
- Although ρ and ω cannot be distinguished in the e^+e^- channel because the spectra are overlapped, ϕ is isolated and easier to analyze.
- Observation of invariant mass spectra of vector mesons in the e^+e^- decay channel to reduce the spectral distortion by final-state interaction in the nuclear matter.
- Observation of slowly moving mesons in the laboratory frame to enhance the probability of decay inside nuclei. The typical $\beta\gamma$ (= p/m) of mesons is less than two.
- Good mass resolution (less than ∼10 MeV/c^2) to observe the small modification of ϕ mesons.
- Use of a high-intensity incident beam to compensate for the very small branching ratio to the e^+e^- channel (ϕ: 2.96×10^{-4}, ρ: 4.54×10^{-5}, ω: 6.95×10^{-5}) and small target thickness (∼0.1% interaction length) to reduce the background due to the γ conversions in the target material.

Many other experiments[6] fro measuring dilepton spectra seem to be unable to satisfy one (or more) of the above conditions. In the completed experiments, CERES at SPS collected statistics that were too small to observe the ϕ meson modifications. NA60 at SPS has higher statistics than E325, but worse mass resolution (more than 20 MeV/c^2 for ϕ). In the running experiments, both HADES at GSI and CLAS at JLab seem to have lower statistics and worse mass resolution than E325 for the time being; however, they may achieve the same level as E325 with possible improvements within the next few years. As a result, E325 is (and will be) a best experiment for measuring the ϕ modification, at least for several years, till our new experiment is conducted. In future experiments, CBM at GSI/FAIR is designed to cover the relatively more forward regions than that of our new experiment. Thus the statistics of slowly moving ϕ they could collect will be lower than that of our new experiment by a certain order of magnitude.

To collect ∼100 times as high statistics as E325, we plan to construct a new spectrometer and to use the primary proton beam (30 or 50 GeV) at an intensity of 1×10^{10} pps from the 50-GeV PS. In the expected factor of a hundred, about a factor of two is provided by the increase in the production cross section of ϕ with a higher incident energy, about five is provided by the larger coverage of the planned spectrometer, and remaining factor of ten is from the higher intensity of the incident beam. To cover the larger acceptance and to cope with the higher interaction rate, R&D of new technology such as a Hadron Blind Detector (HBD) to electron identification and a tracker with a Gas Electron Multiplier (GEM) is ongoing as shown in the Ref. 7. For the detector simulation for designing the new spectrometer, RIKEN-CCJ is used.

References

1) T. Hatsuda and T. Kunihiro: Phys. Rep. **247**, 221 (1994), etc.
2) K. Ozawa et al.: Phys. Rev. Lett. **86**, 5019 (2001); M. Naruki et al.: Phys. Rev. Lett. **96**, 092301 (2006).
3) R. Muto et al.: nucl-ex/0511019
4) http://jkj.tokai.jaeri.go.jp/
5) http://www-ps.kek.jp/jhf-np/LOIlist/LOIlist.html
6) I. Tserrya: Euro. Phys. J. C **43**, 399 (2005).
7) A. Frankel et al.: Nucl. Instrum. Methods Phys. Res. A **546**, 466 (2005).

Mass data processing for RHIC-PHENIX experiment

H. Torii, K. Aoki,[*1] F. Ellinghaus,[*2] K. O. Eyser,[*3] C. Hagemann,[*4] R. Han,[*5] T. Ichihara, S. Kametani, A. Kral,[*6] T. Liska,[*6] P. Mikes,[*7] A. Morreale,[*3] J. Seele,[*2] M. Stepanov,[*8] S. Yokkaichi, I. Younus,[*4] Y. Watanabe, for the PHENIX Collaboration

The entire system of the PHENIX[1)] detectors consists of various detectors of which the number of channels varies from one hundred to sixty thousand. Signals from all the channels are digitized in front-end electronics, collected through the PHENIX data acquisition system,[2)] and recorded in the PHENIX raw data format (PRDF). In off-line analysis,[3)] it is critical to reconstruct the properties of detected particles, for example, momentum and energy, from the raw data. The information reconstructed from the PRDF is stored in a data summary table (DST) file. During 2005, we accumulated 260 TB of PRDF files, which corresponds to an overall luminosity of 3.78 pb^{-1}, in polarized proton and proton collisions. The PRDF files were also transferred[4)] to a high-performance storage system (HPSS) at RIKEN. The processing of such mass data and its technique are unique in the world. Here, we will report the technical highlights of this data processing.

Our goal is to reconstruct DSTs from PRDFs and to transfer back the outputs into the RHIC computing facility (RCF) at Brookhaven National Laboratory (BNL). Figure 1 shows a schematic view of the data stream. First of all, 25 PRDF files are transfered from HPSS into a local disk of the Linux machine at the RIKEN super-combined cluster (RSCC). For each 25 file, we run reconstruction programs based on ROOT,[a)] an object-oriented analysis framework developed at CERN. The outputs of DSTs and smaller DSTs, named nano-DSTs, are saved back into HPSS. We have 20 different types of nano-DSTs, which contain only the information selected for the purpose of specific physics analysis and with different triggers. For each type, we aggregate 25 nano-DST files, which are from 25 PRDF files, into one file. The aggregated nano-DST file for each type is transfered to HPSS and the network file system (NFS). Then, we transfer them to RCF by bbftp,[b)] a file transfer software optimized for large files, and to dCache,[c)] a mass data storage system. The Load Sharing Facility (LSF) system was adopted to manage the schedule of all the sequential steps. It took about 30 hours to process one cycle.

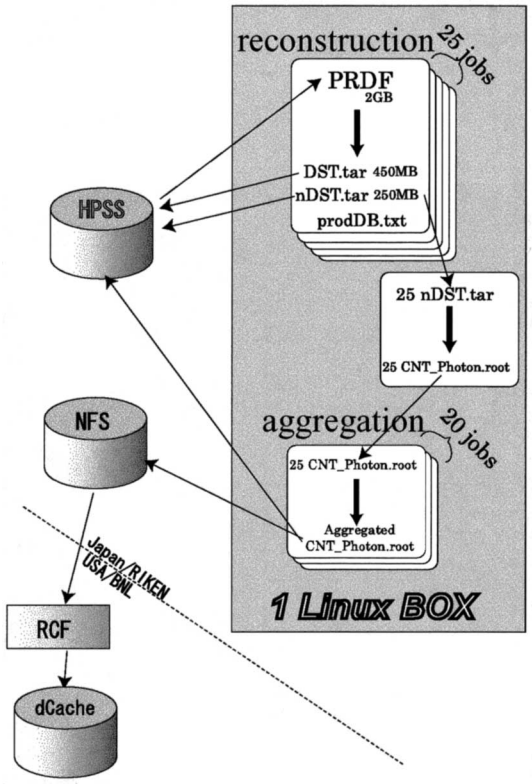

Fig. 1. Schematic drawing of the mass data stream. See text for details.

We used 128 Linux machines of the RSCC system in parallel.

Results of the PHENIX online system[3)] together with the status of the data acquisition system were stored in a PostgreSQL database at RCF. Since they are very important in the reconstruction process, the database was copied into a server at RIKEN every day or every week during data processing. In order to ensure that the reconstruction was performed with the latest copy, we kept a time stamp of the copy that was used for each DST and nano-DST.

We ran a maintenance macro periodically to detect failure of the entire cycle. The macro checked that 1) all 25 PRDFs were reconstructed properly, 2) aggregated nano-DSTs were transfered properly to HPSS, and 3) aggregated nano-DSTs were transferred properly to RCF. When the macro detected a failure, the reconstruction and aggregation were performed again. Since some PRDFs were obtained with a special setting of the trigger, some aggregated nano-DSTs exceeded the 2 GB limitation of the file system. We divided 25

*1 Kyoto University
*2 University of Colorado, USA
*3 University of California, USA
*4 University of New Mexico, USA
*5 Peking University, China
*6 Czech Technical University, Czech Republic
*7 Charles University, Czech Republic
*8 New Mexico State University, USA
a) See http://root.cern.ch
b) See http://doc.in2p3.fr/bbftp
c) See http://www.dcache.org

PRDFs into 2 or 3 sets in such a case of failure. For nano-DSTs tagged as good by the maintenance macro, we ran a quality assurance program in order to check the aggregated nano-DSTs. The program evaluated histograms that were created during the reconstruction and put the results into a database that could be utilized later in physics analysis.

In order to maintain the production constant over a long period, it is important to monitor the entire process frequently. We formed monitoring shifts among us to cover 24 hours per day. One monitor living in Japan covers 12 hours, and the other in USA covers the other 12 hours. Figure 2 shows an example of the monitoring windows distributed on a web server, which the monitors checked every three hours, 4 times per day. The reconstruction speed shown in Fig. 2 (a) is very important since it is sensitive to HPSS access. Figure 2 (b) shows the transfer speed from RIKEN to BNL. If the speed drops to less than 1 MB/sec, trouble may have arisen on the internet network between RIKEN and BNL. Since these figures were updated every 5 minutes, we can judge that the drop recorded in Fig. 2 (b) was a short drop over a couple of hours. An electric log book, ELOG,[d] was employed to report any observed irregularity. When at least one of the monitoring windows is out of range typically for more than 6 hours, we enter a message on the ELOG and then call an expert. In the case of monitors in the USA, we send an e-mail to the cell phone of the expert instead of making an international telephone call.

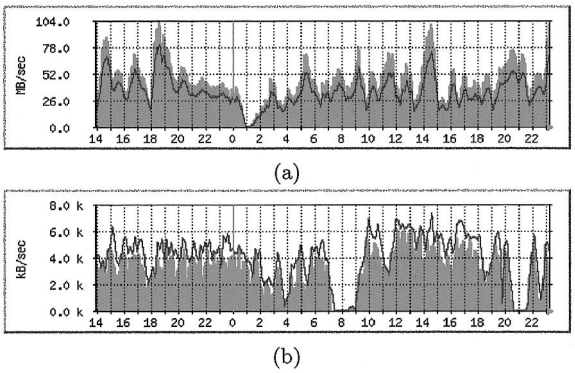

Fig. 2. Monitoring window of (a) production speed for DST + nano-DST (filled hist) and DST only (line), (b) transfer speed from RIKEN to RCF (filled hist) and from RCF to dCache (line) in units of MB/sec as a function of time in a unit time of one hour. These diagrams were taken from the web page for monitoring on July 15th, 2005.

From 260 TB of PRDFs, 42 TB DST and 26 TB nano-DSTs were produced during the reconstruction, and 22 TB aggregated nano-DSTs in total were transferred to RCF. The process speed was limited by the speed of transfer from and to HPSS. The transfer speed was 45 MB/s on average, which was lower than the theoretical estimate. This may be attributed to the fact that requests for different PRDFs occurred regardless of the physical ordering of the PRDFs on the HPSS tape. For the future, there is room to improve the speed by managing the requests according to the ordering in the tape. Figure 3 shows a history of the amount of processed PRDF per day after Jun 10th, 2005, when we started this process. Except for some trouble midway, such as that due to a crash of the hard disk, we succeeded in keeping the process speed constant for almost three months.

In summary, we successfully finished the data processing of the PHENIX raw data of 260 TB at RSCC and sent 22 TB of the output back to RCF. Since the size and processing time were huge, we collaborated internationally in order to maintain the process. We suceeded in processing the mass data in three months.

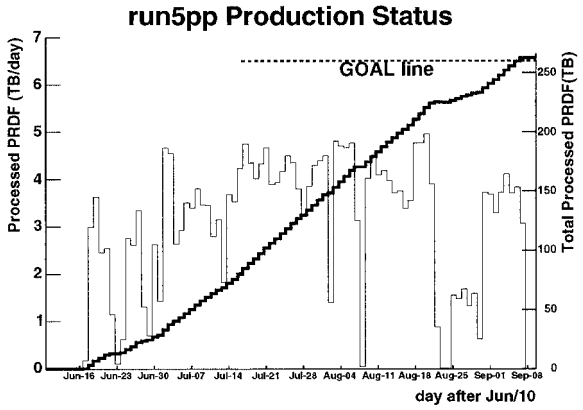

Fig. 3. Data production speed (left axis) and total size of processsed data (right axis). The total size of PHENIX raw data, 260 TB, is shown as "Goal."

References

1) K. Adcox et al.: Nucl. Instrum. Methods Phys. Res. A **499**, 469 (2003).
2) S. S. Adler et al.: Nucl. Instrum. Methods Phys. Res. A **499**, 560 (2003).
3) S. S. Adler et al.: Nucl. Instrum. Methods Phys. Res. A **499**, 593 (2003).
4) Y. Watanabe et al.: RIKEN Accel. Prog. Rep. **39**, 222 (2006).

[d] See http://midas.psi.ch/elog

Large-scale data transfer in realtime over the Pacific

Y. Watanabe, M. Chiu,[*1] H. Hiejima,[*1] T. Ichihara, S. Kametani, M. L. Purschke,[*2] S. Yokkaichi, and D. Yu[*2]

In October 2004, one decision was made that all pp collision data produced at the PHENIX detector in the next experiment (Run 5) will be transferred and analyzed at CCJ as soon as possible. This is because the computing resources of the RHIC Computer Facility (RCF) at Brookhaven National Laboratory (BNL) are expected to be fully occupied for more than one year analyzing the heavy-ion collision data produced in the last experiment (Run 4) and Run 5, and there is no room for the pp data. However, a delay in getting the results is a very serious problem for us (the spin physics group).

The expected volume of the pp data was 300 TB $\sim$ 500 TB in two months, which required a sustained transfer bandwidth of 60 MB/s $\sim$ 100 MB/s between BNL and RIKEN. There were two technical options: One was a well-established method of transporting tape cartridges via airplanes (Fig. 1), and the other was transfer via the network. We had already experienced more than 10 MB/s sustained data transfer and expected to achieve about 40 MB/s with a minor upgrading of the former method. There are several disadvantages of the former method as follows:

- It requires much manpower to handle cartridges, which means that it cannot be achieved by a fully automated operation.
- It takes more than one week to be ready for analysis at CCJ even when using the fastest transfer system via airplanes.

Fig. 1. A container stores up to 60 tape cartridges (200 GB/cartridge). The transfer of a filled up container (12 TB) in one week means a sustained transfer of about 20 MB/s.

In the latter method, although the network bandwidth between BNL and RIKEN had already reached about 100 MB/s, we had a slower transfer experience ($\sim$ 5 MB/s) of actual data using "bbFTP".[1)] It means that much improvement is expected for global-scale data transfer using suitable software. Indeed, it is highly advantageous to obtain actual data immediately after the experiment at the opposite side of the globe.

Thanks to Dantong Yu who succeeded in transferring test data of about 70 MB/s between BNL and CERN, we also easily achieved the transfer of about 70 MB/s between BNL and RIKEN using "GridFTP".[2)] We decided to use the network transfer as the first option and the transfer via airplanes as the backup (Fig. 2). A NAT equipment (ccjexp) is needed to set between a global address area and a private address area, on which storage PCs of PHENIX DAQ system ('phnxbox' 1 $\sim$ 6) are placed. We prepared four PCs ('ccjbox' 1 $\sim$ 4) as the buffer for received data at CCJ, each of which has two disks (2 TB$\times$2).

Each transfer period is separated by disks of the 'Bufferbox'es of the PHENIX DAQ system. PHENIX shift crews initiated the transfer of all data files in the disk to the 'ccjbox'es at CCJ when a disk was filled up. On the other hand, when a disk of the 'ccjbox'es is nearly full which is poured data from BNL as the buffer, the buffer is switched to another disk and starts to transfer data to CCJ-HPSS from the previous buffer disk automatically.

The actual data transfer was started in early April, immediately after the beginning of the pp collision experiment. The transfer rate is generally more than

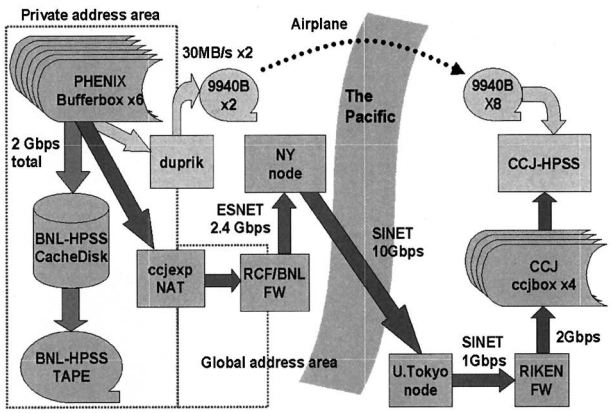

Fig. 2. ESNET[3)] and SINET,[4)] which are connected to BNL and RIKEN, respectively, have a junction in New York. The bottleneck of the route is 1 Gbps between RIKEN and the University of Tokyo, in which a node of SuperSINET[5)] is placed.

[*1] University of Illinois, USA
[*2] Brookhaven National Laboratory, USA

50 MB/s as shown in Fig. 3. To achieve the rate, some kernel parameters related the network configuration in /etc/sysctl were tuned to optimize the transfer speed. Fortunately, we encountered only some minor problems during the 11 weeks of the experiment period, such as a few network troubles and one disk failure; otherwise, we succeeded in transferring 260 TB of data using only the network shown in Fig. 4. It is noteworthy that the transfer project was completed only two days after the end of Run 5. We may say that it was nearly "Realtime transfer". This accomplishment was mentioned in "CERN Courier": "This seems to be the first time that a data transfer of such magnitude was sustained over many weeks in actual production".[6)]

We replaced the file system of the 'ccjbox'es from ext3 (defacto standard of LINUX) to xfs[7)] in the early stage of the transfer project. Both file systems had no problems except for reading files written with GridFTP and/or bbFTP. The speed of reading files from the ext3 file system was about 10 MB/s and it was

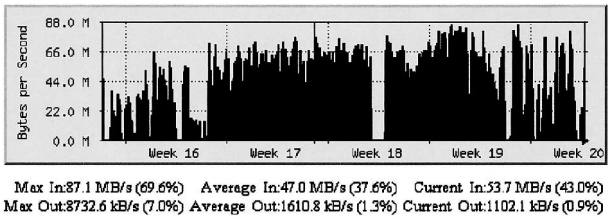

Fig. 3. Typical transfer rate history measured at RIKEN. The rate variation is caused by many factors such as network trouble/congestion, buffer trouble and status of the experiment.

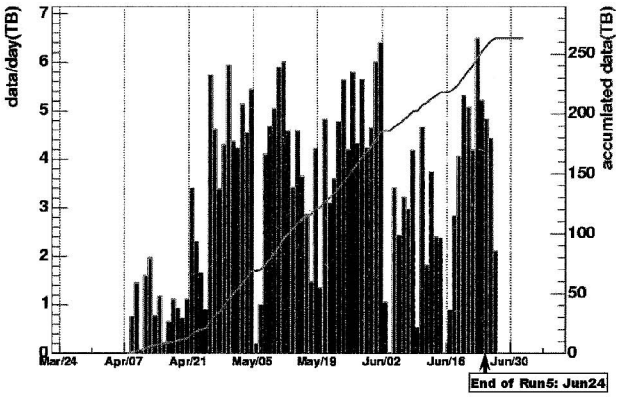

Fig. 4. Transfer rate (bar graph: in TB/day) and aggregated volume (line graph: in TB). The transfer project was completed only two days after the end of the experiment.

three times slower than that from xfs. The technique used by both GridFTP and bbFTP, may be ill-suited for the ext3 file system. We considered that by this technique, many small fragments of a file are transferred simultaneously with multistreams and eventually reconstructed in a file at the destination.

References

1) http://doc.in2p3.fr/bbftp/
2) http://www.globus.org/grid_software/data/gridftp.php
3) http://www.es.net/
4) http://www.sinet.jp/english/index.html
5) http://www.sinet.jp/english/super_sinet.html
6) http://www.cerncourier.com/main/article/45/7/15
7) http://oss.sgi.com/projects/xfs/

CCJ operation in 2004–2005

S. Kametani, H. En'yo, Y. Goto, H. Hamagaki,* T. Ichihara, Y. Watanabe, and S. Yokkaichi

RIKEN PHENIX Computing Center in Japan (RIKEN CCJ) is a large-scale computing system mainly for the analysis of RHIC-BNL[1] physics: the study of the spin structure of a nucleon and QGP search. CCJ performs the role as the simulation center, the Asian regional computing and the production of Data Summary Tape (DST) from experimental raw data in PHENIX.[2]

CCJ is composed of calculation nodes, a mass-storage system, a medium-scale storage system using RAID, and a networking system that connects these components to each another. These systems are installed in the main research building with a cooling system and uninterruptible power supplies. The system is integrated with RIKEN Super Combined Cluster (RSCC) of Advanced Center for Computing and Communication.[a] RSCC and CCJ share the mass storage system, and one-eighth of RSCC calculation nodes are dedicated to CCJ. Users can access CCJ from an outside network only via two SSH servers, one operated by Solaris and the other by Linux.

All the 166 calculation nodes of CCJ and 128 nodes of RSCC have dual CPUs (Intel Pentium III 700 MHz–1.4 GHz and Intel Pentium4 2.0 GHz for CCJ, Intel Xeon 3.06 GHz for RSCC), 1(CCJ)/2(RSCC) GByte of memory, 2 GByte of swap and 10–100 GBytes of local work area. The operating system was migrated from Redhat 8.0 to Scientific Linux 3.0.3 in March and October 2005 to follow up the PHENIX analysis framework installed at RHIC Computing Facility (RCF). CPU allocation is performed using the batch job system. CCJ is adopting LSF[3] as the batch job system. RSCC adopts NEC's NQSII/ERSII. However, NQS is not designed well for our use in experimental nuclear physics, e.g., to process thousands of tasks per day. As the redundancy of NQS is also worse than that of LSF, LSF is employed also for RSCC nodes dedicated to CCJ.

CCJ includes service nodes locally. The user directory and the PHENIX analysis library are stored in RAIDs and are shared by all the CCJ and RSCC calculation nodes with NFS. The PHENIX library is mirrored once a day through OpenAFS with two Linux servers (dual Xeon 2.6/2.4 GHz and 1/2 GByte memory). The mirrored library is also exported to other domestic collaborators with rsync. Following the shift of the calibration database architecture of PHENIX from Objectivity/DB to PostgreSQL in 2004, the local service of PostgreSQL on CCJ has been started. The backup of the PHENIX database is copied to CCJ once a day. The local database service is managed on the Linux server whose performance is sufficiently high (Xeon 3.0 GHz, 2 GByte memory).

The mass storage system has a capacity of 0.8 PByte using 4000 cartridges of tapes with a 200 GByte size each. The cartridges are handled by the StrageTek PowerHorn 9310 tape robot system and eight 9940B tape drives which read/write tape with 30 MBytes/sec. These manipulations and data accesses are managed by the High Performance Storage System (HPSS)[4] 4.5 on five IBM p630 with AIX. The mass storage system stores PHENIX raw experimental data (all the p + p experiments for all the year, heavy-ion experiment for the first and second years), DST (the same as raw data), compact DST called nDST (all the year both for p + p experiments and heavy-ion experiments) and user analysis data archives.

The medium-scale storage system decreases loads on the mass storage system. The system includes five SUN machines and three Linux machines connected to RAID systems with the Fiber Channel (FC) interface. The total capacity of the RAIDs was 28.6 TBytes in April 2005. As that volume is not sufficient, the buffer system of RIKEN-BNL data transfer system (3.8 TBytes) is temporarily diverted into the medium-scale storage system.

These systems are connected with the Gigabit Switch Network with Cisco Catalyst 4506 for fast I/O. The connection for service nodes is 1000Base-SX and that for calculation nodes is 100Base-T.

The main activities of CCJ in 2004–2005 were the transfer of raw data of PHENIX fifth-year p + p experiment, the DST production for the fourth- and fifth-year p + p experimental data and the spin analysis of the fifth-year experimental data. The first activity, raw data transfer from BNL to RIKEN, was achieved during the fifth-year experiment. About 270 TByte data were transferred with GridFTP simultaneously with the experiment. Details are described in this volume.[5] For this purpose, four RAIDs and servers are introduced as a buffer system before transferring data into the mass storage system.

The second activity, the production of DST was performed for PHENIX fourth- and fifth-year p + p experimental data. In particular, for the fifth-year experimental data, simultaneous production with data transfer, that is, simultaneous with experiment, was carried out as a trial. The status of the production was monitored 24 hours by worldwide PHENIX collaborators with HTTP.

During the summer of 2005, an analysis workshop was held at RIKEN for the spin analysis of fifth-year experimental data. To put all the nDST in the medium-scale storage system, two RAID systems were

* Center for Nuclear Study, Graduate School of Science, University of Tokyo

a) http://accc.riken.jp

additionally installed in June 2005. The total capacity of these two RAIDs is 13.6 TBytes. Two SUN Fire V40 machines were also installed as corresponding servers. As Solaris10 for x86 does not support "pftp," the interface of HPSS, servers are operated by Scientific Linux 4.0.

Other analytical activities can be found on the web page: http://ccjsun.riken.go.jp/ccj/proposals/. Achievements of those activities are reported on this volume.

As for maintenance, CCJ encountered several troubles. The first trouble was the memory leak and system crash of the NIS/user home server. The server was operated by Solaris2.6 whose support service by the vendor is now discontinued. Presently, those services are moved to another machine that is operated by Solaris8. The OS upgrading of the phased out server is being planned. The Hard Disk Drive (HDD) of RAID crashed several times and the broken disk was changed. The file system crashed once due to a crash of another HDD during the rebuilding of RAID, however, the system could be restored without causing further problems. There were two troubles with the FC interface: one was a damaged fiber cable and the other was the broken FC HUB. These damaged cable and broken HUB were already changed. Eighteen nodes of the calculation node crashed due to hardware problems. One of the nodes was fixed by changing HDD. In total in the past year,[6] 35% of the calculation nodes crashed. These nodes were installed in 1999–2001 and the performance of these nodes are much lower than newer nodes. The effect of the phaseout is quite negligible with respect to the total performance of CCJ. The incidence of system crashes of calculation nodes and the subsystem of HPSS increased slightly with the increase in loads on the system due to DST production and the analysis workshop.

Figure 1 shows the total capacity and the used space of RAIDs for each RHIC year. The volume of fifth-year nDST data reached 26 TBytes but only 18 TByte data is in RAIDs due to the limited remaining space. The subsequent analysis of third- and fourth-year data is consuming a space of 4 TBytes. The usage of volume by each analysis activity is growing more than 10 TBytes and the disk volume is nearly close to the limit. The shortage of capacity is a serious problem for the planned reproduction of DST for fifth-year data and for future analysis. A further upgrading of the medium-scale storage system is highly expected and is being discussed.

The usage of HPSS volume is shown in Fig. 2. The current limit of HPSS volume is 0.8 TByte and an extension is possible only up to 1 PByte. The plan for HPSS upgrade is being considered carefully: adding tapes into another silo and/or the introduction of newer robot/tape systems.

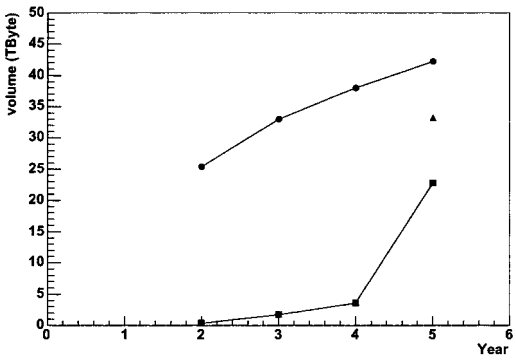

Fig. 1. Volume space of RAIDs at each RHIC experimental year. Circles indicate total volume, squares the space consumed by all the nDST stored and triangle total used volume. "Total volume" does not include the buffer region of RIKEN-BNL transfer system. The system is close to its limit.

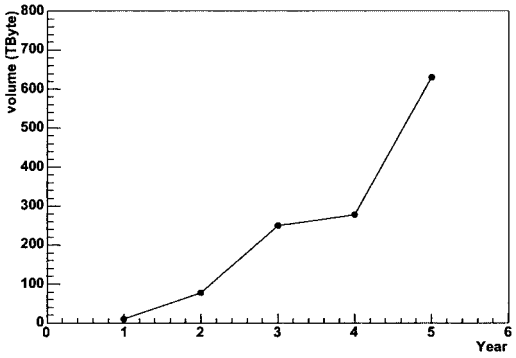

Fig. 2. Volume usage of HPSS for each RHIC experimental year. The HPSS system is also close to its limit of 1 PByte.

References

1) M. Harrison, T. Ludlam, and S. Ozaki: Nucl. Instrum. Methods Phys. Res. A **499**, 235 (2003).
2) D. P. Morrison et al.: Nucl. Phys. A **638**, 565c (1998).
3) http://www.platform.com/products/LSF/
4) http://www.hpss-collaboration.org/hpss/index.jsp
5) Y. Watanabe et al.: RIKEN Accel. Prog. Rep. **39**, 222 (2006).
6) S. Yokkaichi et al.: RIKEN Accel. Prog. Rep. **38**, 247 (2005).

Pumping ^{229m}Th by hollow-cathode discharge [III]

H. Haba, M. Hara,[*1] T. T. Inamura, Y. Kasamatsu,[*2] H. Kikunaga,[*3] T. Mitsugashira,[*1] T. Nakanishi,[*3] T. Ohtsuki,[*4] A. Shinohara,[*2] Y. Suzuki,[*1] K. Takamiya,[*5] S. Watanabe,[*1] A. Yokoyama,[*3] and H. Yuki[*4]

We proposed a new method of populating the "3.5-eV isomer" in ^{229}Th by hollow-cathode electric discharge.[1,2] This exotic isomer has long been sought but as yet not confirmed. Last year, we found no long-lived isomer but only a sign of α decay with a half-life shorter than 20 minutes.[3] Measurement was carried out as follows. The hollow cathode with a sample of ^{229}Th subjected to electric discharge was removed from the tube after switching off the discharge, and the sample was dissolved to make an α source. About 20 minutes after the discharge, α spectra were measured successively for 10 minutes. If the sign of a short-lived isomer is confirmed, then it will be an epoch-making discovery in this field of spectroscopy, since the isomer was first postulated in 1976.[4] To examine an α decay shorter than 20 minutes, we have installed an α detector inside the hollow-cathode discharge tube.

Figure 1 shows our new setup with an α-measurement assembly: (1) a Si detector (ORTEC B-type with 150-mm^2 active area and 300-μm depleted depth), (2) a light-shield housing made of Al, and (3) a thin light-tight-film (4-μm Mylar coated with Al 80 nm thick) window. As was described in our last reports,[2,3] we use Ar gas at a pressure of 200 Pa in the discharge tube, a discharge current of 100 mA or 200 mA and a voltage of about 300 V (constant current mode). We achieved light shielding sufficient for detecting α particles during the discharge. The energy resolution with the Al-coated Mylar window is about 80 keV full width at half maximum (fwhm) for ^{241}Am 5486-keV alphas. (For the same alphas, the detector has an energy resolution of 17 keV fwhm in vacuum at room temperature; about 40 keV fwhm at an Ar-gas pressure of 200 Pa without the Al-coated Mylar window.) This resolution with the Mylar window is not sufficient for identifying individual α lines but it is sufficient for recording α spectra.

Now we can measure α particles during the electric discharge and the change in their yields with time immediately after switching off the discharge. A preliminary measurement using the present setup suggests that there is a delayed α component with a half-life shorter than 16 minutes. Full measurement will be carried out shortly at the Oarai branch of the Institute for Materials Research, Tohoku University.

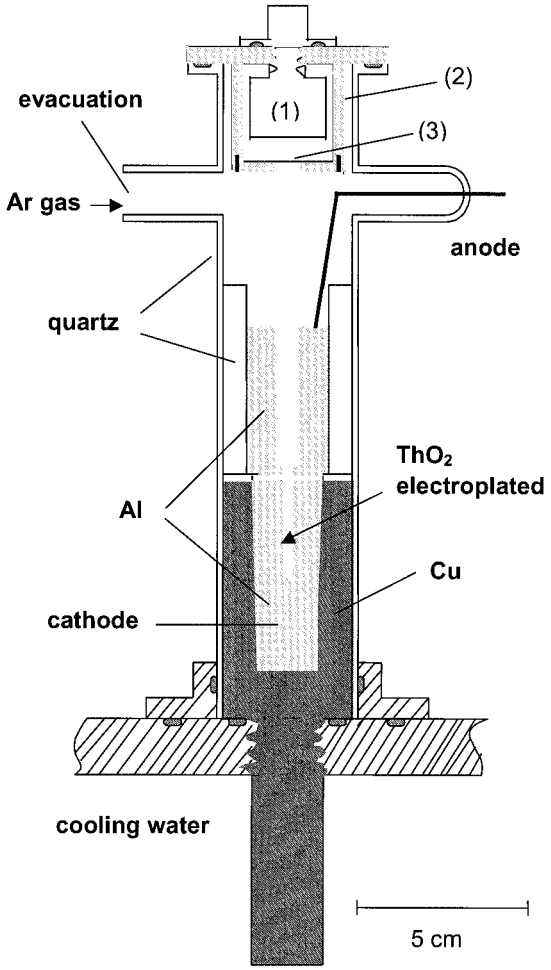

Fig. 1. Schematic cross-sectional view of our hollow-cathode discharge tube with α-measurement assembly: (1) SSD, (2) light-shield housing, and (3) thin light-tight-film window.

References

1) H. Haba et al.: RIKEN Accel. Prog. Rep. **37**, 263 (2004).
2) T. T. Inamura, T. Mitsugashira, and the Oarai collaboration: Hyperfine Interact., in press.
3) S. Enomoto et al.: RIKEN Accel. Prog. Rep. **38**, 249 (2005).
4) L. A. Kroger and C. W. Reich: Nucl. Phys. A **259**, 29 (1976).

[*1] Oarai Branch, Institute for Materials Research, Tohoku University
[*2] Graduate School of Science, Osaka University
[*3] Graduate School of Natural Science and Technology, Kanazawa University
[*4] Laboratory of Nuclear Science, Tohoku University
[*5] Research Reactor Institute, Kyoto University

Status report on RIKEN ECR ion source operation

Y. Higurashi, T. Nakagawa, M. Kidera, H. Haba, T. Aihara, M. Kase, A. Goto, and Y. Yano

In 2005, we successfully produced two special ion beams (^{70}Zn, ^{238}U) from RIKEN 18 GHz ECRIS and an intense Ar beam from the liquid-He-free superconducting ECR ions source for nuclear physics experiments. One of the requirements of the RIKEN RI beam factory (RIBF) project is the production of U ion beams.[1] We therefore study how to produce a beam of U ions. As the first trial, we used UF_6 for the production of the U ion beam from an ECR ion source. When using UF_6, it does not require an oven nor an insertion system for the solid rods to be vaporized under plasma sputtering. It is possible to produce U ions in the same manner as in the case of producing gaseous elements. Figure 1 shows a cross-sectional view of the RIKEN 18 GHz ECRIS and a schematic drawing of the UF_6 bottle. Details of the description of the RIKEN 18 GHz ECRIS and its performance are described in Ref. 2. The UF_6 bottle (50 cm^3 in volume) was connected by a gas-feeding tube via a variable slow-leak valve to control the flow rate of UF_6 vapor. About 3 g of UF_6 was filled in to the UF_6 bottle. No gas-mixing method was applied during the present experiments. To minimize contamination, the plasma chamber wall was covered up with a thin aluminum tube of 1 mm thickness, which is easily replaceable. Furthermore, the aluminum surface emits several secondary electrons per primary electron impact, which helps increase plasma density.[3]

Figure 2 shows the charge state distribution of U ions. The ion source was tuned for the production of U^{21+} ions. The injected microwave power was 260 W. The gas pressures of the plasma chamber and extraction stages were 9.0×10^{-7} and 1.0×10^{-7} Torr, respectively. The extraction voltage was 10 kV. Figure 3 shows the summary of the beam intensity of multicharged U ions at the extraction voltage of 12 kV.

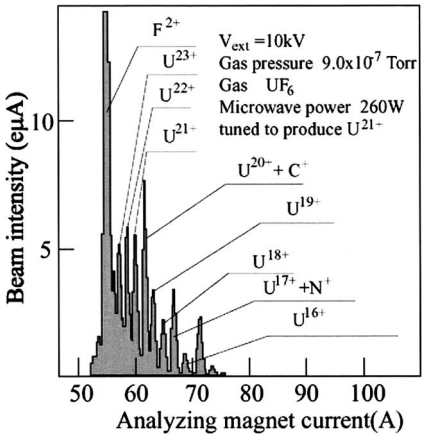

Fig. 2. Charge state distribution of U ions. The ion source was tuned for the production of the U^{21+} ions.

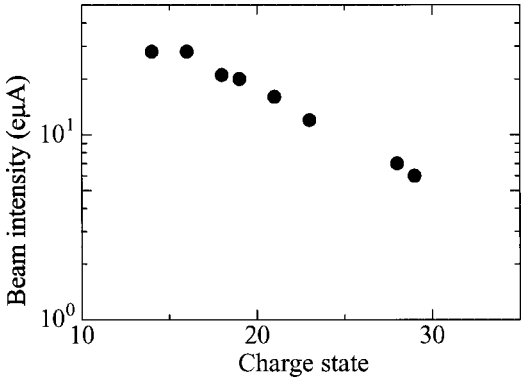

Fig. 3. Beam intensity of multicharged U ions at extraction voltage of 12 kV.

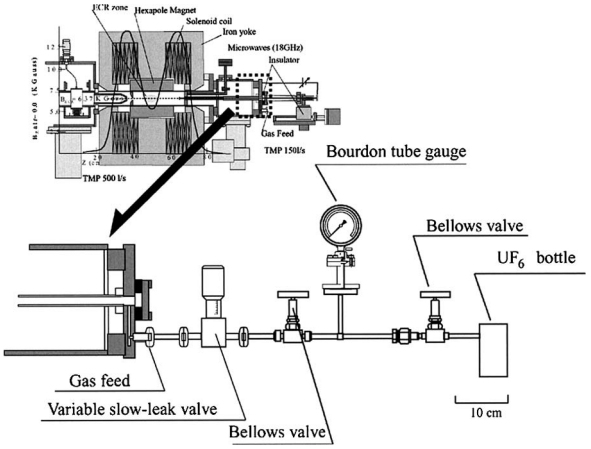

Fig. 1. Cross-sectional view of RIKEN 18 GHz ECRIS and schematic drawing of UF_6 bottle.

Recently, an intense ^{70}Zn beam has been strongly demanded for use in the search for a new superheavy element (atomic number of 113).[4]. The goal of superheavy element search experiments was to generate an intense beam of $Zn^{14+,16+}$ions (at least 2–3 pμA) from the ion source for as long as possible without a break minimize the experimental time, because the estimated cross section of the reaction is very small [smaller than pb (10^{-36} cm^2)]. To produce ^{70}Zn ions, we used the direct insertion method. At first, we measured the beam intensity of Zn ions from a natural ZnO rod. The size of the rod was $4 \times 4 \times 40$ mm^3. To check the effect of ionized gas (base gas for the production of plasma) on beam stability and intensity, we chose He and O_2 gases as ionized gases. Usually,

for the production of Zn ions, O_2 gas is better than He gas, because the ion cooling effect of O ions on Zn ions is much better than that of He ions.[5] However, in this experiment, the beam intensity of Zn ions produced using He gas is more stable than that produced using O_2 gas. For this reason, we used He gas as an ionized gas. Usually, we have to set the rod near the ECR zone to obtain sufficient vapor pressure from a high-melting-point material, such as ZnO. (The melting point of ZnO is 1975°C.) However, remarkably, the position of rod tip (L) was 3 cm, which was 10 cm from the ECR zone, to obtain a 50 eμA $^{64}Zn^{15+}$ ion beam. To understand this phenomenon, we need too carry out further investigations. Practically, it was advantageous to obtain a stable beam, because the solid rod does not cause the instability of the plasma.

Based on these experimental results, we attempted to produce the ^{70}Z ion beam with a ^{70}ZnO rod. Figure 4 shows the charge state distribution of ^{70}Zn ions. The RF power was 560 W, the gas pressure was 7.4×10^{-7} Torr, and the extraction voltage was 15.6 kV. Using this method, we successfully produced an intense beam of $^{70}Zn^{16+}$ (~ 2 pμA) for 43 days without break for superheavy element search experiments.

To accelerate the intense Ar beam (~ 1 pμA) up to 63 MeV/u using the heavy-ion linac-ring cyclotron accelerator complex, we produced the Ar^{9+} ion beam from the superconductiong ECR (SC-ECR) ion source (RAMSES).[3]

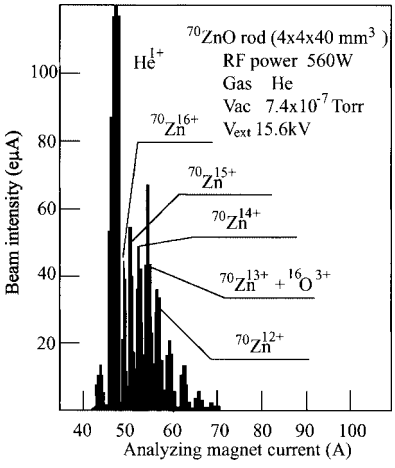

Fig. 4. Charge state distribution of ^{70}Zn ions from RIKEN 18 GHz ECR ion source produced by direct insertion. The ion source was tuned to produce $^{70}Zn^{16+}$.

The typical beam intensity of Ar^{9+} from an ion source is approximately 13 pμA. Figure 5 shows the charge state distribution of Ar ions. The ion source was tuned for the production of Ar^{9+} ions. The injected microwave power was 210 W. The gas pressures of the plasma chamber and extraction stages were 3.0×10^{-7} and 2.7×10^{-7} Torr, respectively. The extraction voltage was 15.8 kV. Using this ion source, we obtained a high transmission efficiency of 95% from the ion source to the RFQ linac and successfully supplied ~ 1 pμA of Ar beam on the target for nuclear physics experiments.

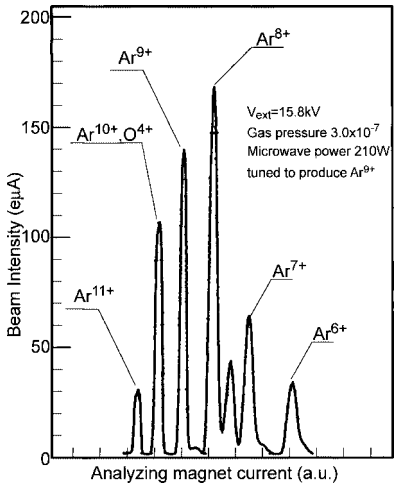

Fig. 5. Charge state distribution of Ar ions. The ion source was tuned for the production of Ar^{9+} ions.

References

1) Y. Yano: Proc. 17th Int. Conf. on Cyclotrons and Their Applications, Tokyo, 2004-10 (Japan Particle Accelerator Physics Society, 2005), p. 169.
2) T. Nakagawa, Y. Higurashi, M. Kidera, T. Aihara, M. Kase, and Y. Yano: Nucl. Instrum. Methods Phys. Res. B **226**, 392 (2004).
3) T. Nakagawa, T. Kurita, M. Kidera, M. Imanaka, Y. Higurashi, M. Tsukada, S. M. Lee, M. Kase, and Y. Yano: Rev. Sci. Instrum. **73**, 513, (2002).
4) K. Morita, K. Morimoto, D. Kaji, T. Akiyama, S. Goto, H. Haba, E. Ideguchi, R. Kanungo, K. Katori, H. Koura, H. Kudo, T. Ohnishi, A. Ozawa, T. Suda, K. Sueki, H. S. Xu, T. Yamaguchi, A. Yoneda, A.Yoshida, and Y. L. Zhao: J. Phys. Soc. Jpn. **73**, 2593 (2004).
5) A. Drentje, A. Girard, D. Hitz, and G. Melin: Rev. Sci. Instrum. **71**, 623 (2000).

Production of high intensity $^7Li^{3+}$ ion beam

Y. Ohshiro,* S. Watanabe,* S. Yamaka,* Y. Higurashi, and S. Kubono*

At the AVF cyclotron facility in RIKEN, high intensity $^7Li^{3+}$ ion beams were successfully produced by a Hyper ECR ion source[1] using a micro-oven method for nuclear astrophysics experiments at the CRIB separator[2] this year. To production of intense $^7Li^{3+}$ ions, a crucible insertion method has been developed to feed the vapor of metallic elements into the discharge chamber. The method is applicable to production of high current stable ion beams from low melting-point material like Li. Thereby, the maximum beam current of 75 eμA was produced by the Hyper ECR ion source. This current was roughly equivalent to the value obtained at Dubna.[3]

According to CRIB scientific programs, one of the key ions required is the high intensity $^7Li^{2+}$ and $^7Li^{3+}$ beams. The $^7Li^{2+}$ ions were preliminary produced by a rod insertion method[4] using LiF solid material, and used for the experiment at CRIB. The maximum beam intensity of $^7Li^{2+}$ extracted from the source was 48 eμA, a $^7Li^{3+}$ beam intensity of about 3.5 eμA (See Table 1). However, in this case, the beam intensity decreased drastically by a bad vacuum pressure, because the LiF rod (melting point being 870°C) evaporated quickly by the higher RF power required than for $^7Li^{2+}$ ion production.

In order to produce a high intensity $^7Li^{3+}$ beam, a crucible insertion method has been developed. A schematic drawing of the crucible insertion system in the Hyper-ECR ion source is shown in Fig. 1. The system consists of a container (called a crucible) of stainless steel with a heat-resistant attachment of Ta (called a cap) and a thin cylindrical Ta sheet (called a hot liner) placed inside the discharge chamber to prevent the condensation of metal at the chamber wall. The crucible that contained metallic Li was placed near the ECR zone to vaporize and supply the material into the ECR zone. Moreover, a hot liner was set on the discharge chamber wall with a 0.5 mm gap. The hot liner inside the discharge chamber provides a better condition to produce intense beams for elements of solids with relatively low melting point.

Since the ions of $^7Li^{3+}$ and $^{14}N^{6+}$ cannot be separated by the mass analyzer of the ECR ion source,

Table 1. ^{7}Li beam intensities produced.

	$^7Li^{2+}$ (eμA)	$^7Li^{3+}$ (eμA)
Rod method	48	3.5
Crucible method	200	75

* Center for Nuclear Study, Graduate School of Science, University of Tokyo

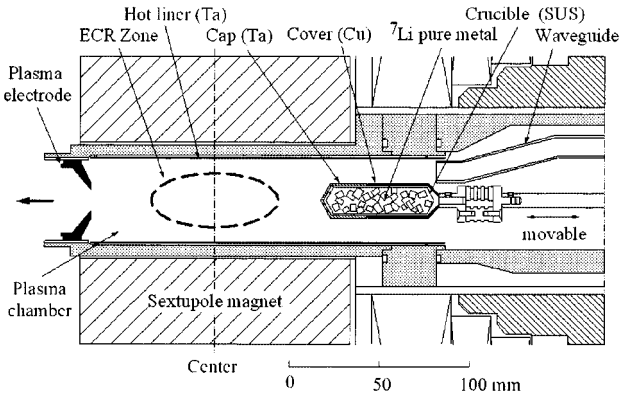

Fig. 1. Schematic drawing of crucible insertion system in Hyper-ECR ion source.

the beam intensities of $^7Li^{3+}$ were first estimated by comparing them with the quantity of the $^{14}N^{5+}$ ions (indicated by the dotted line in Fig. 2). Then, the intensity ratio of $^7Li^{3+}$ was measured by the cyclotron. The $^7Li^{3+}$ ion beam was injected axially together with the $^{14}N^{6+}$ beam into the cyclotron. But, the $^{14}N^{6+}$ ions were well separated by the cyclotron. In the case of $^7Li^{3+}$ injection, the transmission efficiency from the ECR source to the exit of the cyclotron was about 4–6%.

The operating conditions of the ECR ion source for $^7Li^{3+}$ production were as follows. The two peaks of the mirror fields were 10.5 kG and 11.5 kG, and the length of the ECR zone was approximately 70 mm. The RF (14.2 GHz) power was approximately 320 W, and helium gas was fed into the discharge chamber as a supporting gas. The vacuum pressure was 7×10^{-7} Torr in operation.

A nice feature of this crucible insertion system is that the beam intensity can be change by moving the

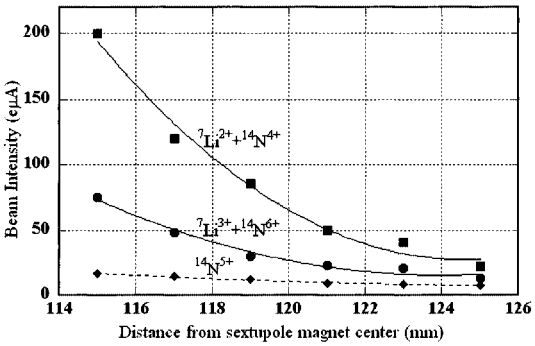

Fig. 2. The beam intensity obtained as a function of distance to the crucible from the center of the sextupole magnet.

crucible position. The beam intensity increases when moved closer to the ECR zone. Figure 2 shows the beam intensity obtained as a function of distance to the tip of the crucible from the center of the sextupole magnet. As an example, the $^{7}Li^{3+}$ beam intensity was 75 eμA at the distance of 115 mm, and $^{7}Li^{2+}$ ions was 200 eμA at the same distance.

The Li consumption was approximately 15 mg/h in long-term operation (up to 6 days) with the $^{7}Li^{3+}$ injected current of 20–40 eμA. The crucible has a length of 52 mm and the useful volume is about 9 cm^3. Thus, this method will be able to provide the beam for about 300–350 hours.

A further development on the stability and the intensity is in program for long-term operation.

References

1) Y. Ohshiro et al.: RIKEN Accel. Prog. Rep. **36**, 279 (2003).
2) Y. Yanagisawa et al.: Nucl. Instrum. Methods Phys. Res. A **539**, 74 (2005).
3) S. L. Bogomolov et al.: Proc. 13th Int. Workshop on ECR Ion Sources, Cern, Geneva, Switzerland, 1999-5 (CERN, 1999), p. 71.
4) Y. Ohshiro et al.: RIKEN Accel. Prog. Rep. **38**, 253 (2005).

Conceptual design of a 28 GHz superconducting ECR ion source

T. Nakagawa, M. Kidera, Y. Higurashi, J. Ohnishi, H. Saitoh, A. Goto, and Y. Yano

To achieve 1 pμA of U ion beam at 350 MeV/u, higher than 15 pμA of U^{35+} ion beam is required from an ion source, unless we use the first charge stripper. To produce such intense beam of highly charged heavy ions, we have to use a higher magnetic mirror ratio and a higher microwave frequency ($>$ 18 GHz) to increase plasma density and ion confinement time.

Figure 1 shows the schematic drawing and magnetic field strength of the superconducting ECR ion source which has an operational frequency of 28 GHz. To obtain a larger plasma volume, we use a special geometrical arrangement of the solenoid coils (Flat $B_{\min}$ configuration) as shown in Fig. 1. Using this arrangement, we obtain the volume 3–4 times larger than that for classical magnetic field configuration. A sextupole field is generated by six racetrack coils wounded around a pole piece. To obtain a good plasma confinement at 28 GHz, we need a maximum mirror magnetic field strength of 4 T and a radial field strength of 2 T.

Calculations using the three dimensional codes TOSCA were used to develop the superconducting magnet structure. The inner and outer diameters of solenoid coil 1 were 290 and 450 mm, respectively. The estimated total stored energy was 300 kJ under this condition.

We found that the magnetic field gradient at the resonance zone plays an essential role in increasing the plasma density and electron temperature. Magnetic field gradient strongly depends on the minimum magnetic field strength ($B_{\min}$) of the mirror field.[1,2] Using this coil arrangement as shown in Fig. 1, we can change $B_{\min}$ without changing maximum magnetic field (B_{ext} and B_{inj}) independently to optimize the magnetic field gradient at the resonance zone.

The inner diameter and length of the plasma chamber are 15 and 50 cm, respectively. The plasma chamber wall is made of Al to donate cold electrons to the plasma to decrease plasma potential.[3,4] Note that Al is very resistant to plasma etching. This reduces contamination in the plasma of the ions from the wall. A biased electrode is installed to obtain the same effect as that of the Al chamber wall.[5] The cooling of all surfaces in contact with the plasma using water minimizes the temperature effects caused by plasma and microwave heating at high microwave power.

At lower microwave frequency ($<$ 18 GHz), one of the high performance ECR ion sources is the AECR-U at the LBL, which has an operational frequency of 14 GHz.[6] The beam intensity of U^{35+} ions is about 16 eμA at an RF power of 1 kW as shown in Fig. 2.

The volume of the resonance zone of the new RIKEN SC-ECR ion source described here is 10-fold larger

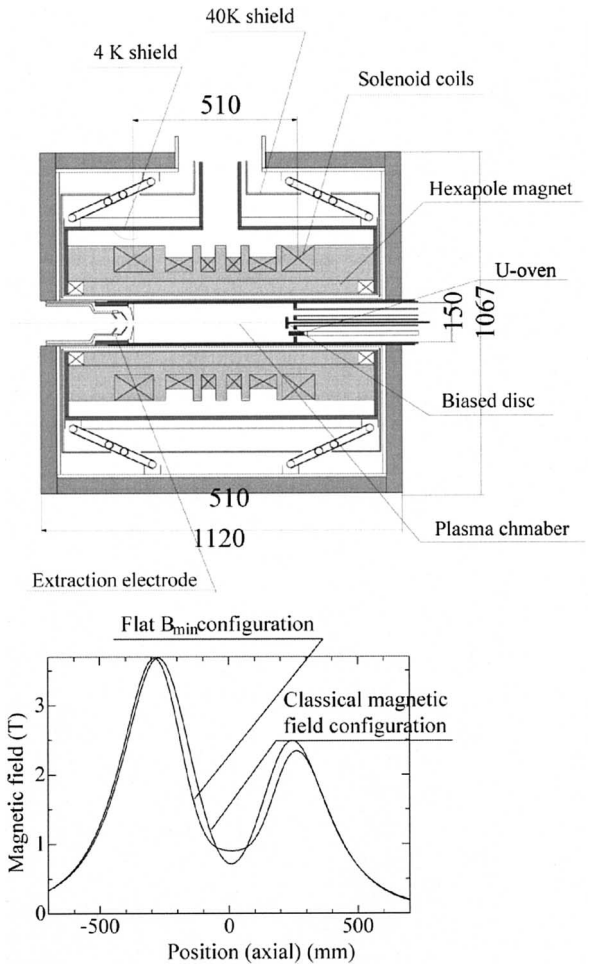

Fig. 1. Schematic drawing of SC-ECRIS and magnetic field configuration.

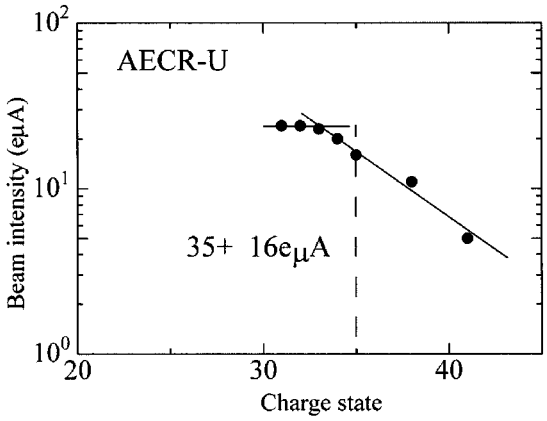

Fig. 2. Beam intensity of U ions from AECR-U.

than that of the AECR-U. The microwave frequency is two-fold higher than that of the AECR-U. This means that in principle the new ion source can produce an intensity 40-fold higher than that of the AECR-U. However, we have to use a higher microwave power ($\sim$10 kW) to obtain sufficiently high electric field gradient at the resonance zone, because the plasma chamber volume is quite large (about 8 L), which is $\sim$10–fold large volume of the AECR-U.

The expected total current from the ion source is higher than 10 mA. In this case, the normalized emittance of highly charged heavy ions is estimated to be $1\,\pi$mm$\cdot$mrad, which is mainly caused by the space charge effect. Under this condition, we have to supply a very high extraction voltage (higher than 60 kV) to obtain a good emittance (unnormarized emittance of $\sim$150 pmm$\cdot$mrad) for matching the acceptance of the RFQ linac. The ion source will be equipped with a movable accel-decel extraction system not only to improve the extraction conditions, but also to compensate for the space charge effect.

References

1) H. Arai, M. Imanaka, S. M. Lee, Y. Higurashi, T. Nakagawa, M. Kidera, T. Kageyama, M. Kase, Y. Yano, and T. Aihara: Nucl. Instrum. Methods Phys. Res. A **491**, 9 (2002).
2) M. Imanaka, T. Nakagawa, H. Arai, I. Arai, and S. M. Lee: Nucl. Instrum. Methods Phys. Res. B **237**, 647 (2005).
3) T. Nakagawa: Jpn. J. Appl. Phys. **30**, L930 (1991).
4) T. Nakagawa, Y. Miyazawa, M. Hemmi, T. Chiba, N. Inabe, M. Kase, T. Kageyama, O. Kamigaito, A. Goto, and Y. Yano: Jpn. J. Appl. Phys. **35**, 4077 (1996).
5) S. Biri, T. Nakagawa, M. Kidera, Y. Miyazawa, M. Hemmi, T. Chiba, N. Inabe, M. Kase,T. Kageyama, O. Kamigaito, A. Goto, and Y. Yano: Nucl. Instrum. Methods Phy. Res. B **152**, 386 (1999).
6) Z. Q. Xie: Rev. Sci. Instrum. **69**, 625 (1998).

Improvement for stable operation of flattop acceleration system of AVF cyclotron

S. Kohara, O. Kamigaito, N. Sakamoto, M. Kase, T. Chiba, K. Masuda,[*1]
Y. Chiba, S. Watanabe,[*2] K. Kumagai, and A. Goto

The flattop acceleration system in the AVF cyclotron has been developed to improve the transmission efficiency and energy spread of beams. The additional resonator was installed in August 2001. The flattop accelerating voltage was generated by the superposition of the fundamental and third harmonics on the dee and a beam of good quality was successfully obtained in a beam acceleration test.[1)] However, we encountered a serious problem on atmospheric discharge at the lower ceramics insulator support for the main coaxial resonator, which is shown in Fig. 1, when the maximum flattop accelerating voltage was generated. The discharge does not occur when the dee is excited with a fundamental voltage only even at the maximum. The reason for this difference is that the peak voltages of the fundamental and third harmonics are cumulatively superposed at the ceramics insulator support, because the phase of the third harmonics is inverted between the dee and the ceramics insulator support while that of the fundamental is unchanged.

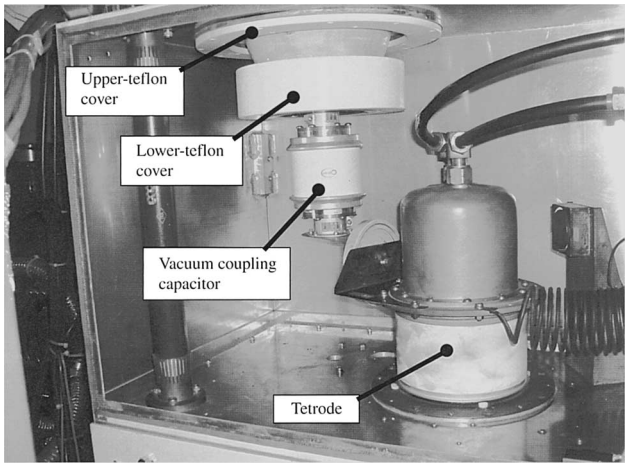

Fig. 2. Photograph of inside of main amplifier, in which teflon covers are attached to lower ceramics insulator support.

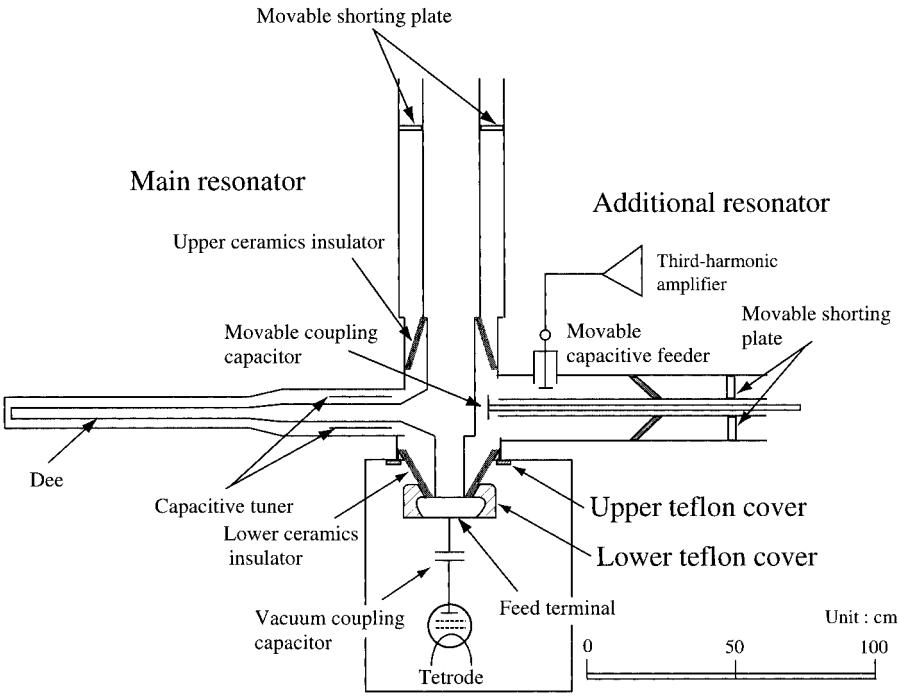

Fig. 1. Cross-sectional view of main resonator equipped with additional resonator for flattop acceleration system and power amplifiers. Teflon covers are attached to the upper and lower sides of the lower ceramics insulator support.

*1 SHI Accelerator Service, Ltd.
*2 Center for Nuclear Study, University of Tokyo

Moreover, the discharge occurs mainly at the lower ceramics, not at the upper ceramics, due to the geometrical asymmetry of the system.

To clarify this discharge problem, teflon covers were manufactured and attached to the upper and lower sides of the lower ceramics insulator. They were used to suppress the emission of electrons at a high potential. A photograph of the inside of the main amplifier, in which the teflon covers are attached to the lower ceramics insulator support, is shown in Fig. 2. After attaching the teflon covers, the atmospheric discharge hardly occurred in the power test of the flattop acceleration system. The voltages of the fundamental and third harmonics can be stably generated at 45 kV and 5 kV, respectively, when the fundamental frequency was 16.3 MHz.

Reference

1) S. Kohara et al.: Nucl. Instrum. Methods Phys. Res. A **526**, 230 (2004).

Study of new flat-top resonator for RRC

L. Stingelin, A. Goto, O. Kamigaito, N. Sakamoto, and Y. Yano

Flat-top resonators are commonly used in cyclotrons to add a third[1,2] or fifth[3] harmonic to the accelerating voltage. The resulting broader acceleration voltage reduces the energy spread of particle bunches and hence the extraction losses of the cyclotron, which is usually the limiting factor for beam intensity. Since the beam losses in the RIKEN Ring Cyclotron (RRC) might limit the beam intensity of the RIKEN Accelerator Research Facility, a design study for a flat-top resonator was launched.

The flat-top will be achieved by a third-harmonic resonator with a frequency range of 54–120 MHz and a total peak gap voltage of approximately 135 kV. This new resonator could replace the "valley box SE," where currently only phase probes and four vacuum pumps are located. Its boundaries are limited by the positions of the first and last turns, the injection and extraction bending magnets and the sector magnets "east" and "south" as indicated in Fig. 1. Therefore, the available space is small and it is challenging to find a resonator shape that fits into the cyclotron.

In the first step, three different types of resonator geometry were investigated. The three-dimensional electromagnetic eigenmode solver in ANSYS[4] was used to simulate and compare a single-gap resonator with two double-gap resonators, one operated in the fundamental mode with a phase shift of 180° between the gaps and the other operated in a higher mode with a doubled opening angle and a phase shift of 0°. For all three types of resonator geometry, a geometry was found that fits into the valley box. However, the double gap resonator in the fundamental mode showed the most promising characteristics. It can be inserted into one half of the valley box, leaving the other half of the valley box free for the phase probes and the vacuum pumps. Furthermore, it requires less rf power than the other resonators and requires no intensive cooling on the sidewalls close to the injection and extraction magnets. However, the double-gap design has the disadvantage of a reduced efficiency for some harmonic numbers, since the Dee angle is fixed and therefore cannot have the optimal value for all the harmonic modes of the cyclotron. Furthermore, the use of one half of the valley-box leads to small particle momentum kicks in the radial direction, since one gap is necessarily not perfectly perpendicular to the trajectory of the particles.

In the second step, a refined simulation model of the double-gap resonator was created, enabling the direct three-dimensional analysis of the surface fields and the rf parameters. The full parametrization of the simulation geometry was very convenient for the efficient optimization of the resonator geometry. Due to mirror symmetry of the geometry with respect to the beam plane, only one half of the structure had to be simulated. This type of simulation used approximately 180,000 elements, 270,000 nodes and the solver required approximately 700 MBytes of memory when second-order tetrahedral elements (ANSYS-type "HF119") were used. The calculation times were approximately five minutes for preprocessing, including the generation of geometry and meshing, approximately one hour for solving and approximately ten minutes for post processing.

It was found that, at higher frequencies, a design with two stems (see Fig. 2) is superior to a design with one stem only. Preliminary simulation results pre-

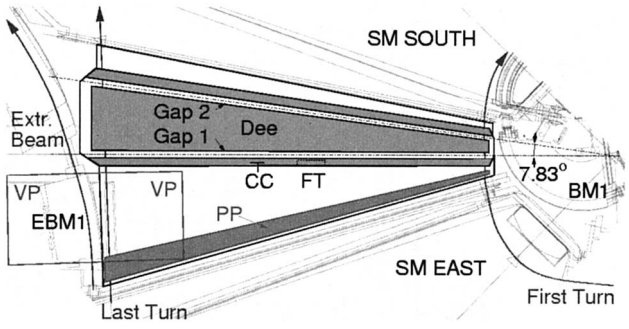

Fig. 1. Top view of proposed valley box with flat-top resonator: phase probes (PP), capacitive coupler (CC), fine tuner (FT), injection, extraction bending magnets (BM1, EBM1) and sector magnets (SM).

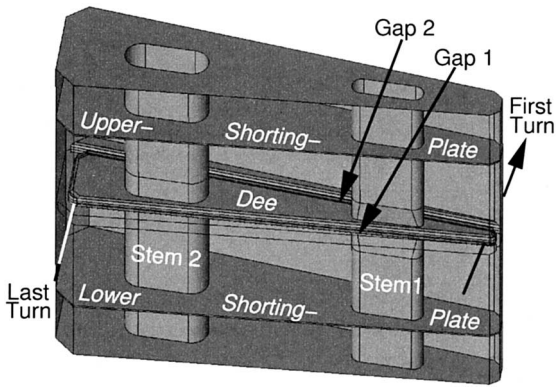

Fig. 2. Flat-top resonator with removed sidewall. The shorting plates are set to an operation frequency of 68 MHz. The rf-geometry has an approximately 2.64 m maximum length, 0.68 m maximum width and 2 m maximum height.

dicted a maximum quality factor of $Q_0 = 13,900$ at an operation frequency of 85 MHz and a minimum quality factor of $Q_0 = 12,000$ at 120 MHz. Figure 3 shows that coarse tuning of the resonator can be achieved by changing the vertical position of the shorting plates. A resonance frequency of 52.6 MHz is reached at a distance of 1.0 m from the beam plane and 120 MHz is reached at a distance of 23.5 cm for example. The bellows for the adjustment of the resonance frequency must therefore reach approximately 77 cm beyond the upper and lower cavity wall.

For the calculation of the gap voltage distribution in Fig. 4 and the power requirement in Fig. 5, the fields were then scaled according to the following procedure. The mean gap voltage is adjusted to be equal to the sum of the mean gap voltage of the main resonators, divided by nine. The calculations are performed for a peak voltage of 300 kV in the gaps of the main resonators. Actual field values and power requirements at

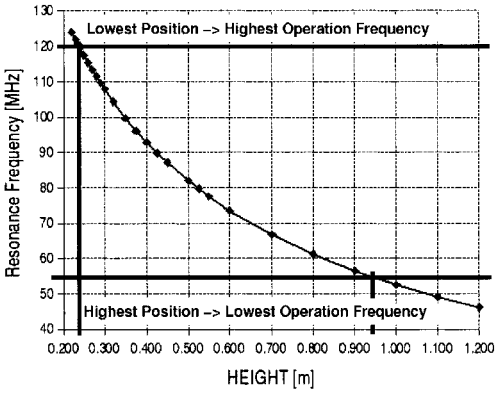

Fig. 3. Coarse tuning of resonator operation frequency. The distance of the shorting plate to the beam plane is indicated.

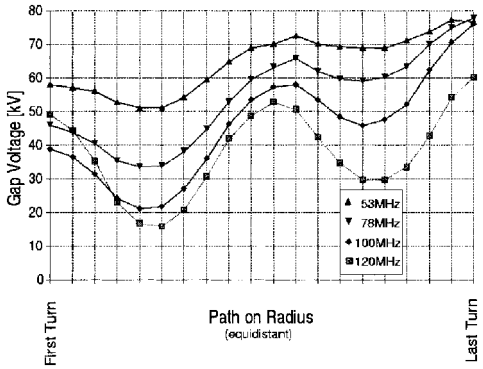

Fig. 4. Gap voltages for gap 1 in function of radius. Voltage distributions are shown for four different operation frequencies. Gap 2 has approximately the same gap voltage distribution.

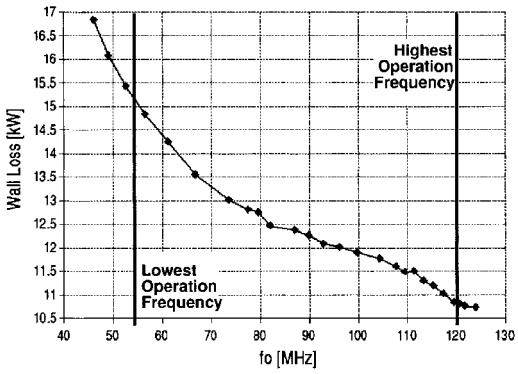

Fig. 5. Power requirement in function of operation frequencies. Power losses in rf contacts are not taken into account.

frequencies lower than 90 MHz will be smaller because of limitations in the main resonators at corresponding frequencies.

Since the flat-top voltages are decelerating, a radially decreasing gap voltage in Fig. 4 leads to a compression of the particle bunches by the rf magnetic field and increasing gap voltage to decompression.[5] The resulting effect on the particle distribution will be analyzed by detailed beam dynamic simulations.

The highest current density in the shorting plate of 23 A/cm was found at an operation frequency of 113 MHz and the maximum electric field in the resonator of 3.7 MV/m at a frequency of 90 MHz. This field strength is lower than half of Kilpatrick's electric field limit.[6]

In the future, we will investigate the mechanical and thermal design of the resonator and finalize the coupling[7] and fine-tuning method. In addition, the rf parameters will be optimized further.

This work is supported by the Japanese Society for the Promotion of Science as postdoctoral fellowship. Support of the RIKEN Computing Center is also gratefully acknowledged for providing the necessary simulation resources.

References

1) W. Joho: Proc. 11th Int. Conf. on Cyclotron and Their Applications, Tokyo, 1986-10 (Ionics Publishing Company, 1987), p. 31.
2) S. Kohara et al.: Nucl. Instrum. Methods Phys. Res. A **526**, 230 (2004).
3) J. L. Conradie: Proc. 14th Int. Conf. on Cyclotron and Their Applications, Cape Town, South Africa, 1995-11 (World Scientific, Singapore, 1996), p. 249.
4) http://www.ANSYS.com
5) T. Fujisawa: Nucl. Instrum. Methods Phys. Res. A **292**, 1 (1990).
6) W. D. Kilpatrick: Rev. Sci. Instrum. **28**, 824 (1957).
7) P. Balleyguier: Part. Accel. **34**, 113 (1997).

Status of control and beam interlock system for RARF and RIBF

M. Kobayashi-Komiyama, M. Fujimaki, I. Yokoyama, and M. Kase

We report two major achievements for the control system of RARF and RIBF this year; one is the replacement and expansion of the EPICS control network system, and the other is the introduction of the new beam interlock system to RARF.

We have started to control the magnet power supplies of SRC and some of the pieces of beam diagnostic equipment of IRC using EPICS this year. Following this expansion of the control system and considering the total number of devices that will be controlled by EPICS in one or two years, we faced a problem in our EPICS control network system. Because it was constructed as a flat one, we could assign a smaller number of control devices to the network than our needs. We can assign up to 128 control devices in the previous system. Considering only the N-DIM system, which is used as a controller of beam diagnostic equipment and a vacuum system among others, more than 100 IP addresses are required in RARF and RIBF because each N-DIM uses one IP address. Because we use not only N-DIMs but also other controllers such as PLC, server computers and PCs for the operator interface in the network, we have to expand the control network system. Therefore, we discussed with Fujitsu Corporation about the best solution for the expansion of our network system.

The new network system is shown in Fig. 1. It was designed to have five subnetworks in the system. The first subnetwork is used for the VME, its server computer, PCs for an operator interface and high-level control computers that work for data archiving and alarm systems among others. The second subnetwork is used for N-DIM for the Faraday cup control and vacuum control and their server computer. The third subnetwork is used for the N-DIM for a beam profile monitor and radial probe and their server computer. The fourth subnetwork is used for PLC and its server computer, and the last subnetwork is used for the maintenance of the network system itself. We newly introduced one Cisco's Catalyst 4506 device as a router and nine Catalyst 2950 devices as edge switches, and set up optical fiber cables among them. The router was placed at the control room of Nishina building, which is the main control room of RARF and RIBF. Three edge switches were placed in Nishina building, and four in Linac building, and two in RIBF accelerator building. We replaced our control network in summer. The performance of the network in terms of communication speed and stability is equal to that of the previous network. It has worked well without any troubles.

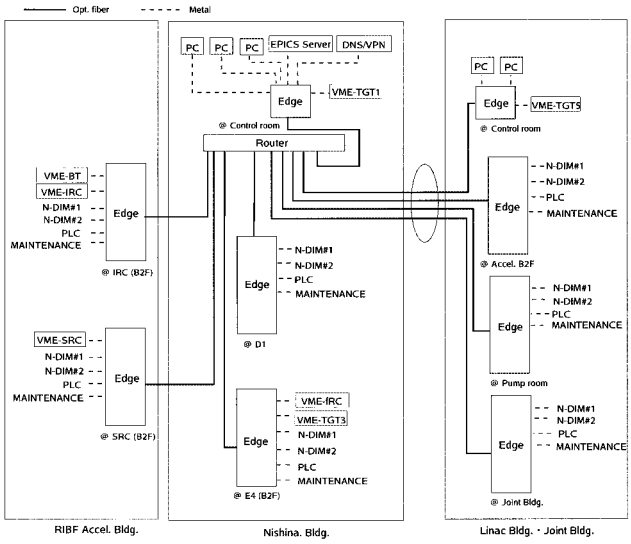

Fig. 1. Structure of RARF and RIBF control network system.

In RARF, we have been using a beam interlock system that is based on CAMAC-CIM/DIM for approximately 20 years. We have to expand it to include fRC and its beam transport line in one year. However, it is not a good idea to expand an old system such as CAMAC. Therefore, we introduced a new beam interlock system using PLC to RARF in addition to the current system. The new system will include signals from RRC, fRC and their beam transport line placed from the joint building to E1. The development of a prototype of the system started in 2001, and the prototype has been working as a beam interlock system in RILAC for approximately three years. When we designed the RRC-fRC beam interlock system on the basis of the prototype, we expanded its function. The structure of the system is shown in Fig. 2, and details of the system are described in another paper.[1] The main features of the system are as follows:

- The system is constructed using five Melsec PLCs

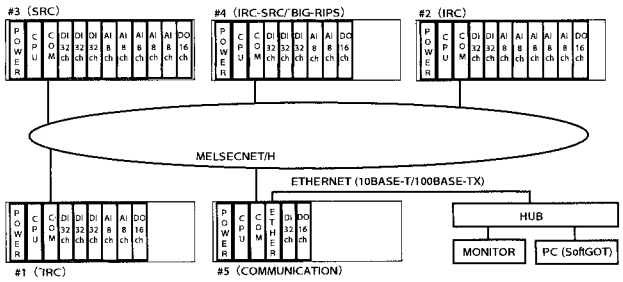

Fig. 2. Structure of beam interlock system for RRC/fRC.

and connected to each other with optical fiber cables.

- The beam is stopped by the beam chopper at the exit of the ion source of RILAC within 5 seconds after the system receives a digital or analog interlock signal.
- We can set an interlock signal pattern depending on the type of beam or operation mode at one time by downloading a file from PC to PLC as well as by setting each signal manually (new function).

Each PLC station is set at the following place: three stations are placed at the corridor of a controlled area in Nishina building, one station is set at the control room in Nishina building and the last one is set at the joint building. As a first step in using this system, we replaced the control system for reading beam current from the baffle slits of the entrance and exit areas of the RRC from the CAMAC-CIM/DIM to N-DIM, and those 27 signals were connected to three stations of the beam interlock system. We confirmed that it works well during a beam service time in October. We are going to include more input signals such as those from the vacuum system or magnet power supplies gradually next year.

Reference

1) M. Kobayashi-Komiyama et al.: Proc. 2nd Annu. Meet. of Particle Accelerator Society of Japan and 30th Linear Accelerator Meet. in Japan, Tosu, 2005-7 (2005), p. 615.

Longitudinal profile monitor using plastic scintillator for RARF

T. Watanabe, M. Kase, M. Wakasugi, N. Fukunishi, and Y. Yano

New plastic scintillation profile monitors have been fabricated to evaluate energy and a longitudinal profile of heavy-ion beams for the RIKEN Accelerator Research Facility (RARF). Two sets of longitudinal profile monitors were installed into the transport line of the RIKEN heavy-ion linac (RILAC) and the RIKEN ring cyclotron (RRC). Preliminary experimental results obtained using the heavy-ion beam are described in this article.

When a scintillation material is struck by a charged particle, some fluorescence photons are created by the electron energy loss due to the collision of the beam particle with the target. These photons can be amplified by a photomultiplier that has extremely high sensitivity, and converted to a logical pulse by a discriminator. Finally, the longitudinal beam profile can be obtained by using a time-to-digital converter (TDC), which digitizes the time lag between start (detector pulse) and stop (bunch clock) and stores the events into the memory of the TDC. Furthermore, the energy of the beam can be measured on the basis of the time of flight (TOF) of the beam using a longitudinal profile monitor set. The plastic scintillators are chosen for our monitors because they are cheap and easy to produce in nearly every mechanical shape. In the present work, the plastic scintillating material is the NE-102 with a size of $30 \times 30\,\mathrm{mm}^2$, a thickness of 0.5 mm and a decay constant of 2.4 ns. The specifications of the photomultiplier are tabulated in Table 1 and a photo and a schematic drawing of the longitudinal profile monitor are shown in Figs. 1 and 2, respectively. The plastic scintillation is pneumatically driven by the pneumatic rotary feeder.

Prior to the energy measurements by the TOF method, preliminary measurements of the longitudinal profile of the heavy-ion beam were carried out. For the experimental measurements, one plastic scintillation profile monitor set that was installed in the beam transport line of RILAC was used. Taking into account the conversion time of the TDC (Lecroy 2228A) of approximately 100 μs, the individual particles can be counted using scintillators if the count rate is less than

Table 1. Specifications of photomultiplier.

Multiplier tube	Hamamatsu R7400U
Type	Metal packaged
Tube Size	Dia.16 mm
Photocathode Area Size	Dia.8 mm
Wavelength (Peak)	420 nm
Gain Typ.	7.0×10^5
Anode Rise Time Typ.	0.78 ns

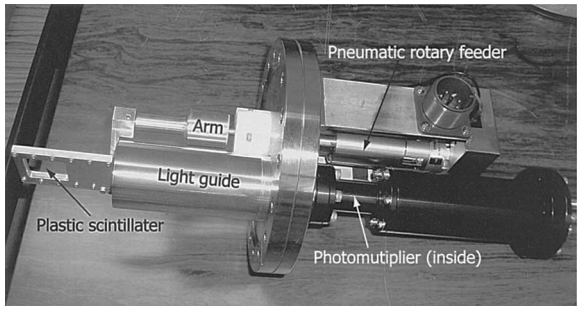

Fig. 1. Photo of longitudinal profile monitor using plastic scintillator.

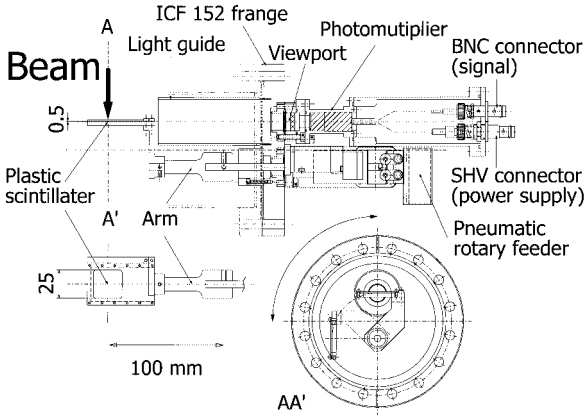

Fig. 2. Schematic drawing of longitudinal profile monitor using plastic scintillator.

10^4. The time difference data between the pulse signal detected by the plastic scintillator and the bunch clock (RF signal) is stored and the time spectrum can be obtained as a result. The time spectra measured using an $^{40}Ar^{9+}$ (3.65 MeV/u) beam, which represent the longitudinal beam profile, are shown in Fig. 3. These measurements show a beam bunching effect in a rebuncher, which was operated at a frequency of 37.75 MHz (a period of 26.49 ns). By subtracting the background and the data with less than 30% of the amplitude and fitting these data using Gaussian curves, it has been found that the FWHM of the longitudinal phase width was compressed from 65.0° to 50.8°. To maintain the minimal background, the Ar beam was attenuated to between 200 cps to 300 cps using slits in these measurements. Next, let us evaluate the time resolution of this system, taking into account the following factors:

(1) The time resolution ΔT_t of the TDC has been measured to be less than 100 ps, which was calibrated using a precise clock generator, and the

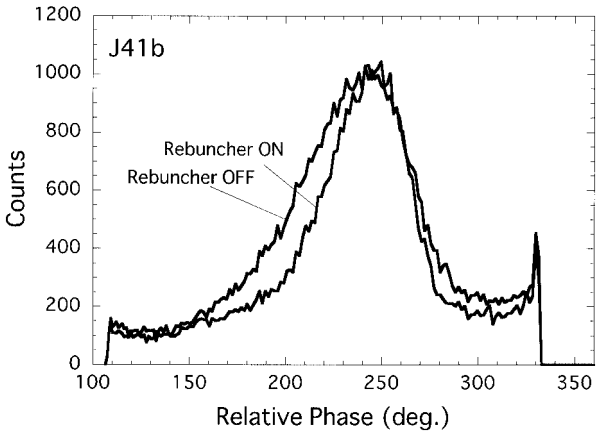

Fig. 3. Measured time spectra of $^{40}Ar^{9+}$ (3.65 MeV/u) beam, which represent longitudinal beam profiles. These measurements show a beam bunching effect in a rebuncher. By subtracting the background and the data with less than 30% of the amplitude and fitting these data using Gaussian curves, it has been found that the FWHM of the longitudinal phase width was compressed from 65.0° to 50.8°.

jitter (ΔT_j) of the photomultiplier was 50 ps.

(2) The time for the beam to pass through the plastic scintillator (T_p) is 19 ps because the ratio (β) of beam velocity (v) to light velocity (c) was 0.08832 ($v = \beta c$) and the thickness of the plastic scintillator was 0.5 mm.

(3) Since the beam size (R_b) is typically 30 mm, the maximum time difference ($\Delta T_b = R_b/c$) in the time it takes for the photons to reach the photomuptiplier through the light guide is 100 ps.

(4) The fitting error of the Gaussian curve (ΔT_f) is 40 ps.

The total time resolution of this system ΔT_{total} can then be evaluated to be approximately 156 ps using the following equation.

$$\Delta T_{total} = \sqrt{\Delta T_t^2 + \Delta T_j^2 + T_p^2 + \Delta T_b^2 + \Delta T_f^2}.$$

In the next step of the experiment, the precise energy measurements of the heavy ion will be carried out by the TOF method.

Beam current measurement using HTS-SQUID monitor for RRC

T. Watanabe, M. Kase, Y. Sasaki,[*1] S. Watanabe,[*2] T. Ikeda, T. Kawaguchi,[*3] and Y. Yano

This year, a prototype of a highly sensitive beam current monitor with a high-temperature superconducting (HTS) SQUID and an HTS magnetic shield,[1–7] that is the HTS-SQUID monitor, has been installed in the beam transport line of the RIKEN Ring Cyclotron (RRC). Unlike other existing facilities, the HTS-SQUID monitor allows us to measure the DC of high-energy heavy-ion beams nondestructively in such a way that the beams are diagnosed in real time and the beam current extracted from the RRC can be recorded without interrupting the beam user's experiments.

This system consists of two vacuum chambers completely separated from each other: one for a cryostat in which the HTS SQUID, an HTS magnetic shield and an HTS current sensor are cooled, and the other for a beam chamber in which a beam passes through. In the present work, all these HTS fabrications are cooled by a low-vibration pulse-tube refrigerator that has a refrigeration power of 11 W at a temperature of 77 K. The operation temperature can be set in the range of 64 K to 90 K (the critical temperature of the HTS SQUID) using a heater, because the pulse-tube refrigerator is capable of cooling the system to temperatures lower than liquid-nitrogen temperature. Furthermore, it is possible to stabilize the temperature of the HTS SQUID with an accuracy of 5 mK using a PID feedback controller, which has four thermometers and a heater. The temperature of the cold head was measured as a function of time. Consequently, the deviation in the temperature over a period of 18 hours was controlled within 3.4 mK (1σ).[7] Both the HTS magnetic shield and the HTS current sensor were fabricated by dip coating[8] a thin Bi_2-Sr_2-Ca_2-Cu_3-O_x (Bi-2223) layer on 99.9% MgO ceramic substrates. The HTS-SQUID system (Model BMS-G manufactured by Tristan Technologies) is composed of a low-noise HTS-SQUID gradiometer (Y-Ba_2-$Cu_3O_{7-\delta}$).[9]

In addition to current measurement, an important function has been performed in which the beam position can be measured by dividing the thin-layer HTS current sensor into two parts and by setting a SQUID on each bridge.[10] It is our expectation that the HTS-SQUID monitor will be capable of measuring beam current and beam position simultaneously in real time.

Prior to the beam measurements in the RRC hall, preliminary measurements were successfully carried out as follows: (1) the first beam test of the HTS-SQUID monitor in the beam transport line for the electron cyclotron resonance (ECR) ion source in the CNS experimental hall and (2) the second beam measurement at the E1 experimental hall in RIKEN to measure the current of the high-energy heavy-ion beam.[7] This year, aiming at practical use for accelerator operations, the authors installed the HTS-SQUID monitor system in the beam transport line (Fig. 1 (a)) in the RRC hall (Fig. 1 (b)). However, the SQUID electric circuit, which has the dynamic range of 100 dB (from 1 μA to 0.1 A) and the frequency range from DC to 25 kHz, did not function normally due to the following reasons: (1) an RF background is caused by the high-power RF cavities of the RRC, which can produce a total power of 0.6 MW; (2) a large stray magnetic field is induced by the main magnetic field of the RRC (max. 1.67 T); (3) there are a neutron radiation dose of 25.5 Sv and a gamma radiation dose of 3.0 Sv for a period of one year. The radiation doses of neutrons and gamma rays were measured using an ionization chamber and a ^{3}He proportional counter, respectively. The actual radiation doses where the HTS-SQUID monitor is installed should be higher than the above values, because both dosimeters are located 4 m above the HTS-SQUID monitor. These data gave tentative criteria for the judgment of safety for radiation damage. After overcoming these difficulties by reinforcing the RF shield and hiding the flux-locked loop (FLL) circuit with lead and concrete blocks, there were no more problems with the beam current measurement. As a result, a 10 μA $^{40}Ar^{15+}$ beam intensity (63 MeV/u) was successfully measured with a 500 nA resolution, shown in Fig. 2, where a 1 μA beam produced $6.5\times10^{-3}\Phi_0$ of magnetic flux at the input coil of the HTS SQUID. Futhermore, a long recording of the extracted Ar beam current from the RRC without interrupting the beam user's experiments for approximately 4 hours was achieved, as is shown in Fig. 3 (a). In this recording, several dips in beam intensity due to

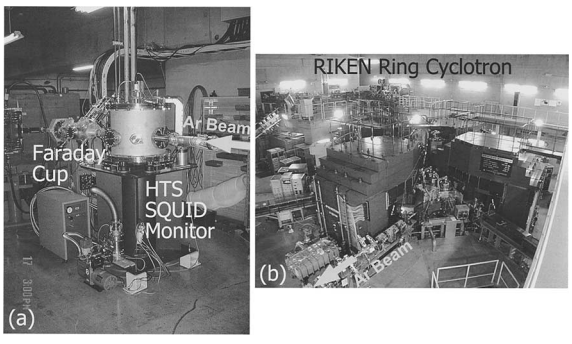

Fig. 1. The authors installed the HTS-SQUID monitor system in the beam transport line (a) and in the RRC hall (b).

*1 Matsushita Electric Industrial
*2 Center for Nuclear Study, Graduate School of Science, University of Tokyo
*3 KT Science Ltd.

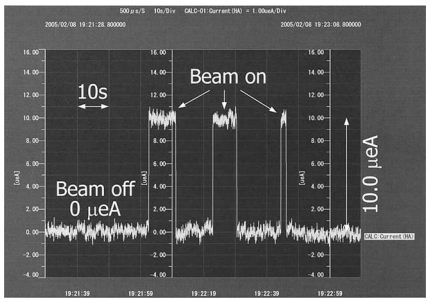

Fig. 2. A 20 μA $^{40}Ar^{15+}$ beam intensity (63 MeV/u) was succesfully measured in real time with a 500 nA resolution, where a 1 μA beam produced $6.5\times10^{-6}\Phi_0$ of magnetic flux at the input coil of the HTS SQUID.

ECR ion source discharge can be observed at irregular intervals of 10 seconds to 60 minutes. Figure 3 (b) shows a magnified image of Fig. 3 (a), which indicates that dips in current caused by ECR ion source discharge recovered within 400 ms. The current signals were analyzed by a fast Fourier transform (FFT) for a frequency domain, and the results are shown in Fig. 4. The amplitudes of ripples modulated on the beam current increased with beam current. All recording and control systems are connected to a PC-based data acquisition system. Through the Ethernet, these systems are linked to a laptop in the main control room located 200 m from the RRC hall. The sampling time for data acquisition is 500 μs and 100 data points are averaged to one data to improve the signal-to-noise ratio.

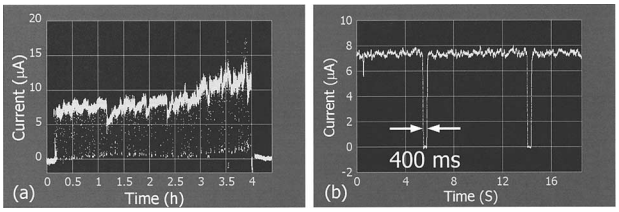

Fig. 3. (a) Measurement of 63 MeV/u Ar beam extracted from RRC, which could be recorded for approximately 4 hours without interrupting beam user's experiments. (b) Magnified image of (a) showing dips in current caused by ECR ion source discharge, which recovered within 400 ms.

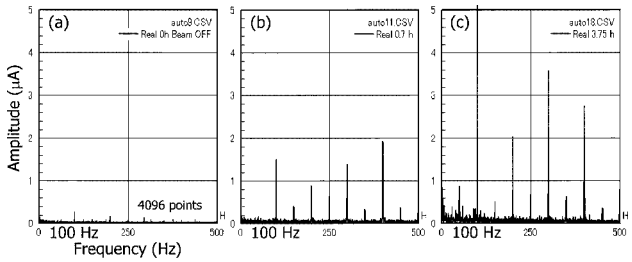

Fig. 4. Results analyzed by fast Fourier transform (FFT), which were measured at 0 h (beam off) (a), 0.7 h (b) and 3.75 h (c) in Fig. 3 (a).

In this study, the authors intended to determine the possibility of measuring the DC of high-energy heavy-ion beams nondestructively and in real time. Despite being performed in an environment with strong gamma ray and neutron flux radiations, RF background and large magnetic stray fields, measurements were successfully carried out. Although the intensity of a sub-microampere beam can be measured, a limit of minimum current higher than two orders of magnitude is required for fainter beam measurement. The possibility of fabricating the new HTS bridge circuit and introducing high-permeability cores into the SQUID through two holes has been investigated.[10] Figure 5 shows a picture of the new SQUID and the high-permeability cores. A test using a simulated beam current shows a 50-fold improvement in gain because the coupling efficiency of the transfer of the magnetic field produced by the simulated beam current to the SQUID is improved.

The authors are grateful to R. L. Fagaly and M. Faley for valuable insights into the HTS-SQUID system and also thank S. Ono, B. Mizuno, H. Kanada, S. Kojima and N. Koshio for their fruitful collaboration.

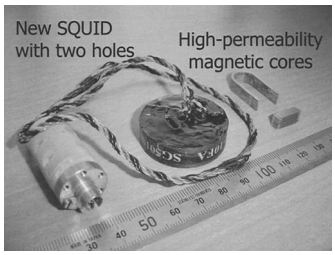

Fig. 5. Picture of new SQUID with two holes and high-permeability cores.

References

1) T. Watanabe et al.: RIKEN Accel. Prog. Rep. **35**, 314 (2002).
2) T. Watanabe et al.: Proc. 8th European Particle Accelerator Conf., Paris, France, 2002-6 (EPS-IGA, 2002), p. 1995.
3) T. Watanabe et al.: RIKEN Accel. Prog. Rep. **36**, 331 (2003).
4) T. Watanabe et al.: CNS Annu. Rep. **59**, 71 (2003).
5) T. Watanabe et al.: Proc. 14th Symp. on Accelerator Science and Technology, Tsukuba, 2003-11 (KEK, 2003), p. 99.
6) T. Watanabe et al.: RIKEN Accel. Prog. Rep. **37**, 310 (2004).
7) T. Watanabe et al.: Supercond. Sci. Technol. **17**, S450 (2004).
8) Y. Ishikawa et al.: Advances in Supercond. (Proc. ISS'91) **4**, 1076 (1992) .
9) M. I. Faley et al.: IEEE Trans. Appl. Supercond. (ASC2000) **11**, 1383 (2001).
10) T. Watanabe et al.: RIKEN Accel. Prog. Rep. **38**, 273 (2005).

Automatic sample changer for biological samples

H. Ryuto*, T. Abe, N. Fukunishi, Y. Hayashi, M. Kase, and Y. Yano

An automatic sample changer was constructed in compliance with numerous requests to irradiate a large number of biological samples. The automatic sample changer realizes undisturbed irradiation on more than 500 sample containers filled with biological samples without interruption for renewals of samples by hand at the heavily shielded beam line. Before the installation of the automatic sample changer, the maximum number of sample containers that were automatically irradiated by the automatic irradiation system[1] was from 5 to 9 according to the size of the sample containers, so from 56 to 100 times renewal of sample containers would be required to irradiate 500 sample containers. Therefore, the automatic sample changer allows effective use of limited beam time.

Figure 1 shows a schematic view of the automatic sample changer installed as a part of the automatic irradiation system. The movable table for samples of the automatic irradiation system was replaced with the automatic sample changer. The slits were also replaced with slits that can be remote-controlled.

The automatic sample changer consists of a movable table and six stages for cassettes. The cassettes are designed for accepting sample containers. Biological samples are filled into one of the sample containers. Typical sample containers are, for example, 5-cm-wide, 7.5-cm-high, and 1.25-cm-deep plastic boxes, and approximately 3-, 6-, and 9-cm-diameter plastic petri dishes. The sample containers are set into the cassettes, and then the cassettes are placed on the stages of the automatic sample changer. Seventeen cassettes fill one stage. The numbers of sample containers that can be set into the cassettes are from 4 to 12 according to the size of the sample containers. Because most of the cassettes can contain more than 5 sample containers, the maximum number of sample containers that can be automatically irradiated is more than 500. The cassettes are circulated among stages by lifts and air cylinders placed both on the upstream and downstream sides of the stages. One of the cassettes is picked up by a transfer arm on the upstream side of the topmost stage and carried to the beam position

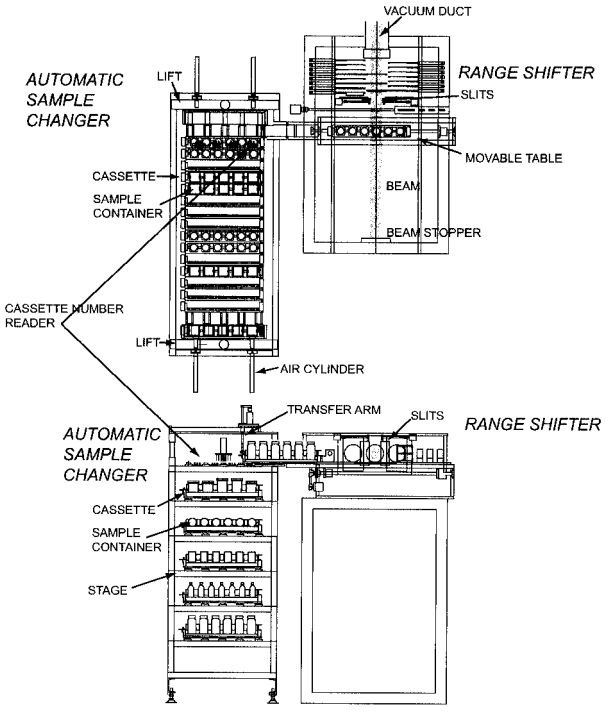

Fig. 1. Schematic view of automatic sample changer together with range shifter. The side view and view from downstream are shown.

by a movable table. The cassettes are numbered, and the cassette numbers are detected by detectors before being picked up by the transfer arm. The slits are automatically positioned at a certain width determined by the size of the sample containers indicated by the cassette number. The selections of absorber thicknesses and doses are specified by two-dimensional bar codes affixed on the sample containers.

The automatic sample changer was used in experiments, and showed good performance.

Reference

1) H. Akiyoshi, N. Fukunishi, M. Kase, Y. Yano, T. Abe, and Y. Yoshida: RIKEN Accel. Prog. Rep. **36**, 291 (2003).

* Formerly, H. Akiyoshi

Design of rebuncher between RRC and fRC

T. Aoki,* O. Kamigaito, N. Fukunishi, N. Sakamoto, L. Stingelin, and A. Goto

The beam extracted from the RRC will be injected to the fRC through a beam line of 100 m. The phase width of the beam keeps growing; the bunch length of the beam becomes a twofold during the transport. In addition, the fRC is operated at a frequency a threefold of that of the RRC. Therefore, a phase width of $\pm 5.0°$ during RRC extraction becomes $\pm 29°$ during fRC injection. Thus, injection becomes difficult.

Therefore, a rebuncher between the RRC and the fRC is indispensable for improving injection efficiency. It is required to keep the beam phase within $\pm 7.5°$ during fRC injection.

This rebuncher is also expected to regulate the change in beam energy caused by the variation of the thickness of the charge stripper after the RRC. For this purpose (acceleration mode), gap voltage should be as high as possible.

The basic parameters required for the rebuncher are 1) installation position, 2) voltage, 3) frequency, and 4) number of gaps. These parameters were determined as described below.

First, the longitudinal motion of the beam was investigated to determine the position and voltage. Assuming a longitudinal emittance of an erected ellipse of $\pm 0.06\%$ in momentum and $\pm 5°$ in phase for the output beam from the RRC,[1] the position and the voltage were determined so as to get the erected ellipse with a phase width of less than $\pm 7.5°$ during the injection of the fRC. To meet this condition, the position was determined 60 m downstream of the RRC. The required voltage was 930 kV at RRC frequency.

Next, rebuncher frequency and gap number were determined. As is well known, the actual gap voltage is proportional to the inverse of the harmonic number. On the other hand, the phase width at the rebuncher is proportional to the harmonic number. To keep the phase width less than $\pm 30°$, the harmonic number of 6 was chosen; the resonant frequency of the rebuncher was 110 MHz. Furthermore, the gap number of 4 was chosen to reduce the required gap voltage; the designed voltage was 38.8 kV. The length of the rebuncher was 1 m.

The rebuncher cavity was designed using the MAFIA code. RF characteristics were evaluated for the three cavity types shown in Fig. 1.

The results are shown in Table 1. The shunt impedance R_s is defined as follows:

$$R_s = \frac{4(V_1 + V_2)^2}{2P}, \tag{1}$$

where P is the power dissipation in the cavity. V_1 and

* Department of Physics, School of Science, The Graduate University of Tokyo

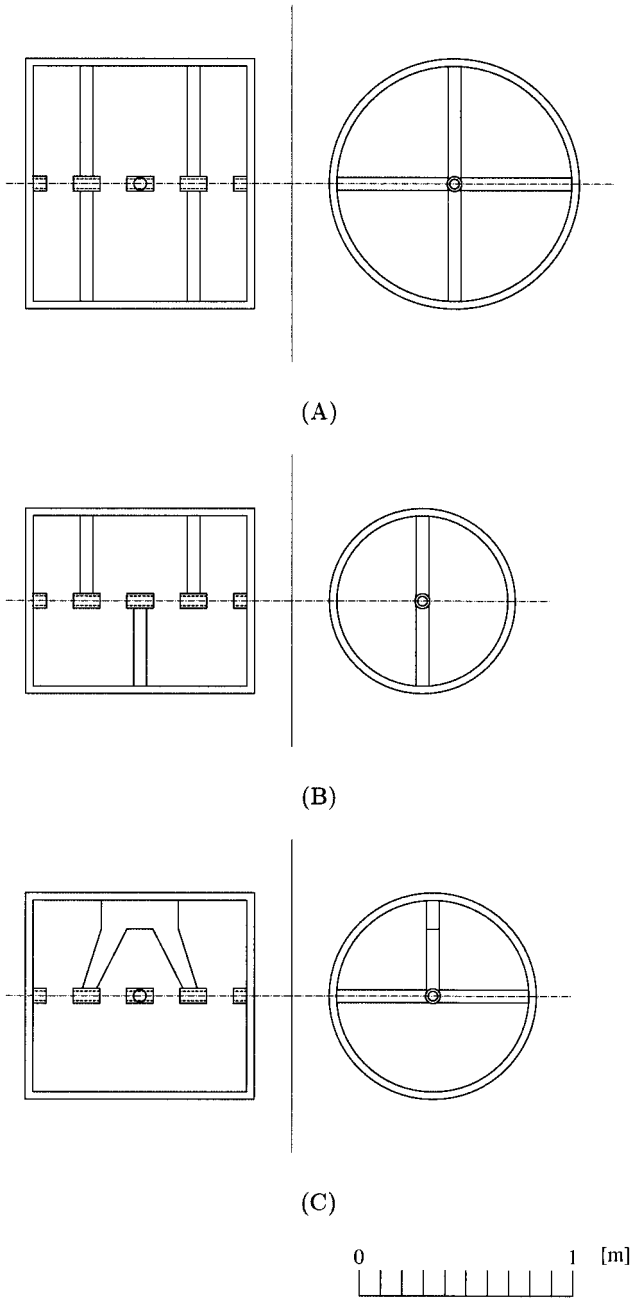

Fig. 1. Three cavity structures evaluated by MAFIA calculation; (A) interdigital H (IH) structure, (B) crossed-bar H(CH) structure, and (C) adopted structure.

Table 1. RF characteristics of three cavity models shown in Fig. 1.

Type	R_s [MΩ]	Q	V_2/V_1
A	22.59	25760	2.43
B	38.82	25680	2.43
C	33.36	26095	1.24

V_2 denote the end-gap voltage and center-gap voltage, respectively.

Type (C) has the minimum voltage ratio V_2/V_1,

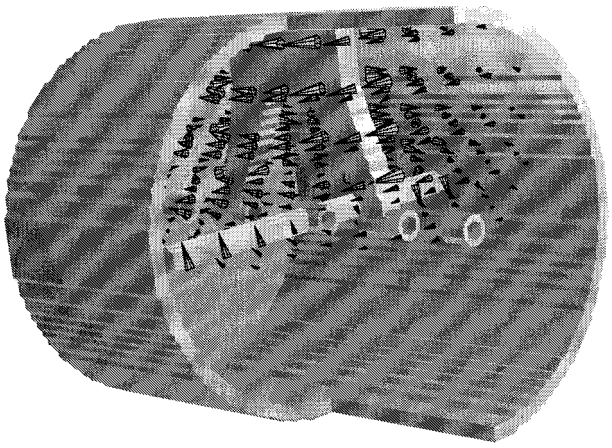

Fig. 2. Magnetic field distributions of fundamental mode of rebuncher cavity.

which means the peak electric field can be reduced for a given total voltage ($2\,[V_1 + V_2]$). This feature will be useful for the acceleration mode. Another advantage of this type is that the electromagnetic field does not exist in the lower half of the cavity, as shown in Fig. 2, where the pumping port might be placed without the disturbance of the resonant field. Therefore, type (C) was adopted, although its shunt impedance is not the highest.

The detailed design of the mechanical structure is underway. At the same time, a 1/3-scaled model is being fabricated.

Reference

1) R. Taki: Master's Thesis at Michigan State University (2003).

Magnetic field measurements of RIKEN fRC

N. Inabe, N. Fukunishi, J. Ohnishi, H. Ryuto, S. Yokouchi, M. Nagase, E. Ikezawa, M. Kase, A. Goto, Y. Yano, and T. Mitsumoto*

RIKEN fixed-Frequency Ring Cyclotron (fRC)[1,2] is a postaccelerator of the existing RIKEN Ring Cyclotron (RRC). Its role is to accelerate heavy ions such as xenon and uranium up to 51 MeV/nucleon, which is essential for producing 350-MeV/n xenon and uranium beams in the RIBF project. The isochronous magnetic fields of fRC are basically produced by iron poles with a very detailed design.[1] This scheme is possible because fRC is a fixed frequency machine and magnetic field distributions are basically the same for all ions, except for small differences between ions with different mass-to-charge ratio. To compensate for these small differences, trim coils will be used in fRC, as well as to compensate for the deformation effects of magnet poles caused by vacuum and electromagnetic forces and to correct harmonic fields produced by magnetic inflection channels. Because these effects are relatively small, the number of trim coils and their maximum excitation currents are significantly reduced compared with frequency-tunable cyclotrons such as RRC and IRC.[3] As a result, the trim coils of fRC were designed to correct only 2% of the magnetic field distributions as a whole. It means that 1% of unexpected error in a magnetic field distribution is not acceptable in fRC.

The construction of fRC started in 2002 and its four sector magnets were completed at the Niihama works of Sumitomo Heavy Industries, Ltd. in March 2005. In the final stage of the fabrication, these four sector magnets were initially assembled and precisely positioned as they will be positioned in the RIKEN site as a preparation of its final assembly in RIKEN. Hence, we carried out magnetic field measurements of fRC at Niihama works in March and April 2005.

We carried out various types of magnetic field measurements. Radial distributions on hill centerlines were measured for all sector magnets with various excitation currents. Radial distribution on the centerline of S (South) valley and azimuthal distributions on an edge region of ES sector magnets were also measured. In addition, stray fields from sector magnets were also measured around the sector magnets. Figure 1 and Table 1 show the summaries of the position and methods of magnetic field measurements, respectively.

The magnetic field distributions with the main coil excitations were measured for various excitation currents. The distributions on the hill centerlines are shown in Fig. 2 for the 615 A of an excitation current, which corresponds to uranium acceleration. The differences between the four sector magnets are less than 50 gausses for 615-A excitation. The differences become large for 480-A excitation, but still remain within 80

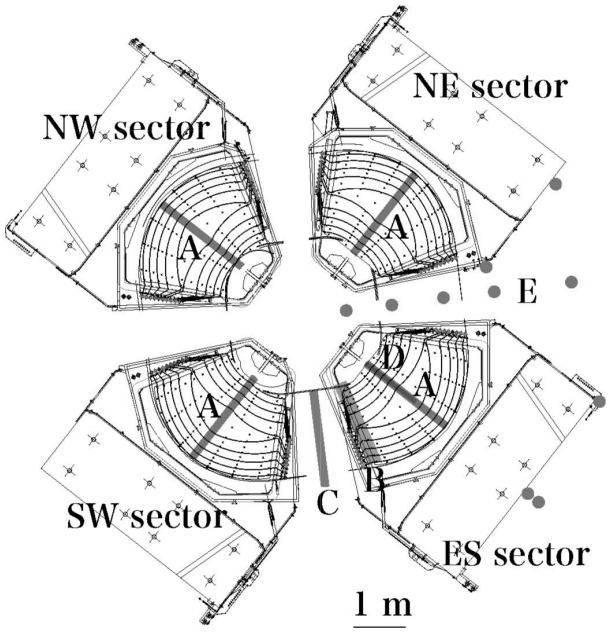

Fig. 1. Plane figure of fRC. Labels from "A" to "E" represent the different kinds of magnetic field measurements. For details, see Table 1. Circles show the positions where measurement "E" was performed.

Table 1. Summary of magnetic field measurements. The symbols δR and $\delta\theta$ indicate the interval between successive two points in the measurements of radial and azimuthal directions, respectively.

Label	probe	Measured quantities	Excitation current (A)
A	NMR	Radial distribution ($\delta R = 20$ mm)	615, 550, 480, 350
B	Hall probe	Azimuthal distribution ($\delta R = 50$ mm, $\delta\theta = 5$ mm)	615, 550, 480
C	Hall probe	Radial distribution ($\delta R = 5$ mm)	615, 480
D	NMR	Radial distribution ($\delta R = 5$ mm)	615[§], 480[§]
E	3-axis hall meter	Stray fields	$0 \sim 650$

[§] No.5 trim coil was excited to 100 A.

* Sumitomo Heavy Industries, Ltd.

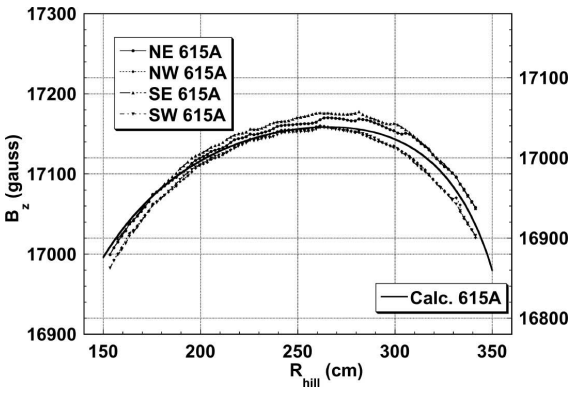

Fig. 2. Radial distributions of magnetic fields excited by 615 A.

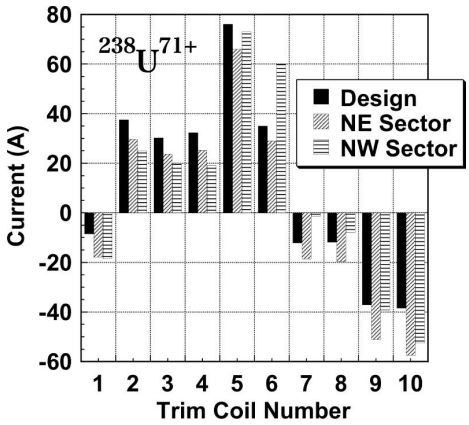

Fig. 3. Estimation of trim coil currents for uranium acceleration. Trim coil currents are estimated on the basis of the observed magnetic fields of NE and NW sector magnets compared with the design value.

gausses for the whole range of operation from 350-A excitation to 615-A excitation. These small differences can be corrected by bypassing power supplies for the main coils of the sector magnets. The differences in magnetic field profile between observations and the design are also less than 50 gausses, which correspond to 0.3% of the magnetic field. Because the present 0.3% difference is not negligible for fRC, we estimated the excitation currents of the trim coils under the assumption that magnetic field errors averaged over equilibrium orbits are proportional to the errors on the hill centerline. The results are summarized in Fig. 3. The deviations from the design values for trim coil currents are less than 20 A, which should be compared with the maximum currents of the trim coils, 200 A for injection and extraction regions and 100 A for other regions. The present deviations are acceptable if our assumption holds. To verify the present assumption, it is necessary to measure field maps over the whole acceleration regions. However, we do not plan to measure field maps because a mapping apparatus is very expensive. In addition, magnetic field calculations give us good starting values of trim coil currents for actual acceleration because the accuracy of calculation is 0.3% as mentioned above. Our expectation is that these errors are smoothed out in averaging over equilibrium orbits. It is very difficult to find a mechanism for enhancing the observed errors in orbit averaging.

Magnetic field distributions in the edge and valley region are also reproduced well by our magnetic field calculations. Stray fields from sector magnets produce 30 gausses for increasing the currents of the main coils. The present data will be used to determine the thickness of magnetic shields for devices such as a flow switch, which do not work properly even under very low magnetic fields. In the magnetic field measurements at Niihama works, we obtained very few data on magnetic fields excited by trim coils. We plan to measure the magnetic fields on the hill centerlines excited by the trim coils at RIKEN because saturation properties for exciting trim coil currents are also important information in actual acceleration. These measurements will be performed next spring.

References

1) N. Inabe et al.: Proc. 17th Int. Conf. on Cyclotrons and Their Applications, Tokyo, 2004-10 (Japan Particle Accelerator Physics Society, 2005), p. 200.
2) T. Mitumoto et al.: Proc. 17th Int. Conf. on Cyclotrons and Their Applications, Tokyo, 2004-10 (Japan Particle Accelerator Physics Society, 2005), p. 384.
3) J. Ohnishi et al.: Proc. 17th Int. Conf. on Cyclotrons and Their Applications, Tokyo, 2004-10 (Japan Particle Accelerator Physics Society, 2005), p. 197.

Construction of the rf resonators for the fRC

N. Sakamoto, O. Kamigaito, S. Kohara, A. Goto, N. Inabe, M. Kase, and Y. Yano

In-flight radioisotope beam production with uranium (350 MeV/u) is one of the most important issues of the RIBF. A four-sector ring cyclotron, fRC, has been designed and built to realize an uranium acceleration scheme.[1] The beam frequency (f_{beam}) from the injector RRC is 18.33 MHz. A high energy gain of 1 MV/turn at an extraction radius is required to obtain a large turn separation.

The fRC has two acceleration resonators, namely, E- and W-resonators. The design value of the acceleration voltage is 500 kV/resonator. Since it has been decided to utilize an existing 100 kW amplifier,[2] the parallel shunt resistance is required to be larger than 1.25 MΩ.

Due to the limitation of space, the single-gap-type resonator with the frequency (f_{frc}) of the third harmonic of f_{beam} is chosen, while the rf frequency of the injector RRC (f_{RRC}) is 18.33 MHz, Therefore, flat-top systems, which broaden the longitudinal acceptance, are necessary. The design parameters of the rf resonators are summarized in Table 1.

The construction of the acceleration resonators started in 2003. A schematic of the resonators is shown in Fig. 1. The rf power is fed through an inductive loop feeder. Block tuners are used to tune the resonant frequency by $\Delta f/f \sim 1\%$. The rf characteristics of the resonators have been investigated and optimized using a three-dimensional code, MAIFA.

Table 1. Key parameters of rf characteristics.

Resonator	acceleration	flattop
Frequency [MHz]	54.99	164.97
No. of resonators	2	1
Gap	single gap	
Maximum gap voltage [kV]	500	180
Wall loss [kW]	85	15
Tuner	Block Tuner	
$\Delta f/f$ [%]	1.5	2.5

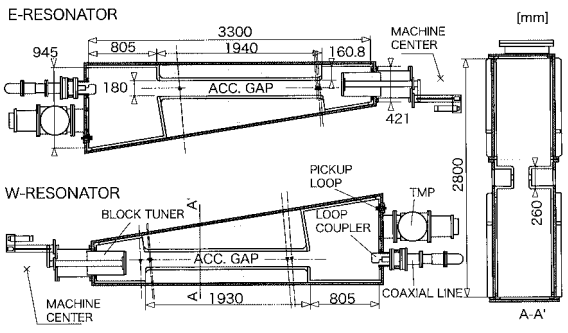

Fig. 1. Schematic drawing of acceleration cavity.

This year, the fabrication was finished and low-power tests were performed. The frequency of the resonator is shown with Q-values in Fig. 2. A frequency of 54.99 MHz is not covered. Some modification of the cavity is required. Otherwise the operational frequency decreases by 1%. The parallel shunt resistance of the resonator was also measured by a perturbation method and is as large as 1.5 MΩ. The required rf power will be approximately 85 kW. The measured rf characteristics are summarized in Table 2. The Q-values and the parallel shunt resistances are approximately 60% of the calculated ones. The final stage amplifier is of the grounded grid type using a tetrode (RS2058CJ) power tube. The maximum output power is 100 kW at a frequency of 54.99 MHz.

The frequency of the flat-top resonator is $3 \cdot f_{acc}$ and the maximum gap voltage is 180 kV. The maximum wall loss is 20 kW. The flat-top resonator is under construction. The construction of the amplifier for the flat-top resonator, which is also of the grounded grid type based on the 4CW5000E tetrode tube, has already been finished. The commissioning of the rf system is planned to start in April 2006.

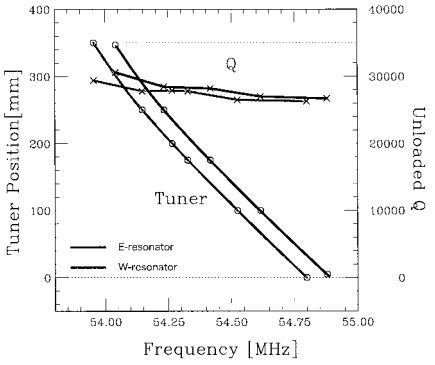

Fig. 2. Frequency and Q-value plots.

Table 2. Rf characteristics of acceleration resonators. The block tuners are set at 100 mm.

Res #	frequency[MHz]	Q	Rs[MΩ]
E	54.57	26120	1.46
W	54.52	27200	1.53

References

1) N. Inabe et al.: Proc. 17th Int. Conf. on Cyclotrons and Their Applications, Tokyo, 2004-10 (Particle Accelerator Society of Japan, 2005), p. 200.
2) Y. Murakami et al.: Proc. 12th Symp. on Accelerator Science and Technology, Wako, 1999-10 (1999), p. 239.

First cool down and excitation test of superconducting sector magnets for SRC magnets

H. Okuno, J. Ohnishi, K. Yamada, H. Hasebe, T. Maie, K. Ikegami, A. Goto, M. Kase, and Y. Yano

In August 2005 the assembling of superconducting sector magnets for the SRC[1] was completed as shown in Fig. 1. After that we performed the first cool down and excitation test until Nov. 7, 2005. The history of the first cool down and excitation test is shown in Table 1. We turned on the main compressors on Aug. 30, 2005, and continued the purification of the cryogenic system until Sept. 17 to remove impurities such as oxygen, nitrogen and water among others in helium gas at less than 0.5 ppm. The cool down started on Sept. 19, and finished on Oct. 13 for the first time as shown in Fig. 2. The coils and supporting structures were cooled by temperature-controlled helium gas, which was supplied by tuning the inlet valves of the four turbines and bypass valves that were installed to skip each turbine. All the main coils became superconducting state on Oct. 13 at about 1:00AM when the supply gas temperature was 8.4 K and the coil outlet temperature was 9.6 K. The cool down was successfully completed within 24 days. After the cool down, the excitation test of the superconducting coils started from Oct. 21.[2] The coil currents were increased daily, checking reactions between the power supply and cryogenic system. On Nov. 7 all the coils were fully excited to generate the maximum field of 3.8 T. The maximum currents are 5000 A for the main coil and 3000 A for the superconducting trim coil. The fast and slow down tests were performed at various currents. Data analysis is now in progress.

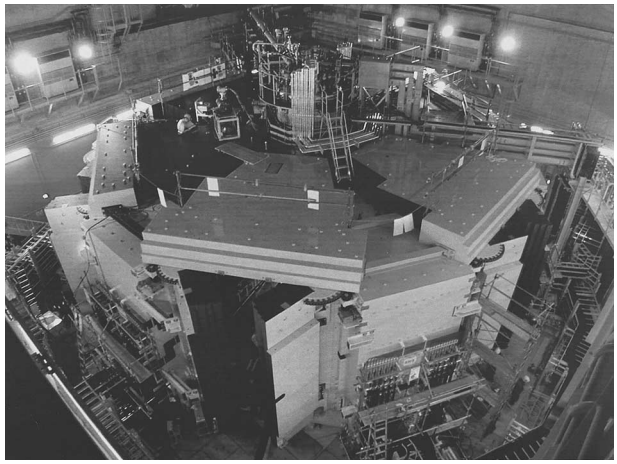

Fig. 1. Photo of SRC.

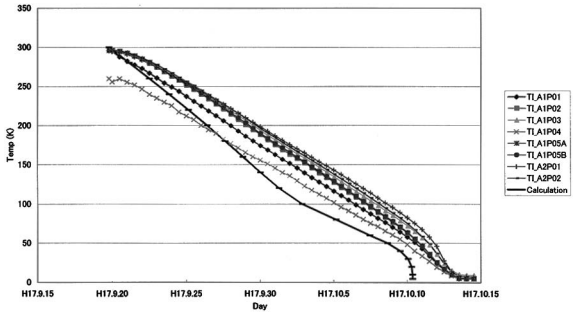

Fig. 2. First cool down curves of SRC. The curves show temperatures (SM1) of the main coil vessels (TI_A1P0, TI_A1P02), connecting plates (TI_A1P03), He supply (TI_A1P04), He return (TI_A1P05A, TI_A1P05B) and the superconducting trim coils (TI_A2P01, TI_A2P02). A prediction from a simple calculation is also shown in the graph.

Table 1. History of first cool down and excitation test.

Date	Events
8/30 – 9/17	Purification
9/19 –	Cool down
10/13 1:00AM	Main coils became superconducting state.
10/16	Level of liquid helium reached operation level.
10/21	Excitation test started. (Imain = 100)
10/27	Excitation test (Imain=1000 A, Itrim=1000A)
10/31	Excitation test (Imain = 3000 A, Itrim = 3200 A (Maximum current))
10/6	Excitation test (Imain = 5000 A(maximum current))
10/7	Excitation test (Imain = 5000 A, Itrim = 3000 A)

References

1) H. Okuno et al.: Proc. 17th Int. Conf. on Cyclotorons and Their Applications, Tokyo, 2004-10 (Japan Particle Accelerator Physics Society, 2005), p. 373.
2) J. Ohnishi et al.: RIKEN Accel. Prog. Rep. **39**, 252 (2006).

First excitation of the SRC superconducting sector magnets

J. Ohnishi, H. Okuno, K. Yamada, M. Nagase, K. Ikegami, H. Hasebe, T. Maie, N. Fukunishi, M. Kase, A. Goto, and Y. Yano

Each of the SRC sector magnets has a pair of superconducting main coils and four pairs of superconducting trim coils. Their power supply system is composed of one power supply for the main coils, four power supplies for the trim coils, and fourteen auxiliaries used for the adjustment of the magnetic field among the sector magnets.[1] The nominal currents are 5000 A for the main coils and 3000 A for the trim coils, respectively. The SRC sector magnets were cooled to the liquid helium temperature for one month from September 19, 2005.[2]

Excitation of the sector magnets was started on October 21. Firstly, the current control of the power supplies was confirmed to be normal by monitoring the voltage ripples while the main coil and the trim coils were excited in turn up to 1000 A. The current ramping rates were 1 A/s for the main coils and 5 A/s for the trim coils. However, the rate was set to be 0.5 A/s for the main coil to suppress the temperature rise of the trim coils due to the eddy current loss to within 0.2 K.

Secondly, the tests for quench protection of the superconducting coils were performed at the main coil currents of 1000 A and 3000 A. In the tests, the coils are disconnected from their power supplies and coil currents are discharged rapidly with dump resistors (fast discharge test). The sequence and time lag in the disconnection of the power supplies and the damping time of the coil currents were confirmed to be designed by measuring the voltages and currents of all coils. Figure 1 shows waveforms of the voltages generated in the main and trim coils. In the fast discharge test in which the main coil current of 3000 A was damped with a resistor of 0.3 Ω, the voltage waveform of the main coil, which corresponds to that of the coil current, was in agreement with the calculated one in which the change of the coil inductance was taken into account. The parameters of the quench detection were set as follows: voltage greater than 0.5 V was generated for longer than 0.5 s in one of the main coils; voltage greater than 0.1 V was generated for longer than 0.5 s in one of the trim coils.

On November 6, after the tests at a low current level, the main coils were successfully excited up to 5000 A without quenching. On the following day, the current of the four trim coils was increased to the nominal current of 3000 A in turn under a condition in which the main coil was excited at 5000 A. As a result, the full excitation of all coils was achieved. Figure 2 shows an excitation curve of the sector magnet as a function of the main coil current. The position of the measurement was 5.45 m from the center of the SRC on the centerline of the sector magnet near the last circulating orbit. Figure 3 shows the magnetic field distribution measured tentatively with a Hall probe along the centerline of sector magnet SM5 when the main coil was excited to 5000 A and four trim coils were excited to 3000 A. The data are in agreement with the results of TOSCA calculation within 0.5%.

The coil current was increased while monitoring the magnetic force acting on the coils using 208 strain gauges attached to the coil vessels and their thermally insulated supports. The strength of the electromagnetic force in the radial direction is shown in Fig. 4. The measured values are in agreement with the results calculated by TOSCA, and they are smaller than the design strength of 900 kN in the radial supports of the coils. On the other hand, the electromagnetic forces in

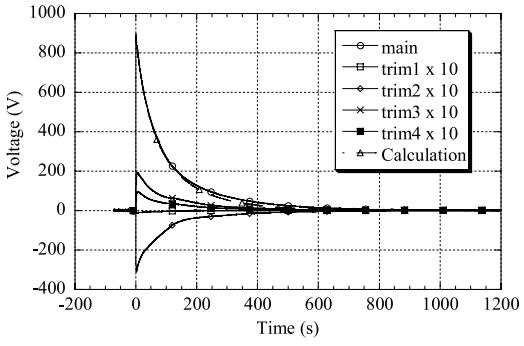

Fig. 1. Voltages generated in the main and trim coils in the fast discharge test when only the main coil is excited at 3000 A. The voltages for the trim coils are plotted by ten times.

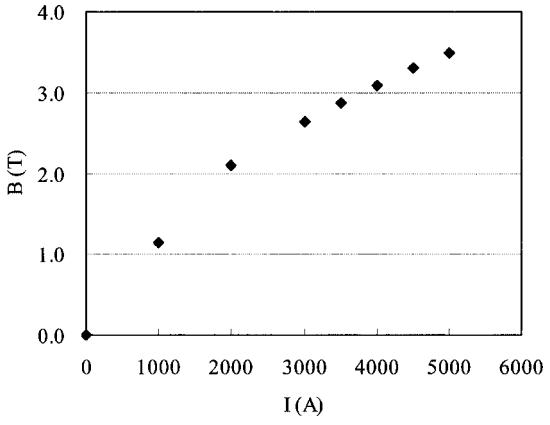

Fig. 2. Excitation curve of the superconducting sector magnet.

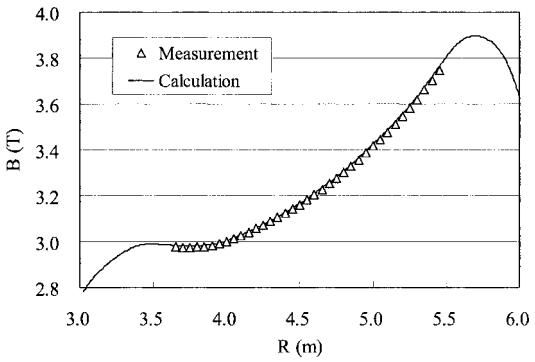

Fig. 3. Magnetic field distribution along the centerline of sector magnet SM5. The currents are 5000 A and 3000 A for the main coil and the four trim coils, respectively.

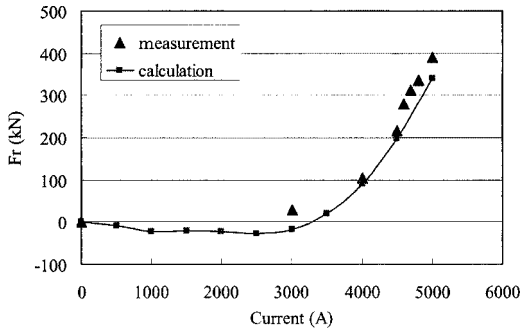

Fig. 4. The magnetic force acting on a pair of main coils (cold mass) in the radial direction. This was measured with strain gauges attached to the radial support.

the azimuthal and vertical directions were balanced, and no large one-sided force was detected in their supports.

The excitation tests were terminated due to the leakage of the thermal insulation vacuum on November 8. After repair and re-cooling, the measurement of the current stability and the test for fast damping from the maximum current will be performed, followed by magnetic field mapping for about three months.

References

1) J. Ohnishi et al.: RIKEN Accel. Prog. Rep. **36**, 301 (2003).
2) H. Okuno et al.: RIKEN Accel. Prog. Rep. **39**, 251 (2006).

Present status of liquid-helium supply and recovery system

K. Ikegami, H. Okuno, T. Yoshida, K. Nakano, T. Maie, H. Hasebe, H. Fukuda, M. Nakamura, and M. Kase

The liquid-helium supply and recovery system,[1] which can generate liquid helium at a rate of 200 ℓ/h from pure helium gas, has been stably operated since the beginning of April 2001. The volumes of liquid helium supplied per year are listed in Table 1. The volume supplied has gradually increased over the years since 2001.

Figure 1 is a schematic diagram of the liquid-helium supply and recovery system.

An impure gas cadre with a volume of 1800 m^3 was added to the system at the beginning of April because the volume of recovered helium gas increased. At the beginning of August, the turbine which is indicated as T1 in the figure was replaced by a new one, because the T1 turbine broke down after approximately 3500 hours of operation. Two types of compressor for recovering and liquefying helium gases were overhauled due to regulations on high-pressure safety and were inspected by the high-pressure gas safety institute of Japan.

To measure the helium purity and gas flow rate of the recovered helium gas, a recovery helium gas observation system is being built on Wako campus. The recovery helium gas observation system consists of a control system placed in the liquid-helium supply and recovery building and five recovery stations, which are equipped with a helium purity sensor and a gas flow meter. The recovery stations are indicated on the Wako campus map shown in Fig. 2. The first recovery station is near the cooperation center building for the advanced device laboratory located on the south side of the RIKEN campus. The second recovery station is in front of the chemistry and material physics building for the nanoscience project. The third recovery station is in the RIKEN main research building and is connected to the frontier research building and the frontier material research facility building. The forth recovery station is behind the east brain science building. The fifth recovery station will be located between the Nishina memorial building and the RIBF accelerator building. Each station is connected to the control system through optical fiber cables. Information regarding helium purity and gas flow rate among others can always be accessed at the liquid-helium control room.

Table 1. Volumes of liquid helium supplied per year from 2001 to 2004.

Year	Amount of supplied liquid helium (kℓ)
2001	28
2002	40
2003	52
2004	55

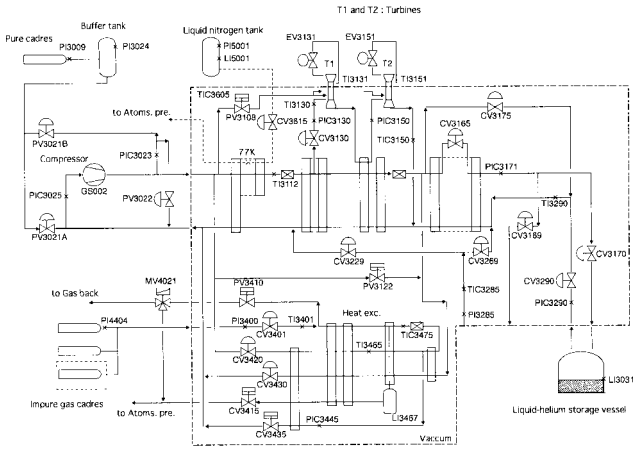

Fig. 1. Schematic diagram of liquid-helium supply and recovery system.

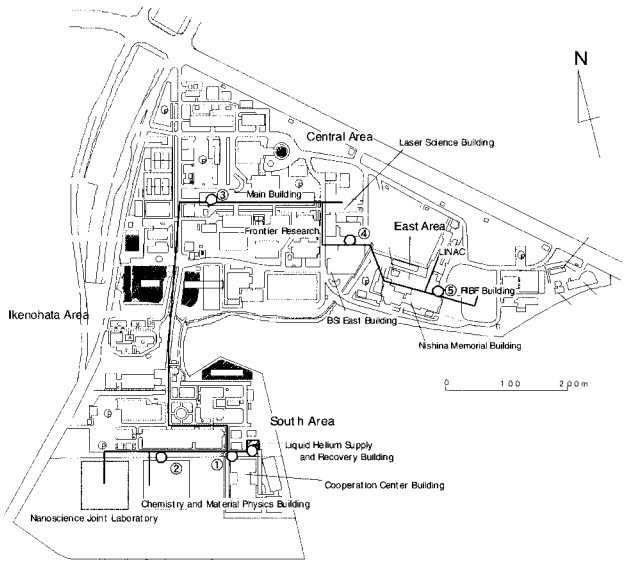

Fig. 2. Map of recovery stations on Wako campus. The recovery stations are indicated as ① to ⑤ in the figure.

Reference

1) K. Ikegami et al.: RIKEN Accel. Prog. Rep. **34**, 349 (2001).

Power supplies for magnets in RARF/RIBF

A. S. Banerjee,* M. Nagase, E. Ikezawa, J. Ohnishi, and M. Kase

A magnet power supply system is one of the main constituents of an accelerator facility. Precise and stabilized DC power supplies for excitation of coils of DC magnets are required for Accelerator application in order to have a high-quality beam output as required for various experiments. A large number of DC power supplies used in RARF/RIBF are shown in Table 1. A list of typical DC magnet power supplies is given in Table 2. Some power supplies have been used for more than 26 years, whereas the power supplies for RIBF have been fabricated recently. The differences between new and old ones will be reported.

These power supplies are basically current-regulated DC power supplies. The current rating of these power supplies varies from 5 to 5200 A required for various applications of the accelerator system. The current stability of these power supplies is an important factor as it has direct impact on the stability of the magnetic field and hence the stability of the beam. The required current stability depends on the function of the magnet concerned. The current stability must be less than 5 ppm is required for the power supplies for the main coil in the cyclotron sector magnets.

In the old power supplies, stability degradation due to changes in the characteristics of a resistive-type feedback current sensor has been noted. The resistive-type current sensor was directly cooled by water and the temperature is controlled to 35 ± 1°C to avoid a variation of characteristics with temperature. However a change in their characteristics has taken place due to corrosion. This has degraded the stability of the power supply. To solve this problem DC current transformer (DCCT) sensors have been used in place of the resistive type sensor. DCCT sensors do not require cooling as the current is sensed by magnet coupling.

In a current feedback loop of old power supplies, a DAC and DC amplifier are enclosed in a box, which is heated to 45°C using a thermostat-controlled oven to avoid changes in the characteristics of the elements which effect the current stability. However, in this method, the surface temperature of several sensitive elements rises over a value much higher than 45°C. Frequent failure of some elements is noted at this temperature. To solve this problem, Peltier coolers are used, which are able to keep the temperature at a low value of 25°C. It may be noted that the burden resistor of DCCT is also kept in the Peltier cooler.

The combination of the DCCT current sensor and the Peltier cooler gives a long-term stability of around 5 ppm to a DC power supply. The new power supplies in RIBF have been designed on the basis of this combination. The old power supplies in RARF should also be modified accordingly. Already, the modification is incorporated in 21 old power supplies including the power supplies for the cyclotron's main coils.

The SRC is a large-scale superconducting device, which was introduced to the facility for the first time. When a quench occurs in the superconducting coil, a special circuit is very important in protecting the coil from damage. A diagram of the SRC main coil power supply[1] is shown in Fig. 1. The power supply must discharge the energy stored in the coil by decreasing the coil current rapidly within 60 s (time constant of the main coil) through a pair of dump resistors (R_1 in Fig. 1) so that the temperature rise of the coil by Joul heating and the voltage generated are maintained at an acceptable level to protect the coil from both thermal and insulation damages. A slow discharge scheme is also adopted to discharge the current within 1200 s for any other fault in the power supply and cryogenic cooling system to avoid loss of liquid helium due to eddy current in the fast discharge.

Table 1. Number of DC power supplies for magnets in RARF/RIBF.

Accelerator Facility		*Commissioning year*	*No.of Power Supplies*
RARF	RILAC	1981	121
	AVF	1989	13
	RRC	1986	85
	BT	1986/1990	267
RARF/RIBF	fRC	2006	43
RIBF	IRC	2006	64
	SRC	2006	79
	BT	2006	236

BT: Beam tranport line

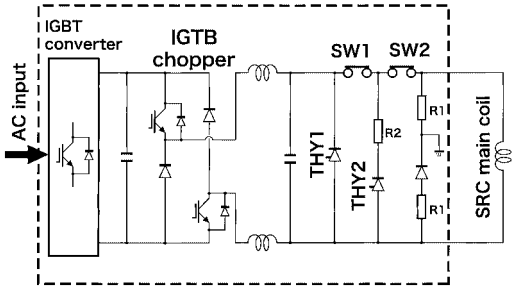

Fig. 1. Diagram of SRC main coil power supply.

* Visiting Scientist from VECC, India

Table 2. List of typical power supplies in RARF/RIBF.

Power Supply		Type	I_{max}	P_{max}	Stability	Regulating	Current	Computer	Yr. of	Remarks
Name	Magnet		(A)	(kW)	(PPM)	Element	Sensor	Interface	Product.	
ECR 1	IS - MIR	L	800	68	100	Tr	Res-Mn	-	1986	
90BM	BT - DM	L	160	5	50	Tr	Res-Mn	-	1986	
SOL-RO	BT - SO	S	230	9	10	FET-PWM	DCCT	GPIB	2000	Air cooled
SCECR-1	IS - MIR	S	120	0.7	2000	FET-PWM	Res-Mn	WE	1999	Air cooled
C1-160/32	BT - DM	S	160	5	100	FET-PWM	Res-Mn	WE	1986	Air cooled
SOL-RO	BT - SO	L	360	15	50	Tr	Res-Mn	GPIB	1986	
SOL-BT	BT - SO	L	460	35	50	Tr	Res-Mn	-	1986	
DQN1-1	BT - QM	L	176	4	500	Tr	Res-Mn	GPIB	1986	
DT1-1	DT - QM	S	30	0.6	500	FET-PWM	Res-Mn	NIO	2002	Air cooled
SQ-12	BT - QM	S	130	1000	500	FET-PWM	Res-Mn	NIO	2002	Air cooled
DT2-5	DT - QM	S	110	2.2	500	FET-PWM	Res-Mn	NIO	2002	Air cooled
DT4-3	DT - QM	L	140	1	200	Tr	Res-Mn	GPIB	1979	
TQPS1	BT - QM	S	175	6	1000	Tr	Res-Zr	GPIB	2000	
90BM(VM)	BT - DM	L	210	17	100	Tr	Res-Mn	GPIB	1979	
A-Q1P	BT - QM	L	160	4	100	Tr	Res-Mn	CIM/DIM	1986	
A-D1(DM3)	BT - DM	L	200	12	50	Tr	DCCT*	CIM/DIM	1986	Renewed*
TQPS5	BT - QM	S	150	4	50	FET-PWM	Res-Mn	GPIB	1999	Air cooled
QPS1(A-Q2)	BT - QM	L	160	4	1000	Tr	Res-Zr	NIO	2000	
AVF-MAIN	SM - Main	L	1200	288	5	Tr + Thy-PR	DCCT*	CIM/DIM	1988	Renewed*
AVF-C6	SM - Trim	L	250	5	10	Tr + Thy-PR	DCCT*	CIM/DIM	1988	Renewed*
AVF-MGCH	EXT - MDC	L	912	82	50	Tr + Thy-PR	Res-Zr	CIM/DIM	1988	
RRC-M1	SM - Main	L	1072	446	5	Tr + Thy-PR	DCCT*	CIM/DIM	1984	Renewed*
RRC-M2	SM - Main	L	1071	129	5	Tr + Thy-PR	DCCT*	CIM/DIM	1984	Renewed*
RRC-TA1	SM - Trim	L	333	7	50	Tr + Thy-PR	Res-Zr	CIM/DIM	1984	
RRC-MIC1	INJ - MIC	L	805	12	50	Tr + Thy-PR	Res-Zr	CIM/DIM	1984	
RRC-MDC1	EXT - MDC	L	1010	15	50	Tr + Thy-PR	Res-Zr	CIM/DIM	1984	
IRC-M1	SM - Main	L	450	217	5	Tr + Thy-PR	DCCT	NIO	2001	
IRC-M2	SM - Main	L	450	181	5	Tr + Thy-PR	DCCT	NIO	2001	
IRC-TRIM1	SM - Trim	S	400	4	10	FET-PWM	DCCT	NIO	2001	
IRC-MIC1	INJ - MIC	S	800	16	10	FET-PWM	DCCT	NIO	2001	
IRC-MDC1	EXT - MDC	S	1200	36	10	FET-PWM	DCCT	NIO	2001	
SRC-P0	SM - Main	S	5200	182	5	IGBT-PWM	DCCT	NIO	2002	SC-coil
SRC-P1	SM - Trim	L	3200	26	10	Tr + Thy-PR	DCCT	NIO	2002	SC-coil
SRC-NT1	SM - Trim	S	1200	40	100	IGBT-PWM	DCCT	NIO	2002	
SRC-MIC1	INJ - MIC	L	2950	183	100	Tr + Thy-PR	DCCT	NIO	2002	
SRC-MDC1	EXT - MDC	L	320	10	100	Tr + Thy-PR	DCCT	NIO	2002	
SRC-SBM	INJ - DM	L	500	8	100	Tr + Thy-PR	DCCT	NIO	2002	SC-coil
A-DM40	BT - DM	L	443	80	10	Tr + Thy-PR	DCCT	CIM/DIM	1986	
A-Q9	BT - QM	L	152	4	100	Tr	Res-Zr	CIM/DIM	1986	
A-ST9	BT - ST	L	5	0.2	100	Tr	Res-Mn	CIM/DIM	1986	Air cooled
BT-D1	BT - DM	L	300	30	100	Tr	DCCT	NIO	2000	Renewed
BT-QA2	BT - QM	L	160	7	1000	Tr	Res-Zr	NIO	2002	
BT-ST1	BT - ST	S	8	0.6	1000	FET-PWM	Res-Mn	NIO	2002	Air cooled

IS: ion source, BT: beam transport, DT: drift tube in linac, SM: sector magnet of cyclotron, INJ: injection sytem of cyclotron, EXT: extraction sytem of cyclotron.

MIR: mirror coil, SO: solenoid coil, DM: dipole magnet, QM: quadrupole magnet, Main: main coil, Trim: trim coil, MIC: magnetic inflection channel, MDC: magnetic deflection channel, ST: steering magnet.

L: linear-type with a transistor-dropper, S: switching-type

Res-Mn: resistor of Manganin, Res-Zr: resister of Zeraninn, DCCT: DC current transformer.

Tr: transistor, PWM: pulse width modulator, Thy-PR: thyristor pre-reguration,

Both linear mode and switching mode power supplies are used. Linear (i.e., transistor-dropper)-mode power supplies are generally bulky and especially low in efficiency because of considerable power loss in their series pass element, although they are simple in design and have no high frequency noise problem. Recent advances in semiconductor, magnetic and passive technologies have made switching power supplies an ever more popular choice in the power conversion arena. Switching power supplies are smaller and have higher efficiency, of the order of around 90%. Using the proper shields and noise filters has solved the high-frequency noise problem in a switching-mode power supply. Moreover, for a high DC current requirement, switching-mode power supply modules can be stacked in parallel conveniently with equal current sharing among the modules. Hence, the choice for all future DC power supplies will be of the switching mode type.

Computer interfaces are incorporated in these power supplies for controlling and monitoring them from a remote control room. In the very early stage, GPIB was chosen as interfaces in RILAC. In RARF, the original RIKEN CIM-DIM system has been used. New power supplies, fabricated after 2000, have been designed using commercially available network IO (NIO). In the course of changing the old power supplies, old interface are being converted into NIO. In RARF/RIBF, two kinds of interfaces, CIM-DIM and NIO will be used in the future.[2)]

References

1) J. Ohnishi et al.: RIKEN Accel. Prog. Rep. **36**, 301 (2003).
2) M. K. Komiyama et al.: RIKEN Accel. Prog. Rep. **38**, 256 (2005).

Status of beam transport line from SRC to BigRIPS

K. Kusaka, T. Kubo, Y. Mizoi,[*1] and N. Kakutani[*2]

In the RI-Beam Factory (RIBF) project, energetic heavy-ion beams from the SRC will be delivered to the projectile fragment separator, called BigRIPS,[1] to produce RI beams. The beam transport line from the SRC to the BigRIPS has been constructed on the basis of a design study reported elsewhere.[2]

A layout of the beam line, together with the SRC and the BigRIPS separator, is schematically shown in Fig. 1. A primary beam extracted from the SRC is transferred from the SRC room to the IRC room using a quadrupole quartet (QQ). A beam shutter is installed in the wall between the SRC room and the IRC room for tuning of the SRC. In the IRC room, a dipole magnet, D1, changes the direction of the beam by 20° together with quadrupole multiplets, TQ and DQ. A pair of beam steering magnets are also installed after the DQ. The beam is then transported to the BigRIPS target using two 50° dipole magnets (R1-D1 and R1-D2), a quadrupole doublet (R1-DQ), and two quadrupole triplets (R1-TQ1 and R1-TQ2).

In Table 1, the main parameters of the dipoles are listed. It should be mentioned that the two dipoles R1-D1 and R1-D2 are 2-Tesla normal conducting bending magnets.[3]

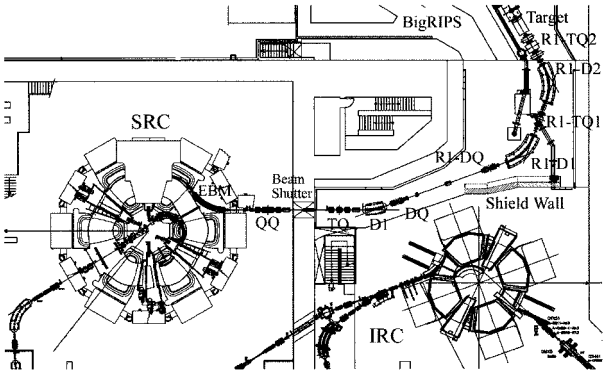

Fig. 1. Schematic layout of beam line from SRC to BigRIPS target.

Table 1. Main parameters of dipoles.

	D1	R1-D1/D2
Max. Field [T]	1.6	2.0
Bending Angle [degree]	20	50
Bending Radius [mm]	5000	4020
Pole Gap [mm]	60	60
Current [A]	320	650
Coil Resistance [mΩ]	175	205
Weight [ton]	12	39

*1 Osaka Electro-Communication University
*2 Toshiba Corporation

For the quadrupoles, we have constructed 5 types of quadrupole magnet as listed in Table 2. Q420a is a building block used to form the quadrupole multiplets QQ, TQ, DQ, and R1-DQ, and its design has been reported elsewhere.[4]

Q220 and Q420, with a maximum field gradient of 24 T/m, form the quadrupole triplet R1-TQ1. All these quadrupole multiplets have a bore diameter of 70 mm. On the other hand, the bore diameter of the quadrupole triplet R1-TQ2, consisting of Q400 and Q800, is 110 mm, so that the primary beam is focused on the target with a small spot size.

The fabrication of these magnets and their power supplies started in 2004 and finished in the early summer of 2005. All the magnets were successfully tested and magnetic field measurements were performed at the factory. They have been installed in the RIBF building together with power supplies and vacuum chambers for beam diagnosis (see Figs. 2–4). All cabling and plumbing, including installation of beam ducts and vacuum evacuation systems, finished in the summer of 2005. Excitation tests of the magnet system and evacuation tests of the vacuum system were successfully performed.

A radiation shield wall between the beam line elements and the IRC has also been constructed (Fig. 5). It consists of a 500-mm-thick iron wall and concrete

Table 2. Main parameters of quadrupoles.

	Q420a	Q220	Q420	Q400	Q800
Max. Field Gradient [T/m]	15	24	24	17.5	17.5
Bore Diameter [mm]	70	70	70	110	110
Yoke Length [mm]	420	220	240	400	800
Current [A]	160	240	220	390	350
Coil Resistance [mΩ]	146	152	219	124	269
Weight [kg]	350	380	650	1950	3700

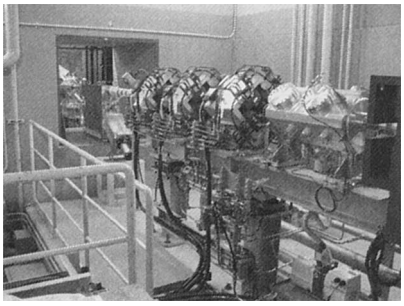

Fig. 2. Beam shutter, installed in wall between SRC and IRC room, together with quadrupole triplet TQ.

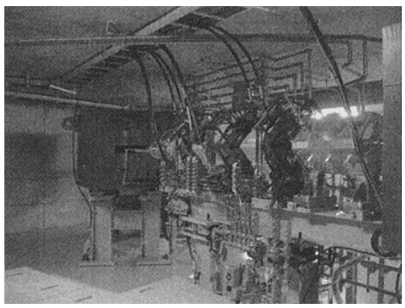

Fig. 3. 2-Tesla dipole R1-D1 and quadrupole triplet R1-TQ1. Shielding blocks can also be seen behind R1-D1.

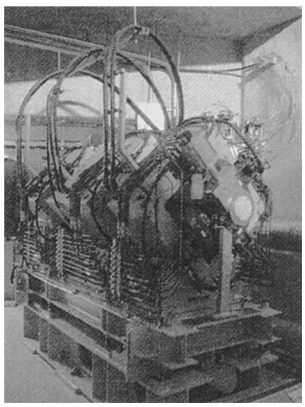

Fig. 4. Large-bore quadrupole triplet R1-TQ2.

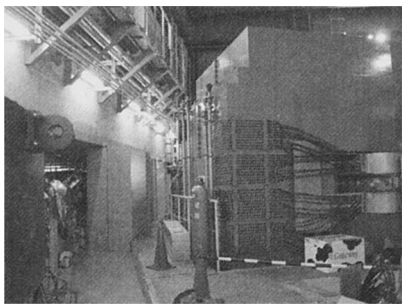

Fig. 5. Radiation shield wall and IRC.

blocks. The iron part consists of approximately 430 plates of steel with a thickness of 22 mm. The concrete blocks are of rectangular shape with a square cross section; 24 pieces of concrete blocks form the 500-mm-thick wall behind the iron wall.

References

1) T. Kubo et al.: RIKEN Accel. Prog. Rep. **39**, 259 (2006).
2) K. Kusaka et al.: RIKEN Accel. Prog. Rep. **35**, 297 (2002).
3) T. Nagafuchi et al.: RIKEN Accel. Prog. Rep. **33**, 234 (2001); Y. Mizoi et al.: RIKEN Accel. Prog. Rep. **35**, 305 (2002).
4) N. Fukunishi et al.: RIKEN Accel. Prog. Rep. **34**, 329 (2001).

Status of BigRIPS separator project

T. Kubo, K. Kusaka, K. Yoshida, A. Yoshida, T. Ohnishi, N. Fukuda, M. Ohtake, Y. Yanagisawa, H. Sakurai, T. Motobayashi, and Y. Yano

The BigRIPS separator[1] and phase-I RI-beam delivery line[2] are under construction for the RI beam factory (RIBF) project with the aim of being commissioned in early 2007. Figure 1 shows a schematic layout of the BigRIPS separator and delivery line along with the RIBF cyclotrons.

The BigRIPS separator is designed to be a superconducting in-flight separator employed for the production and separation of RI beams. It is characterized by two major features: large acceptances and a two-stage separator scheme. The large acceptances are achieved using large-aperture superconducting quadrupoles, allowing the efficient production of RI beams using the in-flight fission of uranium beams as well as projectile fragmentation. The two-stage separator scheme makes it possible to deliver tagged RI beams as well as to realize two-stage isotopic separation. In the RI-beam tagging mode, the first stage of the BigRIPS separator serves to produce and separate RI beams, while the second stage is employed to identify RI-beam species in an event-by-event mode.

The BigRIPS separator is followed by the phase-I RI-beam delivery line, which serves to transport RI beams to experimental setups placed downstream. The delivery line is designed to work also as a zero-degree forward spectrometer called ZDS.[2] In this operational mode of the delivery line, ZDS is employed to analyze and identify projectile reaction residues in secondary-reaction studies of the RI beams.

The fabrication of the BigRIPS magnets consisting of fourteen superconducting triplet quadrupoles (STQs)[3,4] and six room-temperature dipoles was finished in a Toshiba factory in 2004. All the magnets were successfully tested off-line in the factory before being shipped to RIKEN. The first-stage magnets consisting of five STQs and two dipoles were installed in the BigRIPS hall in 2004, along with the liquid-helium cryogenic plant.[5] The installation of the second-stage magnets, which is presently under way, will be completed in March 2006. Field-map measurement is being prepared for some of the second-stage STQs and dipoles. We plan to perform an on-line excitation test of all the magnets in April 2006.

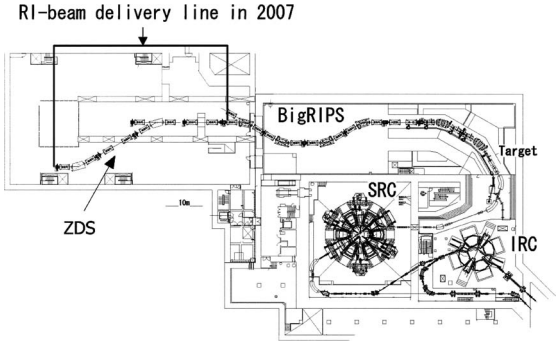

Fig. 1. Schematic layout of RI beam factory in 2007. The BigRIPS separator and phase-I RI-beam delivery line are shown along with the RIBF cyclotrons.

The cryogenic plant[6] is employed to cool the first-stage STQs by supplying liquid helium and 70 K gas helium in a refrigeration mode through a transfer line system. From 2004 to 2005, the test operation of the cryogenic plant has been carried out several times in different operational modes and conditions. The cooling capacity of the cryogenic plant has been measured to be approximately 510 W at liquid helium temperature by a stand-alone operation of the refrigerator. The thermal heat load of the transfer line system, which consists of a joint box, a 50-m-long transfer line and five valve boxes, has been measured to be approximately 100 W in a test operation in which the connection tubes between the valve boxes and the STQs were bypassed. In this case, the liquid and 70 K gas helium coming out of the valve boxes directly returned to the transfer line without going into the STQs. The measured heat load of the transfer line system was initially found to be much larger than this value, because the 70 K thermal shields were not properly fabricated in some parts of the transfer line and because of a small vacuum leakage in a cryogenic valve. The head load of 100 W has been achieved after repairing those faults. In combination with the results of the off-line test of the STQs, the total heat loads to the cryogenic plant have been estimated to be approximately 210 W: 100 W for the transfer-line system, 20 W for the STQs and 90 W for cooling the current leads. Hence, the cryogenic plant has the extra cooling capacity of approximately 300 W. This will be employed to cope with the heat loads caused by the neutron radiation from the production target and the beam dump of the BigRIPS separator.

The test operation to cool down the first-stage STQs was carried out in late 2004. It took approximately three weeks to cool the five STQs down to liquid-helium temperature from room temperature. The next cooling-down operation is scheduled in early 2006 in order to make an on-line excitation test of the STQs and a simulation test of the radiation heat loads. We plan to start continuous operation of the cryogenic plant in summer 2006.

The STQs of the BigRIPS second stage are cooled

by a small refrigeration system, which is mounted on the cryostat of each STQ.[3] The system consists of a GM cryocooler to cool 70 K shields and a GM/JT cryocooler to recondense evaporating helium gas in the coil vessel of the STQs. The precooling using liquid nitrogen as well as liquid helium is needed to make the cryocoolers operational. The second-stage STQs have been precooled at RIKEN since they were shipped to RIKEN after being warmed up. It takes about eight days to precool each STQ. Most of the STQs are presently kept at liquid-helium temperature by continuous operation of the cryocoolers. Figure 2 shows a photograph of those STQs.

The focal-plane chambers, which are to be placed at the eight focuses of the BigRIPS separator, have been fabricated along with their vacuum pump system. The focal-plane chambers are equipped with focal-plane devices such as the slit system, the energy-degrader system, the foil/target ladder system, and the detector stand system. They are to be used for isotopic separation, RI-beam tagging and beam diagnoses, in combination with beam-line detectors mounted on the detector stands.[7] With respect to the beam-line axis, the position of the focal-plane devices is adjustable by remote control. For some devices, only the in/out position can be controlled. Testing of the control system is in progress for the focal-plane devices and the vacuum pump system. The installation of the focal-plane chambers into the BigRIPS beam line is scheduled in early 2006.

The beam-line detectors are presently being fabricated or designed. They are mounted in the focal-plane chambers to measure the position and angle, energy loss, and time-of-flight (TOF) of RI beams. A delay line parallel-plate avalanche counter (DL-PPAC)[8] is employed to measure the position and angle. A multisampling ion chamber (MUSIC) with tilted foil electrodes[9] is employed for the energy loss measurement, while a thin plastic scintillation counter is employed for the TOF measurement. The data acquisition system of the beam-line detectors has been designed.

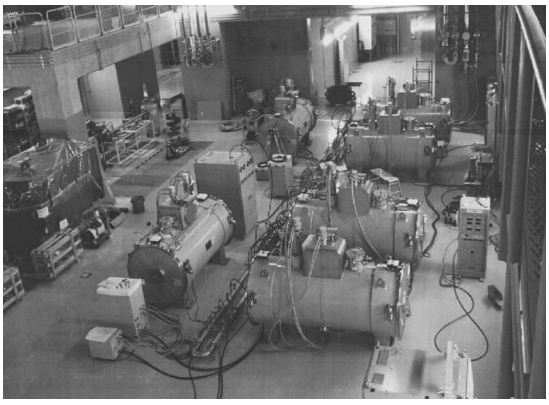

Fig. 2. Photograph of second-stage STQs. They were precooled and kept at liquid-helium temperature by continuous operation of the cryocoolers mounted on the cryostat of the STQs, and are awaiting installation into the BigRIPS beam line.

The production target and beam dump of the BigRIPS separator are exposed to the high heat loads from primary heavy-ion beams. The maximum beam power is as high as 83.3 kW, corresponding to the case of a ^{238}U beam at 350 MeV/nucleon and 1 pμA. To cope with such a high heat load, a rotating-disk target system cooled by water has been developed for the production target.[10] A water-cooling scheme using a Cu screw tube and a Cu swirl tube has been adopted for the beam dump, because those tubes significantly improve the heat transfer coefficient of water flow, so that the temperature of the beam dump can be reduced.[11] Final detailed designs of the target and the beam dump system, based on a heat-load simulation by ANSYS code, are in progress. They will be fabricated by March 2006.

A final design of the radiation shields for the BigRIPS first stage is in progress. The radiation shields consist of approximately 200 concrete blocks and some iron blocks, and the total weight amounts to approximately 4000 tons. They will be fabricated and installed by autumn 2006.

The RI-beam delivery line consists of ten STQs and two dipoles, which have the same designs as the second-stage magnets of the BigRIPS separator. The fabrication and installation of those magnets will be finished in March 2007. The focal-plane chambers for the delivery line are also presently being fabricated.

References

1) T. Kubo: Nucl. Instrum. Methods Phys. Res. B **204**, 97 (2003).
2) Y. Mizoi et al.: RIKEN Accel. Prog. Rep. **38**, 297 (2005).
3) K. Kusaka et al.: IEEE Trans. Appl. Supercond. **14**, 310 (2004).
4) K. Kusaka et al.: RIKEN Accel. Prog. Rep. **37**, 297 (2004).
5) K. Kusaka et al.: RIKEN Accel. Prog. Rep. **38**, 291 (2005).
6) T. Kubo et al.: RIKEN Accel. Prog. Rep. **36**, 316 (2003).
7) K. Yoshida et al.: RIKEN Accel. Prog. Rep. **38**, 293 (2005).
8) H. Kumagai et al.: Nucl. Instrum. Methods Phys. Res. A **470**, 562 (2001).
9) K. Kimura et al.: Nucl. Instrum. Methods Phys. Res. A **538**, 608 (2005).
10) A. Yoshida et al.: RIKEN Accel. Prog. Rep. **38**, 296 (2005).
11) Y. Mizoi et al.: RIKEN Accel. Prog. Rep. **36**, 318 (2003).

Design of rf-linacs of new injector to RIKEN Ring Cyclotron

O. Kamigaito, N. Fukunishi, T. Nakagawa, H. Saito, and A. Goto

The recent success in the synthesis of the super heavy element (SHE)[1] using the RILAC (RIKEN linear accelerator) - CSM (charge-state multiplier) - GARIS (gas-filled recoil ion separator) system strongly encourages us to further pursue the search for heavier SHEs and to more extensively study physical and chemical properties of SHEs. This compels us to provide a longer machine time for these experiments. However, the SHE research and RIBF research conflict with each other, because both of them use the RILAC.

Therefore, a new additional injector linac to the RRC has been proposed, which will make it possible to concurrently conduct the SHE and RIBF research studies. The new injector, which will be placed in the RRC vault, will be used exclusively to produce primary beams of 350 MeV/u from the SRC.

The injector is designed to accelerate ions with a mass-to-charge ratio of 7, aiming at heavy ions such as $^{136}Xe^{20+}$ and $^{238}U^{35+}$, up to an energy of 680 keV/u in the cw mode. It consists of an ECR ion source of 18 GHz,[2] a low-energy beam transport (LEBT) section including a buncher, an RFQ linac based on the four-rod structure, and three drift-tube linacs (DTL) based on the quarter-wavelength resonator (QWR). The rf-resonators are operated at a fixed rf-frequency, like the fRC. Strong quadrupole magnets will be placed into the beam line between the rf-resonators.[5] The output beam is injected to the RRC without charge stripping.

A schematic drawing of the rf-linacs is shown in Fig. 1. The input energy to the RFQ is chosen to be 4 keV/u; the maximum extraction voltage of the ion source is 28 kV. In order to increase the acceleration gradient in the injector, the resonant frequency of the resonators is set to be 36.66 MHz, which is twice the rf frequency of the RRC. The input beam is bunched in the RRC frequency (18.33 MHz) before entering the RFQ. This helps to reduce the beam loss caused by the higher rf-mode operation of the injector linacs.

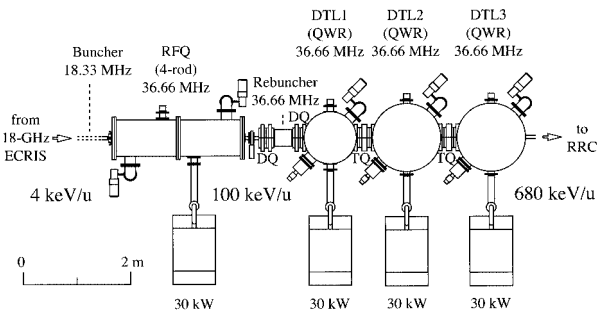

Fig. 1. Schematic drawing of rf-linacs of new injector. DQ and TQ stand for quadupole doublet and quadupole triplet, respectively.

The parameters of the RFQ were determined using the PARMTEQ code. By compromising the RFQ length and defocusing force in the first DTL, the output energy of the RFQ was set to be 100 keV/u. The input emittance was assumed to be 200π mm·mrad at 4 keV/u, which corresponds to a normalized value of 0.6π mm·mrad.[2] The main parameters are listed in Table 1.

The parameters in Table 1 are similar to those used in a four-rod RFQ constructed by NISSIN Electric Co., Ltd. in 1993.[3] The measured shunt impedance of this RFQ, which has a vane length of 222 cm and a resonant frequency of 33.3 MHz, is 47.6 kΩ. On the basis of this shunt impedance, the estimated power loss in our RFQ is about 20 kW.

The buncher in the LEBT section is one of the most important components in the injector. The PARMTEQ simulation shows that nearly 80% of the input beam is captured in the required rf-buckets of 18.33 MHz when the buncher is used, whereas the capture efficiency is less than 50% without it. It was also found that the phase width and energy width can be reduced significantly with the buncher, as shown in Fig. 2. The detailed design of the buncher as well as the study of the LEBT system is under way.

The DTL parameters are optimized by calculating the beam dynamics and rf-characteristics alternatively. A computer program, developed for the CSM design,[4] is used for the beam tracking simulation, whereas the computer code MAFIA is used for the estimation of the rf-power consumption.

The beam envelopes in the DTLs are shown in Fig. 3, which were calculated for the designed output beam

Table 1. Design parameters of RFQ.

Frequency (MHz)	36.6
Duty	100 %
Mass-to-charge ratio (m/q)	7
Input energy (keV/u)	4
Output energy (keV/u)	100
Input emittance (mm·mrad)	$200\,\pi$
Vane length (cm)	214
Intervane voltage (kV)	42.2
Mean aperture (r_0: mm)	7.98
Min. aperture (a: mm)	4.55
Max. modulation (m)	2.41
Beam margin	1.35
Focusing strength (B)	6.8
Max. defocusing strength (Δ_{rf})	-0.225
Final synchronous phase	$-30°$

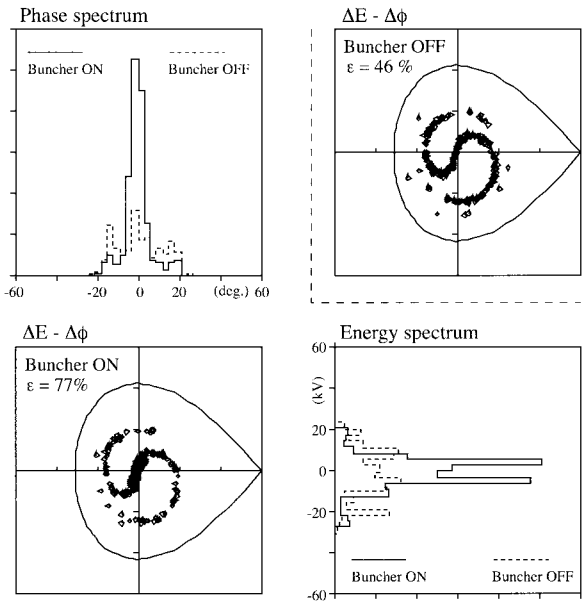

Fig. 2. Longitudinal distribution of output beam of RFQ simulated using PAMTEQ code. A buncher in the LEBT section was included in the simulation, where the position of the buncher was assumed to be 2 m upstream of the RFQ entrance. The dashed lines show the particle distribution without the buncher. The capture efficiencies (ϵ) are also indicated.

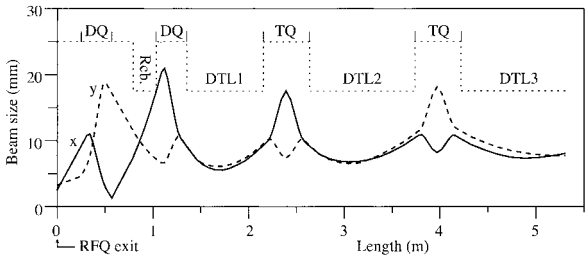

Fig. 3. Beam envelopes of all distributions of test particles included in tracking simulation, where the number of test particles is 2,000. The dotted lines indicate the bore radius of the drift tubes and the inner radius of the beam pipes in the quadrupole magnets.

of the RFQ with a normalized transverse emittance of 0.6π mm·mrad. The beam spreads to more than ± 20 mm in the quadrupole magnets, for which we assume a magnetic field gradient of 40 T/m in order to make the magnet length as short as possible; this is important in preventing the phase width of the accelerated beam from spreading widely. The design of these strong quadrupole magnets is described in the following paper.[5)]

The designed structure of the DTLs is similar to that of the CSM resonators.[4)] The inner diameter of the resonators ranges from 0.8 to 1.1 m, depending on the beam energy. The maximum electric field on the drift tubes is kept below 1.2 Kilpatrick. Table 2 shows the main parameters of the DTLs. The power losses estimated with the MAFIA code ranges from 6 to 17 kW, as shown in the table.

The required rf-power of the amplifiers will be 30 kW, considering the estimated power losses mentioned above and the deterioration of the quality factors of the real resonators. The amplifier of the present FC-RFQ, which has a maximum output of 40 kW, can be referred to as a guideline for the amplifier design.

Table 2. Design parameters of DTLs.

Resonator	DTL1	DTL2	DTL3
Frequency (MHz)	36.6	36.6	36.6
Duty	100 %	100 %	100 %
Mass-to-charge ratio (m/q)	7	7	7
Input energy (keV/u)	100	220	450
Output energy (keV/u)	220	450	680
Length (= Diameter: m)	0.8	1.1	1.1
Height (m)	1.6	1.7	1.8
Gap number	10	10	8
Gap voltage (kV)	110	210	260
Gap length (mm)	20	50	65
Drift tube aperture (a: mm)	17.5	17.5	17.5
Peak surface field (MV/m)	8.2	9.4	9.7
Synchronous phase	$-25°$	$-25°$	$-25°$
Power (100% Q: kW)	6	12	17

References

1) K. Morita et al.: J. Phys. Soc. Jpn. **73**, 1738 (2004).
2) T. Nakagawa et al.: RIKEN Accel. Prog. Rep. **39**, 263 (2006).
3) H. Fujisawa et al.: Nucl. Instrum. Methods Phys. Res. A **345**, 23 (1994).
4) O. Kamigaito et al.: Rev. Sci. Instrum. **76**, 013306 (2005).
5) N. Fukunishi et al.: RIKEN Accel. Prog. Rep. **39**, 264 (2006).

New 18 GHz ECR ion source for new injector system

T. Nakagawa, M. Kidera, Y. Higurashi, O. Kamigaito, N. Fukunishi, H. Saitoh, A. Goto, and Y. Yano

As described in Ref. 1, the construction of a new additional injector system for RRC has been proposed for carrying out both SHI research and RIBF research simultaneously in the RIKEN accelerator facility. The new system, which consists of an ECR ion source, an RFQ linac and a heavy ion linac, will be used to inject intense beams of heavy ions to the ring cyclotron. The ECR ion source will be constructed for producing intense beam of medium charge state of heavy ions, such as Ar^{8+}, Kr^{13+} and Xe^{20+}.

Figure 1 shows a schematic drawing of the new RIKEN 18 GHz ECR ion source. The new source has an additional solenoid coil between two solenoid coils as shown in Fig. 1. We found that the magnetic field gradient at the resonance zone plays an essential role in increasing the plasma density and electron temperature.[2] The field gradient strongly depends on the minimum magnetic field strength (B_{min}) of the mirror field. Using this coil arrangement, we can change B_{min} without changing the maximum magnetic field (B_{ext} and B_{inj}) independently to optimize the magnetic field gradient at the resonance zone. The maximum magnetic field strength of the mirror field will be 1.4 T. Figure 2 shows the magnetic field configuration for Ar and Xe ion beam production.

To confine plasma radially, we use a hexapole magnet which consists of 36 segments of permanent magnets.

The inner diameter and length of the plasma chamber are 78 and 300 mm, respectively. The magnetic field strength at the surface of the inner wall of the plasma chamber is 1.25 T. To evacuate the plasma chamber to the order of 10^{-8} Torr, 150 and 300 l/s turbo molecular pumps will be used.

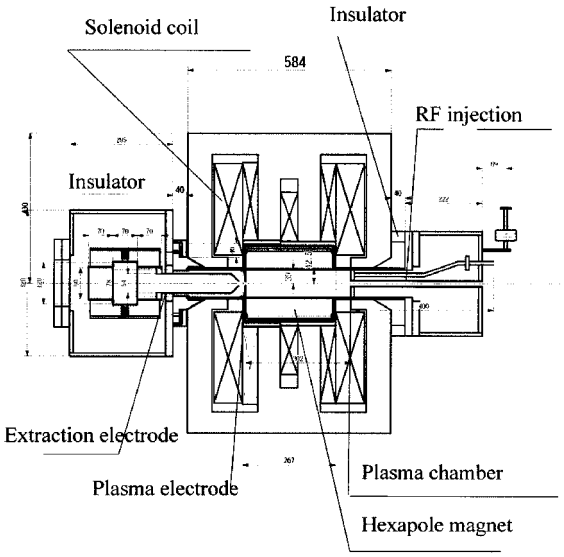

Fig. 1. Schematic drawing of new 18 GHz ECRIS.

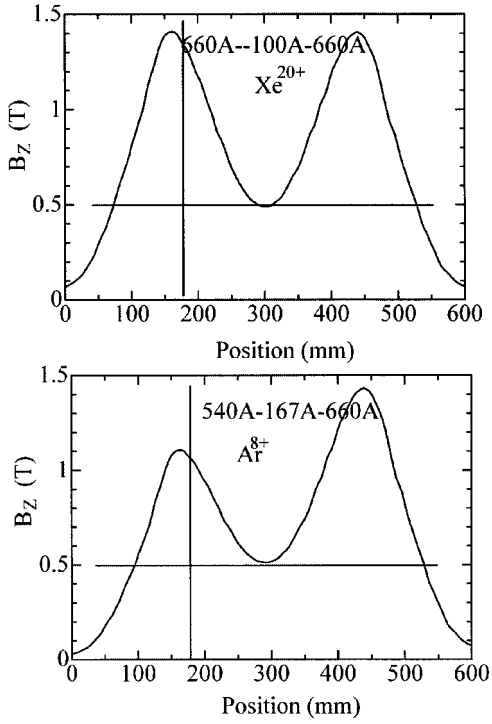

Fig. 2. Magnetic field configuration for production of Ar^{8+} and Xe^{20+}

To protect the hexapole magnet from demagnetization by a high temperature, the plasma chamber takes double wall structure for flowing the cooling water. The inner wall of plasma camber is covered by thin aluminum cylinder to supply the cold electrons to the plasma.[3] The movable negatively biased disc will be installed in the plasma chamber to tune plasma potential.[4] These methods are very useful for increasing the beam intensity of highly charged heavy ions from the ECR ion source.

References

1) O. Kamigaito et al.: RIKEN Accel. Prog. Rep. **39**, 261 (2006).
2) M. Imanaka et al.: Nucl. Instrum. Methods Phys. Res. B **237**, 647 (2005).
3) T. Nakagawa et al.: Jpn. J. Appl. Phys. **35**, 4077 (1996).
4) S. Biri et al.: Nucl. Instrum. Methods Phys. Res. B **152**, 386 (1999).

Design studies on quadrupole magnets of new injector to RRC

N. Fukunishi, O. Kamigaito, H. Saito, and A. Goto

A new injector linac for the existing Riken Ring Cycloton (RRC) is proposed to realize the RIKEN RI beam Factory project[1] and further experiments on superheavy element search in RIKEN.[2] Both projects require the use of the existing RIKEN Linear Accelerator (RILAC) and are incompatible with each other without the new injector system for the RRC. The new injector linac is designed exclusively to produce 350 MeV/nucleon primary beams.[3]

To obtain sufficient transverse focusing, the new injector linac requires two types of quadrupole magnets with very high magnetic-field gradients (0.4 T/cm). The maximum beam size estimated in ion optical calculations is 45 mm. Hence, the pole-tip field should be approximately 1 T, which is nearly twice as large as the maximum pole-tip field of usual quadrupole magnets used in the beam transport system of the existing facility. The present requirement is near the limit of the conventional normal conducting magnet. The effective lengths were 6 and 10 cm for a short quadrupole magnet (Q_s) and a long quadrupole magnet (Q_l), respectively. These quadrupole magnets will be used as quadrupole doublets (Q_s + Q_s) and quadrupole triplets (Q_s + Q_l + Q_s). An additional requirement for these magnets is compactness in the beam axis direction. The space allowed for coils is 4 cm for each side in the beam direction. Because the existing facility does not use this type of compact and high field-gradient quadrupole magnet, we investigated whether conventional normal conducting quadrupole magnets fulfill the present requirements.

Our design studies started with the quadrupole magnet in the IH linac of the Institute for Nuclear Study, Tokyo University, manufactured by Sumitomo Heavy Industries, Ltd.[4] The bore diameter was chosen to be 50 mm for both short and long quadupoles. We performed magnetic field calculations to optimize magnet shapes to obtain better excitation properties. The magnetic field calculations were performed using the TOSCA code.[a] In the magnetic field calculations, we use the BH curve given in the TOSCA code as a default, the effectiveness of which was sufficiently investigated by comparisons with magnets fabricated in the RIBF project.[5] Figure 1 shows a perspective view of a short quadrupole magnet. The excitation properties and effective length of the quadrupole magnets are shown in Figs. 2 and 3, respectively. For the long quadrupole magnet, a 0.41 T/cm field gradient is excited by 11900 ampere turns per pole, which corresponds to an overall current density of 6 A/mm^2. On the other hand, the field gradient of the short quadrupole remains 92% of the requirement with an excitation current of 14900 ampere turns per pole (=7.5 A/mm^2). It is not effective to increase excitation current for well-saturated magnets and one method of increasing field gradient is reducing the bore diameter from 50 mm to 48 mm. In this case, it is preferable to

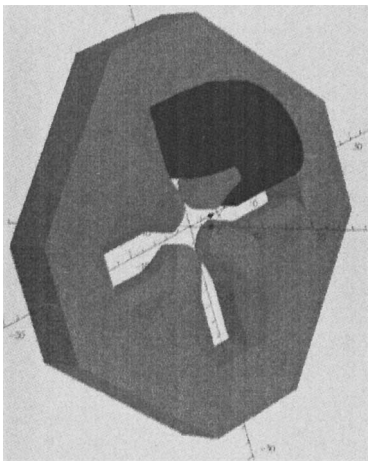

Fig. 1. Perspective view of short quadrupole.

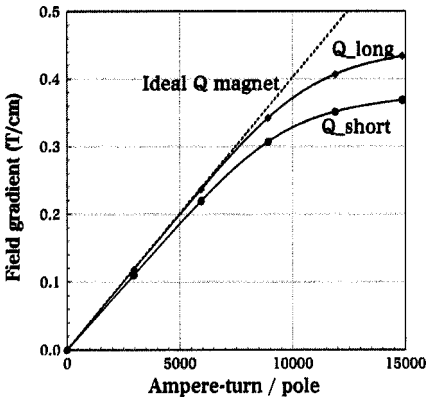

Fig. 2. Excitation property of quadrupole magnets.

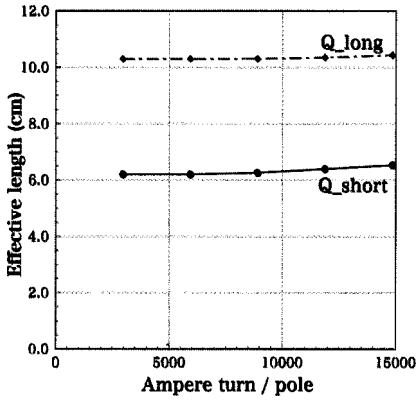

Fig. 3. Effective length of quadrupole magnets.

[a] Vector Field Ltd.

Table 1. Cooling water conditions of the quadrapole magnets.

	Q_s		Q_l	
Number of turns/pole	50		50	
Maximum current (A)	300		300	
Conductor size (mm)	4×6 with 2×4 hole		4×6 with 2×4 hole	
Current density (A/mm^2)	19.23		19.23	
Cooling water path	2		2	
	Inner path	Outer path	Inner path	Outer path
Coil length (m)	11.6	15.0	13.5	17.1
Resistance (Ω)	0.0128	0.0166	0.0149	0.0189
Power consumption (kW)	1.15	1.49	1.34	1.72
Pressure drop (MPa)	0.49	0.49	0.49	0.49
Velocity of cooling water (m/sec)	2.44	2.11	2.24	1.95
Water flow rate (l/min)	1.17	1.01	1.08	0.94
Temperature rise of water (°C)	14.1	21.1	17.7	25.9

adopt a lozenge-shaped beam duct.

The cooling water conditions of the coil were also estimated. The results are summarized in Table 1. The maximum temperature rise of the cooling water is 26°C with a pressure drop of 0.49 MPa, which is acceptable in our facility. In summary, we found the design of normal conducting quadrupole magnets, which fulfill the requirements from the new injector system, even though we need additional optimization for the short qudrupole magnet.

References

1) Y. Yano et al.: Proc. 17th Int. Conf. Cyclotrons and Their Applications, Tokyo, 2004-10 (Particle Accelerator Society of Japan, 2005), p. 169.
2) K. Morita et al.: J. Phys. Soc. Jpn. **73**, 1738 (2004).
3) O. Kamigaito et al.: RIKEN Accel. Prog. Rep. **39**, 261 (2006).
4) M. Tomizawa et al.: INS-Rep-1145 (1996).
5) N. Fukunishi et al.: RIKEN Accel. Prog. Rep. **34**, 329 (2001).

Compact design of damped cavity using SiC HOM absorbers

J. Watanabe[*1] M. Izawa,[*2] T. Koseki, N. Nakamura,[*3] K. Nakayama,[*1] H. Sakai,[*3] K. Sato,[*1] H. Suzuki,[*1] and H. Takaki[*3]

For electron storage rings with intense beam currents, the suppression of the coupled-bunch instability due to higher-order modes (HOMs) in rf cavities is one of the most important issues for stable operation. In this paper, we present a compact design of the higher-order modes (HOMs) damped cavity using microwave absorbers. The design is based on the cavity installed in the Photon Factory (PF) storage ring of KEK.[1,2] The PF-type cavity has a large-diameter beam duct made of a silicon-carbide (SiC) microwave absorber. The HOMs that have a frequency higher than the cut-off frequency of the beam duct are guided out of the cavity and dissipated by the absorber. The PF-type cavity has also been adopted at the New SUBARU ring of the University of Hyogo and at the SAGA Light Source in Tosu city, Saga prefecture.[3]

The PF-type cavity has a total length of more than 1.3 m in the longitudinal direction.[2] The length is relatively large and a shorter design is preferable to save the length of the cavity section in a storage ring and to provide space for installing an insertion device in a straight section together with the cavities. Recently, we have proposed a shorter design of the PF-type damped cavity. In the shorter design, a pair of cavities can be installed in a 2 m straight space as shown in Fig. 1, a cross-sectional view of a half of the pair of cavities.

The shorter design was obtained by eliminating the tapered duct between cavities and adjusting the length and position of the SiC duct. In addition, the diameter of the beam duct is reduced from 140 mm, the size of the original PF-type cavity, to 125 mm. As a result, the shunt impedance of the accelerating mode becomes 8.2 MΩ, which is 6% larger than that of the original PF-type cavity. However, reducing the beam-duct diameter increases the HOM impedances and the number of trapped HOMs, which are not damped by the SiC duct because their frequencies are below the cut-off frequency of the beam duct. In order to damp the trapped modes, three HOM dampers with rod-shaped coupling antennas[4,5] are employed.

Figure 2 shows a 3D view of the cavity with thee HOM dampers. Two dampers are attached to the longitudinal center position of the cavity in horizontal and vertical directions. In contrast, the third HOM damper is placed at an off-centered position to couple the TM012- and TM022-like modes. Figure 3 shows the electric field of the TM022-like mode and the position of the off-centered damper. The off-centered damper can couple the electric field of the TM012- and TM022-like modes effectively and reduce their impedances.

The new design presented in this paper has been adopted in a 3.0-GeV storage ring of the Australian Synchrotron Project (ASP), which is under construction in Melbourne.[6] The main parameters of the rf

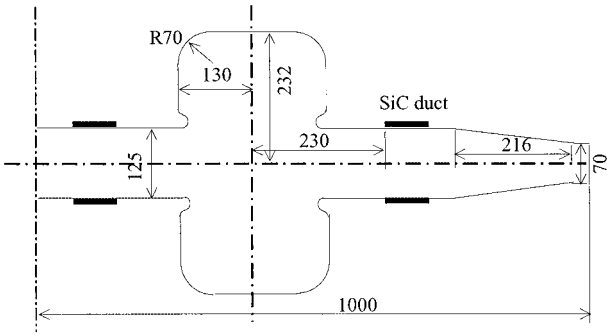

Fig. 1. Cross-sectional view of shorter design of damped cavity.

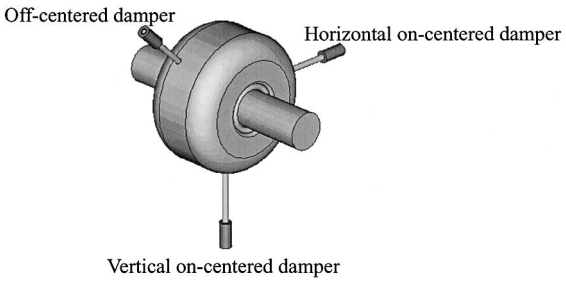

Fig. 2. Schematic drawing of rf cavity with three HOM dampers.

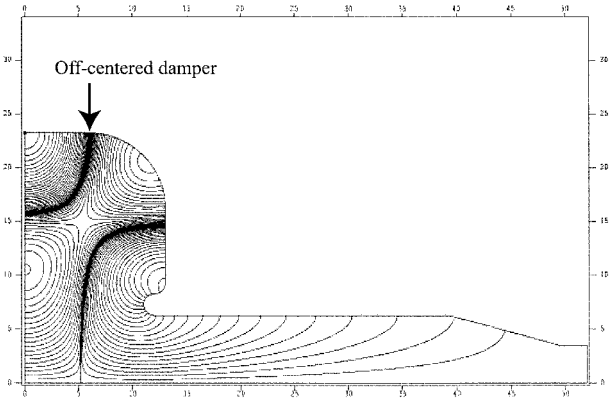

Fig. 3. Field distribution of TM022-like mode.

*1 Toshiba Corporation
*2 High Energy Accelerator Research Organization (KEK)
*3 Institute for Solid State Physics, University of Tokyo

cavity for the ASP ring are listed in Table 1.

Figure 4 shows the manufactured high-power models of the cavity for the ASP ring. Photographs of the on-centered and off-centered HOM dampers are shown in Figs. 5 and 6, respectively. The HOM dampers have a rod-shaped antenna followed by a coxial waveguide.

Table 1. Main parameters of rf cavity for ASP ring.

Frequency [MHz]	499.654
Number of cavities	4
Rf voltage/cavity [MV]	0.75
Coupling constant	1.7
Shunt impedance [MΩ]	8.2
Unloaded Q	> 30000
Nominal beam current [mA]	200

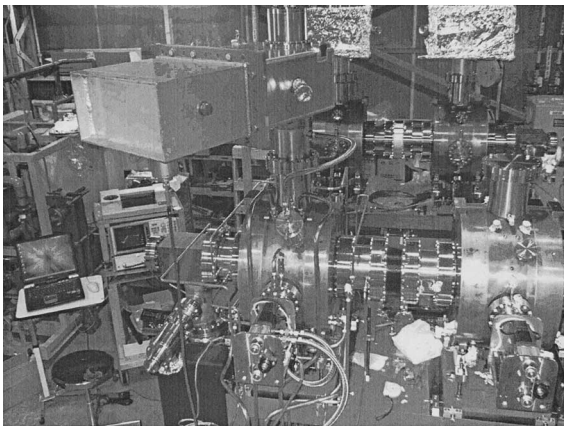

Fig. 4. Photograph of cavities for ASP ring.

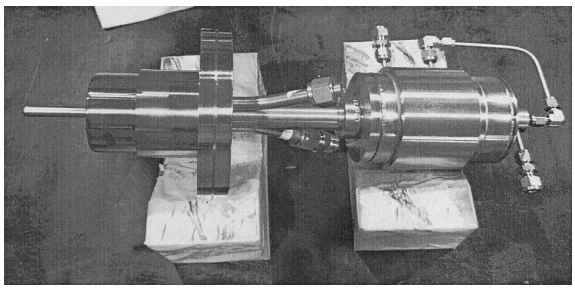

Fig. 5. Photograph of on-centered damper.

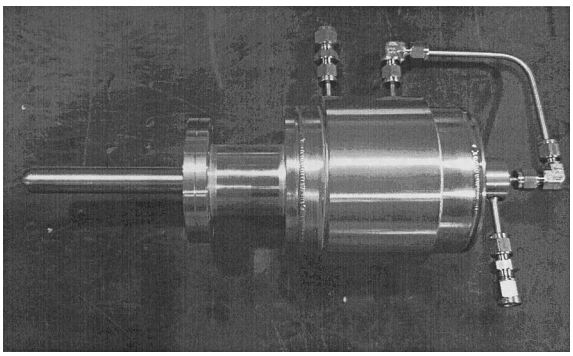

Fig. 6. Photograph of off-centered damper.

A cylindrical SiC piece made of the same material as the absorber at the beam duct is attached to the end of the coaxial waveguide and absorbs the extracted HOM power. The design of the HOM dampers is based on the structure described in the Ref. 5, but modified so as to dissipate higher rf power, which is required for the ASP ring. We have measured rf characteristics of the cavity with the HOM dampers at a low power level. It is confirmed that the Q-values of all trapped HOMs except TM011V- and TM011H-like modes are damped below the critical values so as not to induce the coupled-bunch instabilities in the ASP ring. For TM011H- and TM011V-like modes, which do not couple the rod-shaped antenna of the HOM dampers, their frequencies are detuned well by the tuner block attached to the on-centered damper so as not to coincide with the coupled-bunch mode frequencies.

Now, we are carrying out high-power conditioning of the cavities and HOM dampers, together with the other components such as input couplers and movable tuners. They will then be sent to Melbourne afterwards.

References

1) T. Koseki, M. Izawa, and Y. Kamiya: Rev. Sci. Instrum. **66**, 1926 (1995).
2) M. Izawa et al.: J. Synchrotron Radiat. **5**, 369 (1998).
3) T. Tomimasu et al.: Proc. PAC2003 (2003), p. 902.
4) T. Koseki et al.: Proc. EPAC1998 (1998), p. 1776.
5) T. Koseki et al.: Nucl. Instrum. Methods Phys. Res. A **467/468**, 91 (2001).
6) J. Watanabe et al.: Proc. PAC2005 (2005), p. 3076.

Highly charged ion generation using Nd-glass laser

S. Kondrashev,[*1] T. Kanesue,[*2] M. Okamura, and K. Sakakibara[*3]

At present, the laser ion source (LIS) is the most intense source to fill synchrotron rings in a single turn injection mode using highly charged ions.[1)] One of the most promising methods of intense highly charged ion beam extraction and acceleration is the direct plasma injection scheme (DPIS), proposed in RIKEN a few years ago.[2)] About 35 mA of C^{4+} ions and 17 mA of C^{6+} ions were accelerated by RFQ up to 100 keV/u using DPIS.[3)] As the next step, DPIS will be tested to accelerate intense highly charged ion beams of heavier elements.

Laser-produced plasma parameters (charge state distribution, currents and ion pulse durations) have to be specified before conducting acceleration tests. A 3 J/30 ns Nd-glass laser (B.M. Industries model 511 DNS13 laser courtesy of Center for Nuclear Study, Tokyo University) was used to generate highly charged ions of different elements from ^{12}C to ^{181}Ta. Lenses with focal lengths of 100 mm and 300 mm were used to focus laser beam onto a target surface at an incident angle 30 degrees. Taking into account 0.5 m as a typical disergence for such type of lasers, focal spot size can be estimated to be 50 μm and 150 μm for these cases and the maximum laser power densities reach 10^{12} W/cm^2 and 10^{11} W/cm^2 at the target surface respectisely. A Faraday cup (FC) for measuring ion current and an electrostatic ion analyzer (EIA) for measuring charge state distribution were placed at distances of 2.4 m and 3.7 m from the target normal to the target surface respectively. The detailed description of the experimental setup and focal position search procedure can be found in Refs. 4 and 5. Special attention was paid to carry out correct measurements: the linear range of secondary electron multiplier (SEM) voltage was found and used for all measurements; the widths of the first and second slits of the EIA were chosen to be 100 μm and 10 mm respectively to minimize the possible influence of space-charge effects inside the analyzer.

Having an entire set of FC and EIA data, ion currents, pulse durations, energy ranges and numbers of ions with different charge states were specified for ^{12}C, ^{27}Al, ^{48}Ti, ^{56}Fe, ^{74}Ge, ^{93}Nb and ^{181}Ta targets for two different laser power densities: 10^{12} W/cm^2 and 10^{11} W/cm^2 (except for the ^{48}Ti, ^{56}Fe and ^{74}Ge targets). The independence of secondary electron emission coefficient on the energy and charge state of registered ions was supposed. Ion charge states with the highest current (for 10^{12} W/cm^2 - 1, for 10^{11} W/cm^2 - 3) and maximal registered ion charge states (for 10^{12} W/cm^2 - 2, for 10^{11} W/cm^2 - 4) are summarized in Table 1 for all elements together with corresponding ionization potentials[6)] (in eV). From Table 1, one can clearly separate two groups of elements: highly charged ions with ionization potentials in the range 500–1000 eV were registered for all elements between ^{12}C and ^{56}Fe; at the same time, ions with about-one-order-less ionization potentials were registered for elements between ^{74}Ge and ^{181}Ta.

The most probable reason for such a big difference is recombination losses of highly charged ions during laser-produced plasma expansion into vacuum. Special measurements were performed to verify recombination losses in the case of the Ta target. FC was placed at three different distances (L) from the target: 32.5 cm (defined by the geometry and possible breakdown of the FC suppressor), 142 cm and 242 cm. Time structures of FC currents recorded at these distances from the target were scaled to one distance according to the L^{-3} law[7)] and no difference among all three curves was found. This means that there are no recombination losses of ions in Ta plasma at distances longer than 32.5 cm from the target and recombination processes should take place at shorter distances. Another interesting result obtained is the existence of two different groups of ions for all elements and laser power densities used in experiments: the faster group has a very weak dependence of energy on ion charge state, and the slower group always follows the low $E_z = 0.5\,\mathrm{keV}\cdot z$ (where z is the charge state and E_z is the energy of ions with charge state z corresponding to maximum ion current) with very high accuracy.

Table 1. Ion charge states with highest current and maximal registered ion charge states for different elements of periodic table.

	$^{12}C^{6+}$	$^{27}Al^{10+}$	$^{48}Ti^{10+}$	$^{56}Fe^{14+}$	$^{74}Ge^{5+}$	$^{93}Nb^{4+}$	$^{181}Ta^{4+}$
1	476	427	227	404	87	39.6	36.3
2	$^{12}C^{6+}$	$^{27}Al^{11+}$	$^{48}Ti^{13+}$	$^{56}Fe^{17+}$	$^{74}Ge^{8+}$	$^{93}Nb^{7+}$	$^{181}Ta^{6+}$
	476	471	738	1168	200	120	92.7
3	$^{12}C^{4+}$	$^{27}Al^{6+}$	-	-	-	$^{93}Nb^{4+}$	$^{181}Ta^{2+}$
	67.6	207				39.6	14.5
4	$^{12}C^{6+}$	$^{27}Al^{9+}$	-	-	-	$^{93}Nb^{7+}$	$^{181}Ta^{6+}$
	476	343				120	92.7

*1 Institute of Theoretical and Experimental Physics, Russia
*2 Department of Energy Science and Engineering, Kyushu University
*3 Department of Energy Sciences, Tokyo Institute of Technology

References
1) S. Kondrashev et al.: Proc. EPAC2004 (2004), p. 1402.
2) M. Okamura et al.: Laser Part. Beams **20**, 451 (2002).
3) H. Kashiwagi et al.: Rev. Sci. Instrum. **75**, 1569 (2004).
4) K. Sakakibara et al.: RIKEN Accel. Prog. Rep. **39**, 105 (2006).
5) T. Kanesue et al.: RIKEN Accel. Prog. Rep. **39**, 106 (2006).
6) Th. A. Carlson et al.: At. Data, **2**, 63 (1970).
7) B. Sharkov and S. Kondrashev: Proc. EPAC1996 (1996), p. 1550.

Carbon beam using DPIS†

M. Okamura, S. Kondrashev,*1 K. Sakakibara,*2 and T. Kanesue*3

Since 2004, we have been studying carbon beam acceleration using the direct plasma injection scheme (DPIS). A newly designed 100 MHz RFQ was fabricated at the Institute for Applied Physics, Goethe University, Frankfurt. The deposited energy on a carbon target and the pulse width of the CO_2 laser were measured to be 1.2 J and 85 ns (FWMS), respectively. The charge state distribution of the laser carbon plasma was examined before acceleration. In the first peak, excluding the tail that appears after 2 μs, the main content was C^{4+} (50%) and the rest of the ions consisted of C^{5+} (35%) and C^{3+} (15%).

The carbon target was placed at a position 320 mm upstream from the beginning of the vanes. A small stage for optics that included the target, a concave focusing lens and a plasma guide pipe, which directly faced the vanes, was isolated and surrounded completely by a grounded vacuum box. Up to 100 kV could be applied to the stage and the applied voltage was set to 60 kV for C^{4+} beam acceleration. An electrostatic analyzer was installed after the RFQ. Its bending radius was 100 mm and the distance between positive and negative electrodes was 5 mm. Two Faraday cups were placed before and after the analyzer.

The accelerated beam was analyzed, and acquired separated beam currents are shown in Fig. 1. To obtain $^{3+}$, $^{4+}$ and $^{5+}$ beam currents, voltages of 20 kV, 15 kV and 12 kV, respectively, were applied to the electrodes. Since all the ions were extracted with the stage voltage of 60 kV, all the unaccelerated ions can be bent by the analyzer with at an applied voltage of 3 kV. Therefore, it was difficult to investigate the contents of the unaccelerated beam.

The electrostatic analyzer only has a small opening, which corresponds to about 2.5% of the momentum acceptance instead of 10% of the energy spreads of the beam extracted from the RFQ. This means that the analyzed current only represented a small portion of the beam that was sliced out from 2.5% of the momentum window. Of course, the beam being accelerated was captured by a longitudinal RF bucket and its momentum distribution was caused by a synchrotron oscillation in the RFQ. Then the obtained current should be affected by the distribution pattern in the bucket. Also, in comparison with the beam size after the RFQ, the opening could only sample a small solid angle. The beam divergence after the RFQ of each charge state depends on space charge forces and the effects should not be identical for all the charge states.

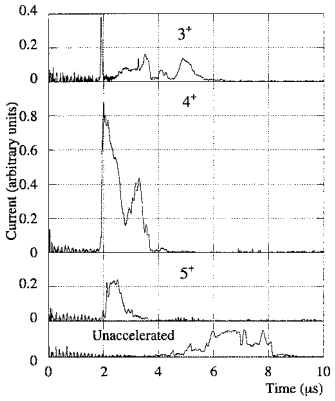

Fig. 1. Analyzed beam pulse.

Note that the information specified in Fig. 1 provides us only a rough quantitative analysis.

The C^{4+} and $^{5+}$ beams were shown from 1.9 μs to 3.8 μs. The C^{3+} beam had a longer pulse period, which lasted up to 5.6 μs. When we applied the integrated areas of each charge state indicated in Fig. 1 to the total accelerated current measured using the Faraday cup just after the RFQ, the C^{4+} occupied more than 60% of the beam which corresponded to 6.3×10^{10} particles.

Since the injection bias voltage was 60 kV, the C^{3+} beam only has a kinetic energy of 180 keV instead of the designed value of 240 keV. Even in this condition, some portions of the injected C^{3+} beam were captured and were accelerated up to 1.2 MeV.

The tail of the current, which started from 4 μs, mainly consisted of the unaccelerated beams that were assumed to originate from C^{1+}, $^{2+}$ and $^{3+}$. Some particles of C^{4+} and $^{5+}$ that were longitudinally lost from the acceleration RF buckets might be contained in the tail.

The unaccelerated beam still has a high intensity. This is evidence that an intense beam from the DPIS can be captured transversely through the entire length of the cavity by the RFQ focusing force. If we have a long unmodulated section in the beginning of the vanes, pulse width can be expanded due to the momentum spread and space charge repulsion force. Using an adequate beam injection energy, the pulse duration of the extracted beam might be controlled without significant beam loss.

Reference

1) M. Okamura, T. Katayama, R. A. Jameson, T. Takeuchi, T. Hattori, and H. Kashiwagi: Laser Part. Beams **20**, 451 (2002).

† Condensed from the article in ICIS05 proceedings

*1 Institute for Theoretical and Experimental Physics, Russia
*2 Tokyo Institute of Technology
*3 Kyusyu University

Routine work for radiation safety in ring cyclotron facility

Y. Uwamino, S. Fujita, H. Sakamoto, R. Hirunuma, H. Mukai,[*1] A. Horigome,[*2] T. Yamaki, and N. Yukawa

We report here the residual radioactivity and leakage radiation level at the RIKEN Ring Cyclotron (RRC) facility.

Residual radioactivity in the facility was measured at various locations using AE133V ionization-chamber gamma-ray survey meters of Applied Engineering Inc. The scheduled overhaul started immediately after the experiment that was carried out with an ^{56}Fe beam of 83 MeV/nucleon in the E2 experimental vault from July 30 to August 2, 2005. The dose rates at the deflectors of the injector AVF cyclotron and RRC were found to be 2 mSv/h and 20 mSv/h on August 9 and 10, respectively.

In addition to the above measurement, dose rates inside the injector AVF cyclotron were measured on October 14, 2004. The dose rates were 3.6 mSv/h at the deflector and 0.46 mSv/h at the magnetic channel. A minor rearrangement was carried out with the deflector after the measurement.

During the period from October 1, 2004 to September 30, 2005, the dose rates were measured along the beam lines after almost every experiment. Spots **a**–**x**, marked by bullets in Fig. 1, are the places where the dose rates exceeded 30 μSv/h. Table 1 summarizes the observed dose rates and gives the dates on which the measurements were performed. The maximum dose rate was found to be 850 μSv/h at the beam dump in the E3 experimental vault denoted by **u** in Fig. 1. Whenever we observed a high dose rate, we roped-off the area and posted a warning sign indicating that it was dangerous to remain for a long time in that place.

We paid particular attention to measuring the leakage radiations in and around the RRC facility when a 63-MeV/nucleon ^{40}Ar beam of 750 pnA intensity was stopped by a Faraday cup, FC-D50, in the beam distribution corridor, without any local shield. Aloka TPS-451BS neutron rem counters and AE133V gamma-ray survey meters were used. The measured results are shown in Table 2. The leakage was found to be small compared with the legal limits, which are 25 μSv/h for **A**–**D** in the radiation controlled area and 2.6 μSv/h for **E** at the boundary of the radiation controlled area.

We also continuously monitored the leakage radiation from the RRC facility using neutron and gamma-ray active area monitors and passive monitors with thermoluminescence dosimeter (TLD). The passive

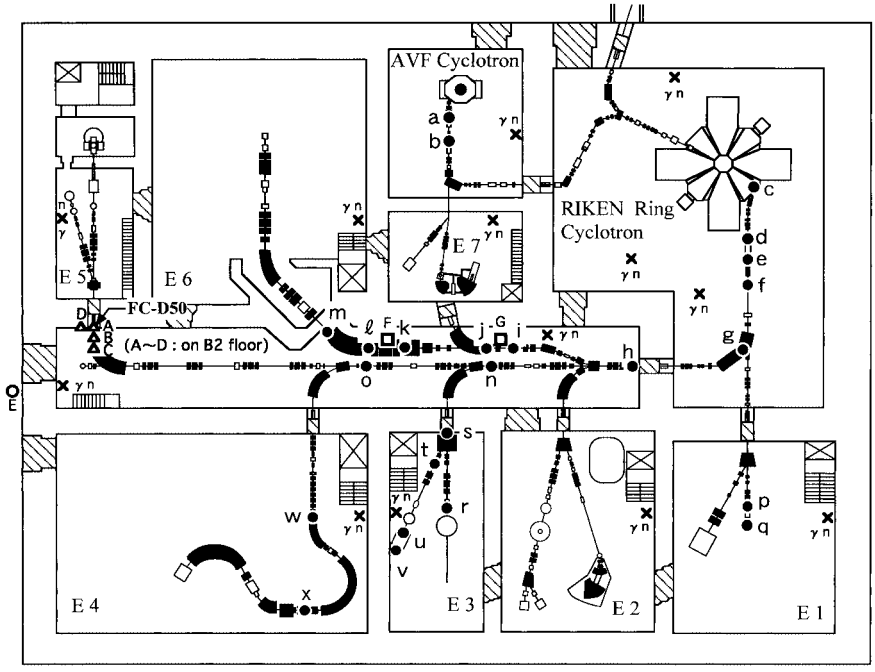

Fig. 1. Layout of RIKEN Ring Cyclotron facility as of 2005. Measured locations of residual radioactivity along the beam lines are indicated by bullets **a**–**x**. Locations of leakage neutron and gamma-ray measurements when an ^{40}Ar beam was stopped at FC-D50 are indicated by open triangles **A** to **D** and open circle **E**. Open squares **F** and **G** are the positions of TLD-rem measurements.

*1 Japan Environment Research Corporation
*2 Tokyo University of Science

Table 1. Summary of dose rates measured along the beam lines with ionization-chamber survey meters. Detection points **a**–**x** indicate measured locations shown in Fig. 1.

Detection point	Measured dose rate (μSv/h)	Date	Particle	Energy (MeV/u)	Intensity (enA)	Period (days)
a	120	Aug 12, '05	Fe-56	83	200	3
b	200	Aug 12, '05	Fe-56	83	200	3
c	90	Aug 12, '05	Fe-56	83	200	3
d	110	Aug 12, '05	Fe-56	83	200	3
e	500	Jan 5, '05	Zn-70	63	6500	7.5
f	100	Aug 12, '05	Fe-56	83	200	3
g	60	Jan 5, '05	Zn-70	63	6500	7.5
h	30	Jan 5, '05	Zn-70	63	6500	7.5
i	60	Jan 5, '05	Zn-70	63	6500	7.5
j	150	Jan 5, '05	Zn-70	63	6500	7.5
k	300	Aug 12, '05	Fe-56	83	200	3
l	90	Aug 12, '05	Fe-56	83	200	3
m	150	Aug 12, '05	Fe-56	83	200	3
n	35	Aug 12, '05	Fe-56	83	200	3
o	90	Aug 12, '05	Fe-56	83	200	3
p	80	Jun 28, '05	N-14	135	3100	0.5
q	55	Jun 28, '05	N-14	135	3100	0.5
r	80	Jun 8, '05	p	135	1	0.5
s	40	Oct 28, '04	N-14	135	3800	1
t	35	Oct 28, '04	N-14	135	3800	1
u	850	Dec 15, '04	N-14	135	2200	1
v	200	Dec 15, '04	N-14	135	2200	1
w	700	Jun 8, '05	p	135	10	1
x	90	Jun 8, '05	p	135	10	1

Table 2. Measured dose rates in and around RRC facility when 63-MeV/nucleon 750-pnA ^{40}Ar beam was stopped by Faraday cup, FC-D50, without any local shield. Measured points are shown in Fig. 1.

Measured point	Neutron dose rate (μSv/h)	Gamma dose rate (μSv/h)	Remark
A	1.0	0.2	directly below Faraday cup, on B2 floor
B	1.3	0.4	1 m south from A
C	0.8	0.2	2 m south from A
D	0.8	0.2	1 m west from A
E	0.8	0.1	outside shielding door of beam distribution corridor

neutron dosimeter was developed by us, and it measures the neutron effective dose.

The leakage radiations were below the detection limit of the environmental area monitors placed near the site boundary. We evaluated the radiation level at the boundary of the radiation controlled area measured using an area monitor installed in the computer room on the ground floor immediately above a bending magnet that guided the beams from the RRC vault to the distribution corridor, and it was approximately 9.6 μSv/y, which was much lower than the allowable dose limit (1 mSv/y).

The results obtained with the passive dosimeters placed around the radiation controlled area were below the detection limit, which was approximately 0.2 mSv/y, and the results obtained with them placed in the RRC facility at points **F** and **G** in Fig. 1 were 3.5 mSv/y and 1.6 mSv/y, respectively. The legal dose limits for these positions were 50 mSv/y.

VI. LIST OF PUBLICATIONS

1. Accelerator development and accelerator physics

V. Banerjee, A. Chakrabarti, A. Bandyopadhyay, T. K. Bhaumik, M. Mondal, T. K. Chakraborty, H. Pande, O. Kamigaito, A. Goto, and Y. Yano: "The design of a radio frequency quadrupole LINAC for the RIB project at VECC Kolkata", Pramana J. Phys. **59**, No. 6, pp. 957–962 (2002).

P. Strasser, K. Nagamine, T. Matsuzaki, K. Ishida, Y. Matsuda, K. Itahashi, and M. Iwasaki: "Progress in muonic atom spectroscopy with RI beams", Nucl. Phys. A **746**, 621c–624c (2004).

Y. Nagashima, F. Saito, Y. Itoh, A. Goto, and T. Hyodo: "Measurement of Cu K-shell and Ag L-shell ionization cross sections by low-energy positron impact", Phys. Rev. Lett. **92**, No. 22, pp. 223201-1–223201-4 (2004).

J. Ohnishi, T. Mitsumoto, A. Goto, M. Kase, M. Nagase, and Y. Yano: "Construction status of the magnet system for the RIKEN intermediate-stage ring cyclotron", Proccdings of the 1st Annual Meeting of Particle Accelerator Society of Japan/The 29th Linear Accelerator Meeting in Japan, Funabashi, 2004–8, Funabashi, pp. 224–226 (2004).

A. Goto: "Cyclotrons 2004", J. Particle Accelerator Society of Japan **2**, No. 1, pp. 58–62 (2005).

M. Kawaguchi, K. Ushida, S. Kashiwagi, R. Kuroda, T. Kuribayashi, M. Kobayashi, Y. Hama, and M. Washio: "Development of compact picosecond pulse radiolysis system", Nucl. Instrum. Methods Phys. Res. B **236**, 425–431 (2005).

G. Bonomi, M. Amoretti, P. Bowe, C. Canali, C. Carraro, C. Cesar, M. Charlton, M. Doser, A. Fontana, M. Fujiwara, R. Funakoshi, P. Genova, J. Hangst, R. Hayano, L. Jorgensen, A. Kellerbauer, V. Lagomarsino, R. Landua, E. Rizzini, M. Macri, N. Madsen, G. Manuzio, P. Montagna, D. Mitchard, A. Rotondi, G. Testera, A. Variola, L. Venturelli, Y. Yamazaki, D. van der Werf, and N. Zurlo: "Antihydrogen production mechanisms in ATHENA", Nucl. Phys. A **752**, 97c–100c (2005).

R. Taki, H. Okamura, N. Fukunishi, H. Ryuto, N. Sakamoto, K. Sekiguchi, and A. Goto: "Response of a germanium detector to energetic heavy ions", Nuclear Instruments and Methods in Physics Research A **545**, 269–272 (2005).

M. Komiyama, M. Kase, and M. Fujimaki: "Beam interlock system at RIKEN RI beam factory", Proccdings of the 2nd Annual Meeting of Particle Accelerator Society of Japan/The 30th Linear Accelerator Meeting in Japan, Tosu, 2005–7, Particle Accelerator Society of Japan, Tosu, pp. 615–617 (2005).

H. Ryuto, T. Abe, N. Fukunishi, M. Kase, and Y. Yano: "Heavy-ion beam irradiation system for biological samples in RIKEN", Proceedings of International Symposium on Novel Techniques in Nano-Biology 2005 (ISNB05), (Biology Research Center of Industrial Accelerators and others), Naju, Korea, 2005–4, BRCIA, Naju, pp. 24–32 (2005).

O. Kamigaito, M. Kase, N. Sakamoto, Y. Miyazawa, E. Ikezawa, N. Fukunishi, S. Kohara, M. Fujimaki, M. Hemmi, T. Chiba, Y. Chiba, H. Ryuto, A. Goto, and Y. Yano: "Construction of a booster linac for the RIKEN heavy-ion linac", Rev. Sci. Instrum. **76**, 013306-1–013306-11 (2005).

T. Tominaka: "Calculations using the helical filamentary structure for current distributions of twisted superconducting multifilamentary composites", Supercond. Sci. Technol. **18**, 634–643 (2005).

T. Tominaka: "Two-dimensional magnetic fields of pie-shaped conductors", Supercond. Sci. Technol. **18**, 881–887 (2005).

H. Imao, N. Kawamura, K. Ishida, T. Matsuzaki, Y. Matsuda, A. Toyoda, and K. Nagamine: "Dependence of muon-catalyzed *d-d* fusion on the ortho-para ratio in solid and liquid deuterium", Phys. Lett. B **632**, 192–196 (2006).

2. Nuclear physics and nuclear instrumentation

D. Kharzeev, A. Krasnitz, and R. Venugopalan: "Anomalous chirality fluctuations in the initial stage of heavy ion collisions and parity odd bubbles", Phys. Lett. B **545**, 298–306 (2002).

A. Yoshimi, K. Asahi, and S. Emori: "Nuclear spin maser and atomic electric dipole moment of 129Xe", Czech. J. Phys. **53**, No. Suppl. B, pp. B227–B233 (2003).

D. Kaji, K. Morita, K. Morimoto, Y. Zhao, A. Yoneda, T. Suda, A. Yoshida, H. Kudo, K. Katori, and I. Tanihata: "Status of heavy element synthesis in RIKEN", J. Radioanal. Nucl. Chem. **255**, No. 1, pp. 77–80 (2003).

M. Golovkov, Y. T. Oganessian, D. Bogdanov, A. Fomichev, A. Rodin, S. Sidorchuk, R. Slepnev, S. Stepantsov, G. Ter-Akopian, R. Wolski, V. Gorshkov, M. Chelnokov, M. Itkis, E. Kozulin, A. Bogatchev, N. Kondratiev, I. Korzyukov, A. Yukhimchuk, V. Perevozchikov, Y. Vinogradov, S. Grishechkin, A. Demin, S. Zlatoustovskiy, A. Kuryakin, S. Fil'chagin, R. Il'kayev, F. Hanappe, T. Materna, L. Stuttge, A. Ninane, A. A. Korsheninnikov, E. Nikolski, I. Tanihata, P. Roussel-Chomaz, W. Mittig, N. Alamanos, V. Lapoux, E. Pollacco, and L. Nalpas: "Evidences for resonance states in ^{5}H", Phys. Lett. B **566**, 70–75 (2003).

T. Blum, P. Chen, N. Christ, C. Cristian, C. Dawson, G. Fleming, R. D. Mawhinney, S. Ohta, G. Siegert,

A. Soni, P. Vranas, M. Wingate, L. Wu, and Y. Zhestkov: "Kaon Matrix Elements and CP Violation from Quenched Lattice QCD: The 3-Flavor Case", Phys. Rev. D **68**, 114506-1–114506-70 (2003).

T. Katayama, T. Suda, and I. Tanihata: "Status of MUSES project and electron RI collider at RIKEN", Phys. Scr. T **104**, 129–143 (2003).

Y. Motizuki and S. Kumagai: "Radioactivity of the Key Isotope ^{44}Ti in SN 1987A", AIP Conf. Proc. **704**, 369–374 (2004).

A. Ozawa: "Measurements of reaction cross-sections and determination of nucleon matter density distributions", Horizons World Phys. **244**, 301–321 (2004).

T. Asano, T. Wada, M. Ohta, T. Ichikawa, S. Yamaji, and H. Nakahara: "Dynamical calculation of multimodal nuclear fission of fermium nuclei", J. Nucl. Radiochem. Sci. **5**, 1–5 (2004).

K. Morita, K. Morimoto, D. Kaji, S. Goto, H. Haba, E. Ideguchi, R. Kanungo, K. Katori, H. Koura, H. Kudo, T. Ohnishi, A. Ozawa, J. Peter, T. Suda, K. Sueki, I. Tanihata, F. Tokanai, H. Xu, A. V. Yeremin, A. Yoneda, A. Yoshida, Y. L. Zhao, and T. Zheng: "Status of heavy element research using GARIS at RIKEN", Nucl. Phys. A **734**, 101–108 (2004).

A. Ozawa: "Recent experiments for interaction and reaction cross-sections", Nucl. Phys. A **734**, 315–318 (2004).

D. Kameda, K. Asahi, H. Ueno, A. Yoshimi, H. Watanabe, H. Miyoshi, K. Shimada, J. Murata, Y. Kobayashi, G. Kato, S. Emori, W. Sato, and H. Ogawa: "Recent result from the nuclear moment measurements using a spin polarized radioactive beam", Nucl. Phys. A **734**, 481–484 (2004).

S. Sugimoto, K. Ikeda, and H. Toki: "Charge- and parity-projected Hartree-Fock study with the tensor force of light nuclei", Nucl. Phys. A **738**, 240–244 (2004).

A. Yoshimi, H. Ueno, W. Sato, H. Watanabe, Y. Kobayashi, J. Murata, H. Miyoshi, K. Shimada, and K. Asahi: "Study on the transient field at very high velocities for the g-factor measurement of excited states in unstable nuclei", Nucl. Phys. A **738**, 519–522 (2004).

S. Sugimoto, K. Ikeda, and H. Toki: "Charge- and parity-projected Hartree-Fock method for the strong tensor correlation and its application to the alpha particle", Nucl. Phys. A **740**, 77–94 (2004).

M. Wakasugi, T. Suda, and Y. Yano: "A new method for electron-scattering experiments using a self-confining radioactive ion target in an electron storage ring", Nuclear Instruments and Methods in Physics Research A **532**, 216–223 (2004).

S. Nishimura, Y. Nishi, M. Kurata-Nishimura, I. Tanihata, M. A. Famiano, M. E. Howard, D. Reitzner, E. E. Smith, and R. N. Boyd: "Half-life measurement of neutron-rich nuclei and future at RIBF", Origin Matter and Evolution of Galaxies 2003: Proceedings of International Symposium on Origin Matter and Evolution of Galaxies 2003, (CNS, RIKEN, and others), Wako, 2003–12, World Scientific, Hackensack, pp. 304–315 (2004).

Z. Elekes, Z. Dombradi, A. Krasznahorkay, H. Baba, M. Csatlos, L. Csige, N. Fukuda, Z. Fulop, Z. Gacsi, J. Gulyas, N. Iwasa, N. Kinugawa, S. Kubono, M. Kurokawa, X. Liu, S. Michimasa, T. Minemura, T. Motobayashi, A. Ozawa, A. Saito, S. Shimoura, S. Takeuchi, I. Tanihata, P. Thirolf, Y. Yanagisawa, and K. Yoshida: "Decoupling of valence neutrons from the core in ^{16}C", Phys. Lett. B **586**, 34–40 (2004).

T. Suzuki, H. Bhang, G. Franklin, K. Gomikawa, R. Hayano, T. Hayashi, K. Ishikawa, S. Ishimoto, K. Itahashi, M. Iwasaki, T. Katayama, Y. Kondo, Y. Matsuda, T. Nakamura, S. Okada, H. Outa, B. Quinn, M. Sato, M. Shindo, H. So, P. Strasser, T. Sugimoto, K. Suzuki, S. Suzuki, D. Tomono, A. M. Vinodkumar, E. Widmann, T. Yamazaki, and T. Yoneyama: "Discovery of a strange tribaryon $S^0(3115)$ in ^{4}He (stopped K^-, p) reaction", Phys. Lett. B **597**, 263–269 (2004).

Z. Elekes, Z. Dombradi, A. Saito, N. Aoi, H. Baba, K. Demichi, Z. Fulop, J. D. Gibelin, T. Gomi, H. Hasegawa, N. Imai, M. Ishihara, H. Iwasaki, S. Kanno, S. Kawai, T. Kishida, T. Kubo, K. Kurita, Y. Matsuyama, S. Michimasa, T. Minemura, T. Motobayashi, M. Notani, T. Ohnishi, H. Ong, S. Ota, A. Ozawa, H. Sakai, H. Sakurai, S. Shimoura, E. Takeshita, S. Takeuchi, M. Tamaki, Y. Togano, K. Yamada, Y. Yanagisawa, and K. Yoneda: "Bound excited states in ^{27}F", Phys. Lett. B **599**, 17–22 (2004).

D. Fang, T. Yamaguchi, T. Zheng, A. Ozawa, M. Chiba, R. Kanungo, T. Kato, K. Morimoto, T. Ohnishi, T. Suda, Y. Yamaguchi, A. Yoshida, K. Yoshida, and I. Tanihata: "One-neutron halo structure in ^{15}C", Phys. Rev. C **69**, 034613-1–034613-6 (2004).

K. Sekiguchi, H. Sakai, H. Witala, K. Ermisch, W. Gloeckle, J. Golack, M. Hatano, H. Kamada, N. Kalantar-Nayestanaki, H. Kato, Y. Maeda, J. Nishikawa, N. Andreas, T. Ohnishi, H. Okamura, T. Saito, N. Sakamoto, S. Sakoda, Y. Sato, K. Suda, A. Tamii, N. Uchigashima, T. Uesaka, T. Wakasa, and K. Yako: "Polarization transfer measurement for ^{1}H($\vec{d}$,$\vec{p}$)^{2}H elastic scattering at 135 MeV/nucleon and three-nucleon force effects", Phys. Rev. C **70**, 014001-1–014001-17 (2004).

Y. Yamaguchi, C. Wu, T. Suzuki, A. Ozawa, D. Fang, M. Fukuda, N. Iwasa, T. Izumikawa, H. Jeppesen, R. Kanungo, R. Koyama, T. Ohnishi, T. Ohtsubo, W. Shinozaki, T. Suda, M. Takahashhi, and I. Tanihata: "Density distribution of ^{17}B from a reaction cross-

section measurement", Phys. Rev. C **70**, 054320-1–054320-6 (2004).

N. Imai, H. Ong, N. Aoi, H. Sakurai, K. Demichi, H. Kawasaki, H. Baba, Z. Dombradi, Z. Elekes, N. Fukuda, Z. Fulop, A. Gelberg, T. Gomi, H. Hasegawa, K. Ishikawa, H. Iwasaki, E. Kaneko, S. Kanno, T. Kishida, Y. Kondo, T. Kubo, K. Kurita, S. Michimasa, T. Minemura, M. Miura, T. Motobayashi, T. Nakamura, M. Notani, T. Onishi, A. Saito, S. Shimoura, T. Sugimoto, M. Suzuki, E. Takeshita, S. Takeuchi, M. Tamaki, K. Yamada, K. Yoneda, H. Watanabe, and M. Ishihara: "Anomalously hindered $E2$ strength $B(E2; 2_1^+ \rightarrow 0^+)$ in ^{16}C", Phys. Rev. Lett. **92**, 062501-1–02501-4 (2004).

D. Cortina-Gil, J. Fernandez-Vazquez, T. Aumann, T. Baumann, J. Benlliure, M. J. Borge, L. V. Chulkov, U. DattaPramanik, C. Forssen, L. M. Fraile, H. Geissel, J. Gerl, F. Hammache, K. Itahashi, R. Janik, B. Jonson, S. Mandal, K. Markenroth, M. Meister, M. Mocko, G. Munzenberg, T. Ohtsubo, A. Ozawa, Y. Prezado, V. Privora, K. Riisager, H. Scheit, R. Schneider, G. Schreider, H. Simon, B. Sitar, A. Stolz, P. Strmen, K. Summerer, I. Szarka, and H. Weick: "Shell structure of the near-dripline nucleus 23O", Phys. Rev. Lett. **93**, No. 6, pp. 062501-1–062501-4 (2004).

T. Matsuura, T. Hatsuda, K. Iida, and G. Baym: "Thermal phase transition of dense QCD", Proceedings of International Conference on Color Confinement and Hadrons in Quantum Chromodynamics: Confinement 2003, Wako, 2003–7, World Scientific, Singapore, pp. 346–357 (2004).

Y. Motizuki, H. Madokoro, and T. Shimizu: "Core-collapse supernovae induced by anisotropic neutrino radiation", Proceedings of International Confrence in Honour of the 60th Birthday of Marcel Arnould: The Future Astronuclear Physics From Microscopic Puzzles to Macroscopic Nightmares, (University Libre de Bruxelles), Brussels, Bergium, 2003–8, A. Jorissen and others, EDP Sciences, Les Ulis, pp. 163–171 (2004).

Y. Motizuki, T. Tachibana, S. Goriely, and H. Koura: "Required precision of mass and half-life measurements for r-process nuclei planned at future Radioactive-Ion-Beam facilities", Proceedings of International Confrence in Honour of the 60th Birthday of Marcel Arnould: The Future Astronuclear Physics From Microscopic Puzzles to Macroscopic Nightmares, (University Libre de Bruxelles), Brussels, Bergium, 2003–8, A. Jorissen and others, EDP Sciences, Les Ulis, pp. 227–234 (2004).

K. Sekiguchi, H. Sakai, H. Okamura, A. Tamii, T. Uesaka, K. Suda, N. Sakamoto, T. Wakasa, Y. Sato, T. Ohnishi, K. Yako, S. Sakoda, H. Kato, Y. Maeda, M. Hatano, J. Nishikawa, T. Saito, N. Uchigashima, N. N. Kalantar, and K. Ermisch: "Measurement of Nucleon-Deuteron Scattering as a Good Probe to Study Three Nucleon Forces", Proceedings of the International Symposium on A New Era of Nuclear Structure Physics (NENS03), (Niigata University), Kurokawa-mura, Niigata Pref., 2003–11, World Scientific, Singapore, pp. 17–21 (2004).

D. Kameda, K. Asahi, H. Miyoshi, K. Shimada, G. Kato, S. Emori, G. Kijima, H. Ueno, A. Yoshimi, H. Watanabe, T. Haseyama, Y. Kobayashi, J. Murata, W. Sato, and H. Ogawa: "g-factor measurement of ^{19}N", Proceedings of the International Symposium on A New Era of Nuclear Structure Physics (NENS03), (Niigata University), Kurokawa-mura, Niigata Pref., 2003–11, World Scientific, Singapore, pp. 231–235 (2004).

K. Iida, K. Oyamatsu, and B. A. Sarhan: "Deducing the density dependence of the symmetry energy from unstable nuclei", Proceedings of the International Symposium on A New Era of Nuclear Structure Physics (NENS03), (Niigata University), Kurokawa-mura, Niigata Pref., 2003–11, World Scientific, Singapore, pp. 342–343 (2004).

H. Miyoshi, K. Shimada, K. Asahi, D. Kameda, K. Sakai, S. Emori, G. Kato, H. Ueno, A. Yoshimi, H. Watanabe, Y. Kobayashi, J. Murata, W. Sato, H. Ogawa, and W. D. Schmidt-Ott: "Low-energy of polarized RI atomic beam", Proceedings of the International Symposium on A New Era of Nuclear Structure Physics (NENS03), (Niigata University), Kurokawa-mura, Niigata Pref., 2003–11, World Scientific, Singapore, pp. 357–358 (2004).

K. Shimada, K. Asahi, H. Miyoshi, D. Kameda, K. Sakai, S. Emori, G. Kato, G. Kijima, M. Tsukui, A. Yoshimi, H. Ueno, Y. Kobayashi, H. Watanabe, T. Haseyama, and J. Murata: "Developement of an extraction chamber for the RI atomic beam resonance method", Proceedings of the International Symposium on A New Era of Nuclear Structure Physics (NENS03), (Niigata University), Kurokawa-mura, Niigata Pref., 2003–11, World Scientific, Singapore, pp. 363–364 (2004).

K. Oyamatsu and K. Iida: "Equation of state of nuclear matter, neutron rich nuclei in laboratories and pasta nuclei in neutron star crusts", Prog. Theor. Phys. Suppl., No. 156, pp. 137–138 (2004).

K. Iida, K. Oyamatsu, and B. A. Sarhan: "Deducing the density dependence of the symmetry energy from unstable nuclei", Prog. Theor. Phys. Suppl., No. 156, pp. 139–140 (2004).

H. Madokoro, T. Shimizu, and Y. Motizuki: "Importance of prolate neutrino radiation in core-collapse supernovae: The reason for the prolate geometry of SN1987A?", Publ. Astron. Soc. Jpn. **56**, 663–669 (2004).

K. Iida: "Color superconductivity in finite quark matter", Soryushiron Kenkyu **108**, No. 5, pp. E7–E9 (2004).

H. Ueno, K. Asahi, H. Ogawa, D. Kameda, H. Miyoshi,

A. Yoshimi, H. Watanabe, K. Shimada, W. Sato, K. Yoneda, N. Imai, Y. Kobayashi, M. Ishihara, and W. D. Schmidt-Ott: "Nuclear moments of nuclei in the neighborhood of the neutron drip line", The Labyrinth in Nuclear Structure: Proceedings of International Conference on The Labyrinth in Nuclear Structure, an EPS Nuclear Physics Divisional Conference, (NCSR Demokritos and others), Crete, Greece, 2003–7, A. Bracco and C. A. Kalfas, American Institure of Physics, New York, pp. 135–142 (2004).

H. Madokoro, T. Shimizu, and Y. Motizuki: "Effects of small-scale fluctuations of neutrino flux in supernova explosions", Cosmic Explosions On the 10th Anniversary of SN1993J (IAU Colloquium 192), Valencia, Spain, 2003–4, J. M. Marcaide and K. W. Weiler, Springer-Verlag, Berlin, pp. 309–314 (2005).

T. Inakura, H. Imagawa, Y. Hashimoto, M. Yamagami, S. Mizutori, and K. Matsuyanagi: "Soft octupole vibrations on superdeformed states in nuclei around ^{40}Ca suggested by Skyrme-HF and self-consistent RPA calculations", Eur. Phys. J. A **25**, Suppl. 1, 545–546 (2005).

K. Yoshida, T. Inakura, M. Yamagami, S. Mizutori, and K. Matsuyanagi: "Microscopic structure of negative-parity vibrations built on superdeformed states in sulfur isotopes close to the neutron drip line", Eur. Phys. J. A **25**, Suppl. 1, 557–558 (2005).

M. Yamagami: "Collective excitations induced by pairing anti-halo effect", Eur. Phys. J. A **25**, Suppl. 1, 569–570 (2005).

M. Yamagami and V. Nguyen: "Pairing effects on the collectivity of quadrupole states around ^{32}Mg", Eur. Phys. J. A **25**, Suppl. 1, 573–574 (2005).

M. Yamagami: "Impact of self-consistent pairing correlations; spatial structure change of quasiparticles and enhanced low-lying collectivity in neutron drip line nuclei", International Symposium on Correlation Dynamics in Nuclei, Tokyo, 2005–1∼2, Institute of Physics Publishing, London, pp. 213–214 (2005).

C. Wu, Y. Yamaguchi, A. Ozawa, I. Tanihata, J. Dongxing, H. Hui, Z. Tao, L. Zhihuan, and Y. Yanlin: "Neutron removal reactions of ^{17}C", J. Phys. G **31**, 39–47 (2005).

N. D. Dang: "Giant resonances at zero and finite temperatures", J. Phys. G **31**, S1697–S1700 (2005).

N. D. Dang and A. Arima: "Role of thermal pairing in reducing the giant dipole resonance width at low temperature", Key Topics in Nuclear Structure: Proceedings of the 8th International Spring Seminar on Nucelar Physics, (University of Naples), Paestum, Italy, 2004–5, World Scientific, Singapore, pp. 409–416 (2005).

Y. Ishida, M. Wada, and H. Wollnik: "A multi-reflection time-of-flight mass spectrometer for mass measurements of short-lived nuclei", Nucl. Instrum. Methods Phys. Res. B **241**, 983–985 (2005).

J. Pinard, H. T. Duong, D. Marescaux, H. H. Stroke, O. Redi, M. Gustafsson, T. Nilsson, S. Matsuki, Y. Kishimoto, K. Kominato, I. Ogawa, M. Shibata, M. Tada, J. R. Persson, Y. Nojiri, S. Momota, T. Inamura, M. Wakasugi, P. Juncar, T. Murayama, T. Nomura, M. Koizumi, and ISOLDE Collaboration: "Precision hfs of ^{126}Cs ($T_{1/2} = 1.63$ m) by ABMR", Nucl. Phys. A **753**, 3–12 (2005).

R. Kanungo, Z. Elekes, H. Baba, Z. Dombradi, Z. Fulop, J. Gibelin, A. Horvath, Y. Ichikawa, E. Ideguchi, N. Iwasa, H. Iwasaki, S. Kawai, Y. Kondo, T. Motobayashi, M. Notani, T. Ohnishi, A. Ozawa, H. Sakurai, S. Shimoura, E. Takeshita, S. Takeuchi, I. Tanihata, Y. Togano, C. Wu, Y. Yamaguchi, Y. Yanagisawa, A. Yoshida, and K. Yoshida: "Search for an isomeric state in ^{19}C", Nucl. Phys. A **757**, 315–328 (2005).

R. G. Zegers, A. L. Cole, H. Akimune, S. M. Austin, D. Bazin, A. M. van den Berg, G. P. Berg, J. Brown, I. Daito, Y. Fujita, M. Fujiwara, K. Hara, M. N. Harakeh, G. W. Hitt, M. E. Howard, J. Janecke, T. Kawabata, T. Nakamura, H. Ueno, H. Schatz, B. M. Sherrill, and M. Steiner: "Weak interaction strengths for supernovae calculations via the (t, 3He) reaction on medium-heavy nuclei", Nucl. Phys. A **758**, 67c–70c (2005).

T. Yamazaki: "Two-particle wave function in four dimensional Ising model", Nucl. Phys. B (Proc. Suppl.) **140**, 338–340 (2005).

K. Ishida, K. Nagamine, T. Matsuzaki, and N. Kawamura: "Muon catalyzed fusion", Nucl. Phys. B (Proc. Suppl.) **149**, 348–350 (2005).

P. Strasser, K. Nagamine, T. Matsuzaki, K. Ishida, Y. Matsuda, and M. Iwasaki: "Muonic atoms of radioactive nuclei", Nucl. Phys. B (Proc. Suppl.) **149**, 390–392 (2005).

A. Kohama, K. Iida, and K. Oyamatsu: "Global view of nuclei in the black sphere picture", Nucl. Study **49**, No. 6, pp. 27–31 (2005).

T. Matsuzaki, K. Nagamine, K. Ishida, N. Kawamura, H. Imao, Y. Matsuda, M. Iwasaki, S. Nakamura, M. Kato, H. Sugai, M. Tanase, K. Kudo, A. Uritani, H. Harano, and G. H. Eaton: "Particle correlations in t+t reactions studied by muon catalyzed t-t fusion", Nucl. Study **49**, No. 6, pp. 191–196 (2005).

Y. Yanagisawa, S. Kubono, T. Teranishi, K. Ue, S. Michimasa, M. Notani, J. He, Y. Ohshiro, S. Shimoura, S. Watanabe, N. Yamazaki, H. Iwasaki, S. Kato, T. Kishida, T. Morikawa, and Y. Mizoi: "Low-energy radioisotope beam separator CRIB", Nuclear Instruments and Methods in Physics Research A **539**, 74–83 (2005).

R. Kanungo, Z. Elekes, H. Baba, Z. Dombradi, Z. Fulop, J. Gibelin, A. Horvath, Y. Ichikawa, E. Ideguchi, N. Iwasa, H. Iwasaki, S. Kawai, Y. Kondo, T. Motobayashi, M. Notani, T. Ohnishi, A. Ozawa,

H. Sakurai, S. Shimoura, E. Takeshita, S. Takeuchi, I. Tanihata, Y. Togano, C. Wu, Y. Yamaguchi, Y. Yanagisawa, A. Yoshida, and K. Yoshida: "Excited states in neutron rich boron isotopes", Phys. Lett. B **608**, 206–214 (2005).

Y. Akaishi, A. Dote, and T. Yamazaki: "Strange tribaryons as K-mediated dense nuclear systems", Phys. Lett. B **613**, 140–147 (2005).

H. Ueno, D. Kameda, G. Kijima, K. Asahi, A. Yoshimi, H. Miyoshi, K. Shimada, G. Kato, D. Nagae, S. Emori, T. Haseyama, H. Watanabe, and M. Tsukui: "Magnetic moments of $^{30}_{13}Al_{17}$ and $^{32}_{13}Al_{19}$", Phys. Lett. B **615**, 186–192 (2005).

Y. L. Ye, D. Y. Pang, D. X. Jiang, T. Zheng, Q. J. Wang, Z. Li, X. O. Li, Y. C. Ge, C. Wu, G. L. Zhang, Q. Y. Hu, J. Wang, Z. Q. Chen, A. Ozawa, Y. Yamaguchi, R. Kanungo, and I. Tanihata: "Quasielastic scattering of 6He on 9Be at 25 MeV/nucleon", Phys. Rev. C **71**, 014604-1–014604-8 (2005).

N. D. Dang: "Particle-number conservation within self-consistent random-phase approximation", Phys. Rev. C **71**, 024302-1–024302-10 (2005).

M. Takashina, Y. Enyo, and H. Sakuragi: "^{16}C inelastic scattering studied with microscopic coupled-channels method", Phys. Rev. C **71**, 054602-1–054602-7 (2005).

A. Kohama, K. Iida, and K. Oyamatsu: "Reaction cross section described by a black sphere approximation of nuclei", Phys. Rev. C **72**, 024602-1–024602-5 (2005).

M. Yamagami: "Continuum effects for many-body correlations in nuclei close to the neutron drip line", Phys. Rev. C **72**, 064308-1–064308-11 (2005).

T. Inamura: "Laser methods in the study of nuclei, atoms and molecules", Phys. Scr. **71**, C1–C4 (2005).

A. Yoshimi, K. Asahi, S. Emori, M. Uchida, and S. Oshima: "Low-frequency nuclear spin maser and search for atomic EDM of ^{129}Xe", Proceedings of 16th International Spin Physics Symposium (SPIN 2004), (Istituto Nazionale di Fisica Nucleare), Trieste, Italy, 2004–10, World Scientific Publishing, Singapore, pp. 247–250 (2005).

N. D. Dang: "Nuclear giant resonances", Proceedings of 9th Asia Pacific Physics Conference (APPC 2004), (Vietnam Academy of Science and Technology), Hanoi, Vietnam, 2004–10, Institute of material Science, Hanoi, pp. 1–4 (2005).

M. Yamagami: "Novel coordinate space representation for deformed loosely-bound nuclei", Proceedings of YITP Workshop on New Developments in Nuclear Self-Consistent Mean-Field Theories (MF05), Kyoto, 2005–5∼6, Kyoto University, Kyoto, p. 46 (2005).

H. Koura, T. Tachibana, M. Uno, and M. Yamada: "Nuclidic mass formula on a spherical basis with an improved even-odd term", Prog. Theor. Phys. **113**, 305–325 (2005).

M. Yamagami, K. Yoshida, and K. Matsuyanagi: "Comparative Study of Octupole Excitations on Superdeformed States in ^{32}S, ^{36}S, ^{40}Ca and ^{50}S", Prog. Theor. Phys. **113**, 1251–1272 (2005).

H. Haba and D. Kaji: "A new element from Japan!? Discovery of the element 113", Radiochem. News **11**, 45–46 (2005).

3. Atomic and solid-state physics

S. Ohira-Kawamura, M. Tamura, R. Kato, I. Watanabe, and M. Iwasaki: "μSR study on magnetic property of [Pd(dmit)$_2$] salts", J. Phys. IV **114**, 355–356 (2004).

R. Lehnert and I. Shimamura: "Theoretical aspects of antihydrogen studies", J. Plasma Fusion Res. **80**, No. 12, pp. 1006–1011 (2004).

H. Torii, N. Kuroda, H. Higaki, R. Funakoshi, and N. Oshima: "The production, deceleration and cooling of the slow antiproton beam, and the production and control of the positron plasma", J. Plasma Fusion Res. **80**, No. 12, pp. 1012–1021 (2004).

M. Hori, M. Fujiwara, N. Kuroda, and A. Mohri: "Observation of antiproton beams and nonneutral plasmas", J. Plasma Fusion Res. **80**, No. 12, pp. 1022–1026 (2004).

M. Fujiwara: "Production of cold antihydrogen in a nested trap", J. Plasma Fusion Res. **80**, No. 12, pp. 1027–1030 (2004).

Y. Kanai, A. Mohri, and M. Hori: "Next generation traps for confinement of extraction of antihydrogen atoms", J. Plasma Fusion Res. **80**, No. 12, pp. 1031–1034 (2004).

Y. Yamazaki: "Efficient accumulation of antiprotons and positrons, production of slow mono-energetic beams, and their applications", Mater. Sci. Forum **445-446**, 430–434 (2004).

K. Kubo, Y. Kobayashi, Y. Yamada, Y. Nemoto, T. Saito, Y. Sakai, H. Shoji, C. Yonezawa, H. Matsue, and M. Nakada: "Neutron In-beam Mössbauer Spectroscopy with a Parallel Plate Avalanche Counter", AIP Conf. Proc. **765**, 348–351 (2005).

B. Juhasz, D. Barna, J. Eades, R. Hayano, M. Hori, D. Horvath, W. Pirkl, E. Widmann, and Y. Yamazaki: "Measurement of the ground-state hyperfine structure of antihydrogen", AIP Conf. Proc. **796**, 243–246 (2005).

A. Rotondi, M. Amoretti, C. Amsler, G. Bonomi, P. Bowe, C. Canali, C. Carraro, C. Cesar, M. Charlton, M. Doser, A. Fontana, M. Fujiwara, R. Funakoshi, P. Genova, J. Hangst, R. Hayano, L. Jorgensen, A. Kellerbauer, V. Lagomarsino, R. Landua, E. Lodi-Rizzini, M. Macri, N. Madsen, G. Manuzio, P. Montagna, H. Pruys, C. Regenfus, D. Mitchard, G. Testera, A. Variola, L. Venturelli, Y. Yamazaki, D. P. van der Werf, and N. Zurlo: "Results from

ATHENA", AIP Conf. Proc. **796**, 285–290 (2005).
W. Bertsche, A. Boston, P. D. Bowe, C. L. Cesar, S. Chapman, M. Charlton, M. Chartier, A. Deutsch, J. Fajans, M. Fujiwara, R. Funakoshi, D. Gill, K. Gomberoff, D. Grote, J. S. Hangst, R. Hayano, M. Jenkins, L. V. Jorgensen, N. Madsen, D. Miranda, P. Nolan, K. Ochanski, A. Olin, R. D. Page, L. Posada, F. Robicheaux, E. Sarid, H. H. Telle, J. L. Vay, J. Wurtele, D. P. van der Werf, and Y. Yamazaki: "The ALPHA experiment: A cold antihydrogen trap", AIP Conf. Proc. **796**, 301–308 (2005).
N. Kuroda, H. Torii, M. Shibata, Y. Nagata, D. Barna, M. Hori, K. Komaki, and Y. Yamazaki: "Antiproton and electron plasma behavior and its control for production of ultraslow antiproton beams", AIP Conf. Proc. **796**, 321–324 (2005).
H. Torii, N. Kuroda, M. Shibata, Y. Nagata, D. Barna, M. Hori, A. Mohri, K. Komaki, and Y. Yamazaki: "Extraction of ultra-slow antiproton beams and their physics application", AIP Conf. Proc. **796**, 413–416 (2005).
T. Kurahashi, Y. Kobayashi, S. Nagatomo, T. Tosha, T. Kitagawa, and H. Fujii: "Oxidizing intermediates from the sterically hindered iron salen complexes related to the oxygen activation by nonheme iron enzymes", Inorg. Chem. **44**, No. 22, pp. 8156–8166 (2005).
Y. Yamazaki: "Physics and Applications of Slow Highly Charged Ions: A Brief Overview", J. Vac. Soc. Jpn. **48**, No. 8, pp. 461–465 (2005).
Y. Iwai and Y. Kanai: "Slow highly charged ions and solid surfaces", J. Vac. Soc. Jpn. **48**, No. 8, pp. 478–482 (2005).
C. Kondo, Y. Takabayashi, T. Muranaka, S. Masugi, T. Azuma, K. Komaki, A. Hatakeyama, Y. Yamazaki, E. Takada, and T. Murakami: "X-ray yields from high-energy heavy ions channeled through a crystal: their crystal thickness and projectile dependences", Nucl. Instrum. Methods Phys. Res. B **230**, 85–89 (2005).
Y. Nakai, T. Ikeda, Y. Kanai, T. Kambara, N. Fukunishi, K. Komaki, C. Kondo, T. Azuma, and Y. Yamazaki: "Resonant coherent excitation of 2s electron of Li-like Fe ions to the $n = 3$ states", Nucl. Instrum. Methods Phys. Res. B **230**, 90–95 (2005).
N. Okabayashi, K. Komaki, and Y. Yamazaki: "Potential sputtering and kinetic sputtering from a water adsorbed Si(100) surface with slow highly charged ions", Nucl. Instrum. Methods Phys. Res. B **232**, 244–248 (2005).
N. Nakamura, M. Terada, Y. Nakai, Y. Kanai, S. Ohtani, K. Komaki, and Y. Yamazaki: "SPM observation of nano-dots induced by slow highly charged ions", Nucl. Instrum. Methods Phys. Res. B **232**, 261–265 (2005).
Y. Kanai, Y. Nakai, Y. Iwai, T. Ikeda, M. Hoshino, K. Nishio, H. Masuda, and Y. Yamazaki: "X-ray measurements of highly charged Ar ions passing through a Ni microcapillary: coincidence of L X-rays and final charge states", Nucl. Instrum. Methods Phys. Res. B **233**, 103–110 (2005).
H. Shimada, Y. Nakai, H. Oyama, K. Ando, T. Kambara, A. Hatakeyama, and Y. Yamazaki: "Recoil-ion momentum spectroscopy of multiply charged argon ions produced by intense ($\sim 10^{16}$ W cm^{-2}) laser light", Nucl. Instrum. Methods Phys. Res. B **235**, 221–225 (2005).
M. Hoshino, T. Kambara, R. H. Schuch, and Y. Yamazaki: "Multi-electron processes in large-angle scattering between slow Ne^{q+} (q = 1, 2 and 3) and Ar", Nucl. Instrum. Methods Phys. Res. B **235**, 347–351 (2005).
N. Okabayashi, K. Komaki, and Y. Yamazaki: "Energy- and angular-distributions of F^+ ions emitted from a F-terminated Si(100) surface with slow highly charged ions", Nucl. Instrum. Methods Phys. Res. B **235**, 438–442 (2005).
M. Terada, N. Nakamura, Y. Nakai, Y. Kanai, S. Ohtani, K. Komaki, and Y. Yamazaki: "Observation of an HCI-induced nano-dot on an HOPG surface with STM and AFM", Nucl. Instrum. Methods Phys. Res. B **235**, 452–455 (2005).
Y. Iwai, Y. Kanai, Y. Nakai, T. Ikeda, M. Hoshino, H. Oyama, K. Ando, H. Masuda, K. Nishio, H. Torii, K. Komaki, and Y. Yamazaki: "X-rays emitted from N ions transmitted through a thin Ni microcapillary target", Nucl. Instrum. Methods Phys. Res. B **235**, 468–472 (2005).
N. Oshima, M. Niigaki, M. Lebois, A. Mohri, K. Komaki, and Y. Yamazaki: "Simultaneous cooling of highly charged ions with electrons and positrons", Nucl. Instrum. Methods Phys. Res. B **235**, 504–508 (2005).
N. Kuroda, H. A. Torii, K. Yoshiki-Franzen, Z. Wang, S. Yoneda, M. Inoue, M. Hori, B. Juhász, D. Horváth, H. Higaki, A. Mohri, J. Eades, K. Komaki, and Y. Yamazaki: "Confinement of a large number of antiprotons and production of an ultraslow antiproton beam", Phys. Rev. Lett. **94**, 023401-1–023401-4 (2005).
N. Madsen, M. Amoretti, C. Amsler, G. Bonomi, P. Bowe, C. Carraro, C. Cesar, M. Charlton, M. Doser, A. Fontana, M. Fujiwara, R. Funakoshi, P. Genova, J. Hangst, R. Hayano, L. Jorgensen, A. Kellerbauer, V. Lagomarsino, R. Landua, E. Lodi-Rizzini, M. Macri, D. Mitchard, P. Montagna, H. Pruys, C. Regenfus, A. Rotondi, G. Testera, A. Variola, L. Venturelli, D. P. van der Werf, Y. Yamazaki, and N. Zurlo: "Spatial distribution of cold antihydrogen formation", Phys. Rev. Lett. **94**, 033403-1–033403-4 (2005).
L. Jorgensen, M. Amoretti, G. Bonomi, P. Bowe, C. Canali, C. Carraro, C. Cesar, M. Charlton, M. Doser, A. Fontana, M. Fujiwara, R. Funakoshi, P.

Genova, J. Hangst, R. Hayano, A. Kellerbauer, V. Lagomarsino, R. Landua, E. Rizzini, M. Macri, N. Madsen, D. Mitchard, P. Montagna, A. Rotondi, G. Testera, A. Variola, L. Venturelli, D. P. van der Werf, and Y. Yamazaki: "New source of dense, cryogenic positron plasmas", Phys. Rev. Lett. **95**, 025002-1–025002-5 (2005).

A. Mohri, Y. Kanai, Y. Nakai, and Y. Yamazaki: "Non-neutral plasma confinement in a cusp-trap and possible application to anti-hydrogen beam generation", Physics with Ultra Slow Antiproton Beams, Wako, 2005–3, American Institute of Physics, New York, pp. 147–158 (2005).

K. Nagamine: "Muonic anti-hydrogen: formation and test of CPT theorem", Physics with Ultra Slow Antiproton Beams, Wako, 2005–3, American Institute of Physics, New York, pp. 159–164 (2005).

M. Wada and Y. Yamazaki: "Antiprotonic Radioactive atom for nuclear structure studies", Physics with Ultra Slow Antiproton Beams, Wako, 2005–3, American Institute of Physics, New York, pp. 223–241 (2005).

H. Torii, N. Kuroda, M. Shibata, Y. Nagata, D. Barna, M. Hori, J. Eades, A. Mohri, K. Komaki, and Y. Yamazaki: "Production of ultra-slow antiproton beams", Physics with Ultra Slow Antiproton Beams, Wako, 2005–3, American Institute of Physics, New York, pp. 293–306 (2005).

N. Kuroda, H. Torii, M. Shibata, Y. Nagata, D. Barna, D. Horvath, M. Hori, J. Eades, A. Mohri, K. Komaki, and Y. Yamazaki: "Control of plasmas for production of ultraslow antiprotons beams", Physics with Ultra Slow Antiproton Beams, Wako, 2005–3, American Institute of Physics, New York, pp. 307–317 (2005).

V. Varentsov, N. Kuroda, Y. Nagata, H. Torii, M. Shibata, and Y. Yamazaki: "ASACUSA Gas-Jet Target: Present status and future development", Physics with Ultra Slow Antiproton Beams, Wako, 2005–3, American Institute of Physics, New York, pp. 328–340 (2005).

4. Radiochemistry, radiation chemistry, and radiation biology

F. Yatagai: "Mutation Induced by Heavy Charged Particles", Biol. Sci. Space **18**, No. 4, pp. 224–234 (2004).

A. Toyoshima, H. Haba, K. Tsukada, M. Asai, K. Akiyama, I. Nishinaka, Y. Nagame, D. Saika, K. Matsuo, W. Sato, A. Shinohara, H. Ishizu, M. Ito, J. Saito, S. Goto, H. Kudo, H. Kikunaga, N. Kinoshita, C. Kato, A. Yokoyama, and K. Sueki: "Elution curve of rutherfordium (Rf) in anion-exchange chromatography with hydrofluoric acid solution", J. Nucl. Radiochem. Sci. **5**, 45–48 (2004).

T. Shinonaga and S. Ambe: "Translocation of radionuclides of Co, Zn, Se, Rb, Y, Tc, and Re into organs of tomato plant via roots", Biol. Trace Elem. Res. **104**, 71–82 (2005).

H. Haba: "Atom-at-a-time chemistry of the super heavy elements: Anion-exchange chromatography of element 104, rutherfordium", Kagaku to Kogyo **58**, 105–108 (2005).

T. Abe and S. Yoshida: "Mutation breeding (Heavy ion beam)", Nogyo Gijutsu Taikei Addendum, Rural Culture Association, Tokyo, pp. 124-2–124-11 (2005).

T. Abe: "Ion-beam irradiation on mutation breeding for ornamental plants", Proceedings of the 5th Technical Seminar on Accelerator Application, (Radiation Application Development Association), Kagoshima, 2005–10, Radiation Application Development Association, Kagoshima, pp. 53–57 (2005).

5. Material Analysis

N. Inada, K. Maeda, and J. Kawai: "Strong X-ray emission from electrified insulators", Anal. Sci. **21**, 877–880 (2005).

K. Maeda, K. Hasegawa, M. Maeda, K. Ogiwara, and H. Hamanaka: "Rapid chemical state analysis in air by highly sensitive high-resolution PIXE using a v. Hamos crystal spectrometer", X-Ray Spectrometry **34**, 389–392 (2005).

6. RIKEN-BNL Collaboration

S. George and W. Vogelsang: "Threshold resummation and rapidity dependence", J. High-Energy Phys., pp. 02(2001)016-1–02(2001)016-24 (2001).

N. Ishii, H. Suganuma, and H. Matsufuru: "The thermal width of the glueball at non-zero temperature", Nucl. Phys. B (Proc. Suppl.) **119**, 484–486 (2003).

N. Ishii, H. Suganuma, and H. Matsufuru: "The thermal glueball in SU(3) anisotropic lattice QCD", Quark Confinement and the Hadron Spectrum V, (National Institute for Nuclear Physics and Milano University), Gargnano, Italy, 2002–9, World Scientific, Singapore, pp. 387–389 (2003).

T. Izubuchi: "B_K from two-flavor dynamical domain wall fermions", Nucl. Phys. B (Proc. Suppl.) **129/130**, 266–268 (2004).

T. Doi, Y. Kondo, and M. Oka: "Meson-baryon couplings from QCD sum rules", Phys. Rep. **398**, 253–279 (2004).

S. S. Adler, Y. Akiba, A. V. Bazilevsky, G. M. Bunce, A. Deshpande, H. En'yo, D. E. Fields, B. Fox, Y. Goto, M. Grosse Perdekamp, T. Ichihara, K. Imai, M. Ishihara, O. Jinnouchi, N. Kamihara, H. Kobayashi, K. Kurita, Y. Mao, J. Murata, H. Ohnishi, K. Okada, N. Saito, H. Sato, T. Shibata, A. Taketani, K. Tanida, J. Tojo, H. Torii, Y. Watanabe, S. Yokkaichi, and PHENIX Collaboration: "J/ψ production in Au-Au collisions at

$\sqrt{s_{NN}}$ = 200 GeV", Phys. Rev. C **69**, 014901-1–014901-10 (2004).

K. Adcox, A. Bazilevsky, G. M. Bunce, A. Deshpande, H. En'yo, Y. Goto, M. Grosse Perdekamp, N. Hayashi, T. Ichihara, K. Imai, M. Ishihara, B. Jacak, K. Kurita, Z. Li, Y. Mao, J. Murata, N. Saito, T. Sakuma, H. Sato, T. Shibata, M. Sugioka, A. Taketani, E. Taniguchi, J. Tojo, H. Torii, Y. Watanabe, S. Yokkaichi, and PHENIX Collaboration: "Single identified hadron spectra from $\sqrt{s_{NN}}$ = 130 GeV Au+Au collisions", Phys. Rev. C **69**, 024904-1–024904-29 (2004).

S. S. Adler, Y. Akiba, A. V. Bazilevsky, G. M. Bunce, A. Deshpande, H. En'yo, D. E. Fields, B. Fox, Y. Goto, M. Grosse Perdekamp, T. Ichihara, K. Imai, M. Ishihara, O. Jinnouchi, N. Kamihara, H. Kobayashi, K. Kurita, Y. Mao, J. Murata, H. Ohnishi, K. Okada, N. Saito, H. Sato, T. Shibata, A. Taketani, K. Tanida, J. Tojo, H. Torii, Y. Watanabe, S. Yokkaichi, and PHENIX Collaboration: "Identified charged particle spectra and yields in Au+Au collisions at $\sqrt{s_{NN}}$ = 200 GeV", Phys. Rev. C **69**, 034909-1–034909-32 (2004).

S. S. Adler, Y. Akiba, A. V. Bazilevsky, G. M. Bunce, A. Deshpande, H. En'yo, D. E. Fields, B. Fox, Y. Goto, M. Grosse Perdekamp, T. Ichihara, K. Imai, M. Ishihara, O. Jinnouchi, N. Kamihara, H. Kobayashi, K. Kurita, Y. Mao, J. Murata, H. Ohnishi, K. Okada, N. Saito, H. Sato, T. Shibata, A. Taketani, K. Tanida, J. Tojo, H. Torii, Y. Watanabe, S. Yokkaichi, and PHENIX Collaboration: "High-p_T charged hadron suppression in Au+Au collisions at $\sqrt{s_{NN}}$ = 200 GeV", Phys. Rev. C **69**, 034910-1–034910-20 (2004).

Y. Hatta and K. Fukushima: "Linking the chiral and deconfinement phase transitions", Phys. Rev. D **69**, 097502-1–097502-4 (2004).

T. Doi, N. Ishii, M. Oka, and H. Suganuma: "Thermal effects on quark-gluon mixed condensate $g\langle\bar{q}\sigma_{\mu\nu}G_{\mu\nu}q\rangle$ from lattice QCD", Phys. Rev. D **70**, 034510-1–034510-5 (2004).

S. Prelovsek, C. Dawson, T. Izubuchi, K. N. Orginos, and A. Soni: "Scalar meson in dynamical and partially quenched two-flavor QCD: lattice results and chiral loops", Phys. Rev. D **70**, 094503-1–094503-13 (2004).

S. S. Adler, Y. Akiba, A. V. Bazilevsky, G. M. Bunce, A. Deshpande, H. En'yo, D. E. Fields, B. Fox, Y. Goto, M. Grosse Perdekamp, T. Ichihara, K. Imai, M. Ishihara, O. Jinnouchi, N. Kamihara, H. Kobayashi, K. Kurita, Y. Mao, J. Murata, H. Ohnishi, K. Okada, N. Saito, H. Sato, T. Shibata, A. Taketani, K. Tanida, J. Tojo, H. Torii, Y. Watanabe, S. Yokkaichi, and PHENIX Collaboration: "J/ψ Production from Proton-Proton Collisions at $\sqrt{s}$ = 200 GeV", Phys. Rev. Lett. **92**, No. 5, pp. 051802-1–051802-6 (2004).

S. S. Adler, Y. Akiba, A. V. Bazilevsky, G. M. Bunce, A. Deshpande, H. En'yo, D. E. Fields, B. Fox, Y. Goto, M. Grosse Perdekamp, T. Ichihara, K. Imai, M. Ishihara, O. Jinnouchi, N. Kamihara, H. Kobayashi, K. Kurita, Y. Mao, J. Murata, H. Ohnishi, K. Okada, N. Saito, H. Sato, T. Shibata, A. Taketani, K. Tanida, J. Tojo, H. Torii, Y. Watanabe, S. Yokkaichi, and PHENIX Collaboration: "Bose-Einstein Correlations of Charged Pion Pairs in Au+Au Collisions at $\sqrt{s_{NN}}$ = 200 GeV", Phys. Rev. Lett. **93**, No. 15, pp. 152302-1–152302-6 (2004).

S. S. Adler, Y. Akiba, A. V. Bazilevsky, G. M. Bunce, A. Deshpande, H. En'yo, D. E. Fields, B. Fox, Y. Fukao, Y. Goto, M. Grosse Perdekamp, K. Hasuko, J. M. Heuser, T. Horaguchi, T. Ichihara, K. Imai, M. Ishihara, O. Jinnouchi, N. Kamihara, M. Kaneta, A. Kiyomichi, H. Kobayashi, K. Kurita, Y. Mao, H. Ohnishi, H. Okada, K. Okada, V. L. Rykov, N. Saito, H. Sato, T. Shibata, A. Taketani, K. Tanida, M. Togawa, J. Tojo, H. Torii, Y. Watanabe, S. Yokkaichi, and PHENIX Collaboration: "Double Helicity Asymmetry in Inclusive Mid-Rapidity π^0 Production for Polarized $p+p$ Collisions at $\sqrt{s}$ = 200 GeV", Phys. Rev. Lett. **93**, No. 20, pp. 202002-1–202002-6 (2004).

S. S. Adler, Y. Akiba, A. V. Bazilevsky, G. M. Bunce, A. Deshpande, H. En'yo, D. E. Fields, B. Fox, Y. Goto, M. Grosse Perdekamp, T. Ichihara, K. Imai, M. Ishihara, O. Jinnouchi, N. Kamihara, H. Kobayashi, K. Kurita, Y. Mao, J. Murata, H. Ohnishi, K. Okada, N. Saito, H. Sato, T. Shibata, A. Taketani, K. Tanida, J. Tojo, H. Torii, Y. Watanabe, S. Yokkaichi, and PHENIX Collaboration: "Measurement of Nonrandom Event-by-Event Fluctuations of Average Transverse Momentum in $\sqrt{s_{NN}}$ = 200 GeV Au+Au and $p+p$ Collisions", Phys. Rev. Lett. **93**, No. 9, pp. 092301-1–092301-6 (2004).

T. Izubuchi: "The electromagnetic splitting and ${g_\mu}^{-2}$ light-by-light contribution", Proceedings of RIKEN BNL Research Center Workshop **68**, 99–104 (2004).

T. Nishikawa, A. Iwazaki, O. Morimatsu, and M. Ohtani: "Coexistence of color ferromagnetic state and color superconducting state", Soryushiron Kenkyu **109**, No. 6, p. 82 (2004).

M. Oka, J. Sugiyama, and T. Doi: "Pentaquark baryons in the QCD sum rule", Nucl. Phys. A **755**, 391c–394c (2005).

N. Ishii, T. Doi, H. Iida, M. Oka, F. Okiharu, and H. Suganuma: "Penta-quark in anisotropic lattice QCD", Nucl. Phys. A **755**, 467–470 (2005).

M. Ohtani and K. Ohta: "Spin polarized Skyrmions in the $U_{EM}(1)$ gauged Wess-Zumino action", Nucl. Phys. A **755**, 661–664 (2005).

K. Adcox, Y. Akiba, K. Aoki, A. Bazilevsky, G. M. Bunce, A. Deshpande, H. En'yo, D. E. Fields, B. Fox, Y. Fukao, Y. Goto, M. Grosse Perdekamp,

T. Hachiya, K. Hasuko, N. Hayashi, J. Heuser, T. Horaguchi, T. Ichihara, K. Imai, M. Ishihara, B. Jacak, O. Jinnouchi, F. Kajihara, N. Kamihara, M. Kaneta, A. Kiyomichi, H. Kobayashi, K. Kurita, Z. Li, Y. Mao, J. Murata, H. Onishi, H. Okada, K. Okada, V. Rykov, N. Saito, T. Sakuma, H. Sato, T. Shibata, K. Shoji, M. Sugioka, T. Tabaru, A. Taketani, K. Tanida, E. Taniguchi, M. Togawa, J. Tojo, H. Torii, Y. Tsuchimoto, Y. Watanabe, W. Xie, S. Yokkaichi, and PHENIX Collaboration: "Formation of dense partonic matter in relativistic nucleus-nucleus collisions at RHIC: Experimental evaluation by the PHENIX Collaboration", Nucl. Phys. A **757**, 184–283 (2005).

T. Izubuchi: "Hadron spectrum and decay constant from $N_F = 2$ domain wall QCD", Nucl. Phys. B (Proc. Suppl.) **140**, 237–239 (2005).

N. Ishii, T. Doi, H. Iida, M. Oka, F. Okiharu, and H. Suganuma: "Penta-quark anti-decuplet in anisotropic lattice QCD", Nucl. Phys. B (Proc. Suppl.) **140**, 269–271 (2005).

K. Hashimoto and T. Izubuchi: "Static $\bar{Q}$-Q potential from $N_f = 2$ dynamical domain-wall QCD", Nucl. Phys. B (Proc. Suppl.) **140**, 341–343 (2005).

T. Doi, N. Ishii, M. Oka, and H. Suganuma: "The lattice QCD simulation of the quark-gluon mixed condensate $g\langle\bar{q}\sigma_{\mu\nu}G_{\mu\nu}q\rangle$ at finite temperature and the phase transition of QCD", Nucl. Phys. B (Proc. Suppl.) **140**, 559–561 (2005).

N. Ishii, T. Doi, H. Iida, M. Oka, F. Okiharu, and H. Suganuma: "Anisotropic lattice QCD studies of penta-quark anti-decuplet", PENTAQUARK04: Proceedings of the International Workshop, (RCNP and JASRI), Harima, 2004–7, World Scientific, Singapore, pp. 316–323 (2005).

J. Sugiyama, T. Doi, and M. Oka: "Pentaquark baryon from the QCD sum rule with the ideal mixing", PENTAQUARK04: Proceedings of the International Workshop, (RCNP and JASRI), Harima, 2004–7, World Scientific, Singapore, pp. 354–357 (2005).

S. S. Adler, Y. Akiba, A. Bazilevsky, G. M. Bunce, A. Deshpande, H. En'yo, D. E. Fields, B. Fox, Y. Goto, M. Grosse Perdekamp, T. Ichihara, K. Imai, M. Ishihara, O. Jinnouchi, N. Kamihara, H. Kobayashi, K. Kurita, Y. Mao, J. Murata, H. Onishi, K. Okada, N. Saito, H. Sato, T. Shibata, A. Taketani, K. Tanida, J. Tojo, H. Torii, Y. Watanabe, S. Yokkaichi, and PHENIX Collaboration: "Systematic studies of the centrality and $\sqrt{s_{NN}}$ dependence of the $dE_T/d\eta$ and $dN_{ch}/d\eta$ in heavy ion collisions at midrapidity", Phys. Rev. C **71**, 034908-1–034908-25 (2005).

S. S. Adler, Y. Akiba, A. Bazilevsky, G. M. Bunce, A. Deshpande, H. En'yo, D. E. Fields, B. Fox, Y. Fukao, Y. Goto, M. Grosse Perdekamp, K. Hasuko, N. Hayashi, J. Heuser, T. Horaguchi, T. Ichihara, K. Imai, M. Ishihara, O. Jinnouchi, N. Kamihara, M. Kaneta, A. Kiyomichi, H. Kobayashi, K. Kurita, Y. Mao, J. Murata, H. Onishi, H. Okada, K. Okada, V. Rykov, N. Saito, H. Sato, T. Shibata, A. Taketani, J. Tojo, H. Torii, Y. Watanabe, S. Yokkaichi, and PHENIX Collaboration: "Jet structure of baryon excess in Au+Au collisions at $\sqrt{s_{NN}} = 200\,\mathrm{GeV}$", Phys. Rev. C **71**, 051902-1–051902-6 (2005).

S. S. Adler, Y. Akiba, A. Bazilevsky, G. M. Bunce, A. Deshpande, H. En'yo, D. E. Fields, B. Fox, Y. Goto, M. Grosse Perdekamp, N. Hayashi, T. Ichihara, K. Imai, M. Ishihara, O. Jinnouchi, N. Kamihara, H. Kobayashi, K. Kurita, Y. Mao, J. Murata, H. Onishi, K. Okada, N. Saito, H. Sato, T. Shibata, A. Taketani, K. Tanida, J. Tojo, H. Torii, Y. Watanabe, S. Yokkaichi, and PHENIX Collaboration: "Production of ϕ mesons at midrapidity in $\sqrt{s_{NN}} = 200\,\mathrm{GeV}$ Au+Au collisions at relativistic energies", Phys. Rev. C **72**, 014903-1–014903-23 (2005).

S. S. Adler, Y. Akiba, A. Bazilevsky, G. M. Bunce, A. Deshpande, H. En'yo, D. E. Fields, B. Fox, Y. Goto, M. Grosse Perdekamp, N. Hayashi, T. Ichihara, K. Imai, M. Ishihara, O. Jinnouchi, N. Kamihara, H. Kobayashi, K. Kurita, Y. Mao, J. Murata, H. Onishi, K. Okada, N. Saito, H. Sato, T. Shibata, A. Taketani, K. Tanida, J. Tojo, H. Torii, Y. Watanabe, S. Yokkaichi, and PHENIX Collaboration: "Measurement of single electron event anisotropy in Au+Au collisions at $\sqrt{s_{NN}} = 200\,\mathrm{GeV}$", Phys. Rev. C **72**, 024901-1–024901-10 (2005).

N. Ishii, T. Doi, H. Iida, M. Oka, F. Okiharu, and H. Suganuma: "Pentaquark baryon in anisotropic lattice QCD", Phys. Rev. D **71**, 034001-1–034001-11 (2005).

A. Iwazaki, O. Morimatsu, T. Nishikawa, and M. Ohtani: "Quantum Hall states of gluons in dense quark matter", Phys. Rev. D **71**, 034014-1–034014-12 (2005).

K. Iida, T. Matsuura, M. Tachibana, and T. Hatsuda: "Thermal phase transitions and gapless quark spectra in quark matter at high density", Phys. Rev. D **71**, 054003-1–054003-15 (2005).

K. Iida: "Magnetic vortex in color-flavor locked quark matter", Phys. Rev. D **71**, 054011-1–054011-7 (2005).

S. S. Adler, Y. Akiba, A. Bazilevsky, G. M. Bunce, A. Deshpande, H. En'yo, D. E. Fields, B. Fox, Y. Goto, M. Grosse Perdekamp, N. Hayashi, T. Ichihara, K. Imai, M. Ishihara, O. Jinnouchi, N. Kamihara, H. Kobayashi, K. Kurita, Y. Mao, J. Murata, H. Onishi, K. Okada, N. Saito, H. Sato, T. Shibata, A. Taketani, K. Tanida, J. Tojo, H. Torii, Y. Watanabe, S. Yokkaichi, and PHENIX Collaboration: "Midrapidity direct-photon production in $p+p$ collisions at $\sqrt{s} = 200\,\mathrm{GeV}$", Phys. Rev. D **71**, 071102-1–071102-7 (2005).

K. Fukushima and K. Iida: "Collective excitations in a superfluid of color-flavor locked quark matter", Phys. Rev. D **71**, 074011-1–074011-16 (2005).

K. Iida: "Feedback effects on the pairing interaction in color superconductors near the transition temperature", Phys. Rev. D **72**, 054025-1–054025-7 (2005).

N. Ishii, T. Doi, Y. Nemoto, M. Oka, and H. Suganuma: "Spin 3/2 Penta-quarks in anisotropic lattice QCD", Phys. Rev. D **72**, 074503-1–074503-15 (2005).

S. S. Adler, Y. Akiba, A. Bazilevsky, G. M. Bunce, A. Deshpande, H. En'yo, D. E. Fields, B. Fox, Y. Goto, M. Grosse Perdekamp, N. Hayashi, T. Ichihara, K. Imai, M. Ishihara, O. Jinnouchi, N. Kamihara, H. Kobayashi, K. Kurita, Y. Mao, J. Murata, H. Onishi, K. Okada, N. Saito, H. Sato, T. Shibata, A. Taketani, K. Tanida, J. Tojo, H. Torii, Y. Watanabe, S. Yokkaichi, and PHENIX Collaboration: "Centrality dependence of charm production from a measurement of single electrons in Au+Au collisions at $\sqrt{s_{NN}} = 200\,\mathrm{GeV}$", Phys. Rev. Lett. **94**, 082301-1–082301-6 (2005).

S. S. Adler, Y. Akiba, A. Bazilevsky, G. M. Bunce, A. Deshpande, H. En'yo, D. E. Fields, B. Fox, Y. Fukao, Y. Goto, M. Grosse Perdekamp, K. Hasuko, J. Heuser, T. Horaguchi, T. Ichihara, K. Imai, M. Ishihara, O. Jinnouchi, N. Kamihara, M. Kaneta, A. Kiyomichi, H. Kobayashi, K. Kurita, Y. Mao, H. Onishi, H. Okada, K. Okada, V. Rykov, N. Saito, H. Sato, T. Shibata, A. Taketani, K. Tanida, M. Togawa, J. Tojo, H. Torii, Y. Watanabe, S. Yokkaichi, and PHENIX Collaboration: "Nuclear modification factors for hadrons at forward and backward rapidities in deuteron-gold collisions at $\sqrt{s_{NN}} = 200\,\mathrm{GeV}$", Phys. Rev. Lett. **94**, 082302-1–082302-6 (2005).

S. S. Adler, Y. Akiba, A. Bazilevsky, G. M. Bunce, A. Deshpande, H. En'yo, D. E. Fields, B. Fox, Y. Goto, M. Grosse Perdekamp, N. Hayashi, T. Ichihara, K. Imai, M. Ishihara, O. Jinnouchi, N. Kamihara, H. Kobayashi, K. Kurita, Y. Mao, J. Murata, H. Onishi, K. Okada, N. Saito, H. Sato, T. Shibata, A. Taketani, K. Tanida, J. Tojo, H. Torii, Y. Watanabe, S. Yokkaichi, and PHENIX Collaboration: "Deuteron and antideuteron production in Au+Au collisions at $\sqrt{s_{NN}} = 200\,\mathrm{GeV}$", Phys. Rev. Lett. **94**, 122302-1–122302-6 (2005).

S. S. Adler, Y. Akiba, A. Bazilevsky, G. M. Bunce, A. Deshpande, H. En'yo, D. E. Fields, B. Fox, Y. Goto, M. Grosse Perdekamp, N. Hayashi, T. Ichihara, K. Imai, M. Ishihara, O. Jinnouchi, N. Kamihara, H. Kobayashi, K. Kurita, Y. Mao, J. Murata, H. Onishi, K. Okada, N. Saito, H. Sato, T. Shibata, A. Taketani, K. Tanida, J. Tojo, H. Torii, Y. Watanabe, S. Yokkaichi, and PHENIX Collaboration: "Centrality dependence of direct photon production in $\sqrt{s_{NN}} = 200\,\mathrm{GeV}$ Au+Au collisions", Phys. Rev. Lett. **94**, 232301-1–232301-6 (2005).

S. S. Adler, Y. Akiba, K. Aoki, A. Bazilevsky, G. M. Bunce, A. Deshpande, H. En'yo, D. E. Fields, B. Fox, Y. Fukao, Y. Goto, M. Grosse Perdekamp, T. Hachiya, K. Hasuko, N. Hayashi, J. Heuser, T. Horaguchi, T. Ichihara, K. Imai, M. Ishihara, O. Jinnouchi, S. Kametani, N. Kamihara, M. Kaneta, A. Kiyomichi, H. Kobayashi, K. Kurita, Y. Mao, J. Murata, H. Onishi, K. Okada, V. Rykov, N. Saito, H. Sato, T. Shibata, K. Shoji, T. Tabaru, A. Taketani, K. Tanida, J. Tojo, H. Torii, Y. Tsuchimoto, Y. Watanabe, W. Xie, S. Yokkaichi, and PHENIX Collaboration: "Saturation of azimuthal anisotropy in Au+Au collisions at $\sqrt{s_{NN}} = 62\text{-}200\,\mathrm{GeV}$", Phys. Rev. Lett. **94**, 232302-1–232302-6 (2005).

S. S. Adler, Y. Akiba, A. Bazilevsky, G. M. Bunce, A. Deshpande, H. En'yo, D. E. Fields, B. Fox, Y. Goto, M. Grosse Perdekamp, N. Hayashi, T. Ichihara, K. Imai, M. Ishihara, O. Jinnouchi, N. Kamihara, H. Kobayashi, K. Kurita, Y. Mao, J. Murata, H. Onishi, K. Okada, N. Saito, H. Sato, T. Shibata, A. Taketani, K. Tanida, J. Tojo, H. Torii, Y. Watanabe, S. Yokkaichi, and PHENIX Collaboration: "Measurement of transverse single-spin asymmetries for midrapidity production of neutral pions and charged hadrons in polarized $p + p$ collisions at $\sqrt{s} = 200\,\mathrm{GeV}$", Phys. Rev. Lett. **95**, 202001-1–202001-6 (2005).

T. Doi, N. Ishii, Y. Nemoto, M. Oka, and H. Suganuma: "Anisotropic lattice QCD study of pentaquark baryons in spin 3/2 channel", Proceedings of Science (LAT2005), 064-1–064-6 (2005).

H. Iida, T. Doi, N. Ishii, and H. Suganuma: "J/Ψ at high temperatures in anisotropic lattice QCD", Proceedings of Science (LAT2005), 184-1–184-6 (2005).

M. Ohtani and K. Ohta: "Spin polarized Skyrmions in the $\mathrm{U_{EM}}(1)$ gauged Wess-Zumino term", Soryushiron Kenkyu **111**, No. 3, p. 18 (2005).

VII. LIST OF PREPRINTS

2005

RIKEN-AF-NP

462 Y. Akaishi, A. Doté, and T. Yamazaki: "Strange tribaryons as $\bar{\mathrm{K}}$-mediated dense nuclear systems"

463 Y. Hashimoto and T. Horibata: "Tilted axis rotation in hartree-fock framework"

464 M. Takashina, Y. Kanada-En'yo, and Y. Sakuragi: "^{16}C inelastic scattering studied with microscopic coupled-channels method"

465 M. Yamagami: "Spatially extended coherence induced by pairing correlation in low-frequency vibrational excitations of neutron drip line nuclei"

466 T. Yamazaki: "Overview: deeply bound nuclear states of pions and kaons"

467 Y. Akaishi: "Kaonic helium atoms in relation to kaonic nuclear bound states"

468 P. Kienle, Y. Akaishi, and T. Yamazaki: "Momentum correlation in the three-body decay of high-density $\bar{\mathrm{K}}$ nuclear clusters: $N\ N\ N\ \bar{K} \rightarrow N + N + \Lambda$"

469 S. Michimasa, S. Shimoura, H. Iwasaki, M. Tamaki, S. Ota, N. Aoi, H. Baba, N. Iwasa, S. Kanno, S. Kubono, K. Kurita, M. Kurokawa, T. Minemura, T. Motobayashi, M. Notani, H. J. Ong, A. Saito, H. Sakurai, E. Takeshita, S. Takeuchi, Y. Yanagisawa, and A. Yoshida: "Proton single-particle states in the neutron-rich ^{23}F nucleus"

470 T. Matsumoto, T. Egami, K. Ogata. Y. Iseri, M. Kamimura, amd M. Yahiro: "Coulomb breakup effects on the elastic cross section of $^{6}\mathrm{He} + ^{209}\mathrm{Bi}$ scattering near coulomb barrier energies"

RIKEN-AF-AC

Not applicable

VIII. PAPERS PRESENTED AT MEETINGS

1. Accelerator development and accelerator physics

M. Kidera, T. Nakagawa, S. Enomoto, K. Takahashi, K. Igarashi, M. Fujimaki, E. Ikezawa, O. Kamigaito, M. Kase, and Y. Yano: "Novel technique for trace element analysis using ECRIS and heavy ion linear accelerator", 16th International Conference on ECR Ion Sources (ECRIS 04), Berkeley, USA, Sept. (2004).

N. Fukunishi, A. Goto, O. Kamigaito, M. Kase, H. Okuno, N. Sakamoto, R. Taki, M. Wakasugi, Y. Yano, and H. Okamura: "Beam quality studies on RIKEN Ring Cyclotrons and RI Beam Factory project", 17th International Conference on Cyclotrons and Their Applications (Cyclotrons 2004), Tokyo, Oct. (2004).

H. Ryuto, N. Fukunishi, A. Goto, H. Hasebe, N. Inabe, M. Kase, Y. Yano, and S. Yokouchi: "Charge stripping plan of the RIKEN RI-Beam Factory", 17th International Conference on Cyclotrons and Their Applications (Cyclotrons 2004), Tokyo, Oct. (2004).

M. Kase, T. Fujinawa, E. Ikezawa, K. Yamaguchi, and Y. Yano: "Co-generation system for the RIBF accelerators", 17th International Conference on Cyclotrons and Their Applications (Cyclotrons 2004), Tokyo, Oct. (2004).

N. Sakamoto, A. Goto, O. Kamigaito, M. Kase, and Y. Yano: "Construction of the RF-resonator for the RIKEN Superconducting Ring Cyclotrons(SRC)", 17th International Conference on Cyclotrons and Their Applications (Cyclotrons 2004), Tokyo, Oct. (2004).

J. Ohnishi, M. Fujimaki, N. Fukunishi, A. Goto, K. Ikegami, O. Kamigaito, M. Kase, K. Kumagai, M. Nagase, H. Okuno, N. Sakamoto, T. Tanabe, Y. Yano, S. Yokouchi, and T. Mitsumoto: "Construction status of the RIKEN Intermediate-stage Ring Cyclotron (IRC)", 17th International Conference on Cyclotrons and Their Applications (Cyclotrons 2004), Tokyo, Oct. (2004).

M. Komiyama, M. Fujimaki, M. Kase, I. Yokoyama, and J. Odagiri: "Control system for the RIKEN accelerator research facility and RI-Beam Factory", 17th International Conference on Cyclotrons and Their Applications (Cyclotrons 2004), Tokyo, Oct. (2004).

S. Enomoto, H. Haba, R. Hirunuma, K. Igarashi, S. Motomura, H. Takeichi, and D. Kaji: "Development of a gas-jet-coupled multitracer system for multitracer production and its application for bioscience", 17th International Conference on Cyclotrons and Their Applications (Cyclotrons 2004), Tokyo, Oct. (2004).

N. Inabe, N. Fukunishi, A. Goto, M. Kase, H. Ryuto, N. Sakamoto, Y. Yano, S. Yokouchi, and T. Mitsumoto: "Fixed-frequency Ring Cyclotron (fRC) in RIBF", 17th International Conference on Cyclotrons and Their Applications (Cyclotrons 2004), Tokyo, Oct. (2004).

T. Tominaka, H. Okuno, S. Fujishima, M. Ohtake, T. Chiba, J. Ohnishi, K. Ikegami, A. Goto, and Y. Yano: "Helium vapor-cooled current leads for the RIKEN SRC", 17th International Conference on Cyclotrons and Their Applications (Cyclotrons 2004), Tokyo, Oct. (2004).

M. Kidera, T. Aihara, Y. Higurashi, M. Kase, T. Nakagawa, and Y. Yano: "Intense heavy ion beam production from RIKEN ECRISs", 17th International Conference on Cyclotrons and Their Applications (Cyclotrons 2004), Tokyo, Oct. (2004).

H. Hasebe, M. Kase, H. Ryuto, and Y. Yano: "Long-lived carbon stripper foils for intense heavy-ion beams", 17th International Conference on Cyclotrons and Their Applications (Cyclotrons 2004), Tokyo, Oct. (2004).

H. Okuno, N. Fukunishi, A. Goto, K. Ikegami, M. Nagase, J. Ohnishi, T. Tominaka, Y. Yano, and S. Yokouchi: "Magnets for the RIKEN Superconducting Ring Cyclotron", 17th International Conference on Cyclotrons and Their Applications (Cyclotrons 2004), Tokyo, Oct. (2004).

M. Kase, M. Fujimaki, N. Fukunishi, A. Goto, Y. Higurashi, E. Ikezawa, N. Inabe, O. Kamigaito, M. Kidera, S. Kohara, M. Komiyama, M. Nagase, T. Nakagawa, H. Okuno, H. Ryuto, M. Wakasugi, Y. Yano, S. Yokouchi, and Y. Ohshiro: "Present status of the RIKEN Ring Cyclotron", 17th International Conference on Cyclotrons and Their Applications (Cyclotrons 2004), Tokyo, Oct. (2004).

Y. Yano: "RI beam factory project at RIKEN", 17th International Conference on Cyclotrons and Their Applications (Cyclotrons 2004), Tokyo, Oct. (2004).

T. Tanabe, T. Emoto, M. Kase, K. Kumagai, T. Masuoka, and K. Yoshida: "RIKEN RI-Beam Factory power supply control system", 17th International Conference on Cyclotrons and Their Applications (Cyclotrons 2004), Tokyo, Oct. (2004).

H. Ryuto, N. Fukunishi, A. Goto, H. Hasebe, N. Inabe, M. Kase, Y. Yano, and S. Yokouchi: "Rotating carbon disk stripper for intense heavy-ion beams", 17th International Conference on Cyclotrons and Their Applications (Cyclotrons 2004), Tokyo, Oct. (2004).

K. Hidume, D. Ueyama, R. Kuroda, S. Minamiguchi, A. Oshima, Y. Hama, M. Washio, J. Urakawa, H. Hayano, S. Kashiwagi, and K. Ushida: "Soft X-ray generation using inverse Compton scattering at Waseda University", 47th Symposium on Radiation Chemistry, (Japanese Society of Radiation Chemistry), Sapporo, Oct. (2004).

A. Goto: "Status of the RIKEN RI Beam Facotry Project", Indian Particle Accelerator Conference 2005 (InPAC-2005), (Variable Energy Cyclotron Center and Department of Atomic Energy), Koltaka, India, Mar. (2005).

P. Bakule and Y. Matsuda: "Generation of slow muons by laser ionization of muonium", International Workshop on Muon Science Instrumentation (MSI-05), (JSP Core-to-Core Program on Development of Advanced Muon and Positron Beam), Tsukuba, Mar. (2005).

H. Ryuto, T. Abe, N. Fukunishi, M. Kase, and Y. Yano: "Heavy-ion beam irradiation system for biological samples in RIKEN", International Symposium on Novel Techniques in Nano-Biology 2005 (ISNB05), (Biology Research Center of Industrial Accelerator, Dongshin University and others), Jeollanamdo, Korea, Apr. (2005).

H. Ryuto, N. Fukunishi, A. Goto, H. Hasebe, N. Inabe, O. Kamigaito, M. Kase, Y. Yano, and S. Yokouchi: "Charge strippers in the RIKEN RI-beam factory", 2005 Particle Accelerator Conference (PAC05), (Oak Ridge National Laboratory and Thomas Jefferson National Accelerator Facility), Knoxville, USA, May (2005).

H. Ryuto, N. Fukunishi, H. Hasebe, S. Yokouchi, A. Goto, M. Kase, and Y. Yano: "Preperation of charge strippers for the RIKEN RI-beam factory", Workshop on Accelerator Operations 2005 (WAO2005), (Fermi National Accelerator Laboratory), Bloomingdale, USA, May (2005).

Y. Matsuda: "Generation of low energy muon with laser resonant ionization of muonium atoms", 7th International Workshop on Neutrino Factories and Superbeams (NuFact 05), (Laboratori Nazionali di Frascati), Rome, Italy, June (2005).

E. Ikezawa, N. Inabe, T. Kageyama, N. Fukunishi, M. Kase, M. Fujimaki, T. Fujinawa, A. Goto, H. Hasebe, Y. Higurashi, O. Kamigaito, M. Kidera, T. Nakagawa, S. Kohara, N. Sakamoto, M. Komiyama, M. Nagase, M. Wakasugi, T. Watanabe, H. Okuno, H. Ryuto, S. Yokouchi, A. Yoneda, Y. Ohshiro, and Y. Yano: "Present status of accelerators in RIKEN accelerator research Facility", 2nd Annual Meeting of Particle Accelerator Society of Japan/30th Linear Accelerator Meeting in Japan, Tosu, July (2005).

Y. Yamazaki: "Nanodots formation with slow highly charged ions", 17th International Conference on Ion-Surface Interactions (ISI-2005), (Moscow Aviation Institute), Zvenigorod, Russia, Aug. (2005).

M. Kidera, T. Nakagawa, K. Takahashi, S. Enomoto, K. Enomoto, M. Fujimaki, E. Ikezawa, O. Kamigaito, M. Kase, A. Goto, and Y. Yano: "Improvement of RIKEN ECRIS-AMS", 11th International Conference on Ion Sources (ICIS05), Caen, France, Sept. (2005).

T. Watanabe, M. Kase, Y. Sasaki, S. Watanabe, T. Ikeda, T. Kawaguchi, and Y. Yano: "Current and position beam monitor with HTS SQUIDs and HTS magnetic shield for the RIKEN Ring Cyclotron", 7th European Conference on Applied Superconductivity (EUCAS '05), (Vienna University of Technology), Vienna, Austria, Sept. (2005).

T. Watanabe, M. Kase, S. Watanabe, T. Ikeda, T. Kawaguchi, and Y. Yano: "Current and Position Monitor with HTS SQUIDs and HTS Magnetic Shield for RRC", Seminar at Paul Scherrer Institute, Villigen, Switzerland, Sept. (2005).

T. Watanabe, M. Kase, Y. Sasaki, S. Watanabe, T. Kawaguchi, and Y. Yano: "Measurement and analysis system using HTS SQUID for heavy ion beam", 62nd workshop on Forum of Superconductivity Science and Technology, (The Society of Non-Traditional Technology), Tokyo, Nov. (2005).

2. Nuclear physics and nuclear instrumentation

T. Suda: "Electron scattering off unstable nuclei", International Workshop 32nd on Gross Properties of Nuclei and Nuclear Excitations, (GSI), Hirschegg, Austria, Jan. (2004).

S. Sugimoto, K. Ikeda, and H. Toki: "Charge- and parity-projected Hartree-Fock method with deformation", 59th Annual Meeting of the Physical Society of Japan, Fukuoka, Mar. (2004).

K. Ishida, K. Nagamine, T. Matsuzaki, N. Kawamura, Y. Matsuda, M. Iwasaki, H. Imao, M. Kato, H. Sugai, M. Tanase, S. Nakamura, K. Kudo, N. Takeda, and G. H. Eaton: "Magnetic field effect in muon catalyzed fusion in D-T mixtures", Present status and future of muon science at RIKEN-RAL Muon Facility, Wako, May (2004).

S. Sugimoto, K. Ikeda, and H. Toki: "Charge- and parity-projected Hatree-Fock method for the strong tensor correlation and its application to the alpha particle", International Nuclear Physics Conference (INPC2004), (Chalmers University of Technology and Goteborgs University), Goteborg, Sweden, June–July (2004).

K. Sekiguchi, H. Sakai, H. Okamura, A. Tamii, T. Uesaka, K. Suda, N. Sakamoto, M. Hatano, T. Wakasa, Y. Sato, T. Ohnishi, K. Yako, S. Sakoda, H. Kato, Y. Maeda, J. Nishikawa, T. Saito, N. Uchigashima, N. N. Kalantar, and K. Ermisch: "Deuteron-Proton Scattering at Intermediate Energies and Three-Nucleon Forces", International Nuclear Physics Conference (INPC2004), (Chalmers University of Technology and Goteborgs University), Goteborg, Sweden, June–July (2004).

H. Ueno, K. Asahi, D. Kameda, H. Miyoshi, A. Yoshimi, K. Shimada, G. Kato, S. Emori, G. Kijima, M. Tsukui, H. Watanabe, T. Haseyama, Y. Kobayashi, and M. Ishihara: "Spin-polarized radioactive-isotope beams and the measurement of

nuclear moments", International Nuclear Physics Conference (INPC2004), (Chalmers University of Technology and Goteborg University), Goteborg, Sweden, June–July (2004).

T. Yamazaki: "Two-particle wave function in four-dimensional Ising model", LATTICE 2004: 22nd International Symposium on Lattice Field Theory, (Fermi National Accelerator Laboratory), Batavia, USA, June (2004).

Y. Motizuki: "Research on the r-process nucleosynthesis in the coming decade", RIBF-UEC/RIKEN Workshop on Physics of Unstable Nuclei: Past Decade and the Future, (RIBF-UEC), Wako, June (2004).

P. Strasser, K. Nagamine, T. Matsuzaki, K. Ishida, Y. Matsuda, and M. Iwasaki: "Muonic atoms of radioactive nuclei", 6th International Workshop on Neutrino Factories and Superbeams (NuFact 04), Osaka, July–Aug. (2004).

Y. Motizuki: "The r-process nucleosynthesis in a multi-dimensional supernova model", 8th International Symposium on Nuclei in the Cosmos (NIC8), (TRIUMF), Vancouver, Canada, July (2004).

H. Ueno, A. Yoshimi, H. Watanabe, T. Haseyama, Y. Kobayashi, K. Asahi, D. Kameda, H. Miyoshi, K. Shimada, G. Kato, S. Emori, G. Kijima, M. Tsukui, and H. Ogawa: "Nuclear-moment measurements of light neutron-rich nuclei", International Symposium on Exotic Nuclei (EXON 2004), (JINR and RIKEN, and others), St. Petersburg, Russia, July (2004).

M. Wada: "The Universal Slow-RI-beem Facility at RIKEN RIBF", International Symposium on Exotic Nuclei (EXON 2004), (JINR and RIKEN, and others), St. Petersburg, Russia, July (2004).

A. Yoshimi, K. Asahi, S. Emori, and M. Tsukui: "Nuclear spin maser oscillation of 129Xe by means of optical-detection feedback", 13th International Conference on Hyperfine Interactions & 17th International Symposium on Nuclear Quadrupole Interaction, (Rheinische Friedrich-Wilhelms-Universitat Bonn and others), Bonn, Germany, Aug. (2004).

T. Saito, H. Sakai, T. Ikeda, K. Itoh, T. Uesaka, T. Kawabata, H. Kuboki, M. Sasano, Y. Sato, K. Suda, K. Sekiguchi, A. Tamii, Y. Maeda, N. Matsui, and K. Yako: "Experimental test of Bell's inequality via the ^{1}H(d, ^{2}He)n reaction", 19th European Conference on Few-Body Problems in Physics, Groningen, The Netherlands, Aug. (2004).

K. Sekiguchi: "Exploring Three Nucleon Forces through dp Scattering at Intermediate Energies", 19th European Conference on Few-Body Problems in Physics, Groningen, The Netherlands, Aug. (2004).

T. Yamazaki, S. Aoki, M. Fukugita, K. Ishikawa, N. Ishizuka, Y. Iwasaki, K. Kanaya, T. Kaneko, Y. Kuramashi, M. Okawa, A. Ukawa, and T. Yoshie: "I = 2 S-wave pion scattering phase shift with two flavor fullQCD", Meeting of the Division of Particles and Fields of the American Physical Society (DPF2004), Riverside, USA, Aug. (2004).

S. Sugimoto, K. Ikeda, and H. Toki: "Study of ^{8}Be with the charge- and parity-projected Hartree-Fock method", 2004 Autumn Meeting of the Physical Society of Japan, Aomori and Kochi, Sept. (2004).

T. Yamazaki: "Two-particle wave function in four dimensional Ising model", 2004 Autumn Meeting of the Physical Society of Japan, Aomori and Kochi, Sept. (2004).

M. Takashina, H. Sakuragi, and Y. Iseri: "Effect of halo structure on ^{11}Be+^{12}C elastic scattering", 4th International Conference on Exotic Nuclei and Atomic Masses (ENAM 04), (Physics Division, Oak Ridge National Laboratory), Pine Mountain, USA, Sept. (2004).

A. Yoshimi, K. Asahi, S. Emori, M. Tsukui, and S. Oshima: "Low-frequency nuclear spin maser and search for atomic EDM of 129Xe", 16th International Spin Physics Symposium (SPIN 2004), (Istituto Nazionale di Fisica Nucleare (INFN)), Trieste, Italy, Oct. (2004).

A. Yoshimi, K. Asahi, S. Emori, M. Tsukui, and S. Oshima: "Spin maser of 129Xe nuclei at low magnetic field by optical spin detection", International Conference on Laser Probing (LAP2004), (Argonne National Laboratory), Argonne, USA, Oct. (2004).

T. Yamazaki, S. Aoki, M. Fukugita, K. Ishikawa, N. Ishizuka, Y. Iwasaki, K. Kanaya, T. Kaneko, Y. Kuramashi, M. Okawa, A. Ukawa, and T. Yoshie: "I = 2 S-wave pion scattering phase shift with two-flavor full QCD", Workshop on the Physics Programme of the RBRC and UKQCD QCDOC Machines, Upton, USA, Nov. (2004).

T. Gomi, T. Motobayashi, Y. Ando, N. Aoi, H. Baba, K. Demichi, Z. Elekes, N. Fukuda, Z. Fulop, U. Futakami, H. Hasegawa, Y. Higurashi, K. Ieki, N. Imai, M. Ishihara, K. Ishikawa, N. Iwasa, H. Iwasaki, S. Kanno, Y. Kondo, T. Kubo, S. Kubono, M. Kunibu, K. Kurita, Y. Matsuyama, S. Michimasa, T. Minemura, M. Miura, H. Murakami, T. Nakamura, M. Notani, S. Ota, A. Saito, H. Sakurai, M. Serata, S. Shimoura, T. Sugimoto, E. Takeshita, S. Takeuchi, Y. Togano, K. Ue, K. Yamada, Y. Yanagisawa, K. Yoneda, and A. Yoshida: "Study of the stellar ^{22}Mg(p,γ)^{23}Al reaction with Coulomb dissociation method", 21th Meeting between Astrophysicists and Nuclear Physicists, (Universite Libre de Bruxelles), Brussels, Belgium, Dec. (2004).

T. Matsuzaki: "Muon catalyzed t-t fusion and the related problems", Workshop on "Recent development of few body physic and the prospect", (RCNP), Ibaraki, Dec. (2004).

D. Nagae, K. Asahi, H. Miyoshi, K. Shimada, A. Yoshimi, M. Uchida, H. Ueno, J. Murata, W. D.

Schmidt-Ott, Y. Kobayashi, T. Haseyama, D. Kameda, G. Kato, S. Emori, G. Kijima, S. Oshima, T. Arai, and M. Takemura: "Development of stopping, extraction and neutralization system for atomic beam resonance method", 1st International Symposium on Nanometer-scale Quantum Physics (nanoPHYS'05), Tokyo, Jan. (2005).

N. D. Dang: "Giant resonances at zero and finite temperature", International Conference on the Interface between Nuclear Structure, Astrophysics and Reactions (NUSTAR '05), (University of Surrey), Guildford, UK, Jan. (2005).

M. Hoshino, T. Kambara, Y. Kanai, R. Schuch, and Y. Yamazaki: "Multiple-electron processes in a collision of slow highly charged ion with atom", RIKEN Symposium on Studies on Condensed Matter Physics, Atomic Physics, Hyperfine Interactions and Biomedical Sciences using RIKEN Accelerators, Wako, Jan. (2005).

Y. Motizuki: "The r-process nucleosynthesis in core-collapse supernova explosions induced by anisotropic neutrino radiation", 2005 Spring Annual Meeting of Astronomical Society of Japan, Hino, Mar. (2005).

H. Madokoro: "Two-Dimensional Numerical Simulation of Core-Collapse Supernovae With Anisotropic Neutrino Radiation", 2005 Spring Annual Meeting of Astronomical Society of Japan, Hino, Mar. (2005).

N. D. Dang: "Giant resonances at zero and finite temperatures", 229th ACS National Meeting, (American Chemical Society), San Diego, USA, Mar. (2005).

N. Aoi: "γ-ray spectroscopy of neutron rich $N = 40\sim50$ nuclei with proton inelastic scattering.", 60th Annual Meeting of Physical Society of Japan, Noda, Mar. (2005).

A. Kohama, K. Iida, and K. Oyamatsu: "Energy dependence of black-sphere radius", 60th Annual Meeting of Physical Society of Japan, Noda, Mar. (2005).

Y. Motizuki, H. Madokoro, T. Tachibana, and S. Goriely: "The r-process nucleosynthesis in two-dimensional core-collapse supernova explosions", 60th Annual Meeting of Physical Society of Japan, Noda, Mar. (2005).

H. Madokoro: "Two-Dimensional Numerical Simulation of Core-Collapse Supernovae With Anisotropic Neutrino Radiation", 60th Annual Meeting of Physical Society of Japan, Noda, Mar. (2005).

N. D. Dang: "Particle-number conservation within the self-consistent RPA", Cyclotron Institute Colloquium, (Texas A&M University), College Station, USA, Mar. (2005).

T. Matsuzaki: "An in-situ tritium gas-handling system for muon catalyzed fusion research at the RIKEN-RAL Muon Facility", International Workshop on Muon Science Instrumentation (MSI-05), (JSP Core-to-Core Program on Development of Advanced Muon and Positron Beam), Tukuba, Mar. (2005).

K. Ishida: "Muon catalyzed fusion experiment with high-intensity pulsed muon beams", International Workshop on Muon Science Instrumentation (MSI-05), (JSP Core-to-Core Program on Development of Advanced Muon and Positron Beam), Tsukuba, Mar. (2005).

Y. Motizuki, K. Takahashi, A. Bamba, K. Makishima, Y. Yano, H. Motoyama, M. Igarashi, K. Kamiyama, K. Suzuki, and H. Niko: "Supernova legacy investigated with Antarctic ice core drilled at Dome-Fuji station", NIPR Symposium on Frontiers of Physics, Chemistry, and Biology in Antarctic Ice Studies, (National Institute of Polar Research), Tokyo, Mar. (2005).

Y. Motizuki: "Research activities of RIKEN in relation with the r-process nucleosynthesis", Seminar at Institut d'Astronomie et d'Astrophysique, Universite Libre de Bruxelles, Brussels, Belgium, Mar. (2005).

Y. Motizuki: "The r-process nucleosynthesis in a two-dimensional core-collapse supernova model", Theoretical Nuclear Physics 'Donshu' Conference, (KEK-IPNS), Tsukuba, Mar. (2005).

Y. Motizuki: "How to make a good presentation at an international conference II", RIBF NAP (Nuclear Astrophysics Project) Seminar, Wako, May (2005).

A. Kohama, K. Iida, and K. Oyamatsu: "Looking at nuclei in the black sphere picture", RIKEN RIBF International Workshop on "Collective motions in unstable nuclei: experiments vs. theories", Wako, May (2005).

M. Yamagami: "Spatially extended coherence induced by pairing correlations in neutron drip line nuclei", RIKEN RIBF International Workshop on "Collective motions in unstable nuclei: experiments vs. theories", Wako, May (2005).

M. Wada: "Slow RI-beams using RF ion guide and Space-charge effect in the gas cell", Radioactive Ion Beam-Targets and Ion Sources, (Oak Ridge National Laboratory), Oak Ridge, USA, May (2005).

M. Yamagami: "Novel coordinate space representation for deformed loosely-bound nuclei", YITP Workshop on New Developments in Nuclear Self-Consistent Mean-Field Theories (MF05), Kyoto, May–June (2005).

K. Ishida: "Muon catalyzed fusion", 7th International Workshop on Neutrino Factories and Superbeams (NuFact 05), (Laboratori Nazionali di Frascati), Rome, Italy, June (2005).

M. Takashina: "^{16}C inelastic scattering studied with microscopic coupled-channels method", Direct Reactions with Exotic Beams (DREB2005), (Michigan State University), East Lansing, USA, June (2005).

S. Takeuchi, N. Aoi, H. Baba, T. Kubo, T. Fukui, Y. Hashimoto, K. Ieki, N. Imai, H. Iwasaki, S. Kanno, Y. Kondo, K. Kurita, T. Minemura, T.

Motobayashi, T. Nakabayashi, T. Nakamura, T. Okumura, T. Onishi, S. Ota, H. Sakurai, S. Shimoura, R. Sugo, D. Suzuki, H. Suzuki, M. Suzuki, E. Takeshita, M. Tamaki, K. Tanaka, Y. Togano, and K. Yamada: "Proton inelastic scattering on ^{34}Si and ^{32}Mg", Direct Reactions with Exotic Beams (DREB2005), (Michigan State University), East Lansing, USA, June (2005).

T. Matsumoto: "The method of continuum-discretized coupled-channels for four-body breakup reactions", Direct Reactions with Exotic Beams (DREB2005), (Michigan State University), East Lansing, USA, June (2005).

K. Ishida: "Muon catalyzed fusion", Workshop on Neutrino Factories and Superbeams (NuFact-J 05), (Tokyo institute of technology), Tokyo, June (2005).

K. Asahi, A. Yoshimi, M. Uchida, S. Emori, and S. Oshima: "Nuclear spin maser with novel masing mechanism and search for atomic EDM in ^{129}Xe", 5th Circum-Pan-Pacific Symposium on High Energy Spin Physics (SPIN 2005), (Tokyo Institute of Technology), Tokyo, July (2005).

Y. Motizuki: "History of supernovae and solar activity investigated with Antarctic ice", NIES (National Institute for Environmental Studies) Seminar, Tsukuba, July (2005).

Y. Ishida, M. Wada, Y. Yamazaki, and H. Wollnik: "Compact time-of-flight mass spectrometer of high resolving power: MR-TOF", 30th Annual Meeting of the Society for Atomic Collision Reserach, Wako, Aug. (2005).

N. Aoi: "Exotic structure of unstable nuclei revealed through a g-ray spectroscopy technique", 4th CNS International Summer School (CISS05), Wako, Aug. (2005).

M. Takashina, E. K. Yoshiko, and Y. Sakuragi: "^{16}C inelastic scattering studied with microscopic coupled-channels method", 2nd Joint Meeting of the Nuclear Physics Divisions of the APS and JPS (Hawaii 2005), Maui, USA, Sept. (2005).

T. Egami, K. Ogata, T. Matsumoto, E. Hiyama, Y. Iseri, M. Kamimura, and M. Yahiro: "Four-body CDCC analysis of ^{6}He+^{209}Bi scattering near Coulomb barrier energies", 2nd Joint Meeting of the Nuclear Physics Divisions of the APS and JPS (Hawaii 2005), Maui, USA, Sept. (2005).

H. Ueno: "Ground-state nuclear moments of neutron-rich *p*- and *sd*-shell nuclei", 2nd Joint Meeting of the Nuclear Physics Divisions of the APS and JPS (Hawaii 2005), Maui, USA, Sept. (2005).

E. Takeshita, N. Aoi, S. Ota, S. Takeuchi, H. Suzuki, H. Baba, S. Bishop, T. Fukui, Y. Hashimoto, H. Ong, E. Ideguchi, K. Ieki, N. Imai, H. Iwasaki, S. Kanno, Y. Kondo, T. Kubo, K. Kurita, K. Kusaka, T. Minemura, T. Motobayashi, T. Nakabayashi, T. Nakamura, T. Nakao, M. Niikura, T. Okumura, T. Onishi, H. Sakurai, S. Shimoura, R. Sugo, D. Suzuki, M. Suzuki, M. Tamaki, K. Tanaka, Y. Togano, and K. Yamada: "Inelastic proton scattering on the neutron rich Cr isotopes", 2nd Joint Meeting of the Nuclear Physics Divisions of the APS and JPS (Hawaii 2005), Maui, USA, Sept. (2005).

A. Yoshimi, K. Asahi, M. Uchida, and S. Oshima: "Nuclear spin maser at low frequency and atomic EDM of ^{129}Xe", 2nd Joint Meeting of the Nuclear Physics Divisions of the APS and JPS (Hawaii 2005), Maui, USA, Sept. (2005).

M. Yamagami: "Pairing correlations in deformed nuclei close to the neutron drip line", 2nd Joint Meeting of the Nuclear Physics Divisions of the APS and JPS (Hawaii 2005), Maui, USA, Sept. (2005).

I. Nakagawa: "Polarization Measurement of 100 GeV Proton Beams at RHIC with CNI pC polarimeter", 2nd Joint Meeting of the Nuclear Physics Divisions of the APS and JPS (Hawaii 2005), Maui, USA, Sept. (2005).

S. Takeuchi, N. Aoi, H. Baba, T. Fukui, Y. Hashimoto, K. Ieki, N. Imai, H. Iwasaki, S. Kanno, Y. Kondo, K. Kurita, T. Minemura, T. Motobayashi, T. Nakabayashi, T. Nakamura, T. Okumura, T. Onishi, S. Ota, H. Sakurai, S. Shimoura, R. Sugo, D. Suzuki, H. Suzuki, M. Suzuki, E. Takeshita, M. Tamaki, K. Tanaka, Y. Togano, and K. Yamada: "Proton inelastic scattering on ^{34}Si and ^{32}Mg", 2nd Joint Meeting of the Nuclear Physics Divisions of the APS and JPS (Hawaii 2005), Maui, USA, Sept. (2005).

M. Yamagami: "Spatially extended coherence induced by pairing correlation in low-frequency vibrational excitation of neutron drip line nuclei", 2nd Joint Meeting of the Nuclear Physics Divisions of the APS and JPS (Hawaii 2005), Maui, USA, Sept. (2005).

Y. Motizuki: "Observation project of the nonthermal universe: from the world of the elements to that of nuclides", 6th Symposium on High Energy Astrophysics Association in Japan, Tokyo, Sept. (2005).

Y. Motizuki: "X-or gamma-rays from supernovae in glacial ice?", International Workshop on Astronomy with Radioactivities V: From Gamma Rays to Stardust, (Clemson University), Clemson, USA, Sept. (2005).

M. Yamagami: "Continuum effects for many-body correlations in nuclei close to the neutron drip line", Nuclear Structure Near the Limits of Stability (INT-05-3), (Institute for Nuclear Theory), Seattle, USA, Sept. (2005).

M. Yamagami: "Continuum effects for many-body correlations in nuclei close to the neutron drip line", RIKEN RIBF Mini-Workshop: Pairing Correlations in Unstable Nuclei, Wako, Sept. (2005).

M. Yamagami: "Continuum effects for many-body correlations in nuclei close to the neutron drip line", Tensor force and many-body correlations in nuclei, (Yukawa Institute for Theoretical Physics, Kyoto University), Kyoto, Sept. (2005).

Y. Motizuki: "History of supernovae and solar activity investigated with Antarctic ice core: Can we perform a related experiment at SPring-8?", 147th SPring-8 Seminar, Harima, Oct. (2005).

Y. Motizuki, H. Madokoro, T. Tachibana, S. Goriely, and K. Takahashi: "The r-process nucleosynthesis in a 2-D supernova model: Multi-dimensional effect", 2005 Fall Annual Meeting of Astronomy Society of Japan, Sapporo, Oct. (2005).

H. Madokoro: "Two-Dimensional Numerical Simulation of Core-Collapse Supernovae Induced by Anisotropic Neutrino Radiation", 2005 Fall Annual Meeting of Astronomy Society of Japan, Sapporo, Oct. (2005).

H. Ueno: "Production of spin-oriented unstable nuclei via the projectile-fragmentation reaction", 11th International Workshop on Polarized Sources and Targets (PST05), (RIKEN and CNS), Tokyo, Nov. (2005).

Y. Motizuki and H. Madokoro: "The r-process nucleosynthesis in a 2-Dimensional supernova model", International Symposium on Origin of Matter and Evolution of Galaxies (OMEG05)): New Horizon of Nuclear Astrophysics and Cosmology, Tokyo, Nov. (2005).

H. Ueno: "RI spin laboratory project", RIKEN RI Beam Factory Technical Advisory Committee Meeting, Wako, Nov. (2005).

T. Matsumoto, T. Egami, E. Hiyama, K. Ogata, Y. Iseri, M. Kamimura, and M. Yahiro: "Four-body CDCC analyses of ^{6}He+^{12}C and ^{6}He+^{209}Bi scattering", RIKEN-CNS RIBF International Workshop "Correlation and Condensation: New Features in Loosely Bound and Unbound Nuclear States", Wako, Dec. (2005).

H. Ueno: "Nuclear moments of neutron-rich Al isotope", RIKEN-CNS RIBF International Workshop "Correlation and Condensation: New Features in Loosely Bound and Unbound Nuclear States", Wako, Dec. (2005).

M. Yamagami: "Pairing correlation in deformed neutron-rich nuclei", RIKEN-CNS RIBF International Workshop "Correlation and Condensation: New Features in Loosely Bound and Unbound Nuclear States", Wako, Dec. (2005).

M. Yamagami: "Continuum effects for many-body correlations in medium mass neutron-rich nuclei", YITP Workshop on Binding Mechanism and New Dynamics in Weakly Bound Systems, (Yukawa Institute for Theoretical Physics, Kyoto University), Kyoto, Dec. (2005).

M. Takashina: "Analysis of ^{12}C, ^{16}O(α,α') reaction using BEC wave function", YITP Workshop on Binding mechanism and new dynamics in weakly bound systems, (Yukawa Institute of Theoretical Physics, Kyoto University), Kyoto, Dec. (2005).

3. Atomic and solid-state physics

S. Ohira-Kawamura, M. Tamura, R. Kato, I. Watanabe, and M. Iwasaki: "μSR study on magnetic property of [Pd(dmit)$_2$] salts", 5th International Symposium on Crystalline Organic Metals, Superconductors and Magnets (ISCOM' 2003), Port-Bourgenay, France, Sept. (2003).

M. Hoshino, Y. Kanai, M. Kitajima, Y. Nakai, Y. Yamazaki, and H. Tanaka: "The study of double-electron catpure processes in slow C^{4+}-He collisions", Genshi/Bunshi hannou so katei ni okeru ryuushi soukan, Okazaki, June (2004).

Y. Fukuyama, Y. Moriwaki, and Y. Matsuo: "Stabilization of Ba^{+*}-He exciplex below the critical temperature at 3.3 K: Formation and dissociation of Ba^{+*}-He", 1st Atomic, Molecular and Optical Science Forum, Tokyo, July (2004).

H. Ueno, K. Asahi, W. Sato, A. Yoshimi, H. Watanabe, Y. Kobayashi, H. Miyoshi, J. Murata, K. Shimada, D. Kameda, G. Kato, S. Emori, and T. Haseyama: "Study on the transient field at high velocities", 13th International Conference on Hyperfine Interactions & 17th International Symposium on Nuclear Quadrupole Interaction, (University of Bonn), Bonn, Germany, Aug. (2004).

M. Hoshino, Y. Kanai, Y. Yamazaki, T. Kambara, and R. Schuch: "The study of multiple electron processes in close collisions of slow Ne^{2+} with Ar", 29th Annual Meeting of the Society for Atomic Collision Research, Sendai, Aug. (2004).

M. Hoshino, T. Kambara, Y. Kanai, Y. Yamazaki, and R. Schuch: "Multi-electron Processes in close, single collisions between slow Ne^{2+} and Ar", 2004 Autumn Meeting of the Physical Society of Japan, Aomori and Kochi, Sept. (2004).

Y. Miyamoto, M. Hoshino, Y. Kanai, Y. Nakai, M. Kitajima, Y. Yamazaki, and H. Tanaka: "Single and double electron capture processes for slow highly charged ion (N^{5+})-He collisions", 2004 Autumn Meeting of the Physical Society of Japan, Aomori and Kochi, Sept. (2004).

L. Pichl, R. Suzuki, M. Hoshino, M. Kimura, Y. Li, and R. J. Buenker: "Theoretical study of double electron capture in collisions of $C^{4+}$with He", 2004 Autumn Meeting of the Physical Society of Japan, Aomori and Kochi, Sept. (2004).

Y. Iwai, Y. Nakai, Y. Kanai, T. Ikeda, M. Hoshino, K. Nishio, H. Masuda, and Y. Yamazaki: "Coincidence measurements of L X-rays and final charge state for Ar^{13+} ions passing through Ni microcapillaries", 15th International Workshop on Inelastic Ion-Surface Collisions (IISC-15), (The Japan Society of Applied Physics), Ise, Oct. (2004).

Y. Matsuo: "Laser spectroscopy and producing spin-polarization of atoms with unstable nuclei trapped in superfluid helium", RIKEN Symposium on Research

Projects Dedicated to RIPS in the RIBF Configuration, Wako, Oct. (2004).

Y. Fukuyama, Y. Moriwaki, and Y. Matsuo: "Formation and dissociation of Ba^{+*}-He exciplex in cold He gas: characteristic behavior of cold collision process", Symposium on Physics and Chemistry of Atoms, Molecules and Ions in Quantum Condensed Phases, (Advanced Science Research Center of JAERI), Tokai-mura, Ibaraki Pref., Dec. (2004).

Y. Matsuo, Y. Fukuyama, T. Kobayashi, T. Furukawa, H. Izumi, Y. Arakawa, I. Wakabayashi, K. Kawai, S. Morinobu, T. Shimoda, and A. Hatakeyama: "Long electric spin relaxation time of Cs atoms in superfluid helium: towards laser spectroscopy of atoms with unstable nuclei", Symposium on Physics and Chemistry of Atoms, Molecules and Ions in Quantum Condensed Phases, (Advanced Science Research Center of JAERI), Tokai-mura, Ibaraki Pref., Dec. (2004).

Y. Nakai: "Resonant Coherent Excitation of Fast Highly Charged Ions", RIKEN Symposium on 9th Studies on Condensed Matter Physics, Atomic Physics, Hyperfine Interactions and Biomedical Sciences Using RIKEN Accelerators, Wako, Jan. (2005).

Y. Fukuyama, Y. Moriwaki, and Y. Matsuo: "Laser-induced fluorescence spectra of Ba^{+*}-He exciplexes produced in cold He gas", Symposium on reaction mechanism cross-over by resonance control, (ISAS, JAXA), Sagamihara, Jan. (2005).

I. Shimamura and A. Igarashi: "Resonance analysis in terms of the time-delay matrix: the effect of poles of the time-independent S matrix", Workshop on Atomic and Molecular Processes in Space, (ISAS, JAXA), Sagamihara, Jan. (2005).

Y. Yamazaki: "High senstive detection of surface-adsorbed hydrogen atoms with slow highly charged ions", 52nd Spring Meeting 2005 of The Japan Society of Applied Physics and Related Societies, Saitama, Mar.–Apr. (2005).

Y. Yoshida, Y. Kobayashi, A. Yoshida, H. Ueno, K. Hayakawa, K. Yukihira, F. Ambe, and F. Shimura: "In-situ observation of the diffusion process of Fe atoms in Si matrix by 57Mn/57Fe in-beam mössbauer spectroscopy", 60th Annual Meeting of Physical Society of Japan, Noda, Mar. (2005).

Y. Matsuo, N. Yonekura, T. Kobayashi, Y. Fukuyama, and T. Nakajima: "Production of highly spin-polarized ions and electrons by resonant photoionization of Sr atoms to the 4s5d autoionizing states", 60th Annual Meeting of Physical Society of Japan, Noda, Mar. (2005).

Y. Yamazaki: "Nanodots formation with slow highly charged ions", Physics at EBIT and Advanced Research Light Sources (PEARL 2005), (Fudan University and Lund University), Hainan, China, Mar. (2005).

Y. Yamazaki: "New Techniques for Trapping Antiprotons, Positrons, and Antihydrogen Atoms", International Conference on Low Energy Antiproton Physics (LEAP'05), Bonn, Germany, May (2005).

T. Furukawa, Y. Matsuo, A. Hatakeyama, Y. Fukuyama, T. Kobayashi, H. Izumi, and T. Shimoda: "Electron spin depolarization of Cs atoms in superfluid helium", 2nd Atomic, Molecular and Optical Science Forum, Wako, June (2005).

Y. Kanai, M. Hoshino, T. Kambara, Y. Yamazaki, R. Hellhammer, and N. Stolterfoht: "Two dimensional images of ions transmitted through insulator capillaries under beam guiding conditions", 24th International Conference on Photonic, Electronic and Atomic Collisions (ICPEAC 2005), Rosario, Argentina, July (2005).

Y. Fukuyama, Y. Moriwaki, and Y. Matsuo: "Cold Collision of Ba^{+*} with He: Formation, Dissociation and Vibrational Relaxation of Ba^{+*}-He exciplexes", International Quantum Electronics Conference 2005 and the Pacific Rim Conference on Lasers and Electro-Optics 2005 (IQEC/CLEO-PR 2005), (Science Council of Japan and others), Tokyo, July (2005).

T. Furukawa, Y. Matsuo, A. Hatakeyama, Y. Fukuyama, T. Kobayashi, and T. Shimoda: "Long Electronic Spin Relaxation Time of Cs Atoms in Superfluid Helium", International Quantum Electronics Conference 2005 and the Pacific Rim Conference on Lasers and Electro-Optics 2005 (IQEC/CLEO-PR 2005), (Science Council of Japan and others), Tokyo, July (2005).

Y. Matsuo, Y. Fukuyama, and Y. Moriwaki: "Temperature and Pressure Control of Cold Helium Gas above Liquid Helium for Laser Spectroscopy of Atoms and Molecules in Helium Gas of 3-30 K", 24th International Conference on Low Temperature Physics (LT24), (Department of Physics and University of Florida), Orlando, USA, Aug. (2005).

Y. Kanai, M. Hoshino, T. Ikeda, T. Kambara, Y. Yamazaki, R. Hellhammer, and N. Stolterfoht: "Ion-beam guide effect of insulator capillaries", 30th Annual Meeting of the Society for Atomic Collision Reserach, Wako, Aug. (2005).

Y. Iwai, Y. Kanai, Y. Nakai, T. Ikeda, M. Hoshino, H. Oyama, K. Ando, H. Masuda, K. Nishio, H. Torii, K. Komaki, and Y. Yamazaki: "Study of the resonant electron capture and decay processes for N ions using microcapillary targets", 30th Annual Meeting of the Society for Atomic Collision Reserach, Wako, Aug. (2005).

S. Tsutsui, J. Uemura, H. Kobayashi, T. Tazaki, S. Nasu, Y. Kobayashi, Y. Yoda, H. Onodera, H. Sugiwara, D. T. Matsuda, D. Kikuchi, H. Sato, C. Sekine, and I. Shirotani: "Elastic properties of filled-skutterudite compounds probed by Mössbauer nuclei", International Conference on the Applications

of the Mössbauer Effect (ICAME2005), Montpellier, France, Sept. (2005).

K. Kubo, Y. Kobayashi, H. Nonaka, Y. Yamada, Y. Sakai, H. Shoji, and H. Matsue: "Neutron in-beam Mössbauer spectroscopic study of iron disulfide at room temperature", International Conference on the Applications of the Mössbauer Effect (ICAME2005), Montpellier, France, Sept. (2005).

Y. Kobayashi, H. Nonaka, J. Miyazaki, K. Kubo, H. Ueno, A. Yoshimi, H. Miyoshi, D. Kameda, K. Shimada, D. Nagae, K. Asahi, and Y. Yamada: "Reactions of ^{57}Mn implanted into solid oxygen", International Conference on the Applications of the Mössbauer Effect (ICAME2005), Montpellier, France, Sept. (2005).

Y. Yoshida, Y. Kobayashi, A. Yoshida, H. Ueno, K. Hayakawa, K. Yukihira, F. Shimura, and F. Ambe: "The formation process of substitutional Fe atoms via interstitial Fe atoms jumping into vacancies in Si", International Conference on the Applications of the Mössbauer Effect (ICAME2005), Montpellier, France, Sept. (2005).

H. Shimada, Y. Yamazaki, Y. Nakai, H. Oyama, K. Ando, and A. Hatakeyama: "Momentum distributions of multiply charged argon ions produced at barrier-suppression ionization regime", Joint Conference on Ultrafast Optics 5 and Applications of High Field and Short Wavelength Sources 11(UFO/HFSW 2005), (The Optical Society of America and others), Nara, Sept. (2005).

Y. Yamazaki: "Accumulation,Cooling,Diagnostics,and Manipulation of Antiprotons and Positrons", The Physical Society of Japan 2005 Autumn Meeting, Kyotanabe, Sept. (2005).

M. Hoshino, T. Kambara, Y. Kanai, R. H. Schuch, and Y. Yamazaki: "Charge state correlations in large-angle scattering between slow Ne ion and Ar atom", The Physical Society of Japan 2005 Autumn Meeting, Kyotanabe, Sept. (2005).

H. Saitoh, Y. Enomoto, Y. Kanai, A. Mohri, and Y. Yamazaki: "Formation of finite length thermalized non-neutral plasma in an inhomogeneous magnetic field", The Physical Society of Japan 2005 Autumn Meeting, Kyotanabe, Sept. (2005).

T. Ikeda, Y. Kanai, T. Nebiki, T. Narusawa, and Y. Yamazaki: "Ion-beam guide effect of glass capillaries", The Physical Society of Japan 2005 Autumn Meeting, Kyotanabe, Sept. (2005).

Y. Kanai, M. Hoshino, T. Ikeda, T. Kambara, R. Hellhammer, N. Stolterfoht, and Y. Yamazaki: "Ion-beam guide effect of insulator capillaries", The Physical Society of Japan 2005 Autumn Meeting, Kyotanabe, Sept. (2005).

A. Mohri, H. Saitoh, Y. Kanai, and Y. Yamazaki: "Nonneutral plasma with a finite lengh in thermal equilibrium formed in an axially symmetric nonuniform magnetic field", The Physical Society of Japan 2005 Autumn Meeting, Kyotanabe, Sept. (2005).

Y. Nagata, A. Mohri, N. Kuroda, H. Torii, M. Shibata, H. Saitoh, Y. Kanai, K. Komaki, and Y. Yamazaki: "Production of polarized anti-hydrogen beam: a simulation of the orbit of anti-hydrogen atoms emerging out of a cusp trap", The Physical Society of Japan 2005 Autumn Meeting, Kyotanabe, Sept. (2005).

Y. Miyamoto, M. Hoshino, Y. Kanai, Y. Nakai, M. Kitajima, D. Tanaka, and Y. Yamazaki: "Single and double electron capture processes in slow N^{5+}-He collisions", The Physical Society of Japan 2005 Autumn Meeting, Kyotanabe, Sept. (2005).

Y. Iwai, Y. Kanai, Y. Nakai, T. Ikeda, M. Hoshino, H. Oyama, K. Ando, H. Masuda, K. Nishio, H. Torii, K. Komaki, and Y. Yamazaki: "Study of the resonant electron capture and decay processes for N ions using metal microcapillary targets", The Physical Society of Japan 2005 Autumn Meeting, Kyotanabe, Sept. (2005).

Y. Yamazaki: "HCI-capillary interactions: Towards Nano-beam formation and applications", International Workshop on Interdisciplinary Research with Slow Ion Beams 2005 (IRSIB 05), (Centre Interuniversitaire de Ressources Informatiques de Lorraine and others), Caen, France, Oct. (2005).

T. Matsuzaki, K. Ishida, N. Kawamura, H. Imao, Y. Matsuda, M. Iwasaki, K. Nagamine, S. Nakamura, M. Kato, H. Sugai, A. Uritani, H. Harano, and G. H. Eaton: "Temperature dependence of muon transfer rate to the accumulated ^{3}He in T_2 solid obseved in the muon catalyzed t-t fusion process", ISSP Workshop on Science of Hydrogen in Solid, (The Insititute of Solid State Physics), Kashiwa, Nov. (2005).

T. Matsuzaki: "Studies of molecular magnetism with μSR method under multiple extreme conditions at RIKEN-RAL Muon Facility", RIKEN Symposium on Molecular Ensemble 2005, Wako, Nov. (2005).

T. Ikeda, Y. Kanai, T. Kojima, T. Nebiki, T. Narusawa, and Y. Yamazaki: "Production of a sub-micron sized highly charged ion beam using glass capillary", 6th Ion Beam Analysis of Surface, (JSAP), Kyoto, Dec. (2005).

Y. Iwai, Y. Kanai, Y. Nakai, T. Ikeda, M. Hoshino, H. Oyama, K. Ando, H. Masuda, K. Nishio, H. Torii, K. Komaki, and Y. Yamazaki: "Study of the formation and decay of multiply and highly excited states in the interaction of N ions using Ni microcapillary target", 6th Ion Beam Analysis of Surface, (JSAP), Kyoto, Dec. (2005).

4. Radiochemistry, radiation chemistry, and radiation biology

R. Hirunuma, K. Igarashi, H. Saito, Y. Miyazawa, H. Haba, H. Takeichi, T. Abe, and S. Enomoto: "Accumulation of various metals in Lotus japonicus using

the multitracer technique", 124th Annual Meeting of the Pharmaceutical Society of Japan, Osaka, Mar. (2004).

K. Ishibashi, T. Suzuki, T. Togawa, R. Hirunuma, H. Haba, S. Enomoto, K. Nishio, and S. Tanabe: "Study of metal sensitivity and detoxification mechanism in cisplatin resistant cell line", 124th Annual Meeting of the Pharmaceutical Society of Japan, Osaka, Mar. (2004).

S. Ohata, T. Suzuki, T. Togawa, K. Nishio, R. Hirunuma, H. Haba, S. Enomoto, and S. Tanabe: "Study on Cadmium-resistance in MRP5-overproducing cell line", 124th Annual Meeting of the Pharmaceutical Society of Japan, Osaka, Mar. (2004).

R. Hirunuma, K. Igarashi, H. Saito, Y. Miyazawa, H. Haba, H. Takeichi, T. Abe, and S. Enomoto: "Research on purification of soil and water pollution by the heavy metals using Lotus japonicus", 14th Symposium on Roles of Metals in Biological Reactions, Biology and Medicine (SRM 2004), (The Pharmaceutical Society of Japan), Shizuoka, June (2004).

T. Abe, H. Saito, T. Matsuyama, H. Ryuto, N. Fukunishi, Y. Yano, and S. Yoshida: "Morphological mutants of rice by heavy ion-beam irradiation", 18th International Conference on Plant Growth Substances (IPGSA Conference 2004), (International Plant Growth Substances Association), Canberra, Australia, Sept. (2004).

Y. Kobayashi: "Application of in-beam mossbauer spectroscopy to inorganic chemistry", 1st TRIAC Workshop, (KEK), Tokai-mura, Ibaraki Pref., Sept. (2004).

W. Sato: "Applications of the on-line perturbed angular correlation method to condensed matter science", 1st TRIAC Workshop, (KEK), Tokai-mura, Ibaraki Pref., Sept. (2004).

H. Saito, T. Abe, N. Fukunishi, H. Ryuto, K. Miyazaki, T. Kusumi, K. Suzuki, and S. Yoshida: "Mutation breeding by heavy-ion beam irradiation on *Verbena hybrida*: isolation and characterization of sterile mutants", 5th International Symposium on In Vitro Culture and Horticultural Breeding (5th IVCHB Symposium), (International Sciety for Horticultural Sciences), Debrecen, Hungary, Sept. (2004).

K. Kubo, Y. Kobayashi, Y. Nemoto, Y. Yamada, Y. Sakai, H. Shoji, C. Yonezawa, and H. Matsue: "A neutron in-beam mossbauer spectrum of iron disulfide", 2004 Annual Meeting on the Japan Society of Nuclear and Radiochemical Sciences and 48th Symposium on Radiochemistry, Tokyo, Oct. (2004).

W. Sato, H. Ueno, H. Watanabe, H. Miyoshi, A. Yoshimi, D. Kameda, J. Kaihara, K. Shimada, T. Ito, S. Suda, Y. Kobayashi, A. Shinohara, and K. Asahi: "Application of the on-line pAC method to condensed matter studies", 2004 Annual Meeting on the Japan Society of Nuclear and Radiochemical Sciences and 48th Symposium on Radiochemistry, Tokyo, Oct. (2004).

K. Kubo, Y. Kobayashi, Y. Yamada, Y. Nemoto, T. Saito, Y. Sakai, H. Shoji, C. Yonezawa, H. Matsue, and M. Nakada: "Neutron in-beam Mössbauer spectroscopy with a parallel plate avalanche counter", International Symposium on Industrial Applications of the Mössbauer Effect, Madrid, Spain, Oct. (2004).

Y. Kobayashi: "Applications of short-lived RI beam to chemistry", RIKEN Symposium on Research Projects Dedicated to RIPS in the RIBF Configuration, Wako, Oct. (2004).

K. Kubo: "Chemical states of krypton compounds", RIKEN Symposium on Research Projects Dedicated to RIPS in the RIBF Configuration, Wako, Oct. (2004).

W. Sato: "Materials science using on-line PAC method", RIKEN Symposium on Research Projects Dedicated to RIPS in the RIBF Configuration, Wako, Oct. (2004).

Y. Yoshida: "Materials science with GeV-energy implantations: Compared with low energy ion implantations", RIKEN Symposium on Research Projects Dedicated to RIPS in the RIBF Configuration, Wako, Oct. (2004).

Y. Yamada: "Mossbauer Spectra of Thin Fe Foil Produced by Laser Evaporation", Special Research Meeting on New Developments in Solid State Physics with Probes of Radiation and Nuclei, (Kyoto University Research Reactor Institute), Kumatori-cho, Osaka Pref., Nov. (2004).

Y. Kobayashi: "Oxidation states of Fe atoms implanted into solid oxygen", Special Research Meeting on New Developments in Solid State Physics with Probes of Radiation and Nuclei, (Kyoto University Research Reactor Institute), Kumatori-cho, Osaka Pref., Nov. (2004).

Y. Yamamoto, H. Saito, T. Matsuyama, H. Ryuto, T. Abe, N. Fukunishi, and S. Yoshida: "Genetic mutation by heavy ion beam irradiation", *Arabidopsis thaliana* Workshop 2004, (The University of Tokyo), Tokyo, Nov. (2004).

Y. Kobayashi: "Chemical states of Fe atoms implanted into solid oxygen", RIKEN Symposium on Studies on Condensed Matter Physics, Atomic Physics, Hyperfine Interactions and Biomedical Sciences using RIKEN Accelerators, Wako, Jan. (2005).

M. Tomita: "Effect of heavy ion irradiation on cell killing and DNA double-strand break repair", RIKEN Symposium on Studies on Condensed Matter Physics, Atomic Physics, Hyperfine Interactions and Biomedical Sciences using RIKEN Accelerators, Wako, Jan. (2005).

Y. Yamamoto: "For evaluation of genetic effects on plants by heavy ion beam irradiation", RIKEN Symposium on Studies on Condensed Matter Physics, Atomic Physics, Hyperfine Interactions and Biomed-

ical Sciences using RIKEN Accelerators, Wako, Jan. (2005).

Y. Yoshida: "Jump process of Fe atoms in Si", RIKEN Symposium on Studies on Condensed Matter Physics, Atomic Physics, Hyperfine Interactions and Biomedical Sciences using RIKEN Accelerators, Wako, Jan. (2005).

T. Abe: "Development of ion-beam breeding technology", 56th CIST Colloquium for Faculty of Photonics Science, (Chitose Institute of Science and Technology), Chitose, Feb. (2005).

H. Haba: "Future plans for superheavy element chemistry (Experiment)", 3rd Workshop on Nuclear and Chemical Properties of Heavy Elements, (Kyoto University Research Reactor Institute), Kumatori-cho, Osaka Pref., Mar. (2005).

K. Kubo, Y. Kobayashi, H. Nonaka, Y. Yamada, Y. Sakai, H. Shoji, and H. Matsue: "A mossbauer spectroscopic study on the products of neutron induce reaction in irondisulfide", 85th National Meeting of the Chemical Society of Japan, Yokohama, Mar. (2005).

Y. Kobayashi, H. Nonaka, J. Miyazaki, K. Kubo, H. Ueno, H. Miyoshi, D. Kameda, K. Shimada, D. Nagae, and Y. Yamada: "Chemical States of 57Fe Decayed from 57Mn after Implantation into Solid Oxygen", 85th National Meeting of the Chemical Society of Japan, Yokohama, Mar. (2005).

Y. Kitamoto, D. Saika, K. Matsuo, Y. Tani, H. Hasegawa, T. Yoshimura, W. Sato, N. Takahashi, H. Haba, S. Enomoto, and A. Shinohara: "Development of an on-line solvent extraction apparatus for superheavy element chemistry", 85th National Meeting of the Chemical Society of Japan, Yokohama, Mar. (2005).

H. Haba, K. Tsukada, K. Akiyama, M. Asai, A. Toyoshima, Y. Ishii, I. Nishinaka, T. Sato, Y. Nagame, J. Saito, M. Ito, S. Goto, H. Kudo, Y. Oura, and K. Sueki: "Reversed-phase extraction chromatography of Zr and Hf in the TBP/HCl system: Model experiments for chemical characterization of element 104, rutherfordium", 85th National Meeting of the Chemical Society of Japan, Yokohama, Mar. (2005).

H. Saito, M. Nakano, H. Ryuto, N. Fukunishi, and T. Abe: "Mutation induction by heavy-ion beam irradiation in daylily, *Hemerocallis hybrida*", 2005 Spring Meeting of Japanese Society for Horticultural Science, Tsukuba, Apr. (2005).

M. Tomita, M. Aoki, and Y. Furusawa: "Molecular response of DNA double-starand break repair proteins to DNA clustered damages", Heisei16nendo HIMAC Kyodo Riyo Kenkyu Seika Happyokai, (National Institute of Radiological Sciences), Chiba, Apr. (2005).

T. Morishita, H. Yamaguchi, K. Degi, H. Asaumi, Y. Hase, A. Tanaka, T. Abe, H. Saito, and S. Yoshida: "Dose responce and mutation effects of ion beams and gamma rays irradiation in perilla seeds", 2nd Meeting of the Ion Beam Breeding Society, Wako, May (2005).

H. Ryuto, H. Saito, Y. Yamamoto, Y. Hayashi, N. Fukunishi, M. Kase, T. Abe, and Y. Yano: "Heavy-ion beam irradiation system for biological samples in RIKEN", 2nd Meeting of the Ion Beam Breeding Society, Wako, May (2005).

K. Ohkoshi, T. Nagashima, Y. Nishikawa, R. Hayashi, M. Ohara, Y. Ito, T. Abe, K. Sakamoto, N. Fukunishi, and H. Ryuto: "Induction of glutinous rice mutants and characteristics of its progenies", 2nd Meeting of the Ion Beam Breeding Society, Wako, May (2005).

N. Ohtsubo, R. Aida, T. Abe, and S. Yoshida: "Modification of chrysanthemum by ion beam irradiation", 2nd Meeting of the Ion Beam Breeding Society, Wako, May (2005).

K. Furukawa, S. Kobayashi, K. Sakamoto, T. Ozaki, and T. Abe: "Mutation breeding of orchids by ion beam", 2nd Meeting of the Ion Beam Breeding Society, Wako, May (2005).

I. Honda, K. Kikuchi, S. Matsuo, M. Fukuda, H. Saito, T. Abe, and S. Yoshida: "Short internode and pericarp mutants of sweet pepper *Capsicum annuus* L. induced by heavy ion irradiation", 2nd Meeting of the Ion Beam Breeding Society, Wako, May (2005).

M. Tomita, T. Funayama, S. Wada, Y. Kobayashi, and T. Sakashita: "Imaging analysis of the mechanisms of low dose radiation-induced DNA double-strand break repair", 14th TIARA Research Review Meeting, (Takasaki Radiation Chemistry Research Establishment, JAERI), Takasaki, June (2005).

Y. Yamamoto, H. Saito, H. Ryuto, N. Fukunishi, S. Yoshida, and T. Abe: "Effective mutagenesis of Arabidopsis by heavy ion beam-irradiation", 17th International Botanical Congress, Vienna, Austria, July (2005).

H. Saito, Y. Hayashi, T. Kanaya, K. Suzuki, and T. Abe: "Sterile mutant of *Verbena hybrida* induced by heavy-ion beam irradiation and wild species *V. peruviana* exhibit self-incompatible phenotype", 17th International Botanical Congress, Vienna, Austria, July (2005).

C. Ikari, N. Shitsukawa, S. Shimada, T. Abe, K. Sakamoto, H. Saito, and K. Murai: "Einkorn wheat mutant, *mvp*, which shows maintained vegetative phase is caused by mutation of wheat *APETALA*1", 10th International Congress of SABRAO, (The Society for the Advancement of Breeding Researches in Asia and Oceania), Tsukuba, Aug. (2005).

C. Ikari, N. Shitsukawa, S. Shimada, T. Abe, K. Sakamoto, H. Saito, and K. Murai: "Einkorn wheat mutant, *mvp*, which shows maintained vegetative phase is caused by mutation of wheat *APETALA*1", 47th Symposium in 107th and 108th Congress of the Breeding Society of Japan, Tsukuba, Aug. (2005).

H. Ichida, T. Koba, T. Abe, and T. Matsuyama: "*Mesorhizobium loti* and *Bradyrhizobium japonicum* genome scanning by virtual image restriction landmark genome scanning (Vi-RLGS)", 15th Annual Meeting of Japanese Society of Plant Microbe Interactions, Takamatsu, Sept. (2005).

D. Saika, Y. Kitamoto, K. Matsuo, T. Tashiro, T. Takabe, T. Yoshimura, W. Sato, N. Takahashi, H. Haba, S. Enomoto, and A. Shinohara: "Development of online solvent extraction system with microchip", 2005 Annual Meeting on the Japan Society of Nuclear and Radiochemical Sciences and 49th Symposium on Radiochemistry, Kanazawa, Sept. (2005).

T. Takabe, Y. Kitamoto, D. Saika, K. Matsuo, T. Tashiro, T. Yoshimura, H. Haba, D. Kaji, and A. Shinohara: "Development of the gas-jet transport system for the superheavy element chemistry using the RIKEN AVF cyclotron", 2005 Annual Meeting on the Japan Society of Nuclear and Radiochemical Sciences and 49th Symposium on Radiochemistry, Kanazawa, Sept. (2005).

S. Kamataki, K. Morishita, H. Haba, and A. Yokoyama: "Distribution coefficients measured with non-carrier tracers of Zr-88 and Hf-175 on TBP-Resin in hydrochloric acid and nitric acid solutions", 2005 Annual Meeting on the Japan Society of Nuclear and Radiochemical Sciences and 49th Symposium on Radiochemistry, Kanazawa, Sept. (2005).

A. Toyoshima, H. Haba, K. Tsukada, M. Asai, K. Akiyama, S. Goto, Y. Ishii, W. Sato, K. Matsuo, D. Saika, Y. Kitamoto, A. Yokoyama, M. Sakama, Y. Oura, I. Nishinaka, T. Sato, T. Ichikawa, M. Hirata, S. Ichikawa, K. Sueki, A. Shinohara, H. Kudo, Y. Nagame, H. Nakahara, and M. Schaedel: "Fluoride complexation of rutherfordium", 2005 Annual Meeting on the Japan Society of Nuclear and Radiochemical Sciences and 49th Symposium on Radiochemistry, Kanazawa, Sept. (2005).

K. Washiyama, Y. Kanayama, H. Haba, S. Enomoto, and R. Amano: "Production and application of lead-203 (^{203}Pb) isotope for nuclear medicine", 2005 Annual Meeting on the Japan Society of Nuclear and Radiochemical Sciences and 49th Symposium on Radiochemistry, Kanazawa, Sept. (2005).

A. Toyoshima, H. Haba, K. Tsukada, K. Akiyama, M. Asai, Y. Ishii, Y. Tome, I. Nishinaka, T. Ichikawa, T. Sato, S. Ichikawa, Y. Nagame, W. Sato, K. Matsuo, Y. Kitamoto, T. Tashiro, A. Shinohara, T. Ikezawa, M. Sakamaki, S. Goto, H. Kudo, M. Arai, S. Kamataki, A. Yokoyama, Y. Oura, and K. Sueki: "Reversed-phase extraction chromatography of rutherfordium in the TBP-HCl system", 2005 Annual Meeting on the Japan Society of Nuclear and Radiochemical Sciences and 49th Symposium on Radiochemistry, Kanazawa, Sept. (2005).

Y. Kitamoto, D. Saika, K. Matsuo, T. Takabe, T. Tashiro, W. Sato, N. Takahashi, T. Yoshimura, H. Haba, S. Enomoto, T. Mitsugashira, and A. Shinohara: "Separation of the actinide elements by capillary electrophoresis and derivation of the ion radius", 2005 Annual Meeting on the Japan Society of Nuclear and Radiochemical Sciences and 49th Symposium on Radiochemistry, Kanazawa, Sept. (2005).

S. Motomura, S. Enomoto, H. Haba, Y. Gono, and Y. Yano: "Multitracer imaging by strip germanium telescope", 2nd Joint Meeting of the Nuclear Physics Divisions of the APS and JPS (Hawaii 2005), Maui, USA, Sept. (2005).

H. Haba: "Present status of the superheavy element chemistry in RIKEN", Scientific Meeting of the Kyoto University Research Reactor Institute, Osaka, Sept. (2005).

T. Abe: "Ion-beam irradiation on mutation breeding for ornamental plants", 5th Technical Seminar on Accelerator Application, (Radiation Application Development Association), Kagoshima, Oct. (2005).

Y. Kobayashi, Y. Tsuruoka, K. Kubo, H. Nonaka, Y. Yamada, Y. Sakai, H. Shoji, W. Sato, A. Shinohara, Y. Watanabe, and H. Matsue: "Mossbauer spectroscopic study of 57Fe species produced by 56Fe(n,gamma)57Fe Reaction in iron disulfide", Asia-Pacific Symposium on Radiochemistry 2005 (APSORC-05), Beijing, China, Oct. (2005).

H. Saito, Y. Hayashi, H. Ryuto, N. Fukunishi, T. Abe, T. Kanaya, M. Sugiyama, K. Suzuki, T. Terakawa, N. Ohtsubo, and R. Aida: "Induction of sterile mutants by heavy-ion beam irradiation in horticultural plants", 11th Radiation Process Symposium, (Radiation Application Development Association), Tokyo, Dec. (2005).

Y. Kobayashi, H. Nonaka, J. Miyazaki, K. Kubo, H. Ueno, A. Yoshimi, H. Miyoshi, D. Kameda, K. Shimada, D. Nagae, and Y. Yamada: "^{57}Mn implantation Mössbauer study into solid oxygen", International Chemical Congress of Pacific Basin Societies (PACIFICHEM 2005), Honolulu, USA, Dec. (2005).

K. Kubo, Y. Tsuruoka, Y. Kobayashi, Y. Yamada, Y. Sakai, H. Shoji, W. Sato, Y. Watanabe, and H. Matsue: "Mössbauer Spectroscopic Study of the Chemical Effects of Neutron Capture Reaction in Iron Disulfide", International Chemical Congress of Pacific Basin Societies (PACIFICHEM 2005), Honolulu, USA, Dec. (2005).

5. Material Analysis

T. Kuribayashi, K. Ushida, S. Kashiwagi, M. Kawaguchi, R. Kuroda, H. Hirama, Y. Hama, and M. Washio: "Development of picosecond pulse radiolysis system at Waseda University", 47th Symposium on Radiation Chemistry, (Japanese Society of Radiation Chemistry), Sapporo, Oct. (2004).

6. RIKEN-BNL Collaboration

K. Hasuko, M. Grosse-Perdekamp, J. S. Lange, A. Ogawa, and V. Siegle: "Future Measurements of Spin Dependent Fragmentation Functions in e+e- Annihilation at Belle", 8th Conference on the Intersections of Particle and Nuclear Physics (CIPANP 2003), New York, USA, May (2003).

N. Ishii and H. Suganuma: "Properties of Thermal Glueballs", International Conference on Color Confinement and Hadrons in Quantum Chromodynamics: Confinement 2003, (International Research Center of Science (IRCS) and RIKEN), Wako, July (2003).

K. Hashimoto and T. Izubuchi: "Static quark potential from two flavor dynamical domain-wall QCD", 59th Annual Meeting of the Physical Society of Japan, Fukuoka, Mar. (2004).

K. Sudo and M. Hirai: "Theoretical prospects on π^0 double spin asymmetry at RHIC", 59th Annual Meeting of the Physical Society of Japan, Fukuoka, Mar. (2004).

K. Sudo and M. Hirai: "Comment on π^0 double spin asymmetry at RHIC", RIKEN-TODAI Mini-Workshop on "Topics in Hadron Physics at RHIC", Wako, Mar. (2004).

K. Sudo and M. Hirai: "Effects of $\Delta g(x)$ on the π^0 spin asymmetry at RHIC", 12th International Workshop on Deep Inelastic Scattering (DIS2004), High Tatras, Slovakia, Apr. (2004).

T. Izubuchi: "Hadron Spectrum and Decay Constants from $N_F = 2$ Domain-Wall QCD", LATTICE 2004: 22nd International Symposium on Lattice Field Theory, (Fermi National Accelerator Laboratory), Batavia, USA, June (2004).

K. Hashimoto and T. Izubuchi: "Static $\bar{Q}$-Q Potential from N_f=2 Dynamical Domain-Wall QCD", LATTICE 2004: 22nd International Symposium on Lattice Field Theory, (Fermi National Accelerator Laboratory), Batavia, USA, June (2004).

K. Hashimoto and T. Izubuchi: "Analysis of Static Quark Potential in Domain-Wall QCD", 2004 Autumn Meeting of the Physical Society of Japan, Aomori and Kochi, Sept. (2004).

K. Sudo and H. Yokoya: "Charm-associated W boson production at RHIC and polarized s quark distribution", 2004 Autumn Meeting of the Physical Society of Japan, Aomori and Kochi, Sept. (2004).

K. Okada and PHENIX Collaboratio: "Measurement of prompt photon in $\sqrt{s} = 200\,\mathrm{GeV}$ pp collisions", 2004 Autumn Meeting of the Physical Society of Japan, Aomori and Kochi, Sept. (2004).

M. Togawa and PHENIX Collaboratio: "Measurement of single electron spectrum in $\sqrt{s} = 200\,\mathrm{GeV}$ p-p collisions at RHIC-PHENIX", 2004 Autumn Meeting of the Physical Society of Japan, Aomori and Kochi, Sept. (2004).

H. Okada, I. Alekseev, N. Saito, and D. Svirida: "Measurement of the analyzing power in pp elastic scattering in the peak CNI region at RHIC", 2004 Autumn Meeting of the Physical Society of Japan, Aomori and Kochi, Sept. (2004).

O. Jinnouchi, I. G. Alekseev, A. Bravar, G. Bunce, S. Dhawan, H. Huang, G. Igo, V. P. Kanavets, K. Kurita, H. Okada, H. Spinka, N. Saito, and J. Wood: "Measurement of the analyzing power of proton-carbon elastic scattering in the CNI region at RHIC", 2004 Autumn Meeting of the Physical Society of Japan, Aomori and Kochi, Sept. (2004).

Y. Goto: "Single transverse-spin asymmetry measurement in neutral pion and charged hadron production at PHENIX", 2004 Autumn Meeting of the Physical Society of Japan, Aomori and Kochi, Sept. (2004).

T. Izubuchi: "Lattice QCD with dynamical domain wall fermions", Lattice QCD simulations via International Research Network (ILFT04), (CCS, University of Tsukuba and KEK), Izu, Sept. (2004).

K. Okada and PHENIX Collaboratio: "Measurement of prompt photon in $\sqrt{s} = 200\,\mathrm{GeV}$ pp collisions", 16th International Spin Physics Symposium (SPIN 2004), (ICTP), Trieste, Italy, Oct. (2004).

S. Kojima, H. Tatsukawa, Y. Suzuki, M. Okuno, and M. A. Zern: "Potential role of polyamines as regulators of blood vessel formation and hepatic apoptosis via controling activity of tissue transglutaminase", 2004 International Conference on Polyamines: Functions and Clinical Application, Kisarazu, Nov.–Dec. (2004).

T. Izubuchi: "The electromagnetic splitting and ${g_\mu}^{-2}$ light-by-light contribution", Workshop on the Physics Programme of the RBRC and UKQCD QCDOC Machines, (RIKEN), Upton, USA, Nov. (2004).

K. Iida: "Magnetic vortex in color-flavor locked quark matter", 60th Annual Meeting of Physical Society of Japan, Noda, Mar. (2005).

M. Ohtani, T. Hatsuda, and S. Digal: "Phase transitions of color superconductor in the Ginzburg-Landau approach on the lattice", 60th Annual Meeting of Physical Society of Japan, Noda, Mar. (2005).

H. Kawamura, J. Kodaira, H. Shimizu, and K. Tanaka: "Q_T resummation in transversely polarized Drell-Yan process", International Conference on QCD and Hadronic Physics, (Pekin University), Beijing, China, June (2005).

H. Kawamura, J. Kodaira, H. Shimizu, and K. Tanaka: "Q_T resummation in transversely polarized Drell-Yan process", 5th Circum-Pan-Pacific Symposium on High Energy Spin Physics (SPIN 2005), (Tokyo Institute of Technology), Tokyo, July (2005).

M. Ohtani, T. Hatsuda, and S. Digal: "Thermal phase transition of color superconductivity with Ginzburg-Landau effective action on the lattice", Workshop on Extreme QCD, (University of Wales, Swansea),

Swansea, UK, Aug. (2005).

K. Iida: "Feedback effects on the pairing interaction in color superconductors near the transition temperature", 2nd Joint Meeting of the Nuclear Physics Divisions of the APS and JPS (Hawaii 2005), Maui, USA, Sept. (2005).

M. Ohtani, A. Iwazaki, O. Morimatsu, and T. Nishikawa: "Vortex excitation and quark spectrum in color ferromagnetic state in cold dense matter", 2nd Joint Meeting of the Nuclear Physics Divisions of the APS and JPS (Hawaii 2005), Maui, USA, Sept. (2005).

K. Iida: "Phase transitions in dense matter and quark stars", 2005 Fall Annual Meeting of Astronomy Society of Japan, Sapporo, Oct. (2005).

H. Kawamura, J. Kodaira, H. Shimizu, and K. Tanaka: "Q_T resummation in transversely polarized Drell-Yan process", 7th International Symposium on Radiative Corrections, (Sokendai and KEK), Hayama-machi, Kanagawa Pref., Oct. (2005).

K. Iida: "Phase transitions in dense matter and quark stars", Particle-, Nuclear-, and Astro-Physics Colloquium, (Tokyo Institute of Technology), Tokyo, Oct. (2005).

M. Ohtani, S. Digal, and T. Hatsuda: "Thermal phase transition of color superconductivity with Ginzburg-Landau action on the lattice", Japan-Korea Mini-Workshop on QCD and hidden local symmetry in matter under extreme conditions, (Nagoya University), Nagoya, Nov. (2005).

IX. LIST OF SYMPOSIA

(Jan.–Dec. 2005)

1) Studies on Condensed Matter Physics, Atomic Physics, Hyperfine Interactions and Biomedical Sciences Using RIKEN Accelerators
28 Jan., Wako, Atomic Physics Lab., RIKEN

2) International Symposium on Correlation Dynamics in Nuclei (CDN05)
31 Jan.–4 Feb., Tokyo, Heavy Ion Nuclear Physics Lab., RIKEN

3) International Workshop on "Chiral Restoration in Nuclear Medium"
15–17 Feb., Wako, Advanced Meson Science Lab., RIKEN

4) Classical and Quantum Aspects of the Color Glass Condensate
7–11 Mar., New York, USA, RBRC, RIKEN

5) Jet Correlations at RHIC
10–11 Mar., New York, USA, RBRC, RIKEN

6) Workshop on Physics with Ultra Slow Antiproton Beams
14–16 Mar., Wako, Atomic Physics Lab., RIKEN

7) RIKEN One-day Workshop on Breakup Reactions
15 Apr., Wako, Heavy Ion Nucl. Phys. Lab., RIKEN

8) Particles and Nuclei, the Playing Fields of Physics
24 Apr., Tokyo, Radiation Lab., RIKEN

9) Detector Workshop
11 May, Wako, Radiation Lab., RIKEN

10) RIKEN RIBF International Workshop "Collective Motions in Unstable Nuclei: Experiments vs. Theories"
24–26 May, Wako, Heavy Ion Nucl. Phys. Lab., RIKEN

11) RBRC QCDOC Computer Dedication and Symposium
1–3 June, New York, USA, RBRC, RIKEN

12) RIKEN Cluster Project Status Report
3 June, Wako, Heavy Ion Nucl. Phys. Lab., RIKEN

13) Spin Fest Workshop At Nikko
17–18 Aug., Nikko, Radiation Lab., RIKEN

14) RIBF Workshop on Study of Nuclear Spectroscopy with Stopped/Slow RI Beam
9 Sep., Wako, Applied Nuclear Physics Lab., and Atomic Physics Lab., RIKEN

15) Mini Workshop on "Pair Correlation in Unstable Nuclei"
12–13 Sep., Wako, Heavy Ion Nucl. Phys. Lab., RIKEN

16) Single Spin Asymmetries
27–29 Sep., New York, USA, RBRC, RIKEN

17) Mini Workshop on "Two-Neutron Correlation in Loosely Bound Nucleus"
19–20 Oct., Wako, RI Physics Lab., RIKEN

18) International Symposium on Origin of Matter and Evolution of Galaxies (OMEG05)
8–11 Nov., Tokyo, Heavy Ion Nuclear Physics Lab., RIKEN

19) International Symposium on the 15 Years of Spectrometer SMART and New Turn to RIBF
11–12 Nov., Wako, Heavy Ion Nuclear Physics Lab., RIKEN

20) 11th International Workshop on Polarized Sources and Targets
14–17 Nov., Tokyo, Heavy Ion Nuclear Physics Lab., Applied Nuclear Physics Lab., and Atomic Physics Lab., RIKEN and CNS

21) RHIC-SPIN-J Physics Discussion No.60
3 Dec., Wako, Radiation Lab., RIKEN

22) RIKEN-CNS RIBF International Workshop "Correlation and Condensation: New Features in Loosely Bound and Unbound Nuclear States"
8–10 Dec., Wako, Heavy Ion Nucl. Phys. Lab., RIKEN

23) Odderon Searches at RHIC
12 Dec., New York, USA, RBRC, RIKEN

24) Heavy Flavor Productions & Hot/Dense Quark Matter
15 Dec., New York, USA, RBRC, RIKEN

25) Workshop on Nuclear Physics Collaboration between Germany and Japan
16–17 Dec., Wako and Tokyo, Heavy Ion Nuclear Physics Lab., RIKEN

X. LIST OF SEMINARS

(Jan.–Dec. 2005)

RIKEN Nuclear Physics Monthly Colloquium

1) T. Nagae, KEK (Tsukuba), 17 May
"Nuclear physics at J-PARC"

2) S. A. Bass, Duke University and RBRC (USA), 7 June
"The quest for the quark-gluon-plasma"

3) P. Kienle, Technische Universität München (Germany), 21 June
"Pions in nuclei, a probe of chiral restoration"

4) H. Horiuchi, Kyoto University (Kyoto), 19 July
"Diverseness of nuclear structure"

5) H. En'yo, RIKEN (Wako), 1 Nov.
"In the quest of proton spin mystery"

6) G. Bollen, MSU (USA), 21 Nov.
"Thermalized beams from projectile fragmentation at the NSCL – First experiments and future developments"

7) K. Makishima, University of Tokyo (Tokyo), 22 Dec.
"Search for nucleosynthesis in the cosmos"

8) K. Masuda, Nagoya University (Nagoya), 22 Dec.
"Study of 14C abundance in Yaku-Sugi cedar by AMS method and clues to solar activity and super novae"

Nuclear Physics Seminar

1) Y. Ishimaru, Ochanomizu University (Tokyo), 20 Jan.
"Trace of r-process elements recorded in Galaxy formation stage"

2) I. Talmi, Weizmann Institute of Science (Israel), 9 Feb.
"Structure of light neutron righ nuclei"

3) L. Guo, Ibaraki University (Mito), 10 Feb.
"To what extent does the self-consistent mean-field exist?"

4) P. Ring, Technische Universität München (Germany), 28 Feb.
"Collective modes and isospin properties of nuclei far from stability"

5) A. E. L. Dieperink, Kernfysisch Versneller Instituut (The Netherland), 2 Mar.
"Nuclear physics aspects of neutron stars: Equation of state and thermal evolution"

6) T. Otuki, Tohoku University (Sendai), 18 Mar.
"Electron-capture decay rate of ^{7}Be encapsulated in C_{60} cages"

7) A. M. Bernstein, MIT (USA), 31 Mar.
"The Pi Meson: From Yukawa to QCD"

8) A. M. Mukhamedzhanov, Cyclotron Institute, Texas A&M University (USA), 14 Apr.
"Can spectroscopic information be extracted from transfer reactions?"

9) V. Y. Denisov, Institute for Nuclear Research (Ukraine), 10 May
"Nucleus-nucleus potential and superheavy element production"

10) Zs. Dombrádi, Institute of Nuclear Research (ATOMKI) (Hungary), 20 May
"In-beam gamma ray spectroscopy close to the neutron dripline"

11) D. T. Khoa, Institute for Nuclear Science & Technique, VAEC (Vietnam), 23 May
"Microscopic study of the quasi-elastic nuclear scattering"

12) M. Chiu, University of Illinois (USA), 11 July
"Sivers Measurement using back to back dihadrons"

13) D. Kawall, RBRC (USA), 20 July
"Testing fundamental symmetries with molecules"

14) K. N. Barish, UCR (USA), 20 July
"High p_T measurements at RHIC"

15) Z. Li, BNL (USA), 25 July
"Si detector development and radiation hardness for nuclear and high energy physics experiments at BNL and around the world"

16) T. Mibe, Ohio University (USA), 25 July
"High statistics search for θ + in $\gamma + d \rightarrow K+ + K- + p(n)$ reaction"

17) H. Okada, Kyoto University (Kyoto), 1 Aug.
"Absolute polarimetry in RHIC – How to measure the beam polarization? What is the principle?"

18) I. Nakagawa, RIKEN (Wako), 1 Aug.
"Silicon-tungsten calorimeter for the forward direction in the PHENIX experiment at RHIC"

19) A. Kral, Czech Technical University in Prague (Czech), 8 Aug.
"Introduction to grid computing"

20) K. Aoki and K. Shoji, Kyoto University (Kyoto), 8 Aug.
"Trigger upgrade for high momentum muons to study the spin-flavor structure of the proton at RHIC-PHENIX"

21) T. Liska, Czech Technical University in Prague (Czech), 22 Aug.
"Massive data production on distributed computation environment"

RIBF Nuclear Physics Seminar

1) J. Terasaki, RIKEN (Wako), 26 Oct.
"Neutron number dependence of strength functions and incompressibility"

2) T. Noro, Kyushu University (Fukuoka), 2 Nov.
"Nuclear medium effects studied by (p, 2p) reaction"

3) T. Kobayashi, Tohoku University (Sendai), 2 Nov.
"(p, 2p) reaction from carbon isotopes"

4) M. Smith, Oak Ridge National Laboratory (USA), 14 Nov.
"The rare isotope accelerator – Future U.S. facility for probing nuclei and exploding stars"

5) S. Amari, University of Washington (USA), 15 Nov.
"Nuclear synthesis recorded in meteorolite"

6) A. A. Ogloblin, Kurchatov Institute (Russia), 29 Nov.
"Some new points of interest in physics of exotic proton-rich nuclei"

7) R. Seki, California State Univ. Northridge/ Caltech (USA), 6 Dec.
"Quantum Monte Carlo Lattice calculation of thermal properties of low-density neutron matter"

8) P. Moeller, LANL (USA), 15 Dec.
"Nuclear shape isomers, shape coexistence, and nuclear ground state reflection and axial shape asymmetries"

9) G. C. Hillhouse, University of Stellenbosch (South Africa), 15 Dec.
"Relativistic predictions of polarization phenomena in exclusive proton-induced proton-knockout reactions"

Radiation Lab.

1) Y. Akaishi, KEK (Tsukuba), 18 Jan.
"Stracture and production of strange tribaryon"

2) T. Doi, RBRC, 29 Mar.
"Pentaquark baryon from QCD sum rule/lattice QCD"

3) Y. Hatta, RBRC, 29 Mar.
"Perturbative odderon in the color glass condensate"

4) K. Kondo, Waseda University (Tokyo)/Tukuba University (Tsukuba), 12 Apr.
"Topics on top quark: discovery. DLM. outlook"

5) R. Seidl, University of Illinois (USA), 20 June
"Measurements of chiral-odd fragmentation functions at Belle"

6) G. Schnell, Tokyo Institute of Technology (Tokyo), 20 June
"Transverse-spin physics at HERMES"

Atomic Physics Lab.

1) K. Omori, Institute for Molecular Science (Okazaki), 22 Feb.
"Phase sensitive memory in molecular wave packets: How to READ and WRITE with molecules"

2) N. Cherepkov, State University of Aerospace Instrumentation (Russia), 25 Feb.
"Non-dipole effects in photoionization of atoms at low energies"

3) K. Wendt, Johannes Gutenberg University Mainz (Germany), 30 Mar.
"Laser and ion source development for production and spectroscopy of exotic species"

4) F. Vedel, Universite de Provence (France), 19 Apr.
"Recent results with a single trapped Ca^+ ion"

5) Z.-C. Yan, University of New Brunswick (Canada), 10 June
"High-precision studies of few-body coulombic systems"

6) B. D. DePaola, Kansas State University (USA),

10 June
"Measurement of population dynamics in coherent excitation"

7) T. Wang, Lanzhou University (China), 12 July
"Approaches on the study of highly charged ion and solid surface interaction"

8) K. Zrost, Max-Plank Institute for Nuclear Physics (Germany), 12 July
"Interaction of intense optical few cycle pulses with atoms"

9) L. Tribedi, Tata Institute of Fundamental Research (India), 19 Aug.
"Some aspects of the interference effect in fact ion collisions with H2"

10) H. Schmidt-Boecking, University Frankfurt (Germany), 22 Aug.
"The COLTRIMS reaction microscope – The tool to explore the secrets of inner atomic and molecular dynamics"

11) J. Burgdoefer, Vienna University of Technology (Austria), 13 Sep.
"From hollow atoms to nanobeams"

12) T. Koshikawa, Osaka Electro-Communication University (Neyagawa), 16 Sep.
"New trend of surface research by using LEEM and PEEM"

13) K. Sakimoto, ISAS, JAXA (Sagamihara), 30 Sep.
"Collisions of antiprotons with atoms and molecules"

14) R. Schuch, Stockholm University (Sweden), 4 Oct.
"The GSI future facility 'FAIR' and atomic physics in strong fields"

15) I. Izosimov, V. G. Khlopin Radium Institute (Russia), 4 Oct.
"Applications of lasers in chemistry and physics in khlopin radium"

16) J. Sunchan, IPNS, KEK (Tsukuba), 14 Oct.
"Study on the diffusion of Li in solids using short-lived radioactive ion beams"

17) H. Winter, Humboldt-University of Berlin (Germany), 2 Dec.
"Studies on ultrathin films using grazing ion scattering"

Advanced Meson Science Lab.

1) T. Ito, University of Tennessee (USA), 6 Jan.
"Basic physics using a ultra-slow neutron"

2) K. Morita, RIKEN (Wako), 17 Jan.
"The newly observed 113th element"

3) H. Ejiri, Osaka University (Osaka)/ICU (Mitaka), 31 Jan.
"Neutrino masses by bb decays and MOON (Mo Observatory Of Neutrinos)"

4) P. Kienle, Technische Universität München (Germany), 28 Mar.
"Precision spectroscopy of exotic atoms and mesonic nuclear states"

5) K. Hachitani, Chiba University (Chiba), 4 Apr.
"Novel properties in filled skutterudite systems studied by magnetic resonance"

6) H. Nemura, RIKEN (Wako), 18 Apr.
"Study of strange few-body systems"

7) Y. Kobayashi, RIKEN (Wako), 30 May
"The research of material sciences by use of the in-beam Mossbauer spectroscopy"

8) K. S. Myint, Mandalay University (Myanmar), 20 July
"Structure and decay of tightly bound K^-NN three – body kaonic nucleus

9) H. Sakai, University of Tokyo (Tokyo), 5 Sep.
"Einstein was wrong? – Entangled two-proton spin – correlation experiment for a test of Bell's inequality (a test of EPR paradox)"

10) M. Iio, RIKEN (Wako), 4 Nov.
"Development of the polarized deuterium target for spin dependent nuclear fusion experiment in the low energy region"

11) H. Ohnishi, RIKEN (Wako), 21 Nov.
"Study of the dense matter created in reletivistic heavy ion collisions"

12) H. Nemura, RIKEN (Wako), 5 Dec.
"Pentaquark state of Λ (1405)"

RIBF Program

1) H. Geissel, GSI (Germany), 27 Apr.
"FAIR project at GSI"

2) L. Stingelin, PSI (Switzerland), 9 June

"Beam-cavity interactions in high power cyclotrons"

3) J. Beyer, Physikalisch-Technische Bundesanstalt Berlin (PTB) (Germany), 8 Aug.
"Concept for a CCC-beam current monitor for the metrology light source of PTB"

RIKEN BNL Research Center

1) F. Yuan , RBRC (USA), 13 Jan.
"Understanding single spin asymmetry in QCD"

2) C. Kouvaris, MIT (USA), 14 Jan.
"A hot bottle of water for aging neutron stars"

3) M. Golterman, San Francisco State University (USA), 18 Jan.
"Before sailing on a domain-wall sea"

4) J. Ferrandis, BNL (USA), 19 Jan.
"Supersymmetry breaking as the origin of flavor"

5) Y. Shamir, Tel-Aviv University (Israel), 19 Jan.
"Locality of the staggered-fermion determinant: renormalization-group approach"

6) T. Lappi, Helsinki (Finland), 21 Jan.
"Particle production in the classical field model for heavy ion collisions"

7) R. S. Longacre, BNL (USA), 21 Jan.
"Bubble model for central events in AuAu collisions at RHIC"

8) A. Kagan, FNAL (USA), 26 Jan.
"$e^+e^- \rightarrow$ M1 M2 and annihilation in B decays"

9) Y. Hatta, RBRC (USA), 27 Jan.
"Perturbative odderon in the color glass condensate"

10) H. Nastase, Brown University (USA), 28 Jan.
"Black hole production, the Froissart bound, the soft pomeron from AdS-CFT"

11) N. Brambilla, University of Milano (Itary), 31 Jan.
"Nonrelativistic effective field theories of QCD"

12) D. Rainwater, University of Rochester (USA), 2 Feb.
"Pseudo-axions in little higgs models"

13) M. Forbes, MIT (USA), 3 Feb.
"Aspects of high density QCD: gapless superconductivity and Kaon condensation"

14) D. Toublan, University of Illinois (USA), 4 Feb.
"QCD at small chemical potential"

15) T. Plehn, Max-Planck Institute for Physics (Germany), 9 Feb.
"Theory tools for supersymmetry at the LHC"

16) A. Gal, Hebrew University (Israel), 11 Feb.
"Traces of θ^+ (1540) pentaquark in K+-nucleus phenomenology"

17) B. Nelson, University of Pennsylvania (USA), 16 Feb.
"Massive neutrinos and string theory"

18) T. Ikeda, RBRC (USA), 17 Feb.
"Balitsky-Kovchegov equation and the Froissart bound"

19) D. Boer, Vrije Universiteit Amsterdam (The Netherlands), 18 Feb.
"Azimuthal asymmetries from hadronic versus QCD vacuum effects"

20) O. Mena, FNAL (USA), 23 Feb.
"Cosmic neutrino spectroscopy and the early universe"

21) T. Sugihara, RBRC (USA), 24 Feb.
"Real-time simulation of quantum states with density matrix RG"

22) T. Kinoshita, Cornell University (USA), 2 Mar.
"Theory of lepton g-2: recent improvement of QED terms"

23) T. Kaneko, KEK (Tsukuba)/BNL (USA), 3 Mar.
"Light hadron spectroscopy from CP-PACS/ JLQCD"

24) B. Holstein, University of Amherst (USA), 4 Mar.
"Hadronic parity violation"

25) I. Stewart, MIT (USA), 9 Mar.
"Factorization in b-decays and the soft-collinear effective theory"

26) H. Abuki, YITP, Kyoto University (Kyoto), 10 Mar.
"Crossover from BCS to Bose-Einstein condensation in the relativistic superfluid: boson formation above the critical temperature"

27) K. Ohnishi, YITP, Kyoto University (Kyoto), 17 Mar.
"Non-equilibrium critical phenomena in the QCD phase transitions"

28) F. Petriello, Johns Hopkins University (USA), 23 Mar.
"High precision QCD at hadron colliders"

29) G. Dunne, University of Connecticut (USA), 24 Mar.
"Mass dependence of the fermion determinant in an instanton background"

30) H. Baer, Florida State University (USA), 30 Mar.
"Direct, indirect and collider searches for neutralino dark matter in SUSY models with non-universality"

31) M. Perelstein, Cornell University (USA), 6 Apr.
"Two topics in cosmoparticle physics"

32) N. Itoh, Sophia University (Tokyo), 7 Apr.
"Relativistic corrections to the Sunyaev-Zeldovich Effect for cluster of galaxies"

33) R. Kitano, IAS (USA), 13 Apr.
"Scenarios for supersymmetry cosmology and phenomenology"

34) K. Tuchin, BNL (USA), 14 Apr.
"Black holes at RHIC?"

35) D. Morrissey, University of Chicago (USA), 20 Apr.
"Dark matter and a baryon asymmetry from supersymmetry"

36) T. Doi, RBRC (USA), 21 Apr.
"Pentaquark baryon in anisotropic lattice QCD"

37) I. Stamatescu, University Heidelberg (Germany), 4 May
"Learning from incomplete information and the mathematical structure behind it"

38) K. Fukushima, RBRC (USA), 5 May
"Recent problems in color superconductivity"

39) G. Salam, University of Paris VI (France), 19 May
"Impact of higher orders in the high-energy limit of QCD"

40) A. Freitas, FNAL (USA), 25 May
"Exploring supersymmetric dark matter in the stop co-annihilation region at colliders"

41) B. Sinha, Saha Institute (India), 27 May
"The changing panorama of physical sciences – The indian kaleidoscope"

42) F. Zantow, BNL (USA), 16 June
"The QGP phase, the coupling, Debye-screening and quarkonium binding"

43) H. Koura, ORNL (USA)/JAERI (Tsukuba), 23 June
"Properties of unstable nuclei predicted by nuclear mass formula: superheavy nuclei and r-process nucleosynthesis"

44) A. Baltz, BNL/RBRC (USA), 30 June
"e^+e^- pairs to all orders in $Z\alpha$: SPS and RHIC data; b = 0 limit"

45) S. Kretzer, BNL/RBRC (USA), 7 July
"Fragmentation functions: Fit update & inclusion of masses"

46) I. V. Heide, Bielefeld (Germany), 8 July
"Pion form-factors from the lattice QCD"

47) K. Agashe, John Hopkins University (USA), 13 July
"Warped compactifications: Flavor, unification and dark matter"

48) S. Jeon, McGill (Canada), 15 July
"Charge transfer fluctuations as a QGP signal"

49) T. Matsuura, University of Tokyo (Tokyo), 21 July
"Color superconductivity in Ginzburg-Landau approach"

50) G. Nayak, SUNY (USA), 22 July
"Soft gluon production from constant chromo-electric field at one loop level via Schwinger mechanism"

51) A. Patel, Banglore (India), 10 Aug.
"Large-N QCD at strong transverse gauge coupling"

52) M. Strikman, Penn State University (USA), 18 Aug.
"Probing small x QCD in ultaperipheral collisions at LHC"

53) T. Falter, BNL (USA), 19 Aug.
"Hadron attenuation in nuclear DIS and HIC"

54) L. Frankfurt, Tel Aviv University (Israel), 25 Aug.
"On the critical phenomena in small x physics"

55) Y. Akiba, RBRC (USA), 30 Aug.
"News from quark matter (I): Perspectives from PHENIX and STAR speakers"

56) J. Dunlop, BNL (USA), 30 Aug.
"News from quark matter (I): Perspectives from PHENIX and STAR speakers"

57) Y. Kovchegov, Ohio State University (USA), 30 Aug.
"Can thermalization be derived from Feynman diagrams?"

58) T. Yamazaki, RBRC (USA), 8 Sep.
"$\Delta I = 3/2$ kaon weak matrix elements with nonzero total momentum"

59) J. Laiho, FNAL (USA), 14 Sep.
"Staggered chiral perturbation theory and heavy light form factors"

60) T. Umeda, BNL (USA), 15 Sep.
"Study of charmonia at finite temperature in quenched lattice QCD"

61) E. Leader, Imperial College (UK), 21 Sep.
"Higher twist and positivity constraints in polarized deep inelastic scattering"

62) J. Jia, Columbia University (USA), 23 Sep.
"Systematic study of back to back jets in PHENIX"

63) T. Tait, ANL (USA), 28 Sep.
"Exploring warped space"

64) A. Rebhan, Vienna University of Technology (Austria), 30 Sep.
"Quark-gluon plasma instabilities in the hard-loop approximation"

65) S. Dutta, University of Delhi (India), 5 Oct.
"Measurement of higgs gauge boson couplings at NLC"

66) J. Bartels, University Hamburg (Germany), 6 Oct.
"On the Pomeranchuk singularity and vector boson reggeization in electroweak theory"

67) P. Levai, KFKI Research Institute for Particle and Nuclear Physics (RMKI) (Hungary), 6 Oct.
"Molecular dynamics simulation of strongly interacting quark matter"

68) J. Kotanski, Jagiellonian University (Poland), 7 Oct.
"Reggeized gluon states and anomalous dimensions in QCD"

69) S. Chang, New York University (USA), 12 Oct.
"Higgs limits with a new standard model singlet"

70) A. Dumitru, Frankfurt University, 13 Oct.
"Instabilities in an anistropic quark-gluon plasma"

71) S. Leupold, University of Giessen (Germany), 14 Oct.
"Weinberg sum rules, four-quark condensates and chiral restoration"

72) R. Dermisek, IAS (USA), 19 Oct.
"Escaping large fine tuning and little hierarchy problems in NMSSM"

73) U. Maor, Tel Aviv University (Israel), 20 Oct.
"Gap survival probabilities and the fate of diffraction at exceedingly high energies"

74) F. Gelis, CEA/SPhT (France), 21 Oct.
"High density effects on quark production in pA and AA collisions"

75) S. Bar-Shalom, Technion (Israel), 26 Oct.
"Massive neutrinos in a grounds-up approach"

76) W. Kinney, Buffalo, SUNY (USA), 28 Oct.
"Inflation in the age of WMAP"

77) E. Lunghi, FNAL (USA), 2 Nov.
"B $\rightarrow$ Xs l l: status, phenomenology and implications for SUSY"

78) C. Korthals-Altes, University Marseile (USA), 3 Nov.
"Quasi-particles and k-tensions in hot QCD"

79) T. Hirano, Columbia University (USA), 4 Nov.
"Perfect fluidity of sQGP core and dissipative hadronic corona"

80) M. Wingate, University of Washington (USA), 9 Nov.
"Field theoretic methods for nonrelativistic fermion gases"

81) K. Okada, RBRC (USA), 10 Nov.
"Direct photon production in p + p collisions at sqrt(s) = 200 GeV"

82) H. Davoudiasl, University of Wisconsin (USA), 16 Nov.
"Detecting solar axions using Earth's magnetic field"

83) P. Levai, KFKI Research Institute for Particle and Nuclear Physics (RMKI) (Hungary), 17 Nov.

"Molecular dynamics simulation of strongly interacting quark matter"

84) S. Sasaki, RBRC (USA), 18 Nov.
"Spin physics from the lattice"

85) A. Ipp, ECT, Trento (Itary), 18 Nov.
"Thermodynamics of large N_f QCD at finite chemical potential for weak and strong couplings"

86) G. Perez, LBNL (USA), 30 Nov.
"Observing dark energy via neutrino detectors"

87) D. Teaney, SUNY (USA), 1 Dec.
"Heay quark diffusion and lattice correlators"

88) M. Pepe, University of Bern (Switerland), 2 Dec.
"The problem of confinement in lattice gauge theory"

89) B. Lillie, University of Chicago (USA), 7 Dec., "Off-the-wall higgs in the randall-sundrum model"

90) K. Tuchin, Iowa State University (USA), 8 Dec.
"Thermalization of color glass condensate"

91) E. Ponton, Columbia University (USA), 9 Dec.
"Resonances from two universal extra dimensions"

92) J. Ruppert, Duke University (USA), 9 Dec.
"Mach cones in an evolving medium"

XI. LIST OF PERSONNEL

Accelerator Research Program, RIKEN Frontier Research System

Program Director
Yasushige YANO

Supervisor for Accelerator Research Program
Hiromichi KAMITSUBO

Members
Hiromu OKAZOE[*1] Atsushi YAMANAKA[*2]

[*1] Temporary Employee
[*2] Visiting Contract Officer

Visiting Members
Masayasu ISHIHARA

Accelerator Operation Group

Group Director
Masayuki KASE

Members
Mieko KOGURE

Visiting Members
Dung NGUYEN (INST, Vietnam)

RILAC Team

Team Leader
Masayuki KASE

Members
Eiji IKEZAWA

AVF Team

Team Leader
Masayuki KASE

Members
Tadashi KAGEYAMA

RRC Team

Team Leader
Masayuki KASE

Members
Naohito INABE

SRC Team

Team Leader
Masayuki KASE

Members
Hiroki OKUNO

Beam Technology Development Team

Team Leader

Masayuki KASE

Members

Kiyoshi OGIWARA
Keiko KUMAGAI
Tamaki WATANABE
Sachiko ITO
Tadashi FUJINAWA[*2]
Shigeru YOKOUCHI[*2]
Makoto NAGASE
Masaki FUJIMAKI
Nobuhisa FUKUNISHI
Hiromichi RYUTO[*1]
Misaki KOBAYASHI-KOMIYAMA[*2]
Jiro FUJITA[*3]

[*1] Contract Researcher
[*2] Contract Technical Scientist
[*3] Temporary Employee

Visiting Members

Hiroaki ASAI (JAXA)
Toshiya CHIBA
Masahiko HAYASHI (JAXA)
Masatake HEMMI
Yoshiya IIDE (JAXA)
Naomi IKEDA (JAXA)
Chihiro KAMEZAWA (JAXA)
Kazuie KIMURA
Masanori KOSHIMIZU (Grad. Sch. Eng., Tohoku Univ.)
Satoshi KUBOYAMA (JAXA)
Masahiko MIDORIKAWA (JAXA)
Hideo MIKAMI (SHI Accel. Serv. Ltd.)
Yoshitoshi MIYAZAWA
Hideharu OHIRA (JAXA)
Katsumi OKA (JAXA)
Osamu OKUDAIRA (Adv. Res. Inst. Sci. Eng., Waseda Univ.)
Hiromitsu OOTOMO (JAXA)
Yohei SATOH (JAXA)
Osamu SHIMADA (JAXA)
Hiroyuki SHINDO (JAXA)
Ichiro YOKOYAMA

Cryogenic Team

Team Leader

Masayuki KASE

Members

Kumio IKEGAMI
Kazushiro NAKANO[*1]
Hiroo HASEBE[*2]
Masato NAKAMURA
Tatsuhiko YOSHIDA[*1]
Takeshi MAIE[*2]

[*1] Temporary Employee
[*2] Technical Staff I

Visiting Members

Ken-ici KATO
Toshiyuki MITO (Natl. Inst. Fusion Sci.)

Accelerator Development Group

Group Director

Akira GOTO

Members
Toshiko NAKAMURA

Ion Source Team

Team Leader
Akira GOTO

Members
Takahide NAKAGAWA
Yoshihide HIGURASHI[*1]
Masanori KIDERA[*2]

[*1] Special Postdoctoral Researcher
[*2] Contract Researcher

Visiting Members
Takehiro MATSUSE (Fac. Text. Sci. Technol., Shinshu Univ.)

Accelerator Team

Team Leader
Akira GOTO

Members
Shigeo KOHARA
Jun-ichi OHNISHI
Osamu KAMIGAITO
Naruhiko SAKAMOTO
Hironori KUBOKI[*]

[*] Junior Research Associate

Visiting Members
Yoshiaki CHIBA
Masatoshi ITO (Cycl. Radioisot. Cen., Tohoku Univ.)
Satoshi KURASHIMA (JAEA, Takasaki)
Lukas STINGELIN (PSI, Switzerland)
Nobumasa MIYAWAKI (JAEA, Takasaki)
Hajime SAITO (SHI Accel. Serv. Ltd.)
Ryoichi WADA (Texas A&M Univ., USA)

Trainees
Takamichi AOKI (Dept. Phys., Grad. Sch. Sci., Univ. Tokyo)
Masahiro ICHIKAWA (Cycl. Radioisot. Cen., Tohoku Univ.)
Keisuke ITOH (Grad. Sch. Sci. Eng., Saitama Univ.)
Hiroaki MATSUBARA (Grad. Sch. Sci., Osaka Univ.)
Ryo MATSUO (Cycl. Radioisot. Cen., Tohoku Univ.)
Yuji TAMESHIGE (Grad. Sch. Sci. Eng., Osaka Univ.)
Tomohiro TERAZONO (Cycl. Radioisot. Cen., Tohoku Univ.)

Nuclear Physics R & D Group

Group Director
Hiroyoshi SAKURAI

Visiting Members
Hirofumi OHTA (Res. Fac. Cen. Sci. Technol., Univ. Tsukuba)

Trainees
Nozomi SATO (Grad. Sch. Sci. Eng., Tohoku Univ.)

BigRIPS Team

Team Leader

Hiroyoshi SAKURAI

Members

Toshiyuki KUBO
Atsushi YOSHIDA
Tetsuya OHNISHI[*1]
Naoki FUKUDA[*3]
Kouichi YOSHIDA
Masao OTAKE
Kensuke KUSAKA[*2]
Eri TAKESHITA[*4]

[*1] Special Postdoctoral Researcher
[*2] Contract Researcher
[*3] Research Associate
[*4] Junior Research Associate

Visiting Members

Toshio KOBAYASHI (Grad. Sch. Sci. Fac. Sci., Tohoku Univ.)
Susumu SHIMOURA (CNS)

GARIS Team

Team Leader

Hiroyoshi SAKURAI

Members

Kosuke MORITA
Daiya KAJI[*1]
Kohji MORIMOTO
Akira YONEDA[*2]

[*1] Special Postdoctoral Researcher
[*2] Contract Technical Scientist

Visiting Members

Shin-ichi GOTO (Niigata Univ.)
Kenji KATORI
Hiroyuki KOURA (JAEA, Tokai)
Hisaaki KUDO (Fac. Sci., Niigata Univ.)
Tetsuya MURAKAMI (Grad. Sch. Sci., Kyoto Univ.)
Toru NOMURA
Keisuke SUEKI (Grad. Sch. Pure Appl. Sci., Univ. Tsukuba)
Fuyuki TOKANAI (Dept. Phys., Yamagata Univ.)
Kenji YOSHINO (Fac. Eng., Miyazaki Univ.)

SLOWRI Team

Team Leader

Yasunori YAMAZAKI

Storage-ring Team

Team Leader

Hiroyoshi SAKURAI

Members

Takashi EMOTO
Tadashi KOSEKI
Masanori WAKASUGI
Yoshitaka YAMAGUCHI[*]

[*] Research Associate

Visiting Members

Akira OZAWA (Inst. Phys., Univ. Tsukuba)

Polarized RI Beam Team

Team Leader

Koichiro ASAHI

Computing and Network Team

Team Leader

Takashi ICHIHARA

Detector Team

Team Leader

Hideto EN'YO

Application and Development Group

Group Director

Yasushige YANO

Members

Kazuya TAKAHASHI
Shuichi ENOMOTO
Masako IZUMI
Teruyo TSUKADA
Shinji MOTOMURA[*1]
Hideki MADOKORO[*2]
Hiroyuki SAITO[*2]
Narumasa MIYAUCHI[*3]
Hideo SHOUJI[*4]
Yousuke KANAYAMA[*5]
Tomoko ABE
Hiroshige TAKEICHI
Tomoki MATSUYAMA
Hiromitsu HABA
Nguyen DINH DANG[*2]
Yuko MOCHIZUKI[*2]
Yoshiharu YAMAMOTO[*2]
Masako HASAMA[*4]
Hiroyuki ICHIDA[*4]

[*1] Special Postdoctoral Researcher
[*2] Contract Researcher
[*3] Technical Staff I
[*4] Part-time Staff I
[*5] Junior Research Associate

Visiting Members

Ryutaro AIDA (Natl. Inst. Floricult. Sci.)
Kazuhiko AKIYAMA (Grad. Sch. Pure Appl. Sci., Univ. Tsukuba)
Ryohei AMANO (Fac. Med., Kanazawa Univ.)
Sachiko AMARI (Washington Univ., USA)
Chang-Hyu BEA (Sunchon Natl. Univ., Korea)
Hiroyuki DAIMON (Osaka Pref. Univ.)
Wenjun DING (Colorado State Univ., USA)
Kazutoyo ENDO (Showa Pharm. Univ.)
Kaori ENOMOTO (Univ. Human Arts Sci.)
Mika FUKUOKA (Tokyo Univ. Fish.)
Koji FURUKAWA (Mukoyama Orchids Co., Ltd.)
Yoshiya FURUSAWA (Natl. Inst. Radiol. Sci.)
Toshinari GODO (Botanic Gardens Toyama)
Yasuyuki GONO
Misako HAMATANI (Hiroshima City Agric. Forest. Promot. Cen.)
Yasuhide HARA (Kanagawa Inst. Agric. Sci.)
Masanori HATASHITA (Wakasa Wan Energy Res. Cen.)
Hiroshi HIDAKA (Fac. Sci., Hiroshima Univ.)
Atsushi HIGASHITANI (Grad. Sch. Life Sci., Tohoku Univ.)
Seiichiro HIMENO (Fac. Pharm. Sci., Tokushima Bunri Univ.)
Akiko HOKURA (Fac. Sci., Tokyo Univ. Sci.)
Ichiro HONDA (Natl. Agric. Res. Cen., Min. Agric. Forest. Fish. Japan)
Mitsugu HORITA (Hokkaido Green-bio Inst.)
Takako IKEDA (Showa Women's Univ.)

Hiroko INAGE (Int. Life Sci. Inst.)
Takashi INAMURA
Toshiaki ISHII (Natl. Inst. Radiol. Sci.)
Nobuyoshi ISHII (Natl. Inst. Radiol. Sci.)
Yuji ITO (Natl. Agric. Res. Cent., Hokkaido Region)
Hiroshi KAGAMI (Shizuoka Citrus Exp. Station)
Takeshi KANAYA (Suntory Flowers, Ltd.)
Si-Yong KANG (Dep. Rad. Plant Breed. Genet., KAERI, Korea)
Shuichi KIMURA (Grad. Sch. Hum. Life Sci., Showa Woman's Univ.)
Tomojirou KOIDE (Riken Vitamin Co., Ltd.)
Masuo KONDOH (Showa Pharm. Univ.)
Tsutomu KUBOYAMA (Ibaraki Univ.)
Kuniko MAEDA
Ken-ichiro MATSUMOTO (Natl. Inst. Health, USA)
Yoshitaka MINAI (Cen. Art. Sci., Musashi Univ.)
Takeshi MINAMI (Dept. Life Sci., Sch. Sci. Eng., Kinki Univ.)
Yutaka MIYAZAWA (Grad. Sch. Life Sci., Tohoku Univ.)
Kazumitsu MIYOSHI (Fac. Bioresour. Sci., Akita Pref. Univ.)
Toshikazu MORISHITA (Inst. Rad. Breeding, Natl. Inst. Agric. Res.)
Shoushichi MOTONAGA
Koji MURAI (Fukui Pref. Univ.)
Tomohiro NABEKURA (Fac. Pharm. Sci., Niigata Univ. Pharm. Appl. Life Sci.)
Yuichiro NAGAME (JAEA, Tokai)
Yukiko NAKANISHI (Grad. Sch. Hum. Life Sci., Showa Woman's Univ.)
Van Chuyen NGUYEN (Jpn. Women's Univ.)
Yasumitsu OGURA (Grad. Sci. Pharm. Sci., Chiba Univ.)
Mio OHNUMA (Inst. Mol. Cell. Biosci., Univ. Tokyo)
Norihiro OHTSUBO (Natl. Inst. Floricult. Sci.)
Tomo OMIYA (Hokkaido Ornamental Plants Veg. Res. Cen.)
Kenji OSAWA (Nagano Agric. Res. Cen.)
Jun SAITO (Iwatsu Test Instrum. Corp.)
Kouichi SAKAMOTO (JAEA, Takasaki)
Tomofumi SAKURAGI (Natl. Inst. Radiol. Sci.)
Hiromu SAKURAI (Kyoto Pharm. Univ.)
Mutsuko SASAKI
Tadashi SATOU (Grad. Sch. Life Sci., Tohoku Univ.)
Hiroaki SERIZAWA (Nagano Veg. Ornamental Crops Exp. Station)
Takiko SHIMADA (Res. Inst. Agric. Resour., Ishikawa Agric. Coll.)
Hiroshi SHIMIZU (Fac. Sci., Hiroshima Univ.)
Atsushi SHINOHARA (Dept. Chem., Grad Sch. Sci., Osaka Univ.)
Fumio SUGAWARA (Tokyo Univ. Sci.)
Masao SUGIYAMA (Hokko Chem. Ind. Co., Ltd.)
Keita SUGIYAMA (Natl. Inst. Veg. Tea Sci.)
Kazunori SUZUKI (Plant Biotech. Inst. Ibaraki Agric. Cen.)
Kenichi SUZUKI (Suntory Flowers, Ltd.)
Toshihiro SUZUKI (Meiji Pharm. Univ.)
Mikiko SUZUKI (Showa Women's Univ.)
Kazuo T. SUZUKI (Grad. Sch. Pharm. Sci., Chiba Univ.)
Hiroyuki SUZUKI (RI Res. Cen., Chiba Univ.)
Takahiro TACHIBANA (Waseda High Sch., Waseda Univ.)
Keiko TAGAMI (Natl. Inst. Radiol. Sci.)
Yoshio TAKAHASHI (Grad. Sch. Sci., Hiroshima Univ.)
Masaaki TAKAHASHI (Grad. Sci. Agric. Biol. Sci., Osaka Pref. Univ.)
Miho TAKAHASHI (Tokyo Univ. Fish.)
Atsushi TAKEDA (Fac. Pharm. Sci., Univ. Shizuoka)
Haruna TAMANO (Fac. Pharm. Sci., Univ. Shizuoka)
Shinzo TANABE (Meiji Pharm. Univ.)
Teruhiko TERAKAWA (Hokko Chem. Ind. Co., Ltd.)
Tadayasu TOGAWA (Meiji Pharm. Univ.)
Ken TOKUHARA (Dogashima Orchid Cen.)

Masanori TOMITA (CRIEPI)
Takehiro TOMITANI (Natl. Inst. Radiol. Sci.)
Hisashi TSUJIMOTO (Fac. Agric., Tottori Univ.)
Shigeo UCHIDA (Natl. Inst. Radiol. Sci.)
Kohshin WASHIYAMA (Fac. Medicine, Kanazawa Univ.)
Masao WATANABE (Fac. Agric., Iwate Univ.)
Tokuko WATANABE (Fac. Fish., Tokyo Univ. Fish.)
Shuhei YAMAJI
Mineo YAMASAKI (Nara Med. Univ.)
Makoto YANAGA (Fac. Sci., Shizuoka Univ.)
Hiroyuki YASUI (Kyoto Pharm. Univ)
Takashi YOSHIMURA (Grad. Sch. Sci., Osaka Univ.)
Akihiko YOKOYAMA (Fac. Sci., Kanazawa Univ.)
Shigekazu YONEDA (Natl. Sci. Museum)
Takuji YOSHIDA (Takii Seed Co., Ltd.)
Shozo YOSHIDA (Nara Med. Univ.)
Yumin ZHAO (Shanghai Jiao Ting Univ., China)

Trainees
Yusuke ADACHI (Grad. Sch. Pharm. Sci., Kyoto Pharm. Univ.)
Tomoko ANDO (Grad. Sch. Hum. Life Sci., Showa Woman's Univ.)
Ryoichi HIRAYAMA (Grad. Sch. Sci. Tecnol., Chiba Univ.)
Yoshitaka KASAMATSU (Grad. Sch. Sci., Osaka Univ.)
Yusuke KITAMOTO (Grad. Sch. Sci., Osaka Univ.)
Yoshitaka MATSUMOTO (Grad. Sch. Medicine., Chiba Univ.)
Keiji MATSUO (Grad. Sch. Sci., Osaka Univ.)
Ryuji MINAYOSHI (Grad. Sch. Sci. Techol., Shizuoka Univ.)
Yohei MITSUBORI (Fac. Sci. Tech., Tokyo Univ. Sci.)
Ryoko ONUMA (Fac. Sci., Tokyo Univ. Sci.)
Daisuke SAIKA (Grad. Sch. Sci., Osaka Univ.)
Tomomasa TAKABE (Grad. Sch. Sci., Osaka Univ.)
Yuki TASHIRO (Grad. Sch. Sci., Osaka Univ.)
Atsushi YUMOTO (Grad. Sch. Pharm. Sci., Meiji Pharm. Univ.)

Safety Group

Group Director
Yoshitomo UWAMINO

Members
Shin FUJITA
Hisao SAKAMOTO[*2]
Rieko HIRUNUMA[*1]
Hiroki MUKAI[*3]

[*1] Contract Researcher
[*2] Contract Technical Scientist
[*3] Visiting Contract Officer

Visiting Members
Koji OISHI (Shimizu Constr. Co., Ltd.)

Cosmic Radiation Laboratory

Head
Kazuo MAKISHIMA

Members
Hiroshi KATO
Yukikatsu TERADA
Mitsuhiro KOHAMA[*]
Toru TAMAGAWA
Tatehiro MIHARA

[*] Special Postdoctoral Researcher

Visiting Members

Yasushi FUKAZAWA (Dept. Phys., Hiroshima Univ.)
Tateo GOKA (JAXA)
Soojing HONG (Dept. Phys., Saitama Univ.)
Yugo KIMOTO (JAXA)
Motohide KOKUBUN (Dept. Phys., Univ. Tokyo)
Tatsuto KOMIYAMA (JAXA)
Haruhisa MATSUMOTO (JAXA)
Hiromasa MIYASAKA (Cal. Inst. Technol., USA)
Motoki NAKAJIMA (Coll. Sci. Technol., Nihon Univ.)
Kazuhiro NAKAZAWA (JAXA)
Yasutomo SASAKI (JAXA)
Tadayuki TAKAHASHI (JAXA)
Kazuhiro TERASAWA (JAXA)
Kazutaka YAMAOKA (Aoyama Gakuin Univ.)

Radiation Laboratory

Head

Hideto EN'YO

Members

Yasuyuki AKIBA
Yuji GOTO
Masahiro OKAMURA
Hiromi SATO
Kiyoshi TANIDA
Kazuaki IKEDA[*1]
Ryotaro MUTO[*1]
Hiroaki OHNISHI[*1]
Masashi OHNO[*1]
Hisayuki TORII[*1]
Masanori HIRAI[*2]
Soichiro KAMETANI[*2]
Hiroyuki KAWAMURA[*2]
Takahiro MORISHIMA[*2]
Munehisa OTANI[*2]
Takenao SHINOHARA[*2]
Junji TOJO[*2]
Takashi ICHIHARA
Itaru NAKAGAWA
Yoshie OTAKE
Atsushi TAKETANI
Yasushi WATANABE
Kenji MISHIMA[*1]
Megumi NARUKI[*1]
Tetsuya OHNISHI[*1]
Hiroyuki TAKEDA[*1]
Johann HEUSER[*2]
Katsuya HIROTA[*2]
Hiroyuki KANO[*2]
Akio KIYOMICHI[*2]
Yoshiyuki ONUKI[*2]
Vladimir L. RYKOV[*2]
Kazutaka SUDO[*2]
Satoshi YOKKAICHI[*2]

[*1] Special Postdoctoral Researcher
[*2] Contract Researcher

Visiting Members

Tomohiro ADACHI (KDN)
Hiroshi AKOH (AIST)
Masahiro AOYAGI (AIST)
Masayuki ASAKAWA (Grad. Sch. Sci., Osaka Univ.)
Kenneth N. BARISH (UCR, USA)
Sasha BAZILVSKY (BNL, USA)
Wolfgang BENTZ (Dept. Phys., Sch. Sci., Tokai Univ.)
Muriel Jane BURWARD-HOY (Dept. Phys., State Univ. New York, Stony Brook, USA)
Mickey CHIU (Dept. Phys., UIUC, USA)
Sanatan DIGAL (Dept. Phys. Grad. Sch. Sci., Univ. Tokyo)
Waled EMAM (UCR, USA)
Frank ELLINGHAUS (Univ. Colorado, USA)
Oleg EYSER (UCR, USA)
Yoshihide FUCHI (KEK)
Hirotsugu FUJII (Grad. Sch. Arts Sci., Univ. Tokyo)
Haruhiko FUNAHASHI (Kyoto Univ.)
Tetsuo HATSUDA (Dept. Phys. Grad. Sch. Sci., Univ. Tokyo)

Toshiyuki HATTORI (Tokyo Inst. Technol.)
Hiro HIEIJIMA (UIUC, USA)
Kensuke HOMMA (Fac. Sci., Hiroshima Univ.)
Kenichi IMAI (Fac. Sci., Kyoto Univ.)
Katsuya ISHIGURO (Kanazawa Univ.)
Noriyoshi ISHII (Tokyo Inst. Technol.)
Edward R. KINNEY (Univ. Colorado, USA)
Ming LIU (LANL, USA)
Jameson ROBERT (Institut Angewandth Physik, Goethe Universität Frankfurt, Germany)
Osamu JINNOUCHI (KEK)
Masashi KANETA (Grad. Sch. Sci., Tohoku Univ.)
Hirotsugu KASHIWAGI (JAEA)
Yuji KAWABATA (Kyoto Univ.)
Takeo KAWASAKI (Fac. Sci., Niigata Univ.)
Jirou KODAIRA (Fac. Sci., Hiroshima Univ.)
Yuji KOIKE (Fac. Sci., Niigata Univ.)
Sergei KONDORASHEV (ITEP, Russia)
Hidekazu KUMAGAI
Shunzo KUMANO (KEK)
Teiji KUNIHIRO (YITP, Kyoto Univ.)
Masahiko KURAKADO (OECU)
Youngil KWON (Dept. Phys., Seoul Natl. Univ., Korea)
Keisuke MAEHATA (Kyusyu Univ.)
Yajun MAO (Sch. Phys., Peking Univ., China)
Yasuo MIAKE (Inst. Phys., Univ. Tsukuba)
Shoichi MIDORIKAWA (Fac. Eng., Aomori Univ.)
Toshiyuki MORII (Fac. Human Dev., Kobe Univ.)
Osamu MORIMATSU (KEK)
Hiroaki MYOREN (Saitama Univ.)
Shoji NAGAMIYA (KEK)
Kenichi NAITO (Hokkaido Univ.)
Sachio NAITOU (KEK)
Hiroshi NAKAGAWA (AIST)
Shogo NAKAMURA (Fac. Educ., Yokohama Natl. Univ.)
Akio OGAWA (Phys. Dept., BNL, USA)
Takayuki OKU (JAEA)
Naohito SAITO (Fac. Sci., Kyoto Univ.)
Koichi SAITO (Fac. Sci. Technol., Tokyo Univ. Sci.)
Harutaka SAKAGUCHI (Fac. Sci., Kyoto Univ.)
Fuminori SAKUMA (Fac. Sci., Kyoto Univ.)
Kenji SASAKI (KEK)
Shinya SAWADA (KEK)
Michiko SEKIMOTO (KEK)
Toshiaki SHIBATA (Tokyo Inst. Technol.)
Kenta SHIGAKI (Fac. Sci., Hiroshima Univ.)
Shigetomo SHIKI (OECU)
Tatsushi SHIMA (Osaka Univ.)
Hirohiko SHIMIZU (KEK)
Mikhail STEPANOV (Phys. Dept., New Mexico State Univ., USA)
Takanori SUGIHARA (Fac. Sci., Hiroshima Univ.)
Toru SUGITATE (Fac. Sci., Hiroshima Univ.)
Jun-ichi SUZUKI (JAEA)
Tsuneo SUZUKI (Kanazawa Univ.)
Tohru TAINO (Saitama Univ.)
Manobu TANAKA (KEK)
Kazuo TANIGUCHI (OECU)
Satoru TERASHIMA (Fac. Sci., Kyoto Univ.)
Manabu TOGAWA (Fac. Sci., Kyoto Univ.)
Thomas THROWE (Phys. Dept., BNL, USA)
Alexander TITOV (Flerov Lab. Nucl. React., JINR, Russia)

Marcus WAGNER (Fac. Sci., Kyoto Univ.)
Satoru YAMADA (JAEA)
Yoshiaki YASUI (Tokyo Manage. Coll.)
Koichi YAZAKI (Tokyo Women's Chr. Univ.)
Imran YOUNUS (Univ. New Mexico, USA)
Juzo ZENIHIRO (Fac. Sci., Kyoto Univ.)

Trainees

Kazuya AOKI (Fac. Sci., Kyoto Univ.)
Robert BENNETT (Dept. Phys. Astron. State Univ. New York, USA)
Kieran BOYLE (Dept. Phys. Astron. State Univ. New York, USA)
Hisato EGUCHI (Fac. Sci., Niigata Univ.)
Kouhei FUJIWARA (Fac. Sci., Niigata Univ.)
Yoshinori FUKAO (Fac. Sci., Kyoto Univ.)
Ran HAN (Peking Univ., China)
Koichi HASHIMOTO (Kanazawa Univ.)
Yoshimasa HIDAKA (Fac. Sci., Univ. Tokyo)
Takuma HORAGUCHI (Tokyo Inst. Technol.)
Yasuyoshi INOUE (Coll. Sci., Rikkyo Univ.)
Taku ITO (Tokyo Inst. Technol.)
Yoshihiko IWAO (Fac. Sci., Kyoto Univ.)
Fukutarou KAJIHARA (CNS)
Takeshi KANESUE (Kyusyu Univ.)
Hiroki KANO (Tokyo Inst. Technol.)
Masahiro KONNO (Inst. Phys., Univ. Tsukuba)
Antonin KRAL (Czech Tech. Univ. Prague, Czech)
Tomas LISKA (Czech Tech. Univ. Prague, Czech)
Kentarou MAWATARI (Fac. Human Develop., Kobe Univ.)
Petr MIKES (Inst. Phys. Prague, Czech)
Koji MIWA (Fac. Sci., Kyoto Univ.)
Astrid MORREALE (UCR, USA)
Takahiro NAGAI (Fac. Sci. Eng., Saga Univ.)
Junji NAGASHIMA (Fac. Sci., Niigata Univ.)
Tomoaki NAKAMURA (Fac. Sci., Hiroshima Univ.)
Yoshifumi NAKAMURA (Kanazawa Univ.)
Kenichi NAKANO (Tokyo Inst. Technol.)
Masato NARISAWA (Saitama Univ.)
Hiromi OKADA (Fac. Sci., Kyoto Univ.)
Ikuo OHTA (Kyusyu Univ.)
Shinsuke OOTA (CNS)
Misaki OUCHIDA (Fac. Sci., Hiroshima Univ.)
Kazuhiko SAKAKIBARA (Tokyo Inst. Technol.)
Joseph SEELE (Univ. Colorado, USA)
Toru SEKIDO (Kanazawa Univ.)
Yosuke SERITA (Saitama Univ.)
Maya SHIMOMURA (Inst. Phys., Univ. Tsukuba)
Kohei SHOJI (Fac. Sci., Kyoto Univ.)
Noriyuki SUGITA (Fac. Sci., Hiroshima Univ.)
Satoshi TAKAGI (Inst. Phys., Univ. Tsukuba)
Junpei TAKANO (Tokyo Inst. Technol.)
Akira TAKANO (Tokyo Inst. Technol.)
Yuji TUCHIMOTO (Fac. Sci., Hiroshima Univ.)
Takashi WATANABE (Tokyo Inst. Technol.)
Kazuo YAMAMOTO (Tokyo Inst. Technol.)
Hiroshi YOKOYA (Fac. Sci., Hiroshima Univ.)
Choong-Jae YOON (Fac. Sci., Kyoto Univ.)
Shota YOSHIMURA (Saitama Univ.)

Radioactive Isotope Physics Laboratory

Head

Hiroyoshi SAKURAI

Members

Takashi ICHIHARA
Shunji NISHIMURA
Toshiyuki SUMIKAMA*
Masayuki YAMAGAMI*
Takashi KISHIDA
Hideaki OTSU
Kanenobu TANAKA*

* Special Postdoctoral Researcher

Visiting Members

Adrian GELBERG (Univ. Koeln., Germany)
Masayuki MATSUO (Fac. Sci., Niigata Univ.)
Takashi NAGATOMO (Inst. Phys., Univ. Tsukuba)
Tetsuo NORO (Fac. Sci., Niigata Univ.)
Hiroyuki OHTA (Inst. Phys., Univ. Tsukuba)
Yuri PENIONZHK (JINR, Russia)

Trainees

Yuhei HASHIZUME (Inst. Phys., Univ. Tsukuba)
Hiroaki MATSUMOTO (Fac. Sci., Kyoto Univ.)

Applied Nuclear Physics Laboratory

Head

Koichiro ASAHI

Members

Yoshio KOBAYASHI
Akihiro YOSHIMI
Daisuke KAMEDA*
Hideki UENO
Tomohito HASEYAMA*

* Special Postdoctoral Researcher

Visiting Members

Minoru ADACHI
Hisazumi AKAI (Grad. Sch. Sci., Osaka Univ.)
Yasuaki EINAGA (Fac. Sci. Eng., Keio Univ.)
Koji HIGASHIYAMA (Grad. Sch. Sci., Univ. Tokyo)
Norimichi KOJIMA (Grad. Sch. Arts Sci., Univ. Tokyo)
Kenya M. KUBO (Div. Natl. Sci., Int. Chr. Univ.)
Takuya KURAHASHI (Inst. Mol. Sci.)
Jun MIYAZAKI (Grad. Sci., Tokyo Univ. Sci.)
Jiro MURATA (Fac. Sci., Rikkyo Univ.)
Masaki MURATA (Grad. Sch. Sci., Univ. Tokyo)
Kazuo MUTO (Grad. Sch. Sci. Eng., Tokyo Inst. Technol.)
Yujiro NAGATA (Coll. Sci. Technol., Aoyama Gakuin Univ.)
Hiromichi NAKAHARA (Grad. Sch. Sci., Tokyo Metrop. Univ.)
Jin NAKAMURA (Dept. Appl. Phys. Chem., Univ. Electro-Commun.)
Saburo NASU (Grad. Sch. Eng. Sci., Osaka Univ.)
Hiroshi OGAWA (Natl. Inst. Adv. Ind. Sci. Technol.)
Takuya OKADA
Hiroyuki SAGAWA (Math. Sci., Univ. Aizu)
Kenji SAKAI (JAEA, CEPAF, Neutron Facility G.)
Wataru SATO (Grad. Sch. Sci., Osaka Univ.)
Kenzi SHIMADA (Grad. Sch. Sci. Eng., Tokyo Inst. Technol.)
Tadashi SHIMODA (Grad. Sch. Sci. Eng., Osaka Univ.)
Satoshi TUTUI (Jpn. Syn. Rad. Res. Inst.)

Makoto UCHIDA (Grad. Sch. Sci. Eng., Tokyo Inst. Technol.)
Masahiko UTSURO (RCNP, Osaka Univ.)
Hiroshi WATANABE (Dept. Nucl. Phys., Australian Natl. Univ.)
Eiichi YAGI (Sch. Sci. Eng., Waseda Univ.)
Yasuhiro YAMADA (Fac. Sci., Tokyo Univ. Sci.)
Yutaka YOSHIDA (Fac. Sci. Technol., Shizuoka Inst. Sci. Technol.)

Trainees

Sounosuke AOKI (Fac. Sci. Technol., Shizuoka Inst. Sci. Technol.)
Takamasa ARAI (Fac. Sci., Tokyo Inst. Technol.)
Shinya FUKAGAI (Sch. Sci. Eng., Waseda Univ.)
Hideki FUKASAWA (Fac. Sci., Tokyo Univ. Sci.)
Masaki HAYASHI (Sch. Sci. Eng., Waseda Univ.)
Tatsuya HAYASHI (Grad. Sch. Sci. Eng., Waseda Univ.)
Naota HIGAMI (Grad. Sch. Sci. Eng., Waseda Univ.)
Kazuhiro HIRABAYASHI (Grad. Sch. Sci. Eng., Waseda Univ.)
Yuichi HIRAISHI (Sch. Sci. Eng., Waseda Univ.)
Sayaka HORIE (Fac. Sci. Technol., Shizuoka Inst. Sci. Technol.)
Takashi IIDA (Sch. Sci. Eng., Waseda Univ.)
Takeshi INOUE (Sch. Sci. Eng., Tokyo Inst. Technol.)
Tomoko KAKUYAMA (Div. Natl. Sci., Int. Chr. Univ.)
Hirokazu KATO (Fac. Sci., Tokyo Univ. Sci.)
Yoshihiro KAWAGUCHI (Div. Natl. Sci., Int. Chr. Univ.)
Hirokazu KAWAMURA (Fac. Sci., Rikkyo Univ.)
Go KIJIMA (Grad. Sch. Sci. Eng., Tokyo Inst. Technol.)
Hiroshi MATSUBA (Grad. Sch. Sci. Eng., Waseda Univ.)
Yoichi MURAKAMI (Sch. Sci. Eng., Waseda Univ.)
Daisuke NAGAE (Grad. Sch. Sci. Eng., Tokyo Inst. Technol.)
Tetsuya NAKAGAWA (Fac. Sci., Tokyo Univ. Sci.)
Akio NAKAMOTO (Grad. Sch. Arts Sci., Univ. Tokyo)
Takanori NAKAYAMA (Fac. Sci. Technol., Shizuoka Inst. Sci. Technol.)
Kentaro NAMIKI (Fac. Sci., Tokyo Univ. Sci.)
Satoshi NISHINO (Fac. Sci. Technol., Shizuoka Inst. Sci. Technol.)
Masashi OHKUBO (Grad. Sch. Arts Sci., Univ. Tokyo)
Yoshinori OKADA (Grad. Sch. Sci. Eng., Waseda Univ.)
Sachiko OSHIMA (Grad. Sch. Sci. Eng., Tokyo Inst. Technol.)
Guillaume PEDOUSSAUT (Div. Natl. Sci., Int. Chr. Univ.)
Kazumasa SAKATA (Fac. Sci. Technol., Shizuoka Inst. Sci. Technol.)
Chika SUGI (Grad. Sch. Sci. Eng., Waseda Univ.)
Kunifumi SUZUKI (Fac. Sci. Technol., Shizuoka Inst. Sci. Technol.)
Shota SUZUKI (Fac. Sci. Technol., Shizuoka Inst. Sci. Technol.)
Kaori TAGUCHI (Grad. Sch. Sci., Tokyo Metrop. Univ.)
Kenichi TAKASE (Sch. Sci. Eng., Tokyo Inst. Technol.)
Akiko TAKEBAYASHI (Sch. Sci. Eng., Waseda Univ.)
Makoto TAKEMURA (Fac. Sci., Tokyo Inst. Technol.)
Yoji TURUOKA (Div. Natl. Sci., Int. Chr. Univ.)
Toru YOSHIDA (Sch. Sci. Eng., Waseda Univ.)

Atomic Physics Laboratory

Head

Yasunori YAMAZAKI

Members

Tadashi KAMBARA
Hitoshi OYAMA
Takao M. KOJIMA
Takane KOBAYASHI
Masaki OURA
Naofumi KURODA[*1]
Tarek Ali Mohamed HASSAN[*1]
Yasuyuki KANAI
Michiharu WADA
Yoichi NAKAI
Tokihiro IKEDA
Yoshihisa ISHIDA[*1]
Takashi NAKAMURA[*1]
Hiroyuki TANAKA[*1]

Masahiro SHIBATA[*2] Haruhiko SAITOH[*2]
Yoshio IWAI[*3]

[*1] Contract Researcher
[*2] Special Postdoctoral Researcher
[*3] Part-time staff supporting research

Visiting Members

Kozo ANDO
Yohko AWAYA (Coll. Art Design Gen. Ed., Musashino Art Univ.)
Toshiyuki AZUMA (Dept. Phys., Tokyo Metrop. Univ.)
Daniel BARNA (KFKI, Hungary)
Joachim BURGDÖRFER (Vienna Univ. Technol., Austria)
Yasuhiro CHIMI (Tokai Res. Estab., JAEA)
Jörg EICHLER (Hahn-Meiter-Inst. Berlin, Germany)
Makoto C. FUJIWARA (TRIUMF, Canada)
Atsushi HATAKEYAMA (Grad. Sch. Arts Sci., Univ. Tokyo)
Akira HITACHI (Kochi Med. Sch.)
Masamitsu HOSHINO (Dept. Phys., Sophia Univ.)
Atsushi ICHIMURA (Inst. Space Astro. Sci.)
Akinori IGARASHI (Fac. Eng., Miyazaki Univ.)
Hideki IIMURA (JAEA)
Norito ISHIKAWA (Tokai Res. Estab., JAEA)
Akio ITOH (Dept. Nucl. Eng., Kyoto Univ.)
Yoh ITOH (Fac. Sci., Josai Univ.)
Akihiro IWASE (Res. Inst. Adv. Sci. Technol., Osaka Pref. Univ.)
Kensuke KAGEYAMA (Fac. Eng., Saitama Univ.)
Ichiro KATAYAMA (KEK)
Kenji KIMURA (Fac. Eng., Kyoto Univ.)
Mineo KIMURA (Grad. Sch. Sci., Kyushu Univ.)
Masashi KITAJIMA (Fac. Sci. Technol., Sophia Univ.)
Tetsuo KOIZUMI (Dept. Phys., Rikkyo Univ.)
Ken-ichiro KOMAKI (Grad. Sch. Arts Sci., Univ. Tokyo)
Chikara KONDOU (Dept. Phys., Grad. Sch. Sci., Univ. Tokyo)
Kenichi KOWARI (Dept. Appl. Phys. Chem., Univ. Electro-Commun.)
Kenro KUROKI (Natl. Res. Inst. Police Sci.)
Michio MATSUZAWA (Dept. Appl. Phys. Chem., Univ. Electro-Commun.)
Akihiro MOHRI
Kanetada NAGAMINE (Inst. Mater. Struc. Sci., KEK)
Nobuyuki NAKAMURA (Inst. Laser Sci., Univ. Electro-Commun.)
Tetsuya NAKAZAWA (Tokai Res. Estab., JAEA)
Takuya NEBIKI (Kochi Univ. Technol.)
Shunsuke OHTANI (Inst. Laser Sci., Univ. Electro-Commun.)
Kunihiro OKADA (Fac. Sci. Technol., Sophia Univ.)
Satoru OKAYASU (Tokai Res. Estab., JAEA)
Brian O'ROURKE (JSPS)
Fumihisa ONO (Fac. Sci., Okayama Univ.)
Nagayasu OSHIMA (AIST)
Patrice PEREZ (C.E.A. Saclay, France)
Lukas PICHL (Found. Comput. Sci. Lab., Univ. Aizu)
Syuiti SAKAGUTI (Fac. Eng., Yamaguchi Univ.)
Akio SAKAI (Vacuum Products Co.)
Reinhold SCHUCH (Phys. Dept., Stockholm Univ., Sweden)
Hans A. SCHUESSLER (Texas A&M Univ., USA)
Hiroyuki SHIMADA (Dept. Phys., Grad. Sch. Sci., Univ. Tokyo)
Noriyuki SHIMAKURA (Fac. Sci., Niigata Univ.)
Isao SHIMAMURA
Nikolaus STOLTERFOHT (Hahn-Meitner-Institut Berlin GmbH, Germany)
Hiroya SUNO (NIFS)
Aiko TAKAMINE (Dept. Phys., Grad. Sch. Sci., Univ. Tokyo)

Michiya TAKEKAWA (Inst. Pure Appl. Phys.)
Hiroyuki TORII (Grad. Sch. Arts Sci., Univ. Tokyo)
Nobuyuki TOSHIMA (Inst. Appl. Phys., Univ. Tsukuba)
Hidetsugu TSUCHIDA (Dept. Nucl. Eng., Kyoto Univ.)
Kazuyuki UEDA (Toyota Technol. Inst.)
Victor VARENTSOV (V. G. Khlopin Radium Inst., Russia)
Tienshan WANG (Lanzhou Univ., China)
Tsutomu WATANABE
Hermann WOLLNIK (Giessen Univ., Germany)
Akira YAGISHITA (KEK)
Nobuhiro YAMANAKA (Sch. Sci., Univ. Tokyo)
Yaming ZOU (Fudan Univ., China)

Trainees

Jacques BABAUD (Appl. Phys., Ecole Centrale Paris, France)
Yoshinori ENOMOTO (Coll. Art Sci., Univ. Tokyo)
Masafumi FUKUZUMI (Grad. Sch. Eng., Osaka Pref. Univ.)
Guillaume JEGOU (Inst. Nucl. Phys., Univ. Paris-Sud Orsay, France)
Vladimir LIOUBIMOV (Texas A&M Univ., USA)
Nobuhiro MAEDA (Grad. Sch. Eng., Osaka Pref. Univ.)
Yasuharu MITSUDA (Chem., Univ. Electro-Commun.)
Yuji MIYAMOTO (Grad. Sch. Sci. Eng., Sophia Univ.)
Yugo NAGATA (Dept. Phys., Grad. Sch. Sci., Univ. Tokyo)
Yuji NAKANO (Dept. Phys., Tokyo Metrop. Univ.)
Koremitsu OGATA (Dept. Phys., Grad. Sch. Sci., Univ. Tokyo)
Shigeki SHIBATA (Dept. Appl. Phys. Chem., Univ. Electro-Commun.)

Heavy Ion Nuclear Physics Laboratory

Head

Tohru MOTOBAYASHI

Members

Toshimi SUDA
Yasushi WATANABE
Akihisa KOHAMA
Yoshiyuki YANAGISAWA
Masaaki TAKASHINA[*1]
Kazunari YAMADA[*1]
Takuma MATSUMOTO[*1]
Shawn BISHOP[*2]
Meiko UESAKA-KUROKAWA[*2]
Mitsutaka YAMAGUCHI[*2]
Alexei A. KORSHENINNIKOV
Yukari MATSUO
Nori AOI
Ken-ichirou YONEDA
Satoshi TAKEUCHI[*1]
Hidetada BABA[*1]
Shinichiro MICHIMASA[*1]
Kiyomi IKEDA[*2]
Kimiko SEKIGUCHI[*2]
Toshimitsu YAMAZAKI[*2]

[*1] Special Postdoctoral Researcher
[*2] Contract Researcher

Visiting Members

Yasuhisa ABE (Yukawa Inst. Theor. Phys., Kyoto Univ.)
Yasuo AOKI (Inst. Phys., Univ. Tsukuba)
Shigeyoshi AOYAMA (Fac. Sci., Niigata Univ.)
Ichiro ARAI (Univ. Tsukuba)
Yoshihiro ARITOMO (JINR, Russia)
Daniel BAZIN (Michigan State Univ., USA)
Didier BEAUMEL (IPN-Orsay, France)
Francis A. BECK (CRN-Strasbourg, France)
Mottelson R BEN (NORDITA, Denmark)
Geoge BERG (Univ. Notre Dame, USA)
Yorick BLUMENFIELD (IPN-Orsay, France)
Alan CHEN (McMaster Univ., Canada)
Silvio CHERUBINI (Katania Univ., Italy)

Marco LA COGNATA (Katania Univ., Italy)
Tien Khoa DAO (Inst. Nucl. Sci. Tech., China)
Zsolt DOMBRADI (Inst. Nucl. Res., Hung. Acad. Sci., Hungary)
Zoltan ELEKES (Inst. Nucl. Res., Hung. Acad. Sci., Hungary)
Yoshiko EN'YO (Kyoto Univ.)
Henning ESBENSEN (Argonne Natl. Lab., USA)
Michel FAMIANO (Michigan State Univ., USA)
Hubert FLOCARD (IPN-Orsay, France)
Yoshihide FUCHI (KEK)
Shinichiro FUJII (Grad. Sch. Sci., Univ. Tokyo)
Yoshitaka FUJITA (Grad. Sch. Sci., Osaka Univ.)
Mamoru FUJIWARA (RCNP, Osaka Univ.)
Tomonori FUKUCHI (Coll. Sci., Rikkyo Univ.)
Mitsunori FUKUDA (Grad. Sch. Sci., Osaka Univ.)
Zsolt FÜLÖP (Inst. Nucl. Res., Hung. Acad. Sci., Hungary)
Ken-ichi FUSHIMI (Tokushima Univ.)
Zoltan GACSI (ATOMKI, Hungary)
Yu-Cheng GE (Peking Univ., China)
Vardir GUIMARAES (Univ. Sao Paulo, Brazil)
Hideki HAMAGAKI (Grad. Sch. Sci., Univ. Tokyo)
Jun HASEGAWA (Fac. Sci., Tokyo Inst. Technol.)
Jianjun HE (Grad. Sch. Sci., Univ. Tokyo)
Satoru HIRENZAKI (Fac. Sci., Nara Women's Univ.)
Khiem LE HONG (Inst. Phys., Natl. Cen. Sci. Technol., Vietnam)
Shen HONG (Dept. Phys., Nankai Univ., China)
Michio HONMA (Aizu Univ.)
TakatoshiI HORIBATA (Fac. Sci., Aomori Univ.)
Hisashi HORIUCHI (Grad. Sch. Sci., Kyoto Univ.)
Hui HUA (Michigan State Univ., USA)
Munetake ICHIMURA (Univ. Air)
Eiji IDEGUCHI (Grad. Sch. Sci., Univ. Tokyo)
Kazuo IEKI (Coll. Sci., Rikkyo Univ.)
Nobuaki IMAI (KEK)
Shigeru ISHIMOTO (KEK)
Hironobu ISHIYAMA (KEK)
Naoyuki ITAGAKI (Grad. Sch. Sci., Univ. Tokyo)
Makoto ITO (Fac. Sci., Univ. Tsukuba)
Akira IWAMOTO (JAEA)
Naohisa IWASA (Grad. Sch. Sci., Tohoku Univ.)
Hironori IWASAKI (Grad. Sch. Sci., Univ. Tokyo)
Takuji IZUMIKAWA (Fac. Sci., Niigata Univ.)
Gal JANOS (ATOMKI, Hungary)
Dang-Xing JIANG (Peking Univ., China)
Lee JU (Chung-Ang Univ., Korea)
Toshiki KAJINO (Natl. Astron. Obs.)
Nasser KALANTAR (Univ. Groningen, The Netherlands)
Gabor KALINKA (ATOMKI, Hungary)
Shoko KANNO (Coll. Sci., Rikkyo Univ.)
Kiyoshi KATO (Grad. Sch. Sci., Hokkaido Univ.)
Seigo KATO (Yamagata Univ.)
Takahiro KAWABATA (Grad. Sch. Sci., Univ. Tokyo)
Paul KIENLE (Tech. Univ. Muenchen, Germany)
Takashi KIKUCHI (Utsunomiya Univ.)
Jang Chan KIM (Chung -Ang Univ., Korea)
Ong Chan KIM (Seoul Univ., Korea)
Kikuo KIMURA (Fac. Sci., Nagasaki Inst. Appl. Sci.)
Koichi KINO (Grad. Sch. Sci., Univ. Tokyo)
Tetsuro KOMATSUBARA (Univ. Tsukuba)
Evgueni KOUZMINE (Kurchatov Inst., Russia)
Attila KRASZNAHORKAY (ATOMKI, Hungary)

Shigeru KUBONO (Grad. Sch. Sci., Univ. Tokyo)
Kazuyoshi KURITA (Coll. Sci., Rikkyo Univ.)
Rubens LICHTENTH (Univ. Sao Paulo, Brazil)
Guan-Hua LIU (Inst. Modern Phys., China)
William LYNCH (Michigan State Univ., USA)
Kazushige MAEDA (Grad. Sch. Sci., Tohoku Univ.)
Yukishige MAEDA (Grad. Sch. Sci., Univ. Tokyo)
Tomohiro MARUNO (Grad. Sch. Sci., Univ. Tokyo)
Kensaku MATSUTA (Grad. Sch. Sci., Osaka Univ.)
Kenichi MATSUYANAGI (Grad. Sch. Sci., Kyoto Univ.)
Jie MENG (Peking Univ., China)
Alberto MENGONI (ENEA, Italy)
Johannes MESSCHENDORP (Univ. Groningen, The Netherlands)
Mototugu MIHARA (Grad. Sch. Sci., Osaka Univ.)
Toshiyuki MINEMURA (KEK)
Shiro MITARAI (Grad. Sch. Sci., Kyusyu Univ.)
Tomoko MIYAGISHI (NIRS)
Yasuo MIYAKE (Inst. Phys., Univ. Tsukuba)
Hiroari MIYATAKE (KEK)
Hiroshi MIZOI (Osaka Electro-Commun. Univ.)
Takahiro MIZUSAKI (Grad. Sch. Sci., Univ. Tokyo)
Peter MOLLER (Los Alamos Natl. Lab., USA)
Sadao MOMOTA (Kochi Univ. Technol.)
Ben MOTTELSON (NORDITA, Denmark)
Hiroyuki MURAKAMI (Coll. Sci., Rikkyo Univ.)
Atsushi MUTA (Inst. Phys., Univ. Tsukuba)
Takayuki MYO (RCNP, Osaka Univ.)
Yasuki NAGAI (RCNP, Osaka Univ.)
Takashi NAKAMURA (Fac. Sci., Tokyo Inst. Technol.)
Takashi NAKATSUKASA (Fac. Sci., Univ. Tsukuba)
Shintaro NAKAYAMA (Tokushima Univ.)
Evgueni NIKOLSKI (Kurchatov Inst., Russia)
Masahiro NOTANI (Argonne National Lab., USA)
Atsuko ODAHARA (Fac. Sci., Osaka Univ.)
Alexei A. OGLOBLIN (Kurchatov Inst., Russia)
Yukimitsu OHSHIRO (Grad. Sch. Sci., Univ. Tokyo)
Masahisa OHTA (Fac. Sci., Konan Univ.)
Hideaki OHTSU (Fac. Sci., Tohoku Univ.)
Takashi OHTSUBO (Fac. Sci., Niigata Univ.)
Hiroyuki OKAMURA (Grad. Sch. Sci., Tohoku Univ.)
Takeo ONISHI (Grad. Sch. Sci., Univ. Tokyo)
Christian OUELLET (McMaster Univ., Canada)
Kazuhiro OYAMATSU (Aichi Shukutoku Univ.)
Kyoichiro OZAWA (Grad. Sch. Sci., Univ. Tokyo)
Kazutaka OZEKI (CYRIC., Tohoku Univ.)
Jonathan PEARSON (McMaster Univ., Canada)
Yuri PENIONZHK (McMaster Univ., Canada)
P. A. Aloy PERERA (Univ. Kalaniya, Sri Lanka)
Gianluca PIZZONE (Katania Univ., Italy)
Chilakamarri RANGACHARYULU (Univ. Saskatchewan, Canada)
Keirin RIKU (Grad. Sch. Sci., Kyushu Univ.)
Hiroyuki SAGAWA (Univ. Aizu)
Aketo SAITO (Grad. Sch. Sci., Univ. Tokyo)
Harutaka SAKAGUCHI (Grad. Sch. Sci., Kyoto Univ.)
Takao SAKAGUCHI (Grad. Sch. Sci., Univ. Tokyo)
Hideyuki SAKAI (Grad. Sch. Sci., Univ. Tokyo)
Mitsuo SAKAI (Grad. Sch. Sci., Univ. Tokyo)
Yoshinori SAKURAGI (Fac. Sci., Osaka City Univ.)
Kimikazu SASA (Univ. Tsukuba)
Yoshiteru SATOU (Fac. Sci., Tokyo Inst. Technol.)

Ryoichi SEKI (Cal. State Univ., Northridge, USA)
Noritaka SHIMIZU (Grad. Sch. Sci., Univ. Tokyo)
Yoshifumi SHIMIZU (Grad. Sch. Sci., Kyushu Univ.)
Toru SHIMOURA (Grad. Sch. Sci., Univ. Tokyo)
Cosimo SIGNORINI (INEN, Italy)
Dorottya SOHLER (ATOMKI, Hungary)
Andreas STOLZ (Michigan State Univ., USA)
Takashi SUGIMOTO (Fac. Sci., Tokyo Inst. Technol.)
Kohsuke SUMIYOSHI (Numazu Coll. Technol.)
Akihiro SUZUKI (Suzuki Corp.)
Masaru SUZUKI (Grad. Sch. Sci., Univ. Tokyo)
Shoji SUZUKI (KEK)
Takeshi SUZUKI (Saitama Univ.)
Toshio SUZUKI (Fac. Eng., Fukui Univ.)
Yasuyuki SUZUKI (Fac. Sci., Niigata Univ.)
Naoki TAJIMA (Fac. Eng., Fukui Univ.)
Tadayuki TAKAHASHI (Inst. Space Astronaut. Sci.)
Yutaka TAKAHASHI (RCNP, Osaka Univ.)
Masatoshi TAKANO (Sci. Eng. Res. Lab., Waseda Univ.)
Noboru TAKIGAWA (Fac. Sci., Tohoku Univ.)
Tadaaki TAMAE (Grad. Sch. Sci., Tohoku Univ.)
Atsushi TAMII (RCNP, Osaka Univ.)
Kazuko TANABE (Otsuma Women's Univ.)
Masahiko TANAKA (KEK)
Takashi TERANISHI (Grad. Sch. Sci., Kyusyu Univ.)
Jun TERASAKI (Univ. North Carolina, USA)
Mariko TERASAWA (Grad. Sch. Sci., Univ. Tokyo)
Manyee TSANG (Michigan State Univ., USA)
Tomohiro UESAKA (Grad. Sch. Sci., Univ. Tokyo)
Yutaka UTSUNO (Tokai Res. Estab., JAEA)
Peter Von BRENTANO (Inst. Kern Phys., Univ. Koeln, Germany)
Takahiro WADA (Fac. Sci., Konan Univ.)
Tomotugu WAKASA (Grad. Sch. Sci., Kyusyu Univ.)
Takashi WAKUI (Tohoku Univ.)
Shinichi WATANABE (Grad. Sch. Sci., Univ. Tokyo)
Yuu WATANABE (KEK)
Shuwei XU (Inst. Modern Phys., Chin. Acad. Sci., China)
Kazuhiro YABANA (Fac. Sci., Niigata Univ.)
Kentarou YAKOU (Grad. Sch. Sci., Univ. Tokyo)
Hidetoshi YAMAGUCHI (Grad. Sch. Sci., Univ. Tokyo)
Takayuki YAMAGUCHI (Fac. Sci., Saitama Univ.)
Shoichi YAMAYA (Grad. Sch. Sci., Univ. Tokyo)
Norio YAMAZAKI (Grad. Sch. Sci., Univ. Tokyo)
Yanlin YE (Peking Univ., China)
Blumenfeld YORICK (IPN-Orsay, France)
Naotaka YOSHINAGA (Fac. Sci., Saitama Univ.)
Yong ZHENG (Grad. Sch. Sci., Univ. Tokyo)
Shan-Gi ZHOU (Peking Univ., China)

Trainees

Takeshi AIBA (Fac. Sci., Niigata Univ.)
Guilherme AMADIO (Grad. Sch. Sci., Univ. Tokyo)
Yoki ARAMAKI (Grad. Sch. Sci., Univ. Tokyo)
Jonathan Michael COOK (Michigan State Univ., USA)
Pham N. DINH (Michigan State Univ., USA)
Natsumi ENDO (Fac. Sci., Tohoku Univ.)
Hisashi FUJIKAWA (Grad. Sch. Sci., Univ. Tokyo)
Hiroki FUJIWARA (Fac. Sci., Osaka Univ.)
Tomonori FUKUCHI (Coll. Sci., Rikkyo Univ.)
Toshiaki FUKUI (Kyoto Univ.)

Yasuro FUNAKI (Fac. Sci., Kyoto Univ.)
Takeshi FURUKAWA (Fac. Sci., Osaka Univ.)
Taku GUNJI (Grad. Sch. Sci., Univ. Tokyo)
Ryosuke HADATE (Coll. Sci., Rikkyo Univ.)
Yoshiko HASHIMOTO (Fac. Sci., Tokyo Inst. Technol.)
Naho HOKOIWA (Fac. Sci., Kyushu Univ.)
Takeshi HOYA (Coll. Sci., Rikkyo Univ.)
Yuichi ICHIKAWA (Grad. Sch. Sci., Univ. Tokyo)
Kiyohiko INAFUKU (Grad. Sch. Sci., Tohoku Univ.)
Kazuhiro ISHIKAWA (Fac. Sci., Tokyo Inst. Technol.)
Tadaaki ISOBE (Grad. Sch. Sci., Univ. Tokyo)
Tatsuhiro ITO (Meiji Univ.)
Ikuko KANAZAWA (Fac. Sci., Saitama Univ.)
Tomomi KATO (Fac. Sci., Niigata Univ.)
Tomomi KAWAHARA (Toho Univ.)
Shoko KAWAI (Coll. Sci., Rikkyo Univ.)
Yoshie KAWAMURA (Fac. Sci., Niigata Univ.)
Aram KIM (Ewha Women's Univ., Korea)
Jang Youl KIM (Chung Ang Univ., Korea)
Mituhisa KITAYAMA (Fac. Sci., Tohoku Univ.)
Kei KOBAYASHI (Fac. Sci., Saitama Univ.)
Mari KOMURO (Fac. Sci., Saitama Univ.)
Yousuke KONDOU (Fac. Sci., Tokyo Inst. Technol.)
Ryo KOYAMA (Fac. Sci., Niigata Univ.)
Hironori KUBOKI (Grad. Sch. Sci., Univ. Tokyo)
Takamasa KUBOKI (Fac. Sci., Saitama Univ.)
Shinichi KUMASHIRO (Fac. Sci., Osaka Univ.)
Chie KUROKAWA (Fac. Sci., Hokkaido Univ.)
Michitarou KUSAKA (Fac. Sci., Tohoku Univ.)
Young Kwan KWON (Chung-Ang Univ., Korea)
Ju Hahn LEE (Chung-Ang Univ., Korea)
Tomohiro MACHIDA (Coll. Sci., Rikkyo Univ.)
Yukie MAEDA (Grad. Sch. Sci., Univ. Tokyo)
Takashi MAEMURA (Fac. Sci., Saitama Univ.)
Tetsuya MASUDA (Coll. Sci., Rikkyo Univ.)
Yohei MATSUDA (Fac. Sci., Tohoku Univ.)
Nobuyuki MATSUI (Coll. Sci., Rikkyo Univ.)
Taizo MATSUMASA (Fac. Sci., Osaka Univ.)
Ryohei MATSUMIYA (Fac. Sci., Osaka Univ.)
Takafumi MATSUYAMA (Fac. Sci., Niigata Univ.)
Kenjiro MIKI (Grad. Sch. Sci., Univ. Tokyo)
Toshiya MIKI (Fac. Sci., Tohoku Univ.)
Kazutaka MIYAKAWA (Fac. Sci., Univ. Tsukuba)
Michal MOCKO (Michigan State Univ., USA)
Tetsuaki MORIGUCHI (Coll. Sci., Rikkyo Univ.)
Kensuke MORIMOTO (Coll. Sci., Rikkyo Univ.)
Konomi MURAKAMI (Fac. Sci., Saitama Univ.)
Takumi NAKABAYASHI (Fac. Sci., Tokyo Inst. Technol.)
Shinpei NAKAJIMA (Fac. Sci., Saitama Univ.)
Atsushi NAKAMURA (Fac Sci., Saitama Univ.)
Ryoko NAKAMURA (Coll. Sci., Rikkyo Univ.)
Taro NAKAO (Grad. Sch. Sci., Univ. Tokyo)
Hiroyuki NAKAYAMA (Grad. Sch. Sci., Univ. Tokyo)
Khai Tuan NGUYEN (Hanoi Univ., Vietnam)
Jun NIKURA (Grad. Sch. Sci., Univ. Tokyo)
Haruki NISHINO (Grad. Sch. Sci., Univ. Tokyo)
Shunpei NOJI (Grad. Sch. Sci., Univ. Tokyo)
Susumu ODA (Grad. Sch. Sci., Univ. Tokyo)
Masafumi OIZUMI (Grad. Sch. Sci., Univ. Tokyo)
Naoto OKAICHI (Fac. Sci., Tokyo Inst. Technol.)

Takashi OKUDA (Fac. Sci., Tohoku Univ.)
Toshifumi OKUMURA (Fac. Sci., Tokyo Inst. Technol.)
Hooi Jin ONG (Grad. Sch. Sci., Univ. Tokyo)
Yosiho OTA (Meiji Univ.)
Andrew ROGERS (Michigan State Univ., USA)
Hiroshi SAENMA (Grad. Sch. Sci., Univ. Tokyo)
Shota SAITO (Grad. Sch. Sci., Univ. Tokyo)
Takaaki SAITO (Grad. Sch. Sci., Univ. Tokyo)
Satoshi SAKAGUCHI (Grad. Sch. Sci., Univ. Tokyo)
Hazuki SAKAI (Coll. Sci., Rikkyo Univ.)
Takashi SAKO (Grad. Sch. Sci., Univ. Tokyo)
Tomoyuki SAKURADA (Coll. Sci., Rikkyo Univ.)
Satoshi SANO (Waseda Univ.)
Makoto SASAKI (Fac. Sci., Osaka Univ.)
Ryoko SASAMOTO (Grad. Sch. Sci., Univ. Tokyo)
Masaki SASANO (Grad. Sch. Sci., Univ. Tokyo)
Tadanori SASANO (Grad. Sch. Sci., Univ. Tokyo)
Junichi SATO (Coll. Sci., Rikkyo Univ.)
Kazunori SATO (Fac. Sci., Niigata Univ.)
Yoko SEKI (Fac. Sci., Tohoku Univ.)
Masatugu SEKIGUCHI (Fac. Sci., Tohoku Univ.)
Ryoko SHINODA (Fac. Sci., Saitama Univ.)
Mayuko SHINOHARA (Fac. Sci., Tokyo Inst. Technol.)
Tokukazu SHINOHARA (Fac. Sci., Tohoku Univ.)
Daisuke SHINOJIMA (Fac. Sci., Niigata Univ.)
Wakako SHINOZAKI (Fac. Sci., Niigata Univ.)
Edward SMITH (Ohio Univ., USA)
Ryohei SUGO (Coll. Sci., Rikkyo Univ.)
Daisuke SUZUKI (Grad. Sch. Sci., Univ. Tokyo)
Hiroshi SUZUKI (Grad. Sch. Sci., Univ. Tokyo)
Ryusuke SUZUKI (Fac. Sci., Hokkaido Univ.)
Kensaku TAKAHASHI (Fac. Sci., Saitama Univ.)
Yoshiyuki TAKAHASHI (Grad. Sch. Sci., Univ. Tokyo)
Maya TAKECHI (Fac. Sci., Osaka Univ.)
Naohiro TAKEMOTO (Fac. Sci., Saitama Univ.)
Hideki TANAKA (Fac. Sci., Niigata Univ.)
Tasutaka TANIGUCHI (Grad. Sch. Sci., Kyoto Univ.)
Yasuo UEKI (Coll. Sci., Rikkyo Univ.)
Hirotaka UENO (Coll. Sci., Rikkyo Univ.)
Yasuo WAKABAYASHI (Fac. Sci., Kyushu Univ.)
Mark WALLACE (Michigan State Univ., USA)
Kiwamu WATANABE (Fac. Sci., Tohoku Univ.)
Yorito YAMAGUCHI (Grad. Sch. Sci., Univ. Tokyo)
Yuzo YAMAMOTO (Coll. Sci., Rikkyo Univ.)
Takuma YASUNO (Fac. Sci., Univ. Tsukuba)
Michiori YOSHITAKE (Fac. Sci., Saitama Univ.)

Advanced Meson Science Laboratory

Head

Masahiko IWASAKI

Members

Teiichiro MATSUZAKI
Haruhiko OUTA
Yasuyuki MATSUDA
Hiroaki OHNISHI
Shinji OKADA[*1]
Takatoshi SUZUKI[*1]
Seiko OHIRA[*2]
Katsuhiko ISHIDA
Isao WATANABE
Kenta ITAHASHI
Takahisa KOIKE[*1]
Hidekatsu NEMURA[*1]
Dai TOMONO[*1]
Pavel BAKULE[*2]

Takao SUZUKI*2 Masami IIO*2

*1 Special Postdoctoral Researcher
*2 Contract Researcher

Visiting Members

Tadashi ADACHI (Grad. Sch. Eng., Tohoku Univ.)
Yoshitami AJIRO (Grad. Sch. Sci., Kyoto Univ.)
Yoshinori AKAISHI
Jun AKIMITSU (Coll. Sci. Eng., Aoyama Gakuin Univ.)
Juichiro ARAI (Fac. Sci., Tokyo Univ. Sci.)
Shingo ARAKI (Grad. Sch. Sci., Osaka Univ.)
Kunio AWAGA (Grad. Sch. Sci., Nagoya Univ.)
George A. BEER (Univ. Victoria, Canada)
Hyoung Chan BHANG (Seoul Natl. Univ., Korea)
Ludmila N. BOGDANOVA (Inst. Theor. Exper. Phys., Russia)
Tara P. DAS (State Univ. New York, USA)
Mark P. FAIFMAN (Kurchatov Inst., Russia)
Yutaka FUJII (Fac. Eng., Fukui Univ.)
Masaki FUJITA (IMR, Tohoku Univ.)
Hideto FUKAZAWA (Grad. Sch. Sci. Eng., Chiba Univ.)
Makoto HAGIWARA (Fac. Eng. Design, Kyoto Inst. Technol.)
Masahira HIRANO (JST)
Emiko HIYAMA (Fac. Sci., Nara Women's Univ.)
Susumu IKEDA (KEK)
Yutaka IKEDO (Toyota Central R&D Labs.)
Shigeru ISHIMOTO (KEK)
Tomoichi ISHIWATARI (Stefan Meyer Inst., Austria)
Atsuko ITO
Ryosuke KADONO (KEK)
Masayasu KAMIMURA
Mineo KATO (Tokai Res. Estab. Dev. Cen., JAEA)
Naritoshi KAWAMURA (KEK)
Jungho KIM (Seoul Natl. Univ., Korea)
Yasushi KINO (Fac. Sci., Tohoku Univ.)
Yoh KOHORI (Fac. Sci., Chiba Univ.)
Youji KOIKE (Grad. Sch. Eng., Tohoku Univ.)
Yoshitaka KUNO (Grad. Sch. Sci., Osaka Univ.)
Syunsuke MAKIMURA (KEK)
Goro MARUTA (Grad. Sch. Sci., Hokkaido Univ.)
Satoru MATSUISHI (Front. Collab. Res. Cen., Tokyo Inst. Technol.)
Yasuhiro MIYAKE (KEK)
Soichiro MIZUSAKI (Coll. Sci. Eng., Aoyama Gakuin Univ.)
Kazuhiko MUKAI (Toyota Central R&D Labs.)
Khin Swe MYINT (Mandalay Univ., Myanmar)
Satoshi N. NAKAMURA (Grad. Sch. Sci., Tohoku Univ.)
Takashi NAKAMURA (Grad. Sch. Sci. Eng., Tokyo Inst. Technol.)
Takayoshi NAKAMURA (Res. Inst. Electron. Sci., Hokkaido Univ.)
Takehito NAKANO (Grad. Sch. Sci., Osaka Univ.)
Nobuhiko NISHIDA (Fac. Sci., Tokyo Inst. Technol.)
Kusuo NISHIYAMA (KEK)
Hiroshi NOZAKI (Toyota Central R&D Labs.)
Yasuo NOZUE (Grad. Sch. Sci., Osaka Univ.)
Vassili V. PEREVOZCHIKOV (Russ. Fed. Nucl. Cen., Russia)
Leonid I. PONOMAREV (Kurchatov Inst., Russia)
Francis L. PRATT (RAL, UK)
Shinichi SAKAMOTO (Tokai Res. Estab. Dev. Cen., JAEA)
Ryoichi SEKI (Cal. State Univ., Northridge, USA)
Koichiro SHIMOMURA (KEK)
Patrick STRASSER (KEK)

Hiroyuki SUGAI (Tokai Res. Estab. Dev. Cen., JAEA)
Jun SUGIYAMA (Toyota Central R&D Labs.)
Haruhiko SUZUKI (Grad. Sch. Nat. Sci. Technol., Kanazawa Univ.)
Kazuyuki TAKAI (Grad. Sch. Sci. Eng., Tokyo Inst. Technol.)
Keiji TAKEDA (Res. Inst. Electron. Sci., Hokkaido Univ.)
Hiroyuki TANAKA (Univ. Cal., Riverside, USA)
Akihiko TANIGUCHI (KURRI, Kyoto Univ.)
Takashi TANIGUCHI (Coll. Sci. Eng., Aoyama Gakuin Univ.)
Eiko TORIKAI (Grad. Sch. Med. Eng. Sci., Univ. Yamanashi)
Akihisa TOYODA (KEK)
Kazuo UEDA (Inst. Solid State Phys., Univ. Tokyo)
Kazuyoshi YAMADA (IMR, Tohoku Univ.)
Arkady A. YUKHIMCHUK (Russ. Fed. Nucl. Cen., Russia)
Johann ZMESKAL (Stefan Meyer Inst., Austria)

Trainees

Hiroshi ABURANO (Grad. Sch. Nat. Sci. Technol., Kanazawa Univ.)
Soichiro ARIMURA (Grad. Sch. Sci., Osaka Univ.)
Truong Cong DUAN (Grad. Sch. Sci., Osaka Univ.)
Ken GOTO (Grad. Sch. Sci., Osaka Univ.)
Kenichi HACHITANI (Grad. Sch. Sci., Chiba Univ.)
Toshio HANAKI (Grad. Sch. Fac. Sci. Technol., Tokyo Univ. Sci.)
Aya HINO (Grad. Sch. Sci., Tohoku Univ.)
Hiroshi IMAO (Grad. Sch. Sci., Univ. Tokyo)
Junho JEONG (State Univ. New York, USA)
Mijung KIM (Seoul Natl. Univ., Korea)
Yoshihiro KUBOTA (Grad. Sch. Sci., Tohoku Univ.)
Sougo KUROIWA (Grad. Sch. Sci. Eng., Aoyama Gakuin Univ.)
Jun MATSUMOTO (Fac. Sch. Sci., Osaka Univ.)
Haruo MIYADERA (Grad. Sch. Sci., Univ. Tokyo)
RISDIANA (Grad. Sch. Eng., Tohoku Univ.)
Masaharu SATO (Grad. Sch. Sci. Eng., Tokyo Inst. Technol.)
Ralph SCHEICHER (State Univ. New York, USA)
Toshiaki TAKAGI (Grad. Sch. Sci., Tohoku Univ.)
Katsunori TAKAHARA (Grad. Sch. Sci. Eng., Tokyo Inst. Technol.)
Hideyuki TATSUNO (Grad. Sch. Sci., Univ. Tokyo)
Yoshitake TODA (Inter. Grad. Sch. Sci. Eng., Tokyo Inst. Technol.)
Yoko TOMITA (Grad. Sch. Sci. Eng., Aoyama Gakuin Univ.)
Maki YAMAZAWA (Grad. Sch. Sci. Eng., Aoyama Gakuin Univ.)
Heejoong YIM (Seoul Natl. Univ., Korea)

Magnetic Materials Laboratory

Head

Hidenori TAKAGI

Members

Hiroko KATORI
Tetsuo HANAGURI
Jobu MATSUNO
Seiji NIITAKA[*1]
Ayako YAMAMOTO[*2]
Hiroki YAMAZAKI
Koshi TAKENAKA
Katsuya IWAYA[*1]
Noriko TSUBOI[*1]
Petra JONSSON[*2]

[*1] Special Postdoctoral Researcher
[*2] Contract Researcher

Visiting Members

Masaaki MATSUDA (JAEA)
Hirokazu TSUNETSUGU (Yukawa Inst. Theor. Phys., Kyoto Univ.)
Kunimitsu UCHINOKURA

Trainees
Hideo NISHIKUBO (Dept. Superconduct., Univ. Tokyo)
Seiichi SATO (Adv. Mater. Sci., Univ. Tokyo)
Tomohiro TAKAYAMA (Adv. Mater. Sci., Univ. Tokyo)

Cellular Physiology Laboratory

Head
Fumio HANAOKA

Members
Fumio YATAGAI

Visiting Members
Koichi ANDO (Natl. Inst. Radiol. Sci.)
Yoshiya FURUSAWA (Natl. Inst. Radiol. Sci.)
Yoshimasa HAMA (Sci. Eng. Inst., Waseda Univ.)
Hisao ITOH (Fac. Med., Chiba Univ.)
Tatsuaki KANAI (Natl. Inst. Radiol. Sci.)
Kiyomi KASAI (Natl. Inst. Radiol. Sci.)
Yasuhiko KOBAYASHI (JAEA)
Masami WATANABE (Radiat. Life Sci. Res. Reactor Inst., Kyoto Univ.)
Shoji YAMASHITA (Natl. Saitama Hosp.)

ADVANCED DEVELOPMENT AND SUPPORTING CENTER

Beam Application Team

Head
Takashi MEGURO

Members
Tomohiro KOBAYASHI
Aiko NAKAO
Kowashi WATANABE

RESEARCH UNIT

Image Information Research Unit (∼ 2005. 11. 15)

Head
Hirohiko M. SHIMIZU

Members
Hiromi SATO
Seiichiro ARIYOSHI[*1]
Kazuaki IKEDA[*1]
Kenji MISHIMA[*1]
Masashi OHNO[*1]
Katsuya HIROTA[*2]
Takahiro MORISHIMA[*2]
Takenao SHINOHARA[*2]

[*1] Special Postdoctoral Researcher
[*2] Contract Researcher

Visiting Members
Tomohiro ADACHI (Daiichi-kiden Co.)
Haruhiko FUNAHASHI (Dept. Phys., Kyoto Univ.)
Masahiko KURAKADO (Dept. Electr. Appl. Phys., Osaka Electro-Commun. Univ.)
Hiroaki MYOREN (Fac. Eng., Saitama Univ.)
Takayuki OKU (JAEA)
Shigetomo SHIKI (Dept. Electr. Appl. Phys., Osaka Electro-Commun. Univ.)
Junichi SUZUKI (JAEA)
Tatsushi SHIMA (RCNP, Osaka Univ.)
Tohru TAINO (Fac. Eng., Saitama Univ.)

Satoru YAMADA (JAEA)

Trainees

Masato NARISAWA (Dept. Electr. Syst., Saitama Univ.)
Yosuke SERITA (Dept. Electr. Syst., Saitama Univ.)
Shota YOSHIMURA (Dept. Electr. Syst., Saitama Univ.)

RIKEN BNL Research Center

Head

Nicholas P. SAMIOS (Director)
Hideto EN'YO (RBRC Associate Director)
Tsung-Dao LEE (Director Emeritus)

Experimental

Group Leader

Hideto EN'YO

Deputy Group Leader

Gerry M. BUNCE

Members

Takashi ICHIHARA
Yasuyuki AKIBA
Yuji GOTO
Kiyoshi TANIDA
Douglas Edward FIELDS[*1]
Masashi KANETA[*2]
Osamu JINNOUCHI[*2]
Junkichi ASAI[*3]
David KAWALL[*1]
Yasushi WATANABE
Atsushi TAKETANI
Itaru NAKAGAWA
Abhay DESHPANDE[*1]
Matthias GROSS PERDEKAMP[*1]
Tsuguchika TABARU[*3]
Kensuke OKADA[*2]
Wei XIE[*4]
Nobuyuki KAMIHARA[*3]

Visiting Members

Yoshinori FUKAO (Kyoto Univ.)
Takuma HORAGUCHI (Tokyo Inst. Technol.)
Naohito SAITO (Kyoto Univ.)
Zheng LEE (BNL, USA)
Akio OGAWA (BNL, USA)
Dominik GABBERT (Univ. Illinois, USA)
Kenichi NAKANO (Tokyo Inst. Technol.)

Theory

Group Leader

Larry MCLERRAN

Deputy Group Leader

Anthony J. BALTZ

Members

Steffen A. BASS[*1]
Takashi IKEDA[*3]
Sangyong JEON[*1]
Thomas SCHAEFER[*1]
Ubirajara van KOLCK[*1]
Werner VOGELSANG[*4]
Sinya AOKI[*1]
Takeshi YAMAZAKI[*2]
Takumi DOI[*3]
Shoichi SASAKI[*4]
Christopher DAWSON[*4]
Thomas BLUM[*4]
Stefan KRETZER[*2]
Takanori SUGIHARA[*3]
Peter PETRECZKY[*4]
Taku IZUBUCHI[*1]
Kei IIDA[*4]
Yoshitaka HATTA[*3]
Feng YUAN[*1]
Kenji FUKUSHIMA[*3]

Ägnes MÖCSY[*2] Denes MOLNAR[*1]
Kirill TUCHIN[*1]

Visiting Members

Miklos GYULASSY (Columbia Univ., USA)
Robert L. JAFFE (Massachusetts Inst. Technol., USA)
Robert MAWHINNEY (Columbia Univ., USA)
Edward SHURYAK (State Univ. New York, Stony Brook, USA)
Shigemi OHTA (KEK)
Hiroshi YOKOYA (Hiroshima Univ.)
Konstantinos ORGINOS (Massachusetts Inst. Technol., USA)
Koichi HASHIMOTO (Kanazawa Univ.)
Tetsufumi HIRANO (Columbia Univ., USA)
Ralf-Christian SEIDL (Univ. Illinois, USA)

[*1] RHIC Physics Fellow, [*2] Research Associate,
[*3] Special Postdoctoral Researcher, [*4] RIKEN BNL Fellow

AUTHOR INDEX